Modelling strategy for the Large-Eddy Simulation of lean hydrogen-air explosions

Jean-Jacques Hok

▶ **To cite this version:**

Jean-Jacques Hok. Modelling strategy for the Large-Eddy Simulation of lean hydrogen-air explosions. Electric power. Université de Toulouse, 2024. English. NNT : 2024TLSEP065 . tel-04654409

HAL Id: tel-04654409

https://theses.hal.science/tel-04654409v1

Submitted on 19 Jul 2024

HAL is a multi-disciplinary open access archive for the deposit and dissemination of scientific research documents, whether they are published or not. The documents may come from teaching and research institutions in France or abroad, or from public or private research centers.

L'archive ouverte pluridisciplinaire **HAL**, est destinée au dépôt et à la diffusion de documents scientifiques de niveau recherche, publiés ou non, émanant des établissements d'enseignement et de recherche français ou étrangers, des laboratoires publics ou privés.

RÉPUBLIQUE FRANÇAISE
Liberté Égalité Fraternité

Université de Toulouse

Doctorat de l'Université de Toulouse

préparé à Toulouse INP

Stratégie de modélisation pour la Simulation aux Grandes Echelles d'explosions de mélanges hydrogène-air pauvres

---

Thèse présentée et soutenue, le 19 juin 2024 par

Jean-Jacques HOK

École doctorale
MEGEP - Mécanique, Energétique, Génie civil, Procédés

Spécialité
Energétique et transferts

Unité de recherche
CERFACS

Thèse dirigée par
Olivier VERMOREL

Composition du jury
Mme Nabiha CHAUMEIX, Présidente, CNRS Centre Limousin Poitou Charente
M. Ronan VICQUELIN, Rapporteur, Université Paris-Saclay
M. Ashwin CHINNAYYA, Rapporteur, ISAE ENSMA
M. Olivier COLIN, Examinateur, IFP Energies nouvelles
M. Olivier VERMOREL, Directeur de thèse, CERFACS

Membres invités

M. Omar Dounia, CERFACS

Résumé — La crise climatique à laquelle le monde est confronté aujourd'hui exige des actions immédiates pour réduire les émissions de carbone. En particulier, une transition énergétique rapide vers des sources plus propres est nécessaire. Parmi de nombreux candidats, l'hydrogène se distingue en tant que vecteur d'énergie décarboné. Cependant, son stockage et son transport en grandes quantités posent des problèmes de sécurité. Après une fuite, mélangé à l'air ambiant, cet hydrogène peut former un mélange hautement inflammable. En cas d'allumage accidentel de ce prémélange, différents scénarios et régimes de combustion sont possibles, en fonction de facteurs tels que la géométrie (dimensions, présence d'obstacles), la composition du mélange, la température, la pression ou le niveau de turbulence. Ces régimes vont de la déflagration lente à la transition vers la détonation dans le pire des cas. Pour prédire les dommages d'une explosion, la Mécanique des Fluides Numérique présente l'avantage d'être plus sûre que les expériences et donne accès à des quantités difficiles ou impossibles à mesurer empiriquement. Cette thèse traite de la prédiction des explosions d'hydrogène-air pauvre en utilisant la Simulation aux Grandes Échelles (SGE ou LES en anglais). Les mélanges pauvres d'H_2-air sont connus pour leur nombre de Lewis subunitaire distinctif, qui caractérise un déséquilibre entre les processus de diffusion moléculaire et thermique avec des conséquences majeures : (1) les flammes H_2-air pauvres sont très sensibles à l'étirement ; (2) elles sont enclines à développer des cellules sur le front de flamme dues à l'instabilité thermo-diffusive. Les deux constituent des mécanismes d'accélération qui impactent la surpression générée lors de l'explosion. Dans ce travail, nous montrons que l'utilisation du modèle de Flamme Épaissie (TF en anglais) pour simuler les flammes à nombre de Lewis subunitaire : (1) induit une amplification de l'effet d'étirement sur la flamme ; (2) combinée à la faible résolution de maillage en LES, filtre les instabilités de front de flamme. Le couplage de ces mécanismes indésirables peut générer une propagation erronée de la flamme qui remet en question la capacité de prédiction de la LES pour les explosions de mélanges H_2-air pauvres. Des efforts nécessaires ont été effectués au cours de cette thèse pour proposer une stratégie de modélisation capable de prédire de manière fiable et précise les explosions d'hydrogène-air pauvre. Un nouveau paradigme est envisagé pour corriger séparément l'amplification des effets d'étirement et modéliser les phénomènes de sous-maille dus à l'instabilité thermo-diffusive. Développées sur des configurations canoniques, ces deux corrections sont ensuite étendues et validées sur des configurations d'explosion plus réalistes.

Mots clés : Combustion ; Hydrogène ; Explosions ; Effects d'étirement ; Instabilités de front de flamme.

Abstract — The climate crisis the world faces today calls for immediate actions to curb down carbon emissions. In particular, a rapid energy transition towards cleaner sources is necessary. Among many candidates, hydrogen stands out as a carbon-free energy vector. However, its storage and transport in big quantities raise safety concerns. Following a leakage, mixed with the surrounding air, this hydrogen can form a highly flammable mixture. In case of accidental ignition of this premix, different combustion scenarios and regimes are possible, depending on factors such as geometry (dimensions, presence of obstacles), mixture composition, temperature, pressure or turbulence level. These regimes range from slow deflagration to the transition to detonation in the worst case. To predict the damage of an explosion, Computational Fluid Dynamics has the advantage of being safer than experiments and gives access to quantities hard or impossible to measure empirically. This thesis deals with the prediction of lean hydrogen-air explosions using Large-Eddy Simulation (LES). Lean H_2-air mixtures are known for their distinctive sub-unity Lewis number, which characterises an unbalance between molecular and heat diffusion processes with major consequences: (1) lean H_2-air flames are strongly sensitive to stretch; (2) they are prone to develop flame front cells due to the thermo-diffusive instability. Both constitute accelerating mechanisms which impact the overpressure generated during the explosion. In this work, we show that the Thickened Flame (TF) approach to simulate sub-unity Lewis flames: (1) induces an amplification of stretch on the flame; (2) combined with the low grid resolution in LES, filters out flame front instabilities. The coupling of these undesired mechanisms can generate an erroneous flame propagation which questions the predictability of LES for lean H_2-air explosions. Much-needed efforts were put during this thesis to propose a modelling strategy capable of reliably and accurately predict lean hydrogen-air explosions. A new paradigm is considered to separately correct the amplification of stretch effects and model subgrid phenomena due to the thermo-diffusive instability. Developed on canonical configurations, these two corrections are then extended and validated on more realistic explosion configurations.

Keywords: Combustion; Hydrogen; Explosions; Stretch effects; Flame front instabilities.

A Paule et Marco, à mon père.

Remerciements

De nombreuses personnes ont largement contribué à la réussite de cette thèse et à l'existence de ce manuscrit. Au travers de ces quelques lignes je tiens à les remercier.

Je commencerai par adresser mes salutations aux partenaires du projet LEFEX qui ont supporté financièrement et techniquement cette thèse. Depuis les premières réunions lorsque je n'étais qu'un jeune stagiaire découvrant la combustion jusqu'aux toutes dernières présentations avant la soutenance, les réunions LEFEX ont été le lieu d'échanges intéressants, enrichissants pour ma formation professionnelle et personnelle. Antoine, Vincent et Bernard, vous avez toujours apporté un avis encourageant à nos travaux tout en nous laissant une liberté suffisante dans le choix des sujets abordés et des directions à suivre. Pour ça je vous remercie.

Je souhaite exprimer toute ma gratitude envers les membres du jury pour avoir accepté d'étudier et évaluer mes travaux de thèse. Merci aux rapporteurs, Ronan et Ashwin, d'avoir pris le temps de lire mon manuscrit dans le détail (ça s'est senti !) et d'avoir écrit votre rapport dans le court délai qui était imposé par le calendrier. Vos remarques très positives m'ont aidé à prendre confiance pour la soutenance et les propositions d'amélioration ont été bienvenues pour finaliser le manuscrit. Merci encore une fois aux deux rapporteurs mais également à Nabiha et Olivier pour les questions et discussions qui ont suivi lors de la soutenance. La bienveillance dont vous avez tous fait preuve a indéniablement contribué à ce que je me sente à l'aise et prenne plaisir à présenter et échanger avec vous.

J'aimerais maintenant remercier mes encadrants de thèse. J'ai eu la chance (et la pression !) d'avoir quatre seniors m'accompagnant tout au long de mon parcours au CERFACS, ça n'est pas donné à tous les thésards ! Tous avec des avis et approches complémentaires, vous avez tour à tour été d'une grande aide pour trouver des solutions et me guider quand j'en avais besoin.
Tout d'abord, Olivier et Thomas m'avez accueilli il y a quatre ans (déjà !) en stage pendant la période pas évidente du premier confinement. J'avoue qu'apprendre la combustion et apprendre AVBP, à partir de quasi-zéro, tout ça à distance, sans réelle discussion avec d'autres thésards plus expérimentés, a été un défi. Mais heureusement qu'on avait nos réunions Teams où vous pouviez m'expliquer ce qu'il manquait. Je dois dire

que ça été drôle quand, au bout de 3 mois de distanciel, à entendre vos voix, j'ai enfin découvert vos têtes ! Merci à vous deux de m'avoir fait confiance et de m'avoir accordé la possibilité de poursuivre en thèse dès les premiers mois, avant même qu'on se rencontre en personne.
Après cette première expérience au CERFACS (et un deuxième confinement plutôt sympathique), ça a été au tour de Quentin et Omar de rejoindre l'équipe. L'équipe au complet prête à résoudre tous les problèmes de la combustion ! Ou pas, parce que les instabilités de front de flamme, bah c'est quand même compliqué ! Mais merci de m'avoir suivi sur ce sujet qui était vraiment nouveau au CERFACS, ça en valait la peine.
Je repense à l'ICDERS à Naples, ma première "vraie" conférence en combustion. Merci à vous Olivier, Thomas, Quentin de m'avoir accompagné là-bas (c'est tombé au mauvais moment pour toi Omar mais comme tu l'as vu on a bien profité pour toi !). Je me sentais (à juste titre ?) comme un gosse accompagné de ses professeurs. Certes ça me mettait encore plus la pression pour réussir ma présentation mais ça m'a peut-être aussi un peu rassuré face à la grande communauté de chercheurs en explosions. Et puis il faut dire que c'était plutôt cool comme évènement, les italiens font de la bonne cuisine ! Sans parler de la soirée "gala" à Capodimonte, l'excursion autour de Naples, à visiter des sites archéologiques sous 38 degrés, ou encore la visite "guidée" de Naples que je vous ai faite vu que j'y étais allé un an plus tôt (coucou Clo', Benou et Laquille !). Bref, tout ça pour dire que faire des conférences avec des seniors, ça peut être sympa !
Pour finir, j'aimerais remercier tout particulièrement Omar et Olivier qui ont eu la lourde tâche de me supporter pendant la phase de rédaction et jusqu'à la soutenance. Lire et relire 300 pages de manuscrit, c'est pas marrant, écouter et réécouter 45 minutes (ou plus) de présentation, c'est pas marrant non plus, mais vous avez été au rendez-vous ! Au bout de quatre ans vous avez fini par apprendre ma personnalité, mon stress permanent (pas toujours apparent...), mon manque de confiance en moi qui me faisait vous demander régulièrement votre avis sur mon travail. Merci à toi Olivier, finalement le seul à avoir pu tout suivre de A à Z, tes avis sont toujours constructifs et m'ont permis d'avoir des présentations bien structurées, dont j'étais fier à la fin, et "une histoire qui se raconte bien" pour reprendre tes mots. Tu as certainement un don pour faire comprendre l'incompréhensible en amenant les choses dans le bon ordre. Avis aux futurs thésards : il y aura TOUJOURS quelque chose à reprendre dans vos présentations, mais ça vaut le coup d'écouter Olivier ! Merci maintenant à toi Omar, l'encadrant que j'ai certainement le plus cotoyé. Ton arrivée dans l'équipe a réellement boosté ma recherche et a d'ailleurs contribué à ce qu'on parte à Naples ! Après ta courte pause d'un an (allez, t'es pardonné), ton retour pour ma dernière année a encore une fois eu son effet : un modèle S-TF avec Nicola (après quelques semaines de dur labeur, à réécrire notre modèle n fois quelque part entre 8 heures et 20 heures). J'ai l'impression que mes travaux n'ont vraiment avancé qu'à partir de ce tremplin. Machine inarrêtable à propositions, à chaque fois que j'arrivais le matin, je savais que t'aurais une nouvelle idée en tête. J'avoue que des fois, il faut s'accrocher pour suivre ton rythme, mais ça paye ! Merci aussi pour nos échanges hors boulot, ça fait du bien de pouvoir discuter d'autre chose avec un senior, merci d'avoir fait "taxi" les fois où on finissait tard le soir.

Je souhaite maintenant remercier tout le personnel sans qui il serait impossible de faire une thèse au CERFACS. Merci Marie, une des premières personnes que j'ai rencontrées au CERFACS, pour m'avoir accueilli, pour nos discussions dans le bus le matin, j'espère que tu profites bien de ta retraite. Merci à Michèle d'avoir été aux petits soins avec tous les thésards, c'est rassurant d'avoir une RH qui se soucie de nous (et oui oui, je poserai mes congés avant la deadline promis !). Merci à Lydia pour nos échanges en pause café et merci pour les nombreuses commandes CSE que j'ai passées ! Merci à Chantal, que je n'ai finalement appris à bien connaître que la dernière année grâce à Antoine, une Tarnaise ! Enfin ! Toujours souriante, de bonne humeur, tu égayes la vie au labo'. Merci à Brigitte pour ton aide indispensable dans toutes ces démarches administratives, conférences, déplacement à Orléans et soutenance de thèse. Merci à la dernière arrivée chez Admin, Philippine, bon courage pour la reprise des activités de Michèle. Merci aussi à toute l'équipe informatique, Gérard, Isa, Fabrice, le CERFACS ne marcherait pas sans vous. Merci particulièrement à Fabrice, qui a passé au total pas mal d'heures au téléphone avec moi pendant ce premier confinement pour débugguer les *blue screens of death* de mon ordi'. Ca n'aura pas suffi et même si j'y étais bien rétissant au départ, passer sur Mac pendant le stage m'a bien sauvé la vie.

Je veux dire maintenant un grand merci à tous les collègues du CERFACS, la grande famille de doctorants, post-docs, stagiaires, ex-stagiaires, etc. qui pour beaucoup sont devenus de vrais amis en dehors du travail. Faire une thèse sans encadrants n'est pas possible, mais faire une thèse sans bons collègues du quotidien est impensable. L'ambiance qui règne au Cerfacs entre tous les non-permanents en fait un lieu plein de vie, qui fait qu'on prend plaisir à venir travailler, alors même qu'on a un manuscrit à terminer. Il y a eu tellement d'expériences, d'évènements, de bons moments au cours des quatre dernières années qu'il m'est impossible de tous les citer.
Je pense forcément aux autres stagiaires qui comme moi ont débuté au CERFACS en distanciel : Clément, Jessica, Jean, Yann, Clément M., Baptiste, Ronan, Barthélémy et le tout dernier arrivé (peut-être un peu grâce à moi) Mehdi. On a un peu été lâchés dans l'arène en arrivant après le confinement, avec des groupes de doctorants déjà formés, mais on a réussi à créer un cercle solide assez rapidement, à se serrer les coudes et à instaurer les afterworks du CERFACS qui perdurent encore aujourd'hui. Clément, premier compagnon de stage, on nous avait mis en contact pour qu'on s'entraide à nos débuts, maintenant tu fais réellement partie de mes amis les plus proches, je suis heureux que nos chemins se soient croisés au CERFACS et qu'on soit restés amis ! Jessica, ma première co-bureau avec qui on a passé des heures à discuter et rire de tout et n'importe quoi, j'avoue que je me demande parfois comment on a réussi à terminer nos rapports de stage ! Il est loin le temps des longues pauses du midi à faire les mots-croisés, tu as maintenant quitté le navire pour un nouveau travail mais on reste toujours en contact (on est encore voisins !). Ah et je ne peux pas parler de Jessica sans parler de Mehdi. Qui aurait cru qu'après cette dernière année à Centrale on se retrouve dans le même labo', et tous les deux en thèse ensemble ? C'était sans compter sur le Covid. Ce n'était sûrement pas la voie que tu avais imaginé après la fin d'école, mais je suis quand même content que tu sois venu au CERFACS et qu'on ait même appris à mieux se connaître pour devenir de vrais

amis. Merci aussi à Jean, le gars du Gers un peu intimidant en apparence (la carrure de militaire n'aide pas !) mais très attachant dès qu'on lui parle, toujours souriant, et toujours là pour remonter le moral, merci et bon courage pour la dernière ligne droite !
Je veux maintenant citer les gars du projet LEFEX : Victor et Soumyo qui étaient déjà là lorsque j'ai débuté, merci de m'avoir aidé à prendre mes marques, Benjamin arrivé presque en même temps que moi, Francís qui est arrivé l'année d'après et qui s'est très rapidement intégré à l'aventure, et enfin les jeunes "affiliés" LEFEX Loïc et Eric. Tout ça fait une team sacrément explosive (oui désolé j'étais obligé de la faire). C'était franchement cool de travailler avec vous, pouvoir avoir des conseils grâce à nos sujets similaires, mais c'était surtout sympa humainement : repas chez les uns, squash et escape games par la suite, hâte de remettre ça !
Après la team LEFEX, parlons du groupe rando' : Thomas, Mouze, Alex, Lukas, Eric (encore), PA, Guigui, Raphaël, Benou, Francís (encore), Marcos, Jorrit, Laura, Pedro et les non-cerfacsiens qu'on a embarqués (coucou Charline, Laquille, Clo', Valéria, Maike, Elia, Johana, Fabien). Je suis content (et pas peu fier) d'avoir participé à créer ce groupe, pour pouvoir souffler de la thèse et prendre un bon bol d'air frais (littéralement) dans les Pyrénées. Certaines sorties ont été plus difficiles que d'autres (cf. la rando' gadou, j'vous avais dit qu'on aurait mieux fait d'aller dans le Tarn ! n'est-ce pas Antoine...), certaines nuits difficiles (je parle bien sûr de la douce mélodie de Marcos ronflant la bouche grande ouverte et écrasant PA), mais dans l'ensemble on a chaque fois passé de très bons moments de rigolade, et ça n'est pas fini car je compte encore continuer à organiser tout ça. Rendez-vous bientôt pour les randonnées-refuge-spa-canoe-fondue-toute-autre-chose-sympa ! PS : le gros-duc à pattes bleues et bec rouge n'existe toujours pas, même avec les supers jumelles que vous m'avez offertes.
Merci de manière générale à tous ceux qui m'ont aidé de près ou de loin à garder le moral en faisant vivre le labo' : Benou, Francís, Eric, Loïc, Mehdi, Jessica, Raphaël, Jean, Alex, Toto, Mouze, Guigui, PA, Lukas, Arthur, Patrick, Nicola, Felix, Nathanaël, Rémi, Héctor, Yann, Clément, Alex D., Laura, Pedro, Susanne, Marcos, Jorrit, Alexis, Victor, Eloïse, Yecine, Carlos, Antony, Mickaël, Christophe, Solène, Thomas L., Nicolas, Jérome, Benoît et les petits nouveaux Mateus, Raquel (merci tous les deux pour les cours express de portugais !) et Noémie, j'espère que je n'ai oublié personne !
Merci au fameux Docteur Mouze, homme au grand coeur, oreille attentive, gardien de Baguera à ses heures perdues, passionné fou de spatial (ne le lancez pas sur les fusées à moins d'avoir une soirée entière devant vous). Tes conseils pour la fin de thèse m'ont vraiment aidé à tenir jusqu'au bout. Ta bonne humeur sans limite et ton rire qu'on entend à trois kilomètres (oui oui) font toujours chaud au coeur.
Merci à Guigui, amateur de drum and bass, fou de F1, grimpeur, coureur et randonneur du dimanche, doctorant éternel du CERFACS. C'est fou de se dire qu'on n'a commencé à se parler qu'à la fin de ma thèse, avec ce séjour à Orléans pour supporter then-soon-to-be-docteur Mouze. Les fins de journée en pause café sans fin et les apéros improvisés à discuter de tout ont vraiment été une bulle d'air pendant ma fin de rédaction. Maintenant que j'ai terminé c'est à ton tour aussi. Je sais que parfois il t'est difficile de trouver la motivation, mais je pense sincèrement que tu peux finir ta thèse, il faut tenir bon !
Merci à Alex, bricoleur confirmé, mi-auvergnat, mi-ardéchois, féru de crevettes et de

chenilles (allez trouver le lien), amateur du vélo de retour de soirée. Cet homme a construit une éolienne pendant sa thèse, et ça, 'faut le faire ! J'espère que tes projets de méthanol en Ardèche pourront bientôt se concrétiser, je te dis *Pouik pouik* !
Merci à Toto, randonneur aguerri, professionnel de la montagne, the Rock en plus petit, plus norvégien, avec plus de cheveux et blond. Plus sérieusement, ta capacité à tenir et rebondir malgré les difficultés que tu as rencontrées pendant ta thèse m'ont toujours impressionné et je me suis dit : si lui y arrive avec tous ces obstacles, je dois pouvoir y arriver aussi. Je suis aussi très content d'avoir initié le groupe rando' avec toi (on reprendra un meilleur rythme quand tu auras rendu ton manuscrit !).
Merci à Francís, imitateur professionnel, puits sans fond de savoir et de références douteuses sur toutes sortes d'animaux, inventeur du Bingo-Poutine-Poulet (BPP) d'afterwork. Merci pour toute ton aide et pour les bons moments partagés. Franchement je dois dire que des fois je suis assez jaloux de ta capacité à comprendre tous les problèmes scientifiques, tes remarques sont toujours précieuses. PS : je trouverai une bière que tu apprécieras, un jour...
Merci à Loïc, jeune insaïen, crossfitteur retraité, autre membre du bureau de la productivité avec Francís. Ton sourire permanent le matin permet de débuter la journée dans la bonne humeur !
Merci à Eric, andorran marathonien et grimpeur, trouvant toujours le moyen de se blesser. Merci pour tes petits messages quotidiens lors de ma rédaction (Clo' commence à être jalouse, attention !), ça m'a toujours fait marrer et motivé pour finir le manuscrit !
Merci à Mehdi, cinéphile, passionné d'aéronautique et d'aviation (au même titre que pour Mouze, vous pouvez lui demander n'importe quoi sur les modèles d'avion, il saura vous répondre). Merci d'avoir fait cette aventure avec moi, merci de m'avoir accueilli à Saint-Chamont et heureux de t'avoir accueilli à Castres et Toulouse.
Merci à Jessica, aka Docteure G, fan incontestable de Taytay. Comme dit plus haut, quatre ans qu'on se connaît et je suis très heureux de te compter parmi mes amies depuis le début. On reste en contact !
Merci à mes Allemands préférés : Lukas et Patrick. Lukas, je me souviens encore de ton arrivée au CERFACS, de notre premier afterwork au Botanist. Ahh tu t'es très vite habitué aux afterworks au point de prendre la relève pour l'organisation, merci ! Dommage que mon niveau d'allemand ait tant régressé ces dernières années, mais promis je m'y remets bientôt pour aller au carnaval de Köln avec Maike et toi. Patrick, je n'ai finalement appris à te connaître que vers la moitié de thèse, mais je n'ai pas été déçu ! Toi aussi tu arrives bientôt à la soutenance, courage ! On reste en contact quand tu seras au Japon.
Merci à Marcos, mon bièrophile fan de parfums. On s'est toujours régalés en venant chez toi, merci de nous avoir fait découvrir le "lait magique" et merci pour la magnifique tasse que tu m'as offerte ! Merci à Raphaël, plongeur pêcheur apnéiste, cinéphile impressionnant, amateur de *fine cuisine* et supporter du Téfécé. Tu te souviens l'excursion avec le groupe rando' ? J'avoue que quand tu nous disais que tu ne randonnais pas beaucoup, on ne s'attendait pas à te voir 500 mètres devant nous en permanence, un vrai bouquetin !
Merci à Arthur, autre passionné du vélo de retour de soirée, pro' de la volatilisation inquiétante (tu te souviens de l'anniversaire de Lukas au Biergarten ?), fin connoisseur de

Pic Saint Loup et enfin, victime collatérale du modèle S-TF (tu vas t'en sortir).
Merci à PA, grenoblois parti s'exiler à Poitiers, puis Toulouse, puis Pau (sérieux, pourquoi ?). Je suis fier de t'avoir initié à l'ornitho', j'espère que ça restera, et hâte que tu reviennes dans notre belle ville !
Je finirai cette vague de remerciements des gens du CERFACS par un type, déjà cité plus haut car faisant partie de quasiment tous les groupes mentionnés : mon frère de thèse Benjamin (aka Benou pour les intimes) bien sûr ! Franchement je ne sais pas ce qu'auraient été ces trois ans et demi sans toi dans le bureau, bien plus tristes c'est sûr. Merci d'avoir égayé la vie au quotidien, à coup de références YouTube impensables, de citations The Office (oui oui chef je terminerai bientôt la série maintenant que j'ai plus de temps), de blagues pourries en tout genre, etc.. On a tous les deux été dans les mêmes galères, et avoir ton soutien a été indispensable. Et je ne peux pas te remercier sans remercier Laquille ! J'avoue que je suis pas peu fier d'avoir trouvé ce surnom qui t'est resté. Véritables amis de tous les jours, avec Clo' on ne passe pas plus de deux semaines sans vous voir, et ça fait plaisir ! Repas chez vous ou chez nous, restos, soirées, anniversaires, sorties, voyages à Naples chez Lorrenzo (il nous a marqués celui-là), aux Canaries, chez les corses et bientôt le Portugal, on ne manque pas une occasion de s'amuser. Je peux également dire que vous étiez là les trois fois où je suis allé aux urgences (drôle de coïncidence quand même...) dans la même année et que par conséquent vous m'avez peut-être sauvé la vie trois fois (pas mal).

Passons maintenant aux amis ne connaissant pas le joyeux zoo du CERFACS. Merci tout d'abord à mes amis du lycée. Compagnons de longue date, compagnons pour la vie, vous avez pu suivre tout mon parcours, m'encourager et me rassurer jusqu'à cette soutenance : Elia, Léa, Clémence et Nico, Allison et Maxime, Alice, Apolline, Manu, Emilie et Akshay. Malgré la distance pour certains, vous êtes encore là après plus de dix ans.
Merci à Elia, ma meilleure partenaire de rando', de sortie, de soirée, de tout en fait. Je suis très heureux de pouvoir toujours compter sur toi, et bien sûr c'est réciproque !
Merci à Léa, globe-trotteuse, pâtissière, agricultrice, community manager, hyperactive dans l'âme. Ta capacité à travailler sans pause, à cumuler les jobs sur différents fronts m'a toujours impressionné. Et encore félicitations pour ton CAP !
Merci à Clémence et Nico, les futurs docteurs (deux vrais médecins !). PACES pour toi Clémence, prépa' pour moi, planning assez chargé, ça ne nous a pas laissé beaucoup de temps pour se voir et tes vieilles blagues m'ont bien manqué, mais je suis toujours content quand on se retrouve ! Et bonne chance pour la dernière année !
Merci à Allison et Maxime, le couple de choc ! Mon p'tit panda, pas du CERFACS mais dans la même galère de thèse, tes avis m'auront rassuré jusqu'à la veille-même de la soutenance. Maintenant que vous êtes de retour sur Toulouse, plus d'excuses, ça sera plus facile de se voir !
Merci à Alice la savoyarde adoptée, malgré la distance on arrive toujours à se capter chaque année. Après toutes ces années je suis content que tu aies enfin trouvé ta voie à Chambéry. Et bonne chance pour le concours !
Merci à Apolline, alors toi t'es vraiment loin et ça fait un bout de temps qu'on s'est pas

croisés. Mais il me tarde de te retrouver à Bruxelles en octobre !
Merci à Manu, mon éleveur de tomates et cacahuètes sur balcon. Tu es toujours là pour les moments importants et ça fait toujours plaisir de passer une soirée avec toi !
Merci à Inès, on n'était pas au lycée ensemble mais on se connaît depuis presque autant de temps grâce à Clo'. Ton trip en Amérique du Sud m'a vraiment fait rêver et j'espère pouvoir faire quelque chose de similaire un jour. On se revoit bientôt à ton retour !
Merci à Emilie et Akshay, autant famille que amis, vous aussi vous êtes partis loin mais je ne désespère pas qu'on fasse un apéro' à Castres, Toulouse, Londres ou même Haridwar qui sait ? Votre mariage en Inde était juste fantastique et m'a vraiment marqué. Ca a été l'occasion de se retrouver à l'autre bout du monde avec toute la famille et les amis. Si on a pu se voir aussi loin, j'imagine qu'on peut se voir en France !
Merci maintenant aux amis rencontrés en prépa'. Du groupe soudé qui s'était formé, MS et Zedette, on s'est perdus de vue et j'en suis désolé. La divergence de nos parcours et la distance entre nos villes n'a sûrement pas aidé mais je pense qu'il n'est jamais trop tard pour reprendre contact. Guillaume et Robin, vous deux aussi avez connu l'épreuve de la thèse, d'ailleurs bon courage Robin pour la soutenance, t'as fait le plus dur ! Carla et CSDO les inséparables, je suis heureux qu'on ait réussi à se voir chaque année depuis tant d'années. Avec Clo' on a beaucoup aimé passer du temps avec vous lorsqu'on s'est retrouvés à Budapest, il faut qu'on remette ça ! Dans tous les cas j'espère pouvoir être là à Paris en octobre pour tous vous revoir !
Merci à Clément (encore une fois), Margaux et Mimine. Depuis les premiers afterworks d'été 2020, le groupe s'est agrandi et on ne s'est plus lâchés avec Benou et Laquille. Je suis vraiment heureux de vous avoir rencontrés et de vous compter parmi mes amis aujourd'hui. Que ce soit à Toulouse, à Frontignan, dans les Pyrénées, en guinguette ou à la plage, ça fait toujours du bien de se retrouver !
Merci à Paul et Lisa, les copains du Muséum. Je ne suis pas retourné aux jardins depuis que Clo' a changé de job mais on arrive à se faire des petits restos régulièrement. Hâte de découvrir de nouvelles cuisines du monde avec vous !
Merci à Thomas et Julie, les exilés à Paris. Comme souvent il est difficile de se voir avec la distance, mais je suis toujours content de recevoir les appels de Thomas pour avoir de vos nouvelles. Même si ce n'est que quelques fois dans l'année j'ai l'impression que c'est comme avant quand on se retrouve à Paris ou dans le sud, ça fait plaisir !
Merci à Nathanaël, mon cher binôme d'école. Encore bravo pour ta thèse, je t'ai enfin rattrapé ! J'espère que tu te plaîs bien à Bordes, on aura peut-être enfin une occasion de randonner (ou grimper ?) ensemble maintenant que tu es descendu dans le sud.

Pour finir je tiens à remercier sincèrement toute ma famille pour le soutien que vou m'apportez depuis toujours.
Lydie, merci de m'avoir accueilli chaleureusement dans la belle-famille dès notre première rencontre. Mon appétit d'ogre t'avait bien surpris à l'époque et même si je me suis un peu calmé, j'adore toujours les petits plats que tu nous prépares avec attention à Clo' et moi. Dans la vie quotidienne tu es une personne droite dans ses bottes, franche et sincère. Que ce soit pendant la prépa' ou au cours de mes années de thèse, tes mots pour me rassurer et me motiver ont toujours eu un effet immédiat, merci beaucoup.

François, l'esprit plus calme, toi aussi tu sais rendre Clotilde heureuse. Merci d'être là pour nous deux. Merci de nous avoir accueillis pendant le premier confinement, c'est finalement chez toi que mon aventure au CERFACS a commencé.
Michelle, tu es certainement la meilleure mamie dont Clotilde puisse rêver. Avec Lydie et Clotilde vous formez un trio de choc ! Toi aussi tu m'as accueilli les bras ouverts dès notre première rencontre. Je prends toujours plaisir à venir te faire un petit coucou quand on passe à Castres.
Merci à Ben et Mathieu, les papous ! Merci de nous accueillir à tout moment à Peyregoux, merci pour tous les bons souvenirs partagés. Les soirées du deuxième confinement chez vous, mêlant chartreuse, jeux de société et bonne cuisine, me manquent vraiment. Ben, mon beau-frère, d'abord merci d'être là pour Clotilde. Le nez dans le guidon je n'arrive pas toujours à la rassurer quand elle se fait du souci. Grâce à ton oreille attentive, tu trouves souvent les bons mots pour la réconforter et la faire rire. Et tu es aussi là dans les bons moments ! On est heureux chaque fois de t'accueillir chez nous pour passer une bonne soirée avec toi. De mon côté, ça m'a touché que tu t'intéresses à ce que je fais et à cette épreuve qu'est la thèse.
Mathieu, je t'ai connu lorsque vous étiez encore à Rabastens avec Ben. Ton boulot te passionnait déjà et aujourd'hui encore. Et en dehors du travail je sais que tu tiens énormément à Ben et Clo', c'est rassurant de se dire qu'ils peuvent compter sur toi.
A toute ma belle famille, merci de m'avoir accueilli, merci de m'avoir soutenu pendant tout ce temps, votre présence le jour de la soutenance m'a grandement touché.

Paule et Marco, je ne vous ai jamais appelés "papi" ou "mamie" mais vous représentez bien plus à mes yeux que ce que ces simples mots veulent dire. Vous avez été présents pour Jean-Marc, Jean-Rémy et moi depuis notre plus jeune âge, à tous les moments importants, chaque anniversaire, chaque diplôme. Je vous retrouve dans nombre de souvenirs heureux de mon enfance, que ce soit chez nous, dans votre jardin à Castres ou encore et surtout à Narbonne, quand on venait déjeuner à la plage et qu'on allait ramasser les coquillages ensemble. Je suis tellement triste que ces souvenirs s'éloignent. La vie nous a séparés et vous me manquez tous les jours. Paule, tes gros bisous sur la joue, tes câlins et ton rire me manquent. Marco, ta bonne humeur et tes blagues me manquent. J'adorais venir chez vous vous écoutez nous parler de votre enfance à Lourdes, de votre jeunesse à Paris, de comment vous avez rencontré papa, de votre croisière en Russie, de la fois où Marco s'est retrouvé en Italie en confondant Genoa et Genova et de plein d'autres choses encore. Vous nous avez quittés mais j'aime penser que vous vous êtes retrouvés, que Paule soupire encore pendant que Marco sort une blague pas drôle.

Merci à mon grand frère Jean-Marc, c'est bien toi qui nous a donné à Jean-Rémy et moi le goût des maths d'abord, puis des sciences en général. Tu as sans doute beaucoup influencé le parcours que j'ai suivi, entre les cours que tu me donnais pendant les vacances d'été quand j'avais 5-6 ans, jusqu'à me parler de Fermat pour les études supérieures. Le premier de la fratrie, tu as instauré la réputation des "frères Hok" auprès de nos enseignants à l'école, au collège et au lycée. Je suis très content pour toi que tu aies atteint ton "endgame" comme tu dis, dans ta vie professionnelle avec un job de prof' dans

lequel tu as l'air parfaitement épanoui, tout comme dans ta vie personnelle avec Eva et maintenant la petite Rune ! Merci donc aussi à toi Eva, Jean-Marc ne se définit pas sans toi. Et puis disons la vérité, il ne ferait pas grand chose sans toi !

Merci à mon petit frère Jean-Rémy. Maman a souvent un regard très protecteur sur toi parce que tu es le petit dernier. Mais je pense que tu es largement plus indépendant qu'elle ne le pense. Toi aussi tu as enfin fini tes études avec brio pour travailler dans un domaine qui te plaît. Après que papa nous ait quittés, j'ai pu compter sur toi pour m'aider et aider maman à la maison et aujourd'hui tu restes celui qui rentre le plus souvent la voir. Merci pour tout ce soutien.

Maman, comment te dire tout l'amour que j'ai pour toi. Je sais que ta vie a été difficile : supporter quatre garçons à la maison ! Plus sérieusement, je sais que tu as joué un grand rôle dans notre famille, en restant parfois dans l'ombre, tu as aidé papa à l'époque à Berlin, tu l'as suivi depuis le début de son commerce à la maison et sur les marchés, tu nous as élevés Jean-Marc, Jean-Rémy et moi en même temps. Pour tout ça merci. Aujourd'hui les rôles se sont inversés : avec papa tu as veillé sur nous pendant plus de vingt ans, à nous maintenant de veiller sur toi. Je comprends à quel point ça doit être difficile pour toi depuis la mort de papa. On est partis tous les trois vivre à Toulouse et tu es restée seule à la maison. Je sais qu'on ne te donnera jamais assez de nouvelles, qu'on ne rentrera jamais assez à la maison, qu'on ne t'appellera jamais assez souvent, mais on t'aime maman. Je suis toujours heureux de t'entendre au téléphone et de te parler en chinois car je n'en ai plus trop l'occasion et je suis aussi très content de t'accueillir à l'appartement à Toulouse !

Papa, tu ne liras jamais ces mots mais j'aime imaginer que tu es quelque part avec nous, à veiller sur nous, à regarder ce qu'on est devenus. Je ne sais pas comment commencer ce paragraphe tellement il y a de choses pour lesquelles je veux te dire merci. Tout le monde le dit et tu l'as toujours su : je te ressemble beaucoup. Bien plus que sur le physique, tu as forgé la personne que je suis devenu aujourd'hui. Tu m'as appris la générosité, le partage et le sens de la famille. Il n'y a qu'à voir tout ce que tu as fait pour notre famille. Tu nous faisais passer avant tout. Tu as travaillé toute ta vie, en abîmant ta santé pour nous préserver, pour qu'on puisse faire des études et ne pas avoir à suivre le même chemin que toi. Avant nous déjà, en aidant tes frères à Berlin et à Castelsarrasin, tu as tout le temps fait passer la famille avant toi. Tu le gardais pour toi mais on sait toutes les épreuves que tu as traversées dans ta vie. Survivant de génocide, tu es reparti de rien en arrivant par hasard à Castres. La famille, les amis et tes clients peuvent le confirmer : toujours souriant, tu n'as jamais laissé transparaître toutes les horreurs que tu as vues et vécues. Tu as donné une chance à la vie pour construire notre belle famille. Pour Jean-Marc, Jean-Rémy et moi tu restes un modèle de persévérance. Plus tard, tu as accueilli Clotilde comme ta propre fille. Notre voyage en Chine et à Hong Kong en 2016 a été un magnifique cadeau. Encore une fois, tu m'as montré l'importance des moments passés en famille, tu nous a donnés des souvenirs pour la vie. Pour tous ces moments de bonheur, pour toutes tes valeurs, merci. Papa, je donnerais tout pour pouvoir te revoir, te dire merci en personne et te serrer dans mes bras. J'aimerais te dire que tout va bien

pour nous, que Jean-Marc a soutenu sa thèse, qu'il a trouvé le travail de prof' dont il rêvait, qu'il est comblé avec Eva et Rune (j'imagine à quel point tu aurais été heureux de la rencontrer), que Jean-Rémy a fini et qu'il a aussi une vie tranquille, qu'on s'occupe tous de maman, que tout va bien pour Clotilde et moi et que au final tu as parfaitement réussi ta vie. C'est peut-être égoïste mais j'aimais beaucoup t'entendre dire "je suis fier de toi mon fils". Alors aujourd'hui c'est à moi de te le dire : je suis fier de toi papa.

Enfin, je voudrais terminer ces remerciements par la personne la plus chère à mes yeux : Clo'. Je ne te le dirai jamais assez : merci ! Merci de m'avoir soutenu pendant tout ce temps, ma thèse t'a donné l'occasion de revoir mes coups de stress de la prépa', sauf que cette fois on habitait dans le même appart' ! Donc merci de m'avoir supporté au quotidien. Merci pour toutes tes tentatives pour me rassurer malgré ma non-réceptivité, mon syndrôme de l'imposteur. Merci d'avoir compris quand j'avais besoin de travailler soirs et week-ends. Au passage merci de m'avoir accepté dans ta vie avec Baguera et merci à Baguera pour son soutien malgré elle, elle a quand même passé pas mal de temps à "télétravailler" devant mon écran... En dehors de la thèse merci d'être encore là aujourd'hui. Tu me supportes aujourd'hui depuis dix ans. Après des débuts dans la galère quand j'étais à Toulouse, toi à Albi, puis toi à Toulouse, moi à Lyon, et maintenant quelques années de vie commune, je n'imagine pas continuer sans toi. Tu me rends heureux et j'espère pouvoir te rendre au moins autant heureuse. Pour citer une personne que j'apprécie particulièrement : je t'aime plus que tout ce qui existe et tout ce qui existe pas !

List of communications

Publications in scientific journals

Detomaso, N., **Hok, J.-J.**, Dounia, O., Laera, D., & Poinsot, T. (2023). A generalization of the Thickened Flame model for stretched flames. *Combustion and Flame*, 258(December), 113080.

Hok, J.-J., Dounia, O., Detomaso, N., Jaravel, T., Douasbin, Q., & Vermorel, O. (2024). A modeling strategy for the Thickened Flame simulation of propagating lean hydrogen – air flames. *International Journal of Hydrogen Energy*, 78(July), 1133–1141.

Presentations in international conferences

Hok J.-J., Dounia O., Vermorel O. & Jaravel T. (2021). Modelling of hydrogen-air explosions in confined environments: effect of flame front thermo-diffusive instability on flame acceleration in a tube. *MATHIAS TotalEnergies conference*, Paris.

Hok J.-J., Vermorel O., Jaravel T. & Douasbin Q. (2022). Modelling of hydrogen-air explosions in confined environments: on the interplay of stretch effects and thermo-diffusive instabilities. *MATHIAS TotalEnergies conference*, Paris.

Hok J.-J., Dounia O., Vermorel O., & Jaravel T. (2022). Effect of Flame Front Thermo-Diffusive Instability on Flame Acceleration in a Tube. *Proceedings of the 28th International Colloquium on the Dynamics of Explosions and Reactive Systems*, Napoli (Italy).

Contents

Nomenclature

AIT	*Auto-ignition temperature*
AMR	*Adaptive Mesh Refinement*
ARC	*Analytically-Reduced Chemistry*
BF	*Bunsen flame*
CFD	*Computational Fluid Dynamics*
CH_2G	*Compressed hydrogen gas*
CFL	*Courant–Friedrichs–Lewy*
CNG	*Compressed natural gas*
CPF	*Counterflow premixed flame*
DL	*Darrieus-Landau*
DNS	*Direct Numerical Simulation*
ENACCEF2	*ENceinte d'ACCeleration de Flame 2*
FCS	*Flame consumption speed*
FDS	*Flame displacement speed*
FSD	*Flame surface density*
GHG	*Greenhouse gas*
HPC	*High-Performance Computing*
ICE	*Internal combustion engine*
IPSF	*Inwardly propagating spherical flame*

JPDF	*Joint probability density function*
LCA	*Life cycle assessment*
LEFEX	*Large-Eddy simulation For gas EXplosions*
LES	*Large-Eddy Simulation*
LH_2	*Liquid hydrogen*
LNG	*Liquefied natural gas*
MIE	*Minimum ignition energy*
OPSF	*Outwardly propagating spherical flame*
PHES	*Pumped hydro-electric storage*
PDF	*Probability density function*
PtG	*Power-to-gas*
RANS	*Reynolds-averaged Navier Stokes*
SCFD	*Safety Computational Fluid Dynamics*
SGS	*Subgrid scales*
SSF	*Steady spherical flame*
S-TF	*Stretched-Thickened Flame*
TD	*Thermo-diffusive*
TD-S-TF	*Thermo-Diffusive-Stretched-Thickened Flame*
TF	*Thickened Flame*
URANS	*Unsteady Reynolds-averaged Navier Stokes*

Chapter 1

Introduction

Sommaire

1.1 Energy crisis and energy transition

The global energy sector is today in a critical stage in many respects. The swelling worldwide demography is accompanied with rising living standards in developing and emerging countries putting considerable pressure on the energy market [1, 2]. Demand is gigantic but stakes are even higher. Energy is so ubiquitous in everyone's life that it has become a geopolitical weapon [3]. The energy crisis of 2022 that has led to skyrocketing electricity bills in Europe echoes that of the 1970s with oil [1]. All this raises the question of energy independence. While international cooperation is needed to build a secure, reliable, efficient and interconnected energy grid, each country might aim at self-sufficiency to become less vulnerable to the ups-and-downs of the energy trade.

Alongside strategical interests, the energy sector also plays a central role in the fight against climate change. So far, its practices have exerted a profound and often detrimental impact on the environment. Dominated by fossil fuels, such as coal, oil, and natural gas, the sector is a major contributor to anthropogenic greenhouse gas (GHG) emissions,

exacerbating climate change and environmental degradation [1]. In 2022, energy-related CO_2 emissions reached an all-time high of 41.3 Gt [4] (see Figure 1.1). Combustion and industrial processes (such as cement, iron, chemicals, etc.) accounted for 89% of that share. The extraction, production, and consumption of these conventional energy sources not only deplete finite resources but also pose severe threats to biodiversity and air and water quality [5]. In light of these challenges, there is an urgent and compelling need to transition towards cleaner and more sustainable energy alternatives. Renewable energy sources like solar, wind, and hydro-power offer viable solutions to mitigate the environmental fallout of traditional energy practices. Embracing these cleaner options not only reduces carbon emissions but also promotes the aforementioned energy independence by allowing an in-house production.

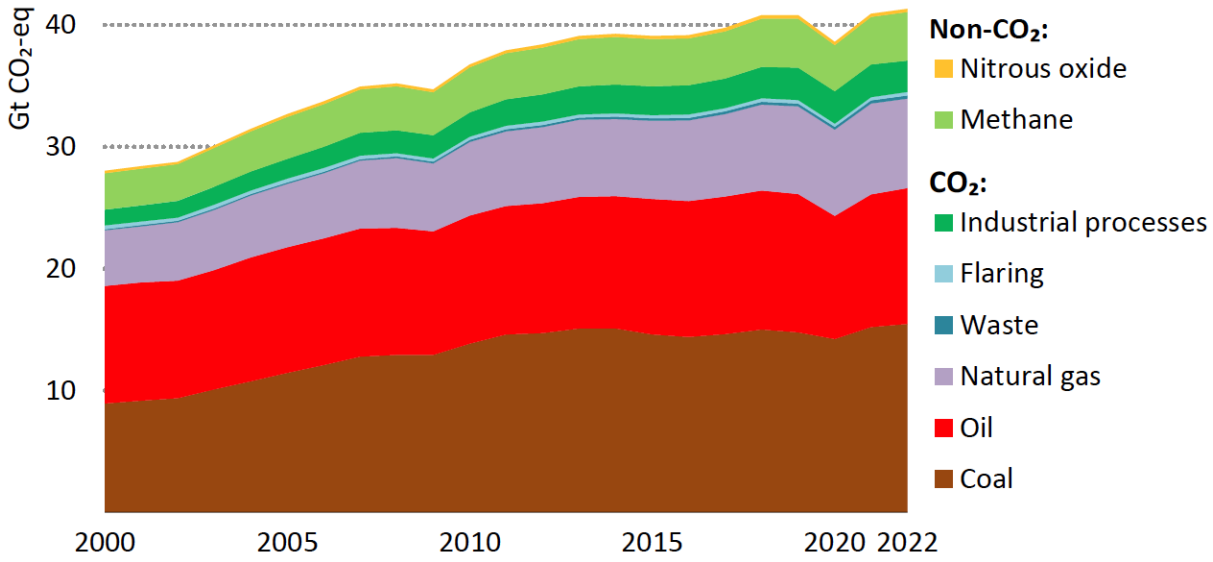

Figure 1.1: Global energy-related greenhouse gas emissions, 2000-2022 [4].

Energy storage is often regarded as the weak point of renewable energies due to the inherent intermittency of their sources [6]. Unlike traditional fossil fuel power plants that can provide a consistent and controllable output, renewables are highly dependent on environmental conditions. Solar power generation is contingent on sunlight, wind power relies on wind speeds, and hydro-power is influenced by water availability. The challenge arises when these resources are not consistently available, leading to fluctuations in energy production. Energy storage becomes crucial to address this intermittency by capturing excess energy during peak production times and releasing it when demand is high or when renewable resources are scarce. Overcoming these challenges is essential to realising the full potential of renewable energy sources and ensuring a reliable and consistent power supply. However, current energy storage technologies face limitations in terms of efficiency, cost, and scalability. Currently, pumped hydro-electric storage (PHES) represents the most widely used technology with a global capacity of approximately 130 GW [7]. Although it has significant potential for development in some areas of the world, it still faces technical and socio-economic barriers such as landscape topology, land use or biodiversity loss to cite a few [8]. Also, some applications, especially in the transport sector,

require embedded energy storage that hydro-power cannot provide. Batteries, a common form of mobile and dispatchable storage, often struggle with capacity, degradation over time, and the environmental and social impact of production and disposal [9–11].

Electrofuels (also called e-fuels) production represents a convenient way of storing excess output from renewable sources. In this so-called power-to-gas (PtG) paradigm, energy is kept within the chemical bonds of carbon-free or low-carbon vectors such as hydrogen, ammonia or methane. It is then recovered by burning these fuels in power plants when needed. It is all the more relevant considering that thermal generation is the biggest source of power and heat in the world today [12]. Using electrofuels also makes sense in the transportation sector and, most particularly, global aviation. Full electrification is indeed awkward in this domain where technical constraints impose high-density energy storage [13–15].

1.2 Hydrogen as an energy vector

Hydrogen gathers all qualities required for a sustainable and resilient energy vector. It has a strong energy density compared to classical carbonated fuels [16] (see Figure 1.2). As a carbon-free molecule, it can be used in industries where thermal power is needed and where emissions are hard to abate (e.g. cement, steel or glass production). Whether burnt in thermal engines or converted to water in fuel cells, the use of hydrogen in vehicles has the potential to strongly reduce pollution from the latter and enhance air quality [6]. Research is currently made to retrofit existing combustion technologies for hydrogen usage [17]. Full life cycle assessments (LCA) are still needed, but a hydrogen-based PtG strategy seems promising to decarbonate the global economy [18].

Although its current production is mainly fossil-fuel-based (through steam methane reforming), efforts are made to develop low-emission technologies such as water electrolysis or ammonia decomposition [19]. According to the International Energy Agency [20], "low-emission hydrogen production can grow massively by 2030 but cost challenges are hampering deployment". Its report encourages further political incentives to tend towards a global hydrogen economy. As a matter of fact, hydrogen can tip the balance in favour of a clean energy transition.

1.3 Risks associated with the use of hydrogen

Unfortunately, every technology comes with its share of drawbacks. The massive deployment of hydrogen technologies is necessary, but must be carried out with care for a safe production, storage, transport and utilisation. H_2 physical properties significantly differ from those of usual hydrocarbons. Despite a high energy density per mass unit, it has a low energy density per volume unit under atmospheric conditions (see Figure 1.2). It

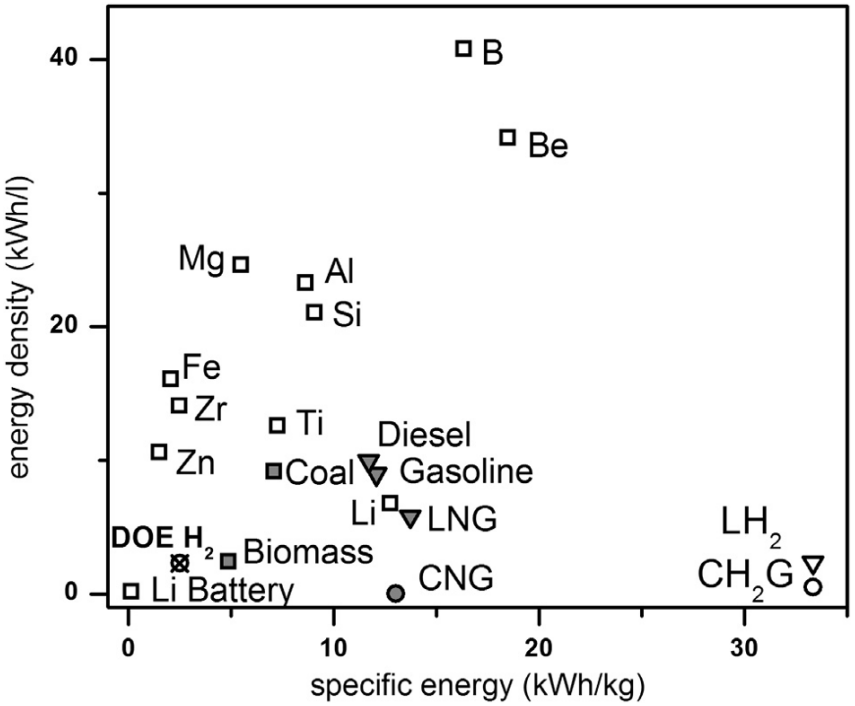

Figure 1.2: Volumetric and gravimetric energy density for various metal fuels [41] compared to batteries [42], hydrogen [43], bio-derived fuels [44], and fossil fuels [43–45] (1 kWh $= 3.6 \times 10^6$ J). Abbreviations used: compressed natural gas (CNG), liquefied natural gas (LNG), compressed hydrogen gas (CH_2G) and liquid hydrogen (LH_2). Gaseous fuels are indicated by (s), liquid fuels by (r) and solid fuels by (h). Open symbols indicate potential zero-carbon fuels. Taken from Bergthorson *et al.* [16].

must be stored under low temperatures or high pressures to reach sufficient density and increase the storage capacity [21]. Given that liquids are much denser than gases, using cryogenic temperatures allows to stockpile a lot of hydrogen within smaller tanks. However, the main challenge is crossing the boiling point of hydrogen which is lower than that of other fuel gases. To give an idea, liquefied hydrogen is stored at -253°C against -162°C for liquefied natural gas [22]. The other solution is compressed hydrogen. Considering its very low density at ambient conditions, hydrogen is usually stored under pressures of 350 bars or 700 bars [23]. Such substantial values induce of course safety issues and require appropriate technologies. Hydrogen storage and transport facilities are not the only place where safety standards must be applied. Investigations of the 2011 accident at Fukushima nuclear power plant has shown that hydrogen played an important role in the disaster. Through domino effect, a series of events has led to tremendous quantities of hydrogen being produced into the reactor building. It ended in an explosion blowing up large sections of the construction which released large amounts of fission products [24].

Safety concerns are also justified by hydrogen diffusion and combustion properties. It has a high capacity for leaking because of the small size of the H_2 molecule. Leakages are hard to detect given that hydrogen is odourless and invisible [25]. What's even more concerning is the high flammability of hydrogen. Usual metrics to evaluate a fuel

ignitability are the minimum ignition energy (MIE), auto-ignition temperature (AIT) and flammability limits. The first quantifies the minimal energy that, when supplied in a single point of space, can ignite and propagate a flame through the mixture. Of course it depends on the gas composition and the global minimum is taken as the MIE. The second quantity, also called kindling point, measures the temperature of a fuel-oxidiser(-diluents) mixture above which it spontaneously ignites without any external source of energy. Lastly, flammability limits are to be understood in terms of mixture composition. Combustion reactions need a fuel and an oxidiser to burn. When one of the two comes in tremendously larger concentrations than the other, combustion cannot be initiated even in the presence of a big source of energy because not enough molecules meet to react. Lower and upper flammability limits are commonly expressed as molar fractions of fuel at 25°C and atmospheric pressure [26]. In Table 1.1, comparison with natural gas regarding the formerly described three metrics shows that hydrogen is more likely to be ignited under ambient conditions [25].

	Hydrogen	Natural gas
MIE [mJ]	0.02	0.30
AIT [°C]	520	580
Flammability limits [v%]	4-75	4-15

Table 1.1: Flammability metrics : Hydrogen vs natural gas

Several sequences of events are conceivable following a fuel leakage. They are summarised in the following flow chart (Figure 1.3). The main distinctions are made between open and confined space and whether an ignition occurs immediately or late. The most damaging scenario is an explosion of the gaseous mixture in a confined space where pressure can build up. Depending on several conditions such as mixture composition, temperature, infrastructure geometry or ignition location, an explosion can take two forms. As long as the combustion wave stays subsonic relative to fresh gases, it is categorised as a deflagration. Deflagrations can cause severe damages with overpressures usually of the order of $\mathcal{O}(0.1 - 1)$ bar under atmospheric conditions with classical fuels. However the effects are mild compared with a detonation which can be seen as a reacting wave coupled with a shock wave [27]. During this type of events, overpressures can reach $\mathcal{O}(1 - 10)$ bars, obviously detrimental to the infrastructures [28]. Owing to the high flammability and burning properties of hydrogen mentioned above, hydrogen explosions are likely to be more destructive. This correlates with the wide detonability range of H_2 situated between 18 % and 59 % in volume [25]. Therefore, even a light leakage of hydrogen represents a danger. Over the past few years, several incidents linked with hydrogen have caused numerous casualties and generated considerable economic losses, e.g. [29–33]:

- Brahegatan, Sweden (1983): hydrogen cylinder explosion in an open street in Stockholm, 16 injured;
- Czech Republic (1990): hydrogen release and explosion due to a leak in a high pressure hydrogen tank, 34 deaths, 10 injured;

- Padua, Italy (2003): hydrogen cylinders involved in a car crash with more than 250 cars on a highway, 13 deaths, +90 injured, hydrogen released and ignited due to the high temperatures caused by the conventional fire;
- Santa Clara, United States (2019): explosion in a hydrogen production and storage facility during a refuelling operation, no casualties, $\sim$ 1000 people impacted during several weeks by the H_2 supply cut;
- Gangwon, South Korea (2019): explosion of a hydrogen reservoir in a research center for water electrolysis, 6 deaths, 2 injured, building completely destroyed;
- Kjorbo, Norway (2019): explosion and fire in a H_2 servicing station, no casualties, nearby highway and roads closed to traffic for several hours, other servicing stations of the same company in Europe, United States and South Korea closed for inspection;

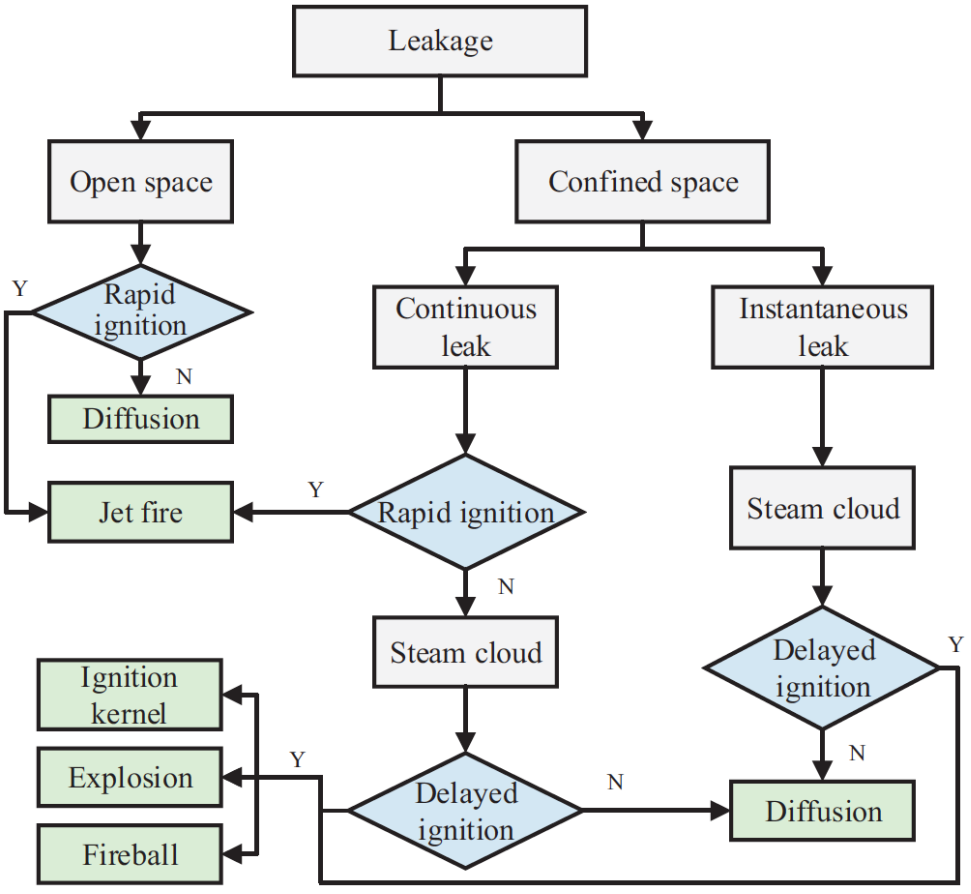

Figure 1.3: Possible hazardous events following a fuel leakage. Adapted from Yang *et al.* [34].

On top of the immediate human and monetary cost, explosion incidents have long-lasting consequences such as environmental pollution and profound social impacts [35]. In the case of hydrogen, it could change the public opinion about it and deter future

developments. The past experience of the Hindenburg accident has marked people's minds and re-emerges today [36]. Explosions must therefore be studied exhaustively to understand their dynamics and design prevention and mitigation devices before hydrogen is deployed widely.

1.4 The need for numerical simulations

In order to avoid future tragedies and failures, to create standards and adopt safety measures, thorough understanding of combustion phenomena must be achieved. To this end, early explosion studies heavily relied on experiments [28]. While an empirical approach gives realistic information that can be later analysed, it is rapidly limited due to extensive costs and dangerousness (owing to the extreme thermal conditions and mechanical stresses inflicted to the material). Sensibility analyses consisting in varying one or several parameters to gauge their impacts on the flame are onerous and painstaking. Besides, experimental diagnostics in large-scale systems are often limited to very little data such as pressure probes and simple video recordings [37–39]. Because of implementation difficulties and of the extremely short time scales involved in explosions, experiment sometimes suffers from a lack of detailed diagnostics about the flow itself. A fine verification of initial conditions (mixture composition, homogeneity, quiescent flow or turbulence regime, etc.) and boundary conditions (impact of surroundings in a free-atmosphere explosion, thermal conditions for a confined explosion, etc.) is also usually complicated, especially at industrially relevant scales. These issues complicate the understanding of experimental observations and may lead to a general lack of repeatability which calls for alternative and complementary analysis tools.

The arrival of the numerical world has found loads of applications in sciences and inexorably changed scientific research. As far as combustion is concerned, Computational Fluid Dynamics (CFD) has significantly increased the knowledge about (reacting) flows. Safety CFD (SCFD) is a particular field for explosion modelling that has developed in recent years and appeals to more and more [40]. Apart from their ease of set-up, simulations allow access to quantities that are hard or quasi-impossible to measure experimentally such as exhaustive spatial distributions and reaction rates. Over the past few decades, the increasing computational power has gradually improved numerical precision. Technical advances in the High-Performance Computing (HPC) field has allowed the use of parallelised codes on supercomputers and computer clusters.

1.5 Towards the LES of explosions: the LEFEX project

As explained in the previous section, numerical simulations are nowadays heavily used in explosion studies. They provide a complementary analysis tool to experimental measurements. Initially, the limitations imparted by computational costs restricted the simulations to the (Unsteady-)Reynolds-Averaged Navier-Stokes ((U)RANS) approach. In this approach, all turbulent scales are modelled and only the mean fields are solved for. This method has proved its capability of reproducing experimental observations in a large range of explosion configurations [41–44]. However, owing to the averaging operation, most of the physics is contained in the models used for turbulent scales. The accuracy of RANS is thoroughly conditioned by the quality of these models, in particular some constants used therein. In practice, such constants can be tuned to match experimental data, thereby fitting the simulation to a particular realisation of an explosion. This questions the predictability of the RANS approach for a priori evaluations of an explosion scenario without experimental measures.

Following the increase in computational resources, the use of Large-Eddy Simulation is now possible. This method consists in spatially filtering Navier-Stokes equations so as to resolve the biggest scales of turbulence only. Although subgrid-scale (SGS) models are required, LES equations capture much more of physical phenomena than RANS approaches. LES is all the more suited to explosions simulations as these are highly unsteady and often involve a wide range of scales. Geometries can be of the order of a few or dozens of meters while flame thickness is close to a few hundred microns and turbulent scales can be a lot smaller. In recent years, the LES concept has made way in the SCFD research community thanks to stronger prediction abilities. It has been successfully applied to a wide range of explosion scenarios, for configurations of various types and scales, different mixture compositions and diverse conditions of temperature and pressure [45–56]. Nevertheless, the LES approach still faces many challenges to improve its accuracy and robustness while ensuring reasonable computational costs. The LEFEX (Large-Eddy simulation For EXplosions) project, involving CERFACS and several industrial partners (TotalEnergies, Air Liquide and GRTGaz), has been specifically designed to address these issues. Several PhDs subjects were part of the LEFEX project, among which: the development of Adaptive Mesh Refinement (AMR) to substantially reduce the computational cost of an explosion LES (theses of Soumyo Sengupta and Benjamin Vanbersel); the use of Deep Learning to assist turbulent combustion models (thesis of Victor Xing); and the application of LES methods to ultra large-scale (industrial) explosion configurations (thesis of Francís Adrián Meziat Ramírez). The present work has also been conducted within this framework to provide a thorough understanding of the modelling issues associated to lean H_2-air explosions.

1.6 Objectives of the thesis

This thesis focuses on the simulation of lean hydrogen-air explosions. Such mixtures are representative of leakage events where small contents of hydrogen are mixed with the surrounding air and ignited. These explosions represent a challenging test case for standard modelling strategies. Indeed, lean hydrogen-air mixtures are subject to several phenomena not commonly observed in other conditions. In particular, they are known for their sub-unity Lewis number which traduces an unbalance between thermal and molecular diffusion processes. This property has multiple consequences on the flame propagation. First, lean H_2-air flames are strongly accelerated by stretch (local quantity measuring the flame surface area increase). On top of that, the sub-unity Lewis number is also at the origin of the thermo-diffusive instability which appears in the form of small-scale cells wrinkling the flame front, thereby enhancing combustion. The presence of these two physical phenomena calls to reconsider classical LES methods for lean H_2-air explosions. Indeed, one may wonder if current methods are able to correctly capture these mechanisms, key to flame acceleration (hence conditioning the severity of the explosion).

The objective of this PhD thesis is to construct an LES framework capable of taking into account the specificities of very lean hydrogen combustion. Most of the manuscript will concentrate on the laminar regime associated to the early stages of flame propagation during an explosion. The detailed experiments carried out at ICARE (spherical bombs) will serve as valuable reference data. Obviously, focusing only on the laminar phase of an explosion is not sufficient to tackle realistic scenarios where turbulence is a major contributor to flame acceleration. A proper solution for the turbulent regime is beyond the scope of this thesis. Instead, the strategy adopted in this work will consist in connecting the approach developed for the laminar regime with the classical turbulent combustion models. Even though this approach may seem naïve, it constitutes a first step towards the complete analysis, understanding and modelling of very lean H_2-air explosions. The pros and cons of this approach will be highlighted in a configuration representative of real explosion scenarios: the ENACCEF2 vessel from ICARE laboratory [57] (Figure 1.4). It has been designed to investigate the flame acceleration in lean hydrogen-air mixtures in a confined and obstructed environment. Despite its reduced size, it is reasonable to say that the ENACCEF2 test rig reproduces key elements of real geometries (notably the level of confinement and obstruction) potentially encountered in H_2 storage or transport facilities. Finally, the main objectives of the present work are:

1. to evaluate the performance of standard methods when applied to the LES of lean hydrogen-air explosions and identify potential deficiencies;

2. to develop the adequate correction models;

3. to apply these models and assess their added value in ENACCEF2, representative of a real lean H_2-air explosion.

Figure 1.4: Photograph of the ENACCEF2 experimental test rig at ICARE laboratory. Taken from [57]

1.7 Thesis outline

To address these objectives, the progression of the manuscript is as follows:

- Chapter 2 lays the basic notions for the understanding of lean hydrogen-air flames;
- Chapter 3 explains the common physical mechanisms responsible for flame acceleration in explosion events;
- in Chapter 4, the Navier-Stokes equations for reactive flows are reminded as well as the numerical framework for the Large-Eddy Simulation of explosions;
- the technical developments of the manuscript start with Chapter 5. It evaluates state-of-the-art methods in the context of lean H_2-air flames in a 2D tube set-up. This configuration is representative of the early stages of a confined explosion like ENACCEF2. In particular, it is shown that the classical Thickened Flame model is unable to correctly predict the explosion. This deficiency results from the coupling of two shortcomings: (1) the stretch response of the flame is incorrectly accounted for; (2) thermo-diffusive instabilities are not resolved on common LES meshes;

- Chapter 6 tackles the first issue by proposing a correction strategy to properly capture stretch effects;
- Chapter 7 presents the second block of the correction with a subgrid model aimed for all thermo-diffusive instabilities not resolved in LES. It is developed on the canonical 2D spherical flame set-up and assessed on 3D spherical flames, both representative of the initial instants following ignition;
- the previous model is extended in Chapter 8 for confined explosions and comes back to the 2D tube configuration of Chapter 5;
- Finally, the model is applied and discussed in Chapter 9 on the full 3D ENACCEF2 explosion test case (confined and obstructed).

Part I

Theoretical background: premixed flames, explosions, and the specificities of hydrogen

Chapter 2

Theoretical concepts of premixed flames

Sommaire

The aim of this chapter is to introduce the necessary quantities and relations used throughout the thesis. Section 2.1 defines fundamental laminar flame characteristics. The asymptotic theory on the flame response to stretch is presented in Section 2.2 and the linear stability theory of flame fronts is presented in Section 2.3. Finally, Section 2.4

shows a decomposition of the turbulent flame speed which is relevant for the present study.

2.1 Laminar flame characteristics

Laminar flame characteristics are central in combustion theory and modelling. This section introduces several flame speed and flame thickness definitions used in the rest of the thesis.

2.1.1 Flame speed definitions

The notion of flame speed represents a keystone in the combustion field. It plays an important role in most turbulent combustion models and is a basic quantity often used to evaluate the reactivity of a mixture [58]. For explosions, it quantifies the combustion wave propagation and determines the potential for damage. Although essential, the notion of flame speed is ambiguous because of the variety of definitions.

2.1.1.1 Laminar flame speed

The most basic and fundamental speed is the *laminar flame speed* S_L^0. It is defined as the speed at which a perfectly planar flame propagates into fresh gases at rest [59]. The flame is then regarded as an interface separating fresh and burnt gases.

To give an idea of where the flames of this thesis sit, Figure 2.1 shows the evolution of S_L^0 with equivalence ratio Φ for hydrogen-air flames under atmospheric conditions. Planar lean H_2-air flames ($\Phi < 1$) propagate at speeds ranging from a couple cm/s for ultra-lean flames to around 2 m/s near-stoichiometry, showing a sharp evolution compared to the rich side. The maximum laminar flame speed is not reached near stoichiometry like for classical carbonated fuels, but at a richer equivalence ratio (around $\Phi \approx 1.5 - 1.7$). This is due to the high diffusivity of hydrogen [58] (see Section 2.2.3 for further details).

2.1.1.2 Kinematic definitions

In spite of its simple definition, the notion of laminar flame speed is not directly applicable to real flames. These are indeed multidimensional, often unsteady and wrinkled. The definition of a flame speed needs further considerations. Intuitively, one can define a speed using a kinematic approach as one would do with a solid in motion. But the question then is which motion to track and also in which frame?

Let's consider a region in the vicinity of a flame. Like in the fully planar case, one can

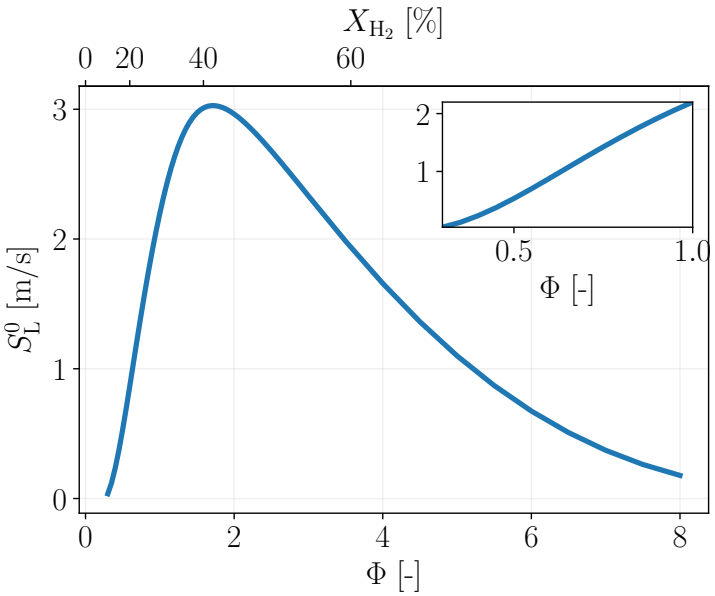

Figure 2.1: Laminar flame speed as a function of equivalence ratio for H_2-air premixed flames under atmospheric conditions. Computed with the detailed mechanism of San Diego [60] (see Sections 4.2.2 and 5.2).

consider the flame front to be an interface between fresh and burnt gases. The motion of this interface can thus be tracked over time to define a propagation speed. In the case of premixed flames, the fresh gases are composed of a mixture of reactants (fuel, oxidiser and other compounds like inert gases, other chemicals from the air, etc.) whereas the hot gases are the products of the combustion (right-hand side terms of the global combustion reaction, remaining excess species and other non-reactive compounds).

The first issue arising from this approach is that this interface has a finite thickness (see Section 2.1.2) because of continuity constraints in the physical quantities (like temperature, velocity, etc.). To be more precise, a flame interface can be defined as a continuous set of isolevel surfaces separating fresh and burnt gases. Straightforward choices for the quantity to base the isolevel on are iso-temperature or iso-density contours. A normalised progress variable c can therefore be defined to measure the combustion process varying from 0 in the reactants to 1 in the products. Typical temperature-based and fuel-based definitions for c are given by [61]:

$$c \equiv \frac{T - T_\mathrm{u}}{T_\mathrm{b} - T_\mathrm{u}} \tag{2.1}$$

$$c \equiv \frac{Y_\mathrm{F} - Y_\mathrm{F,u}}{Y_\mathrm{F,b} - Y_\mathrm{F,u}} \tag{2.2}$$

where T is the temperature and Y_F the fuel mass fraction. Subscript u (resp. b) refers to the unburnt (resp. burnt) side. The flame surface can still be defined as the loci where c takes a particular value $c = c^*$. Nonetheless, as stated by Law [58], uncertainties still come up with this definition. Depending on which quantity is chosen for that isocontour and which value of c^* is chosen, one will not measure the same speeds with the same

precision.

The second problem comes from the wrinkling of the flame itself. Seldom are real flames fully planar (see Figure 2.2). Even when there is no turbulence wrinkling the flame, this latter often tends to be curved, making it difficult to define a global flame speed. Flame speed must then be understood locally. The unit normal vector to the flame front is defined as:

$$\mathbf{n} \equiv -\frac{\nabla \mathbf{c}}{|\nabla \mathbf{c}|} \tag{2.3}$$

The flame propagation is measured along this normal direction (pointing towards fresh gases) at each location along the flame front.

The last input required to define kinematic flame velocities is the reference frame. Because a flame front evolves in a flow, two frames are usually discussed. On the one hand, if an observer watches the flame propagation nearby in a fixed frame (laboratory frame), what they will measure is the *absolute flame speed*, given by:

$$S_\mathrm{a} \equiv \mathbf{w} \cdot \mathbf{n} = \frac{1}{|\nabla \mathbf{c}|} \frac{\partial c}{\partial t} \tag{2.4}$$

where $\mathbf{w}$ is the speed at which a point on an isolevel $c = c^*$ must move to stay on it over time (see Figure 2.2). S_a is a local quantity, varying along and through the flame front, hence depends on c^* as well. But in the case where the flame front is neither thickened, nor thinned by the flow (the distance between isolevels of progress variable does not change over time), S_a is independent of the value of c^* and only varies crosswise along the flame front [62].

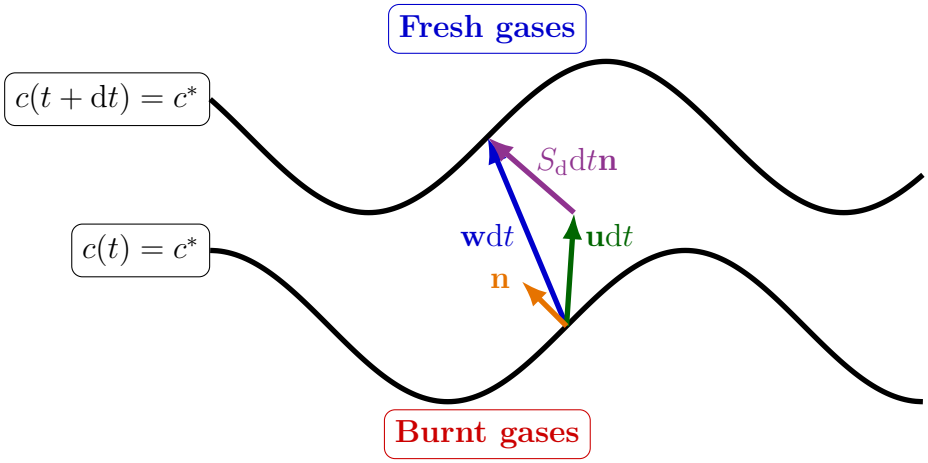

Figure 2.2: Absolute and displacement flame speeds definition.

On the other hand, one can measure the flame front speed relative to the flow, the so-called *flame displacement speed* (FDS):

$$S_\mathrm{d} \equiv (\mathbf{w} - \mathbf{u}) \cdot \mathbf{n} = S_\mathrm{a} - \mathbf{u} \cdot \mathbf{n} \tag{2.5}$$

where $\mathbf{u}$ is the local flow velocity vector. In other words, S_d can be defined in terms of

material derivative of a flame isocontour:

$$S_\mathrm{d} \equiv \frac{1}{|\nabla \mathbf{c}|}\frac{\mathrm{D}c}{\mathrm{D}t} = \frac{1}{|\nabla \mathbf{c}|}\frac{\partial c}{\partial t} + \frac{\mathbf{u}\cdot\nabla \mathbf{c}}{|\nabla \mathbf{c}|} \tag{2.6}$$

S_d is also by essence a local quantity (which depends on the choice of isocontour c^*). It is affected by flow straining, curvature and transport phenomena [63] (see Section 2.2). Most importantly, it changes across the flame front because of the flow dilatation. This means that depending on the value of c^*, one considers a FDS relative to unburnt or burnt mixture. It can lead to significant gaps. For example, one can show that for a perfectly planar flame, S_d varies from S_L^0 in the fresh gases to $(\rho_\mathrm{u}/\rho_\mathrm{b})S_\mathrm{L}^0$ in the hot gases (where ρ represents density) [62]. In order to build meaningful comparisons of FDS at different locations, a density-weighted FDS $\widehat{S_\mathrm{d}}$ is often introduced [64, 65]:

$$\widehat{S_\mathrm{d}} \equiv \frac{\rho}{\rho_\mathrm{u}} S_\mathrm{d} \tag{2.7}$$

The use of FDS along the flame front allows a thorough investigation of local effects of flow and flame curvature on the propagation as will be shown in Chapter 5. However, in complex combustion scenarios, it is more convenient to find a global propagation speed that characterises the evolution of the flame front. In the specific case of explosions in a confined space, the existence of a preferential direction for propagation allows to define a global flame position by taking the "most advanced" point of an isocontour of progress variable in that direction. For instance, if one considers the evolution of a flame ignited in a channel oriented along the x axis and propagating towards increasing x values, the flame is tracked by:

$$x_\mathrm{f}(t) = \max\left\{x \in \mathbb{R} / c(x,t) = c^*\right\} \tag{2.8}$$

And a global flame speed is computed by:

$$v_\mathrm{f} \equiv \frac{\mathrm{d}x_\mathrm{f}}{\mathrm{d}t} \tag{2.9}$$

Figure 2.3 illustrates this tracking method. In experiments, when an optical window is used, this procedure allows to track a single scalar function $x_\mathrm{f}(t)$ to measure the evolution of the flame instead of tracking the displacement of every point of the flame brush. When no optical window is available, the flame is tracked by time-of-arrival photodiodes scattered along the channel [66].

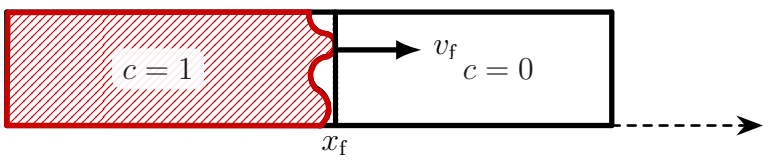

Figure 2.3: Flame front speed in a vessel.

2.1.1.3 Chemical definition

From a chemical point of view, a combustion process is nothing more than an (exothermic) oxido-reduction reaction. In this way, defining the flame speed is straightforward: it must be the speed at which reactants are consumed. This quantity is commonly called the *flame consumption speed* (FCS) and writes [65, 67]:

$$S_\mathrm{c} \equiv -\frac{1}{\rho_\mathrm{u}(Y_\mathrm{F,u} - Y_\mathrm{F,b})} \int_{(\Gamma)} \dot{\omega}_\mathrm{F} \, \mathrm{d}s \tag{2.10}$$

where $\dot{\omega}_\mathrm{F}$ is the fuel production rate (negative). (Γ) defines a streamline normal to the flame front (everywhere parallel to $|\nabla \mathbf{c}|$).

Such expression defines a flame speed independent of the reference frame and the value of c^*. The main drawback is that it cannot be measured in experiments. On the contrary, it is straightforwardly computed in numerical simulations as one can get all fields. More generally, a FCS can be defined from the production rate of any species k of the global reaction [68]:

$$S_\mathrm{c} = \frac{1}{\rho_\mathrm{u}(Y_{k,\mathrm{b}} - Y_{k,\mathrm{u}})} \int_{(\Gamma)} \dot{\omega}_k \, \mathrm{d}s \tag{2.11}$$

2.1.1.4 Summary of flame speed definitions

Table 2.1 summarises the different definitions of flame speed introduced so far as well as their characteristics. The FCS provides an unambiguous definition of flame speed that only varies along the flame. However, it cannot be directly measured in experiments (quantitatively). Kinematic flame speed definitions are more suitable for experimental measurements but their local nature is often hard to capture. Assimilating the flame to an infinitely thin surface provides a first simplification to define speeds varying along but not across the front (like the FCS). To go further, in some cases, the geometry of the flame motivates the choice of a global flame speed. The example of the explosion confined along one direction has been developed here. Another example is discussed in Section 2.2.2.

Flame speed	Definition	Localness	Measurability
Absolute speed S_a	Flame front speed relative to a fixed reference frame	Varies along and across the flame front	Experiments and simulations
Displacement speed S_d	Flame front speed relative to the flow	Varies along and across the flame front	Experiments and simulations
Consumption speed S_c	Speed at which reactants are consumed	Varies along the flame front	Simulations only

Table 2.1: Summary of flame speed definitions.

2.1.2 Flame thickness definitions

Flame thickness is another fundamental characteristic of a flame. From a numerical point of view, it determines the minimum mesh resolution that is necessary to capture the physics of a flame front. Before running a complex case simulation, it is usually necessary to do a first computation of a one-dimensional planar flame to assess the flame thickness. Apart from the pure numerical aspect, the flame thickness also plays a prominent role in combustion theory and modelling. For example, it is compared to the length scales of turbulence (integral length scale and Kolmogorov scale) to evaluate the sensitivity of the flame to turbulence [69, 70].

Like for flame speeds, several definitions exist for flame thickness. One of the most used is the *flame thermal thickness*, given for a planar flame by:

$$\delta_{\mathrm{L}}^{0} \equiv \frac{T_{\mathrm{b}} - T_{\mathrm{u}}}{\max\limits_{x}\left(\left|\frac{\partial T}{\partial x}\right|\right)} \tag{2.12}$$

This approach is based on the temperature profile through the flame as depicted in Figure 2.4. Similarly to the FCS definition, a flame thermal thickness can be evaluated locally on real flames by taking the maximum temperature gradient along the streamline (Γ) defining the flame front:

$$\delta_{\mathrm{L}}^{0} \equiv \frac{T_{\mathrm{b}} - T_{\mathrm{u}}}{\max\limits_{(\Gamma)}\left(|\nabla \mathbf{T}|\right)} \tag{2.13}$$

When the progress variable is temperature-based (Equation (2.1)), the thermal flame thickness corresponds to the inverse of the maximum of its gradient:

$$\delta_{\mathrm{L}}^{0} = \left(\max_{(\Gamma)}\left(|\nabla \mathbf{c}|\right)\right)^{-1} \tag{2.14}$$

Another thickness, called the *diffusive flame thickness* is also often used in the theory:

$$\delta_{\mathrm{d}} \equiv \frac{\lambda_{\mathrm{u}}}{\rho_{\mathrm{u}} C_p S_{\mathrm{L}}^{0}} = \frac{D_{\mathrm{th,u}}}{S_{\mathrm{L}}^{0}} \tag{2.15}$$

where $D_{\mathrm{th,u}}$ is the mixture thermal diffusivity of the fresh gases linking the Fourier thermal conductivity λ, density ρ and the mixture heat capacity at constant pressure C_p:

$$D_{\mathrm{th}} \equiv \frac{\lambda}{\rho C_p} \tag{2.16}$$

While both definitions (2.13) and (2.15) relate to heat diffusion, the thermal thickness can be seen as an effective diffusive thickness.

Flame thickness is one of the main limitations in simulation. Flames are usually very thin (a few hundreds micrometers) and significantly increase computational costs by

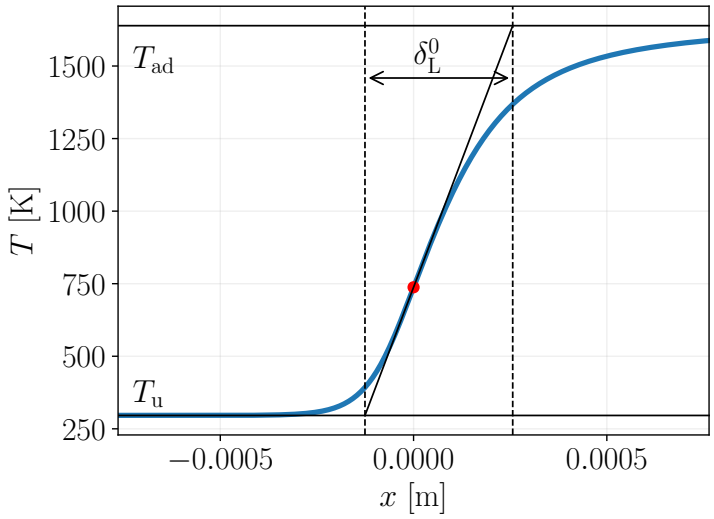

Figure 2.4: Flame thermal thickness definition (distance between the two dashed lines).

driving up the number of cells, even for laminar flows. For instance, Figure 2.5 shows the thermal and diffusive thicknesses for H_2-air flames at ambient conditions. Although the magnitudes differ, both definitions give the same evolution with equivalence ratio. Both reach a minimum above stoichiometry ($\Phi \approx 1.5 - 1.7$) where the laminar flame speed is maximal. Lean flames have the advantage of being thicker, thus reducing the necessary number of cells for a given resolution.

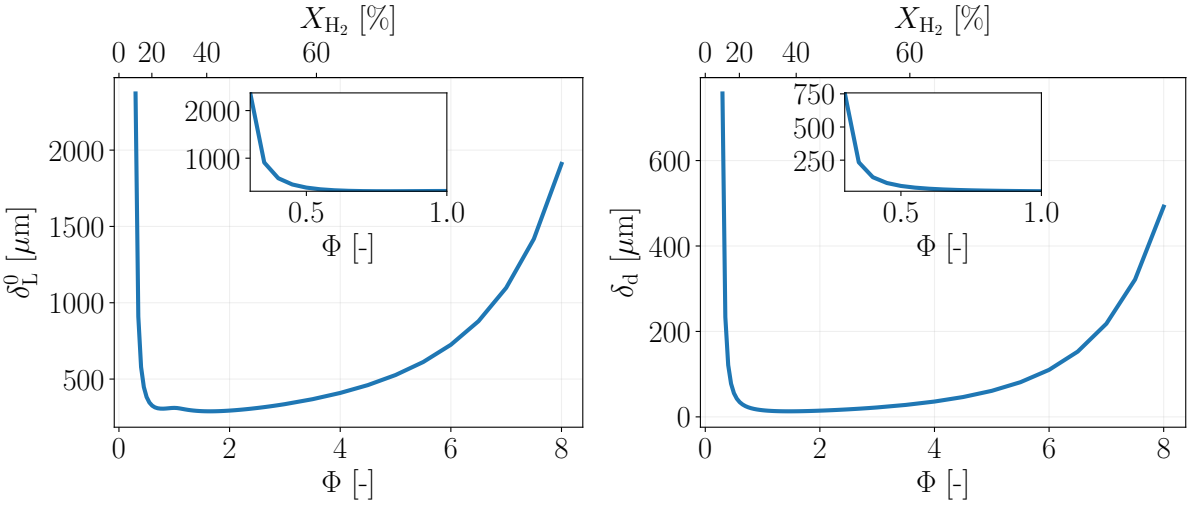

(a) Thermal thickness.

(b) Diffusive thickness.

Figure 2.5: Flame thicknesses as a function of equivalence ratio for H_2-air premixed flames under atmospheric conditions. Computed with the detailed mechanism of San Diego [60] (see Sections 4.2.2 and 5.2).

2.1.3 Flame temperature

The flame temperature is another characteristic of interest to evaluate the combustion process. It is the integrated effect of the heat released by the flame. This same heat is fundamental to thermal technologies such as gas turbines and turboreactors. In 1824, Carnot [71] famously postulated the second law of thermodynamics: the production of work requires the existence of at least two sources of heat, a hot source from which heat is extracted and a cold source into which it is ejected. And the performance of such machine depends on the temperature difference between the two sources, or in Carnot's own words: *"The motive power of heat is independent of the agents employed to realise it; its quantity is fixed solely by the temperatures of the bodies between which is effected, finally, the transfer of caloric"*.

Similarly to the laminar flame speed, the most fundamental temperature is measured on the planar flame and called the *adiabatic flame temperature*. Under several assumptions (among which the fact that the fuel must be the limiting reactant), the adiabatic flame temperature can be approximated by [58, 62]:

$$T_{\mathrm{ad}} \approx T_{\mathrm{u}} + \frac{QY_{\mathrm{F,u}}}{C_p} \tag{2.17}$$

where Q is the heat of reaction per unit mass (heat released by the combustion of 1 kg of fuel). Despite the strongly simplifying assumptions, this relation establishes the fact that all combustion power is converted to sensible energy to heat up the gas from T_{u} to T_{ad}.

Another parameter often found in theoretical studies and related to the flame temperature is the thermal expansion ratio defined by:

$$\begin{aligned} \sigma &\equiv \frac{\rho_{\mathrm{u}}}{\rho_{\mathrm{b}}} \\ &\approx \frac{T_{\mathrm{b}}}{T_{\mathrm{u}}} \end{aligned} \tag{2.18}$$

As its name suggests, σ directly measures the gas expansion produced by the exothermic chemical reaction.

Both T_{ad} and σ are plotted against equivalence ratio for H_2-air flames at ambient conditions in Figure 2.6. Unlike S_{L}^0, the adiabatic flame temperature peaks exactly at stoichiometry.

2.2 Flame stretch

As stated in Section 2.1.1, real flames are never fully planar. Flame fronts interact with their environment which affects their propagation. These effects are quantified through the notion of *flame stretch* described in this section.

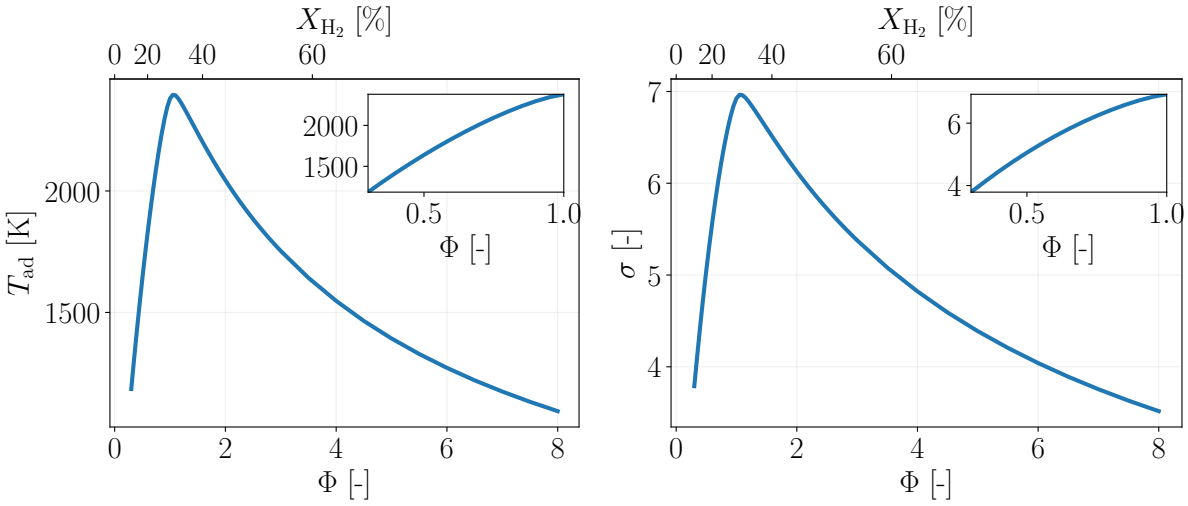

(a) Adiabatic flame temperature.

(b) Thermal expansion ratio.

Figure 2.6: Adiabatic flame temperature and thermal expansion ratio as a function of equivalence ratio for H_2-air premixed flames under atmospheric conditions. Computed with the detailed mechanism of San Diego [60] (see Sections 4.2.2 and 5.2).

2.2.1 Definition

The flame stretch rate $\mathbb{K}$ is defined as follows [72]:

$$\mathbb{K} \equiv \frac{1}{A}\frac{\mathrm{d}A}{\mathrm{d}t} \tag{2.19}$$

where A is a flame surface element. Homogeneous to the inverse of a time, it evaluates the rate of change in local flame surface area: stretch is positive when the area increases and negative otherwise. The word "local" is essential. Non-zero values of stretch don't necessarily mean that the global flame surface is unsteady. As explained by Poinsot and Veynante [62], stationary flames can be stretched in the same time.

To go further, Candel and Poinsot [73] used a pure kinematic approach to express $\mathbb{K}$ with the previously defined flame front velocity $\mathbf{w}$ (Section 2.1.1.2):

$$\mathbb{K} = -\mathbf{nn} : \nabla\mathbf{w} + \nabla \cdot \mathbf{w} \tag{2.20}$$

This relation re-enacts the fact that flame stretch is, generally speaking, a quantity varying along and through the flame front.

Using Equation (2.5) to link $\mathbf{w}$ with the FDS and the flow velocity, flame stretch is equal to [74, 75]:

$$\mathbb{K} = K_\mathrm{s} + S_\mathrm{d}\kappa \tag{2.21}$$

where:

$$K_\mathrm{s} \equiv -\mathbf{n} \cdot \overrightarrow{\overrightarrow{\mathbf{E}}} \cdot \mathbf{n} \tag{2.22}$$

and:

$$\kappa \equiv \nabla \cdot \mathbf{n} \tag{2.23}$$

with $\overrightarrow{\overrightarrow{\mathbf{E}}}$ being the strain rate tensor:

$$\overrightarrow{\overrightarrow{\mathbf{E}}} \equiv \frac{1}{2}\left(\nabla \mathbf{u} + (\nabla \mathbf{u})^{\mathrm{T}}\right) \tag{2.24}$$

Equation (2.21) provides a classical expression for flame stretch involving two components. The first one, K_{s}, is the strain of the flow acting on the flame surface and increasing its local area. The second is directly linked to the flame shape with κ representing the local flame curvature: the motion of a curved flame front naturally increases its area. Figure 2.7c clearly illustrates this geometrical mechanism. Considering a flame element of local curvature κ_0 (corresponding to a local radius of curvature $R_0 = 1/\kappa_0$) spanning over an angle $\mathrm{d}\theta_0$ and propagating at speed $S_{\mathrm{d},0}$, one has:

$$\begin{cases} A(t) = R_0\,\mathrm{d}\theta_0 \\ A(t+\,\mathrm{d}t) = A + \,\mathrm{d}A = (R_0 + S_{\mathrm{d},0}\,\mathrm{d}t)\,\mathrm{d}\theta_0 \end{cases} \tag{2.25}$$

which leads to:

$$\frac{1}{A}\frac{\mathrm{d}A}{\mathrm{d}t} = S_{\mathrm{d},0}\kappa_0 \tag{2.26}$$

Sometimes, it is convenient to recast Equation (2.21) to relate the flame stretch with its absolute flame speed (defined by Equation (2.4)) [65]:

$$\begin{aligned} \mathbb{K} &= \nabla_{\mathbf{t}} \cdot \mathbf{u_t} + (\mathbf{u}\cdot\mathbf{n})\kappa + S_{\mathrm{d}}\kappa \\ &= \nabla_{\mathbf{t}} \cdot \mathbf{u_t} + S_{\mathrm{a}}\kappa \end{aligned} \tag{2.27}$$

where $\nabla_{\mathbf{t}}$ is the surface gradient [75]. This new formulation splits the strain rate into a tangential strain contained in $\nabla_{\mathbf{t}} \cdot \mathbf{u_t}$ (purely aerodynamic, Figure 2.7a) and a normal strain in $(\mathbf{u}\cdot\mathbf{n})\kappa$ (linked to the flame curvature, Figure 2.7b). All effects of non-stationarity are now encompassed in the second term through S_{a}. The tangential strain is sometimes written as [65, 76, 77]:

$$\nabla_{\mathbf{t}} \cdot \mathbf{u_t} = -\mathbf{n} \cdot \nabla \times (\mathbf{u} \times \mathbf{n}) \tag{2.28}$$

Depending on the flame configuration, it can be easier to compute the flame stretch using either Equation (2.19), (2.21) or (2.27). This is illustrated in the next section.

2.2.2 Canonical stretched flames

The decomposition of total flame stretch into strain and curvature introduced by Equations (2.21) and (2.27) is better understood on canonical stretched flames which involve one or several of its components. They are summarised in Figure 2.8. It is shown in each case how the local nature of flame stretch can be bypassed to define $\mathbb{K}$ as a global

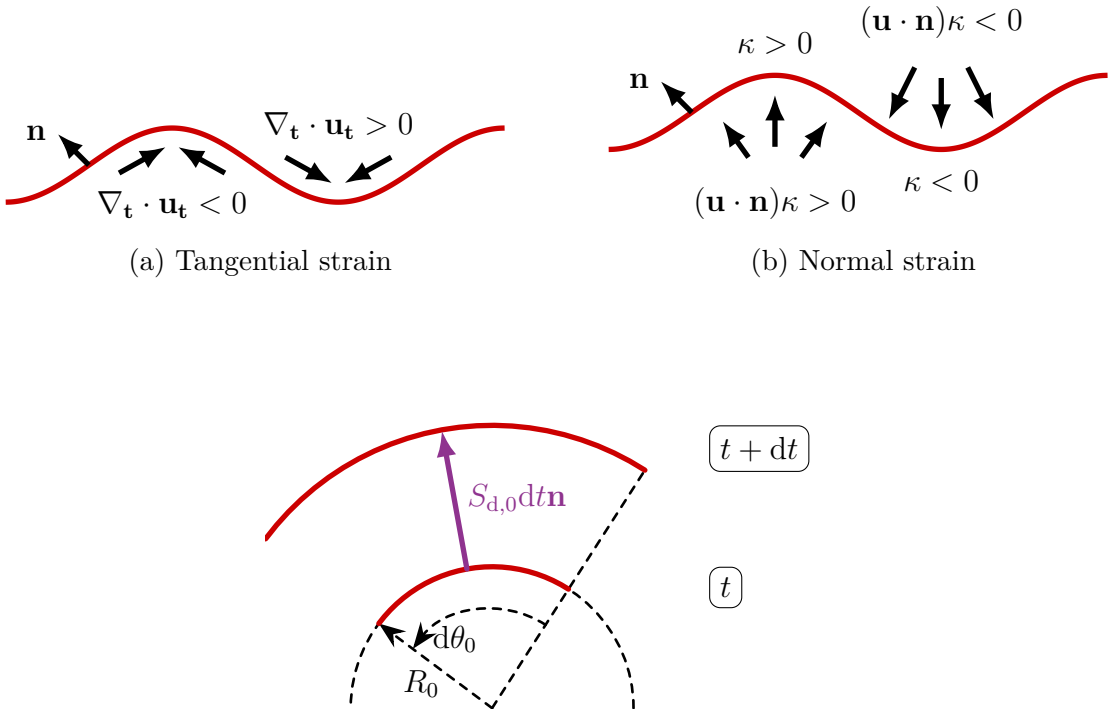

(a) Tangential strain

(b) Normal strain

(c) Flame motion

Figure 2.7: Illustration of different types of flame stretching.

quantity.

Counterflow premixed flame

The counterflow premixed flame (CPF, also called stagnation point flame) is composed of two impinging jets, one with a premixed combustible mixture and the other with burnt products of the combustion (see Figure 2.8a). The governing equations can be found in Kee *et al.* [78, 79]. A planar flame is stabilised in the middle. This set-up is an example of stretched, but stationary flame. Given that the flame is planar, the curvature term of stretch is null and Equation (2.27) reduces to:

$$\mathbb{K} = \nabla_{\mathbf{t}} \cdot \mathbf{u_t} \tag{2.29}$$

The counterflow flame is stretched by pure tangential strain. This strain is non-zero due to the gradient of velocity in the flame tangent plane. In the case of non-reacting potential flows, the analytical solution for the velocity is given by $u = -ax$ and $v = ay$ where a is the velocity gradient. Considering u_1 (resp. u_2) the velocity of the first (resp. second) injector and d the distance between the two injectors, a is constant for a potential flow and equal to $(|u_1| + |u_2|)/d$. In the present reacting case, the combustion alters the velocity field but a keeps the same order of magnitude [62]. The CPF is thus an example where flame stretch can be defined as a global quantity (not varying through the flame). Flame

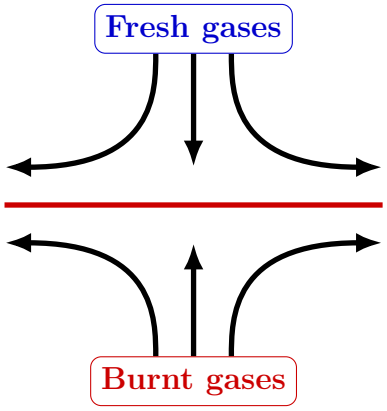

(a) Counterflow premixed flame (CPF).

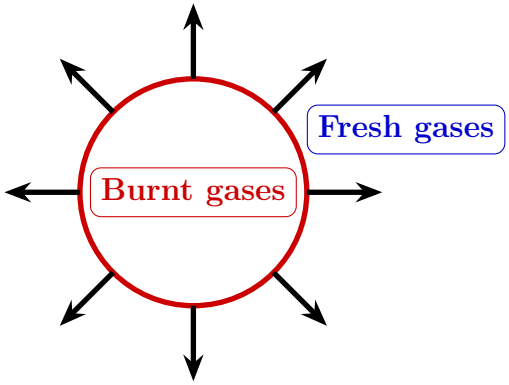

(b) Outwardly propagating spherical flame (OPSF).

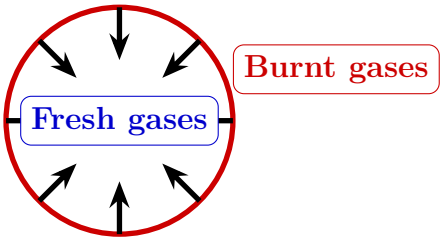

(c) Inwardly propagating spherical flame (IPSF).

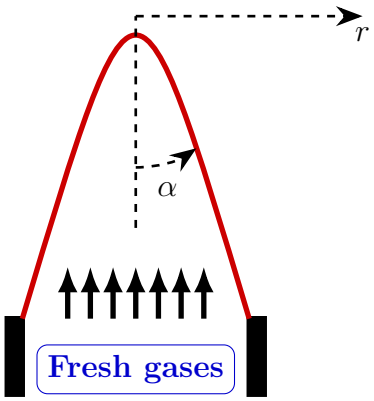

(d) Bunsen flame (BF).

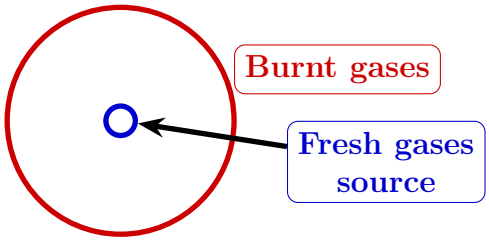

(e) Steady spherical flame (SSF).

Figure 2.8: Canonical stretched flames.

speeds though, remain local. The stationarity of such flame means that:

$$\begin{cases} S_\mathrm{a} = 0 \\ S_\mathrm{d} = -\mathbf{u}\cdot\mathbf{n} \end{cases} \tag{2.30}$$

Outwardly propagating spherical flame

The second canonical configuration is the outwardly propagating spherical flame (OPSF, see Figure 2.8b). It is generated by centrally igniting a perfectly premixed combustible mixture. Owing to the blatant central symmetry, the stretch rate is homogeneous over the whole flame front. A global flame stretch can be estimated using the relation to the flame surface (Equation (2.19)):

$$\mathbb{K} = \begin{cases} \dfrac{1}{r_\mathrm{f}}\dfrac{\mathrm{d}r_\mathrm{f}}{\mathrm{d}t} \text{ for 2D (cylindrical flames)} \\ \dfrac{2}{r_\mathrm{f}}\dfrac{\mathrm{d}r_\mathrm{f}}{\mathrm{d}t} \text{ for 3D (spherical flames)} \end{cases} \tag{2.31}$$

where r_f is the radius of the sphere. Note that the fact that $\mathbb{K}$ is again a global quantity not varying across the flame front is based on the assumption that the front can be identified by a single radius value (hypothesis of infinitely thin flame). Interestingly, $\mathbb{K}$ can also be computed easily from Equation (2.27). Again thanks to the symmetry of the problem, no tangential velocity gradient is expected on the flame front so that:

$$\begin{aligned} \mathbb{K} &= S_\mathrm{a}\kappa \\ &= \frac{\mathrm{d}r_\mathrm{f}}{\mathrm{d}t}\kappa \end{aligned} \tag{2.32}$$

The outwardly propagating spherical flame is not subject to tangential strain, but experiences a normal strain that is proportional to curvature. Regarding the kinematic flame speeds defined in Section 2.1.1, the expression of the absolute flame speed has been shown in Equation (2.31), but for the FDS, the flow velocity is needed. For an infinitely thin flame, Poinsot and Veynante [62] provide an expression for a global FDS:

$$\begin{cases} S_\mathrm{a} = \dfrac{\mathrm{d}r_\mathrm{f}}{\mathrm{d}t} \\ S_\mathrm{d} = \dfrac{\rho_\mathrm{b}}{\rho_\mathrm{u}}\dfrac{\mathrm{d}r_\mathrm{f}}{\mathrm{d}t} \end{cases} \tag{2.33}$$

Inwardly propagating spherical flame

The next flame configuration is very similar but the flame propagates inwards (IPSF, see Figure 2.8c). Using the same considerations, the flame stretch is given by Equation (2.31) and the kinematic flame speeds by Equations (2.33). However, in this case the absolute flame speed is negative, leading to a global negative stretch.

Bunsen flame
The bunsen flame (BF) is one of the best-known combustion set-ups (see Figure 2.8d). Premixed fuel and oxidiser is ejected at constant velocity U_0 at the exit of a circular orifice. A stationary conic flame with apex angle α is stabilised above the burner. Assuming a sharp apex, it has been shown [74, 80] that the stretch rate experienced by a flame element at radial position r is expressed as:

$$\begin{aligned}\mathbb{K} &= -\frac{U_0 \sin(2\alpha)}{2r} \\ &= -\frac{U_0 \cos(\alpha)\sin(\alpha)}{r}\end{aligned} \tag{2.34}$$

Contrary to previous configurations, flame stretch varies locally here. In Equation (2.34), the total stretch rate comes from pure normal straining (noticing that $U_0\cos(\alpha)$ corresponds to the flow velocity projected on the flame front normal ($\mathbf{u}\cdot\mathbf{n}$) and $r^{-1}\sin(\alpha)$ is the curvature κ). The bunsen flame is thus negatively stretched.

Steady spherical flame
The last canonical flame is a remarkable example of a curved and yet unstretched flame (Figure 2.8e). The steady spherical flame (SSF) is indeed curved so that flame stretching may be expected. But the imposed stationarity and central symmetry cancel out all terms of Equation (2.27).

Table 2.2 summarises the different stretch components involved in each of the above flame configurations.

Configuration	**Total stretch**	**Tangential strain**	**Normal strain (curvature-related)**	**Flame motion (curvature-related)**
	$\mathbb{K}$	$\nabla_{\mathbf{t}}\cdot\mathbf{u}_{\mathbf{t}}$	$(\mathbf{u}\cdot\mathbf{n})\kappa$	$S_{\mathrm{d}}\kappa$
CPF	>0	>0	0	0
OPSF	>0	0	>0	>0
IPSF	<0	0	0	<0
BF	<0	0	<0	0
SSF	0	0	0	0

Table 2.2: Summary of stretch components (Equation (2.27)) for canonical flame configurations.

2.2.3 Mixture Lewis number

The effect of stretch on the structure and propagation of a flame is linked with diffusive phenomena. This section defines some transport properties and proposes a phenomenological approach to the flame stretch response.

Mixture transport properties can significantly affect the flame dynamics. Three diffusion coefficients are particularly of interest: the thermal diffusion coefficient D_{th}, the deficient reactant molecular diffusion coefficient D_{D}, and the excess reactant molecular diffusion coefficient D_{E}. From these quantities, the balance between the different diffusion processes is assessed by several variables, namely the ratio between the excess and deficient reactants diffusion coefficients $D_{\mathrm{D}}/D_{\mathrm{E}}$, and the Lewis number of each reactant k:

$$\mathrm{Le}_k \equiv \frac{D_{\mathrm{th}}}{D_k} \tag{2.35}$$

Let's first consider a lean mixture. Subscript D (resp. E) now corresponds to the fuel (resp. the oxidiser). If one of the two reactants, say, the fuel, diffuses faster than the other ($D_{\mathrm{D}}/D_{\mathrm{E}} > 1$), its concentration will increase when approaching the reaction zone (where its gradient is steep), making the mixture closer to stoichiometry. The flame will burn more intensely and its temperature is expected to increase (see Figure 2.6a). Conversely, if the oxidiser diffuses faster ($D_{\mathrm{D}}/D_{\mathrm{E}} < 1$), the mixture becomes leaner and burns less. This mechanism is called *preferential diffusion*.

Now let's assume that the two reactants diffuse at the same rate ($D_{\mathrm{D}}/D_{\mathrm{E}} = 1$), but faster than heat ($\mathrm{Le}_{\mathrm{D}} = \mathrm{Le}_{\mathrm{E}} < 1$). The molecular diffusion of reactants towards the flame front will stoke it whereas the diffusion of heat out of the flame tends to abate it. So when the former is stronger than the latter, combustion is enhanced and a higher flame temperature is expected. The reverse rationale applies for $\mathrm{Le}_{\mathrm{D}} = \mathrm{Le}_{\mathrm{E}} > 1$. This second mechanism is called the *non-unity Lewis number effect*.

In a real flame, the three diffusion coefficients D_{D}, D_{E} and D_{th} are generally different so that a combination of preferential diffusion together with non-unity Lewis number effect exists, sometimes termed *non-equidiffusional effect*. The quantification of their composite effect is made through the definition of an effective Lewis number for the full mixture. It is often agreed upon that for mixtures sufficiently far from stoichiometry, the overall molecular diffusion is driven by the deficient reactant, hence [77, 81, 82]:

$$\mathrm{Le}_{\mathrm{eff}} \approx \mathrm{Le}_{\mathrm{D}} \tag{2.36}$$

But some authors [83, 84] suggest a more general definition accounting for both reactants:

$$\mathrm{Le}_{\mathrm{eff}} = 1 + \frac{(\mathrm{Le}_{\mathrm{E}} - 1) + (\mathrm{Le}_{\mathrm{D}} - 1)\, B}{1 + B} \tag{2.37}$$

In that way, $(\mathrm{Le}_{\mathrm{eff}} - 1)$ is a weighted average of $(\mathrm{Le}_{\mathrm{E}} - 1)$ and $(\mathrm{Le}_{\mathrm{D}} - 1)$. Weight B is given by:

$$B = \begin{cases} 1 + \beta(\Phi - 1) & \text{if } \Phi > 1 \\ 1 + \beta(\Phi^{-1} - 1) & \text{if } \Phi < 1 \end{cases} \tag{2.38}$$

where β is the reduced activation energy, also called Zel'dovich number [85], defined by:

$$\beta \equiv \frac{T_a(T_b - T_u)}{T_b^2} \tag{2.39}$$

where T_a is the activation temperature of the combustion reaction (computed from the chemical activation energy with Boltzmann's constant). Coefficient B brings in chemical parameters controlling the overall diffusion. When the mixture is stoichiometric, the effective Lewis number is simply the non-weighted average of the two reactants Lewis number. When the mixture shifts far from stoichiometry, $B \to \infty$ and the mixture Lewis number reduces to the deficient species one: Equation (2.36) is retrieved.

2.2.4 Flame response to stretch

2.2.4.1 Phenomenology

The previous section has outlined the basic principles behind diffusion processes which influence the flame burning rate. Now, the link with flame stretch is introduced using phenomenological considerations. The three components of total flame stretch introduced in Equation (2.27) can be analysed separately on the canonical configurations presented in Section 2.2.2.

Effect of tangential strain
The rationale developed in Section 2.2.3 can be directly applied to the counterflow premixed flame in a control volume (sketched in Figure 2.8a) corresponding to a section of a streamtube: it loses sensible enthalpy through thermal diffusion and chemical enthalpy by reactants diffusion (both are assumed to be aligned with the normal direction to the flame). If these processes are ill-balanced, say $\mathrm{Le}_{\mathrm{eff}} < 1$, the overall result is enhanced combustion. The other channel by which diffusive mechanisms can improve combustion is through preferential diffusion: if the leaner reactant diffuses faster than the other reactant, the composition gets closer to stoichiometric and the flame burns more intensely. Now if the stretch rate of the CPF is increased (increasing the inlet velocities of both jets), the flame plane will move closer towards the burnt gases to stabilise against the faster incoming flow [86]. The combustion intensification by stretch is consequently amplified.

Effect of normal strain
The effect of flow normal strain on the flame is manifest on the bunsen flame configuration (Figure 2.8d). Assuming a round tip for the conic flame, this same apex constitutes the highest curvature zone of the flame. In this region, the concave shape of the flame surface (relative to the incoming fresh gases) concentrates the diffusion of heat ahead of it. Contrarily, the diffusion of reactants is unfocused. Mixtures for which $\mathrm{Le}_{\mathrm{eff}} < 1$ will thus burn less because of this geometric effect. The negative stretch (evidenced by Equation (2.34)) weakens combustion.

Effect of flame motion

The last ingredient of stretch is the flame motion itself. Its influence on the flame can be comprehended with the outwardly propagating spherical flame. Let's assume like in Section 2.2.2 that the flame can be tracked by an isocontour at radius r_f. If δ_d (defined by Equation (2.15)) describes the flame diffusive thickness on a thermal basis, an analogous thickness $\delta_\mathrm{d,mol}$ can be computed with the flame overall molecular diffusion coefficient ($D_\mathrm{eff} \equiv D_\mathrm{th}/\mathrm{Le}_\mathrm{eff}$). It is within these thicknesses that all diffusion processes come into play. After a small time δt, the flame has consumed reactants and its radius expands of an amount δr_f. This is accompanied by an increase of the volume for both thermal and molecular diffusion. If it is further assumed that r_f is located ahead of the diffusion zone, this change is of the order of [58]:

$$\begin{aligned}
&\frac{4\pi}{3}\left(r_\mathrm{f}+\delta_\mathrm{d}+\delta r_\mathrm{f}\right)^3-\frac{4\pi}{3}\left(r_\mathrm{f}+\delta_\mathrm{d}\right)^3\approx 4\pi\left(r_\mathrm{f}+\delta_\mathrm{d}\right)^2\delta r_\mathrm{f}\\
&\frac{4\pi}{3}\left(r_\mathrm{f}+\delta_\mathrm{d,mol}+\delta r_\mathrm{f}\right)^3-\frac{4\pi}{3}\left(r_\mathrm{f}+\delta_\mathrm{d,mol}\right)^3\approx 4\pi\left(r_\mathrm{f}+\delta_\mathrm{d,mol}\right)^2\delta r_\mathrm{f}
\end{aligned} \tag{2.40}$$

For a sub-unity Lewis number mixture, the molecular diffusion zone is thicker than its thermal counterpart and the flame front motion generates a greater increase in volume for reactant diffusion than for thermal diffusion: combustion is expected to strengthen.

2.2.4.2 Stretched flame speed

Now that the effects of stretch on the flame response and structure have been analysed qualitatively, an attempt to quantify them is presented. Under several hypotheses, theoretical relations give the flame response to stretch. Namely, the asymptotic analysis relies on the following assumptions [87, 88]:

- Low stretch rate;
- Single-step chemistry with an Arrhenius type law;
- High activation energy or equivalently Zel'dovich number β for that reaction;
- Off-stoichiometric mixture composition so that the rate of progress is described by the concentration of the limiting reactant.

This section and the following summarise the main results of this theory.

First, it has been established that the flame speed varies linearly with flame stretch:

$$\begin{aligned}
\frac{S_\mathrm{L}}{S_\mathrm{L}^0} &= 1-\mathcal{L}\frac{\mathbb{K}}{S_\mathrm{L}^0}\\
&= 1-\mathcal{M}\mathrm{Ka}
\end{aligned} \tag{2.41}$$

The slope of the stretched flame speed response with stretch is quantified by the *Markstein length* $\mathcal{L}$ or its non-dimensional version, the *Markstein number* $\mathcal{M}$ defined by:

$$\mathcal{M} \equiv \frac{\mathcal{L}}{\delta_\mathrm{d}} \tag{2.42}$$

where δ_d is the flame diffusive thickness defined by Equation (2.15). Note that a non-dimensional stretch called the Karlovitz number Ka (differs from its homonym used for turbulent flames) has been introduced:

$$\mathrm{Ka} \equiv \frac{\mathbb{K}\delta_\mathrm{d}}{S_\mathrm{L}^0} \tag{2.43}$$

Depending on which flame speed definition is used (see Section 2.1.1), various Markstein lengths and numbers can be retrieved. In particular, the stretched flame consumption speed S_c and displacement speed S_d are given by:

$$\begin{aligned} \frac{S_\mathrm{c}}{S_\mathrm{L}^0} &= 1 - \mathcal{L}_\mathrm{c}\frac{\mathbb{K}}{S_\mathrm{L}^0} \\ &= 1 - \mathcal{M}_\mathrm{c}\mathrm{Ka} \end{aligned} \tag{2.44}$$

$$\begin{aligned} \frac{S_\mathrm{d}}{S_\mathrm{L}^0} &= 1 - \mathcal{L}_\mathrm{d}\frac{\mathbb{K}}{S_\mathrm{L}^0} \\ &= 1 - \mathcal{M}_\mathrm{d}\mathrm{Ka} \end{aligned} \tag{2.45}$$

With the additional hypothesis that the thermal conductivity λ is constant, the early work of Clavin and Joulin [88] has resulted in the following expressions:

$$\mathcal{M}_\mathrm{c} = \frac{\beta\left(\mathrm{Le}_\mathrm{D} - 1\right)}{2(\sigma - 1)} \int_1^\sigma \frac{\ln x}{x - 1}\,\mathrm{d}x \tag{2.46}$$

and:

$$\mathcal{M}_\mathrm{d} = \frac{\sigma \ln \sigma}{\sigma - 1} + \mathcal{M}_\mathrm{c} \tag{2.47}$$

Equations (2.46) and (2.47) echo the analysis carried out in the previous section: diffusive processes play a major role in the flame response to stretch through the Lewis number. Here, the off-stoichiometric assumption has been used to equate the mixture Lewis number to the deficient species Lewis number. If $\mathrm{Le}_\mathrm{D} < 1$ (resp. $\mathrm{Le}_\mathrm{D} > 1$), then the Markstein number for consumption speed is negative (resp. positive) and S_c increases (resp. decreases) with stretch. The same applies for the displacement speed if the Lewis number is sufficiently far from unity. $\mathcal{M}_\mathrm{d}$ contains indeed a second term offsetting its value in comparison with $\mathcal{M}_\mathrm{c}$, linked with thermal expansion. Note also that this term is always positive.

The constant-thermal-conductivity assumption has quickly been relaxed with a temperature-dependency in the following study of Clavin and Garcia [82], yielding the

generalised expressions:

$$\mathcal{M}_{\mathrm{c}} = \frac{\beta\left(\mathrm{Le}_{\mathrm{D}} - 1\right)}{2(\sigma - 1)} \int_1^{\sigma} \frac{\tilde{\lambda}(x)}{x} \ln\left(\frac{\sigma - 1}{x - 1}\right) \mathrm{d}x \tag{2.48}$$

and:

$$\mathcal{M}_{\mathrm{d}} = \frac{1}{\sigma - 1} \int_1^{\sigma} \frac{\tilde{\lambda}(x)}{x} \mathrm{d}x + \mathcal{M}_{\mathrm{c}} \tag{2.49}$$

where $\tilde{\lambda}$ is a reduced thermal conductivity defined by:

$$\tilde{\lambda} \equiv \frac{\lambda(T)}{\lambda_{\mathrm{u}}} \tag{2.50}$$

Note that Equations (2.46) and (2.47) are easily retrieved by setting $\tilde{\lambda} = 1$.

As expressed in Section 2.1.1.2, the flame displacement speed can be source of ambiguity depending on which side of the flame is considered for its definition. That said, some authors have tried to clarify which Markstein length corresponds to the unburnt or burnt side. Based on the work of Matalon [89], Giannakopoulos *et al.* [65] have distinguished two FDS Markstein lengths. In addition, they have replaced the Lewis number Le_{D} in former Equations (2.48) and (2.49) by the mixture effective Lewis number defined by Equation (2.37):

$$\mathcal{M}_{\mathrm{c}} = \frac{\beta\left(\mathrm{Le}_{\mathrm{eff}} - 1\right)}{2(\sigma - 1)} \int_1^{\sigma} \frac{\tilde{\lambda}(x)}{x} \ln\left(\frac{\sigma - 1}{x - 1}\right) \mathrm{d}x \tag{2.51}$$

$$\mathcal{M}_{\mathrm{d}}^{\mathrm{b}} = \frac{1}{\sigma - 1} \int_1^{\sigma} \frac{\tilde{\lambda}(x)}{x} \mathrm{d}x + \mathcal{M}_{\mathrm{c}} \tag{2.52}$$

$$\mathcal{M}_{\mathrm{d}}^{\mathrm{u}} = \frac{\sigma}{\sigma - 1} \int_1^{\sigma} \frac{\tilde{\lambda}(x)}{x} \mathrm{d}x + \mathcal{M}_{\mathrm{c}} \tag{2.53}$$

$\mathcal{M}_{\mathrm{d}}^{\mathrm{b}}$ (resp. $\mathcal{M}_{\mathrm{d}}^{\mathrm{u}}$) corresponds to the Markstein length of a FDS measured on the burnt (resp. unburnt) side of the flame front.

2.2.4.3 Stretched flame temperature

Stretch also affects the temperature of the burnt gases. From the previous considerations on diffusive phenomena in Section 2.2.3, one can deduce that if $\mathrm{Le}_{\mathrm{eff}} > 1$, whenever the flame front is positively stretched, additional heat loss due to flame front enlargement exceeds additional reaction rate induced by reactants diffusion: the flame becomes locally sub-adiabatic.

The first expression for the stretched flame temperature dates back to the study of

Clavin and Williams [90] which states:

$$\frac{T_\mathrm{b} - T_\mathrm{ad}}{T_\mathrm{ad}} = \left(\frac{\mathrm{Le} - 1}{\sigma} \int_1^\sigma \frac{\ln x}{x - 1} \, \mathrm{d}x \right) \mathrm{Ka} \tag{2.54}$$

In their paper, the Lewis number was assumed to be a constant. Like for the Markstein lengths, Equation (2.54) has been generalised for temperature-dependent thermal conductivity by Giannakopoulos *et al.* [65]:

$$\frac{T_\mathrm{b} - T_\mathrm{ad}}{T_\mathrm{ad}} = \left(\frac{\mathrm{Le_F} - 1}{\sigma} \int_1^\sigma \frac{\tilde{\lambda}(x)}{x} \ln\left(\frac{\sigma - 1}{x - 1}\right) \, \mathrm{d}x \right) \mathrm{Ka} \tag{2.55}$$

2.2.4.4 Applicability of the asymptotic theory

As pointed out by Bechtold and Matalon [84], the asymptotic theory has been derived from a single-step reaction pathway assumption and is not expected to quantitatively agree with real-life experiments (which of course rely on complex sets of reactions) on a large range of operating conditions. It is nevertheless useful in that it provides explicit expressions from which global flame properties can be assessed. For example, by measuring the Markstein number from spherical flames stretch response, Jomaas *et al.* [91] have extracted the effective Lewis number of mixtures. In the same vein, Bouvet *et al.* [92] have determined the best Lewis number formulation to characterise the diffusive properties of hydrogen-hydrocarbon blends from similar Markstein number measurements.

The low stretch rate assumption constitutes another caveat of the asymptotic theory hitherto overlooked. Indeed, following the work of Markstein [93], the asymptotic analysis produces a linear dependence of the flame speed with stretch that is based on a small stretch level hypothesis. This is convenient for simple extrapolations towards zero-stretch for laminar flame speed determination from canonical stretched flame configurations (see Section 2.2.2), for instance using [94]:

- the counterflow premixed flame (CPF) technique [95];
- the outwardly propagating spherical flame (OPSF) method [96–98].

However, it is not representative of the behaviour of strongly stretched flames commonly encountered in complex combustion set-ups. These often involve turbulent flows straining highly curved flames completely out of the scope of the linear theory. Even in a laminar regime, non-linear stretch responses are a common thing. In order to extend its applicability, several authors have revisited the asymptotic theory to derive non-linear formulas for the flame stretch response. For instance, the reader may refer to the work of Ronney and Sivashinsky [99] who proposed an expression for spherical flames which is free of the low stretch rate assumption. It has later been successfully applied by Kelley and Law [100] for the extrapolation to the laminar flame speed. Other studies from Law and coworkers [101,

102] use an integral analysis to retrieve the non-linear behaviour. This has the advantage of relaxing the high activation energy hypothesis used by the asymptotic theory.

2.3 Flame front instabilities

Intrinsic flame front instabilities exist considering the flame surface per se, without needing to encompass the environmental features with which it might interact. In that sense, they are opposed to other mechanisms such as thermo-acoustic instabilities. They can appear in different forms and different scales. One of the early mentions of an unstable flame front dates back to 1964 when Markstein [93] observed that rich nitrogen-diluted hydrocarbon-air planar flames can take on a cellular shape (see Figure 2.9). In his experiments, cells width was typically of the order of 0.5-1 cm but varied with the inflow mixture composition. To cite a few other examples, the same phenomenon has been measured on spherical flames by Lind and Whitson [103] and flame propagating in a tube by Quinard *et al.* [104] (see Figure 2.10). Lean hydrocarbon-air mixtures are not spared: Groff [105] experimentally observed cellular instabilities on lean propane-air spherical flames. Last but not least, hydrogen-air flames, which are the focus of this thesis, are also remarkably unstable [91, 106]. All this prompts the following questions: what are the causes of flame front instabilities and what is their impact on flame propagation? The next sections provide an introductory answer to these problems while laying the theoretical relations behind the early dynamics of flame front instabilities. In particular, the asymptotic theory proposes some dispersion relations giving the growth rate of perturbations through a linear stability analysis (small-perturbation assumption). Instabilities can originate from three distinct mechanisms described hereafter:

- Hydrodynamic (also called Darrieus-Landau) instability;
- Thermo-diffusive (also called diffusional-thermal) instability;
- Buoyancy (also called Rayleigh-Taylor) instability.

2.3.1 Darrieus-Landau instabilities

At a hydrodynamic level, the flame front thickness is negligible compared to the length scales of the flow. Under the infinitely thin flame assumption, the flame front can be seen as a discontinuity separating the fresh gases at constant density ρ_u from the burnt gases at density ρ_b. The flame surface then propagates at a constant speed assimilated to its unstretched laminar value S_L^0. This model is often referred to as the *Landau mode* of propagation [58]. To analyse the stability of the system, an initially planar flame wrinkled by an arbitrary perturbation is assumed (see Figure 2.11). Given that the disturbance is only localised in the vicinity of the flame surface, the area of a streamtube far upstream

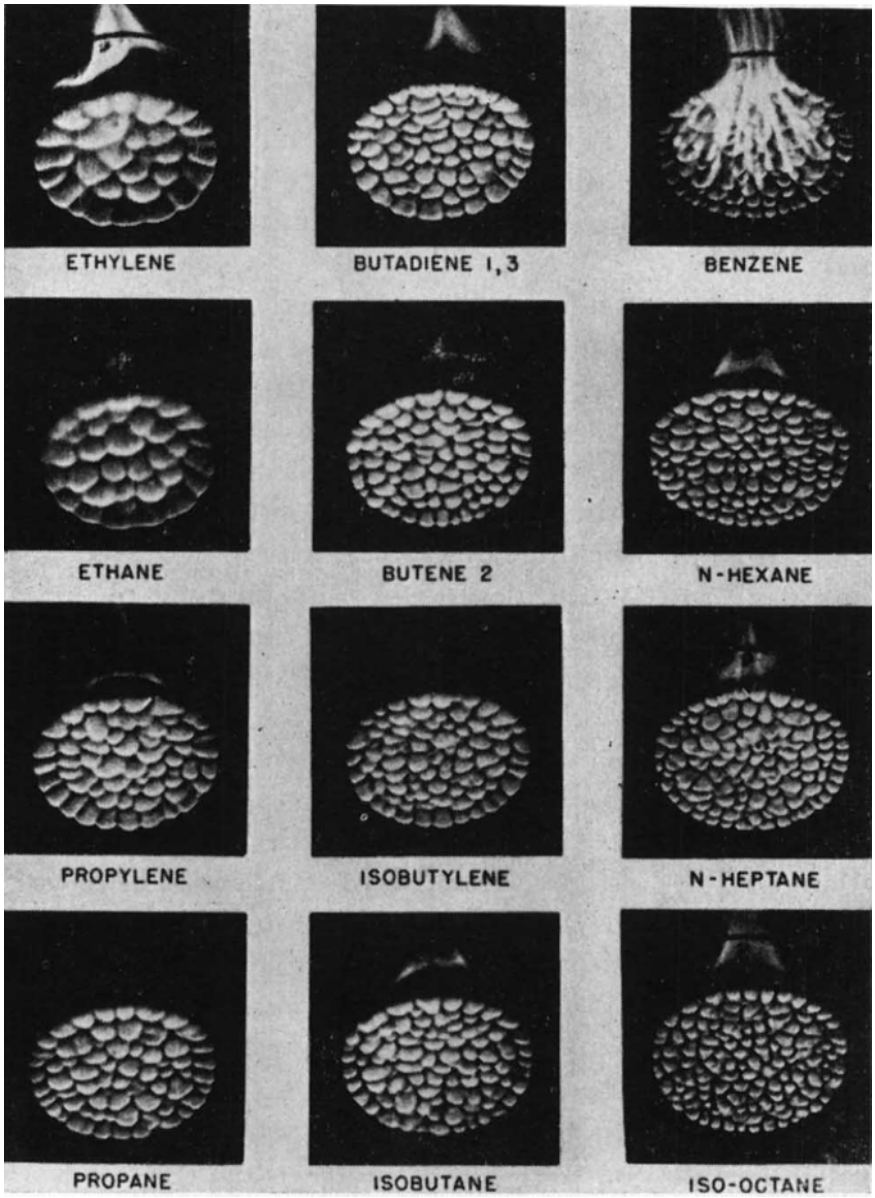

Figure 2.9: Cellular structures on nominally planar flames in fuel-rich hydrocarbon-air-nitrogen mixtures under atmospheric conditions. Taken from Markstein [93].

of the flame must be strictly the same as far downstream. Now, considering the flow velocity jump conditions at the flame interface (illustrated at point P in Figure 2.11), one has that:

- the normal component suffers an abrupt jump due to the density gap;
- the tangential component is conserved.

These conditions imply that the streamlines must diverge (resp. converge) when approaching a segment of the flame that is convex (resp. concave) relative to the unburnt gases. That streamtube widening in convex regions causes the flow to slow down whereas

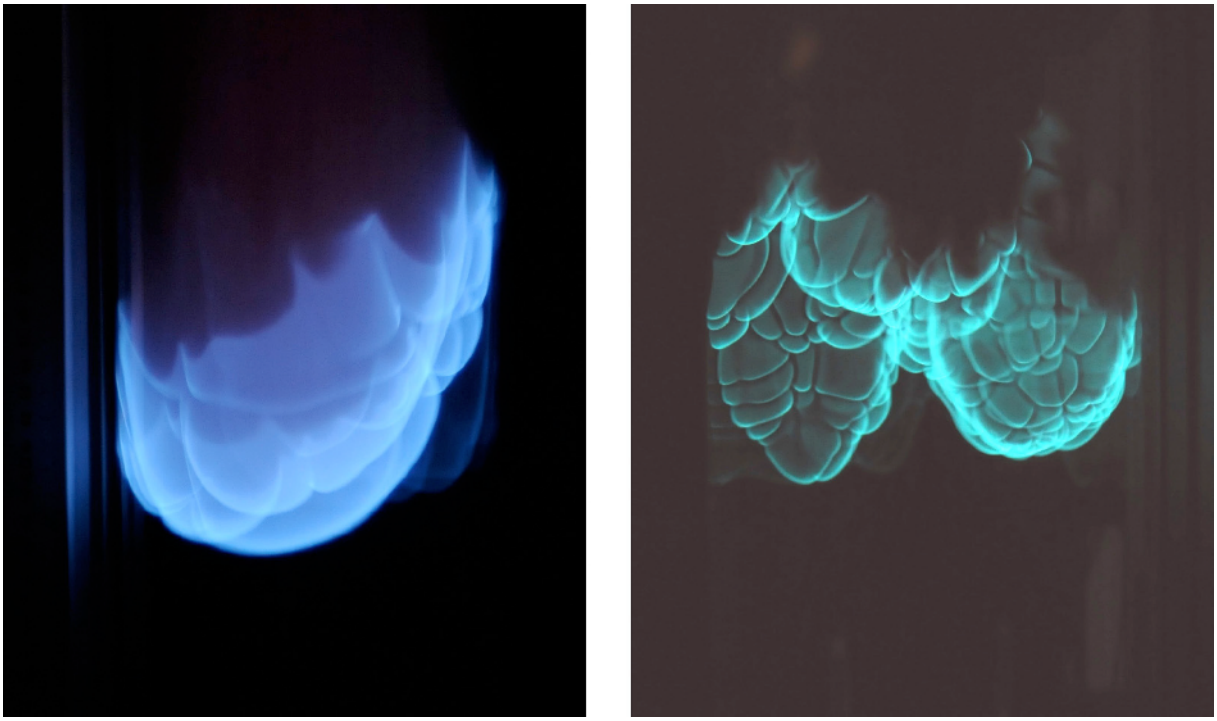

Figure 2.10: Cellular patterns on flames propagating in a tube under atmospheric conditions. Left: CH_4-air ($\Phi = 1.3$). Right: C_3H_8-air ($\Phi = 1.4$). Taken from Quinard *et al.* [104].

it speeds up in concave regions, leading to an amplification of the initial perturbation. The rationale applies to all flames and does not involve any length scale, meaning that all flames are unconditionally unstable to all perturbations. This mechanism is called the *hydrodynamic instability*.

Darrieus [107] and Landau [108] have formalised this mode of instability through the following dispersion relation linking the wave number k and the growth rate ω of a harmonic perturbation:

$$(\sigma + 1)\hat{\omega}^2 + 2\sigma\hat{\omega} - \sigma(\sigma - 1) = 0 \tag{2.56}$$

where $\hat{\omega} = \omega/(S_L^0 k)$ is the normalised growth rate. Because $\sigma > 1$, this second-order polynomial function always has a positive root, yielding:

$$\begin{gathered} \omega = S_L^0 k \omega_{DL} \\ \text{where } \omega_{DL} \equiv \frac{-\sigma + \sqrt{\sigma^3 + \sigma^2 - \sigma}}{\sigma + 1} > 0 \end{gathered} \tag{2.57}$$

The perturbation growth rate is always positive: the unconditional instability obtained above from qualitative reasoning is retrieved quantitatively. Another interesting property can be deduced from Equation (2.57): the growth rate is proportional to the wave number so that small-scale perturbations grow faster than their large-scale counterparts. This feature is nevertheless not valid for wrinkles with a size comparable to the flame thickness. At this level the infinitely thin flame assumption certainly does not hold anymore. In fact,

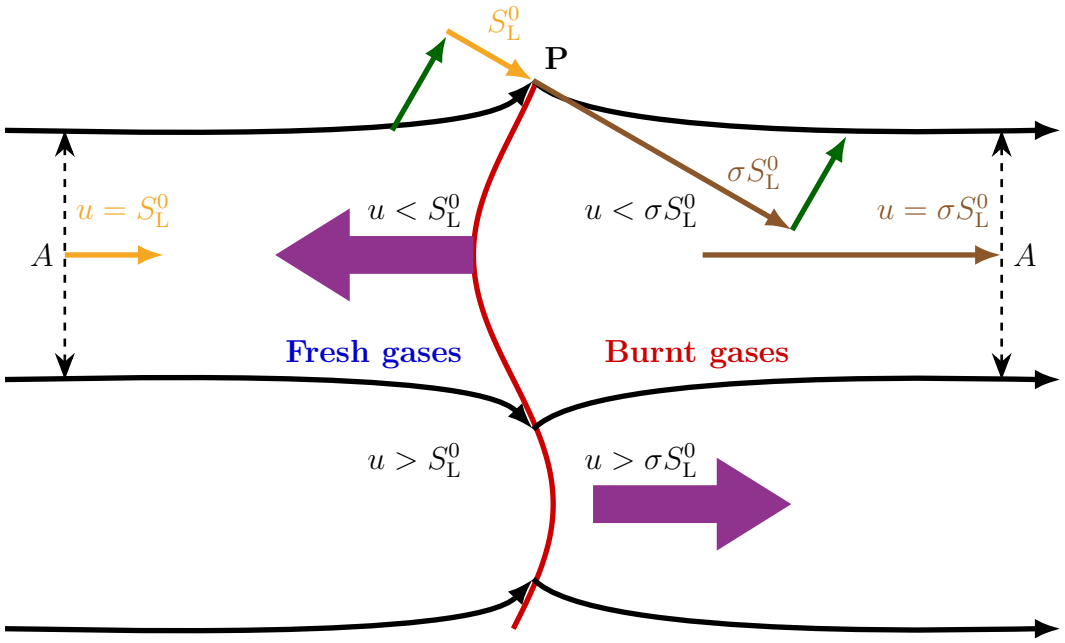

Figure 2.11: Darrieus-Landau instability mechanism.

it is shown in the next section that diffusive phenomena can have a stabilising influence at such small scales, justifying the existence of stable flames in real life despite the presence of hydrodynamic effects.

2.3.2 Thermo-diffusive instabilities

Thermo-diffusive instabilities are due to an unbalance between thermal and molecular diffusion of species. On that account, the Lewis number introduced in Section 2.2.3 proves perfectly relevant. The same formalism as in Section 2.3.1 is adopted here and illustrated in Figure 2.12. Qualitatively, the thermo-diffusive phenomenon results from the combination of two mechanisms.

Geometric and non-unity Lewis number effect
The local curvature generated by a perturbation has opposite effects on heat and reactants. For instance, in a convex segment of the flame, the local curvature leads to an unfocusing of thermal fluxes towards the fresh mixture whereas reactants molecular fluxes are all focused towards the center of curvature in the burnt area. This diffusion asymmetry can destabilise or stabilise the flame front depending on its Lewis number. When the thermal diffusion coefficient is greater than the mixture diffusion coefficient ($\mathrm{Le}_{\mathrm{eff}} > 1$), the enthalpy lost by thermal transport is greater than the enthalpy brought by combustion of incoming reactants. This process tends to stabilise the flame as it dampens the local perturbation. On the contrary, when $\mathrm{Le}_{\mathrm{eff}} < 1$, this curvature effect further destabilises the flame and leads to the formation of cusps on the flame front.

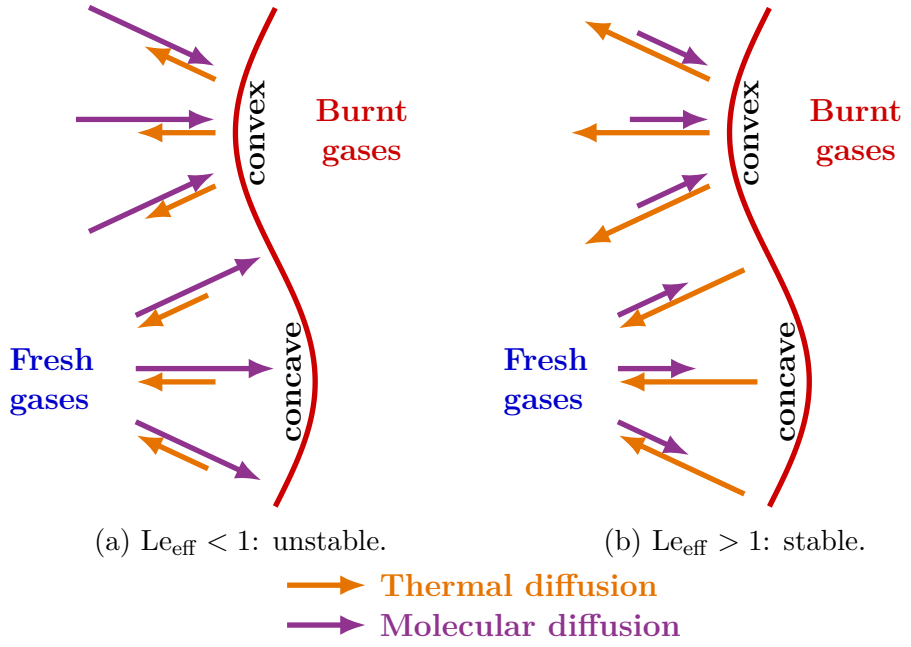

(a) $\mathrm{Le_{eff}} < 1$: unstable. (b) $\mathrm{Le_{eff}} > 1$: stable.

Figure 2.12: Thermo-diffusive instability mechanism.

Preferential diffusion

Second, when the fuel and the oxidiser have different transport properties, that disequilibrium of diffusion can locally modify the fresh mixture equivalence ratio and vary the local flame speed. For example, in lean hydrogen-air mixtures, the fact that hydrogen diffuses faster than oxygen can increase the local flame speed in regions where burnt gases protrude into fresh gases (convex segments). This preferential diffusion thus destabilises the flame front when the fuel diffuses faster than the oxidiser.

Insofar as $\mathrm{Le_{eff}} > 1$, thermal-diffusive phenomena tend to stabilise the flame against Darrieus-Landau instabilities and explain the empirical observation of stable flames. On the contrary, if $\mathrm{Le_{eff}} < 1$, a *thermo-diffusive instability* arises from the coupling of preferential diffusion and curvature effects, and adds up to the Darrieus-Landau instability.

Historically, the thermo-diffusive instability has been first studied as a separate mechanism in the so-called diffusional-thermal theory of premixed flames using an "artificial" constant-density approach [109–111]. This model qualitatively yields the behaviour predicted by the phenomenological approach taken in this section. However, a more general representation accounting for the hydrodynamic instability has been later addressed by Pelce and Clavin [81], Frankel and Sivashinsky [112] and Matalon and Matkowsky [113] and is presented hereafter.

Planar flames

For a planar flame, it is shown that a harmonic perturbation with wave number k has a growth rate given by:

$$\omega = \omega_{\mathrm{DL}} S_{\mathrm{L}}^{0} k - \delta_{\mathrm{d}} \left[B_1 + \beta \left(\mathrm{Le_{eff}} - 1 \right) B_2 + \mathrm{Pr} B_3 \right] S_{\mathrm{L}}^{0} k^2 \tag{2.58}$$

where ω_{DL} is the term previously defined for Darrieus-Landau instabilities (see Equation (2.57)) and B_i are positive coefficients depending solely on the thermal expansion ratio σ [114, 115]. Their most general expressions are given by [116–118]:

$$\begin{cases} B_1 = \dfrac{\sigma}{2\left(\sigma + (\sigma+1)\omega_{\mathrm{DL}}\right)} \left(\dfrac{\sigma\left(2\omega_{\mathrm{DL}} + \sigma + 1\right)}{\sigma - 1} \displaystyle\int_1^\sigma \frac{\tilde{\lambda}(x)}{x}\,\mathrm{d}x + \int_1^\sigma \tilde{\lambda}(x)\,\mathrm{d}x \right) \\ B_2 = \dfrac{\sigma\left(1+\omega_{\mathrm{DL}}\right)\left(\sigma+\omega_{\mathrm{DL}}\right)}{2(\sigma-1)\left(\sigma + (\sigma+1)\omega_{\mathrm{DL}}\right)} \displaystyle\int_1^\sigma \ln\left(\frac{\sigma-1}{x-1}\right)\frac{\tilde{\lambda}(x)}{x}\,\mathrm{d}x \\ B_3 = \dfrac{\sigma}{\sigma + (\sigma+1)\omega_{\mathrm{DL}}} \left((\sigma-1)\tilde{\lambda}(\sigma) - \displaystyle\int_1^\sigma \tilde{\lambda}(x)\,\mathrm{d}x \right) \end{cases} \tag{2.59}$$

Equation (2.58) gives a parabolic shape for $\omega(k)$, as depicted in Figure 2.13. The hydrodynamic mechanism still always has a destabilising effect on the flame surface. But now three components play a role in the range of unstable wavelengths (dictated by the orientation of the parabola):

- B_1 carries the effects of heat diffusion. According to the previous discussion, heat loss by diffusion tends to stabilise the flame. It is retrieved by the positive sign of this term;
- The second term contains the same factor $\beta(\mathrm{Le}_{\mathrm{eff}} - 1)$ that appears in Markstein length expressions (see Section 2.2.4). It shows that the stability to thermo-diffusive phenomena is intimately linked to the flame response to stretch. Mixtures for which $\mathrm{Le}_{\mathrm{eff}} < 1$ (resp. $\mathrm{Le}_{\mathrm{eff}} > 1$) are destabilised (resp. stabilised) by this term;
- $\mathrm{Pr}B_3$ contains the influence of viscosity and is stabilising like thermal diffusion.

Then, the overall stability of the flame is determined by the sign of the sum of these terms. For a given couple (β, σ), there exists a critical Lewis number value $\mathrm{Le}_{\mathrm{eff}}^{\mathrm{c}}$ where the flame switches from unconditional instability to partial stability:

$$\mathrm{Le}_{\mathrm{eff}}^{\mathrm{c}} = 1 - \frac{B_1 + \mathrm{Pr}B_3}{\beta B_2} \tag{2.60}$$

Spherical flames

In the case of spherical flames, a harmonic perturbation is constrained by the periodicity condition. It is usually described by a harmonic order n and amplitude A. Matalon, Matkowsky and Bechtold [89, 119] have established the following dispersion relation:

$$\frac{1}{\mathrm{A}}\frac{\mathrm{dA}}{\mathrm{d}t} = \frac{\dot{r}_{\mathrm{f}}}{r_{\mathrm{f}}} \left\{ \omega_{\mathrm{DL}}^{\mathrm{sph}} - \frac{\delta_{\mathrm{d}}}{r_{\mathrm{f}}} \left[B_1^{\mathrm{sph}} + \beta\left(\mathrm{Le}_{\mathrm{eff}} - 1\right) B_2^{\mathrm{sph}} + \mathrm{Pr}B_3^{\mathrm{sph}} \right] \right\} \tag{2.61}$$

where r_{f} is the flame radius, and B_i^{sph} are coefficients depending solely on σ and n.

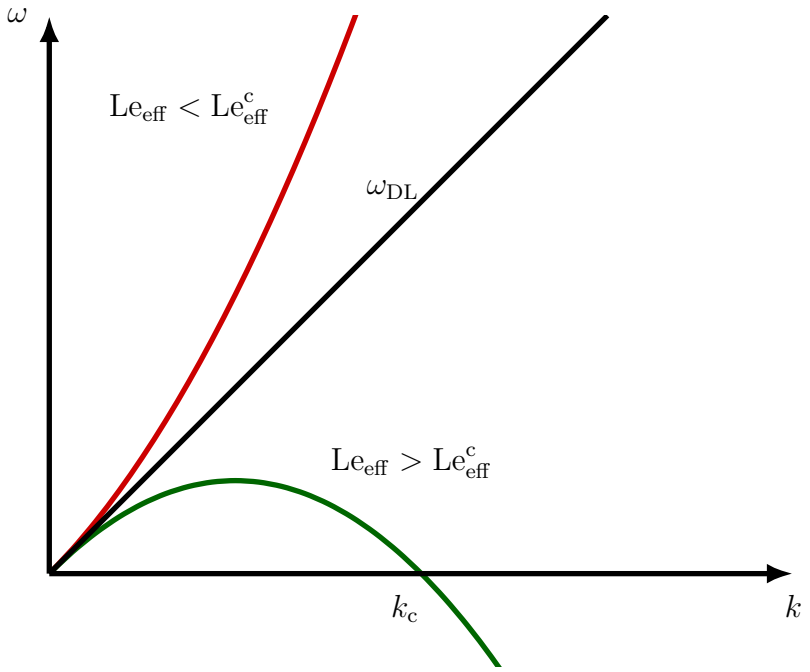

Figure 2.13: Dispersion relation for a planar flame accounting for hydrodynamic and thermo-diffusive effects.

The coefficients coming into play in Equation (2.61) are given by [120]:

$$
\begin{aligned}
\omega_{\mathrm{DL}}^{\mathrm{sph}} &= \frac{-(b-a)+\sqrt{(b-a)^2-4ac}}{2a} \\
B_1^{\mathrm{sph}} &= \begin{array}{l} \frac{\gamma_1}{\sigma\Delta}\Big[(\sigma+1)n^4+\sigma(2\omega_{\mathrm{DL}}^{\mathrm{sph}}+5)n^3 \\ +\left(\omega_{\mathrm{DL}}^{\mathrm{sph}}\sigma-2\sigma^2+\sigma-1\right)n^2 \\ +\sigma(\sigma-7-3\omega_{\mathrm{DL}}^{\mathrm{sph}}-\sigma\omega_{\mathrm{DL}}^{\mathrm{sph}})n-2\sigma(1+\omega_{\mathrm{DL}}^{\mathrm{sph}})\Big] \\ +\frac{\gamma_3}{\sigma\Delta}\left[n\left(n^2-1\right)(n+2)(\sigma-1)\right] \end{array} \\
B_2^{\mathrm{sph}} &= \begin{array}{l} \frac{\gamma_2}{2\Delta} \\ \times\Big\{2n^4+(2\omega_{\mathrm{DL}}^{\mathrm{sph}}\sigma+2\omega_{\mathrm{DL}}^{\mathrm{sph}}+10\sigma-3)n^3 \\ +\Big[2\sigma{\omega_{\mathrm{DL}}^{\mathrm{sph}}}^2+(5\sigma-1)\omega_{\mathrm{DL}}^{\mathrm{sph}}+3\sigma-2\sigma^2-2\Big]n^2 \\ +\Big[\sigma{\omega_{\mathrm{DL}}^{\mathrm{sph}}}^2(1-4\sigma)-\left(14\sigma^2+1\right)\omega_{\mathrm{DL}}^{\mathrm{sph}}+3\ -9\sigma-8\sigma^2\Big]n \\ -2\sigma\left({\omega_{\mathrm{DL}}^{\mathrm{sph}}}^2+4\omega_{\mathrm{DL}}^{\mathrm{sph}}+3\right)\Big\} \end{array} \\
B_3^{\mathrm{sph}} &= \begin{array}{l} \left[2n\left(n^2-1\right)(\sigma-1)/\sigma\Delta\right] \\ \times\Big[(n+2)\left(\tilde{\lambda}_{\mathrm{b}}-\gamma_3\right)-3\left(\tilde{\lambda}_{\mathrm{b}}-1\right)\Big] \end{array}
\end{aligned}
\tag{2.62}
$$

with:

$$\begin{aligned}
\gamma_1 &= \tfrac{\sigma}{\sigma-1}\int_1^\sigma \tfrac{\tilde{\lambda}(x)}{x}\,\mathrm{d}x \\
\gamma_2 &= \tfrac{1}{\sigma-1}\int_1^\sigma \tfrac{\tilde{\lambda}(x)}{x}\ln\left(\tfrac{\sigma-1}{\mathrm{x}-1}\right)\,\mathrm{d}x \\
\gamma_3 &= \tfrac{1}{\sigma-1}\int_1^\sigma \tilde{\lambda}(x)\,\mathrm{d}x \\
\Delta &= 2a\omega_{\mathrm{DL}}^{\mathrm{sph}} + b - 2a \\
a &= (\sigma+1)n+1 \\
b &= 2n^2+(4+5\sigma)n+4 \\
c &= -[(\sigma-1)/\sigma]n^3+2n^2+[3(\sigma+1)-1/\sigma]n+2
\end{aligned} \tag{2.63}$$

Equation (2.61) has a very similar form to the planar flame dispersion relation. It also contains a low-order term representing the destabilising effect of the Darrieus-Landau mechanism and a higher-order term for diffusive phenomena. One major difference with planar flames is that the dispersion relation evolves with the flame propagation. It means that a harmonic mode which is initially stable can become unstable at greater flame radius. The stability at small kernel size is explained by the influence of flame stretch (and more particularly curvature) [89, 121–123]. Phenomenologically, a local disturbance cannot produce a cell if its growth rate is slower than that of the flame expansion. This characteristic will be illustrated in Section 2.3.4. Concretely, that time-dependent stability/instability of the flame can be illustrated by the concept of *instability peninsula*. If the dispersion relation (2.61) is plotted against the flame radius for a large range of harmonics, one obtains Figure 2.14. The plot is coloured by the normalised growth rate of the perturbations. The positive zone (unstable harmonics) is delimited by the black curve and forms the characteristic peninsula shape. The stability at small flame radii is recovered on the left as well as the existence of a critical radius (or Peclet number[1]) for the onset of the TD instability. As the kernel grows, the range of unstable wavelengths widens following two asymptotes [124, 125]:

- the bottom asymptote (low-order harmonics) reaches a constant value n^*. It represents the largest expected cell size and scales with the flame radius: $\lambda_{\max} = 2\pi r_{\mathrm{f}}/n^*$;
- the top branch linearly increases with the flame radius and characterises the smallest cells that can be observed $\lambda_{\min} \propto 2\pi\delta_{\mathrm{d}}$: it is naturally related to the flame thickness.

Both Equations (2.58) and (2.61) express the fact that:

- if the mixture effective Lewis number is small enough, the flame becomes at some point unstable to all perturbation scales;
- if it is higher, diffusive phenomena stabilise small-scale perturbations but long waves stay unstable: Darrieus-Landau instabilities happen at large scales.

[1]The Peclet number for a spherical flame is defined as the flame radius normalised by the flame thickness (the diffusive thickness definition of Equation (2.15) is often used).

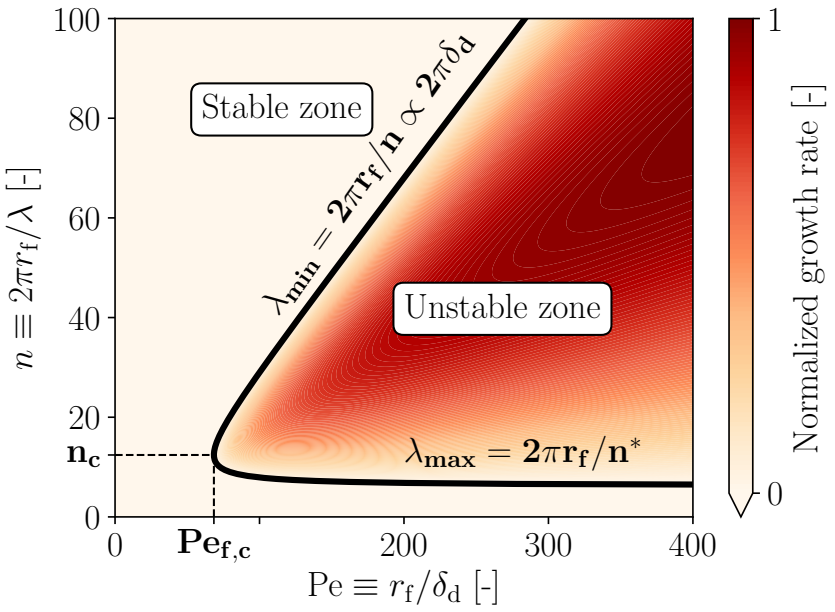

Figure 2.14: Instability peninsula for a TD-unstable spherical flame. Lean H_2-air flame at $\Phi = 0.5$ under atmospheric conditions. The growth rate is arbitrarily normalised by its maximum value over the considered range of $(\mathrm{Pe_f}, n)$.

2.3.3 Buoyancy instabilities

Gravity is seldom accounted for in combustion simulations. Its effects on flame propagation are generally neglected when experimental measurements need to be compared with the theory or numerical simulations [126]. However, it can play a role in either stabilising or destabilising a flame depending on the flame direction of propagation relative to the gravity vector. The unstable scenario has been most studied outside the combustion field under the name of *Rayleigh-Taylor instability*. It happens when a lighter fluid pushes into a heavier fluid. This is exactly the case when the hot gases of a flame ascend by gravity (upward propagation) into the fresh mixture. The main difference with non-reactive flows is that a flame is by essence not driven only by the convective force of gravity. Therefore, the buoyancy instability interacts not only with the general flame dynamics but also with the two previously cited instability mechanisms. A common example of gravity-sensitive flame is the case of a mixture ignited at one end of a closed vertical vessel. This scenario also constitutes a fundamental set-up for explosions in confined areas and is further detailed in Chapter 3. In particular, it will be shown that in the absence of gravity, the dynamics of such flame is driven by the generated flow which has a piston-like effect on the flame tip. Such acceleration acts with or against the gravity body-forces:

- if the flame is ignited at the top of the tube, its propagation goes against the natural convection wanted by buoyancy: the flame is stable;
- if it is ignited at the bottom, its propagation is in the same direction as buoyancy effects and adds up to the classical Rayleigh-Taylor instability mechanism: the flame

is unstable.

Because the buoyancy instability is never happening alone on the flame, it is usually studied in conjunction with other instability mechanisms. Namely, Landau [108] has developed another dispersion relation considering hydrodynamic effects and gravity on the flame front:

$$(\sigma+1)\hat{\omega}^2 + 2\sigma\hat{\omega} - (\sigma - \mathrm{Fr}^{-1})(\sigma-1) = 0 \tag{2.64}$$

where $\mathrm{Fr} \equiv kS_\mathrm{L}^{0\,2}/g$ is the Froude number of a specific wave number k and g the gravitational acceleration. This number quantifies the relative influence of buoyancy due to gravity and chemical effects related to combustion.

Equation (2.64) echoes the former dispersion relation with pure hydrodynamic effects given by Equation (2.57). Its resolution leads to the new root:

$$\omega = \frac{1}{\sigma+1}\left[\sqrt{(\sigma^3+\sigma^2-\sigma)\,S_\mathrm{L}^{0\,2}k^2 - (\sigma^2-1)\,gk} - \sigma S_\mathrm{L}^0 k\right] \tag{2.65}$$

A classical Taylor series expansion for $k \ll 1$ and $k \gg 1$ and for $g > 0$ versus $g < 0$ leads to the following conclusions:

- For downward propagation, disturbances for which $k < g/\left(\sigma S_\mathrm{L}^{0\,2}\right)$ are stable: gravity stabilises long waves;
- For upward propagation, the flame stays unconditionally unstable (as it was the case for pure hydrodynamic effects): gravity further destabilises the flame.

2.3.4 General coupling of instability mechanisms

While the joint effects of Darrieus-Landau and thermo-diffusive instabilities on a planar flame are theoretically explained by Equation (2.58) and the combination of Darrieus-Landau and buoyancy instabilities give rise to Equation (2.64), no general dispersion relation encompassing the three phenomena together is to be found in the literature[1]. On top of that, the dispersion relations presented so far rely on a restrictive small-perturbation assumption: they evaluate the stability of disturbances as they appear on the flame surface but do not predict their long-term non-linear evolution. Nevertheless, a qualitative approach can be associated with experimental measurements of their coupling. To illustrate the various possible interactions between the three instability mechanisms, H_2-air mixtures with different amounts of hydrogen are analysed in the following.

Ultra-lean H_2-air flames: predominance of bulk buoyancy
The effects of buoyancy are known to become important for near-flammability-limit mix-

[1]Law and Sung [102] do provide a general dispersion relation which resembles Equation (2.64) and adds thermo-diffusive effects in the form of a Markstein number. Nevertheless, this response to stretch is arbitrarily chosen rather than demonstrated from conservation equations as it is done in the classical asymptotic theory.

tures. Indeed, their contribution relative to the flame inertial propagation at S_{L}^0 is measured by the Richardson number Ri (somehow close to a Froude number):

$$\begin{aligned} \mathrm{Ri} &\equiv \frac{\Delta\rho g L}{\rho_{\mathrm{u}} {S_{\mathrm{L}}^0}^2} \\ &= \frac{\sigma - 1}{\sigma} \frac{gL}{{S_{\mathrm{L}}^0}^2} \end{aligned} \tag{2.66}$$

The characteristic velocity $\Delta\rho g L/\rho_{\mathrm{u}}$ corresponds to the velocity that a low density gas achieves after rising a distance L [127]. An analysis using orders of magnitude [126] shows that buoyant forces may be neglected for mixtures with $S_{\mathrm{L}}^0 = \mathcal{O}(1\ \mathrm{m/s})$. Under atmospheric conditions, this is usually only the case close to stoichiometry. In off-stoichiometric mixtures, the flame is also subject to the thermo-diffusive instability (following an effective Lewis number analysis).

To understand whether or not gravity plays a significant role on flame stability when compared to the diffusional-thermal path, it is necessary to look at numerical and experimental results. For instance, Patnaik and Kailasanath [128] have simulated two-dimensional nominally planar flames in lean hydrogen-air mixtures subject to gravity. Their data include upward-propagating, downward-propagating flames as well as zero-gravity cases. It is demonstrated that the role of gravity only predominates near the lean flammability limit: a 12% hydrogen-air ($\Phi \approx 0.325$) flame constitutes a limit case that is insensitive to the buoyant forces. Leaner mixtures are either strongly stabilised (downward propagation) or destabilised (upward propagation) by buoyant forces.

As previously mentioned, the stability of spherical flames evolves with time. Since there is no real downward or upward propagation distinction, the result presented in the last paragraph does not hold anymore. Instead, one can only compare cases with or without gravity showing that it has two main impacts:

- Buoyant forces distort the hot flame kernel as a whole in the vertical direction;
- The buoyancy instability mechanism destabilises the flame front at a local level.

The first phenomenon is macroscopic so that its effect can be quantified through a Richardson number defined for the spherical flame as [129]:

$$\begin{aligned} \mathrm{Ri} &\equiv \frac{\sigma - 1}{\sigma} g r_{\mathrm{f}} \left(\frac{\mathrm{d}r_{\mathrm{f}}}{\mathrm{d}t} \right)^{-2} \\ &\approx \frac{\sigma - 1}{\sigma} \frac{g r_{\mathrm{f}}}{\left(\sigma S_{\mathrm{L}}^0\right)^2} \end{aligned} \tag{2.67}$$

Equation (2.67) shows that gravity becomes important for either slow flames, or big kernels. At a given sphere size, it holds sway over normal flame propagation for near-flammability-limit mixtures. In its extreme version, it can lead to so-called *flame balls*

rising in the unburnt mixture with very mild combustion [130]. For example, Anikin *et al.* [131] have succeeded in igniting ultra-lean hydrogen-air flames under atmospheric conditions. Their work (see Figure 2.15) shows that flames with H_2 volume percentage lower than 9% ($\Phi = 0.235$) evolve into a very particular shape that they call "vortex-like". Such flames are almost not cellular at all. Similar dynamics have been observed for nitrogen-diluted rich H_2-air flames by Berger *et al.* [129].

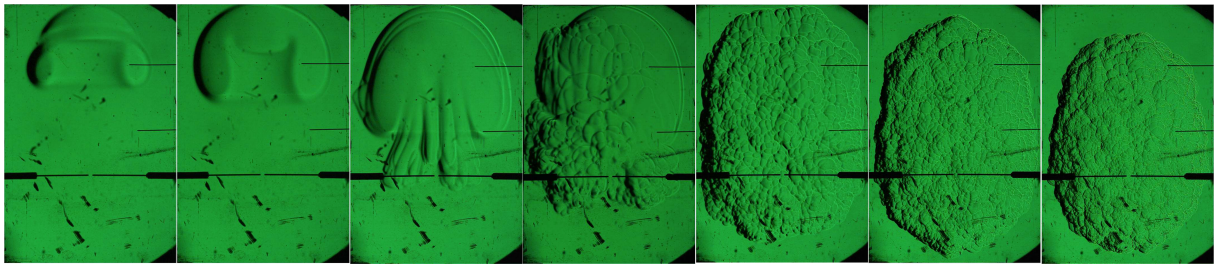

Figure 2.15: Ultra-lean to lean hydrogen-air flames under atmospheric conditions. From left to right: $X_{H_2} = 6 - 7.5 - 8.8 - 9 - 10 - 12 - 16\%$ ($\Phi = 0.152 - 0.193 - 0.230 - 0.235 - 0.264 - 0.325 - 0.453$). Each picture size is 134×200 mm^2. Taken from Anikin *et al.* [131].

Lean H_2-air flames: predominance of Rayleigh-Taylor instability – thermo-diffusive instability

As the hydrogen content is increased from ultra-lean to lean, the Rayleigh-Taylor instability kicks in. Although the flame kernel is still distorted by the bulk gravity effect, cellular structures scatter on the flame front at a local level. These cells are also naturally promoted by the thermo-diffusive instability. Anikin *et al.* [131] add that the apparent asymmetry of their flames above 12% H_2 is due to the influence of the bottom wall of their combustion chamber and would not be observed in a freely-expanding spherical flame. Gravity-induced distortion of the flame kernel is indeed generally not observed for lean hydrogen-air mixtures at such equivalence ratios [132]. Numerous experimental studies about these flames [133–136] show their (statistical) spherical symmetry. The example of the work of Goulier [134] is depicted in Figure 2.16. Although it is hard to distinguish the contribution of Rayleigh-Taylor effects on the cells of a flame front, it is expected to vanish progressively as Φ is increased so that the thermo-diffusive effects take over.

Besides, emphasis must be put on the natural unsteadiness of the cellular structure development on spherical flame fronts. This can be linked to the dispersion relation given by Equation (2.61) which shows that the flame can start as a stable kernel and grow unstable after reaching a critical size. It is evidenced by comparing the flame surface at different instants. Even at lean conditions, the flame kernel is initially smooth (if ignited in a quiescent environment). Figure 2.17 shows experiments from Kim *et al.* [137] at lean ($\Phi = 0.5$) and rich ($\Phi = 2.0$) operating conditions. At the maximal size, the lean flame is strongly perturbed by thermo-diffusive instabilities whereas the rich flame is still smooth. Nevertheless, the Darrieus-Landau instability pathway is present for all flames. Provided that kernels can grow bigger in a laminar regime, thermo-diffusive phenomena are no longer sufficiently stabilising and cells induced by the hydrodynamic instability spread on

the surface. The existence of a critical radius (or equivalently a critical Peclet) for the onset of intrinsic flame front instabilities has been known for decades and is the subject of numerous experimental measurements often aimed at numerical modelling [133, 138–142].

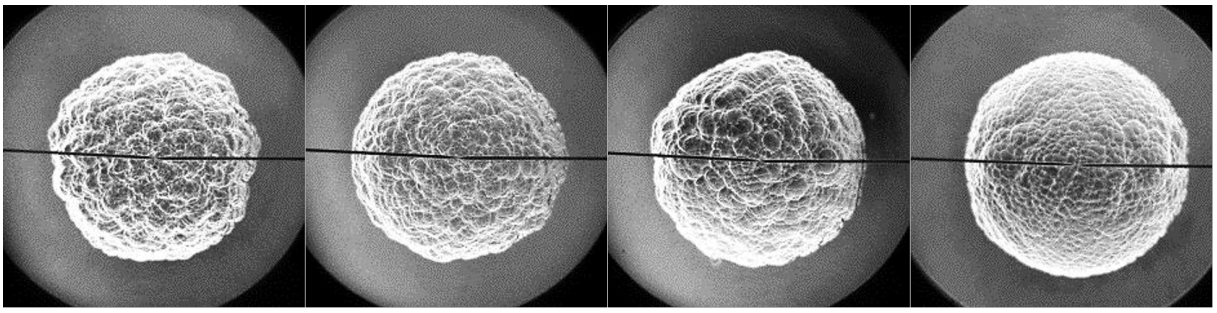

Figure 2.16: Lean hydrogen-air flames under atmospheric conditions. From left to right: $X_{H_2} = 16 - 20 - 24 - 28\%$ ($\Phi = 0.453 - 0.595 - 0.752 - 0.926$). Each picture diameter is 97 mm. Taken from Goulier [134].

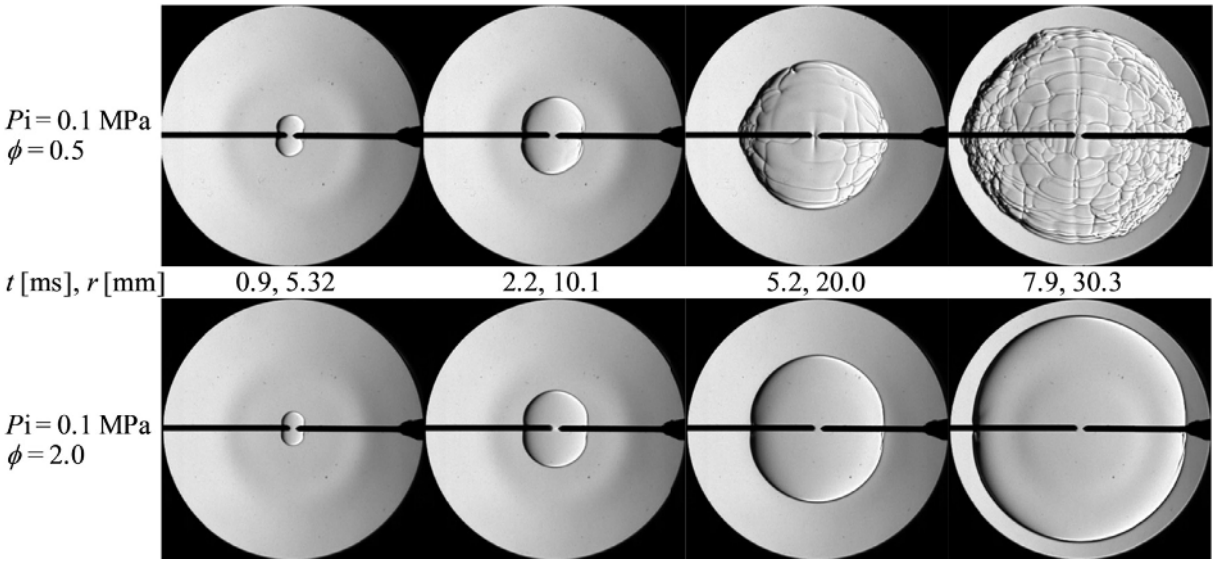

Figure 2.17: Dynamics of hydrogen-air flames under atmospheric conditions. Top: $X_{H_2} = 17.4\%$ ($\Phi = 0.5$). Bottom: $X_{H_2} = 45.7\%$ ($\Phi = 2.0$). Each picture diameter is 100 mm. Taken from Kim *et al.* [137].

Near-stoichiometric and rich H_2-air flames: predominance of Darrieus-Landau instability

When the mixture composition approaches stoichiometry, the effective Lewis number increases (as explained in Section 2.2.3) so that thermo-diffusive instabilities become milder and milder. In this process, the Darrieus-Landau mechanism is no longer attenuated by diffusion and the flames become unstable at large radii. Under atmospheric conditions, the limitations in size for the optical access to the spherical bomb apparatus make it hard to observe hydrodynamically unstable rich H_2-air flames (see for example Figure 2.17 where the rich flame is still smooth). However, higher pressures enhance the instability [106, 141, 143] and allow such visualisation. For instance, Yang *et al.* [106] have assessed the effect of pressure on the flame cellularity at a given size (Figure 2.18).

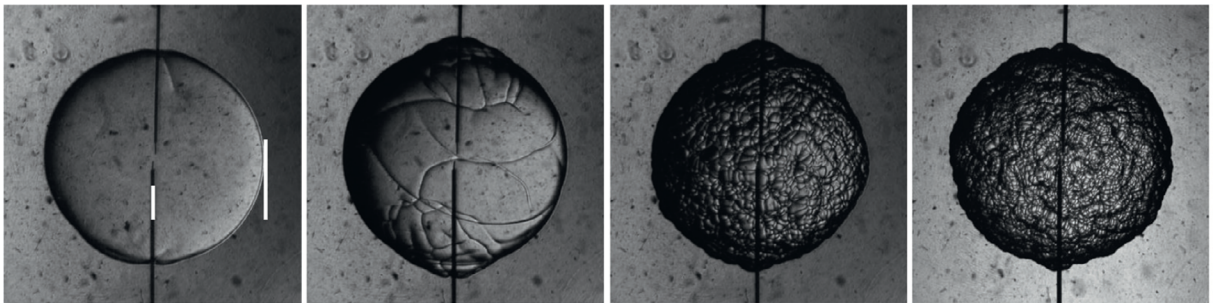

Figure 2.18: Stoichiometric hydrogen-air flames under various pressures. From left to right: $P = 1 - 2.5 - 5 - 10$ atm. Each kernel diameter is 15 mm. Taken from Yang *et al.* [106].

Ultra-rich H_2-air flames: predominance of Darrieus-Landau instability – bulk buoyancy

Very few experimental studies about the stability of ultra-rich hydrogen-air mixtures are to be found in the literature [123, 137, 144, 145]. Though, theoretical considerations can give insights into the driving mechanisms for their propagation. Such flames are known to decelerate with positive stretch. The effective Lewis number of these mixtures is indeed approaching that of O_2. This also conveys the stabilising influence of thermo-diffusive processes. At greater size or higher pressures, these flames will only be subject to the hydrodynamic instability as observed by Kwon *et al.* [123]. Near the upper flammability limit, the extremely low flame speed values will boost the relative effect of gravity as a bulk force so that phenomena similar to the ultra-lean side will be observed.

2.3.5 Implications for combustion theory and modelling

Even though the dispersion relations of the asymptotic theory rely on a set of simplifying assumptions, they allow a fairly good understanding of flame front instabilities origins and early dynamics. These intrinsic phenomena have many practical implications for combustion theory and modelling which become particularly prevalent for the lean hydrogen-air mixtures studied in this manuscript.

The most evident effect of intrinsic instabilities is the flame front wrinkling induced by the cellular patterns development. As will be explained in the next section, this additional wrinkling enhances the flame propagation by providing more space for reactions to occur. In the case of lean hydrogen-air mixtures, the acceleration can be substantial. For example, using direct numerical simulations of statistically planar flames[1] in atmospheric conditions, Howarth *et al.* [146] have measured flame speeds of $2 - 10$ times the laminar flame speed value. If the speed-up ratio is of this order of magnitude on the simplest planar flame, it could be even higher for more complex cases. In particular, intrinsic instabilities can interact with other flame propagation mechanisms classically encountered in explosion scenarios. From a CFD point of view, it means that flame front instabilities

must be modelled.

Flame front instabilities has another practical implication. As has been emphasised in Section 2.1.1.1, the laminar flame speed is one of the most fundamental flame properties for combustion theory, also featuring in most combustion models. Its value generally comes from experiments. The experimental determination of the laminar flame speed often uses the spherical flame extrapolation method [147–155]. It relies on the response to stretch detailed in Section 2.2.4: a laminar spherical flame propagates at a stretched speed that tends towards the laminar flame speed S_L^0 as the kernel grows. However, flame front instabilities can hinder such extrapolations by triggering an acceleration of the flame front as they develop. For the lean hydrogen-air flames considered in this thesis, it is a well-known fact that cellular instabilities complicate the experimental estimation of S_L^0 [98, 148, 149, 151, 154, 156, 157]. The subsequent uncertainty becomes all the more hampering far from stoichiometry where it adds up to the difficulty of measuring very low flame speeds [94, 152, 153, 158].

The last implication that is paramount to this thesis has to do with numerical simulations. The preceding sections have indeed demonstrated that flame front instabilities can appear on a very wide range of length scales. But computational costs being a major limitation for large-scale combustion set-ups, the mesh edge size is often strongly reduced to allow for affordable simulations (see Section 4.3). This means that most small-scale instability cellular patterns cannot be resolved on typical meshes. The modelling of flame front instabilities for large-scale simulations therefore constitutes one of the uppermost issues addressed in the present work.

2.4 Turbulent flame speed decomposition

Section 2.1.1 has introduced the main flame speed definitions found in combustion theory. It has insisted on the local nature of these quantities which vary with the mixture composition, temperature, flow features, etc.. However, it has been established that for propagating flames commonly found in explosion scenarios, it is easier to define a global flame speed, hereafter called *turbulent flame speed* (e.g. the evolution of the most advanced point in a well-chosen direction). This integral quantity results from the sum of local factors influencing the flame front evolution. Such phenomena as flame stretch and intrinsic instabilities have been presented in Sections 2.2 and 2.3. In turbulent regimes, the problem is complicated by the interactions of the combustion wave with turbulent eddies, generating a highly wrinkled flame brush. To better understand the dynamics of flame propagation, this section tries to describe the various factors contributing to the overall turbulent flame speed. It also provides formulas for their estimation that will be used in this manuscript.

[1] The flames are only statistically planar due to the instabilities.

2.4.1 Surface enlargement effect

In a flamelet regime, a flame brush burns according to its chemical flame speed and its total surface area. A larger surface gives indeed more room for the reactions to occur. Under Damkhöler's hypothesis, the resulting turbulent flame speed is based on the laminar flame speed S_{L}^0, enhanced by the flame surface wrinkling Ξ:

$$S_{\mathrm{T}}^0 = \Xi S_{\mathrm{L}}^0 \tag{2.68}$$

The wrinkling factor is defined by:

$$\Xi \equiv \frac{\Sigma}{\Sigma_{\mathrm{ref}}} \tag{2.69}$$

where Σ is the real flame surface area and Σ_{ref} is a reference flame surface area. Several definitions of flame surface area can be found in the literature. For example, it can be computed as the surface of an isocontour [159]:

$$\Sigma \equiv \int_V \delta(c - c^*)|\nabla \mathbf{c}| \, \mathrm{d}V \tag{2.70}$$

where V refers to the whole domain. $|\nabla \mathbf{c}|$ is the local flame surface density (FSD), as used in some turbulent combustion models [160]. The same problem as for the FDS arises: the value of Σ computed using Equation (2.70) usually depends on c^*. In the rest of the thesis, a generalised flame surface definition is preferred [159]:

$$\Sigma \equiv \int_V |\nabla \mathbf{c}| \, \mathrm{d}V \tag{2.71}$$

Definition (2.71) reflects the contribution of all flame isocontours to its total area.

The real difficulty lies in the definition of a reference flame surface. For canonical flames such as statistically spherical and planar flames, such definition is straightforward. But for more complex flames, the choice of Σ_{ref} is ambiguous and usually prevents the computation of S_{T}^0. The global burning intensity is instead quantified for example by the integrated heat release rate, but this latter does not correspond to a flame speed.

2.4.2 Global stretch effect

Equation (2.68) provides a direct relation between the flame surface and its speed. However, it has been shown in Section 2.2 that for lean H_2-air flames, stretch can locally affect the flame velocity. The local stretch factor I_0 is defined at an arbitrary position by:

$$I_0 \equiv \frac{S_{\mathrm{c}}}{S_{\mathrm{L}}^0} \tag{2.72}$$

where S_{c} is the local consumption speed defined in Section 2.1. The global effect of stretch on turbulent flame speed can be assessed by a spatial average on the flame front

$\mathcal{F}$ (surface average), weighted by the FSD (denoted $\overline{\bullet}$):

$$\overline{I_0} \equiv \frac{\int_{\mathcal{F}} I_0 |\nabla \mathbf{c}| \, \mathrm{d}A}{\int_{\mathcal{F}} |\nabla \mathbf{c}| \, \mathrm{d}A} \tag{2.73}$$

As explained in Section 2.1.1.2, in practice, the flame front can be taken as an isosurface of progress variable:

$$\mathcal{F} \equiv \{P \in V / c(P) = c^*\} \tag{2.74}$$

and V is the entire domain. Now, $\overline{I_0}$ must be added to Equation (2.68), yielding:

$$\begin{aligned} S_\mathrm{T} &= \Xi \overline{I_0} S_\mathrm{L}^0 \\ &= \frac{\Sigma}{\Sigma_\mathrm{ref}} \overline{\left(\frac{S_\mathrm{c}}{S_\mathrm{L}^0} \right)} S_\mathrm{L}^0 \end{aligned} \tag{2.75}$$

In practice, the computation of local FCS for all loci of the flame front can be tedious. Indeed, it requires the resolution of a streamline equation for all flame points. This operation can rapidly become costly. Here, another expression for $\overline{I_0}$ is derived. The choice of Σ_ref for complex flame topologies usually prevents the computation of S_T. Fortunately, determining its value is not necessary to evaluate global stretch effects. The turbulent flame speed is also linked to the total fuel consumption through:

$$\begin{aligned} S_\mathrm{T} &\equiv \frac{\Omega}{\Sigma_\mathrm{ref}} \\ &= -\frac{1}{\Sigma_\mathrm{ref}} \frac{1}{\rho_\mathrm{u} (Y_\mathrm{F,u} - Y_\mathrm{F,b})} \int_V \dot{\omega}_\mathrm{F} \, \mathrm{d}V \end{aligned} \tag{2.76}$$

where Ω is the total consumption rate (in m^3/s). In this relation, local stretch effects are directly included in the local fuel consumption $\dot{\omega}_\mathrm{F}$. Comparing Equations (2.75) and (2.76), it comes:

$$\overline{I_0} = -\frac{1}{\Sigma S_\mathrm{L}^0} \frac{1}{\rho_\mathrm{u} (Y_\mathrm{F,u} - Y_\mathrm{F,b})} \int_V \dot{\omega}_\mathrm{F} \, \mathrm{d}V \tag{2.77}$$

All terms of Equation (2.77) can be easily computed on-the-fly in a simulation, whatever the flame configuration. It provides an elegant way of evaluating global stretch effects with simple scalar operations.

Chapter 3

Acceleration mechanisms for explosions in confined and obstructed areas

Sommaire

Chapter 2 has introduced the fundamental quantities commonly used in combustion. Particular attention has been paid towards the description of flame stretch and intrinsic flame front instabilities which represent strong acceleration factors for the lean hydrogen-air mixtures considered in this manuscript. Their effects have been illustrated on canonical flame configurations such as the counterflow premixed flame and the outwardly propagating spherical flame. The latter can to some extent represent free-atmosphere explosions. On the other hand, a lot of accidents happen in confined and obstructed areas. Section 1.3 has illustrated this issue with some past events in such environments as:

- personal living areas;
- industrial buildings and factories;
- pipelines, tanks and other facilities related to the transport and storage of combustible mixtures.

Within a confined space, a flame front interacts with the surrounding walls in multiple ways:

- thermal interactions: the temperature of the walls can mitigate flame acceleration through heat loss [161] (especially in narrow tubes and for slow flames). Another more complicated effect is certainly the thermal load and damage that explosions can cause to materials constituting walls (e.g. through pyrolysis). Such effects are not studied in the present work;

- structural interactions: one of the main practical applications of explosions studies is to evaluate the damage they can induce on the structures through the overpressures that are generated. In addition to the absolute maximum overpressure $P_{\max}$, the severity of an explosion must also be linked to: the maximum rate of pressure rise $(\mathrm{d}P/\mathrm{d}t)_{\max}$, allowing the definition of the so-called deflagration index [154, 162]; and the integral of overpressure over time $\int P\,\mathrm{d}t$ (also called impulse) [43, 163]. Fluid-structure interactions are out of the scope of this thesis;

- flow interactions: the presence of walls certainly modifies the flow in front of the flame in such a way that it can foster flame acceleration. At microscales, wall roughness is known to be conducive to flame acceleration [164–166] but this matter is also out of the scope of this study.

The last item is at the core of explosion studies from the fluid mechanics point of view. An infinite number of geometries can be imagined for explosion scenarios. The severity of explosions depends on a myriad of factors [167, 168] such as the type of fuel and its concentration [28, 169–173], mixing [174, 175], ignition location and energy [38, 171, 172, 176, 177], venting conditions of the chamber [171, 172, 178, 179], presence of obstacles, their geometry and arrangement [173, 180–185]. However, some fundamental acceleration mechanisms can be retrieved in most sequences of events. Two pathways for flame acceleration have been identified for this thesis and are presented in this chapter. Namely, the pure effect of confinement through the so-called finger flame phenomenon, and the effect of obstacles.

3.1 The finger flame phenomenon

This section is dedicated to describing a fundamental mechanism for flame acceleration in smooth tubes: the so-called *finger flame phenomenon*. When a flame propagates through such high-aspect-ratio confined environments, the shape imposed by lateral walls leads to a rapid flame surface area increase accompanied by an exponential flame acceleration. This phenomenon is observed not only in the canonical smooth tube set-up, but also in a number of academic configurations that are representative of real explosion scenarios [57, 186, 187].

3.1.1 Mechanism

The ignition of a premixed combustible mixture at one end of a tube almost constitutes a canonical configuration for flame dynamics studies. First suggested by Clanet and Searby [188] from experimental observations, the theory of finger-shaped flames propagation was later formalised by Bychkov *et al.* [189]. The sequence of events at the early stages has been summarised by Dounia [53] (see Figure 3.1). As suggested in Section 2.1.1, the flame tip is defined as the most advanced point of the flame brush in the direction of the tube while the flame skirt measures its progress towards lateral walls:

- after ignition, the flame stays almost perfectly hemi-spherical for a while, devoid of the lateral walls effect (phases a and b). If the ignition plate is assumed to behave with an adiabatic slip-wall condition, the propagation is very similar to that of a genuine spherical flame. In particular, the flame curvature is highest at this stage, generating strong stretch effects for non-unity Lewis number mixtures (see Section 2.2.4);
- then, as the flame skirt approaches the lateral walls, the confinement forces the flame to take on a tubular or "finger" shape (phase c). The subsequent surface area increase is naturally accompanied by a strong flame acceleration (see Section 2.4.1);
- finally, as soon as the flame skirt touches the lateral wall, a sudden deceleration is observed, induced by the flame surface area shrinking (phase d).

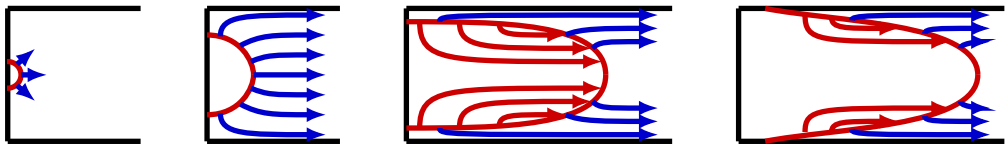

Figure 3.1: Phenomenology of flame propagation in a tube. Reproduced from [53].

3.1.2 Equations

The finger flame acceleration mechanism is quantitatively justified from simple analytical equations. They have first been developed by Bychkov *et al.* [189] and later generalised by Valiev *et al.* [190] to account for weak compressibility effects. The following sections recall the main steps of the rationale as well as the salient points in two canonical geometries. The underlying assumptions are listed below:

- slip walls: any friction at the walls is neglected. It represents a strong assumption given that the matter of this section is about confinement effects on flame acceleration. However, Valiev *et al.* [190] have demonstrated a quantitative agreement of their theory with experiments and numerical simulations. Besides, the contribution

of non-slip boundary conditions to flame speed-up (also known as the *Shelkin mechanism* [164]) is believed to become significant only when the flame skirt has reached the walls and if the tube is long enough [165];

- adiabatic walls: any heat loss at the walls is neglected. Chiefly, the influence of heat transfers at the ignition plate (decelerating the flame) is assumed to be of lower order and slow compared to the finger flame acceleration mechanism [191]. Thermal exchanges with lateral walls only become important for narrow tubes and very slow-burning flames [192–196];
- infinitely thin flame front: the finger flame theory relies on basic hydrodynamic equations which do not take into account the finite structure of the flame front. In particular, any non-unity Lewis number effect (detailed in Section 2.2.4) is discarded.

Planar case

The planar case corresponds exactly to a flame propagating in a two-dimensional tube. It may also be applicable to three-dimensional cases in channels with a rectangular cross-section (provided that the latter has a high aspect ratio). Let's first consider the flow in the vicinity of the tube end wall as depicted in Figure 3.2. Spatial coordinates are non-dimensionalised by the tube radius R_{tube}, velocities by the laminar flame speed S_{L}^0 and time by $R_{\text{tube}}/S_{\text{L}}^0$:

$$\begin{cases} \xi \equiv \frac{x}{R_{\text{tube}}}, & \eta \equiv \frac{r}{R_{\text{tube}}} \\ v \equiv \frac{u_x}{S_{\text{L}}^0}, & w \equiv \frac{u_r}{S_{\text{L}}^0} \\ \tau \equiv t\frac{S_{\text{L}}^0}{R_{\text{tube}}} \end{cases} \tag{3.1}$$

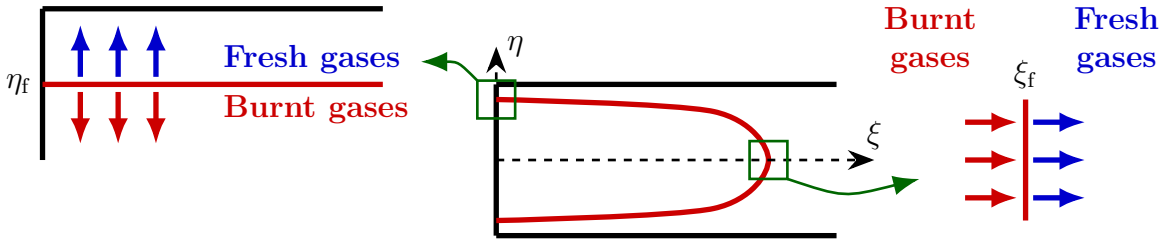

Figure 3.2: Flow close to the flame tip and flame skirt in a finger flame configuration.

In the planar case, the continuity equation is given by:

$$\frac{\partial w}{\partial \eta} + \frac{\partial v}{\partial \xi} = 0 \tag{3.2}$$

Then, assuming a potential flow in the fresh gases and the hot gases separately, and using the boundary conditions, one has:

$$\begin{aligned} v_{\text{u}} &= C_1\xi, \quad w_{\text{u}} = C_1(1-\eta) \\ v_{\text{b}} &= C_2\xi, \quad w_{\text{b}} = -C_2\eta \end{aligned} \tag{3.3}$$

In order to make the link between fresh and hot gases velocity fields, conditions on the flame front are considered. The flame skirt moves towards the lateral wall at the laminar

flame speed increased by the flow velocity ahead of it, namely in adimensional coordinates:

$$\frac{\mathrm{d}\eta_\mathrm{f}}{\mathrm{d}\tau} - w_\mathrm{u} = 1 \tag{3.4}$$

What's more, conservation of tangential velocity and jump in normal velocity through the flame gives:

$$\begin{aligned} v_u - v_b &= 0 \\ w_u - w_b &= \sigma - 1 \end{aligned} \tag{3.5}$$

Injecting expressions (3.3) into Equations (3.4) and (3.5) yields:

$$\frac{\mathrm{d}\eta_\mathrm{f}}{\mathrm{d}\tau} - (\sigma - 1)\,(1 - \eta_\mathrm{f}) = 1 \tag{3.6}$$

This differential equation connects the flame skirt kinematic velocity with its position. Solving it gives the skirt position over time:

$$\eta_\mathrm{f} = \frac{\sigma}{\sigma - 1}\left[1 - \exp(-(\sigma - 1)\tau)\right] \tag{3.7}$$

Applying the same rationale for the flame tip using the flow field in the vicinity of the channel axis, one has:

$$\frac{\mathrm{d}\xi_\mathrm{f}}{\mathrm{d}\tau} - (\sigma - 1)\xi_\mathrm{f} = \sigma \tag{3.8}$$

And solving it gives:

$$\xi_\mathrm{f} = \frac{\sigma}{\sigma - 1}\left[\exp\left((\sigma - 1)\tau\right) - 1\right] \tag{3.9}$$

In physical coordinates, one has:

$$\begin{cases} x_\mathrm{f} = \dfrac{\sigma R_\mathrm{tube}}{\sigma - 1}\left[\exp\left(\dfrac{(\sigma - 1)S_\mathrm{L}^0}{R_\mathrm{tube}}t\right) - 1\right] \\ r_\mathrm{f} = \dfrac{\sigma R_\mathrm{tube}}{\sigma - 1}\left[1 - \exp\left(-\dfrac{(\sigma - 1)S_\mathrm{L}^0}{R_\mathrm{tube}}t\right)\right] \end{cases} \tag{3.10}$$

and:

$$\begin{cases} \dfrac{\mathrm{d}x_\mathrm{f}}{\mathrm{d}t} = \sigma S_\mathrm{L}^0 + \dfrac{(\sigma - 1)S_\mathrm{L}^0}{R_\mathrm{tube}}x_\mathrm{f} \\ \dfrac{\mathrm{d}r_\mathrm{f}}{\mathrm{d}t} = S_\mathrm{L}^0 + (\sigma - 1)S_\mathrm{L}^0\left(1 - \dfrac{r_\mathrm{f}}{R_\mathrm{tube}}\right) \end{cases} \tag{3.11}$$

The flame tip velocity and position are linked by a simple affine relation and most importantly, the flame tip undergoes an exponential acceleration in time. The rate of acceleration is simply expressed as a function of the problem parameters:

- S_L^0: the laminar flame speed represents the reactivity of the mixture. The more reactive, the stronger the finger flame acceleration;
- σ: the thermal expansion ratio also carries a chemical information. It shows the piston-like effect that lies behind the finger flame mechanism. As the combustion

wave propagates in the tube, gases suffer a density drop accompanied by a strong expansion. The impermeability of lateral walls forces that expansion to push along the tube direction thereby accelerating the flame tip;

- R_{tube}: the tube radius is the only geometrical parameter of the model which also conveys the piston effect. The narrower the tube, the stronger the finger flame acceleration. When $R_{\text{tube}} \longrightarrow \infty$, the flame tip recovers a constant speed σS_{L}^0 characteristic of a planar flame propagating away for a wall (no stretch effects are included in the analysis).

Axisymmetric case

Following exactly the same procedure but in an axisymmetric geometry, Valiev *et al.* [190] have established differential equations relating flame skirt and tip velocity and position:

$$\begin{aligned} \frac{\mathrm{d}\eta_{\text{f}}}{\mathrm{d}\tau} - (\sigma-1)\left(1-\eta_{\text{f}}^2\right) &= 1 \\ \frac{\mathrm{d}\xi_{\text{f}}}{\mathrm{d}\tau} - 2\alpha\tanh(\alpha\tau)\xi_{\text{f}} &= \sigma \end{aligned} \tag{3.12}$$

where:

$$\alpha \equiv \sqrt{\sigma(\sigma-1)} \tag{3.13}$$

Solving them yields:

$$\begin{aligned} \eta_{\text{f}} &= \frac{\sigma}{\alpha}\tanh(\alpha\tau) \\ \xi_{\text{f}} &= \frac{\sigma}{2\alpha}\sinh(2\alpha\tau) \end{aligned} \tag{3.14}$$

As $\tau \longrightarrow \infty$, ξ_{f} follows an exponential growth like in the planar case, but with a greater acceleration rate: $2\sqrt{\sigma(\sigma-1)}$ instead of $\sigma - 1$. In dimensional form, one has:

$$\begin{cases} x_{\text{f}} \approx \dfrac{\sigma R_{\text{tube}}}{2\alpha}\left[\exp\left(\dfrac{2\alpha S_{\text{L}}^0}{R_{\text{tube}}}t\right) - 1\right] \\ r_{\text{f}} \approx 1 \end{cases} \tag{3.15}$$

3.1.3 Coupling with other acceleration mechanisms

The finger flame phenomenon can sometimes be coupled with other acceleration mechanisms depending on the mixture properties. In particular, fundamental phenomena such as stretch effects (as introduced in Section 2.2) and intrinsic flame front instabilities (Section 2.3) are also present for the lean hydrogen-air flames considered in this work. Stretch effects are expected to be significant at the early instants after ignition when the hemi-spherical flame has a strong curvature. Also, burning in narrower tubes geometrically leads to stronger flame curvatures during the finger flame phase [197]. On the other hand, the development of cellular instabilities in a tube deviates from the purely spherical theory presented in Section 2.3.2. The coupling depends on the stability of the mixture,

most particularly the ratio between the tube radius and the critical radius for the onset of the instabilities [197, 198]:

- if the tube is large enough, the kernel has time to become fully cellular before entering the finger flame phase;
- if it is too narrow, it leaves less room for instabilities to grow.

This interaction will be quantitatively demonstrated in Section 5.3.6. As an illustration, Figure 3.3 represents a comparison of a stoichiometric and a lean H_2-air flames propagating in a channel [199].

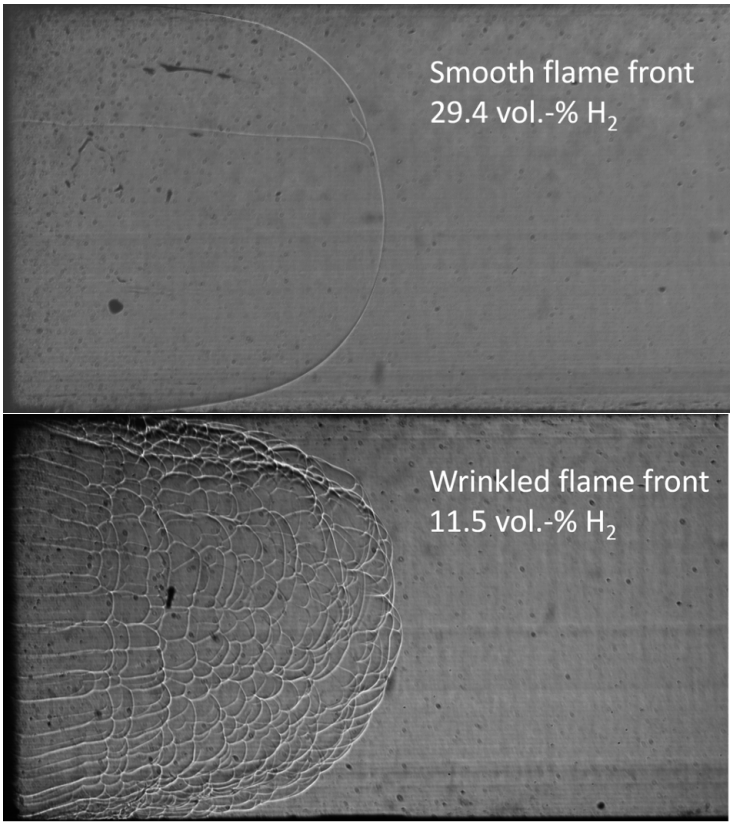

Figure 3.3: Shadowgraphs of a stable (top) and unstable (bottom) hydrogen-air flame propagating in a channel. Taken from [199].

3.2 Effect of obstacles

While the finger flame phenomenon represents a strong acceleration mechanism in the laminar phase of flame propagation in smooth tubes, the addition of obstacles creates new flow features that can further enhance flame propagation. An infinity of obstacle-filled configurations can be imagined. Some studies have focused on particular aspects influencing the intensity of an explosion, such as:

- the shape of the obstacles [180, 184, 200];
- their size [183, 185];
- their arrangement [181, 182].

But fundamentally, the effect of obstacles on flame acceleration can be summarised to some elemental mechanisms that are detailed now.

3.2.1 Flow contraction and jetting mechanisms

When a combustion wave propagates in a confined environment, the thermal expansion of hot products mechanically pushes the fresh gases ahead of it (piston effect as detailed in the previous section). Adding obstacles to the explosion channel has a direct impact in that it locally reduces the cross section. This can be qualified by the obstacles blockage ratio. The contraction leads to a natural acceleration of the flow ahead of the flame. When the latter approaches the obstacle, the tip is accelerated downstream much faster than the rest of the flame. On top of this convective effect, flame acceleration is also supported by the increased flame surface area (pure geometrical effect as detailed in Section 2.4.1) which can in turn also be coupled with stretch effects. Just after the obstacle, the decreased flow velocity (linked to its expansion) causes the flame tip to decelerate. This phenomenon has been observed both experimentally and numerically by Boeck *et al.* [201] on an initially laminar flame (see Figure 3.4). The acceleration of the flow is visible on the right picture. Note also that in the wake of the obstacle, vortical structures are generated and wrinkle the flame front. This mechanism is described in the next section.

The flame acceleration by flow contraction and wrinkling by the shedded vortices is a phenomenon localised around the obstacle which is followed by a decelerating phase (see Figure 3.5, case with one single obstacle). But if several obstacles are aligned in the direction of the flame propagation, the mechanism is repeated at each obstruction to sustain a continuous acceleration [49, 51] (see Figure 3.5, case with two obstacles). The limiting case of a high number of obstacles close to one another has been described by Bychkov *et al.* [202] through the so-called *jetting* phenomenon (illustrated in Figure 3.6). The presence of several rows of obstacles geometrically forms successive chambers for the flame propagation. Given its high velocity, the flame tip leaves unburnt mixture pockets behind as it advances. The delayed burning of these pockets accumulates into a jet flow of hot products along the axis which further pushes the flame tip forward. As this latter accelerates, it leaves even more unburnt pockets behind it, thereby re-fuelling the former jetting mechanism. This positive feedback loop leads to a strong exponential acceleration of the flame.

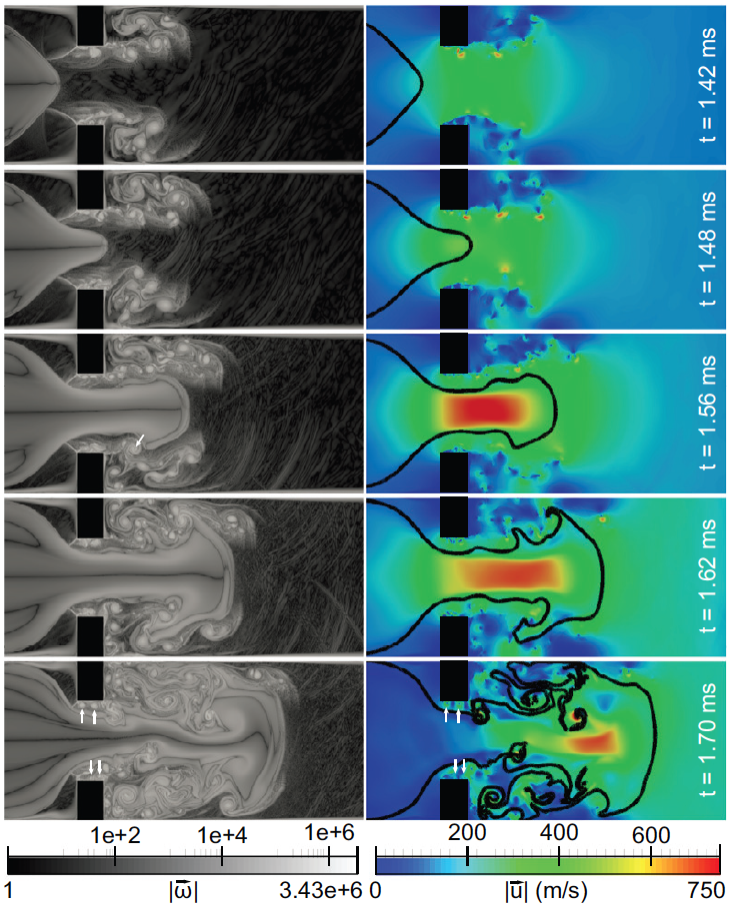

Figure 3.4: Sequences of vorticity magnitude (left) and velocity magnitude (right) of a stoichiometric H_2-O_2 flame ($P = 15$ kPa, $T_u = 300$ K) passing through an orifice plate in a square-section channel. Taken from [201].

3.2.2 Turbulence generation

The last impact of obstacles is one of the most powerful acceleration mechanisms for deflagrations: turbulence-flame interactions. Even when lab-scale experiments are ignited in a purely laminar flow, the vortex generation downtream the obstacles and their interaction with the flame mark the transition to a turbulent regime of propagation. As previously explained, the combustion wave pushes fresh gases ahead of it as it propagates. When obstacles are located in its way, vortical structures are generated behind them. As soon as the flame crosses an obstacle, it is wrinkled by these vortices. The increased surface area enhances combustion which in turn creates a higher flow velocity in the unburnt gases. This positive feedback loop again contributes to considerable flame acceleration. It is illustrated in Figure 3.7 with the work of Vermorel *et al.* [51]. The multiple interactions of a flame front with turbulence is at the core of many combustion studies and the subject of modelling strategies. This will be detailed in the next chapter.

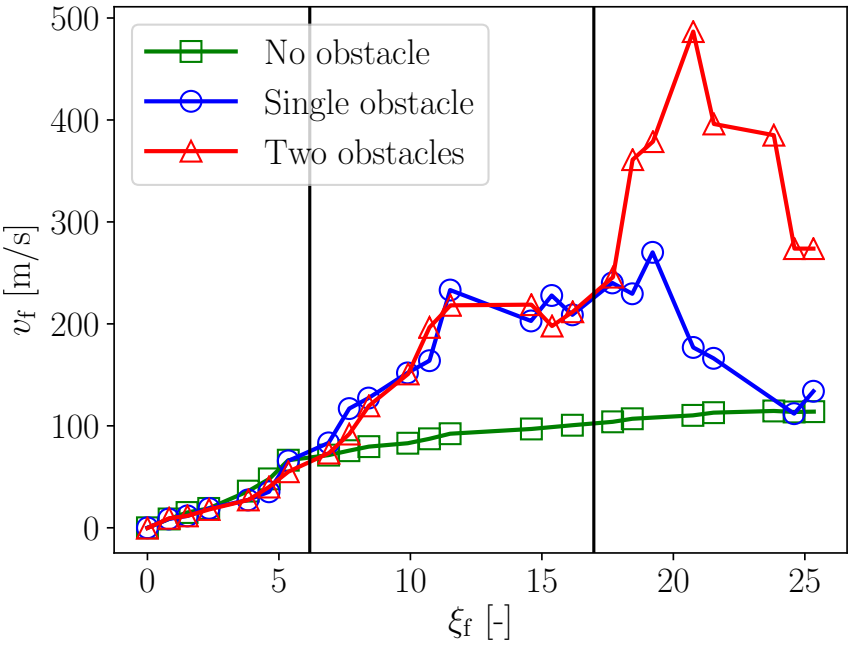

Figure 3.5: Flame tip velocity against flame tip position for a CH_4-air flame at X_{CH_4} = 10% in a semi-closed cylindrical vessel for three configurations (unobstructed, single obstacle and two obstacles with a 30% blockage ratio). Reproduced from Na'inna *et al.* [203].

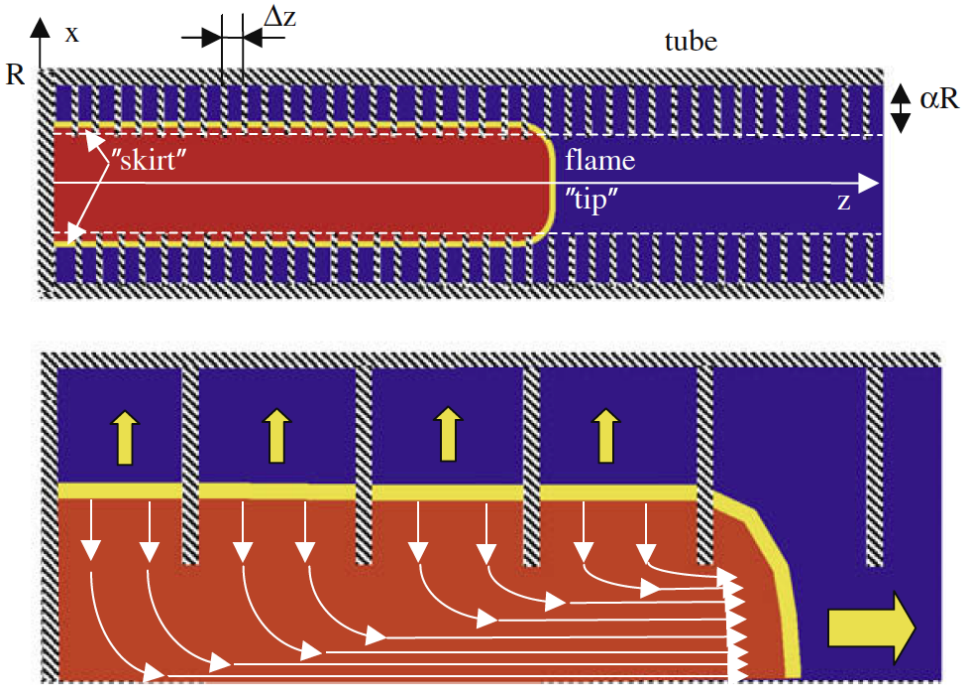

Figure 3.6: Schematic of the jetting mechanism during flame propagation in an obstructed channel. Taken from [204].

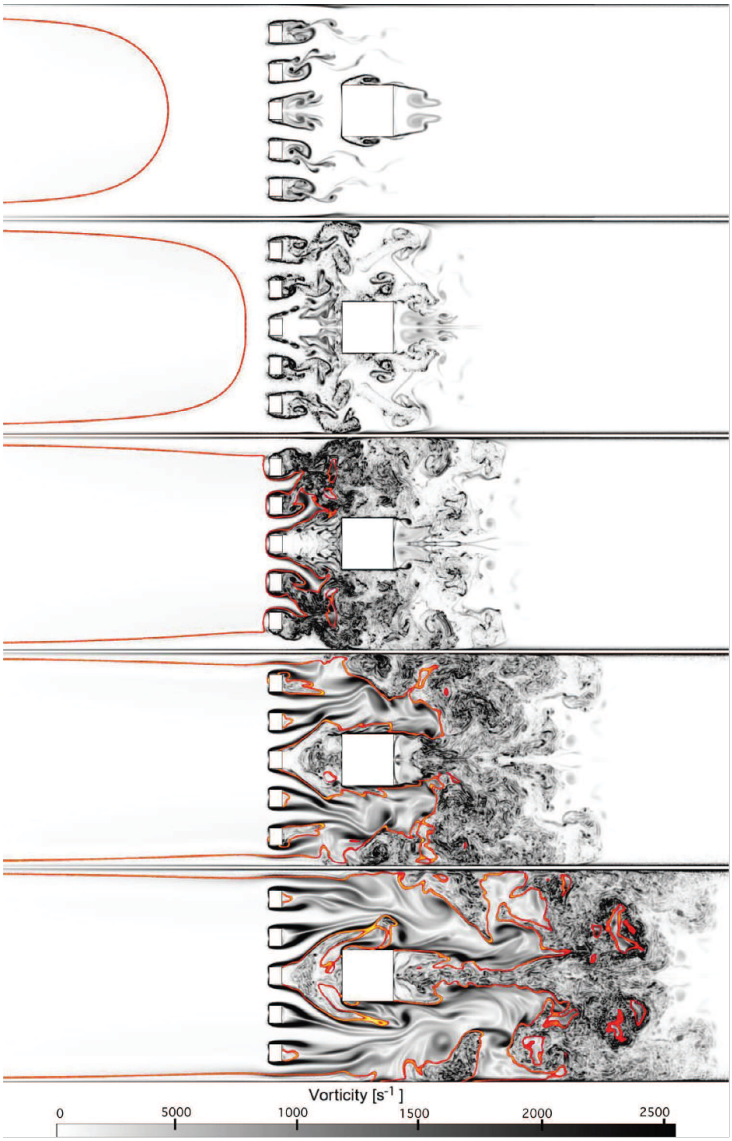

Figure 3.7: Simulation of the so-called Sydney experiment [173, 186] by Vermorel *et al.* [51] showing the turbulence-flame interactions during flame propagation in an obstructed vessel. Isocontour of heat release rate in red.

3.2.3 Coupling with other acceleration mechanisms

In lean hydrogen-air flames, the jetting and turbulent wrinkling mechanisms can also be coupled to the stretch effects and flame front instabilities inherent to these mixtures. Stretch is present all the way through the propagation. It is expected to be particularly effective when the flame is contracted at the passage of obstacles and when it is stretched by turbulence. For flame front instabilities, it is generally agreed upon that cellular structures play a prominent role in the early laminar phase of a deflagration [205, 206]. However, their role in the turbulent regime remains a controversial open question. Some studies suggest a lesser importance compared to turbulence effects [207, 208] whereas others talk about synergistic effects between the two [146, 209, 210]. Figure 3.8 depicts

an experimental observation of a lean H_2-air flame propagating through a series of orifice plates. A general coupling of all formerly described phenomena is present: flame front instabilities is distinguishable at the beginning; it is followed by the jetting and turbulent wrinkling effects.

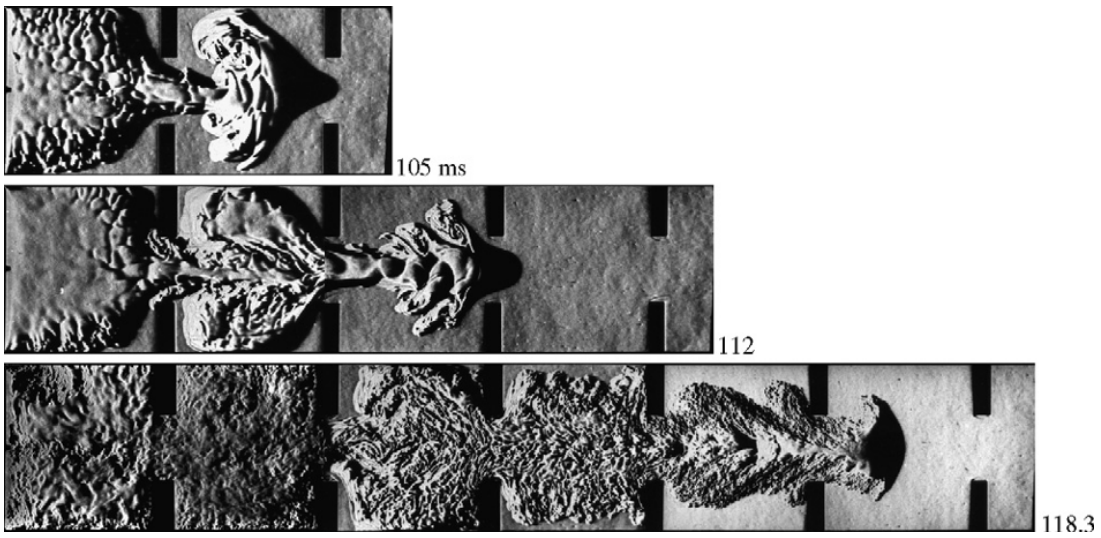

Figure 3.8: Sequence of shadowgraph images of a lean hydrogen-air ($X_{H_2} = 10\%$) flame propagating in an obstructed channel. Taken from [211].

Last but not least, in confined and obstructed explosions, other instability mechanisms can contribute to flame acceleration through surface increase and turbulence generation. Namely the Kelvin-Helmholtz instability associated with shear [206] and the Richtmeyer-Meshkov instability resulting from shock waves impacting the flame front [206, 212, 213].

Chapter 4

Conservation equations and models for reactive flows

Sommaire

This chapter introduces the governing equations of turbulent reacting flows as well as the physical modelling behind them. The general approaches used for their numerical resolution in CFD are outlined. In particular, the concept of Large-Eddy Simulations (LES) and its implementation in the AVBP solver is presented. One major difficulty that arises in turbulent combustion LES is to close the filtered reaction terms which are stiff and highly non-linear. A brief overview of the principal methods found in the

literature is presented. Emphasis is put on the principles and practical implementation of the Thickened Flame formalism that is used in the rest of the thesis.

4.1 Conservation equations

Combustion is a particular subdomain within the fluid dynamics field. Consequently, flames can be described by the general equations of reactive flows which are recalled hereafter.

4.1.1 Multi-species flows

Reactive flows involve multiple species coupled by an ensemble of chemical reactions. Each species k within a mixture of N species can be characterised either by its molar fraction X_k, or by its mass fraction Y_k:

$$\begin{cases} X_k \equiv \dfrac{n_k}{n} \\ Y_k \equiv \dfrac{m_k}{m} \end{cases} \tag{4.1}$$

where n (resp. m) is the number of moles (resp. mass) contained in the system and the subscript k denotes properties specified for the given species k. By definition, one has:

$$\begin{cases} \displaystyle\sum_{k=1}^{N} X_k = 1 \\ \displaystyle\sum_{k=1}^{N} Y_k = 1 \end{cases} \tag{4.2}$$

Given the system volume V, it can also be useful to define the molar concentration $[X_k]$ and mass concentration $[Y_k]$:

$$\begin{cases} [X_k] \equiv \dfrac{n_k}{V} \\ [Y_k] \equiv \dfrac{m_k}{V} \end{cases} \tag{4.3}$$

The whole mixture has a molar mass W given by:

$$\frac{1}{W} = \sum_{k=1}^{N} \frac{Y_k}{W_k} \tag{4.4}$$

and its heat capacities at constant volume C_V and constant pressure C_p are expressed as:

$$\begin{cases} C_V = \sum_{k=1}^{N} Y_k C_{V,k} \\ C_p = \sum_{k=1}^{N} Y_k C_{p,k} \end{cases} \tag{4.5}$$

The heat capacities of each species $C_{V,k}$ and $C_{p,k}$ (and in particular their dependence on temperature) is usually tabulated using polynomial functions (see for instance the NASA polynomials [214]).

4.1.2 Conservation equations

Despite being a research field per se, combustion remains a particular case of reacting flows. Apart from the classical aerodynamic processes, chemistry comes into play. To account for that, flow dynamics is not only governed by the usual Navier-Stokes conservation laws but also by one mass conservation equation for each species. The system is explicitly coupled through chemical source terms traducing the production/destruction of species which globally leads to a significant heat release. On top of that, this exothermicity and the variation in mixture composition implicitly affects thermodynamic and transport properties in time and space. The equations behind these interactions are recalled hereafter. Einstein's summation rule is used in the following sections.

4.1.2.1 Mass conservation

As combustion doesn't produce or consume mass, the global mass conservation equation (continuity equation) is the same as for non-reacting flows:

$$\frac{\partial \rho}{\partial t} + \frac{\partial}{\partial x_i}(\rho u_i) = 0 \tag{4.6}$$

where ρ is the mixture density and u_i the i^{th} component of the velocity vector.

4.1.2.2 Species conservation

As far as species are concerned, their conservation equations write:

$$\frac{\partial \rho Y_k}{\partial t} + \frac{\partial}{\partial x_i}(\rho u_i Y_k) = -\frac{\partial J_{k,i}}{\partial x_i} + \dot{\omega}_k \tag{4.7}$$

where $\dot{\omega}_k$ is the production rate of species k and $J_{k,i}$ is the diffusion flux of species k along the i^{th} direction. $\dot{\omega}_k$ carries the information on reactions (it is null for multi-species

non-reacting flows) and is usually modelled using an Arrhenius law as will be detailed in Section 4.2.2. $J_{k,i}$ is expressed as a function of the diffusion velocity $V_{k,i}$ by:

$$J_{k,i} = -\rho Y_k V_{k,i} \tag{4.8}$$

Because all production and consumption of species have to balance one another, it comes that:

$$\sum_{k=1}^{N} \dot{\omega}_k = 0 \tag{4.9}$$

Moreover, summing all species equations is equivalent to stating that the total mass is conserved and should thus boil down to the continuity equation (4.6). From that, the diffusion velocities and mass fractions have to be solution of:

$$\sum_{k=1}^{N} Y_k V_{k,i} = 0 \tag{4.10}$$

Details on the computation of diffusion velocities $\mathbf{V_k}$ are given in Section 4.2.1.

4.1.2.3 Momentum conservation

Momentum conservation equations for reacting flows look the same as for non-reacting flows and simply write:

$$\begin{aligned} \frac{\partial \rho u_j}{\partial t} + \frac{\partial}{\partial x_i}(\rho u_i u_j) &= \frac{\partial \sigma_{ij}}{\partial x_i} + \rho f_j \\ &= -\frac{\partial p}{\partial x_j} + \frac{\partial \tau_{ij}}{\partial x_i} + \rho f_j \end{aligned} \tag{4.11}$$

where σ_{ij} is the total stress tensor that can be decomposed into the sum of a pressure term p (isotropic part) and a viscous stress tensor τ_{ij} (deviatoric part). The expression of the viscous stress tensor is given in Section 4.2.1. f_j is a volume force acting in the direction j (assumed to be acting in the same manner for all species). For instance, the effect of gravity is encompassed in this term (using $f_j = \mathbf{g} \cdot \mathbf{e_j}$, $\mathbf{g}$ being the gravity acceleration vector and $\mathbf{e_j}$ the unit vector in direction j). Chemical reactions and combustion are not explicitly manifest in the momentum equation which is the same for non-reacting flows. However, combustion affects parameters such as density ρ and the viscous stress as is shown in Section 4.2.1.

4.1.2.4 Energy conservation

The energy conservation equation plays a big role in combustion physics as it handles for example the heat release term from chemical reactions. It can be written in many ways,

all of which are equivalent [62]. Here, the total energy form is chosen:

$$\frac{\partial \rho E}{\partial t} + \frac{\partial}{\partial x_i}\left(\rho u_i E\right) = \dot{\omega}_T - \frac{\partial q_i}{\partial x_i} + \frac{\partial}{\partial x_j}\left(\sigma_{ij} u_i\right) + \rho \sum_{k=1}^{N} Y_k f_i (u_i + V_{k,i}) + \dot{\mathcal{Q}} \tag{4.12}$$

where E is the total energy (sensible + kinetic), $\dot{\omega}_T$ is the heat released by combustion, $\mathbf{q}$ is the energy flux vector due to transport and $\dot{\mathcal{Q}}$ is an external source of energy (e.g. induced by a spark or laser). The expression of the heat flux vector $\mathbf{q}$ is specified in Section 4.2.1. The heat released by chemical reactions is straightforwardly linked to the production/consumption of species by the formation enthalpies of each species using the classical thermodynamical relation:

$$\dot{\omega}_T = -\sum_{k=1}^{N} \Delta h^{\circ}_{\mathrm{f},k} \dot{\omega}_k \tag{4.13}$$

The values of individual formation enthalpies $\Delta h^{\circ}_{\mathrm{f},k}$ at standard conditions is usually found in JANAF tables [215].

4.2 Transport and chemistry modelling

To fully close the system of conservation laws given above (Equations (4.7), (4.11) and (4.12)), molecular ($V_{k,i}$), momentum (τ_{ij}) and energy (q_i) fluxes must be expressed as a function of the other thermodynamical variables and transport coefficients. Besides, expressions for the chemical source terms ($\dot{\omega}_k$) must be provided. They allow the computation of the energy source term ($\dot{\omega}_T$) through Equation (4.13). The overall exothermic reaction of a fuel and an oxidiser is indeed of paramount importance for a flame to exist. However, this macroscopic effect results from the combination of multiple intermediary reactions occurring between numerous species. Accounting for all reactions and species is very costly and does not always prove useful to capture a given flame feature. In this section, an overview of existing transport and chemistry models is presented.

4.2.1 Transport modelling

Transport properties are important ingredients of the equations which dictate the behaviour of reactive flows. They determine the diffusive fluxes which usually act to smooth out gradients present in the system. However, it is shown in this section that there is a multitude of transport coefficients which traduce the numerous interactions between species, momentum and heat. The complexity associated to the transport problem makes it a research field per se. In practical combustion simulations, simplifying assumptions are often made to render the computations tractable. This section gives insights into the general equations which govern transport and introduces the main simplifications found in the literature and used in the rest of the manuscript.

Molecular fluxes

Conservation of species (Equation (4.7)) involves diffusion velocity vectors $\mathbf{V_k}$ for each species k. Their expressions are needed to close the system of equations. Various levels of accuracy (corresponding to various computational costs) are found in the literature. Williams [216] gave the theoretical set of linear equations (generally called Stefan-Maxwell equations) that implicitly link all diffusion velocities to binary mass diffusion coefficients between each pair of species:

$$\begin{aligned}\frac{\partial X_k}{\partial x_i} = &\sum_{j=1}^{N}\left(\frac{X_k X_j}{\mathcal{D}_{kj}}\right)(V_{j,i}-V_{k,i}) + (Y_k - X_k)\frac{1}{p}\frac{\partial p}{\partial x_i} \\ &+\sum_{j=1}^{N}\left[\left(\frac{X_k X_j}{\rho\mathcal{D}_{kj}}\right)\left(\frac{\mathcal{D}_{\mathrm{th},j}}{Y_j}-\frac{\mathcal{D}_{\mathrm{th},k}}{Y_i}\right)\right]\left(\frac{1}{T}\frac{\partial T}{\partial x_i}\right)\end{aligned} \tag{4.14}$$

where $\mathcal{D}_{ij}$ is the binary mass diffusion coefficient of species i into species j, $\mathcal{D}_{\mathrm{th},i}$ is the thermal diffusion coefficient of species i in the mixture (not to be confounded with the thermal diffusivity D_{th} introduced in Equation (2.16)). These coefficients are implicitly retrieved from the kinetic theory of gases but their computation, which involves collision integrals [217] requests the resolution of a linear system depending on local composition, temperature and pressure. To reduce the cost of their evaluation, Ern and Giovangigli [218] have for example proposed an optimised library called EGLIB [219, 220]. The reader may refer to [221, 222] for more details. Equation (4.14) shows that concentration gradients are supported by differences in diffusion velocities, pressure gradients and temperature gradients. Note that the last term corresponds to the *Soret effect*, also called *thermophoresis*. It represents the diffusion of molecules due to temperature gradients and usually drives light (resp. heavy) species towards hot (resp. cold) regions of the domain [216, 223]. It is an example of cross-transport mechanism which adds more complexity to the coupling of conservation laws. This effect is often neglected versus the two other terms [223].

The *multi-component transport* represented by Equation (4.14) allows to both satisfy (4.7), (4.9) and (4.10) and thus (4.6) equations. But solving this system, although linear, for each species, at each position and at each time step of a numerical simulation represents a CPU-time-consuming task. To avoid such costly computations, most codes model diffusion of species by *mixture-averaged transport* using the Hirschfelder and Curtiss approximation [222]:

$$V_{k,i}X_k = -D_k\frac{\partial X_k}{\partial x_i} \tag{4.15}$$

where D_k is an equivalent diffusion coefficient of species k within the mixture taken as a whole. As given by Giovangigli and Smooke [224] and Ern and Giovangigli [218], the latter are expressed as follows:

$$D_k = \frac{1-Y_k}{\sum_{j\neq k} X_j/\mathcal{D}_{jk}} \tag{4.16}$$

The drawback of using an approximation for diffusion velocities is that contrary to the

exact solution of Williams' system [216] (Equation (4.14)), the sum of all species equations in this case does not yield the continuity equation (i.e. conservation of mass is violated). One usual way to get around this is to introduce a correction velocity theoretically given by:

$$V_i^c = \sum_{k=1}^{N} D_k \frac{W_k}{W} \frac{\partial X_k}{\partial x_i} \tag{4.17}$$

Eventually, the species equation used in most codes reads:

$$\frac{\partial \rho Y_k}{\partial t} + \frac{\partial}{\partial x_i} \rho \left(u_i + V_i^c\right) Y_k = \frac{\partial}{\partial x_i} \left(\rho D_k \frac{W_k}{W} \frac{\partial X_k}{\partial x_i} \right) + \dot{\omega}_k \tag{4.18}$$

Another possible solution would be to impose the global mass conservation and the species conservation equations for all but one species and to get the mass fraction of this last species by using Equation (4.2). It allows to use the simple Hirschfelder diffusion velocities model while ensuring mass conservation. This approach does not induce significant errors when a species is substantially more abundant than the others and can be used as a "buffer" species (e.g. N_2 or other diluents).

Viscous stress tensor

The momentum conservation law (Equation (4.11)) introduced the viscous stress tensor τ_{ij}. In the case of Newtonian fluids, it writes:

$$\tau_{ij} = -\frac{2}{3}\mu \frac{\partial u_k}{\partial x_k} \delta_{ij} + \mu \left(\frac{\partial u_i}{\partial x_j} + \frac{\partial u_j}{\partial x_i} \right) \tag{4.19}$$

where δ_{ij} is the Kronecker symbol and μ is the dynamic viscosity of the fluid. Note that in Equation (4.19), the bulk viscosity has been neglected as is classically done [216, 223]. This assumption is not easily justifiable [225] and the reader may refer to [219] for more details on the importance of bulk viscosity. As stated in the previous section, combustion indirectly modifies the conservation of momentum by changing the viscosity μ.

While the notion of viscosity is straightforward and clearly defined for single-species flows, a digression is needed here to clarify what viscosity represents for a multi-species mixture. Following the same rationale as has been done for diffusion coefficients, the computation of the real *multi-component* viscosity is tedious. To make its evaluation tractable, a *mixture-averaged* viscosity is often used. The computation starts from the viscosity of each pure species (again based on the kinetic theory of gases [217]) and then uses an empirical averaging formula for the mixture (such as Wilke's [226] and Bird's [227] laws). This is done for standard conditions.

Heat flux

Heat fluxes in the energy conservation (Equation (4.12)) are mostly due to temperature gradients (through Fourier's law) and diffusion of species through the mixture [216]:

$$q_i = -\lambda \frac{\partial T}{\partial x_i} + \rho \sum_{k=1}^{N} h_{s,k} Y_k V_{k,i} + R^0 T \sum_{k=1}^{N} \sum_{j=1}^{N} \left(X_j \mathcal{D}_{\text{th},k} / W_k \mathcal{D}_{kj} \right) \left(V_{k,i} - V_{j,i} \right) \tag{4.20}$$

where R^0 is the universal gas constant, λ is the Fourier coefficient and $h_{s,k}$ is the sensible enthalpy of species k:

$$h_{s,k} \equiv \int_{T_0}^{T} C_p \, \mathrm{d}T \tag{4.21}$$

and T_0 is a reference temperature. Note that in Equation (4.20), the last term corresponds to the *Dufour effect* which shows that concentration gradients can induce heat fluxes. This cross-transport phenomenon is reciprocal to the Soret effect but it is commonly agreed that the Dufour effect plays a minor role in comparison with the Soret effect in combustion applications [216, 223, 225]. Note also that radiative heat transfers have been neglected in Equation (4.20). The reader may refer to [228–230] for more details on the radiative term.

Similarly to the previous comment on viscosity, the thermal conductivity for a multi-species mixture often uses a *mixture-averaged* formula (such as the laws of Mathur [231] or Mason-Saxena [232, 233]).

Transport modelling in AVBP

As previously explained, the resolution of the exact multi-component molecular transport system for all species [216] is extremely costly. It is usually restricted to 0D and 1D solvers like the open-source code Cantera [234]. In two-dimensional and three-dimensional cases, transport is often modelled. A first simplified model has been proposed above with mixture-averaged diffusion coefficients from Equation (4.16). In the LES calculations using AVBP, the problem is further simplified through the use of *constant Schmidt numbers* Sc_k (defined in Chapter 2) for each species. The diffusion coefficient of species k is computed using:

$$D_k = \frac{\mu}{\rho \mathrm{Sc}_k} \tag{4.22}$$

Equation (4.22) spares the computation of binary diffusion coefficients $\mathcal{D}_{ij}$ (necessary for the mixture-averaged approach, Equation (4.16)) which remains expensive.

A Sutherland law is prescribed for the viscosity μ to account for the effect of temperature:

$$\mu = c_1 \frac{T^{3/2}}{T + c_2} \frac{T_{\mathrm{ref}} + c_2}{T_{\mathrm{ref}}^{3/2}} \tag{4.23}$$

where c_1 and c_2 are given by the model and T_{ref} represents a reference temperature. Sometimes, this law is replaced by a simpler power law:

$$\mu = c_1 \left(\frac{T}{T_{\mathrm{ref}}} \right)^b \tag{4.24}$$

where b is typically chosen between 0.5 and 1.

The last diffusive process to model is the thermal diffusivity or equivalently the thermal conductivity. In AVBP, it is modelled similarly to molecular diffusion coefficients using

a *constant Prandtl number* Pr assumption:

$$\lambda = \frac{\mu C_p}{\mathrm{Pr}} \tag{4.25}$$

To sum up, global transport properties are imposed by a temperature-dependent law for viscosity and constant Prandtl and Schmidt numbers. All diffusion coefficients are deduced from μ, Pr and Sc_k according to the local temperature/density conditions.

The unity Lewis number assumption commonly used with global chemistries is set by imposing constant Schmidt numbers:

$$\mathrm{Sc}_k = \mathrm{Pr}, \forall k \in [\![1, N]\!] \tag{4.26}$$

A review of the various levels of resolution of molecular diffusion (multi-component, mixture-averaged, constant Schmidt and other intermediary approaches) may be found in Hilbert *et al.* [225].

4.2.2 Chemical approaches

In the last section, the species k source term $\dot{\omega}_k$ has been introduced. In real flames, a large number of species react through an even more considerable number of pathways. The production/destruction of a species is the sum of all reactions in which it is involved. For theoretical and numerical analyses, several levels of chemistry description exist. Namely detailed mechanisms, skeletal and reduced mechanisms and global mechanisms.

Detailed chemistries

Detailed mechanisms provide a fine-grain description of all reactions involved in the chemical process. They are intended to be as exhaustive as possible but are still considered as models. In particular, the description of the rate of the reaction is assumed to follow a typical Arrhenius law. A detailed chemical kinetic scheme consists of a set of M elementary reactions. A reversible reaction j can be generically expressed as:

$$\sum_{k=1}^{N} \nu'_{kj} \mathcal{M}_k \rightleftharpoons \sum_{k=1}^{N} \nu''_{kj} \mathcal{M}_k \tag{4.27}$$

where ν'_{kj} and ν''_{kj} are the molar coefficients of the reaction and $\mathcal{M}_k$ symbols designate each species k. For this reaction, the forward rate writes:

$$k_{\mathrm{f},j} = A_{\mathrm{f},j} T^{\beta_j} \exp\left(\frac{-E_{\mathrm{a},j}}{R^0 T}\right) \tag{4.28}$$

$E_{\mathrm{a},j}$ is the activation energy as introduced in Chapter 2, β_j is called the temperature exponent and $A_{\mathrm{f},j}$ the pre-exponential constant. Subscript f denotes here the forward direction of the reaction. The backward rate is related to $k_{\mathrm{f},j}$ through the equilibrium

constant $k_{\mathrm{eq},j}$:

$$k_{\mathrm{r},j} = \frac{k_{\mathrm{f},j}}{k_{\mathrm{eq},j}} \tag{4.29}$$

Subscript r refers to the reverse direction of the reaction. $k_{\mathrm{eq},j}$ is given by the law of mass action. From the forward and backward rates, the progress rate of reaction j is given by:

$$Q_j = k_{\mathrm{f},j} \prod_{k=1}^{N} [X_k]^{\nu'_{kj}} - k_{\mathrm{r},j} \prod_{k=1}^{N} [X_k]^{\nu''_{kj}} \tag{4.30}$$

Finally, the production/destruction rate of a species k can be deduced by:

$$\dot{\omega}_k = W_k \sum_{j=1}^{M} \nu_{kj} Q_j \tag{4.31}$$

where $\nu_{kj} = \nu''_{kj} - \nu'_{kj}$.

Detailed mechanisms are constructed by chemists and validated against experimental data on fundamental phenomena (e.g. shock tube experiments, auto-ignition, extinction, etc.) [235, 236]. They are accurate to reproduce a great variety of combustion processes. However, given that each species requires an additional transport equation, detailed chemical schemes are not suited for the simulation of large-scale combustion set-ups like explosions. On top of the large number of equations, they also represent a bottleneck in terms of time-step. Combustion relies indeed on highly reactive radical species associated to short time-scales, thereby requiring a chemical time-step far below the usual limit imposed by the CFL (Courant–Friedrichs–Lewy) or Fourier number constraints.

Skeletal and reduced chemistries

Skeletal mechanisms come from the reduction of detailed chemistries. Numerical and/or analytical considerations are used to remove species and reactions which are not relevant for the combustion problem of interest and do not significantly modify the scheme behaviour (see for example the DRGEP and lumping methods and the notion of quasi-steady state which relaxes the short time scale problem encountered with detailed mechanisms, the reader may refer to [237] for more details). Such chemical kinetic mechanisms represent a cheaper alternative to detailed schemes that can appropriately be used in the LES of mid-scale set-ups within a limited scope of applicability (notably for the ranges of temperature, pressure and equivalence ratio). Analytically Reduced Chemistries (ARC) have proved efficient in a number of combustion set-ups including spark ignition [238], swirled flames [239–242] and slot burner flames [243].

Global chemistries

In explosion studies, a common strategy is to use global chemical kinetic schemes. They are restricted to an even narrower range of operating conditions but are computationally cheaper than skelelal and reduced mechanisms (less species and reactions, less stiff due to the absence of fast intermediate reactions). Such chemistries can be built ex nihilo by considering the main reactants and products of the fuel oxidation [244]. The limited set

of chemical parameters is then fitted to match some global flame properties of interest (usually the laminar flame speed, adiabatic flame temperature, auto-ignition delay, etc.). Global schemes are remarkably suited for the simulation of explosion configurations which can commonly involve ultra large scales. The fundamental and simplest global chemical scheme only involves fuel F, oxidiser O and product P through a single-step irreversible reaction:

$$\mathrm{F} + \mathrm{O} \longrightarrow \mathrm{P} \tag{4.32}$$

With such simplification, the reaction rate given by Equation (4.30) is reduced to:

$$Q_{1\mathrm{S}} = A[\mathrm{F}]^{n_\mathrm{F}}[\mathrm{O}]^{n_\mathrm{O}} T^{\beta} \exp\left(\frac{-E_\mathrm{a}}{RT}\right) \tag{4.33}$$

where n_F and n_O are the partial orders of reaction associated to the fuel and oxidiser respectively. They can differ from the stoichiometric coefficients because (4.32) is not an elementary reaction. Global chemistries have shown their capabilities to reproduce the fundamental characteristics of many flames in various applications among which lean partially premixed swirled flames [244], spark ignition [245, 246], flame kernel growth in internal combustion engines (ICE) [247], ignition sequence in a gas turbine [248], and most importantly explosions [49, 51, 53, 249].

4.3 Computational resolution approaches (RANS, LES, DNS)

The previous sections have presented the set of conservation equations for reactive flows along with the physical modelling for some specific phenomena such as transport. Now, the numerical resolution of this system of partial differential equations is considered. Navier-Stokes equations are indeed highly non-linear in their general form and CFD remains the only way to get an approximated solution. For that purpose, the problem is discretised in time and in space on a computational grid. The accuracy of CFD depends on the time scales and length scales that are numerically solved for. Three families of approaches are generally distinguished based on the amount of turbulent scales that are resolved/modelled (see Figure 4.1).

Direct Numerical Simulations (DNS)

Direct Numerical Simulation (DNS) is a bruteforce strategy in the sense that all scales of turbulent motion are explicitly resolved. The grid edge size must be typically of the order of the Kolmogorov scale $\Delta x = \mathcal{O}(\eta_\kappa)$ [250, 251] to refine the finest structures of turbulence. A rapid calculation gives an order of magnitude for the required number of cells for a 3D DNS:

$$N_\mathrm{cells} \propto \left(\frac{l_\mathrm{t}}{\eta_\kappa}\right)^3 = {\mathrm{Re}_\mathrm{t}}^{9/4} \tag{4.34}$$

where l_t is the integral length scale of turbulence and Re_t the turbulent Reynolds number:

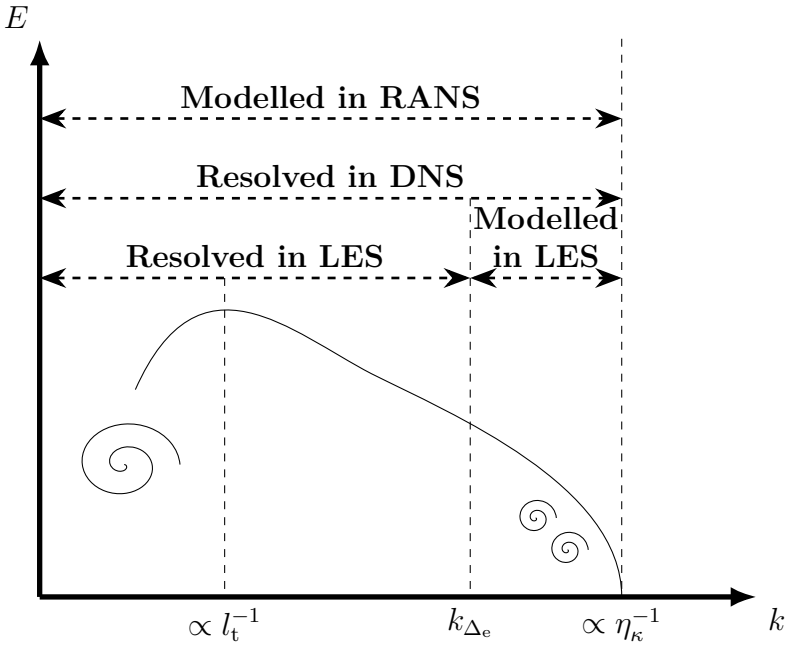

Figure 4.1: Typical turbulent energy spectrum as a function of wave number.

$\mathrm{Re_t} = (\rho u' l_t)/\nu$. Simulations using N_{cells} cells rapidly become out of reach for general engineering problems like explosions. DNS is commonly restricted to small-scale academic cases which give insights into the physics of a particular problem. It will therefore be used in this work on canonical configurations to provide reliable results, from which models for larger configurations can be proposed.

Reynolds-Averaged Navier-Stokes (RANS)
At the opposite of DNS lies the *Reynolds-Averaged Navier-Stokes* (RANS) approach. RANS equations only solve for the mean flow/flame quantities. To obtain these equations, a statistical average is applied to the instantaneous Navier-Stokes conservation laws. Every quantity f is split into its statistical mean and a fluctuation:

$$f = \langle f \rangle + f' \tag{4.35}$$

where $\langle \bullet \rangle$ is the statistical averaging operator and by definition, one has: $\langle f' \rangle = 0$. Because of the non-linear nature of Navier-Stokes equations, the averaging operation reveals unclosed terms. They carry the information of the effects of turbulent motion on the mean field. In the RANS approach, all turbulent scales are modelled (cf. Figure 4.1). Being the cheapest of all CFD approaches, RANS remains a very popular method in many commercial codes. A variant, called URANS (for *Unsteady Reynolds-Averaged Navier-Stokes*) is suited for transient phenomena such as explosions [191, 252–255]. However, (U)RANS is also the least accurate CFD method: in a general context, knowing mean quantities often proves insufficient to characterise unsteady phenomena in turbulent combustion problems [256]. Although some studies [41–44] have proved that RANS simulations of explosion showed good agreement with experiments, it should be reminded that these simulations heavily rely on the quality of the models used for turbulent scales.

Large-Eddy Simulation (LES)
Large-Eddy Simulation (LES) stands in between RANS and DNS strategies. The largest scales of turbulence are resolved on the mesh whereas the rest is modelled (cf. Figure 4.1). LES therefore also needs models for both flow and flame subgrid contributions. It is particularly adapted to the simulation of explosion scenarios for two reasons:

1. its accuracy is expected to be higher than that of RANS because a significant part of the physics is associated with large scales (resolved in LES), thereby alleviating the contribution of the models;

2. explosions are extremely unsteady events. The resolution of some turbulent and flame motions in LES seems relevant to produce correct simulations;

3. the computational cost of LES is considerably decreased in comparison with DNS.

This explains why the LES strategy has been chosen as part of the LEFEX project, which includes this work.

4.4 LES modelling

The following section presents the equations as well as the models used in LES codes. In particular, the Thickened Flame formalism for the LES of explosions is introduced. This model represents a state-of-the-art method for turbulent premixed combustion in large-scale systems and will be used throughout this thesis.

4.4.1 LES filtering

The basic operation behind the LES approach is a filtering (in spectral or physical space) of the Navier-Stokes equations. In physical space, if Δ_e is the LES filter size, filtering a quantity f boils down to:

$$\overline{f}(\mathbf{x}) \equiv \int f(\mathbf{x}) F_{\Delta_e}(\mathbf{x} - \mathbf{x}') \mathbf{dx}' \tag{4.36}$$

where F_{Δ_e} is the filter kernel and $\overline{\bullet}$ denotes the filtering operator. f is then split into the filtered and subgrid components:

$$f = \overline{f} + f'' \tag{4.37}$$

Equation (4.37) is to be compared to the former RANS approach given by Equation 4.35. Instead of splitting each quantity into the average and the statistical fluctuation, it is split into the resolved (filtered) and the subgrid part. In combustion, to account for variable

density, the Favre filtering operator is preferred (denoted by $\widetilde{\bullet}$):

$$\begin{aligned}\overline{\rho}\widetilde{f}(\mathbf{x}) &\equiv \int \rho f(\mathbf{x}) F_{\Delta_e}(\mathbf{x}-\mathbf{x}')\mathbf{dx}' \\ &= \overline{\rho f}\end{aligned} \tag{4.38}$$

Applying the LES filter on Navier-Stokes balance equations yields:

Filtered mass conservation

$$\frac{\partial \overline{\rho}}{\partial t} + \frac{\partial}{\partial x_i}(\overline{\rho}\widetilde{u_i}) = 0 \tag{4.39}$$

Filtered species conservation

$$\frac{\partial \overline{\rho}\widetilde{Y_k}}{\partial t} + \frac{\partial \overline{\rho}\widetilde{u_i}\widetilde{Y_k}}{\partial x_i} = -\frac{\partial}{\partial x_i}\left(\overline{\rho}\left(\widetilde{u_i Y_k} - \widetilde{u_i}\widetilde{Y_k}\right)\right) - \frac{\partial \overline{J_{k,i}}}{\partial x_i} + \overline{\dot{\omega}_k} \tag{4.40}$$

Filtered momentum conservation

$$\frac{\partial \overline{\rho}\widetilde{u_j}}{\partial t} + \frac{\partial}{\partial x_i}\left(\overline{\rho}\widetilde{u_j}\widetilde{u_i}\right) = -\frac{\partial \overline{p}}{\partial x_i} + \frac{\partial}{\partial x_i}\left(\overline{\tau_{ij}} - \overline{\rho}\left(\widetilde{u_i u_j} - \widetilde{u_i}\widetilde{u_j}\right)\right) + \overline{\rho} f_j \tag{4.41}$$

Filtered energy conservation

$$\begin{aligned}\frac{\partial \overline{\rho}\widetilde{E}}{\partial t} + \frac{\partial}{\partial x_i}\left(\overline{\rho}\widetilde{u_i}\widetilde{E}\right) = &-\frac{\partial}{\partial x_i}\left(\overline{\rho}\left(\widetilde{u_i E} - \widetilde{u_i}\widetilde{E}\right)\right) + \overline{\dot{\omega}_T} + \frac{\partial}{\partial x_i}\left(\overline{\lambda\frac{\partial T}{\partial x_i}}\right) \\ &- \frac{\partial}{\partial x_i}\left(\sum_{k=1}^{N}\overline{h_{s,k}J_{k,i}}\right) - \frac{\partial}{\partial x_i}\left(\overline{u_j\left(p\delta_{ij} - \tau_{ij}\right)}\right) + \overline{\dot{\mathcal{Q}}}\end{aligned} \tag{4.42}$$

4.4.2 Closure terms

In the filtered set of conservation equations (4.39)-(4.42), several unclosed terms must be modelled.

Species and enthalpy laminar fluxes
Species and enthalpy laminar fluxes are generally small compared to turbulent fluxes. They can be either neglected or modelled using a simple gradient assumption:

$$\overline{J_{k,i}} = -\overline{\rho}\left(\overline{D_k}\frac{W_k}{\overline{W}}\frac{\partial \widetilde{X_k}}{\partial x_i} - \widetilde{Y_k}\widetilde{V_i^c}\right) \tag{4.43}$$

$$\overline{\lambda\frac{\partial T}{\partial x_i}} = \overline{\lambda}\frac{\partial \widetilde{T}}{\partial x_i} \tag{4.44}$$

$$\sum_{k=1}^{N}\overline{h_{s,k}J_{k,i}} = \sum_{k=1}^{N}\widetilde{h_{s,k}}\overline{J_{k,i}} \tag{4.45}$$

where the filtered correction velocity writes:

$$\widetilde{V_i^{\mathrm{c}}} = \sum_{k=1}^{N} \left(\overline{D_k} \frac{W_k}{\overline{W}} \frac{\partial \widetilde{X_k}}{\partial x_i} \right) \tag{4.46}$$

Filtered transport properties are estimated using resolved quantities:

$$\overline{\mu} = \mu(\widetilde{T}) \tag{4.47}$$

$$\overline{D_k} = \frac{\overline{\mu}}{\overline{\rho}\ \mathrm{Sc}_k} \tag{4.48}$$

$$\overline{\lambda} = \frac{\overline{\mu}\ \overline{C_p}(\widetilde{T})}{\mathrm{Pr}} \tag{4.49}$$

Reynolds stress tensor

The Reynolds stress tensor is closed using classical turbulence models. Under Boussinesq assumption, they are related to a turbulent viscosity μ_{t} by:

$$\widetilde{u_i u_j} - \widetilde{u_i}\widetilde{u_j} = -\mu_{\mathrm{t}} \left(\frac{\partial \widetilde{u_i}}{\partial x_j} + \frac{\partial \widetilde{u_j}}{\partial x_i} - \frac{2}{3}\delta_{ij} \frac{\partial \widetilde{u_k}}{\partial x_k} \right) \tag{4.50}$$

Now, the problem is reduced to modelling μ_{t}. Among the multiple models found in the literature, this work uses the WALE model [257]:

$$\frac{\mu_{\mathrm{t}}}{\rho} = \nu_{\mathrm{t}} = (C_w \Delta_{\mathrm{e}})^2 \frac{\left(s_{ij}^d s_{ij}^d \right)^{3/2}}{\left(\widetilde{s_{ij}}\widetilde{s_{ij}}^{5/2} + \left(s_{ij}^d s_{ij}^d \right)^{5/4} \right.} \tag{4.51}$$

with $C_w = 0.4929$ as a model constant and:

$$s_{ij}^d = \frac{1}{2} \left(\widetilde{g_{ij}}^2 + \widetilde{g_{ji}}^2 \right) - \frac{1}{3} \widetilde{g_{kk}}^2 \delta_{ij} \tag{4.52}$$

$\widetilde{g_{ij}}$ is the resolved velocity gradient. The WALE model has the particular advantage of ensuring a correct asymptotic behaviour at the walls.

Species and enthalpy turbulent fluxes

The species and enthalpy turbulent fluxes are also evaluated using a gradient closure with the resolved terms:

$$\overline{J_{\mathrm{t},ik}} = \overline{\rho} \left(\widetilde{u_i Y_k} - \widetilde{u_i}\widetilde{Y_k} \right) = -\overline{\rho} \left(\overline{D_{\mathrm{t},k}} \frac{W_k}{\overline{W}} \frac{\partial \widetilde{X_k}}{\partial x_i} - \widetilde{Y_k}\widetilde{V_{\mathrm{t},i}^{\mathrm{c}}} \right) \tag{4.53}$$

$$\overline{\rho} \left(\widetilde{u_i E} - \widetilde{u_i}\widetilde{E} \right) = -\overline{\lambda_{\mathrm{t}}} \frac{\partial \widetilde{T}}{\partial x_i} + \sum_{k=1}^{N} \widetilde{h_{\mathrm{s},k}} \overline{J_{\mathrm{t},ik}} \tag{4.54}$$

The turbulent correction velocity is expressed as:

$$\widetilde{V_{\mathrm{t},i}^{c}} = \sum_{k=1}^{N} \overline{D_{\mathrm{t},k}} \frac{W_k}{\overline{W}} \frac{\partial \widetilde{X_k}}{\partial x_i} \tag{4.55}$$

And the turbulent transport coefficients are given by:

$$\overline{D_{\mathrm{t},k}} = \frac{\overline{\mu_{\mathrm{t}}}}{\overline{\rho}\ \mathrm{Sc}_{\mathrm{t},k}} \tag{4.56}$$

$$\overline{\lambda_{\mathrm{t}}} = \frac{\overline{\mu_{\mathrm{t}}}\ \overline{C_p}}{\mathrm{Pr}_{\mathrm{t}}} \tag{4.57}$$

Turbulent Schmidt $\mathrm{Sc}_{\mathrm{t},k}$ and Prandtl Pr_{t} numbers have been fixed to 0.60 in this study.

The last terms that are still unclosed in the LES Navier-Stokes Equations (4.39)-(4.42) are the filtered chemical source terms $\overline{\dot{\omega}_k}$. Because they are highly non-linear and peak at very small-scales, they represent critical components of LES codes at the base of many combustion models [62]. The main turbulent combustion models for premixed flames are discussed in the next section.

4.4.3 Short review of turbulent combustion models for premixed flames

Over the past few decades, several authors have tackled the modelling of the filtered source terms. It resulted in the proposal of a number of strategies based on various paradigms. The main approaches are summarised below. For more comprehensive reviews of all existing approaches, the reader may refer to the works of Veynante and Vervisch [256], Bilger *et al.* [258], Pitsch [259], Poinsot and Veynante [62] or Pope [260].

Geometrical approaches
In some approaches, the flame front is described from a pure geometrical point of view. This kind of strategy often assumes an infinitely thin flame, then considered as an interface between fresh and burnt gases.

In the *G-equation* paradigm (sometimes called *level set approach*) [61, 261], the flame evolution is described by a balance equation for the progress variable (see Equations (2.1) or (2.2) for example):

$$\frac{\partial c}{\partial t} + \frac{\partial \widetilde{\overline{\rho} u_i} \widetilde{c}}{\partial x_i} = \rho_{\mathrm{u}} \overline{S_{\mathrm{T}}}\, |\nabla \widetilde{\mathbf{c}}| \tag{4.58}$$

where $\overline{S_{\mathrm{T}}}$ is the filtered turbulent flame speed (see Section 2.4). The problem of the unclosed filtered source terms is transferred to the choice of a model for $\overline{S_{\mathrm{T}}}$. The closure

is often imposed by:

$$\frac{\overline{S_{\mathrm{T}}}}{S_{\mathrm{L}}^0} = 1 + \alpha \left(\frac{\overline{u'}}{S_{\mathrm{L}}^0} \right)^n \tag{4.59}$$

where α and n are constants determined from experimental correlations or theoretical considerations.

Another family of geometrical approaches is based on the *flame surface density* (FSD, see Section 2.4.1) which measures the available flame surface area per unit volume [160]. In this kind of models, the flame structure is fully decoupled from the wrinkling induced by turbulence-flame interactions. The unclosed filtered chemical source terms are directly taken proportional to the FSD (similarly to Equation (2.75)):

$$\overline{\dot{\omega}_c} = \rho_{\mathrm{u}} S_{\mathrm{L}}^0 I_0 \left| \nabla \widetilde{\mathbf{c}} \right| \tag{4.60}$$

and a balance equation is derived for that filtered FSD $|\nabla \widetilde{\mathbf{c}}|$. Because they provide a convenient way of accounting for many physical phenomena (confinement, instationarity, pressure rise, etc.), FSD-based approaches have been used in a wide range of applications close to explosion configurations Ibrahim *et al.* [46], Gubba *et al.* [262] and Di Sarli *et al.* [263].

Statistical approaches

Following a completely different paradigm, statistical approaches assume that the fluctuations lost at the LES filter scale can be described by a probability density function (PDF) varying in a so-called "phase space" ϕ (not to be confounded with the equivalence ratio Φ). In general, this space is chosen in the form $\phi = (Y_1, Y_2, ..., Y_N, T)$. The probability of being in a specific point of the phase space is defined by $\mathcal{P}(\phi)$. The filtered source terms are simply computed using:

$$\overline{\dot{\omega}} = \int \dot{\omega} \mathcal{P}(\phi) \, \mathrm{d}\phi \tag{4.61}$$

The problem is here transferred to the determination of the PDF $\mathcal{P}$.

A first method is to presume the shape of the PDF (yielding the *presumed PDF* methods family), with the β-PDF being commonly used. The parameters of the β function are directly expressed as a function of the mean $\widetilde{c}$ and variance $\widetilde{c'^2} \equiv \widetilde{(c - \widetilde{c})^2}$ of the progress variable. The mean is readily solved for in the LES equations (resolved field) but an additional balance equation is needed for the variance. Although practical, the presumed PDF method has several disadvantages among which the non-conservation of the unstretched laminar flame speed S_{L}^0 in the absence of turbulence [264]. For that reason, it is often reserved for non-premixed combustion.

In the *stochastic PDF* approach, a transport equation is derived for the complete PDF $\mathcal{P}$ starting from the Boltzmann equation [265]. This approach provides an excellent description of subgrid interactions. However, it gives rise to a complex implementation as well as increased computational costs.

4.4.4 Thickened Flame model

The Thickened Flame (TF or TFLES) model circumvents the problem of modelling stiff reaction terms by artificially thickening the flame to resolve it on a coarse grid [266, 267]. Its principle stems from simple scaling laws for the laminar flame speed and flame thickness (defined in Chapter 2) coming from the asymptotic theory [216, 223]:

$$\begin{cases} S_{\mathrm{L}}^0 \propto \sqrt{DA} \\ \delta_{\mathrm{L}}^0 \propto \sqrt{\dfrac{D}{A}} \end{cases} \tag{4.62}$$

A is the Arrhenius law pre-exponential constant as defined in Equation (4.33) and D represents a characteristic diffusivity. Equations (4.62) express the effects of diffusion and reaction on the global properties of a laminar flame front. If one applies the following transformation:

$$\begin{cases} D \mapsto FD \\ A \mapsto \dfrac{A}{F} \end{cases} \tag{4.63}$$

the flame properties are accordingly modified to:

$$\begin{cases} S_{\mathrm{L}}^0 \mapsto S_{\mathrm{L}}^0 \\ \delta_{\mathrm{L}}^0 \mapsto F\delta_{\mathrm{L}}^0 \end{cases} \tag{4.64}$$

The flame front is thickened by a factor F while conserving the laminar flame speed. F is then chosen to resolve the flame for a given mesh resolution. In practice, the TF model is easily implemented by:

$$\begin{cases} D_{\mathrm{th}} \mapsto FD_{\mathrm{th}} & \\ D_k \mapsto FD_k, & \forall k \in [\![1, N]\!] \\ \dot{\omega}_k \mapsto \dfrac{\dot{\omega}_k}{F}, & \forall k \in [\![1, N]\!] \end{cases} \tag{4.65}$$

For example, the TF model results in the following species conservation equation:

$$\frac{\partial \overline{\rho}\widetilde{Y_k}}{\partial t} + \frac{\partial}{\partial x_i}\overline{\rho}\left(\widetilde{u_i}\widetilde{Y_k}\right) = \frac{\partial}{\partial x_i}\left(F\overline{\rho}\overline{D_k}\frac{W_k}{\overline{W}}\frac{\partial \widetilde{X_k}}{\partial x_i} - \overline{\rho}\widetilde{Y_k}\left(\widetilde{V_i^{\mathrm{c}}} + \widetilde{V_{\mathrm{t},i}^{\mathrm{c}}}\right)\right) + \frac{\overline{\dot{\omega}_k}}{F} \tag{4.66}$$

This common method is applicable in turbulent combustion as well as for laminar flames (it has initially been derived in the context of laminar flame simulations [267]).

4.4.5 Dynamic Thickened Flame model (DTF)

So far, the TF approach has been introduced as a model applied everywhere in the computational domain (F only depending on the local mesh size and flame thickness). The diffusion coefficients are modified even far from the flame front. By doing that, the

model affects regions where the diffusion properties of the mixture are critical such as mixing zones and near the walls. To avoid these spurious effects, the Dynamic TF (DTF) approach has been proposed [268]. To target areas where combustion takes place and apply the TF correction therein, a flame sensor $\mathcal{S}$ is used. The local thickening reads:

$$F = 1 + (F_{\max} - 1)\mathcal{S} \tag{4.67}$$

where $F_{\max}$ is the thickening imposed by the local mesh resolution and flame thickness:

$$F_{\max} = \frac{N_{\mathrm{c}}\Delta x}{\delta_{\mathrm{L}}^0} \tag{4.68}$$

N_{c} is a parameter determining the number of points used to resolve the flame thickness. In practice, it is fixed at $N_{\mathrm{c}} = 7$. The flame sensor is generally based on the fuel consumption rate using an Arrhenius-like expression:

$$\Omega = Y_{\mathrm{F}}^{n_{\mathrm{F}}} Y_{\mathrm{O}}^{n_{\mathrm{O}}} \exp\left(-\Gamma \frac{E_{\mathrm{a}}}{RT}\right) \tag{4.69}$$

and compared to the value of the 1D unstretched flame Ω_0:

$$\mathcal{S} = \tanh\left(\beta' \frac{\Omega}{\Omega_0}\right) \tag{4.70}$$

Constants of the sensor are fixed at $\Gamma = 0.5$ and $\beta' = 50$.

On top of the local targeting for thickening introduced by Equation (4.67) in the DTF model, it is also considered that when thickening is applied, the structure of the flame is fully resolved so that subgrid turbulent fluxes can be set to zero:

$$\begin{cases} \overline{J_{\mathrm{t},ik}} \mapsto (1 - \mathcal{S})\overline{J_{\mathrm{t},ik}} \\ \overline{\rho}\left(\widetilde{u_i E} - \widetilde{u_i}\widetilde{E}\right) \mapsto (1 - \mathcal{S})\overline{\rho}\left(\widetilde{u_i E} - \widetilde{u_i}\widetilde{E}\right) \end{cases} \tag{4.71}$$

4.4.6 Turbulent combustion modelling

The TF model has the advantage of being easily applicable to any (premixed) flame LES. However, thickening the flame front alters its sensitivity to turbulent eddies [269, 270]. Its wrinkling is reduced and the ratio of turbulence and chemical time scales is modified. A scales analysis shows that the flame Damkhöler and Karlovitz[1] numbers are modified

[1]This Karlovitz number related to flame and turbulence scales must not be confused with the Karlovitz number Ka defined in Chapter 2 (by Equation (2.43)) representing non-dimensional flame stretch.

by a factor F. They are defined by:

$$\begin{cases} \mathrm{Da} \equiv \dfrac{\tau_\mathrm{t}}{\tau_\mathrm{c}} = \dfrac{l_\mathrm{t}}{u'} \dfrac{S_\mathrm{L}^0}{\delta_\mathrm{L}^0} \\ \mathrm{Ka} \equiv \dfrac{\tau_\mathrm{c}}{\tau_\kappa} = \dfrac{u_\kappa}{\eta_\kappa} \dfrac{\delta_\mathrm{L}^0}{S_\mathrm{L}^0} \end{cases} \tag{4.72}$$

and become for the thickened flame:

$$\begin{cases} \mathrm{Da} \mapsto \dfrac{\mathrm{Da}}{F} \\ \mathrm{Ka} \mapsto F\mathrm{Ka} \end{cases} \tag{4.73}$$

$\tau_\mathrm{c} = \delta_\mathrm{L}^0 / S_\mathrm{L}^0$ represents a characteristic chemical time scale whereas $\tau_\mathrm{t} = l_\mathrm{t}/u'$ (resp. $\tau_\kappa = \eta_\kappa/u_\kappa$) is the characteristic time scale for the eddies at the integral (resp. Kolmogorov) scale. Da (resp. Ka) measures the flame sensitivity to the largest (resp. smallest) vortices. They are typically used to distinguish turbulent combustion regimes in the Borghi-Peters diagram [69, 70].

To compensate for the lost contribution due to the TF model, an efficiency function is introduced. It originates from the classical Damkhöler's hypothesis (see Section 2.4) which stipulates that the effective turbulent speed S_T^0 of a flame brush is simply related to the laminar flame speed S_L^0 and the wrinkling factor Ξ by $S_\mathrm{T}^0 = \Xi S_\mathrm{L}^0$ (Equation (2.76)). The action of the TF model is to reduce Ξ (flame wrinkling at subgrid scales) so the efficiency function compensates for that:

$$\begin{cases} D_\mathrm{th} \mapsto \mathcal{E} F D_\mathrm{th} \\ D_k \mapsto \mathcal{E} F D_k, & \forall k \in [\![1, N]\!] \\ \dot{\omega}_k \mapsto \mathcal{E} \dfrac{\dot{\omega}_k}{F}, & \forall k \in [\![1, N]\!] \end{cases} \tag{4.74}$$

allows to ensure:

$$\begin{cases} S_\mathrm{L}^0 \mapsto \mathcal{E} S_\mathrm{L}^0 \\ \delta_\mathrm{L}^0 \mapsto F \delta_\mathrm{L}^0 \end{cases} \tag{4.75}$$

$\mathcal{E}$ is defined as the ratio between the wrinkling factors of the unthickened and the thickened flames:

$$\mathcal{E} \equiv \frac{\Xi(\delta_\mathrm{L}^0)}{\Xi(F\delta_\mathrm{L}^0)} \tag{4.76}$$

For example, the TF LES model results in the following species conservation equation:

$$\frac{\partial \overline{\rho} \widetilde{Y_k}}{\partial t} + \frac{\partial}{\partial x_i} \overline{\rho} \left(\widetilde{u_i} \widetilde{Y_k} \right) = \frac{\partial}{\partial x_i} \left(\mathcal{E} F \overline{\rho} \overline{D_k} \frac{W_k}{\overline{W}} \frac{\partial \widetilde{X_k}}{\partial x_i} - \overline{\rho} \widetilde{Y_k} \left(\widetilde{V_i^\mathrm{c}} + \widetilde{V_{\mathrm{t},i}^\mathrm{c}} \right) \right) + \frac{\mathcal{E} \overline{\dot{\omega}_k}}{F} \tag{4.77}$$

The problem is now reduced to the determination of $\mathcal{E}$ (or equivalently for Ξ). Various expressions can be found in the literature [270–274]. In the present work, the model of

Charlette *et al.* [274] is considered.

$$\Xi\left(\delta_{\mathrm{L}}^{0}\right)=\left(1+\min\left[\frac{\Delta_{\mathrm{e}}}{\delta_{\mathrm{L}}^{0}},\Gamma\left(\frac{\Delta_{\mathrm{e}}}{\delta_{\mathrm{L}}^{0}},\frac{u'_{\Delta_{\mathrm{e}}}}{S_{\mathrm{L}}^{0}},\mathrm{Re}_{\Delta_{\mathrm{e}}}\right)\frac{u'_{\Delta_{\mathrm{e}}}}{S_{\mathrm{L}}^{0}}\right]\right)^{\beta} \tag{4.78}$$

Note that Δ_{e} is the effective LES filter size (used in Equation (4.36)). It does not exactly correspond to the mesh edge size Δx. The LES filter size is instead usually taken proportional $\Delta_{\mathrm{e}} \propto \Delta x$ [270, 275]. In Charlette *et al.* [274], it is chosen at $\Delta_{\mathrm{e}} = F\delta_{\mathrm{L}}^{0}$. Γ is a function accounting for the subgrid strain rate (depending on the subgrid velocity fluctuations and on the filter size). The Reynolds number is evaluated at the LES filter size: $\mathrm{Re}_{\Delta_{\mathrm{e}}} = (\rho u'_{\Delta_{\mathrm{e}}}\Delta_{\mathrm{e}})/\nu$ and the expression of Colin *et al.* [270] is used for the velocity fluctuations. Finally, the model constant β is fixed at 0.5 as suggested in the original work of Charlette *et al.* [274].

The TFLES model has been successfully applied to a wide range of applications including anchored, lifted and blown-off flames [268], swirled flames [241, 276–279] and stratified flames [280] to cite a few. As far as propagating flames are concerned, the TFLES approach has also been validated for ignition sequence [248], deflagration [49, 51] and deflagration to detonation transition [53, 56, 281] for instance.

Part II

State of the art of lean hydrogen-air explosions: the Thickened Flame model

Chapter 5

Naïve approach to the LES of lean hydrogen-air explosions

Sommaire

Chapters 2 and 3 have introduced the necessary notions to understand the various factors influencing flame propagation in a lean hydrogen-air explosion. In Chapter 4, a thorough description of the principle of Large-Eddy Simulations has been presented. The goal of this thesis being to provide a modelling strategy for the LES of lean H_2-air explosions, a preliminary study is needed to assess the performance of state-of-the-art models. This chapter aims at identifying the caveats of a naïve LES of such scenarios. A detailed description of the configuration of interest is given in Section 5.1. Section 5.2 presents simulation results using a detailed chemical mechanism and following a two-step programme: several flames are first analysed in Direct Numerical Simulations (without any model) to identify the physical acceleration mechanisms at play; then, the mesh is coarsened and the classical Thickened Flame model is activated to evaluate its effect on flame propagation. Finally, a similar analysis is carried out with a global chemical scheme in Section 5.3. This kind of simplified chemistry is indeed typical in explosion calculations.

5.1 Set-up description

It is commonly agreed that the initial stages of an explosion can have substantial consequences on the following turbulent development. Focus is therefore first put on the initial laminar phase of an explosion. To that end, the configuration studied throughout this chapter consists of a flame ignited at one end of a two-dimensional tube, depicted in Figure 5.1. The reduction to 2D geometry allows affordable Direct Numerical Simulations of the full tube to set a reference for the establishment of dedicated models. Potential 3D effects will be later discussed in Chapter 9.

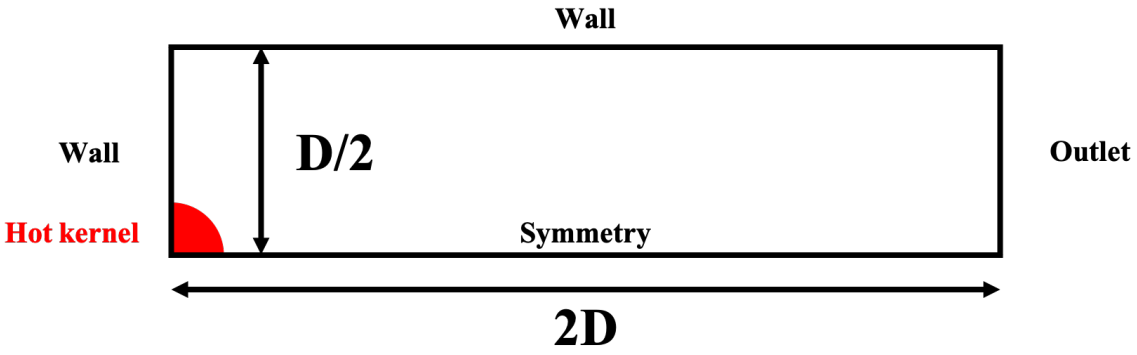

Figure 5.1: Schematic of the 2D tube configuration.

5.1.1 Operating conditions

The present work is devoted to understanding and modelling the dynamics of lean hydrogen-air explosions. Mixtures with equivalence ratios ranging from as lean as $\Phi = 0.325$ to as rich as $\Phi = 7.300$ are studied. Most points are of course in the lean side to evaluate the peculiarities of lean H_2-air flames such as the response to stretch and the propensity for flame front instabilities. A summary of all operating conditions considered as well as their corresponding flame properties is given in Table 5.1. All cases are performed under atmospheric temperature and pressure. Note that the acceleration rate $(\sigma - 1)S_L^0$ of the finger flame mechanism (Equation (3.11), Section 3.1.2) is also provided. The last two cases ($\Phi = 5.916$ and $\Phi = 7.300$) correspond to very rich flames sharing the same acceleration rate $(\sigma - 1)S_L^0$ as their lean counterparts ($\Phi = 0.500$ and $\Phi = 0.400$ respectively) as highlighted in Table 5.1. The comparison between the very rich thermo-diffusively stable cases and their lean unstable equivalent will permit to highlight the coupling of thermodiffusive effects with the finger flame mechanism.

Φ	S_L^0 [m/s]	δ_L^0 [mm]	σ	$(\sigma - 1)S_L^0$ [m/s]	$\mathrm{Le_{eff}}$
0.325	0.074	1.321	3.956	0.219	0.362
0.350	0.120	0.909	4.128	0.377	0.371
0.400	0.236	0.579	4.457	0.816	0.388
0.450	0.375	0.448	4.765	1.411	0.406
0.500	0.533	0.382	5.056	2.162	0.426
0.550	0.704	0.346	5.327	3.046	0.448
0.600	0.883	0.326	5.581	4.045	0.472
0.700	1.247	0.309	6.036	6.280	0.526
0.800	1.596	0.306	6.419	8.648	0.590
0.900	1.916	0.309	6.726	10.970	0.665
1.000	2.199	0.311	6.926	13.028	0.772
1.600	3.014	0.289	6.501	16.578	1.006
5.916	0.705	0.703	4.067	2.162	1.183
7.300	0.303	1.274	3.679	0.811	1.193

Table 5.1: Operating conditions used in the 2D tube set-up with corresponding mixture and flame properties.

5.1.2 Geometry

The aspect ratio of the tube is set to 4. It will be shown later that this tube length is sufficient to properly observe the finger flame acceleration until its end when the flame skirt touches the lateral wall. The reference configuration is set such that the tube radius corresponds to:

$$R_{\mathrm{tube}} = 100\delta_L^0 \tag{5.1}$$

where δ_L^0 is the thermal flame thickness defined in Chapter 2. Ensuring 100 flame thicknesses within the tube radius leaves enough room for thermo-diffusive instabilities to

develop in the initial spherical phase of propagation. Note that the tube radius changes with each operating point (Φ), always satisfying Equation (5.1). This allows a fair comparison between all cases. An analysis of the effects of the tube geometry (varying the $R_{\text{tube}}/\delta_{\text{L}}^0$ ratio) is presented in Section 5.3.6.

5.1.3 Boundary conditions

A symmetry is imposed as a bottom boundary condition to limit the simulation to half-a-tube. It has indeed been shown in Section 3.1 that the flame propagates mainly along the centerline of the tube, driven by the finger flame phenomenon. For lean mixtures, some asymmetry may be introduced by flame front instabilities which are inherently chaotic. However, this effect is believed to be second-order regarding flame acceleration. Different thermal and velocity conditions are possible for the walls of the tube. Knowing that the boundary condition at the ignition plate can trigger the thermo-diffusive instability[1], it is set to an adiabatic slip-wall to let TD cells freely develop in the hemi-spherical phase of propagation. On the other hand, the top wall is imposed as adiabatic no-slip. The no-slip condition at lateral walls can be conducive to flame acceleration through the Shelkin mechanism (see Section 3.1). The heat loss is neglected to stay consistent with the condition imposed on the ignition wall. Finally, the outlet uses the Navier-Stokes Characteristic Boundary Conditions (NSCBC) formalism [282] with a zero relaxation coefficient so as to evacuate all pressure waves generated both by the flame (physical effect) and by the initialisation procedure (numerical effect) presented hereafter.

5.1.4 Initialisation procedure

To initialise the simulations, planar flame profiles computed using the open-source Cantera software [234] are used. They are interpolated on the mesh to form a spherical kernel as shown in Figure 5.1. For the velocity field, an analytical profile determined for spherical flames is imposed following the work of Bonhomme [283]. In 2D, it writes:

$$u_r(r) = \frac{1}{\rho_{\text{1D}}(r) r} \frac{\rho_{\text{1D,u}}}{\rho_{\text{1D,b}}} S_{\text{L}}^0 \int_0^r r \frac{\partial \rho_{\text{1D}}(r)}{\partial r} \, \mathrm{d}r \tag{5.2}$$

where u_r is the radial component of the velocity vector and subscript 1D refers to properties from the planar flame. The use of unstretched planar profiles for the other variables is far from the reality of spherical flames but constitutes a well-established procedure that is commonly applied [49, 51, 53]. Some spurious numerical noise can result from this initialisation but are rapidly evacuated after a short transient period. In any case, the present thesis is not concerned with modelling the ignition of embryonic flame kernels.

[1] If a no-slip condition is imposed, the zero-velocity tangent to the wall forces a perturbation of the flame surface which can become amplified by the natural thermo-diffusive instability. Instead, a spontaneous development of TD cells is preferred.

The reader may refer to Lacaze *et al.* [245] for further details about numerical ignition alternatives. The initial radius is determined by:

$$r_{\mathrm{f},0}^{\mathrm{DNS}} = 2\delta_{\mathrm{L}}^{0} \tag{5.3}$$

This value is set sufficiently low to minimise as much as possible any effects of ignition on the overall flame propagation. As explained in the introduction of the chapter, some calculations involve coarse (LES-like) meshes (they are later presented in Section 5.2.3). These simulations need a larger initial kernel to successfully ignite. If the kernel size is too small, the hot gases profiles can be partially cut out, hence reducing the amount of thermal energy contained therein and hindering flame propagation: the flame is too weak and extinguishes. For these cases, the initial radius is imposed by:

$$r_{\mathrm{f},0}^{\mathrm{LES}} = 20\delta_{\mathrm{L}}^{0} \tag{5.4}$$

5.1.5 Meshes for Direct Numerical Simulations

In order to evaluate the performance of state-of-the-art simulation strategies to capture the dynamics of hydrogen-air flames, a mesh with quadrilateral elements is built for each operating condition. The cell size is chosen to allow $\delta_{\mathrm{L}}^{0}/\Delta x = 10$ cells within the flame thickness. A summary of all meshes parameters is provided in Table 5.2.

Φ	Δx [mm]	$\delta_{\mathrm{L}}^{0}/\Delta x$
0.325	0.132	10
0.350	0.090	10
0.400	0.057	10
0.450	0.044	10
0.500	0.038	10
0.550	0.034	10
0.600	0.032	10
0.700	0.030	10
0.800	0.030	10
0.900	0.030	10
1.000	0.031	10
1.600	0.028	10
5.916	0.070	10
7.300	0.127	10

Table 5.2: Mesh resolutions used in the 2D tube reference DNS ($\delta_{\mathrm{L}}^{0}/\Delta x = 10$) set-up for all operating conditions.

5.2 Detailed mechanism

This section deals with simulations using a detailed chemistry. The chemical kinetic scheme of San Diego (9 species, 21 reactions) [60] is chosen. In the first place, Direct Numerical Simulations are carried out in Sections 5.2.1 and 5.2.2 to identify the main physical mechanisms at play during the flame acceleration in the present 2D tube configuration. In Section 5.2.3, the mesh resolution is progressively decreased and the Thickened Flame model is activated. It aims at evaluating the influence of this classical LES model on hydrogen-air flame propagation.

5.2.1 Effect of equivalence ratio

The effect of mixture composition is analysed in this section. The DNS (using the meshes allowing $\delta_{\mathrm{L}}^{0}/\Delta x = 10$, Table 5.2) at all equivalence ratios are compared. Several snapshots at different instants of flame propagation are shown for $\Phi = 0.350$, $\Phi = 0.700$, $\Phi = 1.000$ and $\Phi = 1.600$ in Figures 5.2 to 5.5. Comparison of the four cases must be taken with care since the flames have different sizes: the tubes dimensions have been scaled with the flame thickness. To give an idea, the tube radius is equal to 909 mm in the leanest case, against 289 mm for the richest. Both lean flames develop cellular patterns characteristic of the thermo-diffusive instability presented in Section 2.3.2. The effective Lewis number (computed using Equation (2.37)) of these mixtures is indeed well below unity at 0.371 and 0.526 respectively. As is expected from the asymptotic theory, the instability is strongest for the leaner $\Phi = 0.350$ case (Figure 5.2). For this mixture, the finger flame phenomenon is visually coupled with flame front instabilities: cells appear during the early spherical stage but continue developing in the subsequent finger flame phase. TD cells create temperature variations within the hot gases: convex zones (protruding into the fresh gases) are superadiabatic and regions near cusps are largely subadiabatic. This is symptomatic of the TD instability as explained in Section 2.3.2. On the other hand, the stoichiometric and rich flames are only very mildly wrinkled (Figures 5.4 and 5.5). Under such conditions, the flame is known to be thermo-diffusively stable. The cusps observed on the flame surface are most probably due to the Darrieus-Landau instability mechanism which only arises at large scales (cf. Section 2.3.1).

To get a quantitative comparison of the DNS at various equivalence ratios, the flame tip position x_{f} is tracked over time (cf. Figure 2.3). For stable flames only subject to the finger flame mechanism, the tip is always located along the centerline of the tube as suggested by the theory. For unstable flames, the front is actually a flame brush wrinkled by cellular instabilities which chaotically develop on the flame surface. As a consequence, the tip is not always located on the symmetry axis of the tube. The flame tip velocity is then computed according to:

$$v_{\mathrm{f}} \equiv \frac{\mathrm{d}x_{\mathrm{f}}}{\mathrm{d}t} \tag{5.5}$$

To conduct a similarity analysis of all cases, x_{f} (resp. v_{f}) is normalised by the tube radius

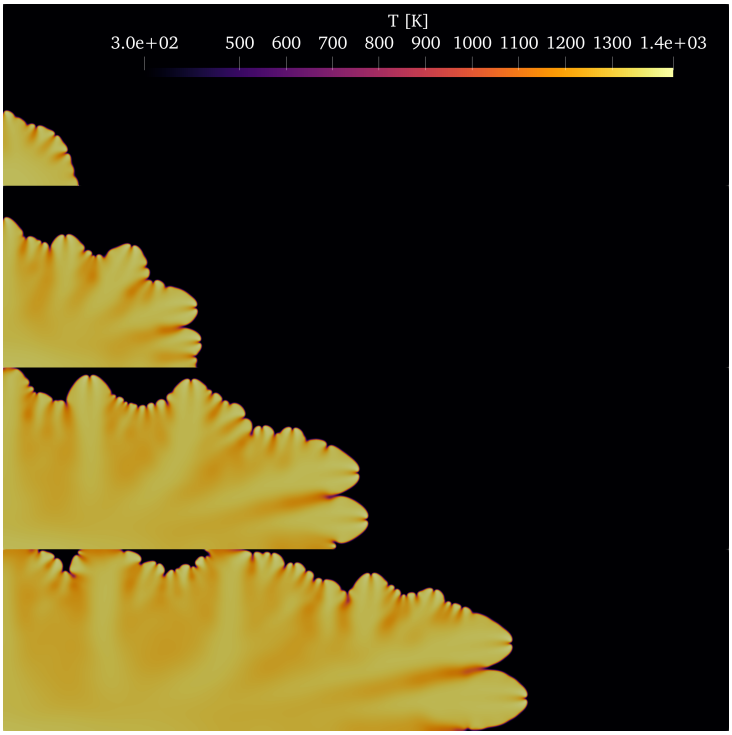

Figure 5.2: Snapshots of temperature field during flame propagation for the DNS ($\delta_{\mathrm{L}}^{0}/\Delta x = 10$) at $\Phi = 0.350$.

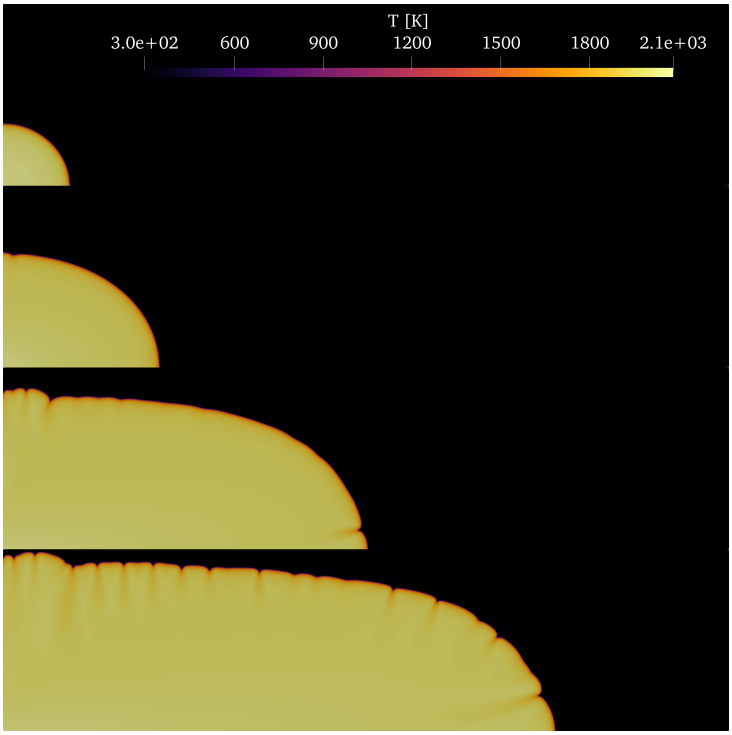

Figure 5.3: Snapshots of temperature field during flame propagation for the DNS ($\delta_{\mathrm{L}}^{0}/\Delta x = 10$) at $\Phi = 0.700$.

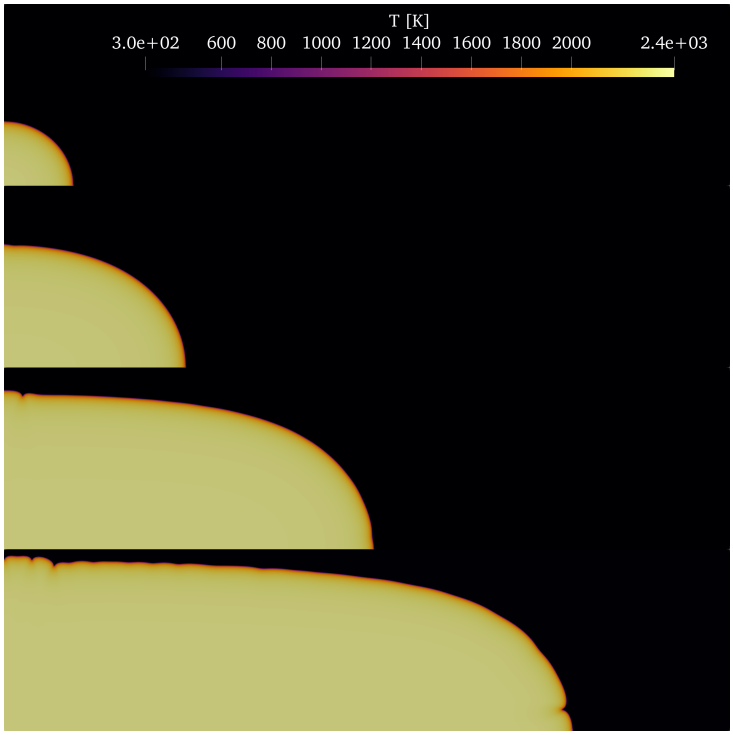

Figure 5.4: Snapshots of temperature field during flame propagation for the DNS ($\delta_{\mathrm{L}}^{0}/\Delta x = 10$) at $\Phi = 1.000$.

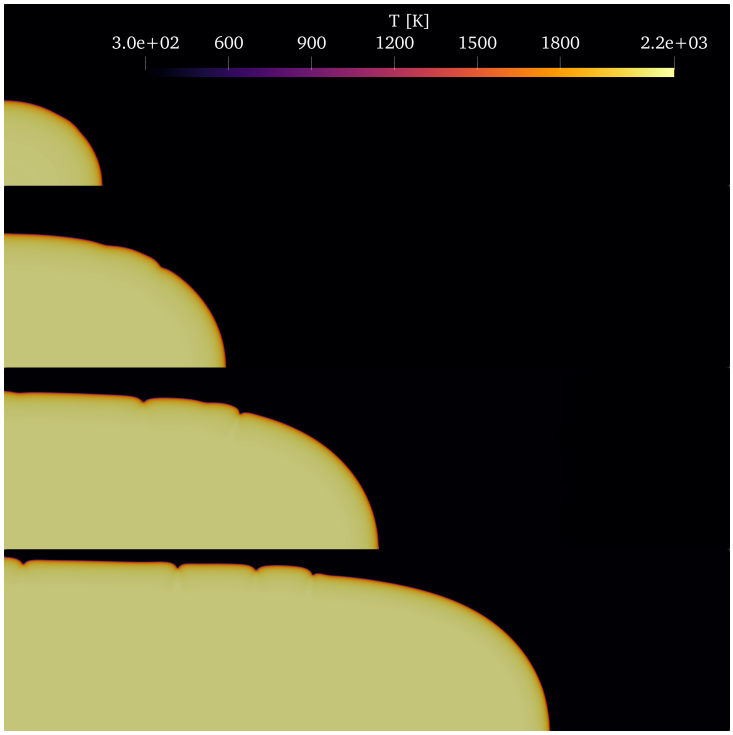

Figure 5.5: Snapshots of temperature field during flame propagation for the DNS ($\delta_{\mathrm{L}}^{0}/\Delta x = 10$) at $\Phi = 1.600$.

(resp. the laminar flame speed):

$$\begin{cases} \xi_{\mathrm{f}} \equiv \dfrac{x_{\mathrm{f}}}{R_{\mathrm{tube}}} \\ S_{\mathrm{f}} \equiv \dfrac{v_{\mathrm{f}}}{S_{\mathrm{L}}^{0}} \end{cases} \tag{5.6}$$

Figure 5.6 shows the normalised flame propagation speed as a function of the normalised tip position. The initial increase of the flame speed happens during the hemi-spherical flame phase (annotated "1") and reflects the influence of stretch. Following ignition, the initial kernel experiences strong curvature effects responsible for the sharp initial acceleration. While the kernel grows, the curvature reduction goes with a short deceleration. The discrepancies between all operating conditions in this normalised space are very weak at this stage of the propagation. After that, all cases undergo a strong acceleration (annotated "2") characteristic of the confinement effect induced by the walls. As soon as the flame skirt touches the lateral wall (instant annotated "3"), the flame velocity declines because of the surface area loss. Comparing the different simulations in this non-dimensional frame allows to get rid of the strong laminar flame speed discrepancies. It also highlights an important conclusion: the acceleration rate of lean hydrogen-air flames is stronger than that of rich flames. This is the macroscopic result of the local burning rate enhanced by stretch effects and thermo-diffusive instabilities. This is further detailed in the next section. The finger flame phenomenon presented in Section 3.1 is usually the driving acceleration mechanism for the early stages of flame propagation in a tube. In the present 2D (planar) case, the rate of the exponential acceleration is theoretically given by Equation (3.11), and in non-dimensional form:

$$S_{\mathrm{f}} = \sigma + (\sigma - 1)\xi_{\mathrm{f}} \tag{5.7}$$

In other words, if all flames were only subject to the finger flame mechanism, all curves would collapse in the phase space given by $(\xi_{\mathrm{f}}, (S_{\mathrm{f}} - \sigma)/(\sigma - 1))$. Such comparison is shown in Figure 5.7. It is seen that rich and near-stoichiometric flames properly follow the finger flame trend (dashed black line). This means that the slight disturbances triggered by the hydrodynamic instability and potential stretch effects have very little influence on the flame propagation for these mixtures. It is expected to become more important in larger tubes allowing for Darrieus-Landau wrinkles to fully develop. On the other hand, lean mixtures are strongly accelerated with decreasing Φ because of thermo-diffusive instabilities and stretch effects which amplify the finger flame acceleration mechanism.

5.2.2 Effect of thermo-diffusive instabilities

The previous section has demonstrated the progressive disappearance of flame front instabilities and the weakening of stretch effects as one goes from very lean to stoichiometric mixtures and beyond. The stabilisation of the flame front results in a milder flame acceleration, eventually collapsing with the pure finger flame theoretical curve. As shown in Section 3.1, the latter is based on an infinitely thin flame assumption which discards

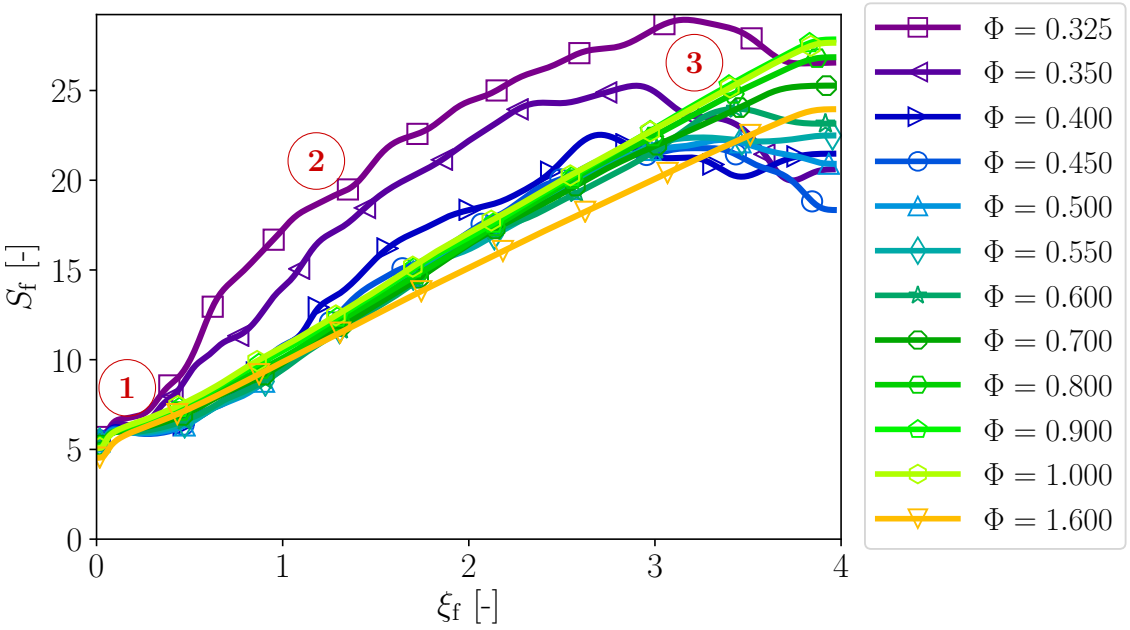

Figure 5.6: Normalised flame speed as a function of normalised flame tip position. 1: hemi-spherical phase. 2: finger flame phase. 3: end of finger flame phase (flame skirt touches the wall).

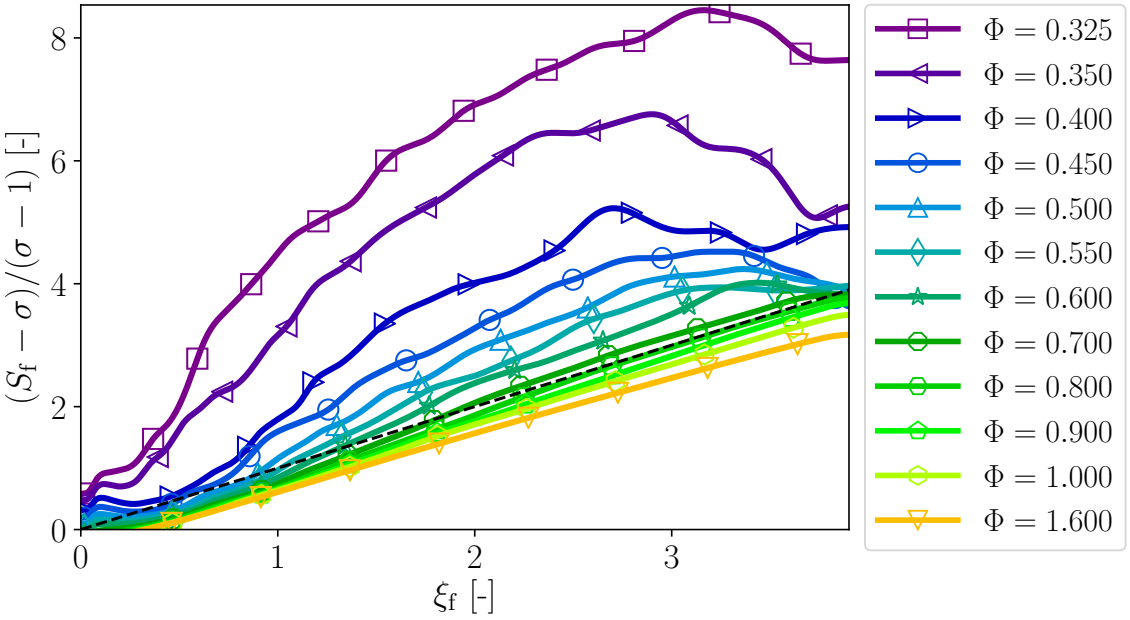

Figure 5.7: Normalised flame speed as a function of normalised flame tip position in another frame determined for finger flame similarity. Dashed black line: finger flame theoretical slope (Equation (3.8)).

all diffusive processes. On the other hand, the birth of thermo-diffusive instabilities is closely linked to the flame response to stretch as made explicit in the asymptotic theory (see Section 2.3.2). Both are related to a mixture Lewis number sufficiently lower

than one. If the mixture is perfectly equidiffusive ($\mathrm{Le}_{\mathrm{eff}} = 1$), they should disappear. Such demonstration is not possible with a detailed kinetic scheme for which unity-Lewis numbers have little meaning. As an attempt to isolate the effects of intrinsic flame front instabilities on the propagation, rich counterparts to lean unstable flames have been determined. As explained in Section 5.1.1, cases $\Phi = 5.916$ and $\Phi = 7.300$ have been chosen to match their lean equivalent $\Phi = 0.500$ and $\Phi = 0.400$ in terms of finger flame acceleration rate $(\sigma - 1)S_{\mathrm{L}}^0$. In the following, each ultra-rich flame has been simulated in the tube corresponding to its lean counterpart. This allows a direct comparison in dimensional coordinates $(x_{\mathrm{f}}, v_{\mathrm{f}})$. Figures 5.8 and 5.9 represent the flame speed as a function of position for both pair of operating points. While rich mixtures closely match the finger flame exponential acceleration, their slope is modest compared to their lean equivalent. This is again due to a combination of factors:

- thermo-diffusive instabilities: flame wrinkling and local stretch effects disappear on the rich side;
- negative stretch response: the overall flame is now smooth, still positively stretched by the flow geometry, but the response to stretch has become negative.

Both contribute to a lesser acceleration of the flame in comparison with lean mixtures. On top of that, the stretch response differences are clearly visible at the beginning of propagation: lean cases suffer an abrupt acceleration due to flame curvature during the spherical stage which is not observed for the ultra-rich cases. The end of the acceleration stage is also more pronounced for the rich cases. This is typical of the pure finger flame mechanism which collapses when the flame skirt reaches the lateral wall and the flame surface rapidly shrinks. In comparison, the lean cases suffer an extended finger flame phase due to the TD wrinkling.

In order to get a proper evaluation of stretch effects on the flames, the local flame consumption speed (defined in Equation (2.10)) as well as the local stretch rate (Equation (2.72)) are computed at several instants of the propagation for cases $\Phi = 0.400$ and $\Phi = 7.300$. The FCS is normalised by the laminar flame speed to yield the stretch factor I_0 as introduced in Section 2.4. Maps of the stretch factor I_0 and stretch rate $\mathbb{K}$ are shown in Figures 5.10 and 5.11 for $\Phi = 0.400$ and Figures 5.12 and 5.13 for $\Phi = 7.300$. The intricate coupling of stretch effects and thermo-diffusive instabilities is clearly visible in the first picture. It is indeed the local stretch response (related to the mixture Lewis number) which dictates the dynamics of TD cells development, inducing intense (resp. moderate) burning in positively stretched crests (resp. negatively stretched cusps). On the contrary, the smooth flame at $\Phi = 7.300$ is globally positively stretched during the whole flame propagation. The high effective Lewis number leads to a negative stretch response evidenced by the sub-unity I_0 levels.

To finalise the stretch response analysis, joint probability density functions (JPDF) of I_0 against $\mathbb{K}$ are displayed in Figure 5.14. The positive (resp. negative) stretch response is demonstrated for the lean (resp. rich) flame. The linear response predicted by the

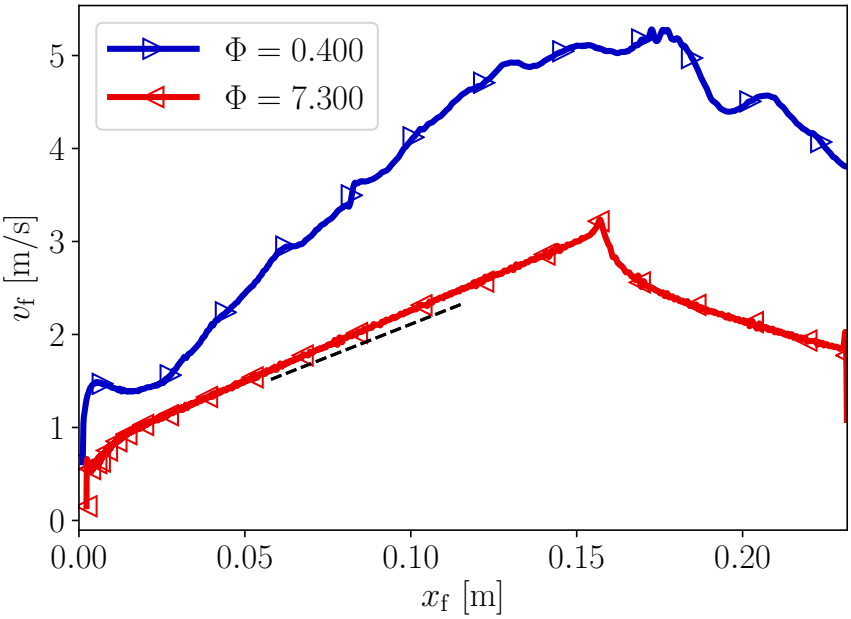

Figure 5.8: Flame speed as a function of flame tip position for $\Phi = 0.400$ and $\Phi = 7.300$. Dashed black line: finger flame theoretical slope (Equation (3.11)).

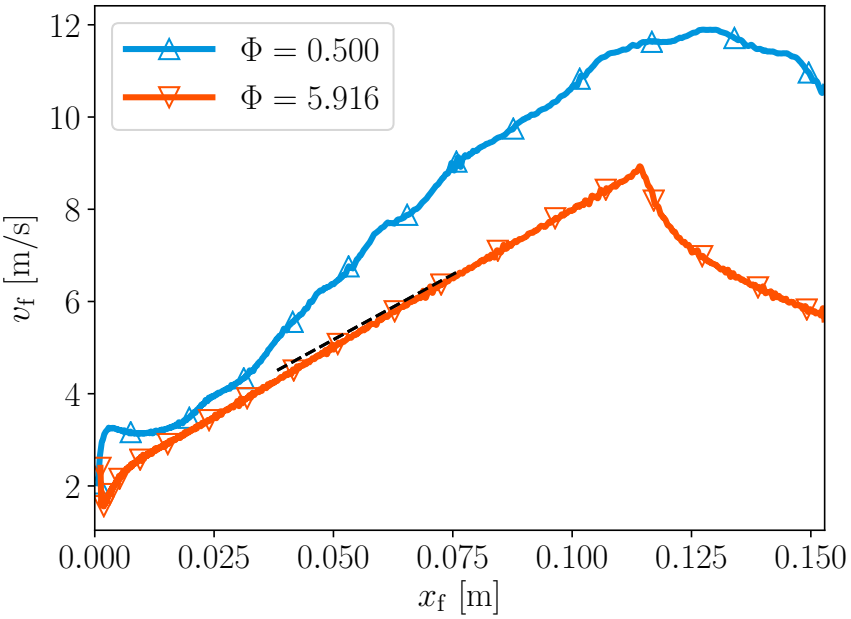

Figure 5.9: Flame speed as a function of flame tip position for $\Phi = 0.500$ and $\Phi = 5.916$. Dashed black line: finger flame theoretical slope (Equation (3.11)).

asymptotic theory is also plotted. The measured FCS do not exactly follow the theoretical curve but it is in qualitative agreement with it. The JPDF of the ultra-rich flame has a highest probability crest following properly a linear trend, whereas a way wider range of stretch rates and burning rates is observed for the unstable case due to the cellular patterns at $\Phi = 0.400$.

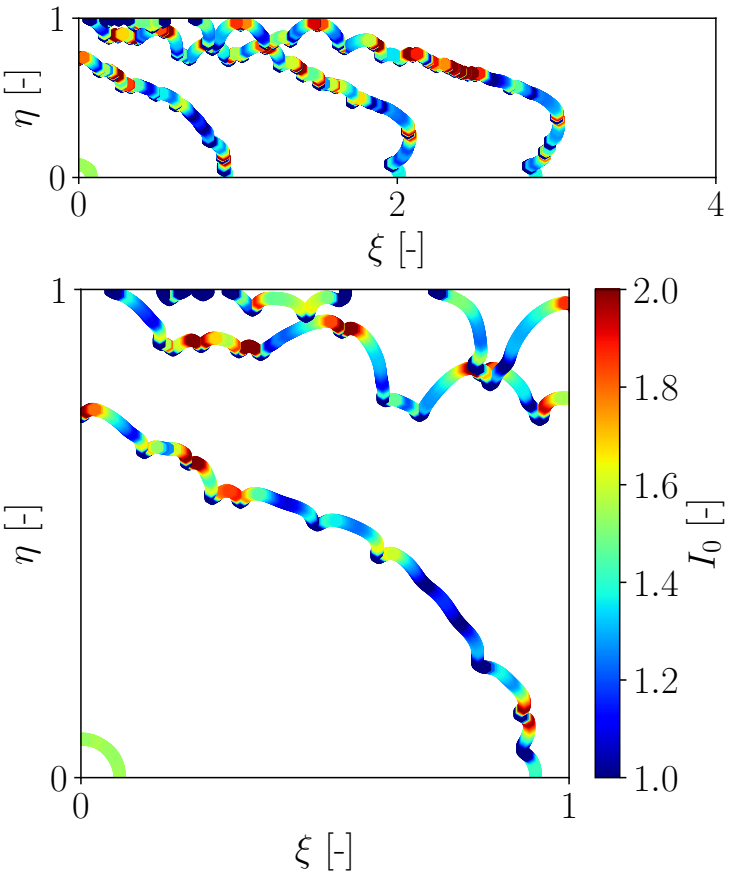

Figure 5.10: Local stretch factor I_0 at several instants during flame propagation for the DNS at $\Phi = 0.400$. Top: global view. Bottom: zoom on the beginning of propagation.

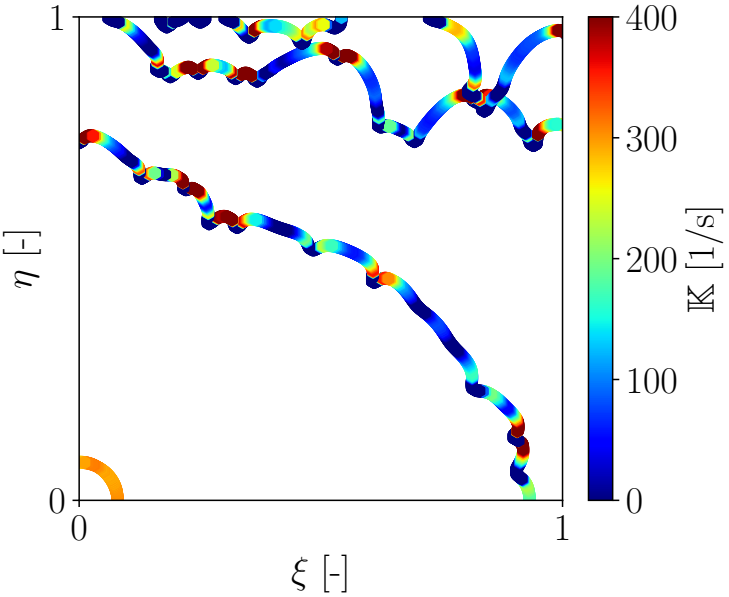

Figure 5.11: Local stretch rate $\mathbb{K}$ at several instants during flame propagation for the DNS at $\Phi = 0.400$.

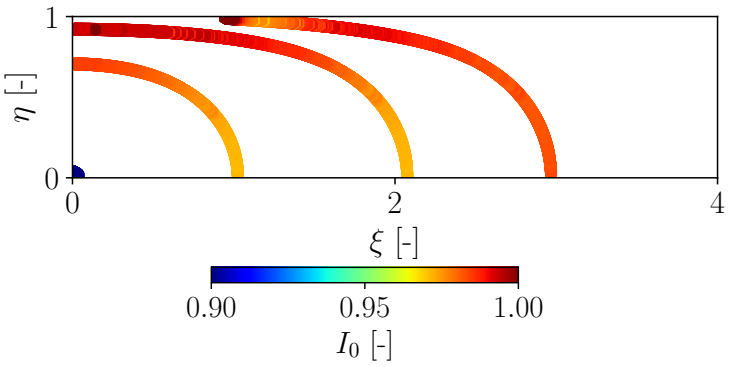

Figure 5.12: Local stretch factor I_0 at several instants during flame propagation for the DNS at $\Phi = 7.300$.

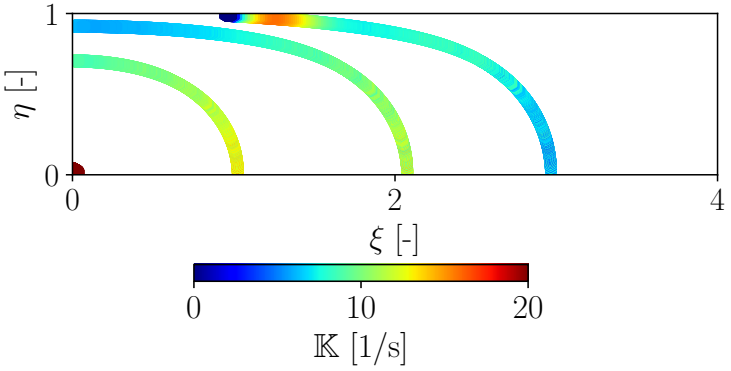

Figure 5.13: Local stretch rate $\mathbb{K}$ at several instants during flame propagation for the DNS at $\Phi = 7.300$.

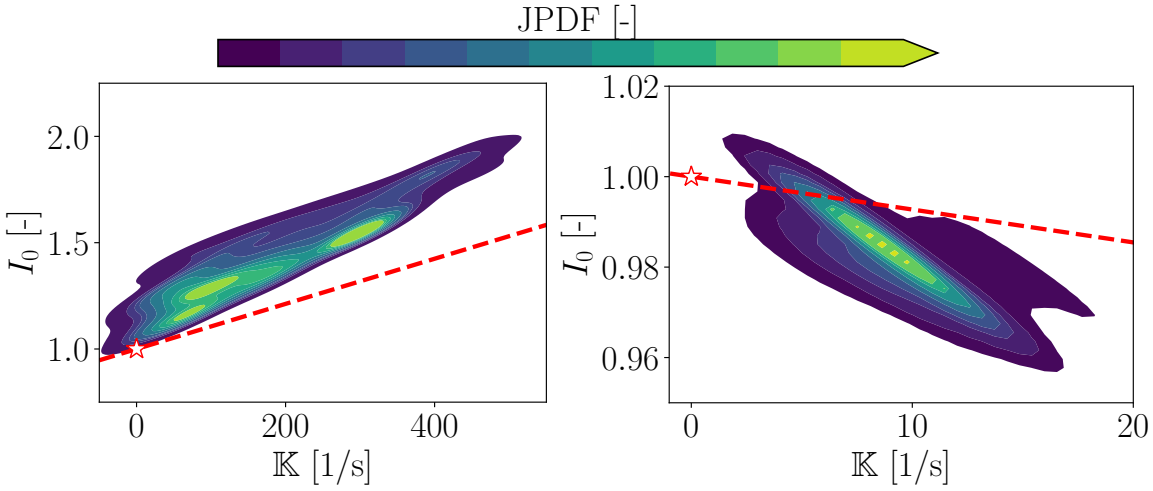

(a) $\Phi = 0.400$. (b) $\Phi = 7.300$.

Figure 5.14: Joint PDF of stretch factor I_0 as a function of total stretch $\mathbb{K}$ for the DNS at $\Phi = 0.400$ and $\Phi = 7.300$. Dashed red line: asymptotic theory (Equation (2.44)). Red star: unstretched laminar value.

5.2.3 Effect of mesh resolution and impact of the flame thickening approach

So far, in-depth analyses of DNS calculations have highlighted the role of sub-unity Lewis number effects on flame propagation. More specifically, the rapid development of thermo-diffusive instabilities interacts with the finger flame phenomenon to yield a considerable flame acceleration. Direct Numerical Simulations have been performed for each operating point on meshes allowing $\delta_L^0/\Delta x = 10$ cells within the flame thickness. This value is expected to be sufficient to resolve the flame structure for classical mixtures [51]. However, lean H_2-air flames develop thermo-diffusive cells at micro-scales of the order of the flame thickness which can question the previous DNS resolution criterion [118, 284, 285]. To ensure that $\delta_L^0/\Delta x = 10$ is enough to capture the proper flame dynamics in the current tube configuration, a highly refined DNS using $\delta_L^0/\Delta x = 20$ is conducted at $\Phi = 1.000$ (TD-stable) and $\Phi = 0.400$ (TD-unstable). In addition, to assess the performance of the standard TF model used in LES, a full mesh convergence study is carried out for these operating conditions. The various mesh resolutions are presented in Tables 5.3 and 5.4. Simulations on coarse meshes ($\delta_L^0/\Delta x \leq 7$) use the previously introduced Thickened Flame formalism (see Section 4.4) with thickening factor F to impose $N_c = F\delta_L^0/\Delta x = 7$. Despite the absence of a turbulence subgrid model (the propagation is mainly laminar here), these cases will be referred to as LES for simplicity.

Δx [mm]	$\delta_L^0/\Delta x$	F	N_c	Approach
0.015	20		20	DNS
0.031	10		10	DNS
0.062	5	1.4	7	LES
0.155	2	3.5	7	LES
0.311	1	7	7	LES
0.622	0.5	14	7	LES
1.556	0.2	35	7	LES

Table 5.3: Mesh resolutions used in the 2D tube set-up for $\Phi = 1.000$.

Δx [mm]	$\delta_L^0/\Delta x$	F	N_c	Approach
0.028	20		20	DNS
0.057	10		10	DNS
0.115	5	1.4	7	LES
0.289	2	3.5	7	LES
0.578	1	7	7	LES
1.157	0.5	14	7	LES
2.894	0.2	35	7	LES

Table 5.4: Mesh resolutions used in the 2D tube set-up for $\Phi = 0.400$.

Stoichiometric case $\Phi = 1.000$

Figure 5.15 depicts several snapshots coloured by heat release rate for the whole flame

propagation. It has been shown in Section 5.2.1 that the reference DNS at $\delta_L^0/\Delta x = 10$ is almost perfectly stable during the whole propagation. It only develops some cellular patterns due to the hydrodynamic instability at large kernel size. The DNS on the finer mesh at $\delta_L^0/\Delta x = 20$ looks in every instant almost identical to the previous simulation with $\delta_L^0/\Delta x = 10$. The introduction of LES meshes with the TF formalism stabilises the flame. However, given that the DNS (both cases $\delta_L^0/\Delta x = 20$ and $\delta_L^0/\Delta x = 10$) are relatively smooth, the first LES is perfectly stable throughout the propagation. Comparing all LES, a difference in terms of heat release rates is observed. While all flames have phenomenologically the same propagation, they burn differently: the TF model dilates the heat release profile to thicken the flame, thus reducing the maximum value for the coarser meshes.

The effects of the TF model is assessed in the phase space in Figure 5.16. As previously mentioned, the DNS ($\delta_L^0/\Delta x = 20$ and $\delta_L^0/\Delta x = 10$) correctly follow the theoretical finger flame acceleration. Switching to the LES at $\delta_L^0/\Delta x = 5$ slightly reduces the finger flame acceleration slope due to the lack of DL instabilities resolution. When the mesh is again coarsened, the acceleration rate no longer significantly changes.

Figure 5.17 provides another angle to see the impact of the TF model by showing the joint PDF of local stretch factor I_0 as a function of the stretch rate for $\delta_L^0/\Delta x = 10$ and $\delta_L^0/\Delta x = 1$. The response to stretch is relatively flat for both cases but the range of $\mathbb{K}$ values is wider in the DNS. It reflects the action of the DL instability.

Lean case $\Phi = 0.400$

On the other side of the spectrum of simulated operating conditions lies the lean case. Figure 5.18 displays the flame shape evolution for the two DNS and several LES. In agreement with what has been stated in Section 5.2.1, the DNS flames ($\delta_L^0/\Delta x = 20$ and $\delta_L^0/\Delta x = 10$) are thermo-diffusively unstable. The wrinkles caused by the instability generate faster-burning zones which grow along with the flame kernel until they split into smaller cells. As explained in Section 2.3.2, flame stretch has a stabilising impact at a local level. When a TD cell expands, the stretch rate diminishes until a critical threshold, allowing the splitting. The macroscopic outcome is the perpetual creation and destruction of TD "fingers". This feature is not predicted by the linear stability theory (which is limited to small perturbations) but commonly observed in experiments and simulations [286–288]. Because of the chaotic nature of the flame front instabilities, their origin and development is also dependent on the numerical set-up (in particular the mesh type of cells, cells arrangement, etc.). As a consequence, cases $\delta_L^0/\Delta x = 20$ and $\delta_L^0/\Delta x = 10$ are not identical but display TD structures which look similar in shapes and scales.

When the resolution is further decreased, $\delta_L^0/\Delta x \leq 5$, the TD structures are progressively lost. The LES at $\delta_L^0/\Delta x = 5$ is still highly unstable. However, one can notice the lesser extent of the cellular patterns. In particular, they appear later than for the DNS reference. This is due to the stabilising effect of the TF model: a thicker flame is harder to wrinkle. This argument is at the basis of subgrid turbulent combustion mod-

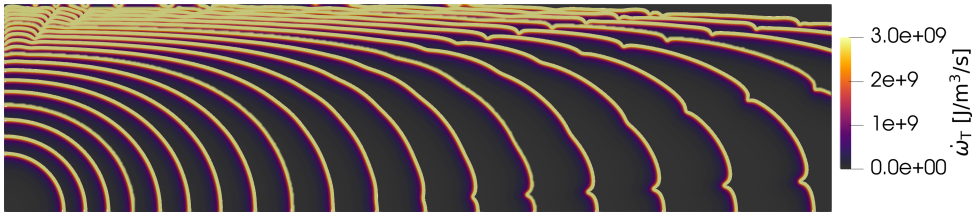

(a) DNS $\delta_L^0/\Delta x = 20$.

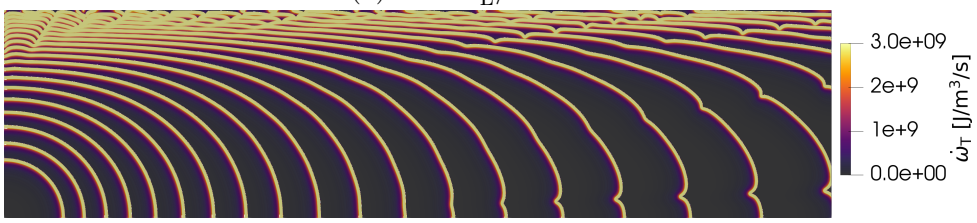

(b) DNS $\delta_L^0/\Delta x = 10$.

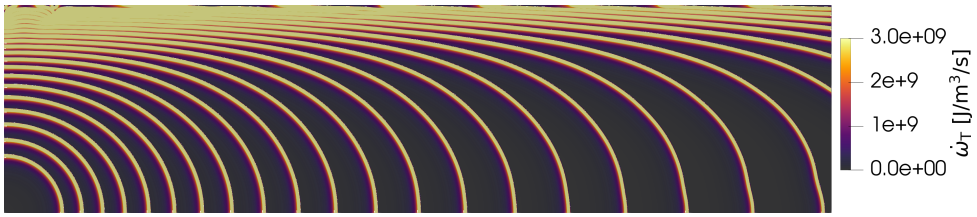

(c) LES $\delta_L^0/\Delta x = 5, F = 1.4$.

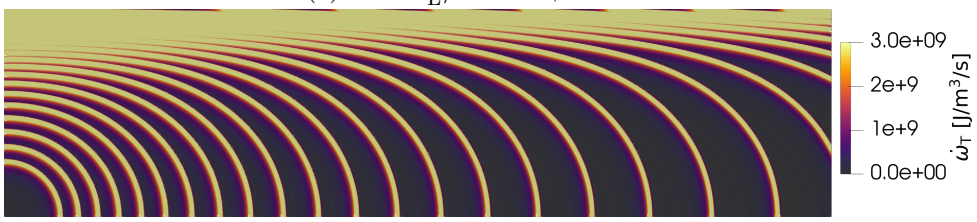

(d) LES $\delta_L^0/\Delta x = 2, F = 3.5$.

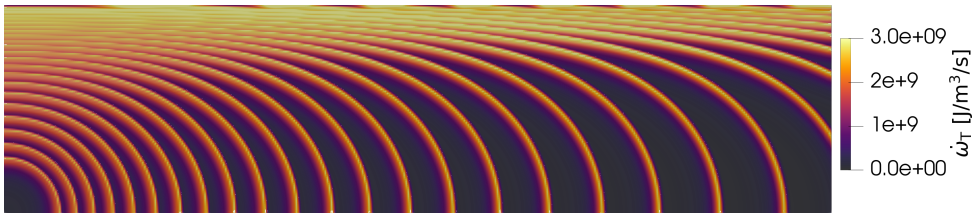

(e) LES $\delta_L^0/\Delta x = 1, F = 7$.

Figure 5.15: Superimposition of heat release rate profiles at several instants ($\Delta t = 10\delta_L^0/(\sigma S_L^0)$ between two consecutive contours) of flame propagation for several mesh resolutions (Table 5.3). $\Phi = 1.000$.

els for TFLES and applies in the same way for flame front instabilities. For the latter, this statement is consolidated by another argument coming from the asymptotic theory presented in Section 2.3.2. The dispersion relation for spherical flames accounting for Darrieus-Landau and thermo-diffusive instability mechanisms is given by Equation (2.61). The TF transform used in LES does not change any parameter except δ_d. It means that the instability peninsula (as shown in Figure 2.14) for a thickened flame is the same as in DNS when plotted in non-dimensional coordinates (Peclet number in abscissa), but

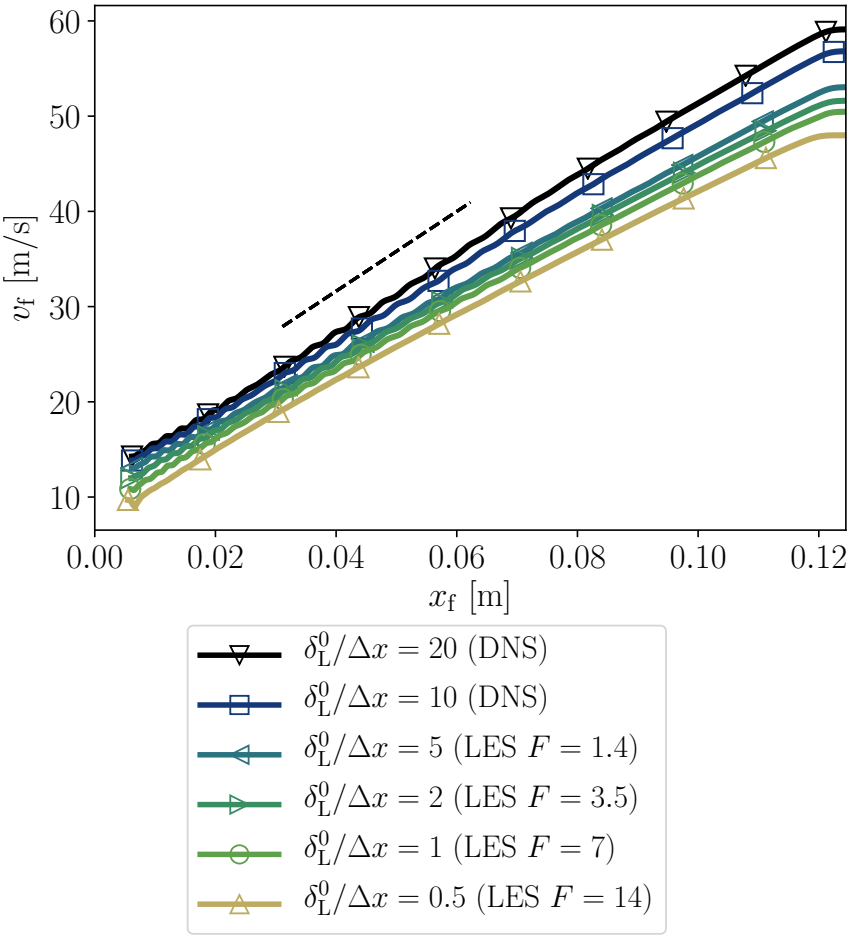

Figure 5.16: Flame speed as a function of flame tip position for several mesh resolutions (Table 5.3). $\Phi = 1.000$. Dashed black line: finger flame theoretical slope (Equation (3.11)).

is dilated in physical coordinates (flame radius in abscissa): the instability is delayed. This feature is schematically shown in Figure 5.19. While the present 2D tube set-up lies outside the validity domain of the asymptotic relations, they still provide a qualitative answer to the observed flame stabilisation.

Case $\delta_L^0/\Delta x = 5$ constitutes an intermediate LES for which TD structures are still captured. Further coarsening the mesh reduces the instability and for the case $\delta_L^0/\Delta x = 1$ the flame is completely stable throughout its propagation.

Figure 5.20 compares the flame evolution for all meshes in the (x_f, v_f) space. The DNS $\delta_L^0/\Delta x = 20$ and $\delta_L^0/\Delta x = 10$ have a similar propagation up to near the end of the finger flame phase. As explained above, this moment takes place when the skirt reaches the lateral wall. But for such unstable flames, this collapsing depends on the shape of the TD structures.

When the resolution is decreased, a non monotonic response of the finger flame acceleration rate with $\delta_L^0/\Delta x$ is observed:

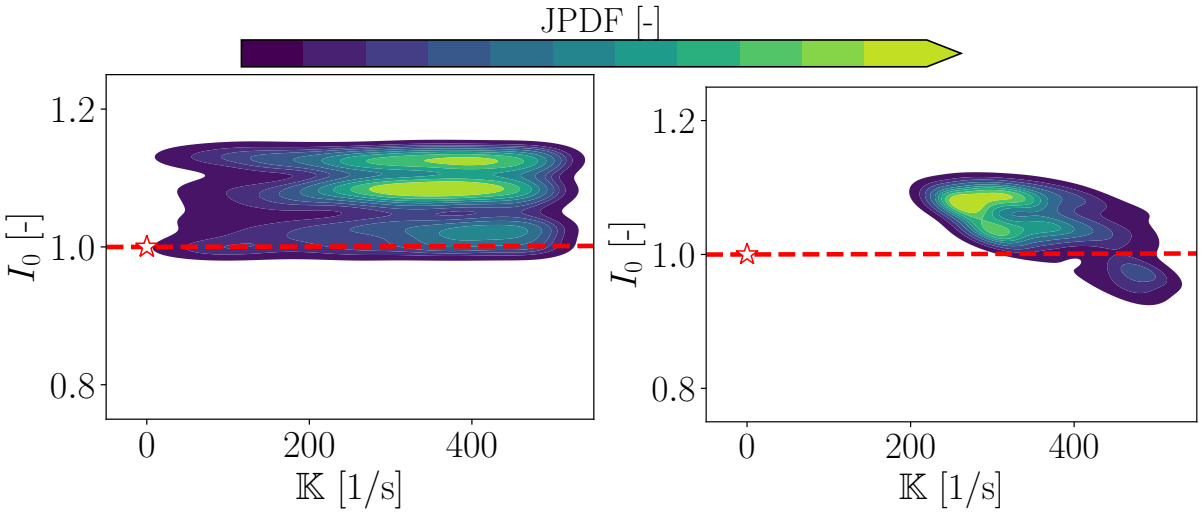

(a) DNS $\delta_L^0/\Delta x = 10$. (b) LES $\delta_L^0/\Delta x = 1, F = 7$.

Figure 5.17: Joint PDF of stretch factor I_0 as a function of total stretch $\mathbb{K}$ for several mesh resolutions (Table 5.3). $\Phi = 1.000$. Dashed red line: asymptotic theory (Equation (2.44)). Red star: unstretched laminar value.

- For $\delta_L^0/\Delta x \geq 2$, the loss of TD cells observed in Figure 5.18 as $\delta_L^0/\Delta x$ is decreased results into a progressive decrease of the global acceleration rate associated to the finger flame. For $\delta_L^0/\Delta x = 2$, the slope of the $v_f - x_f$ curve in the simulation is close to the one predicted by the theory (Equation (3.11)), owing to the stable mode of propagation achieved at this resolution;
- Interestingly, for $\delta_L^0/\Delta x \leq 2$, the finger flame acceleration rate starts increasing with decreasing resolution $\delta_L^0/\Delta x$ (and equivalently increasing thickening factor F). This unexpected behaviour is attributed to the flame response to stretch as discussed below.

An evaluation of the flame local response to stretch demonstrates the aforementioned amplification of stretch effects by the TF formalism. It is shown in Figure 5.21.

The asymptotic theory for stretch presented in Section 2.2 has concluded on a linear evolution of the flame speed at low stretch rates (Equation (2.41)). For higher values (but sufficiently far from the extinction limit), that response becomes non-linear but stays monotonic. The theory also predicts that for the lean H2-air mixtures currently studied, the flame speed increases with stretch. More interestingly, the behaviour (in the linear limit) is proportional to the flame thickness. Here comes the second effect of the TF model used in LES: by thickening the flame front, its response to stretch is amplified:

$$\frac{S_L}{S_L^0} = 1 - F\mathcal{L}\frac{\mathbb{K}}{S_L^0} \tag{5.8}$$

where $\mathcal{L}$ is the Markstein length associated to the non-thickened flame. This mechanism is better demonstrated by evaluating the local flame response to stretch. A joint PDF of

(a) DNS $\delta_L^0/\Delta x = 20$.

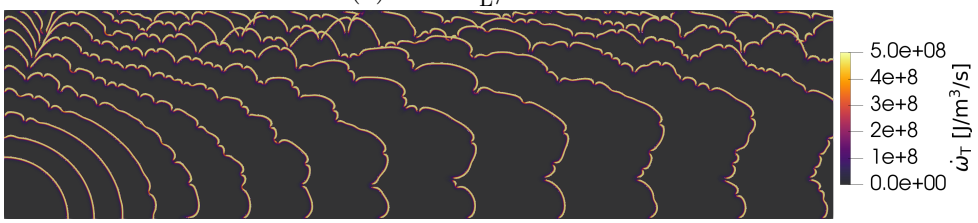

(b) DNS $\delta_L^0/\Delta x = 10$.

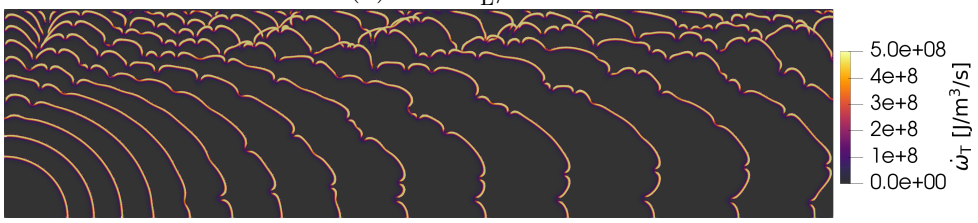

(c) LES $\delta_L^0/\Delta x = 5, F = 1.4$.

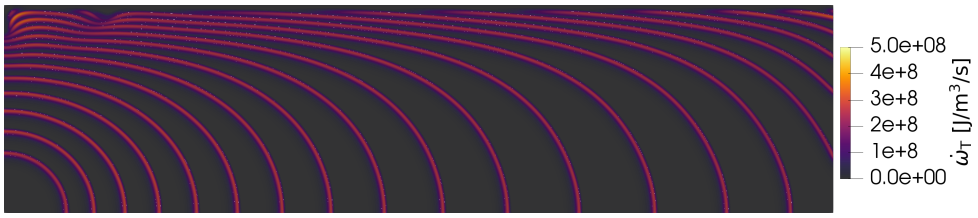

(d) LES $\delta_L^0/\Delta x = 2, F = 3.5$.

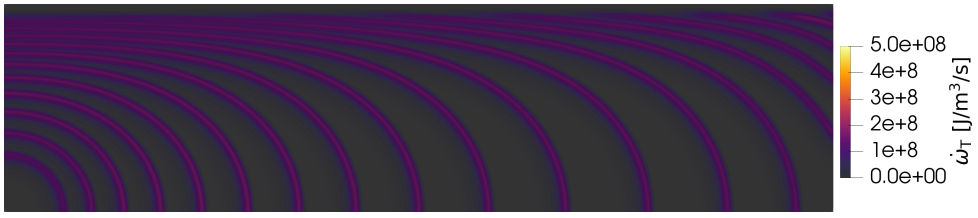

(e) LES $\delta_L^0/\Delta x = 1, F = 7$.

Figure 5.18: Superimposition of heat release rate profiles at several instants ($\Delta t = 10\delta_L^0/(\sigma S_L^0)$ between two consecutive contours) of flame propagation for several mesh resolutions (Table 5.4). $\Phi = 0.400$.

stretch factor I_0 as a function of total stretch $\mathbb{K}$ is computed for all the meshes presented in Figure 5.18. The results are provided in Figure 5.21. The DNS flames both experience a broad spectrum of stretch values related to the thermo-diffusive wrinkling. A local acceleration of the flame front ensues and the positive correlation between FCS and stretch rate reasonably follows the trend predicted by the asymptotic theory (dashed red curve) as it was observed in the previous section. There is no notable difference between cases $\delta_L^0/\Delta x = 20$ and $\delta_L^0/\Delta x = 10$, meaning that thermo-diffusive effects are not more marked

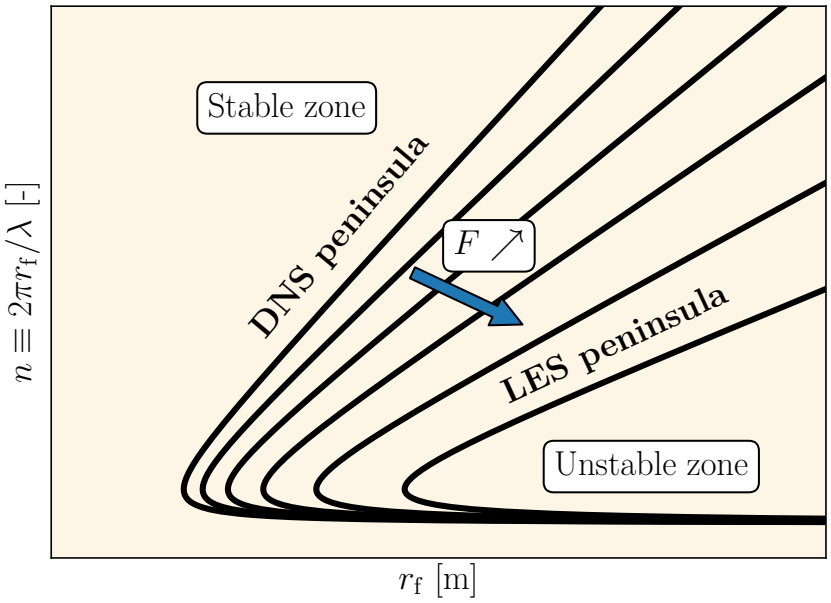

Figure 5.19: Effect of the Thickened Flame model on the instability peninsula.

for the finest mesh. On the other hand, as the resolution decreases and thickening is applied (increasing F to satisfy $N_c = 7$), the global slope of the JPDF increases, implying an overall amplification of the flame response to stretch. This is consistent with the amplification by a factor F of the stretch effect predicted by Equation (5.8) and displayed in Figure 5.21 with dashed green curves. One can therefore conclude that for large F values ($F \geq 3.5$ here), the amplification of the flame response to stretch can become high enough to induce an artificial over-acceleration during flame propagation.

As a matter of fact, applying the classical Thickened Flame model to hydrogen-air flames has multiple consequences depending on the operating conditions:

- For stable flames (near-stoichiometric and rich mixtures at room temperature and pressure), the local response to stretch is amplified. Given that the behaviour of these mixtures with relation to stretch is negative, thicker flames are slowed down in the present 2D tube set-up;
- For unstable flames (lean mixtures at room temperature and pressure), the local response to stretch is also amplified thereby accelerating the flame. But another consequential effect happens in parallel: the flame is more stable. This results from the conjunction of two mechanisms: thickening "physically" stabilises the flame by delaying the onset of the instabilities, and coarser meshes "numerically" stabilise the flame because perturbations cannot be resolved. The loss of thermo-diffusive structures represents an important decelerating phenomenon. The overall LES flame propagation results from the intricate coupling of the stretch response amplification and the TD loss.

The sum of these effects is illustrated by the diagram in Figure 5.22. It represents the

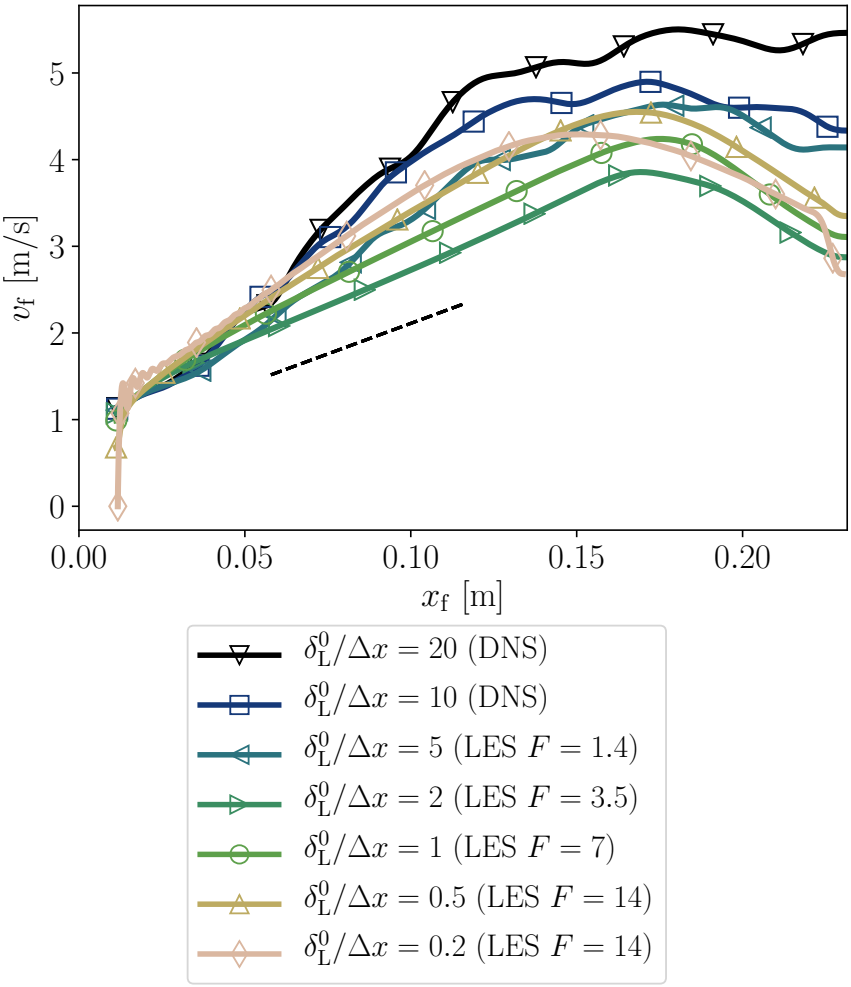

Figure 5.20: Flame speed as a function of flame tip position for several mesh resolutions (Table 5.4). $\Phi = 0.400$. Dashed black line: finger flame theoretical slope (Equation (3.11)).

mean exponential acceleration rate as a function of the thickening factor (or equivalently the inverse of mesh resolution $\Delta x/\delta_L^0$). This rate is computed by taking the average slope in the phase space (x_f, v_f) before the flame skirt hits the lateral wall. It initially decreases following the loss of thermo-diffusive instabilities, and then increases back as soon as the flame is perfectly stable due to the amplification of stretch effects. The strong mesh dependency observed in the present case questions the reliability and predictability of LES simulations. In conclusion, the classical TF approach cannot be directly applied for the simulation of propagating lean hydrogen-air flames.

5.3 Single-step mechanism

The previous section has outlined the consequences of applying the TF model in LES of propagating hydrogen-air flames: (1) a numerical and physical stabilisation of the flame

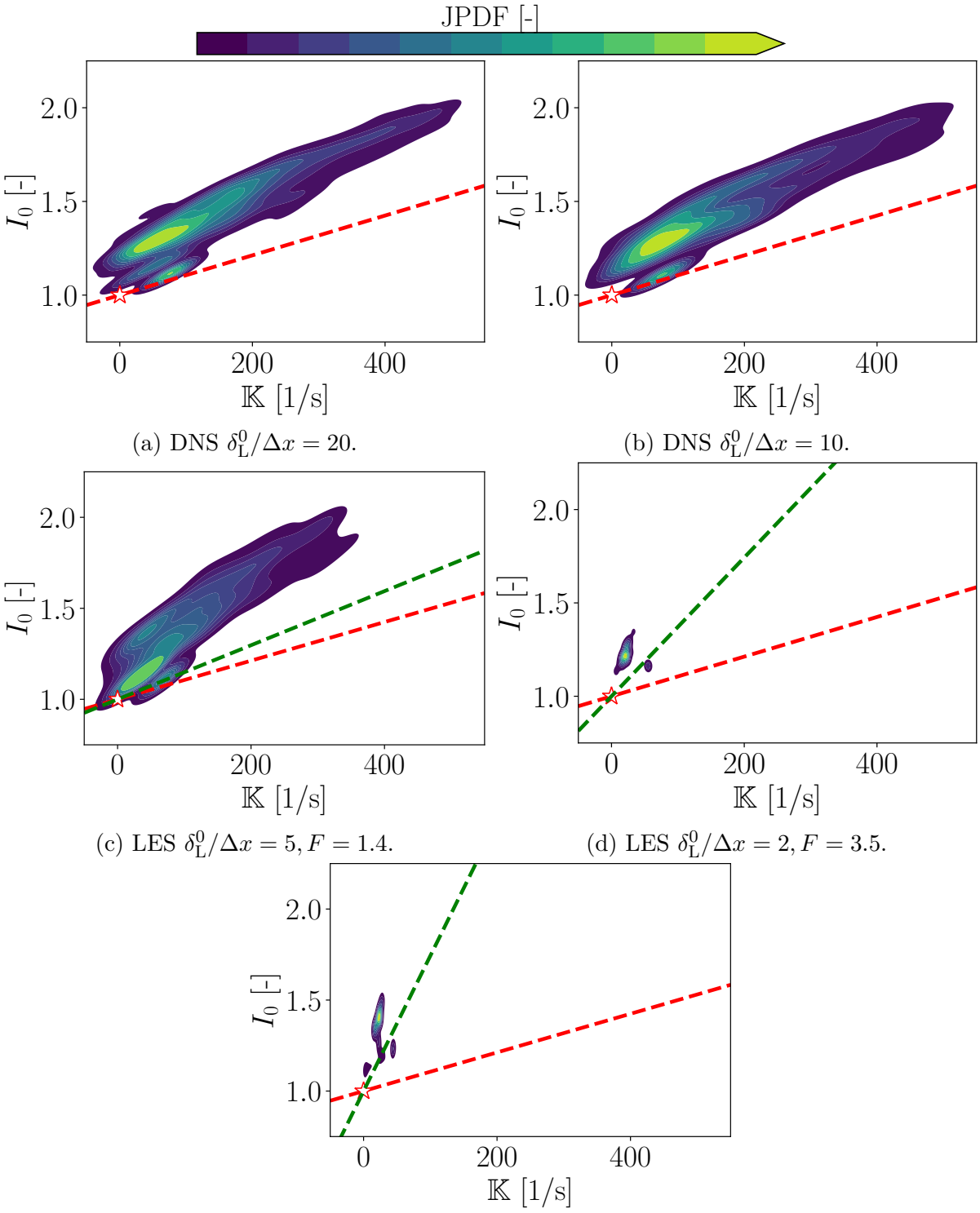

(a) DNS $\delta_L^0/\Delta x = 20$.

(b) DNS $\delta_L^0/\Delta x = 10$.

(c) LES $\delta_L^0/\Delta x = 5, F = 1.4$.

(d) LES $\delta_L^0/\Delta x = 2, F = 3.5$.

(e) LES $\delta_L^0/\Delta x = 1, F = 7$.

Figure 5.21: Joint PDF of stretch factor I_0 as a function of total stretch $\mathbb{K}$ for several mesh resolutions (Table 5.4). $\Phi = 0.400$. Dashed red line: asymptotic theory (Equation (2.44)). Green line: asymptotic theory for the thickening level associated to each LES. Red star: unstretched laminar value.

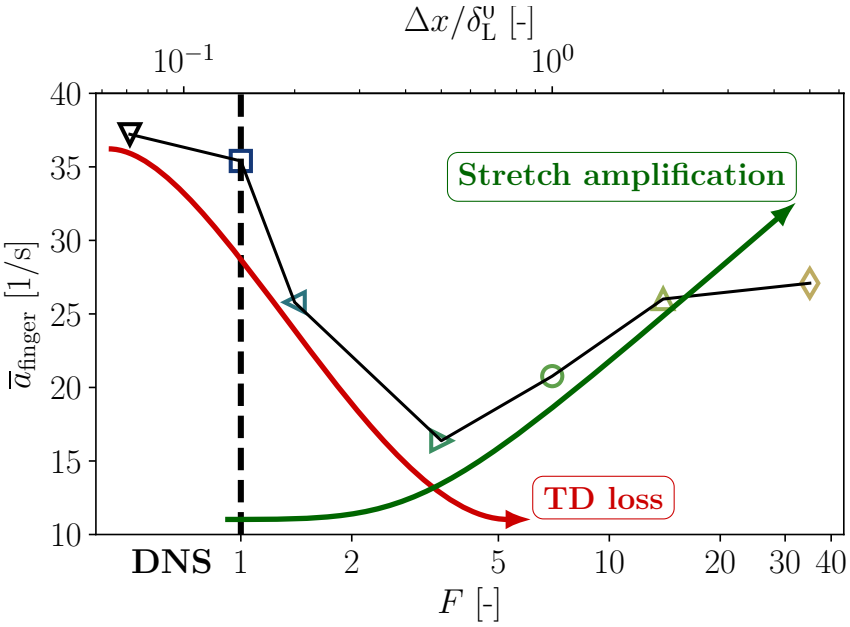

Figure 5.22: Mean exponential acceleration rate during the finger flame phase against thickening factor (or equivalently the inverse of mesh resolution $\Delta x/\delta_L^0$). Red zone: meshes where TD structures are partially resolved.

(deceleration mechanism); (2) an amplification of its response to stretch (acceleration mechanism of lean mixtures only). Until now, a detailed chemical scheme has been used, in particular to obtain a reference DNS that is as reliable as possible. However, in Safety Computational Fluid Dynamics, the considerable size of the explosion configurations often require huge computational resources. In order to reduce these costs, detailed chemical schemes are usually replaced by cheaper equivalent global chemistries (see Section 4.2.2). Several studies have already shown the ability of such chemistries to properly reproduce flame acceleration with common hydrocarbon fuels [45, 46, 262, 289–291]. This section carries out an analysis about the effects of the TF model on the simulation of hydrogen-air flames using simplified chemical kinetics. Focus is put on the lean $\Phi = 0.400$ case which showed the strongest mesh dependency with the detailed mechanism. This section therefore aims at answering two questions:

- is a global chemistry able to correctly capture the dynamics of lean H_2-air flames, as observed with the detailed mechanism?

- the previous section has identified spurious effects of the TF formalism which prevent simulations of lean H_2-air flames from being predictive. Is it also the case for the global chemical schemes commonly used in SCFD?

5.3.1 Global chemistry construction

As explained in Section 4.2.2, global chemical schemes are conceptually different from classical reduced mechanisms. Reduced chemistries are commonly built starting from a detailed chemistry, removing some reactions, lumping species together, etc. based on an exhaustive (analytical or numerical) analysis of the reaction pathways [237]. Conversely, global chemistries can be built from scratch by specifying one or two reactions representative of the overall oxidation of the fuel. They are intended to mimic the global flame parameters (cf. Section 2.1) and only remain valid within a narrow range of operating conditions. On top of the reduced computational cost, one advantage of such mechanisms is to be more comparable to theoretical results. The asymptotic studies presented in Chapter 2 are indeed based on the restrictive assumption of irreversible single-step chemistry. Previous studies [284, 292] have already demonstrated the ability of single-step schemes to capture flame front instabilities.

In this section, an Arrhenius-type single-step irreversible chemistry of the form $2\,H_2 + O_2(\,+\,3.76\,N_2) \longrightarrow 2\,H_2O(\,+\,3.76\,N_2)$ is constructed. In spite of the simplicity of the mechanism, several steps are required to build it. The procedure flowchart is represented in Figure 5.23. Following the method detailed by Sun *et al.* [101], the global activation energy and the global reaction order are determined starting from the San Diego reference mechanism. The latter is arbitrarily split equally in oxidiser and fuel partial reaction orders. After that, the transport properties are specified. This is discussed in detail in the next paragraph. The pre-exponential constant of the Arrhenius law is tuned to ensure the same laminar flame speed S_L^0 as the detailed chemistry. At that point of the procedure, the flame thickness is too low. Single-step chemistries are known to generate thinner flames because of the absence of intermediary reactions [293]. A default thickening factor F_0 is thus applied to match the flame thickness of the detailed mechanism. This thickening uses the same formalism as the TF model (modifying diffusion and reaction terms) but is not used for the same purpose. It is only there to reproduce the properties of the real flame as accurately as possible. Therefore, later mentions of the TF thickening factor F for LES meshes do not include F_0.

To finalise the chemical scheme construction, transport properties must be assigned to each species and to the whole mixture. For the viscosity, the same temperature-dependent law as the San Diego mechanism is imposed (see Section 4.4). Following the constant transport properties formalism used in AVBP, the Prandtl number Pr and the Schmidt number for the 4 species Sc_k are directly extracted from the detailed scheme. This first global chemical scheme is noted *1S-LeRe* (for "Lewis real"), namely because it relies on realistic transport properties for H_2 combustion. By doing so, the mixture effective Lewis number as defined by Equation (2.37) remains conserved the same as that of the San Diego mechanism (identical Zel'dovich number and Lewis numbers for H_2 and O_2). It has been well-understood from the previous chapters that this number plays an important role in the dynamics of lean H_2-air flames. It therefore represents a noteworthy feature of the present global scheme.

In addition to the 1S-LeRe chemistry, another global mechanism (noted *1S-Le1*) is built with a unity Lewis assumption ($\mathrm{Le}_k = 1, \forall k \in [\![1, N]\!]$). Its pre-exponential constant is slightly tuned again to fit the laminar flame speed. Using the same considerations on the asymptotic theory, this scheme will be used as a TD-free and stretch-response-less reference. It allows a proper isolation of the finger flame phenomenon. This was not possible for the detailed chemistry (the unity Lewis is not applicable in the detailed mechanism) for which a tentative rich-equivalent case was built (cf. Section 5.2.2). Unity-Lewis schemes are common in numerical flame simulations [45, 204, 262, 289, 290]. While they have been shown to correctly reproduce the dynamics of hydrocarbon flames, or stoichiometric H_2-air mixtures [181, 294], they may not be suited to the lean H_2-air mixtures studied in this thesis for which the effective Lewis number is known to be far from one.

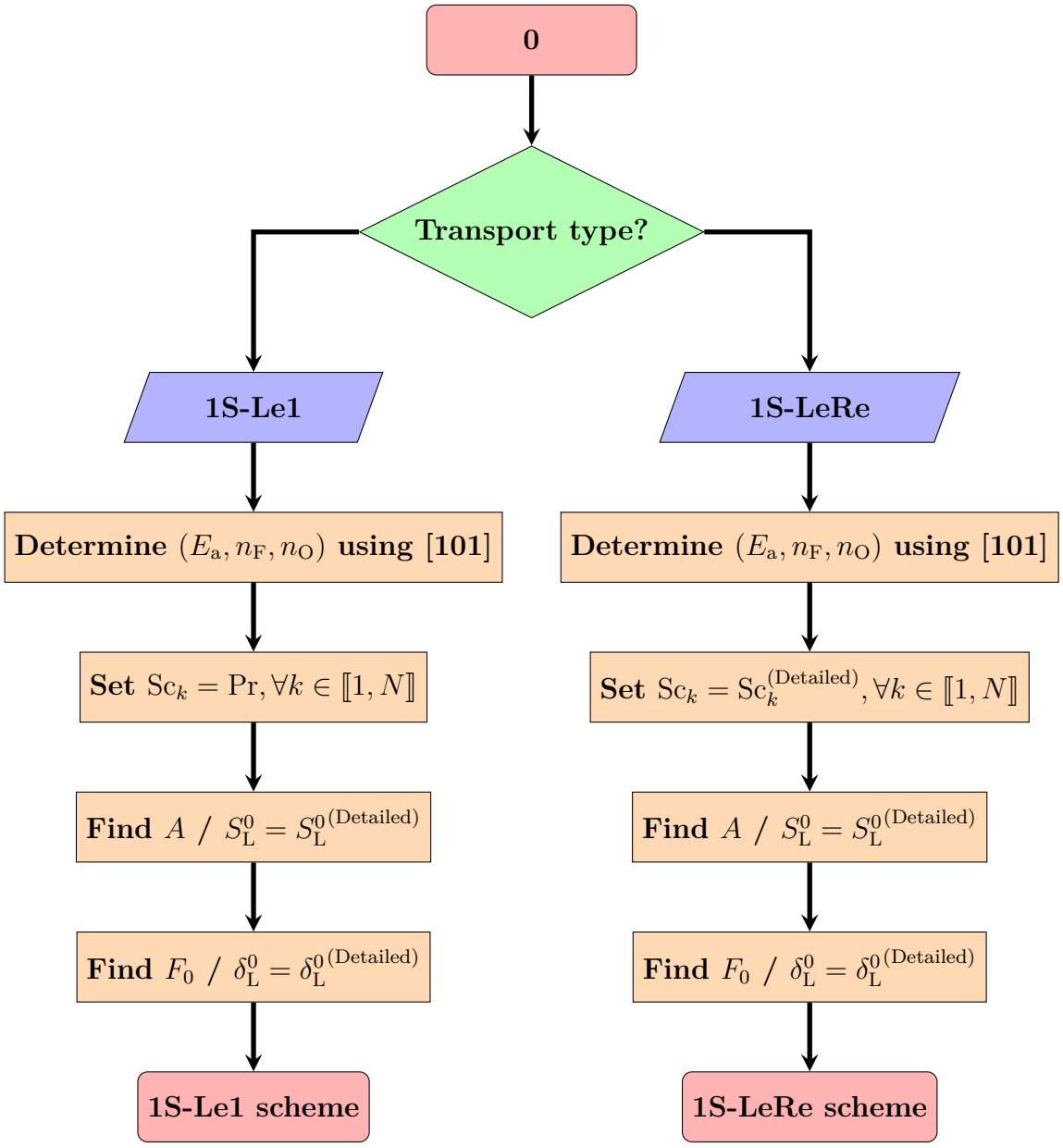

Figure 5.23: Global chemistry construction procedure: 1S-Le1 and 1S-LeRe schemes.

A summary of the chemical and transport properties of both mechanisms is given in Table 5.5.

	1S-LeRe				1S-Le1			
Reaction rate model	$A[H_2]^{n_{H_2}}[O_2]^{n_{O_2}}e^{-E_a/RT}$							
Arrhenius parameters								
A [IU]	1.3×10^{11}				7.5×10^{10}			
E_a [kcal.mol^{-1}]	38.8				38.8			
n_k	H_2	O_2			H_2	O_2		
	0.507	0.507			0.507	0.507		
Transport parameters								
Pr	0.662				0.662			
Sc_k	H_2	O_2	H_2O	N_2	H_2	O_2	H_2O	N_2
	0.226	0.797	0.584	0.906	0.662	0.662	0.662	0.662

Table 5.5: Single-step mechanisms used for H_2-air combustion at $\Phi = 0.400$ and atmospheric conditions.

The numerical set-up used up to now and described in Section 5.1 is kept unchanged (initialisation, boundary conditions, geometry, etc.). In particular, the same mesh resolutions can be used since the flame thickness of the 1S-LeRe and 1S-Le1 schemes are the same as the detailed chemical scheme.

5.3.2 Lewis number effect

The first comparison concerns the DNS (using the mesh allowing $\delta_L^0/\Delta x = 10$, Table 5.4) with the two global chemistries. Figure 5.24 depicts the flame shape evolution coloured by the heat release rate. As expected, the 1S-Le1 case stays perfectly smooth throughout the simulation. This chemistry is indeed insensitive to stretch and thermo-diffusively stable thanks to the unity-Lewis constraint. The burning rate is also relatively homogeneous along the flame surface, evidencing the independence with regards to the local stretch. On the other hand, the 1S-LeRe case is strongly unstable. TD patterns wrinkle the flame front like was observed with the detailed chemistry and cause a great variety of burning intensities. It also highlights an important point: the global chemistry is able to form thermo-diffusive cells.

Figure 5.25 compares the flame velocity as a function of its position for the two DNS. The 1S-Le1 case follows perfectly the finger flame exponential acceleration because it satisfies the assumptions of the theory. Contrarily, the 1S-LeRe flame undergoes a strong acceleration due to the thermo-diffusive instabilities. It must be noted that in the present configuration, the gap between the realistic 1S-LeRe case and the more classical 1S-Le1 case is huge: capturing the effect of TD structures is essential for lean H_2-air flame simulations.

Similarly to what has been done for the detailed chemistry in the last section, a local

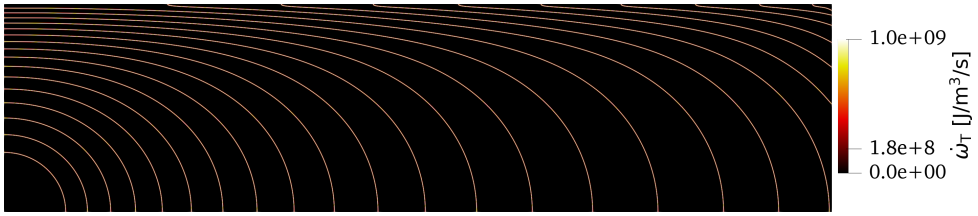

(a) 1S-Le1 scheme.

(b) 1S-LeRe scheme.

Figure 5.24: Superimposition of heat release rate profiles at several instants of flame propagation in DNS ($\delta_L^0/\Delta x = 10$) for the two global chemistries 1S-Le1 and 1S-LeRe. $\Phi = 0.400$.

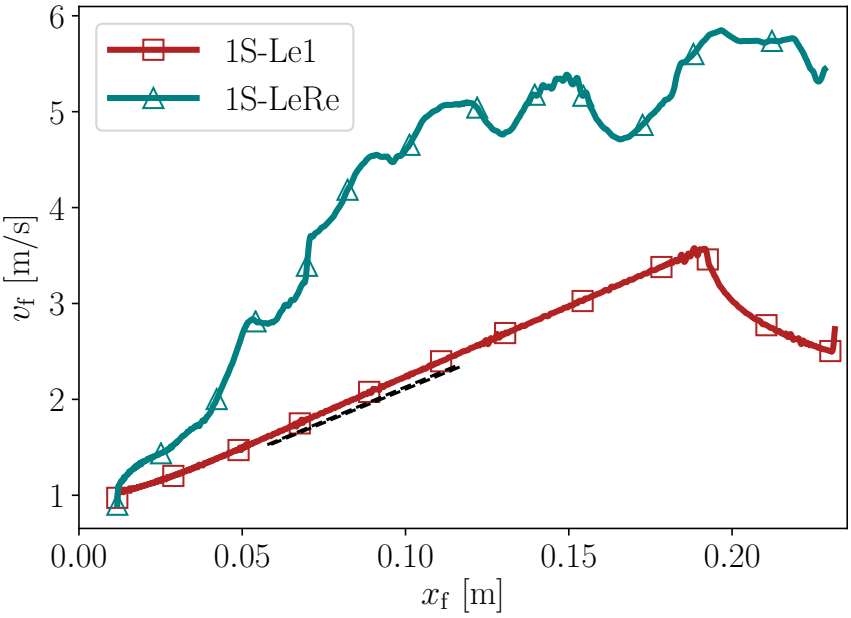

Figure 5.25: Flame speed as a function of flame tip position in DNS ($\delta_L^0/\Delta x = 10$) for the two global chemistries 1S-Le1 and 1S-LeRe. $\Phi = 0.400$. Dashed black line: finger flame theoretical slope (Equation (3.11)).

consumption speed is extracted for the 1S-Le1 and 1S-LeRe DNS. The joint PDF for $I_0(\mathbb{K})$ is shown in Figure 5.26. As expected, the unity-Lewis case yields a globally homogeneous burning rate independent of the local stretch rate. The JPDF is approximately constant and very close to the theoretical curve $I_0(\mathbb{K}) = 1$. Conversely, the real Lewis flame experiences a very wide range of stretch rates associated with the cusps and crests of the TD cells. The stretch response is positive and stronger than the asymptotic theory prediction. Given that the distribution of stretch rates is skewed to greater values (there

are only a couple of isolated zones which are negatively stretched), the FCS is globally higher than S_L^0.

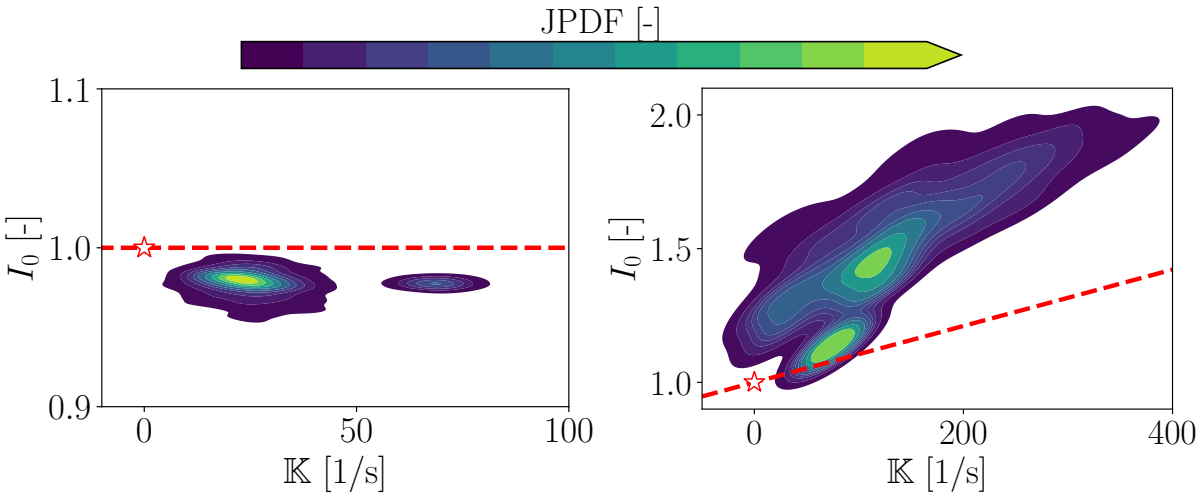

(a) 1S-Le1 scheme. (b) 1S-LeRe scheme.

Figure 5.26: Joint PDF of stretch factor I_0 as a function of total stretch $\mathbb{K}$ for the DNS ($\delta_L^0/\Delta x = 10$) with the two global chemistries 1S-Le1 and 1S-LeRe. $\Phi = 0.400$. Dashed red line: asymptotic theory (Equation (2.44)). Red star: unstretched laminar value.

5.3.3 Effect of mesh resolution for unity Lewis schemes

Similarly to Section 5.2, a mesh dependency analysis is conducted for the 1S-Le1 scheme here. Figure 5.27 represents the flame shapes for various LES (to be compared with the DNS equivalent in the previous Figure 5.24a). Knowing that the flame is already physically stable in the DNS, switching to LES does not introduce any wrinkling of the flame front.

Figure 5.28 confronts the flame speed for all meshes. No significant dependence on the resolution is observed, all simulations correctly follow the finger flame acceleration. The only notable difference appears at the end of the finger flame phase. As previously explained, it is triggered when the flame skirt touches the lateral wall of the tube. When the mesh cell size is increased, the skirt reaches earlier the wall.

5.3.4 Effect of mesh resolution for realistic Lewis schemes

While the 1S-Le1 simulations are relatively independent of the mesh resolution, the same cannot be concluded for the 1S-LeRe chemical scheme. It has indeed been shown that the flame is highly TD-unstable. Under the influence of a similar phenomenon to the detailed chemistry (Section 5.2.3), the Thickened Flame model stabilises the flame front both numerically and physically. Figure 5.29 again shows the progressive disappearance of

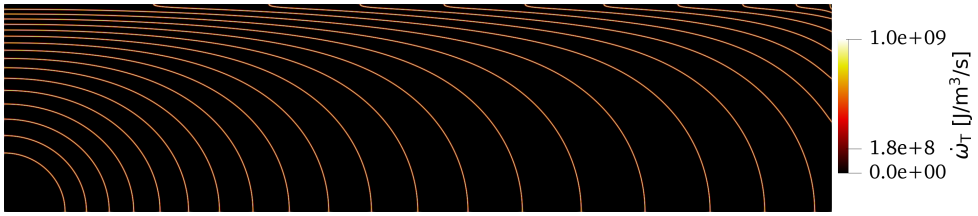

(a) LES $\delta_L^0/\Delta x = 5, F = 1.4$.

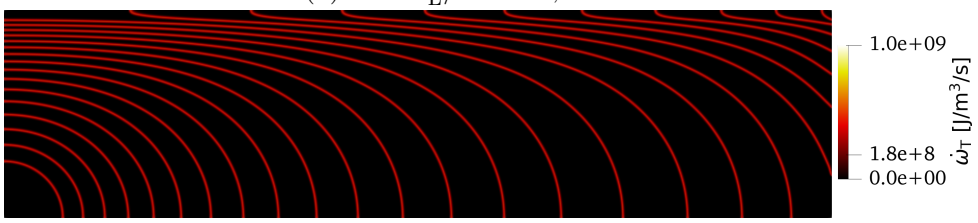

(b) LES $\delta_L^0/\Delta x = 2, F = 3.5$.

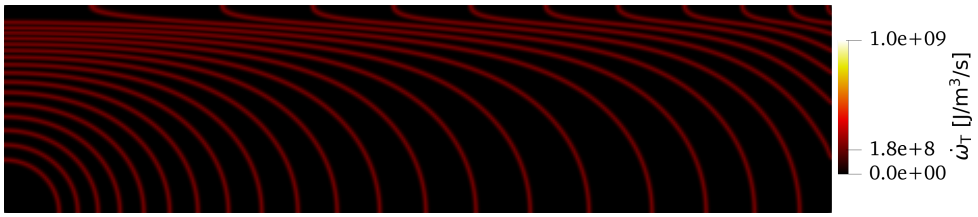

(c) LES $\delta_L^0/\Delta x = 1, F = 7$.

Figure 5.27: Superimposition of heat release rate profiles at several instants ($\Delta t = 10\delta_L^0/(\sigma S_L^0)$ between two consecutive contours) of flame propagation for several mesh resolutions. 1S-Le1 chemistry. $\Phi = 0.400$.

cellular structures induced by mesh coarsening. As soon as the flame becomes completely stable, the amplification of stretch effects is also visible: the heat release rates are globally stronger for coarse meshes.

The loss of wrinkling is once more accompanied by a deceleration of the flame front when switching from DNS to intermediate LES cases (see Figure 5.30). And when the LES flame is smooth, the integrated effect of local stretch amplification translates into a greater acceleration rate. Earlier observed with a detailed chemistry, the same phenomena exist for a global chemical scheme: the classical TF approach cannot be used as-is to simulate lean hydrogen-air flames because its results depend on the mesh resolution.

5.3.5 Comparison with detailed chemistry

The other question that this section tries to answer is whether the current global chemical scheme 1S-LeRe has the capacity to reproduce the propagation predicted by the detailed mechanism. The mechanisms are compared both in DNS and LES modes.

DNS ($\delta_L^0/\Delta x = 10$)
Their flame speed evolution in DNS is presented in Figure 5.31. Overall, a good agree-

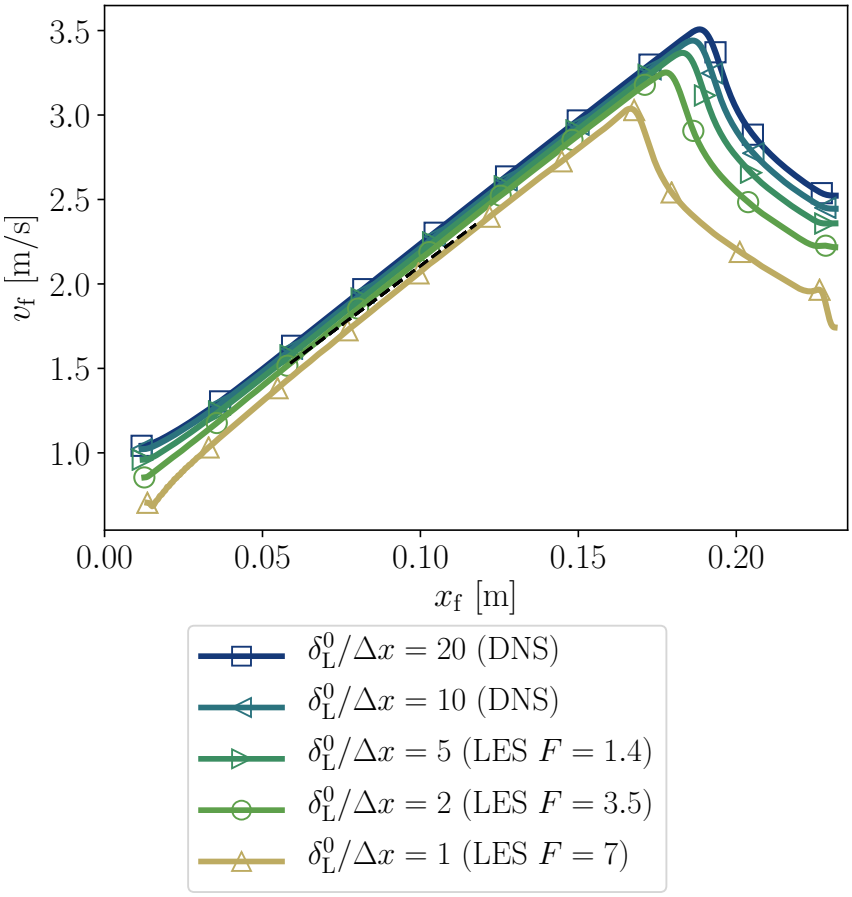

Figure 5.28: Flame speed as a function of flame tip position for several mesh resolutions. 1S-Le1 chemistry. $\Phi = 0.400$. Dashed black line: finger flame theoretical slope (Equation (3.11)).

ment between the 1S-LeRe global chemistry and the detailed chemistry is noted. At the beginning when the flame front is still relatively smooth, both chemistries agree on the same propagation. Around $x_f \approx 0.05$, the curves start to diverge due to disparities in the development of thermo-diffusive cells (see Figure 5.32). The flame simulated with the detailed mechanism seems to form TD structures of larger size in comparison with the single-step chemistry. This splitting results in a slightly different acceleration during the finger flame phase. Consequently, the single-step chemical scheme does not produce the exact same flame front instabilities dynamics as the detailed mechanism, despite bearing the same fundamental parameters (global chemical properties and transport properties). This discrepancy can be explained in two ways:

- the detailed chemistry does not comply with the hypotheses of the asymptotic theory (Section 2.3). The existence of multiple intermediary species and reactions falls out of its scope and can produce a different behaviour [293];
- the asymptotic theory does not predict the full non-linear dynamics of flame front instabilities. As has been said in the dedicated section, it only gives insights to understand the factors influencing their early development.

(a) LES $\delta_L^0/\Delta x = 5, F = 1.4$.

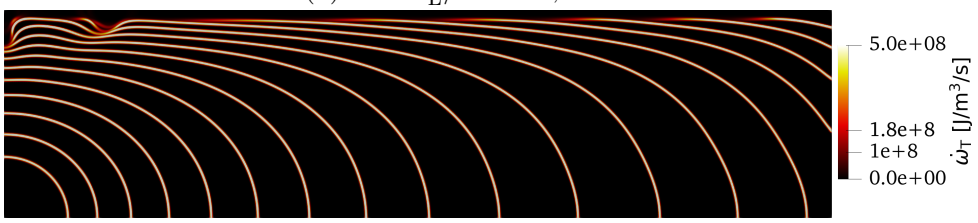

(b) LES $\delta_L^0/\Delta x = 2, F = 3.5$.

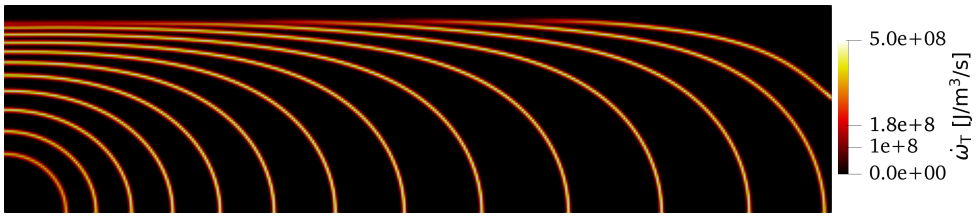

(c) LES $\delta_L^0/\Delta x = 1, F = 7$.

Figure 5.29: Superimposition of heat release rate profiles at several instants ($\Delta t = 10\delta_L^0/(\sigma S_L^0)$ between two consecutive contours) of flame propagation for several mesh resolutions. 1S-LeRe chemistry. $\Phi = 0.400$.

The differences between the detailed and global chemical approaches is better understood in terms of local FCS. The macroscopic flame dynamics corresponds indeed to the integral effect of the local consumption. The comparison of both $I_0(\mathbb{K})$ joint PDFs is displayed in Figure 5.33 for two flame positions corresponding respectively to the smooth flame and the TD-unstable phases. During the first phase of the propagation, the distributions of FCS are both concentrated around a unique point $I_0(\mathbb{K})$ as expected from the uniform stretch experienced by the kernel. The FCS level is slightly higher for the detailed mechanism but not enough to induce a flame tip velocity difference (see Figure 5.31). Later, when the flames become unstable, the TD cells generate a wide range of stretch rates. It now highlights a small stretch response gap between the two chemical schemes. A stiffer response to stretch is remarkable for the single-step mechanism. As observed in Figure 5.31, it now results in a divergence of propagation speeds. The conclusions from this local analysis validate the explanation for the different behaviours that has been guessed above:

1. the detailed and single-step chemistries do not have the same response to stretch;
2. it exacerbates a different TD cells dynamics;
3. and it finally leads to the global propagation divergence.

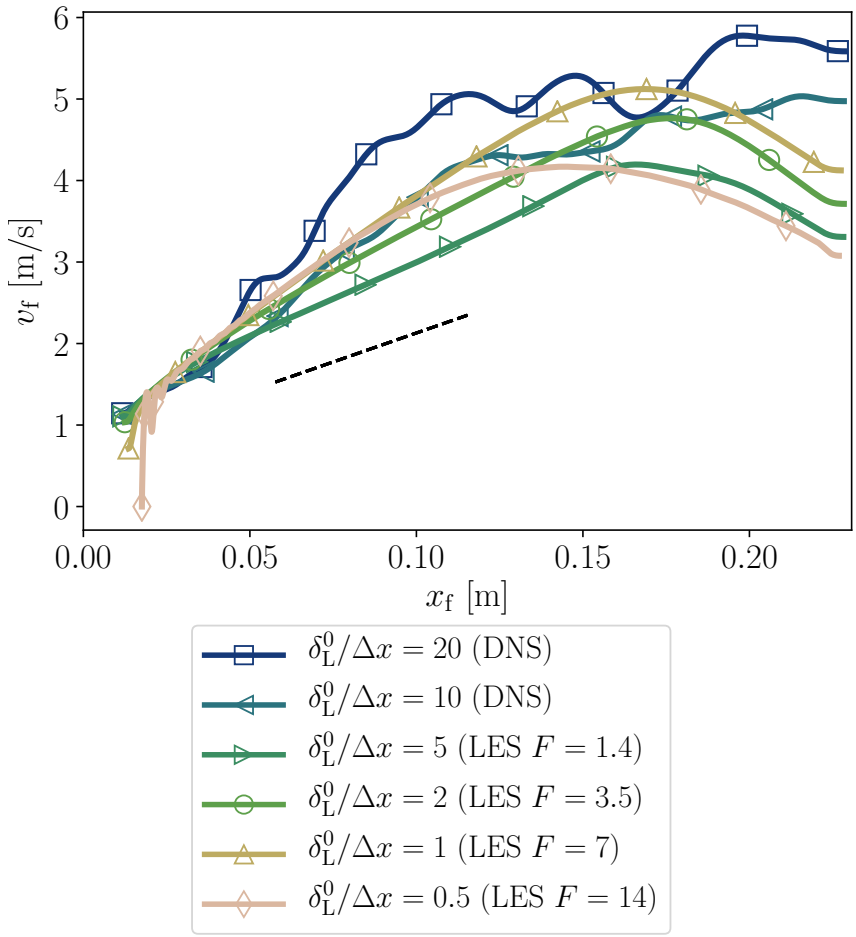

Figure 5.30: Flame speed as a function of flame tip position for several mesh resolutions. 1S-LeRe chemistry. $\Phi = 0.400$. Dashed black line: finger flame theoretical slope (Equation (3.11)).

LES ($\delta_L^0/\Delta x = 1, F = 7$)

The different TD dynamics between the detailed and global mechanisms remains small in DNS mode. However, anticipating that the 1S-LeRe is built for the simulation of large-scale explosions, its behaviour must also be studied in LES. Figure 5.34 compares the evolution of the flame speed for the two schemes in LES mode using the mesh resolution $\delta_L^0/\Delta x = 1$ ($F = 7$). The global divergence in terms of acceleration rate is clearly visible here. Both flames are TD-stable, but the small difference of response to stretch is exaggerated by the TF model. In real explosion scenarios, one can expect:

1. large thickening factors due to the size of configurations;
2. larger stretch rates due to turbulence.

Both phenomena indicate that the 1S-LeRe scheme, albeit being quite close to the detailed scheme reference in DNS, must be replaced by a chemistry that is better-fitted to the detailed mechanism in terms of flame response to stretch.

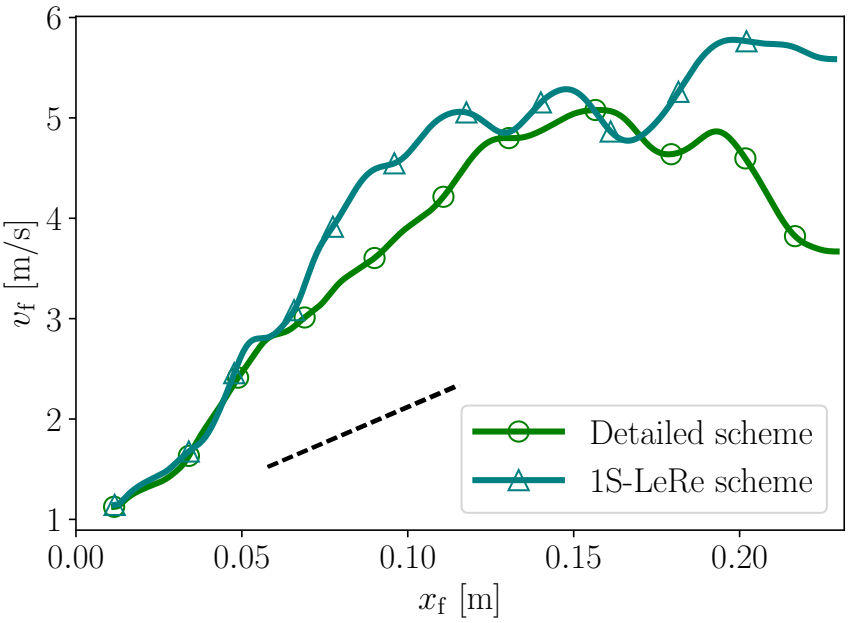

Figure 5.31: Flame speed as a function of flame tip position in DNS ($\delta_L^0/\Delta x = 10$) for the 1S-LeRe global chemistry and the detailed chemistry. $\Phi = 0.400$. Dashed black line: finger flame theoretical slope (Equation (3.11)).

(a) Detailed scheme.

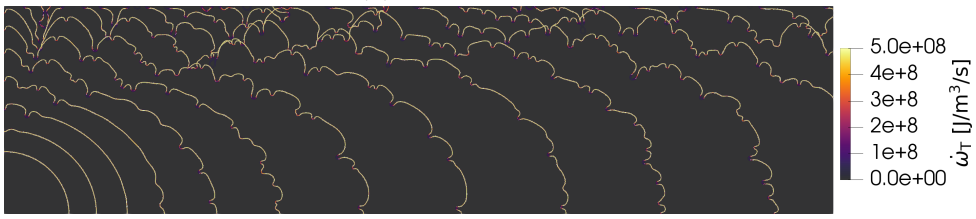

(b) Global 1S-LeRe scheme.

Figure 5.32: Superimposition of heat release rate profiles at several instants of flame propagation in DNS ($\delta_L^0/\Delta x = 10$) for the detailed chemistry and the global chemistry 1S-LeRe. $\Phi = 0.400$.

5.3.6 Effect of tube size on the flame acceleration

The last section of this chapter discusses the interactions between the finger flame phenomenon and flame front instabilities. The goal is to identify the potential predominance of one acceleration mechanism over the other as a function of the tube size. This analysis has been the subject of a publication in the *Proceedings of the 28th International Colloquium on the Dynamics of Explosions and Reactive Systems*. The method used in

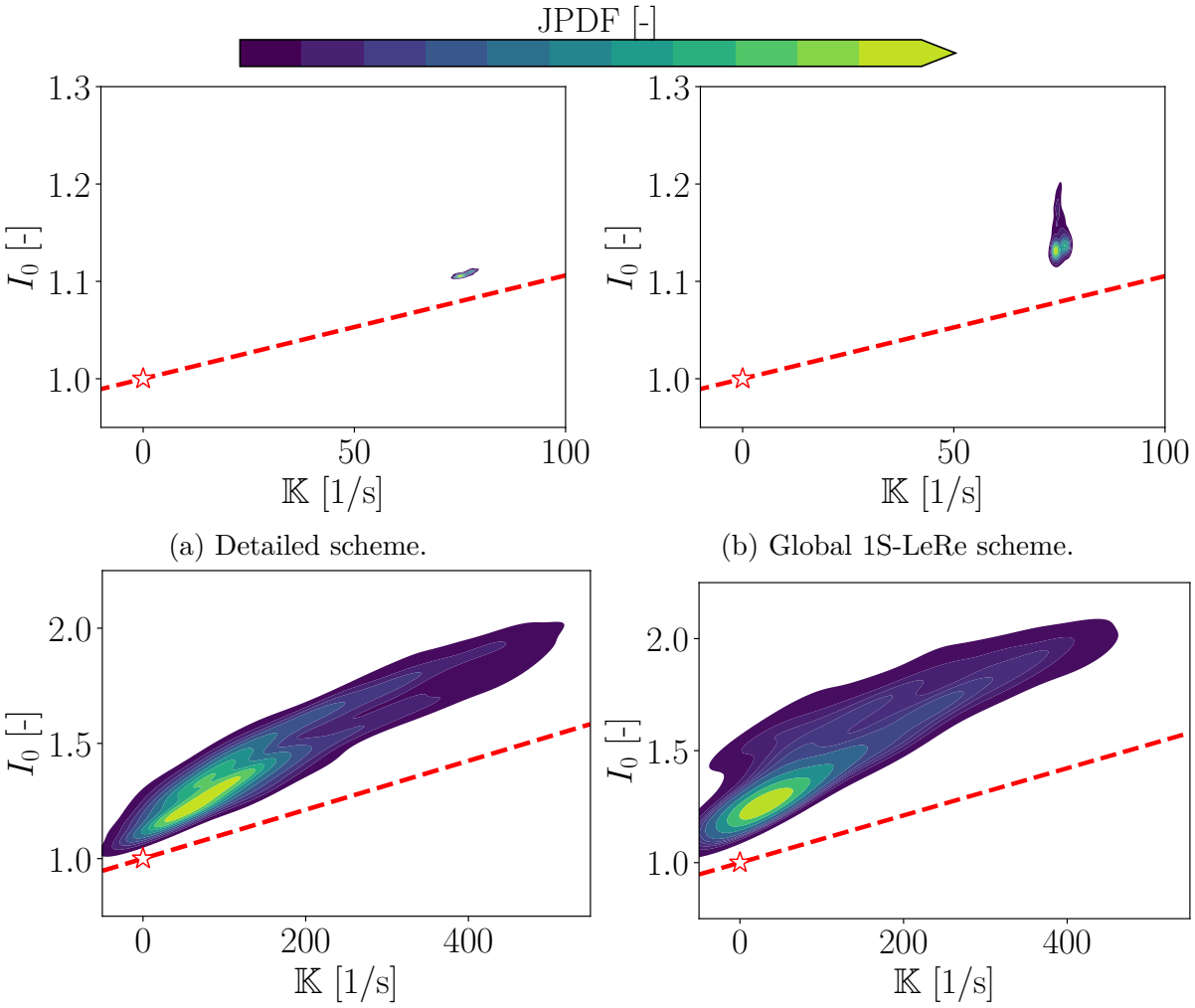

(a) Detailed scheme.

(b) Global 1S-LeRe scheme.

(c) Detailed scheme.

(d) Global 1S-LeRe scheme.

Figure 5.33: Joint PDF of stretch factor I_0 as a function of total stretch $\mathbb{K}$ in DNS ($\delta_L^0/\Delta x = 10$) for the detailed chemistry and the global chemistry 1S-LeRe. $\Phi = 0.400$. Dashed red line: asymptotic theory (Equation (2.44)). Red star: unstretched laminar value. (a-b): Instants corresponding to the smooth phase. (c-d): Instants corresponding to the unstable phase.

this work as well as its main conclusions are summarised herein. Readers may refer to Appendix A to read the full article.

The 2D tube flame configuration is used in different flavours characterised by their radius: a tube noted "M" with radius $R_{\text{tube}} = 500\delta_d$, and a small-sized (resp. supersized) version noted "S" (resp. "L") scaled by a factor 1/2 (resp. $\times 2$). The operating conditions are ($\Phi = 0.356$, $T_u = 296$ K, $P = 1$ atm). In each of these tubes, two DNS are carried out: one with the "realistic" Lewis approach 1S-LeRe, and another with the unity-Lewis 1S-Le1 chemistry.

The various flame propagations can be compared in the normalised phase space (ξ_f, S_f) as depicted in Figure 5.35. The main takeaway messages are:

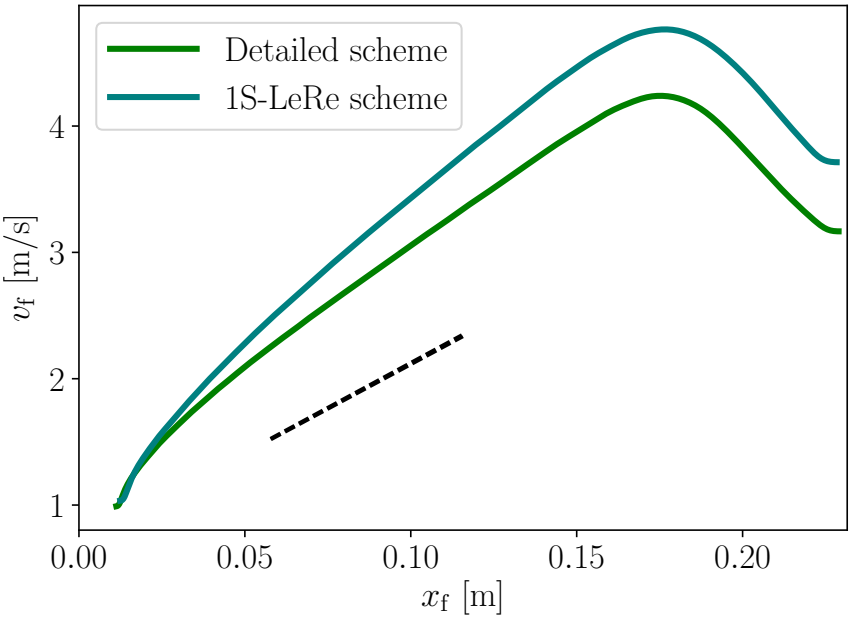

Figure 5.34: Flame speed as a function of flame tip position in LES ($\delta_L^0/\Delta x = 1, F = 7$) for the 1S-LeRe global chemistry and the detailed chemistry. $\Phi = 0.400$. Dashed black line: finger flame theoretical slope (Equation (3.11)).

- the 1S-Le1 flames all strictly follow the finger flame theoretical acceleration. As expected, they do not develop TD cells;
- the 1S-LeRe flames all develop thermo-diffusive instabilities which induce an additional acceleration of the combustion wave;
- this acceleration depends on the tube radius: the wider the tube, the stronger the influence of TD instabilities.

The last point traduces the fact that the relative importance of the finger flame and TD mechanisms depends on the level of confinement. In narrow tubes, the finger flame mechanism is so strong that the effect of the TD instability on flame acceleration becomes negligible. If the tube radius is increased, the influence of TD cells increases and must be taken into account to produce the correct flame acceleration. Therefore, any attempt to model TD effects for LES of confined flame propagation must contain an information on the geometry: a model that does not comply with this rule, fitted for a given tube radius, will fail in a tube of different size.

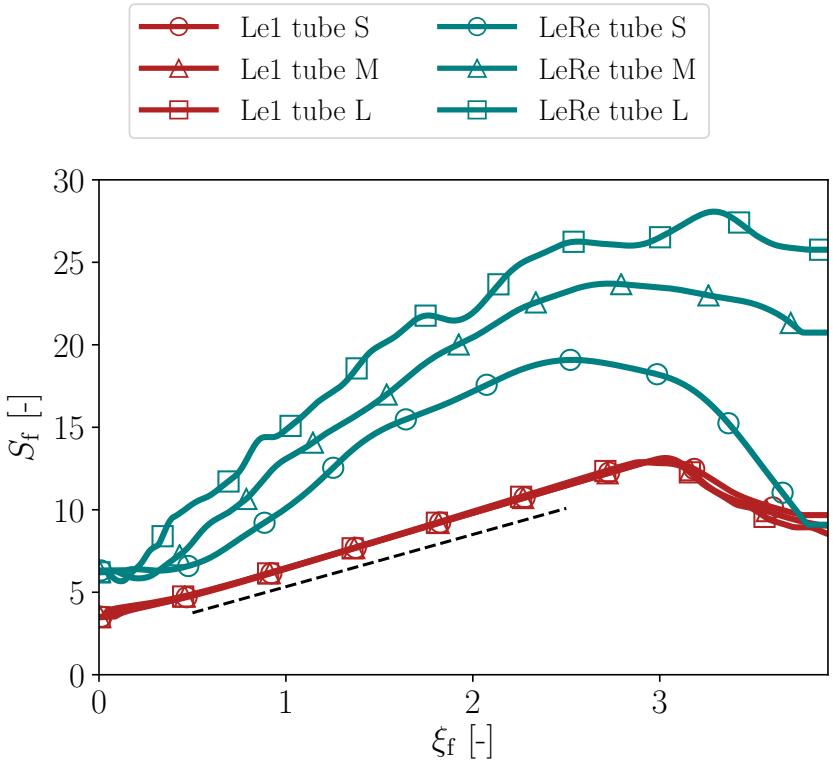

Figure 5.35: Normalised flame speed as a function of normalised flame tip position for all 1S-LeRe and 1S-Le1 DNS. Dashed black line: finger flame theoretical slope (Equation (3.11)).

5.4 Conclusion and implications for the modelling of propagating lean hydrogen-air flames

The main goal of this chapter was to assess the capability of the classical Thickened Flame model to correctly predict lean hydrogen-air flames propagation in the context of a two-dimensional tube configuration, representative of the early stages of an explosion. It has been shown that:

- in Direct Numerical Simulations, a detailed chemical kinetic mechanism is able to capture the onset of flame front instabilities due to thermo-diffusive phenomena for lean H_2-air mixtures under atmospheric conditions. When the equivalence ratio is raised towards stoichiometry, the flame front is progressively smoothened as a result of the increase of the effective Lewis number which conveys a stabilising influence of TD effects. Near-stoichiometric flames are still slightly unstable at large scales due to the ubiquitous Darrieus-Landau mechanism. Compared to a classical exponential acceleration in the pure finger flame theory, unstable cases suffer a stronger acceleration due in particular to the wrinkling added by flame front cells and the subsequent local stretch effects. This mechanism gradually decreases towards stoichiometric and rich mixtures;

- when the mesh resolution is decreased and when the Thickened Flame model is activated, flames become smoother little by little. This is due to two distinctive stabilising factors. First numerically, the larger mesh cell size implies lesser resolution of cellularity. Second, from a physical point of view, thickening a flame delays the onset of instabilities according to the asymptotic theory. The loss of TD structures leads to the deceleration of the flame in LES;

- the former mechanism is acting in parallel of another one: the thickening applied to the flame front also amplifies its response to stretch. Predicted by the asymptotic theory, this behaviour is demonstrated quantitatively on the LES flames. It becomes clearly visible for the LES flames carried out on the coarsest meshes which remain stable throughout their propagation. For the lean mixtures considered in this work (and for positively stretched flames), the amplification of stretch effects generates an additional acceleration;

- the overall propagation in LES results from the interaction of those mechanisms respectively hindering and fostering flame propagation as the mesh resolution is decreased. The main consequence is the inability of classical TFLES to reliably predict lean hydrogen-air explosions.

In addition to these points, the use of global chemical schemes has brought out that:

- in Direct Numerical Simulations, a first global chemistry (noted 1S-LeRe) has been built with transport properties (in particular the species Lewis numbers) extracted directly from the detailed mechanism. It correctly mimics the different phases of flame acceleration: initial stable phase followed by the onset of the thermo-diffusive instability which carries on during the finger flame phase. Overall, the flame propagation is in good agreement with the detailed chemical reference. However, the observed dynamics for the TD cells development slightly differs from the detailed reference. This is most probably due to the discrepancies in terms of stretch response measured on the two flames. When switching to LES mode, these small discrepancies are amplified by the TF model, yielding different flame acceleration scenarios for the global and the detailed mechanisms;

- the effects of using coarse meshes and the Thickened Flame model are the same as identified with the detailed mechanism;

- another global chemistry (noted 1S-Le1) has been constructed using unity Lewis numbers for all species. No significant mesh dependency was observed and all flames perfectly follow the finger flame theoretical acceleration slope. By comparison with the detailed chemistry DNS used as a reference, one can conclude that the classical unity-Lewis assumption used in explosion simulations proves wrong for lean hydrogen-air flames.

In the light of these conclusions, a new modelling strategy for the LES of lean H_2-air flames must be established. Chapters 6 and 7 introduce the main principles behind the innovative approach proposed in this thesis.

Part III

Strategies for correction: the Thermo-Diffusive-Stretched-Thickened Flame model

Chapter 6

Stretch response correction for LES: the Stretched-Thickened Flame (S-TF) model

Sommaire

The naïve approach to the LES of lean hydrogen-air explosions of Chapter 5 has put forward two main issues:

- the Thickened Flame model amplifies the flame response to stretch;

- the use of coarse meshes and high thickening levels filters out flame front instabilities.

This chapter addresses the first issue whereas the second is addressed in the next chapter. Before dealing with thickened flames, one must make sure that the use of global chemistries does indeed produce a response to stretch that is consistent with the detailed chemical reference. Section 6.1 presents a procedure intended to build such stretch-fitted single-step chemical schemes. It provides a baseline for any stretched flame simulation in DNS mode. Then, as the flame gets thickened in a TFLES framework, the amplification of stretch effects appear. For lean hydrogen-air mixtures, it constitutes a substantial artificial accelerating mechanism when the LES mesh resolution is decreased. For small-to-mid-scale explosion scenarios, the thickening factor is usually of the order of $F = \mathcal{O}(10^1 - 10^2)$, making the flame more sensitive to stretch by the same amount. What's more, the high levels of turbulence encountered during turbulent flame acceleration lead to strong flame straining which can aggravate the erroneous behaviour of the TFLES model. A correction strategy, called the Stretched-Thickened Flame (S-TF) model, has been developed during this thesis to rectify the stretch response of thickened flames. This work has been published in the international journal *Combustion and Flame* [295]. In the paper, the S-TF model has only been applied to propane-air flames. In Sections 6.2 to 6.4, the philosophy of the model is explained and the emphasis is placed on its application to the specific case of hydrogen-air flames.

6.1 Stretch response in a DNS framework: a stretch-fitted global chemistry

As a reminder, in Chapter 5, a comparison of the flame propagation in a tube in DNS for the detailed mechanism of San Diego [60] and a basic single-step chemical scheme (called 1S-LeRe) has led to the following conclusions:

- during the early stages of the propagation, both flames are smooth due to the stabilising effect of high curvature. The flame propagation observed with the global chemistry is in good agreement with the detailed chemistry reference;
- as soon as the thermo-diffusive instability arises, the propagation of the two flames diverge. Following a local flame consumption speed analysis, a small gap in terms of stretch response between the detailed and the global kinetic schemes has been observed. It is exacerbated by the high curvatures generated by TD cells. Although the gap in stretch response is small, it is thought to generate a slightly different TD instability dynamics.

In an attempt to reduce this gap, a new methodology to construct a global chemical scheme, called *1S-LeFit*, is proposed. In addition to the laminar flame speed and thermal

flame thickness, the response to stretch is also fitted to the detailed mechanism reference for each operating condition:

- the Arrhenius law pre-exponential constant is used to fit the laminar flame speed;
- a default thickening factor F_0 is applied (with the TF formalism) to match the thermal flame thickness;
- all species Lewis numbers are modified by the same ratio to fit the stretch response. This operation requires the choice of a target stretch $\mathbb{K}_\infty$ which is in practice set at $S_\mathrm{L}^0/\delta_\mathrm{L}^0$, of the order of magnitude of the extinction stretch rate for most flames [295]. The exact optimisation method of the Lewis numbers follows a flowchart similar to the Stretched-Thickened Flame model presented thereafter (see in particular Section 6.3.3).

The 1S-LeFit construction procedure is summarised in Figure 6.1 and the output for the present mixtures at $\Phi = 1.0$ (resp. $\Phi = 0.4$) is given in Table 6.1 (resp. Table 6.2). Note the values of the Schmidt numbers, to be compared with the former 1S-LeRe chemistry (recalled in the right column): for both mixtures, the Schmidt numbers (equivalently the Lewis numbers) are increased to match the stretch response of the detailed mechanism.

	1S-LeFit				**1S-LeRe**			
Reaction rate model	$A[\mathrm{H_2}]^{n_{\mathrm{H_2}}}[\mathrm{O_2}]^{n_{\mathrm{O_2}}}e^{-E_\mathrm{a}/RT}$							
Arrhenius parameters								
A [IU]	2.7×10^{15}				5.6×10^{15}			
E_a [kcal.mol^{-1}]	32.7				32.7			
n_k	$\mathrm{H_2}$	$\mathrm{O_2}$			$\mathrm{H_2}$	$\mathrm{O_2}$		
	0.953	0.953			0.953	0.953		
Transport parameters								
Pr	0.662				0.662			
Sc_k	$\mathrm{H_2}$	$\mathrm{O_2}$	$\mathrm{H_2O}$	$\mathrm{N_2}$	$\mathrm{H_2}$	$\mathrm{O_2}$	$\mathrm{H_2O}$	$\mathrm{N_2}$
	0.444	1.565	1.147	0.779	0.226	0.797	0.584	0.906

Table 6.1: Stretch-fitted 1S-LeFit mechanism used for $\mathrm{H_2}$-air combustion at $\Phi = 1.0$ and atmospheric conditions. The former 1S-LeRe (used in Chapter 5 is recalled for the comparison.

Figure 6.2 compares the response of 1D CPF to strain at $\Phi = 0.4$ for the detailed chemistry, the global 1S-LeRe chemistry used in Chapter 5 and the newly proposed 1S-LeFit mechanism. The 1S-LeRe schemes overreact to stretch when compared to the detailed chemistry reference. It echoes similar observations made on the 2D tube flame in Section 5.3.5. On the contrary, the 1S-LeFit mechanism reproduces the correct behaviour, as expected.

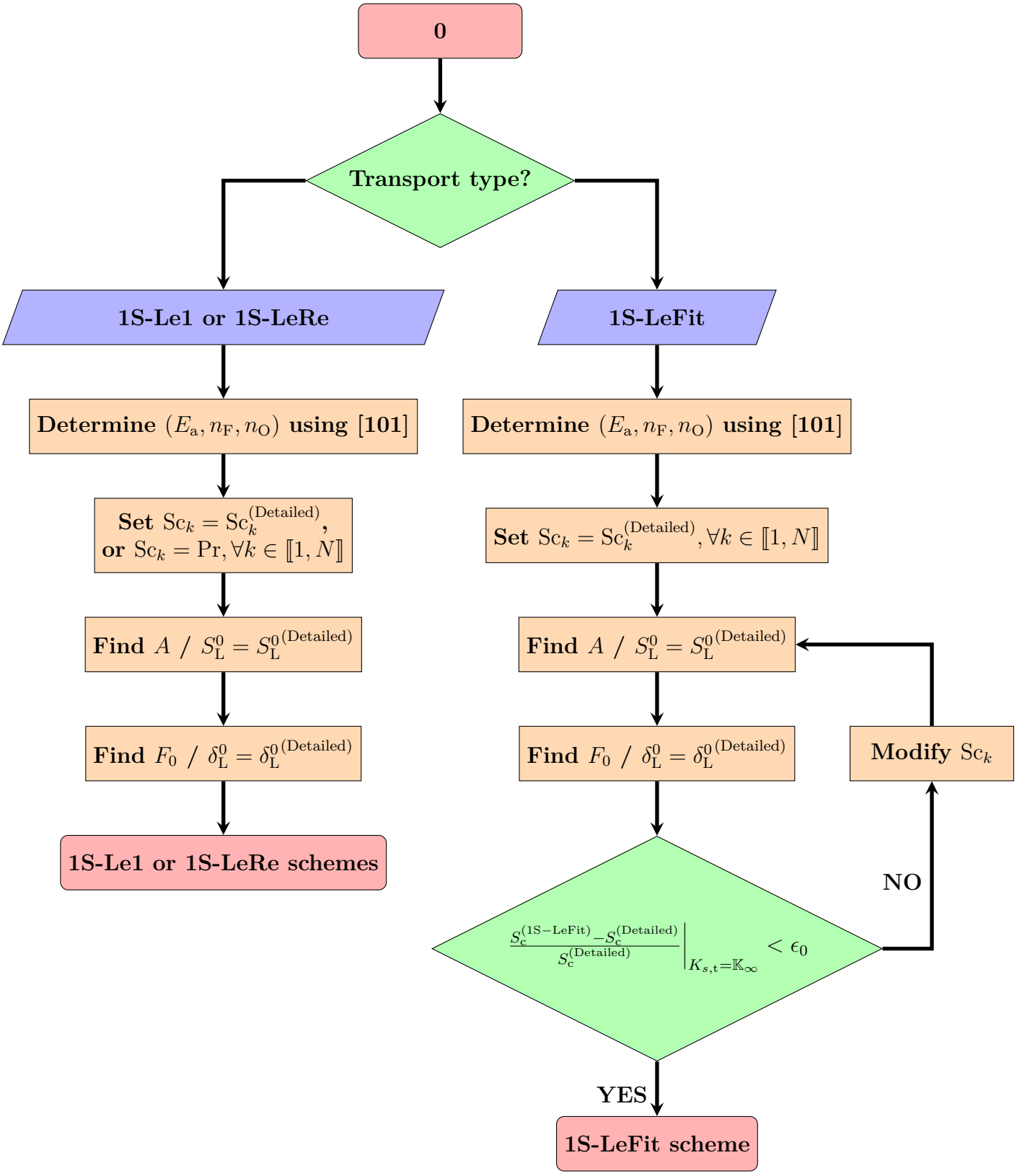

Figure 6.1: Procedure for building a stretch-fitted global chemistry: 1S-LeFit schemes.

	1S-LeFit	1S-LeRe
Reaction rate model	$A[H_2]^{n_{H_2}}[O_2]^{n_{O_2}}e^{-E_a/RT}$	
Arrhenius parameters		
A [IU]	1.1×10^{11}	1.3×10^{11}
E_a [kcal.mol^{-1}]	38.8	38.8
n_k	H_2 O_2 0.507 0.507	H_2 O_2 0.507 0.507
Transport parameters		
Pr	0.662	0.662
Sc_k	H_2 O_2 H_2O N_2 0.301 1.062 0.778 1.207	H_2 O_2 H_2O N_2 0.226 0.797 0.584 0.906

Table 6.2: Stretch-fitted 1S-LeFit mechanism used for H_2-air combustion at $\Phi = 0.4$ and atmospheric conditions.

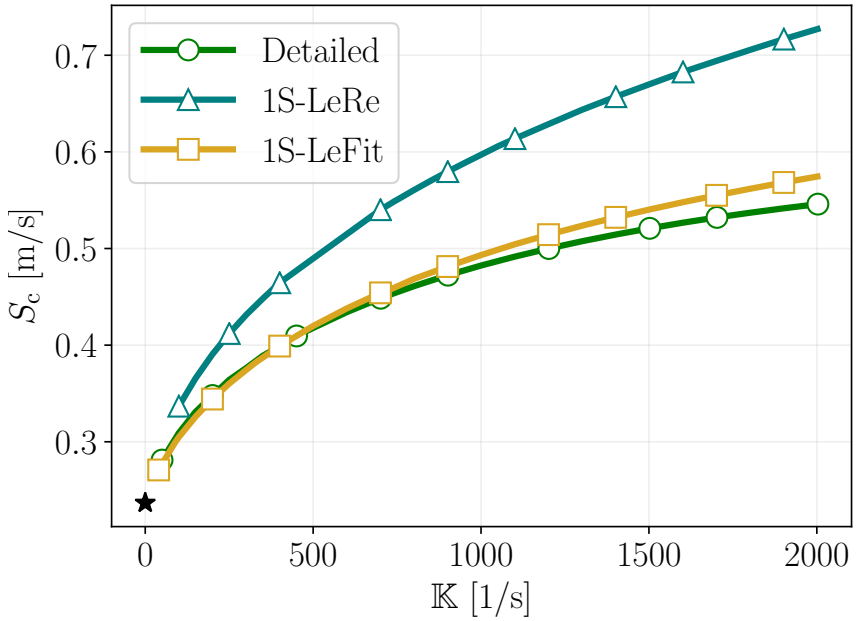

Figure 6.2: Counterflow premixed flame response to strain for the three chemistries at $\Phi = 0.4$. DNS mode ($F = 1$). Black star: laminar flame speed.

6.2 Stretch response in the Thickened Flame LES framework: problem formulation

In Chapter 5, the response to stretch of thickened flames was shown to be amplified by the thickening factor under the classical TF formalism. This section analyses the problem in the reduced 1D counterflow premixed flame configuration.

6.2.1 Thickened Flame model for unstrained laminar flames

To propagate a premixed flame on a coarse grid, Butler and O'Rourke [266, 267] laid the theoretical foundation of the Thickened Flame model (cf. Section 4.4.4), proposing the introduction of a coordinate dilatation ($x \mapsto x^*$) normal to the flame front:

$$x^* = \int^x F \, \mathrm{d}x' \tag{6.1}$$

where F is the thickening factor. For a single-step reaction, the following governing equations for fuel mass fraction Y_F and temperature T for a 1D flame are obtained:

$$\frac{\partial}{\partial t}\left(\rho Y_\mathrm{F}\right) + \frac{\partial}{\partial x^*}\left(\rho u Y_\mathrm{F}\right) = \frac{\partial}{\partial x^*}\left(\rho F D_\mathrm{F} \frac{\partial Y_\mathrm{F}}{\partial x^*}\right) - \frac{\dot{\omega}}{F} \tag{6.2}$$

$$\frac{\partial}{\partial t}\left(\rho T\right) + \frac{\partial}{\partial x^*}\left(\rho u T\right) = \frac{\partial}{\partial x^*}\left(\rho F D_\mathrm{th} \frac{\partial T}{\partial x^*}\right) + \frac{Q}{C_p}\frac{\dot{\omega}}{F} \tag{6.3}$$

where D_F is the fuel mass diffusivity, $\dot{\omega}$ is the reaction rate and Q is the heat of reaction.

As highlighted in [267], the equations are self-similar with respect to the coordinate transformation: the resulting thickened flame solution in the dilated x^* space is equivalent to the original one in the x space. Introducing with $\widehat{\bullet}$ the flame variables obtained with the model transformation, the laminar flame speed of the thickened flame is conserved ($\widehat{S_\mathrm{L}^0} = S_\mathrm{L}^0$), since the integral of the heat release rate is retained (Figure 6.3a) and the laminar flame thickness is increased by a factor F ($\widehat{\delta_\mathrm{L}^0} = F\delta_\mathrm{L}^0$). This is shown in Figure 6.3b, where the temperature-based progress variable $c \equiv (T - T_\mathrm{u})/(T_\mathrm{b} - T_\mathrm{u})$ is plotted in space with $F = 1$ and $F = 10$ for a 1D unstretched laminar flame at $\Phi = 0.4$. These results match scaling laws coming from asymptotic premixed flame theory [62]:

$$\begin{cases} S_\mathrm{L}^0 \propto \sqrt{D_\mathrm{th}\dot{\omega}} \Rightarrow \widehat{S_\mathrm{L}^0} = S_\mathrm{L}^0 \propto \sqrt{F D_\mathrm{th}\dot{\omega}/F}, \\ \delta_\mathrm{L}^0 \propto \frac{D_\mathrm{th}}{S_\mathrm{L}^0} \Rightarrow \widehat{\delta_\mathrm{L}^0} = F\delta_\mathrm{L}^0 \propto \frac{F D_\mathrm{th}}{S_\mathrm{L}^0}. \end{cases} \tag{6.4}$$

Thus, in the canonical TF model, the diffusion coefficients are increased by F while the source terms are reduced by the same factor F:

$$(D_k, D_\mathrm{th}, \dot{\omega}_k) \mapsto (F D_k, F D_\mathrm{th}, \dot{\omega}_k/F) \tag{6.5}$$

where D_k is the diffusion coefficient and $\dot{\omega}_k$ the source term of the species k. A convenient method to explain the S_L^0 conservation is to plot the flame structure in the progress variable space c. The mapping of Equation (6.5) ensures that gradients are perfectly scaled by the thickening factor such that $F\nabla\widehat{c} = \nabla c$ (Figure 6.3c). This guarantees that the consumption speed [62, 296]:

$$\widehat{S_\mathrm{c}} \propto \int \dot{\omega}_\mathrm{F} \, \mathrm{d}x = \int \frac{\dot{\omega}_\mathrm{F}\left(c\right)}{F\nabla\widehat{c}} \, \mathrm{d}c \tag{6.6}$$

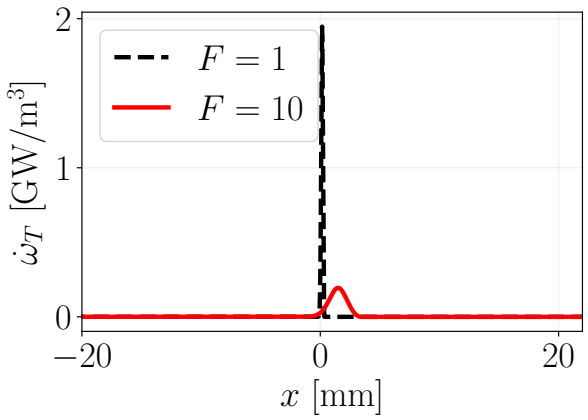

(a) Heat release rate in space coordinate x.

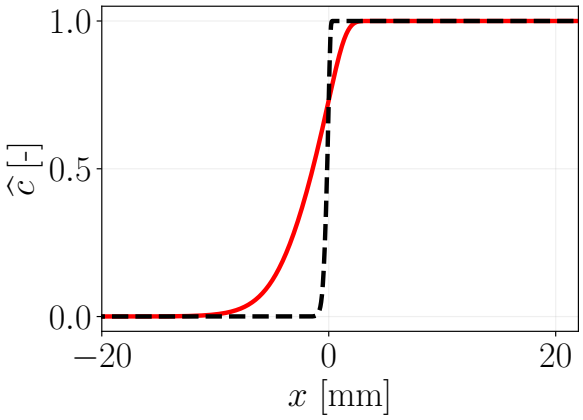

(b) Progress variable $\widehat{c}$, mapped with Equation (6.5), in space coordinate x.

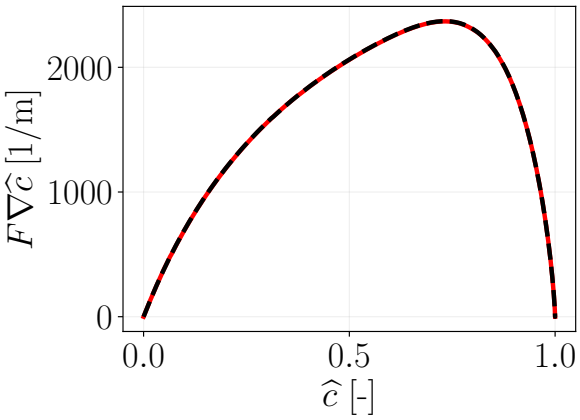

(c) Progress variable gradient in the temperature-based progress variable space.

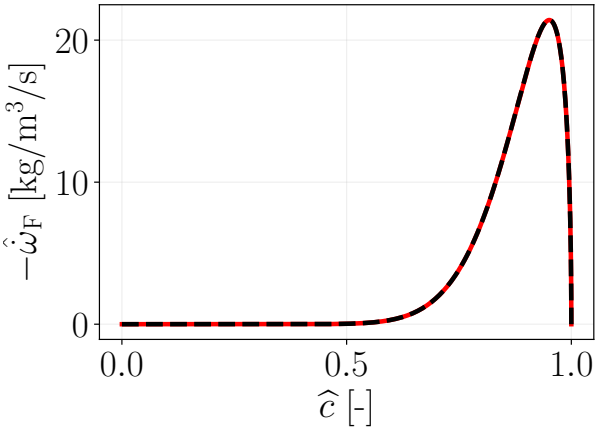

(d) Fuel source term in the temperature-based progress variable space.

Figure 6.3: Classical TF model applied to unstrained H_2-air flames at $\Phi = 0.4$ with $F = 1$ and $F = 10$.

corresponds exactly to S_L^0 for laminar unstrained flames, since $\dot{\omega}_F(c)$ is unchanged (Figure 6.3d) and $F\nabla\widehat{c} = \nabla c$: the flame is thickened and burns locally less, conserving the integral of the heat release rate. This property is not rigorously guaranteed for strained flames as discussed in the next section.

6.2.2 Strained laminar flames and numerical configuration

Numerical configuration

The combined effect between stretch and thickening is analysed now using 1D strained flames results. Popp *et al.* [296] considered a stagnation point flame where reactants and products are injected respectively from the two extreme sides of the domain. This counterflow premixed flame (CPF) configuration has been presented in Section 2.2.2. It is used here to understand the problem from a theoretical point of view and to simulate

how stretch and thickening affect premixed flames[1]. Simulations are carried out with the CANTERA [234] software.

Flame speed and strain rate

Stretch effects will be evaluated through the flame consumption speed, defined by Equation (2.10). As explained in Section 2.2.2, the CPF is subject to pure tangential strain (see Equation (2.29)). For simplicity, this term is denoted $K_{s,\mathrm{t}}$ (tangential component of the total strain) in the following. While multiple formulas of the strain rate of a CPF can be found in the literature, it is reasonable to say that the differences imparted by using one definition over the other remain minimal [298]. Here, a global approximation of $K_{s,\mathrm{t}}$, based on the injection velocity of fresh (u_{u}) and burnt gases (u_{b}), is used:

$$K_{s,\mathrm{t}} = \frac{\mid u_{\mathrm{u}} \mid + \mid u_{\mathrm{b}} \mid}{d} \tag{6.7}$$

with d the length of the computational domain, i.e. the distance between the two injection points.

Operating conditions

The fresh mixture conditions are taken at atmospheric temperature and pressure with equivalence ratios $\Phi = 1.0$ and $\Phi = 0.4$. The use of a stoichiometric point and a lean point allows a direct illustration of the stretch response stiffening and its consequences as one shifts towards the lean side. Flame response is examined for different values of $K_{s,\mathrm{t}}$, by increasing the injection velocities. The domain length d is set at 1 m (substantially greater than δ_{L}^0) to avoid flame-boundary interactions.

6.2.3 Thickened Flame model application to strained flames

Previous works [296] proved that a thickened CPF under the diffusion-reaction transformation (Equation (6.5)) does not conserve its burning velocity $\widehat{S_{\mathrm{c}}}$. This is verified here in Figure 6.4a, where the consumption speed of the strained flames deviates from the exact value ($F = 1$) as soon as $F > 1$. The error increases both with thickening factor F and strain $K_{s,\mathrm{t}}$. This is confirmed by the F-scaled gradient profiles of $\widehat{c}$ shown in Figures 6.4b-6.4c for the case $\Phi = 0.4$. For very small strain values ($K_{s,\mathrm{t}} = 30$ s^{-1}) and low values of F (see the case $F = 2$, Figure 6.4b), the flame structure exhibits a weak sensitivity to thickening and the consumption speed remains close to the reference value at $F = 1$ (whereas the classical TF model in the unstretched case perfectly matches the laminar flame speed). The picture is different when strain is increased (Figure 6.4c), or if thickening is increased (Figure 6.4b case $F = 10$): $F\nabla\widehat{c}$ is not conserved in the temperature-based progress variable domain $\widehat{c}$ and, accordingly, the consumption speed diverges (see Equation (6.6)) from the reference solution at $F = 1$. The mismatch becomes higher by increasing the thick-

[1] Hawkes and Chen [297] highlighted the physical reliability of this configuration for a flamelet approach, showing that the CPF is a coherent representation of the laminar flame structure embedded within a turbulent strained flame.

ening value. Note that in contrast with the propane-air flames in Detomaso *et al.* [295], the present hydrogen-air flames are strongly sensitive to strain. It means that even at very low stretch ($K_{s,\mathrm{t}} = 30$ s^{-1}), the flame profile thickened with $F = 10$ already deviates considerably from the $F = 1$ reference.

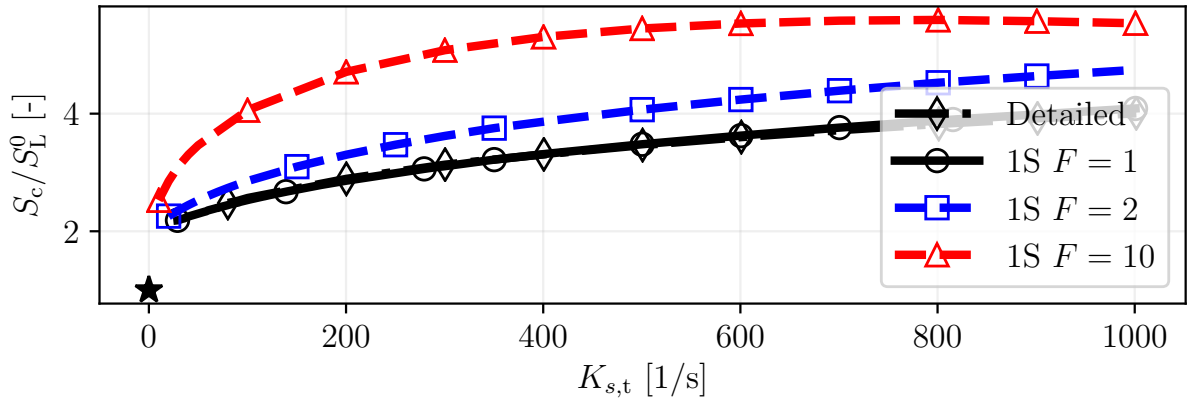

(a) Normalised consumption speed behaviour with respect to the applied strain rate. Detailed scheme [60] at $F = 1$ also plotted for comparison.

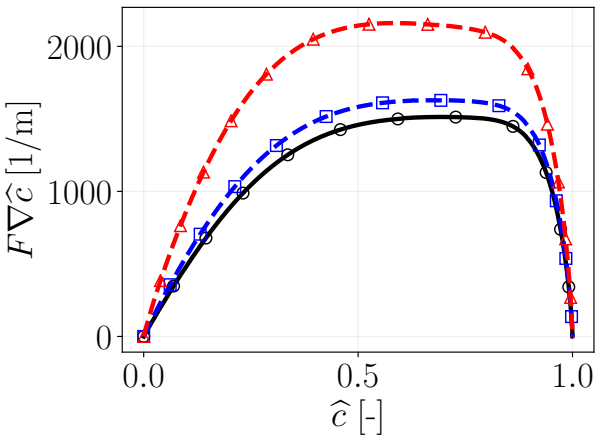

(b) Gradient of the progress variable vs. progress variable $\widehat{c}$ at $K_{s,\mathrm{t}} = 30$ s^{-1}.

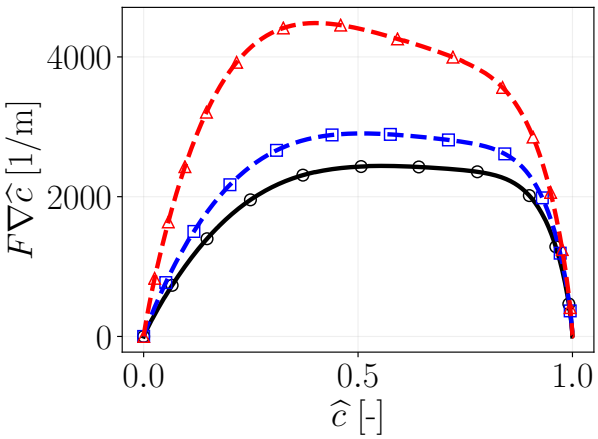

(c) Gradient of the progress variable vs. progress variable $\widehat{c}$ at $K_{s,\mathrm{t}} = 500$ s^{-1}.

Figure 6.4: TF model applied to strained flames with $F = 1$, $F = 2$, $F = 10$ at $\Phi = 0.4$.

This behaviour has been explained in [296] and is briefly recalled here for completeness. Applying the coordinate change of Equation (6.1) to the governing equations of a flame in a stagnation point flow, written on the centerline of the physical domain, yields:

$$-\rho_\mathrm{u}\frac{K_{s,\mathrm{t}}}{F}x^*\frac{\mathrm{d}Y_\mathrm{F}}{\mathrm{d}x^*} = \frac{\mathrm{d}}{\mathrm{d}x^*}\left(\rho F D_\mathrm{F}\frac{\mathrm{d}Y_\mathrm{F}}{\mathrm{d}x^*}\right) - \frac{\dot{\omega}}{F} \tag{6.8}$$

$$-\rho_\mathrm{u}\frac{K_{s,\mathrm{t}}}{F}x^*\frac{\mathrm{d}T}{\mathrm{d}x^*} = \frac{\mathrm{d}}{\mathrm{d}x^*}\left(\rho F D_\mathrm{th}\frac{\mathrm{d}T}{\mathrm{d}x^*}\right) + \frac{Q}{C_p}\frac{\dot{\omega}}{F}. \tag{6.9}$$

Contrary to the unstrained case (Equations (6.2) and (6.3)), the factor F now appears also in the convection term of the relations due to the spatial variation of axial mass flux

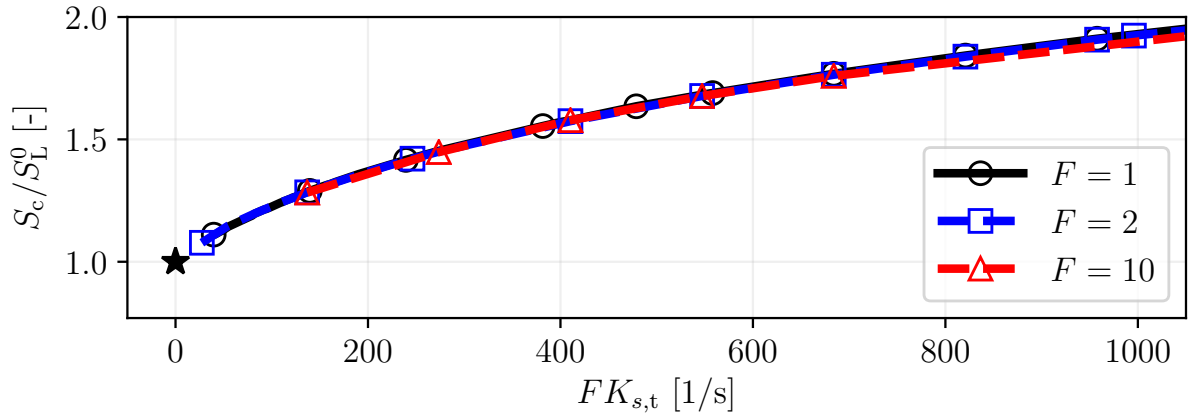

(a) Normalised consumption speed behaviour with respect to the scaled strain rate.

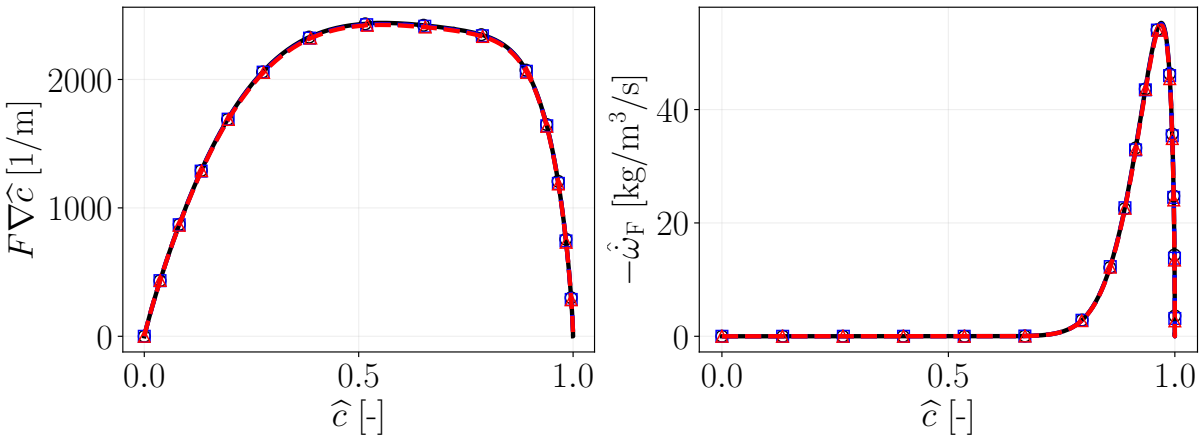

(b) Gradient of the progress variable vs. progress variable $\widehat{c}$ at $FK_{s,t} = 500$ s^{-1}.

(c) Fuel source term vs. progress variable $\widehat{c}$ at $FK_{s,t} = 500$ s^{-1}.

Figure 6.5: TF model applied to strained flames at $\Phi = 0.4$ by applying the convection-diffusion-reaction transformation $(K_{s,t}, D_k, D_{th}, \dot{\omega}_k) \mapsto (K_{s,t}/F, FD_k, FD_{th}, \dot{\omega}_k/F)$.

across the flame front, generating a strained flame.

Equations (6.8) and (6.9) suggest a more complex mapping than Equation (6.5), preserving the flame structures and, thus, all flame properties. In addition to the previous transformations, the strain parameter must also be divided by F:

$$(K_{s,t}, D_k, D_{th}, \dot{\omega}_k) \mapsto (K_{s,t}/F, FD_k, FD_{th}, \dot{\omega}_k/F). \tag{6.10}$$

Figure 6.5a displays the flames burning velocities computed for the three flames at $F = 1$, $F = 2$ and $F = 10$ as a function of the scaled strain rate $FK_{s,t}$. The collapse of all curves confirms the mapping introduced in Equation 6.10. The flame structure is also conserved through this transformation, as illustrated in Figures 6.5b and 6.5c. Thus, as expected, a strained thickened flame reacts to a strain $K_{s,t}/F$ exactly as a non-thickened flame does to a strain $K_{s,t}$: in other words, the diffusion-reaction transformation of Equations (6.5) generates flames reacting to a strain equal to $FK_{s,t}$.

Although the transformation of Equation (6.10) is an exact solution for the CPF problem, it is by no means a general solution for the simulation of strained flames since the transformation $K_{s,\mathrm{t}} \mapsto K_{s,\mathrm{t}}/F$ derives directly from the potential flow assumption adopted to get Equations (6.8) and (6.9) and cannot be implemented in practice in other flow topologies where $K_{s,\mathrm{t}}$ is imposed by the flow. The mapping of Equations (6.10) is therefore not a practical solution to correct stretch effects in CFD codes. A review of alternative solutions is proposed in the next section together with the development of the Stretched-Thickened Flame model.

6.3 Thickened Flame model extensions for strained laminar flames

6.3.1 Existing models

Model	Mapping	Speed matched	Properties conserved
TF [267]	$(D_k, D_{\mathrm{th}}, \dot{\omega}_k) \mapsto (FD_k, FD_{\mathrm{th}}, \dot{\omega}_k/F)$	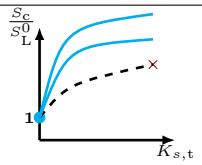	$S_{\mathrm{c}}(K_{s,\mathrm{t}}=0)$
Popp [296]	$(D_k, D_{\mathrm{th}}, \dot{\omega}_k) \mapsto (FD_k, \alpha FD_{\mathrm{th}}, \dot{\omega}_k/F)$	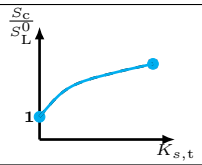	$S_{\mathrm{c}}(K_{s,\mathrm{t}})\ \forall\ K_{s,\mathrm{t}}$ but $K_{s,\mathrm{t}}$ must be known
TF-adapt [52]	$(D_k, D_{\mathrm{th}}, \dot{\omega}_k) \mapsto (F_{\mathrm{sp}} D_k, F_{\mathrm{th}} D_{\mathrm{th}}, \dot{\omega}_k/F_{\mathrm{r}})$	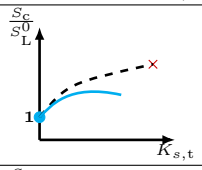	$S_{\mathrm{c}}(K_{s,\mathrm{t}}=0)$, $\frac{\partial S_{\mathrm{c}}}{\partial K_{s,\mathrm{t}}}$ at $K_{s,\mathrm{t}} \longrightarrow 0$ for a linear behaviour
Comer [299]	$(D_k, D_{\mathrm{th}}, \dot{\omega}_k) \mapsto (F^{2-x_0} D_k, F^{2-x_0} D_{\mathrm{th}}, \dot{\omega}_k/F^{x_0})$	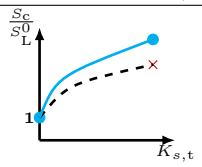	$S_{\mathrm{c}}(K_{s,\mathrm{t}}=0)$, $K_{s,\mathrm{t}}^{\mathrm{ext}}$, $S_{\mathrm{c}}(K_{s,\mathrm{t}}^{\mathrm{ext}})$ not guaranteed
S-TF [295]	$(D_k, D_{\mathrm{th}}, \dot{\omega}_k) \mapsto (F_{\mathrm{sp}} D_k, F_{\mathrm{th}} D_{\mathrm{th}}, \dot{\omega}_k/F_{\mathrm{r}})$	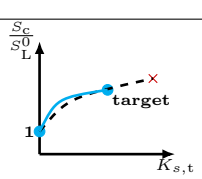	$S_{\mathrm{c}}(K_{s,\mathrm{t}}=0)$, $S_{\mathrm{c}}(K_{s,\mathrm{t}}=\mathbb{K}_\infty)$

Table 6.3: Summary of TF-based methods and their corresponding stretch response.

A brief overview of previously proposed models is summarised in Table 6.3. Popp *et al.* [296] suggested a correction function based on strain rate, plugged inside the diffusion term of the energy conservation equation (Equation (6.9)) in order to recover flame gradients

and, therefore, flame speed. Although it provides the exact burning velocity through a local flame structure adjustment, this approach demands the strain rate computation. The total stretch rate $\mathbb{K}$ evaluation is not immediate in a LES simulation of turbulent flames since it requires complex treatments such as the determination of the local flame displacement speed (see Equation 2.21 for instance).

A different approach relies on the asymptotic theory of stretch response presented in Section 2.2.4.2. In a first-order approximation, the consumption speed of weakly stretched flames is a function of the Lewis number of the mixture, the stretch $\mathbb{K}$, and the resolved laminar flame thickness $F\delta_{\mathrm{L}}^0$:

$$1 - \frac{\widehat{S_{\mathrm{c}}}}{S_{\mathrm{L}}^0} \propto F\delta_{\mathrm{L}}^0 \left(\mathrm{Le}_{\mathrm{eff}}^0 - 1\right) \mathbb{K} \tag{6.11}$$

Equation (6.11) confirms that thickening the flame by factor F increases the slope of the function $\widehat{S_{\mathrm{c}}}/S_{\mathrm{L}}^0 = f(\mathbb{K})$ (Figure 6.4a). However, the same relation may be seen from another point of view: it reveals that for a given value of stretch $\mathbb{K}$, the flame acts as if its Lewis number, or rather, $\left(\mathrm{Le}_{\mathrm{eff}}^0 - 1\right)$ is modified. This observation was the basis of the TF-adapt solution developed by Quillatre [49, 52] who proposed to artificially modify the species Lewis number in order to correct the stretch response. However, since it is based on an asymptotic theory, the success of this approach depends on restrictive hypotheses such as low stretch, single-step chemistry and high Zel'dovich number (cf. Section 2.2.4.2). Recently, Poncet *et al.* [300] improved this theory with a Markstein length adjustment but still only valid for small stretch values.

Finally, Comer *et al.* [299] also suggested a Lewis number modification aiming mainly at matching the extinction strain rate $K_{s,\mathrm{t}}^{\mathrm{ext}}$. However, this correction does not guarantee the consumption speed of the flame at all strain values.

Figure 6.6 shows the flame consumption speed obtained with the TF and TF-adapt models in a 1D CPF for both cases $\Phi = 1.0$ and $\Phi = 0.4$. The maximum strain rate plotted in these diagrams is chosen to be of the order of $\mathcal{O}(S_{\mathrm{L}}^0/\delta_{\mathrm{L}}^0)$ (which, as explained in Section 6.1 has the same magnitude as the extinction limit[1]). As expected, the classical Thickened Flame model fails even for small thickening factors especially at high strains since the flame reacts to $FK_{s,\mathrm{t}}$. TF-adapt improves the flame stretch response (see the case $\Phi = 1.0, F = 2$, Figure 6.6a) but it guarantees the expected flame behaviour only if the thickening factor is kept low. For high strain or high thickening, the linear theory does not hold anymore and the error becomes substantial.

From this review, it is possible to conclude that another approach is required in order to improve the flame transformation when the TF and the TF-adapt models show lim-

[1]Note that counterflow premixed flames used herein are never quenched. As explained in Law [58], when the injection velocity is increased, the flame front moves closer to the stagnation plane. The absence of a wall (replaced by the hot gases jet) leaves room for the flame to cross the stagnation plane and move in the burnt gases side. Instead, the extinction at high strain is usually measured on so-called *twin* counterflow premixed flames, consisting of two impinging jets of fresh combustible mixture.

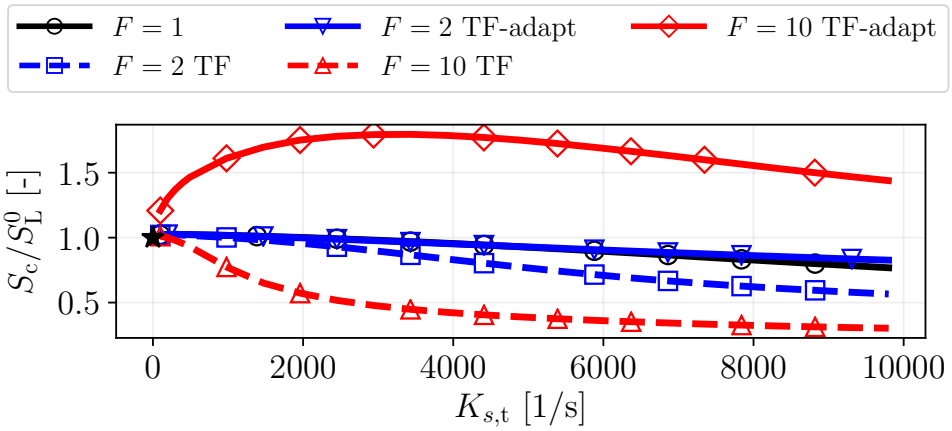

(a) $\Phi = 1.0$

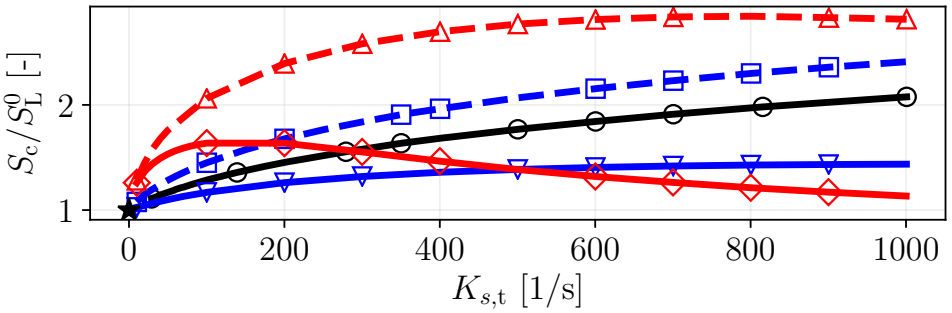

(b) $\Phi = 0.4$

Figure 6.6: Normalised consumption speed behaviour with respect to the applied strain rate. TF and TF-adapt models at $F = 1$, $F = 2$, $F = 10$ for cases $\Phi = 1.0$ and $\Phi = 0.4$.

itations. The Lewis number modification appears to be a convenient solution to correct the behaviour of a stretched thickened flame, especially because it is based on chemistry response and does not require strain or curvature evaluation on the flame front.

A Lewis number optimisation is proposed now, starting from a generalisation of the diffusion-reaction transformation (Equation (6.5)), in order to retrieve the correct flame stretch response regardless of the stretch values. The next section presents the mathematical formulation of this theoretical approach, leading to the definition of the Stretched-Thickened Flame model.

6.3.2 Generalisation of the diffusion-reaction transformation: introduction of the Stretched-Thickened Flame (S-TF) model

The first step of the model is to recognise that differently from the classical Thickened Flame model, thermal diffusion D_{th} and species mass diffusion D_k can be scaled using different factors F_{th} and F_{sp} such that $\widehat{D_{\text{th}}} = F_{\text{th}} D_{\text{th}}$ and $\widehat{D_k} = F_{\text{sp}} D_k$. F_{sp} is set uniquely

for all species to avoid the modification of preferential diffusion effects (see Section 2.2.3). As a consequence, the Lewis number[1] is changed as follows:

$$\widehat{\mathrm{Le}_{\mathrm{eff}}} = \frac{\widehat{D_{\mathrm{th}}}}{\widehat{D_k}} = \frac{F_{\mathrm{th}} D_{\mathrm{th}}}{F_{\mathrm{sp}} D_k} = \frac{F_{\mathrm{th}}}{F_{\mathrm{sp}}} \mathrm{Le}^0_{\mathrm{eff}}. \tag{6.12}$$

Since this Lewis number modification alters the unstretched laminar flame speed, a correction function F_{r} is applied to the Arrhenius pre-exponential factors to conserve S^0_{L}. This procedure leads to a generalisation of the mapping introduced by the classical TF transformation of Equation (6.5):

$$(D_k, D_{\mathrm{th}}, \dot{\omega}_k) \mapsto (F_{\mathrm{sp}} D_k, F_{\mathrm{th}} D_{\mathrm{th}}, F_{\mathrm{r}} \dot{\omega}_k) \tag{6.13}$$

which, as announced, does not take into account the local value of strain.

The factors F_{th}, F_{sp}, F_{r} are unknown a priori: their values can be determined by targeting three specific flame properties. First, the unstretched flame quantities must satisfy:

$$\frac{\widehat{S^0_{\mathrm{L}}}}{S^0_{\mathrm{L}}} = 1 \tag{6.14}$$

$$\frac{\widehat{\delta^0_{\mathrm{L}}}}{\delta^0_{\mathrm{L}}} = F \tag{6.15}$$

where $\widehat{S^0_{\mathrm{L}}}$ and $\widehat{\delta^0_{\mathrm{L}}}$ represent the unstretched laminar flame speed and thickness once the generalised transformation of Equation (6.13) is applied. Equations (6.14) and (6.15) guarantee the unstretched laminar flame speed conservation and the thermal thickness resolution, respectively, as obtained through the classical Thickened Flame model.

Equation (6.15) imposes the thermal diffusion factor F_{th}:

$$\frac{\widehat{\delta^0_{\mathrm{L}}}}{\delta^0_{\mathrm{L}}} = \frac{\widehat{D_{\mathrm{th}}}}{\widehat{S^0_{\mathrm{L}}}} \frac{S^0_{\mathrm{L}}}{D_{\mathrm{th}}} = F_{\mathrm{th}} = F \tag{6.16}$$

showing that, in the S-TF model, the thermal diffusion is still increased by F.

The first constraint (Equation (6.14)) is now used to find F_{r}. Following premixed flame theory [62, 301], the laminar flame speed depends on the square root of the global reaction rate $\dot{\omega}$ and on thermal diffusion and species mass diffusivity:

$$S^0_{\mathrm{L}} \propto \dot{\omega}^{1/2} D^{\alpha}_{\mathrm{th}} D^{\beta}_k \tag{6.17}$$

where α and β are parameters that generalise the laminar flame speed dependency on D_{th} and D_k, or, in other words, on the Lewis number. They are obtained from unstretched laminar flame properties and classical theory for non-unity Lewis number shows that

[1] Note that the Lewis number $\mathrm{Le}^0_{\mathrm{eff}}$ for the 1S-LeFit chemistry corresponds to that obtained after the fitting of the stretch response to the detailed mechanism (see Section 6.1).

$\alpha + \beta = 1/2$ [62, 216]. The procedure to compute α and β is detailed in Appendix A of Detomaso *et al.* [295]. Note that no hypothesis on the complexity of the chemical scheme has been used in Equation (6.17). The laminar flame speed ratio may therefore be expressed as follows:

$$\frac{\widehat{S_{\mathrm{L}}^0}}{S_{\mathrm{L}}^0} = \frac{\left(\dot{\omega} F_{\mathrm{r}}\right)^{1/2} \left(D_{\mathrm{th}} F_{\mathrm{th}}\right)^{\alpha} \left(D_k F_{\mathrm{sp}}\right)^{\beta}}{\dot{\omega}^{1/2} D_{\mathrm{th}}^{\alpha} D_k^{\beta}} = \sqrt{F_{\mathrm{r}}} F_{\mathrm{th}}^{\alpha} F_{\mathrm{sp}}^{\beta} \tag{6.18}$$

The condition $\widehat{S_{\mathrm{L}}^0} = S_{\mathrm{L}}^0$ is fulfilled with the following expression for F_{r}:

$$F_{\mathrm{r}} = \left[\frac{1}{F_{\mathrm{th}}^{\alpha+\beta}} \left(\frac{F_{\mathrm{th}}}{F_{\mathrm{sp}}} \right)^{\beta} \right]^2 = \frac{1}{F} \left(\frac{F}{F_{\mathrm{sp}}} \right)^{2\beta} \tag{6.19}$$

In a multi-step reactions chemistry, F_{r} is applied to all pre-exponential constants. In the classical TF model, one has $F_{\mathrm{sp}} = F$ so that $F_{\mathrm{r}} = 1/F$.

Note that the expressions for F_{th} and F_{r} (Equations (6.16) and (6.19)) allow to impose the unstretched flame properties ($\mathbb{K} = 0$) for any value of F_{sp}. To fix F_{sp}, a third constraint is added to Equations (6.14) and (6.15), which consists in imposing that the thickened flame consumption speed at a certain target strain value, $\mathbb{K}_\infty$, must match the one obtained from the reference solution at $F = 1$:

$$\widehat{S_{\mathrm{c}}}\left(F > 1, K_{s,\mathrm{t}} = \mathbb{K}_\infty\right) = S_{\mathrm{c}}\left(F = 1, K_{s,\mathrm{t}} = \mathbb{K}_\infty\right) \tag{6.20}$$

In practice, to find the value of F_{sp} that satisfies Equation (6.20), an optimisation procedure is used, based on the following objective function ϵ:

$$\min\left(\epsilon\right) = \min\left(\left. \frac{S_{\mathrm{c}}(F=1) - \widehat{S_{\mathrm{c}}}(F)}{S_{\mathrm{c}}(F=1)} \right|_{K_{s,\mathrm{t}}=\mathbb{K}_\infty} \right) \tag{6.21}$$

ϵ measures the difference between the consumption speeds of the flame at $F = 1$ ($S_{\mathrm{c}}(F = 1)$) and at $F > 1$ ($\widehat{S_{\mathrm{c}}}(F)$), evaluated at the target strain $\mathbb{K}_\infty$. An efficient method to minimise ϵ is to use the slope at $K_{s,\mathrm{t}} \longrightarrow 0$ as a shooting parameter to reach $S_{\mathrm{c}}\left(F = 1, K_{s,\mathrm{t}} = \mathbb{K}_\infty\right)$ as shown in Figure 6.7. Formally, this slope is influenced by the mixture Lewis number:

$$\frac{\partial S_{\mathrm{c}}}{\partial \mathbb{K}} \propto \delta_{\mathrm{L}}^0 \left(\mathrm{Le}_{\mathrm{eff}}^0 - 1\right), K_{s,\mathrm{t}} \longrightarrow 0 \tag{6.22}$$

that can be adjusted to match the constraint Equation (6.20). Hence, inside the optimisation loop, the initial slope $\partial S_{\mathrm{c}}/\partial \mathbb{K}$ is changed by modifying the Lewis number $\widehat{\mathrm{Le}_{\mathrm{eff}}}$ according to:

$$\left(\widehat{\mathrm{Le}_{\mathrm{eff}}} - 1\right) \widehat{\delta_{\mathrm{L}}^0} = \left(\mathrm{Le}_{\mathrm{eff}}^0 - 1\right) \delta_{\mathrm{L}}^0 X_0 \tag{6.23}$$

where X_0 is an optimisation variable which depends on the parameter F.

Finally, combining Equation (6.23) with Equation (6.15) gives an expression for the

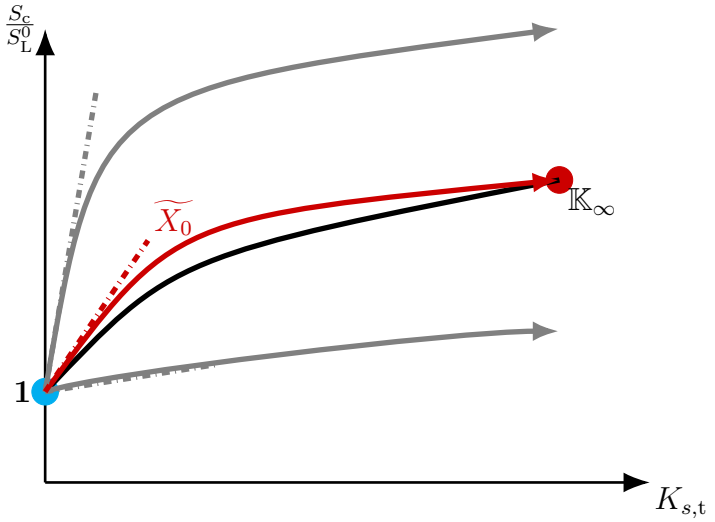

Figure 6.7: Shooting method applied, by changing the parameter X_0, to retrieve the slope $\partial S_c/\partial K_{s,t}$ for $K_{s,t} \longrightarrow 0$ such that the constraint in Equation 6.20 is accomplished. Black curve: reference DNS ($F = 1$) stretch response. Red curve: S-TF model.

species mass diffusion term F_{sp}:

$$F\left(\frac{F_{th}D_{th}}{F_{sp}D_k} - 1\right) = \left(\mathrm{Le}^0_{eff} - 1\right) \Longrightarrow F_{sp} = \frac{F_{th}F\mathrm{Le}^0_{eff}}{F + \left(\mathrm{Le}^0_{eff} - 1\right)X_0} \tag{6.24}$$

Note that F_{sp} depends on the desired thickening F and the mixture Lewis number Le^0_{eff}.

Eventually, the generalised diffusion-reaction transformation factors are obtained:

$$\begin{cases} F_{th} = F \\ F_{sp} = \frac{F^2\mathrm{Le}^0_{eff}}{F+\left(\mathrm{Le}^0_{eff}-1\right)X_0} \\ F_r = \left[\frac{1}{F_{th}^{1/2}}\left(\frac{F_{th}}{F_{sp}}\right)^{\beta}\right]^2 \end{cases} \tag{6.25}$$

which, after mapping, leads to the Lewis number $\widehat{\mathrm{Le}_{eff}}$:

$$\widehat{\mathrm{Le}_{eff}} = \frac{\widehat{D_{th}}}{\widehat{D_k}} = 1 + \frac{\left(\mathrm{Le}^0_{eff} - 1\right)X_0}{F} \tag{6.26}$$

Since a positive Lewis number must be ensured, X_0 is limited to:

$$\begin{cases} X_0 < -\dfrac{F}{\mathrm{Le}^0_{eff} - 1} & \text{if } 0 < \mathrm{Le}^0_{eff} < 1 \\ X_0 > -\dfrac{F}{\mathrm{Le}^0_{eff} - 1} & \text{if } \mathrm{Le}^0_{eff} > 1 \end{cases} \tag{6.27}$$

Thus, according to the original Lewis number $\mathrm{Le}^0_{\mathrm{eff}}$, there is one value of X_0, here defined as $\widetilde{X_0}$, that satisfies Equation (6.20) for a given value of F, able to correct the stretch response of thickened flames.

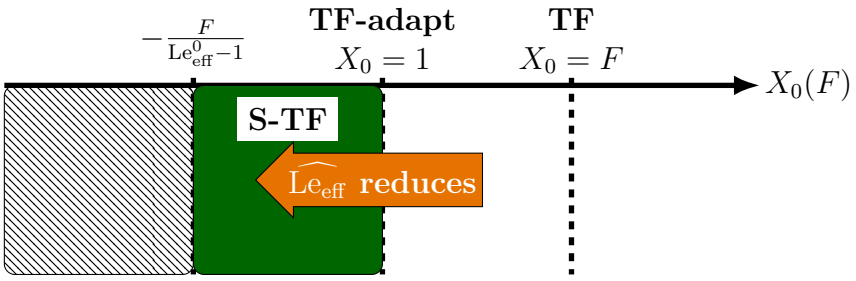

Figure 6.8: Schematic overview of the three different approaches (TF, TF-adapt and S-TF) for $\mathrm{Le}^0_{\mathrm{eff}} > 1$.

Note that Equation (6.25) yields a generalised mapping for all thickened flame models, covering different approaches depending on the value assumed by the function X_0 (see Figure 6.8 for $\mathrm{Le}^0_{\mathrm{eff}} > 1$):

1. $X_0 = F$ yields the Thickened Flame model factors [266, 267]:

$$\begin{cases} F_{\mathrm{th}} = F \\ F_{\mathrm{sp}} = F \\ F_{\mathrm{r}} = 1/F \end{cases} \tag{6.28}$$

   with $\widehat{\mathrm{Le}_{\mathrm{eff}}} = \mathrm{Le}^0_{\mathrm{eff}}$.

2. $X_0 = 1$ corresponds to the TF-adapt model [49]:

$$\begin{cases} F_{\mathrm{th}} = F \\ F_{\mathrm{sp}} = \frac{F^2 \mathrm{Le}^0_{\mathrm{eff}}}{F + \left(\mathrm{Le}^0_{\mathrm{eff}} - 1\right)} \\ F_{\mathrm{r}} = \left[\frac{1}{F_{\mathrm{th}}^{1/2}} \left(\frac{F_{\mathrm{th}}}{F_{\mathrm{sp}}} \right)^{\beta} \right]^2 \end{cases} \tag{6.29}$$

   with $\widehat{\mathrm{Le}_{\mathrm{eff}}} = 1 + \frac{\left(\mathrm{Le}^0_{\mathrm{eff}} - 1\right)}{F}$ as expected from TF-adapt theory.

3. $X_0 = \widetilde{X_0}(F)$, with $\widetilde{X_0}(F) \neq 1$ and $\widetilde{X_0}(F) \neq F$, leads to the Stretched-Thickened Flame model [295], where the $\widetilde{X_0}$ function matches the correct strained flame speed at $\mathbb{K}_\infty$, leading to the following mapping factors:

$$\begin{cases} F_{\mathrm{th}} = F \\ F_{\mathrm{sp}} = \frac{F^2 \mathrm{Le}^0_{\mathrm{eff}}}{F + \left(\mathrm{Le}^0_{\mathrm{eff}} - 1\right) \widetilde{X_0}} \\ F_{\mathrm{r}} = \left[\frac{1}{F_{\mathrm{th}}^{1/2}} \left(\frac{F_{\mathrm{th}}}{F_{\mathrm{sp}}} \right)^{\beta} \right]^2 \end{cases} \tag{6.30}$$

In this case, the Lewis number corresponds to:

$$\widehat{\mathrm{Le}_{\mathrm{eff}}} = 1 + \frac{\left(\mathrm{Le}^0_{\mathrm{eff}} - 1\right)\widetilde{X_0}}{F} \tag{6.31}$$

Note that formally the S-TF model does not guarantee the right slope for $K_{s,\mathrm{t}} \longrightarrow 0$ (Markstein number) trying, instead, to match the thickened flame consumption speed at $K_{s,\mathrm{t}} = \mathbb{K}_\infty$. However, once the optimisation problem is solved and the thickened flame consumption speed matches the one of the reference flame ($F = 1$) at the target stretch value $\mathbb{K}_\infty$, $\widehat{S_\mathrm{c}}$ will be reasonably predicted also for all strain values below $\mathbb{K}_\infty$: the unstrained solution ($K_{s,\mathrm{t}} = 0$) is recovered by construction and the flame speed response to stretch is usually monotonic[1] between $K_{s,\mathrm{t}} = 0$ and $\mathbb{K}_\infty$ (Figure 6.7).

It is convenient to choose the target value $\mathbb{K}_\infty$ in the high strain region to ensure precision over a large range of strain. In most cases, the exact value of $\mathbb{K}_\infty$ is not fundamentally crucial: it is just used to match the correct thickened flame behaviour on an extended set of strain values. $\mathbb{K}_\infty$ can be set of the order of $\mathcal{O}\left(S^0_\mathrm{L}/\delta^0_\mathrm{L}\right)$, or in other words $\mathrm{Ka}_\infty = \mathcal{O}(1)$ because it is close to the extinction strain rate limit. However, contrary to the propane-air flames encountered in Detomaso *et al.* [295], the strong sensitivity to stretch of the lean H_2-air flames[2] encountered in the present manuscript advocates for a proper choice of $\mathbb{K}_\infty$. This will be illustrated in Section 6.4.

The procedure to compute $\widetilde{X_0}$ in the Stretched-Thickened Flame model framework is detailed in the next section.

6.3.3 Optimisation procedure

Figure 6.9 describes the S-TF model optimisation loop followed to compute the function $\widetilde{X_0}$ for a certain thickening factor F. Once the fresh gas conditions have been defined, the code Cantera[3] is used to simulate both unstrained and strained flames. At first, the 1D unstrained flame behaviour is characterised by measuring the parameters α and β of the chemical scheme (see Appendix A of Detomaso *et al.* [295]). After that, strained flames are computed using the CPF configuration: the consumption speed of the reference strained flame at $F = 1$ is computed for the chosen $\mathbb{K}_\infty$ and compared to the value of $\widehat{S_\mathrm{c}}(F > 1)$ of the thickened flame for the same strain value. In general, the classical TF model can be used as an initial guess for the optimisation ($X_0^{\mathrm{init}} = F$). Then the objective function (Equation (6.20)) is minimised. In practice, the algorithm exits the optimisation loop as soon as the error function verifies $\epsilon < \epsilon_0$ (ϵ_0 is a threshold usually set of the

[1] This monotony assumption does not hold anymore at high thickening/strain levels for the present H_2-air mixtures, as illustrated for the TF-adapt curves in Figure 6.6.

[2] This sensitivity must be linked to the aforementioned non-monotonic response to stretch.

[3] The factors F_{th}, F_{sp} and F_{r} have been implemented in the code Cantera.

order of $\mathcal{O}(10^{-3} - 10^{-2})$). The search for the minimum can be done by using different optimisation algorithms such as Newton-Raphson, Broyden's or the Differential Evolution (DE) method [302]. Here the DE approach was used since it proved to be the fastest and most effective in converging on a solution, following a stochastic approach in the research of the best candidate, without relying on gradient methods. During this process, X_0 is updated and the curve slope ($\partial S_\mathrm{c}/\partial K_{s,\mathrm{t}}|_{K_{s,\mathrm{t}}\longrightarrow 0}$) is modified until the constraint on the burning velocity, $\widehat{S_\mathrm{c}}\,(F > 1, \mathbb{K}_\infty) = S_\mathrm{c}\,(F = 1, \mathbb{K}_\infty)$, is satisfied for $X_0 = \widetilde{X_0}$. This process is repeated for different thickening factors, building a $\widetilde{X_0}$ dependency in F as shown in Section 6.4.

Note that although the S-TF model optimisation is done on counterflow flames, it is reasonable to expect that the model stays valid for any nature of stretch. The main hypothesis lies in the fact that the set of species Schmidt numbers is uniquely linked to the response to stretch, no matter its nature. There is no reason why a set of Schmidt numbers which produces a correct response to strain, would yield completely inaccurate results on a flame subject to curvavture-related stretch.

In the next section, the results of the optimisation procedure are validated for the counterflow premixed flame configuration.

6.4 Stretched-Thickened Flame model validation

6.4.1 Stretch response correction

Figure 6.10 reports the consumption speed as a function of the 1D CPF strain for $\Phi = 1.0$ and $\Phi = 0.4$. Curves include the reference $F = 1$, classical TF approach and the S-TF correction at $F = 2$ and $F = 10$. For the S-TF optimisation input, two values of target strain $\mathbb{K}_\infty$ (delimited by the vertical dashed black lines) are tested for the lean case. They correspond to Karlovitz numbers $\mathrm{Ka}_\infty = 1$ and $\mathrm{Ka}_\infty = 1/5$.

Stoichiometric case
In the stoichiometric case, using $\mathrm{Ka}_\infty = 1$ for the S-TF optimisation allows a good reproduction of the reference ($F = 1$) curve both at $F = 2$ and $F = 10$. The error of the classical TF approach (dashed curves) is greatly reduced over the whole range of strain $\mathbb{K} \in [0, \mathbb{K}_\infty]$. These conclusions are similar to those obtained with the propane-air flames of Detomaso *et al.* [295].

Lean case
At $\Phi = 0.4$, a similar conclusion can be drawn at small thickening level ($F = 2$). However, as F is increased, the shooting method described in Section 6.3.3 converges on a non-monotonic behaviour which matches with the reference only at $K_{s,\mathrm{t}} = \mathbb{K}_\infty$. This generates an over-prediction (resp. under-prediction) of the consumption speed for strains below (resp. above) $\mathbb{K}_\infty$. It is directly linked to the strong sensitivity of lean H_2-air flames to

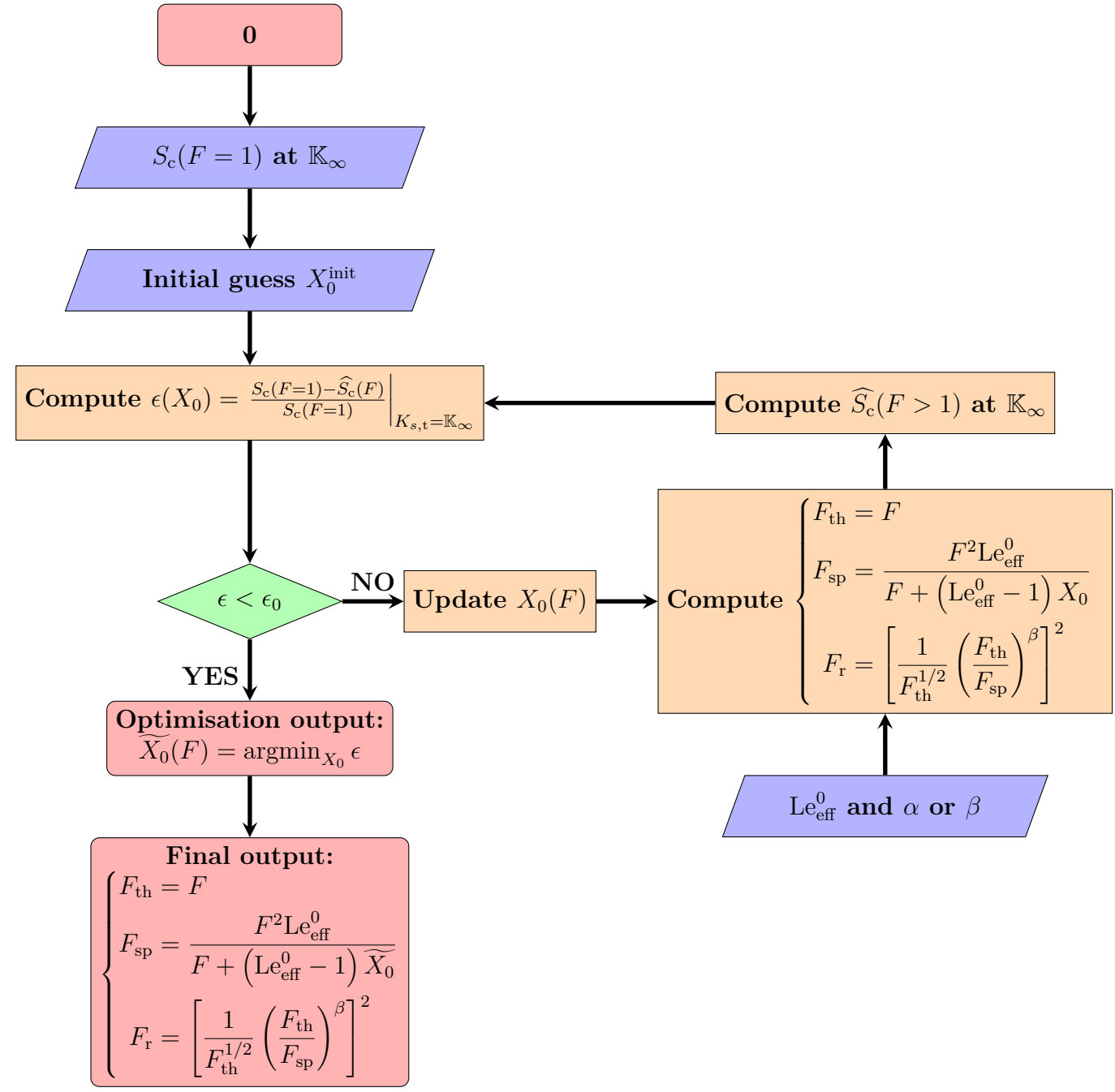

Figure 6.9: Optimisation loop used to obtain S-TF model key parameters $(F_{\text{th}}, F_{\text{sp}}, F_{\text{r}})$ for a given desired thickening F and fixed operating conditions. Consumption speeds of strained flames are computed using the Counterflow Premixed Flame configuration in Cantera.

stretch, mentioned in Chapter 2 and verified in Chapter 5. While the error remains limited at $F = 10$, it rapidly becomes consequential for greater thickening levels. This undesired overshooting questions the performance of the S-TF correction for LES simulations. A workaround is to re-think the choice of target Ka_∞. As explained in [295], the value of

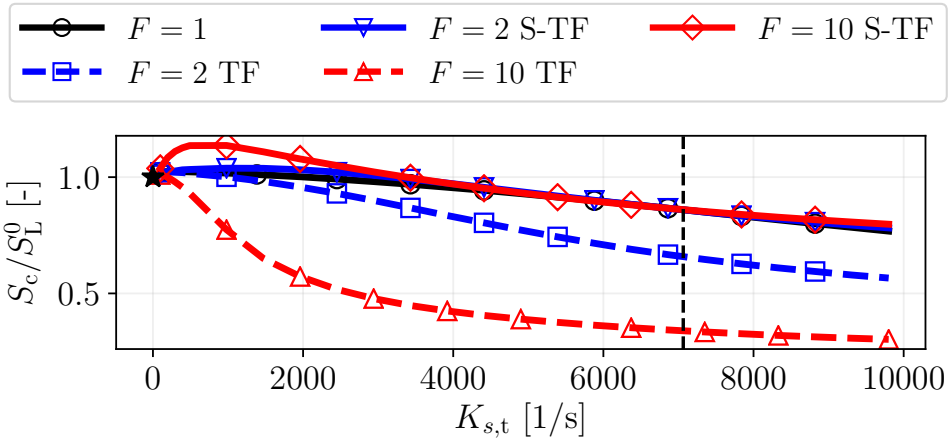

(a) $\Phi = 1.0, \mathrm{Ka}_\infty = 1$.

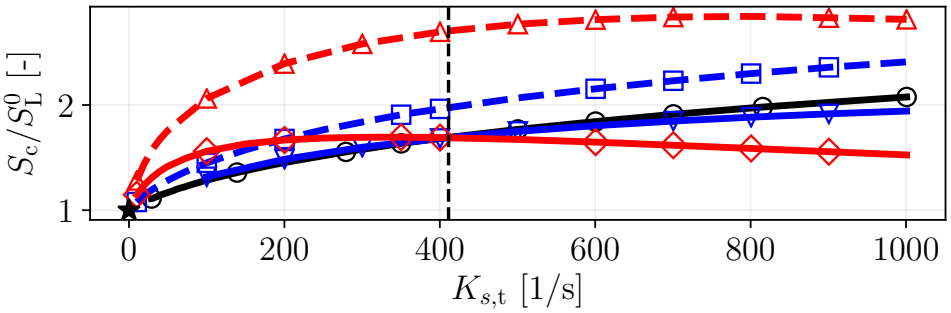

(b) $\Phi = 0.4, \mathrm{Ka}_\infty = 1$.

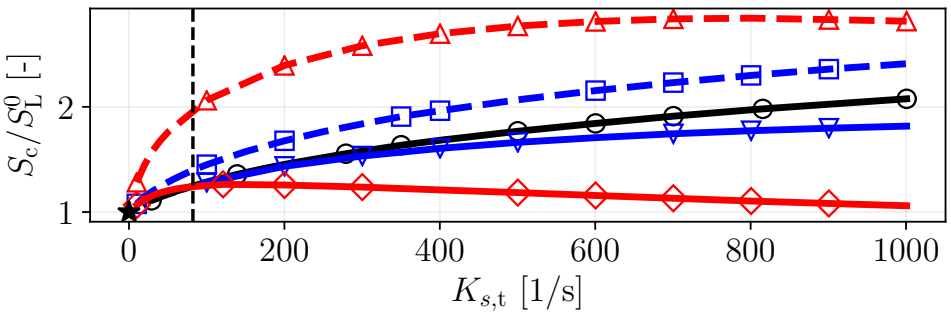

(c) $\Phi = 0.4, \mathrm{Ka}_\infty = 1/5$.

Figure 6.10: Normalised consumption speed behaviour with respect to the applied strain rate. TF and S-TF models at $F = 1$, $F = 2$, $F = 10$ for cases $\Phi = 1.0$ and $\Phi = 0.4$. Dashed black line: $K_{s,t} = \mathbb{K}_\infty$ abscissa.

Ka_∞ can be set according to the range of stretch rates expected for a given flame. For example, in the laminar phase of an explosion, the stretch rate is highest at the ignition (due to the high curvature of the hot kernel) and decreases afterwards[1].

Figure 6.10c depicts the consumption speed versus the strain rate of the classical TF

[1]In the presence of thermo-diffusive instabilities, the cellular patterns can locally generate strongly stretched zones, but these structures vanish in LES (cf. Chapter 5).

and the S-TF correction using $\mathrm{Ka}_\infty = 1/5$ ($\mathbb{K}_\infty \approx 80$ s^{-1}). The reduction of the target stretch for optimisation yields better predictions in the limited zone $\mathrm{Ka} \in [0, 1/5]$. This new correction is expected to be adapted for the LES of the 2D tube flame propagation of Chapter 5. It has indeed been shown that the local stretch rates experienced by the LES flames all fall within this optimal range for sufficient thickening levels (see Figure 5.21). The suitability of $\mathrm{Ka}_\infty = 1/5$ for other flame configurations is further discussed in the next chapters.

6.4.2 Modified Lewis number

Figure 6.11 summarise the results of the optimisation procedure detailed in Section 6.3.3 for a H_2-air premixed flame at $\Phi = 1.0$ and $\Phi = 0.4$ under atmospheric conditions. The modified Lewis number obtained with the TF, TF-adapt and S-TF models (resulting from the transformation given by Equation (6.26)) is plotted against F[1]. Target Karlovitz numbers $\mathrm{Ka}_\infty = 1$ and $\mathrm{Ka}_\infty = 1/5$ are both used for the S-TF input.

Stoichiometric case
The stoichiometric flame has an initial effective Lewis number greater than unity (in the 1S-LeFit chemical scheme, see Section 6.1). Like what has been observed in [295] for propane-air flames (their Lewis number is also greater than unity), the S-TF approach reduces the Lewis number of the stoichiometric flame when the thickening factor increases. Note that this trend is consistent with the TF-adapt strategy, thereby showing that this latter is correct for small thickening levels (or equivalently small strain rates). Nevertheless, the optimisation progressively diverges from the TF-adapt result as F is increased. The modified Lewis number rapidly becomes smaller than unity for $F > 5$ to ensure a correct response to stretch at high strain rates. This feature is retrieved in Figure 6.10a with the positive slope at the origin (characteristic of the $\widehat{\mathrm{Le}_{\mathrm{eff}}} < 1$) in the $F = 10$ case (solid red line).

Lean case
The lean flame exhibit an initial Lewis number smaller than unity. In that case, the S-TF optimisation increases its value when the thickening factor increases. It also diverges from the TF-adapt model, but in constrast with the stoichiometric case, the S-TF approach keeps $\widehat{\mathrm{Le}_{\mathrm{eff}}} < 1$. It is indeed verified in Figures 6.10b and 6.10c where the initial slope for the shooting stays positive.

[1] More details on the correlation of the S-TF optimisation results with the desired thickening factor F can be found in Appendix B.

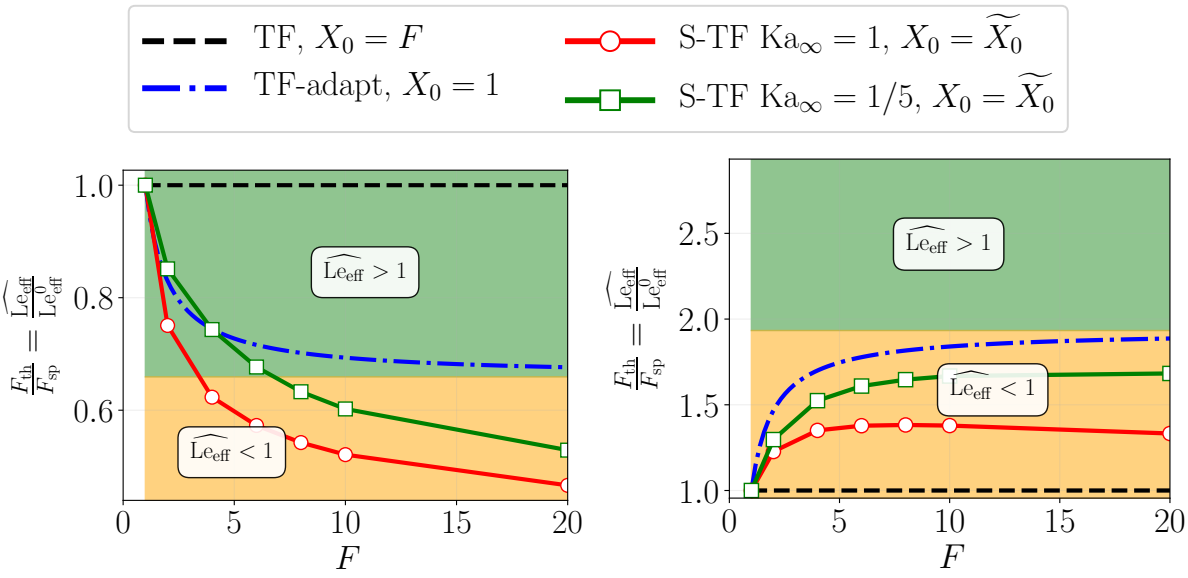

(a) $\Phi = 1.0$. (b) $\Phi = 0.4$.

Figure 6.11: Comparison of the S-TF optimisation results with TF and TF-adapt approaches at different values of thickening for $\Phi = 1.0$ (left) and $\Phi = 0.4$ (right) using $\mathrm{Ka}_\infty = 1$ and $\mathrm{Ka}_\infty = 1/5$.

6.5 Conclusion

It has been shown in previous chapters that the classical Thickened Flame model exaggerates the flame response to stretch. In this chapter, a strategy is proposed to correct this deficiency. The amplification of stretch effects leads to a dependency to the LES mesh resolution which questions the predictability of LES (in particular in explosion scenarios where the flame propagation is driven by stretch effects). Here, the problem is tackled using 1D counterflow premixed flames simulations which have the advantage of being computationally cost-effective. The coupling of the thickening applied to the flame and its sensitivity to stretch is reproduced, confirming the mathematical analysis carried out by Popp *et al.* [296]. In order to produce a LES which properly emulates the real flame response to stretch, two steps are needed.

First, a new procedure to build stretch-fitted global chemistries, called 1S-LeFit is developed. By a general modification of all species Lewis numbers, the response to stretch of the single-step mechanism is matched with a detailed scheme reference. The use of 1S-LeFit schemes allows a good reproduction of stretch effects in DNS ($F = 1$).

Then, the thickening-stretch interaction in LES ($F > 1$) is corrected by the Stretched-Thickened Flame model. It is achieved by modifying the thermal and species diffusivity with different factors as well as adjusting the reaction terms to match specific flame properties. Namely, the diffusion-reaction transformation is generalised and the scaling factor applied on the thermal and species mass diffusion as well as on the reaction terms

are computed to ensure the laminar flame speed conservation, the thermal thickness resolution and the same stretch response between thickened and non thickened flame. In the last constraint, an optimisation function is included to match the stretched flame speed at one large stretch value $\mathbb{K}_\infty$ of the order of $S_\mathrm{L}^0/\delta_\mathrm{L}^0$.

As mentioned in the introduction, this work has been the subject of a publication [295]. While the article focused on propane-air flames, this chapter re-establishes and analyses the model for hydrogen-air mixtures. While similar results are obtained for a stoichiometric flame (Lewis number greater than unity like the propane-air mixtures of [295]), caution is needed for lean mixtures. The main difference comes from their high sensitivity to stretch. Contrary to the previous cases, the choice of target $\mathbb{K}_\infty$ has a significant impact on the resulting S-TF correction at high thickening levels: for strain rates below (resp. above) $\mathbb{K}_\infty$, the consumption speed is over-predicted (resp. under-predicted). The value of $\mathbb{K}_\infty$ must be adapted to the target configuration. Further studies are necessary to build a S-TF model valid at all thickening levels independent of $\mathbb{K}_\infty$.

Still, the S-TF approach suggests a practical solution to overcome TF model limits for stretched flames, without requiring local stretch computation or discrimination between strained, curved or unstretched flame during the simulation. From an implementation point of view, the S-TF model preserves the simplicity of the TF approach and offers a viable solution for complex CFD codes. It provides the first building block for predictive LES of lean hydrogen-air explosions. The next chapter shows the application of the S-TF model to a multidimensional configuration and deals with the second phenomenon symptomatic of lean H_2-air flames identified in Chapter 5: thermo-diffusive instabilities.

Chapter 7

Flame front instabilities correction for LES: the Thermo-Diffusive-Stretched-Thickened Flame (TD-S-TF) model

Sommaire

The naïve approach to the LES of lean hydrogen-air explosions of Chapter 5 has put forward two main issues:

- the Thickened Flame model amplifies the flame response to stretch;
- the use of coarse meshes and high thickening levels filters out flame front instabilities.

While Chapter 6 proposed the Stretched-Thickened Flame model to solve the first point, the present chapter builds upon it to address also the second point with the Thermo-Diffusive-Stretched-Thickened Flame (TD-S-TF) model. This work is the subject of an article published in the *International Journal of Hydrogen Energy* which is recalled below (Section 7.1). An addendum is joined afterwards to provide more information about some aspects not fully discussed in the paper. Namely:

- in Section 7.2.1: a new initialisation method for explosion simulations based on a strained initial profile;
- in Section 7.2.2: details on the practical inputs of the Stretched-Thickened Flame model used in the present chapter;
- in Section 7.2.3: the use of the new stretch-fitted global chemical scheme 1S-LeFit developed in Section 6.1;

Eventually, Section 7.3 deals with the validation of the TD-S-TF model against experimental data on a 3D spherical flame LES. The TD-S-TF model has indeed been initially developed on a 2D spherical flame set-up and requires an appropriate demonstration of its capability to capture the propagation of real flames.

7.1 Thermo-Diffusive-Stretched Thickened Flame model development

This section includes the work on the development of the Thermo-Diffusive-Stretched-Thickened Flame model, published in the *International Journal of Hydrogen Energy.*

A modeling strategy for the Thickened Flame simulation of propagating lean hydrogen-air flames

Jean-Jacques Hok[a,*], Omar Dounia[a], Nicola Detomaso[a], Thomas Jaravel[a], Quentin Douasbin[a], Olivier Vermorel[a]

[a] *CERFACS, 42 avenue Gaspard Coriolis, Toulouse, 31057, France*

Abstract

Even in the laminar regime, lean H_2-air flames are prone to intrinsic Thermo-Diffusive (TD) instabilities which contribute to flame acceleration. Applying the Thickened Flame (TF) strategy to simulate such flames prompts two erroneous behaviors: (1) amplification of the flame sensitivity to stretch due to thickening; (2) inability to capture TD cells onset and development. A new paradigm is proposed based on 2D spherical flames simulations: (1) the flame response to global stretch is corrected by the Stretched-Thickened Flame model, extended here for lean hydrogen mixtures; (2) a TD efficiency function is introduced, encompassing both subgrid wrinkling and subgrid stretch effects due to TD instabilities. These corrections are introduced in the diffusion and reaction terms of the Navier-Stokes equations, in a manner similar to the TF model. The new model accurately reproduces the propagation of these flames, both the early stages governed by global stretch effects and the TD-dominated phase, without adding any significant computational cost.

Keywords: Lean hydrogen-air flames, Spherical flames, Stretch effects, Thermo-diffusive instabilities, Subgrid modeling

*Corresponding author
Phone number: +33 5 61 19 30 66
Email address: hok@cerfacs.fr (Jean-Jacques Hok)

1. Introduction

Over recent years, there has been renewed interest for hydrogen (H_2) to decarbonize combustion-bound industries. However, the burning properties of H_2 significantly differ from those of usual hydrocarbons and raise safety concerns. One of the worst cases is the deflagration to detonation transition (DDT) which usually happens for near-stoichiometric mixtures [1]. But even at low concentrations, H_2 explosions can cause considerable damage. In addition to experiments, these events can also be studied using numerical simulations. Owing to the considerable size of the geometries often involved in this kind of scenarios, Direct Numerical Simulations (DNS) are impossible due to their prohibitive computational costs. Instead, Large-Eddy Simulations (LES) provide a good compromise between cost and accuracy. In this context, among multiple existing strategies (such as the G-equation model [2, 3], flame surface density approaches [4, 5, 6], probability-density function approaches [7, 8], etc.), a very popular and classically used model is the Thickened Flame (TF) model [9]. Even in the absence of turbulence, the TF model is still very useful to resolve premixed flames on a coarse mesh [10, 11, 12]. This paper focuses on the initial evolution of a laminar flame kernel, representative of the first stages of flame acceleration in an explosion. During this phase, lean H_2-air mixtures are subject to several phenomena not usually encountered with conventional hydrocarbon fuels. Indeed, these mixtures are characterized by a sub-unity Lewis number, i.e. an imbalance between thermal and molecular diffusion processes, which can drastically impact the first stages of an explosion [13]:

(1) lean H_2-air flames accelerate with stretch. The initial stages of flame kernel development are accompanied by a global flame stretch (related to the curvature of the spherical kernel) that homogeneously enhances the flame propagation speed. Even if this stretch is resolved, the TF formalism is known to amplify stretch effects on the flame [14, 15, 16]. A recent correction, called the Stretched-Thickened Flame (S-TF) model has been successfully validated in simulations of stretched propane-air flames by Detomaso et al. [17]. However, the suitability of the S-TF approach for lean H_2-air flames, which are considerably more sensitive to stretch, remains to be assessed.

(2) lean H_2-air mixtures are known to form intrinsic flame front instabilities. In asymptotic theory studies [18, 19, 20], this unstable nature is directly linked with the mixture Lewis number. While most flames only experience Darrieus-Landau (DL, also called hydrodynamic) instabilities at large scales

due to the density jump across the flame, lean H_2 mixtures also exhibit thermo-diffusive (TD) instabilities at small scales owing to their sub-unity Lewis number. This phenomenon has been extensively studied experimentally [21, 22, 23, 24, 25, 26, 27, 28] as well as numerically [29, 30, 31, 32, 33] and is recognized as an acceleration mechanism. But such small-scale structures cannot be resolved on coarse meshes. The loss of wrinkling is not the only issue: cellular patterns generate high curvature zones where combustion is promoted by stretch effects. In a TF framework, local stretch effects are not captured: TD instabilities become a subgrid mechanism to model. So far, TD modeling is nascent. Recently, Aniello et al. [34] have developed the TD-TF model which combines the scaling laws of Berger et al. [32] with the TF approach. Unfortunately, this model gives a constant-valued efficiency (for a premixed flame under fixed operating conditions) that may not be representative of the dynamics of TD instabilities on a propagating flame. The TD instability is indeed known to develop on spherical flame kernels only after they have reached a critical radius. After the onset, the TD cells continually grow and split into smaller structures as the flame expands. Therefore, a subgrid model aimed at accounting for their effect on flame acceleration must vary during the propagation.

The objective of the present paper is to provide a modeling strategy for the TF simulation of laminar propagating lean H_2-air flames. Although focus is put on a laminar spherical flame expansion, this case constitutes the first stage of many explosion scenarios. The article is structured as follows: Section 2 describes the simulation framework as well as the results obtained with a naïve TF modeling. It is intended to demonstrate the shortcomings introduced by the TF transform applied to lean H_2-air flames. Then, Section 3 addresses the issue of stretch response. It recalls the basic principles behind the S-TF model and shows its application to hydrogen. Finally, Section 4 outlines three TD modeling approaches for TF simulations and identifies the best one by comparing them with a flame-resolved reference simulation. The article ends with a discussion on possible extensions of the model to complex geometries, in particular for turbulent regime considerations.

2. Naïve TF simulation of a lean hydrogen-air spherical flame

2.1. Set-up description

The two-dimensional spherically-expanding flame configuration is chosen because it is representative of the first stages of an explosion. The flames are computed using the AVBP code developed at CERFACS [35]. It is a massively parallel DNS and LES solver which solves the compressible multi-species Navier-Stokes equations on unstructured grids. More details about the governing equations are provided in [36]. AVBP has been used for a large range of combustion applications, including flame acceleration in gas explosions [37, 38, 39] and even DDT in both internal combustion engines [40, 41], and explosions [42, 43]. The computational domain consists of a quarter of a disk with a radius of 2 m depicted in Fig. 1. The outlet is set sufficiently far from the ignition with a buffer zone to ensure a constant pressure and avoid any influence on the flame expansion. The analysis is restricted within a radius of 0.1 m. Symmetries are imposed on left and bottom boundaries. The simulation of one quarter instead of the full disk has been shown to have no influence on the flame propagation. More details can be found in the Supplementary Material.

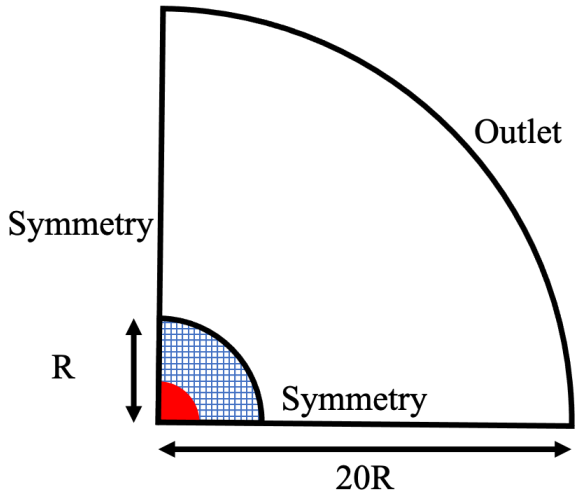

Figure 1: Schematic of 2D spherical domain, boundary conditions and initial flame kernel (in red). Hatched blue zone: region of interest where analyses are made.

Reference flame-resolved simulations (FRS) are computed using a spa-

tial discretization allowing 21 points within one flame thermal thickness δ_{L}^0 ($N_{\mathrm{c}} \equiv \delta_{\mathrm{L}}^0/\Delta x_{\mathrm{FRS}} = 21$). For the TF cases, the mesh resolution is reduced to target different thickening factors F: $\Delta x_{\mathrm{TF}} = F\delta_{\mathrm{L}}^0/7$. The flame is then thickened by a constant F factor to obtain 7 points within it using the classical TF formalism [9]:

$$\begin{cases} D_{\mathrm{th}} \mapsto F D_{\mathrm{th}} \\ D_k \mapsto F D_k \\ \dot{\omega}_k \mapsto F^{-1}\dot{\omega}_k \end{cases} \tag{1}$$

Applied to an unstretched flame, the TF transform (Equation (1)) allows to increase the flame thickness δ_{L}^0 by a factor F without altering the laminar flame speed S_{L}^0. It is based on scaling laws from the asymptotic theory [44]:

$$\begin{cases} \delta_{\mathrm{L}}^0 \propto \dfrac{D_{\mathrm{th}}}{S_{\mathrm{L}}^0} \\ S_{\mathrm{L}}^0 \propto \sqrt{D_{\mathrm{th}}\dot{\omega}} \end{cases} \Rightarrow \begin{cases} \widehat{\delta_{\mathrm{L}}^0} = F\delta_{\mathrm{L}}^0 \propto \dfrac{F D_{\mathrm{th}}}{S_{\mathrm{L}}^0} \\ \widehat{S_{\mathrm{L}}^0} = S_{\mathrm{L}}^0 \propto \sqrt{F D_{\mathrm{th}} F^{-1}\dot{\omega}} \end{cases} \tag{2}$$

where the hat symbol $\widehat{\bullet}$ denotes values after the TF transformation (Equation (1)). $\dot{\omega}$ is the rate of the global reaction.

Table 1 summarizes the different simulations along with their associated mesh properties.

Table 1: Summary of FRS and TF simulations.

Type of simulation	Thickening level F (imposed by the mesh resolution)	$\delta_{\mathrm{L}}^0/\Delta x$	$F\delta_{\mathrm{L}}^0/\Delta x$
FRS	-	21	-
TF	2	3.50	7
TF	4	1.75	7
TF	6	1.17	7
TF	8	0.87	7
TF	10	0.70	7

It is important to state that, the propagation being laminar, no subgrid turbulence model and no turbulent combustion model is used.

The flame kernel is initialized with hot flame products at the center of the sphere, the rest of the domain being filled with the fresh mixture. The transition from unburnt to burnt gases is provided by a 1D strained flame profile obtained with a counterflow premixed flame computation using the open-source Cantera software [45]. This 1D solution is obtained for an estimated

stretch rate associated to the kernel radius $r_{\mathrm{f},0}$ [44]:

$$\mathbb{K}_0 \approx \frac{\sigma_0 S_{\mathrm{L}}^0}{r_{\mathrm{f},0}} \left[1 + \frac{F\delta_{\mathrm{L}}^0}{2r_{\mathrm{f},0}}\right]^{-1} \tag{3}$$

where S_{L}^0 is the laminar flame speed and σ_0 the thermal expansion ratio. This procedure allows to properly reduce the transient phase associated to ignition.

The operating conditions simulated in this study include atmospheric lean H_2-air mixtures at equivalence ratios $\Phi \in [0.4, 0.7]$. For the sake of conciseness, results presented here first focus on the $\Phi = 0.4$ case which is particularly prone to stretch effects and TD instabilities. Other operating points are discussed in Section 4.4. For each operating condition, an irreversible single step chemistry is constructed. The use of global chemical schemes is motivated by: (1) their suitability for the study of large-scale explosions thanks to the decreased computational costs relative to detailed mechanisms; (2) and their capacity to reproduce intrinsic flame front instabilities [46, 47] via global mixture/flame parameters as suggested in the asymptotic theory [18, 19, 20]. They are tuned to match the detailed San Diego mechanism [48] in terms of laminar flame speed, flame thickness and flame response to stretch. The detailed mechanism has proven its validity in a wide range of applications [49]. Starting from the parameters of the detailed scheme, the fitting uses the Arrhenius pre-exponential constant and thermal and molecular diffusivities as degrees of freedom. All molecular diffusivities are modified by the same ratio so that preferential diffusion is unchanged. Fig. 2 illustrates the capacity of the single-step approach to accurately reproduce the flame response to stretch observed with the detailed mechanism. The ordinate corresponds to the consumption speed, defined for a 1D flame as:

$$S_{\mathrm{c}} = -(\rho_{\mathrm{u}}(Y_{\mathrm{F,u}} - Y_{\mathrm{F,b}}))^{-1} \int_{-\infty}^{+\infty} \dot{\omega}_{\mathrm{F}} \mathrm{d}x \tag{4}$$

where ρ_{u} is the fresh gases density, $Y_{\mathrm{F,u}}$ (resp. $Y_{\mathrm{F,b}}$) is the fresh (resp. burnt) gases fuel mass fraction.

2.2. Results

The effect of mesh size on the TF simulation of lean H_2-air flame propagation is assessed here. The flame front shapes at various instants are shown

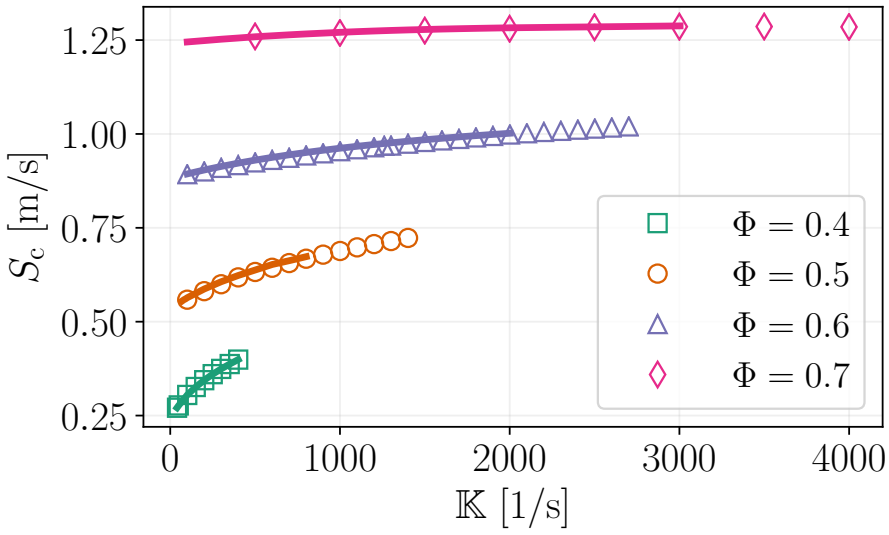

Figure 2: Consumption speed as a function of strain at several equivalence ratios for the detailed (solid lines) and global (symbols) schemes.

in Fig. 3 for decreasing mesh resolutions (hence increasing thickening factors) and compared with the reference FRS case. As expected, the flame is thermo-diffusively unstable in the FRS. By contrast, a progressive loss of wrinkling is observed with the TF flames as the resolution decreases. This effect is attributed to: (1) the stabilizing effect of thickening on the flame structure via enhanced thermal diffusion, and (2) the inability of a given coarse mesh to resolve all relevant cell structures, acting as a spatial filter cutting off short-wave perturbations. The net effect is the emergence of smoother flames as the mesh is coarsened.

To assess the impact of the loss of wrinkling on flame acceleration, the mean radial position r_f is tracked over time. To account for instabilities, r_f is defined as the radius of an equivalent perfect sphere containing the same mass of burnt products as a given wrinkled flame. In the present case of a 2D quarter of disk, it writes:

$$r_\mathrm{f} = \sqrt{\frac{4}{\pi \rho_\mathrm{b} Y_\mathrm{P,b}} \int_\Omega \rho Y_\mathrm{P} \mathrm{d}\Omega} \tag{5}$$

where subscript P refers to products (H_2O in the present case) properties, ρ_b is the burnt gases density and Ω denotes the whole computational domain.

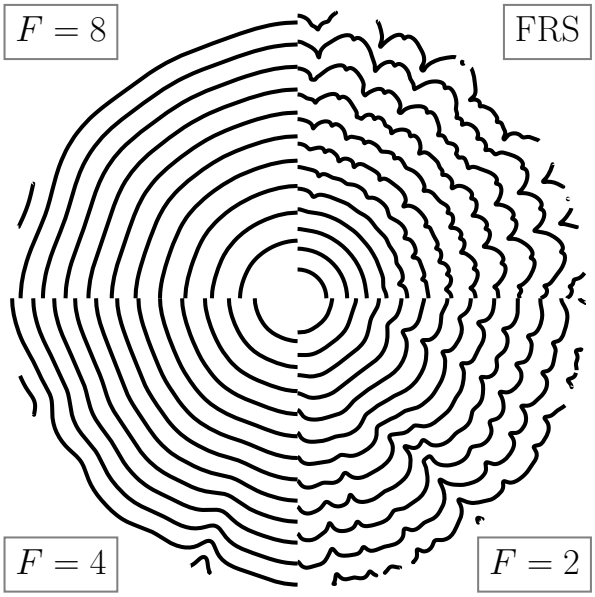

Figure 3: Superimposition of isotherms $T = 800$ K during flame propagation at $\Phi = 0.4$ for several thickening values. Same sampling period for all cases.

Fig. 4 displays the evolution of the flame propagation speed $v_\mathrm{f} \equiv \mathrm{d}r_\mathrm{f}/\mathrm{d}t$ with the flame radial position r_f for different mesh resolutions. Regarding the FRS, the propagation can be split into two phases (delimited by a change of line style on the curves):

1. Globally-stretched phase (solid lines): at the first stage, the flame is perfectly smooth and its speed decreases as the global stretch rate diminishes over time;
2. TD-dominated phase: as soon as the kernel reaches a critical size, the onset and development of the cellular structures observed in Fig. 3 induce an acceleration of the flame owing to the increased flame surface area.

When considering TF simulations, a strong mesh dependency is observed. This can be explained by two phenomena related to each phase of the propagation:

1. Globally-stretched phase (dashed lines): TF flames are smooth like the FRS, but they do not propagate at the same speed. Faster flames are

observed with increased thickening. This is characteristic of the stretch response amplification by the TF model identified in [17];

2. TD-dominated phase: this second stage is still observed for the TF flame at $F = 2$ but disappears at higher thickening levels. The acceleration induced by TD cells is not captured on coarse meshes.

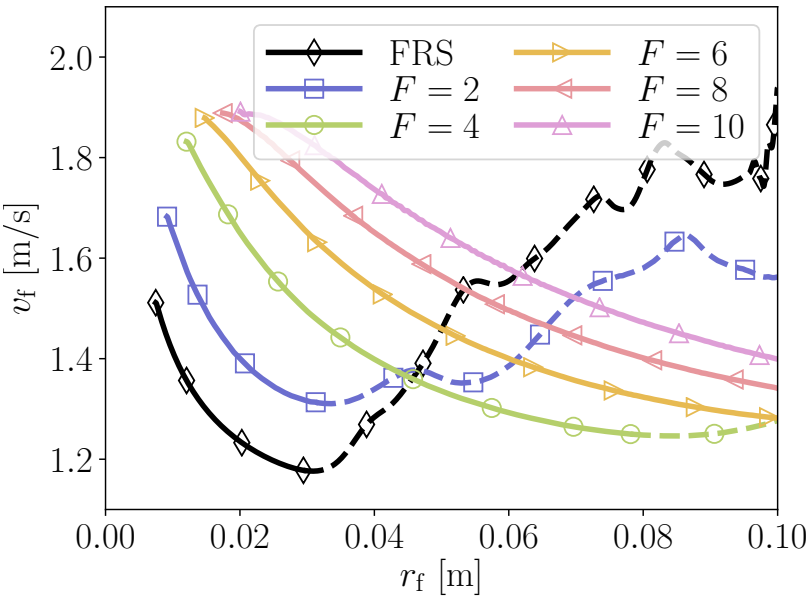

Figure 4: Flame speed as a function of flame position for the classical TF model at various thickening levels. $\Phi = 0.4$. Solid line: globally-stretched phase. Dashed line: TD-dominated phase.

In Fig. 5, the results of Fig. 4 are displayed in the $\mathbb{K}-v_\mathrm{f}$ space to better visualize the coupling of thickening with flame stretch. The flame global stretch rate $\mathbb{K}$ is here defined as $\mathbb{K} \equiv 1/r_\mathrm{f} \mathrm{d}r_\mathrm{f}/\mathrm{d}t$. In this framework, time goes from right (high stretch) to left (low stretch). The flame response to stretch is quantified through a Markstein length defined as the slope $-(\mathrm{d}v_\mathrm{f}/\mathrm{d}\mathbb{K})_{|\mathbb{K}\to 0}$. Given that the current estimation of global stretch rate is no longer valid when TD instabilities appear, the estimation must be carried out for $r_\mathrm{f} < r_\mathrm{f,c}$. The extrapolations for the FRS and all TF simulations are shown in gray lines, indicating an increase of the Markstein length with F and a corresponding amplification of the sensitivity of the flame to stretch.

The results of this section clearly highlight two problems related to the TF simulation of propagating lean H_2-air flames: (1) amplification of the

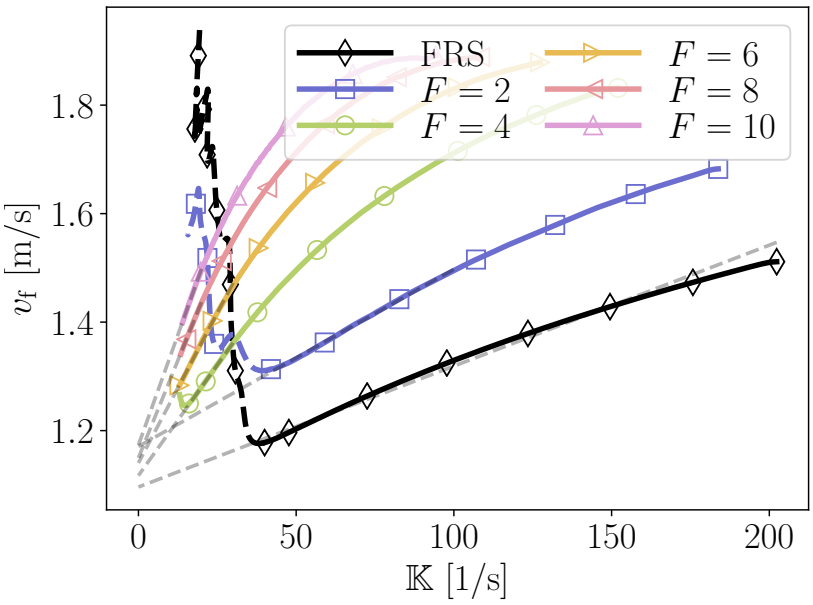

Figure 5: Flame speed as a function of flame global stretch rate for the classical TF model at various thickening levels. $\Phi = 0.4$. Solid line: globally-stretched phase. Dashed line: TD-dominated phase. Gray lines: extrapolations to zero-stretch for Markstein length estimation.

flame response to stretch by the thickening; (2) loss of the contribution of the cellular structures by coarse meshes. The ensuing flame propagations do not conform to the flame-resolved simulation reference and show a strong mesh dependency. This questions the suitability of the classical TF model for the simulation of lean H_2-air propagating flames. Solutions for both problems are presented in the next sections.

3. Stretch response correction

3.1. The Stretched-Thickened Flame model

To address the issue of stretch amplification by the TF transform, the Stretched-Thickened Flame (S-TF) model developed by Detomaso et al. [17] is used. Its principle is briefly recalled here but the reader may refer to the original paper for further details.

In essence, it consists in applying different thickening factors, namely F_{th} for the thermal diffusivity, F_{sp} for all molecular diffusivities and F_{r} for

all species chemical source terms $\dot{\omega}_k$ (by modifying the Arrhenius law pre-exponential constant):

$$\begin{cases} D_{\text{th}} \mapsto F_{\text{th}} D_{\text{th}} \\ D_k \mapsto F_{\text{sp}} D_k \\ \dot{\omega}_k \mapsto F_{\text{r}}^{-1} \dot{\omega}_k \end{cases} \tag{6}$$

Equation (6) can be seen as a generalization of Equation (1) for stretched flames. Such transform is equivalent to modifying the effective Lewis number of the mixture as shown in [17]. This number is indeed computed as a weighted average of the fuel and oxidiser Lewis numbers [19]:

$$\text{Le}_{\text{eff}}^0 = 1 + \frac{(\text{Le}_{\text{E}} - 1) + (\text{Le}_{\text{D}} - 1)\, B}{1 + B} \tag{7}$$

$$B = \begin{cases} 1 + \beta(\Phi - 1) & \text{if } \Phi > 1 \\ 1 + \beta(\Phi^{-1} - 1) & \text{if } \Phi < 1 \end{cases} \tag{8}$$

where Le_{E} (resp. Le_{D}) is the Lewis number of the excess (resp. deficient) reactant and β is the Zel'dovich number [44]. The S-TF transform of Equation (6) modifies the Lewis numbers of the reactants by the same amount $F_{\text{th}}/F_{\text{sp}}$ so that the effective Lewis number of the mixture becomes:

$$\widehat{\text{Le}_{\text{eff}}} = \frac{F_{\text{th}}}{F_{\text{sp}}} \text{Le}_{\text{eff}}^0 \tag{9}$$

The values of coefficients $F_{\text{th}}, F_{\text{sp}}$ and F_{r} are optimized to ensure that the flame is thickened by F and that the flame speeds at the unstretched ($\mathbb{K} = 0$) and a reference high stretch ($\mathbb{K} = \mathbb{K}_\infty$) points are correctly reproduced:

$$\begin{cases} \widehat{\delta_{\text{L}}^0} \approx F \delta_{\text{L}}^0 \\ \widehat{S_{\text{L}}^0} \approx S_{\text{L}}^0 \\ \widehat{S_{\text{L}}}(\mathbb{K}_\infty) \approx S_{\text{L}}(\mathbb{K}_\infty) \end{cases} \tag{10}$$

The hat symbol $\widehat{\bullet}$ now denotes values after the S-TF transformation (Equation (6)). The resulting effective mixture Lewis number controls the behavior at intermediary stretch levels, which is verified a posteriori. In practice the value of $\mathbb{K}_\infty$ depends on the operating conditions. It is chosen so that its non-dimensional form $\text{Ka}_\infty \equiv \mathbb{K}_\infty \delta_{\text{L}}^0 / S_{\text{L}}^0$ (Karlovitz number) is of the order unity, reflecting relatively high stretch levels [17]. The optimization uses 1D

counterflow premixed flame simulations with Cantera. Lean H_2-air flames are strongly sensitive to stretch, hence representing a new test case to extend the validity domain of the S-TF approach.

3.2. Results

The performance of the S-TF model is assessed in Fig. 6 at $F = 2$. This value is already sufficient to analyze the deficiencies of the TF model. Higher F simulations are presented in Section 4.3. In order to facilitate the analysis, the two phases of the propagation are highlighted with the background color. In the globally-stretched stage (in gray), the S-TF model is able to reproduce a stretched flame propagation close to the FRS reference. This validates its use for H_2-air flames. On the contrary, in the subsequent phase (in orange), the current modeling does not account yet for TD instabilities. Solutions for this part are addressed in the next section. It is worth noting that the S-TF flame becomes unstable at a large flame radius ($r_f \approx 0.08$ m) and re-accelerates, which is only due to the low thickening value applied in this particular case, further discussed in Section 4.3.

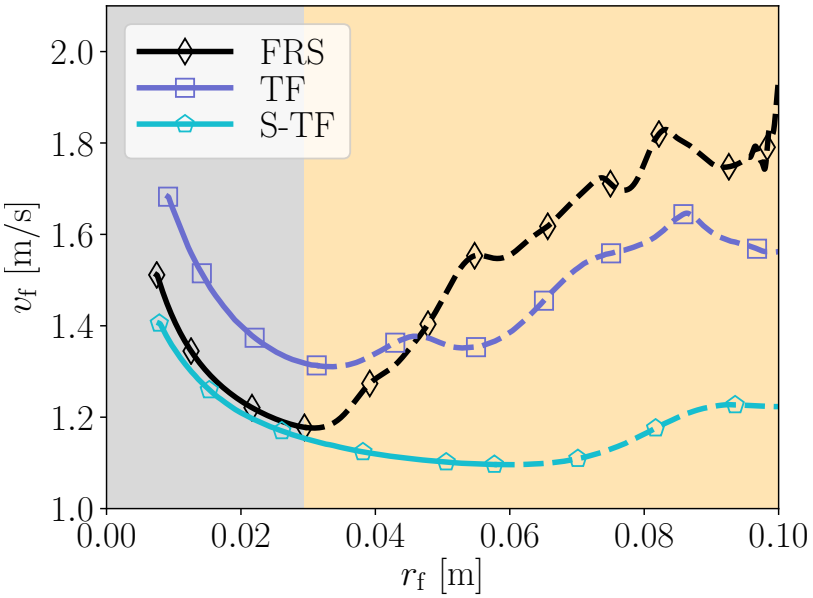

Figure 6: Flame speed as a function of flame radius for the FRS, the naïve TF and the S-TF simulations at $F = 2$. $\Phi = 0.4$. Gray zone: globally stretched phase. Orange zone: TD-dominated phase.

4. Thermo-diffusive instabilities modeling

4.1. Thermo-diffusive instabilities models

Fig. 6 shows that there is still a velocity gap between the stretch-corrected TF simulation and the flame-resolved simulation in the TD-dominated phase. The lost contribution of flame front instabilities to flame acceleration must also be corrected to increase the accuracy of the simulation. Three modeling strategies (summarized in Table 2) are explored in the following.

Table 2: Summary of proposed thermo-diffusive instabilities models.

Model	Resolved stretch effects	TD subgrid wrinkling	TD subgrid stretch effects
Planar-TF	overlooked	modeled with E_{planar} constant	modeled with E_{planar} constant
Fractal-TF	modeled with $E_{\text{fractal}}(r_{\text{f}})$	modeled with $E_{\text{fractal}}(r_{\text{f}})$	modeled with $E_{\text{fractal}}(r_{\text{f}})$
TD-S-TF	corrected by S-TF	modeled with $E_{\text{TDS}}(r_{\text{f}})$	modeled with $E_{\text{TDS}}(r_{\text{f}})$

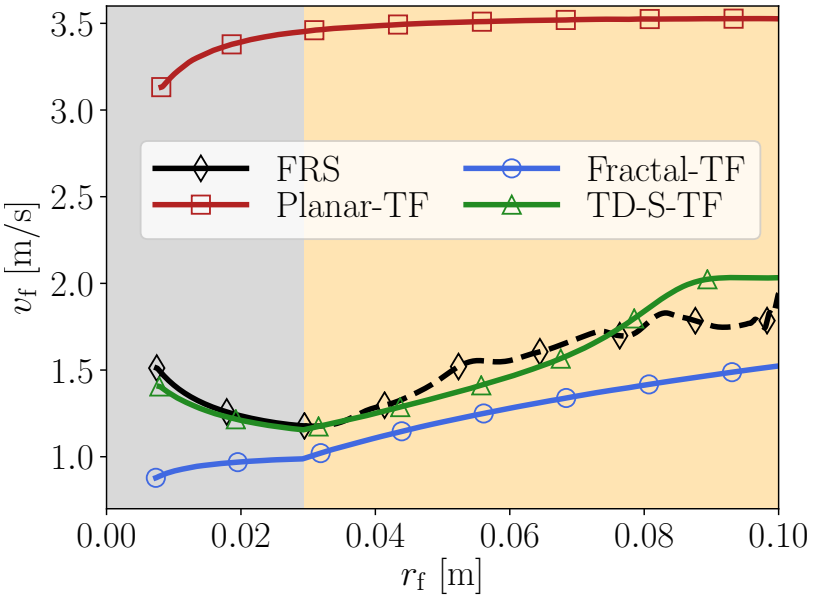

Figure 7: Flame speed as a function of flame radius for the FRS and the three corrected TF simulations at $F = 2$. $\Phi = 0.4$. Gray zone: globally-stretched phase. Orange zone: TD-dominated phase.

4.1.1. Planar-TF model: constant Lewis number effect

First, given that the flame response to global stretch and thermo-diffusive instabilities are both linked to the mixture Lewis number, one way to correct the TF simulation is to lump the two together in a single "Lewis number effect" factor. Such approach is meant to be used with a simplified unity Lewis number chemistry. In so doing, the resolved flame front does not respond to stretch and does not develop any thermo-diffusive instabilities by design. Instead, all combustion enhancement effects related to the sub-unity Lewis are lumped into an efficiency function E_{lam} analogous to turbulent combustion models in classical TF LES:

$$\begin{cases} D_{\text{th}} \mapsto E_{\text{lam}} F D_{\text{th}} \\ D_k \mapsto E_{\text{lam}} F D_k \\ \dot{\omega}_k \mapsto E_{\text{lam}} F^{-1} \dot{\omega}_k \end{cases} \tag{11}$$

The simplest form for this function is a constant E_{planar} that should represent all acceleration mechanisms induced by the sub-unity Lewis number. For example, Berger et al. [32] have extracted a "consumption speed enhancement factor" as a function of operating conditions from 2D planar flames simulations. Aniello et al. [34] have implemented an LES model based on these correlations and validated it on a turbulent swirled flame. This Planar-TF strategy is combined with a unity Lewis single-step chemistry (the pre-exponential factor is fitted to conserve the laminar flame speed) and confronted to the FRS results in Fig. 7 for $F = 2$. In the first phase of propagation, the efficiency E_{planar} (≈ 3.5 here) is activated right from the beginning of the simulation and leads to an overestimation of flame speed as the real flame is still stable. In the following TD-dominated phase, the flame speed reaches a plateau around $E_{\text{planar}}\sigma_0 S_{\text{L}}^0$. Because of its design, this model is only representative of Lewis number effects when the sphere reaches a considerable radius, where it can be locally assimilated to a planar flame. It is not able to capture the transient phase of a propagating unstable flame.

4.1.2. Fractal-TF model: time-varying Lewis number effect

The next level of precision is to account for time-dependency. For unstable spherical flames, fractal approaches exhibit such behavior. They rely on the assumption that intrinsic instabilities follow a fractal topology that drives a self-acceleration of the flame front [22, 50, 51]. In this framework, the flame

speed evolves according to:

$$\frac{\mathrm{d}r_\mathrm{f}}{\mathrm{d}t} \propto r_\mathrm{f}^d \tag{12}$$

where d is the fractal excess.

A large amount of experimental and computational studies have tried to measure d on thermo-diffusively unstable flames. A review by Wu et al. [22] has concluded that $d = 1/3$ is a good approximation. Eq. (12) can then be used to develop a correction model for thermo-diffusive instabilities. Similarly to the first approach, this Fractal-TF model is meant to be used with a unity Lewis chemistry because it contains the entire macroscopic effect of TD cells and stretch effects. An efficiency function evolving with the flame radius is applied to the laminar flame speed:

$$E_\mathrm{fractal} = \max\left(1, \left(\frac{r_\mathrm{f}}{r_\mathrm{f,c}}\right)^d\right) \tag{13}$$

where $d = 1/3$ and $r_\mathrm{f,c}$ is the critical radius for the onset of the instabilities. $r_\mathrm{f,c}$ is expected to differ in 2D and 3D. In the current study, its value is extracted from the 2D FRS but in other 3D applications, experimental data and correlations can directly be found in the literature [52, 53, 54, 55, 56, 57].

Fig. 7 highlights the performance of the Fractal-TF approach. As long as the flame kernel has not reached the critical size $r_\mathrm{f,c}$, $E_\mathrm{fractal} = 1$ and the Fractal-TF model follows a simple stretch-free spherical evolution, leading to an underestimation of the flame speed in the globally-stretched phase. Regarding the subsequent unstable phase of propagation, despite a small offset, the good match with the FRS speed evolution validates the fractal assumption for flame front instabilities. Given that the fractal theory has been explicitly based on unstable spherical flame expansion, it is not surprising that it catches accurately the acceleration of the flame during the TD-dominated phase.

4.1.3. TD-S-TF model: separate stretch and instabilities corrections

The third TD modeling strategy, inspired from the work of Goulier [54], differs from the two previous approaches as it splits Lewis number effects into two contributions: (1) resolved stretch effects (mainly observed during the globally-stretched phase) corrected by the S-TF model, and (2) "TD effects" solely due to the instabilities (wrinkling and local stretch effects), modeled

by an efficiency defined by:

$$E_{\mathrm{TDS}} \equiv v_{\mathrm{f}}/v_{\mathrm{f}}^{\mathrm{smooth}} \tag{14}$$

where $v_{\mathrm{f}}^{\mathrm{smooth}}$ corresponds to the propagation speed of a stable, stretched flame. Resolved stretch effects are gathered in $v_{\mathrm{f}}^{\mathrm{smooth}}$. This third approach called TD-S-TF is expressed as:

$$\begin{cases} D_{\mathrm{th}} \mapsto E_{\mathrm{TDS}} F_{\mathrm{th}} D_{\mathrm{th}} \\ D_k \mapsto E_{\mathrm{TDS}} F_{\mathrm{sp}} D_k \\ \dot{\omega}_k \mapsto E_{\mathrm{TDS}} F_{\mathrm{r}}^{-1} \dot{\omega}_k \end{cases} \tag{15}$$

The analysis carried out by Goulier has allowed to identify a self-similarity space for E_{TDS}:

$$(E_{\mathrm{TDS}} - 1)\mathrm{Le}_{\mathrm{eff}} = f\left(\left(\frac{r_{\mathrm{f}}}{r_{\mathrm{f,c}}} - 1\right)\mathrm{Le}_{\mathrm{eff}}\right) \tag{16}$$

where $\mathrm{Le}_{\mathrm{eff}}$ is the mixture Lewis number (computed using Equation (8)). Fig. 8 shows that the 2D FRS results performed in this work also obey the self-similarity law suggested by the experiments of Goulier for different equivalence ratios Φ. As suggested by [54] and the present FRS, the following formulation of the self-similarity function f can be proposed:

$$\begin{aligned} f(X) &= \begin{cases} 1 & \text{if } X < 0 \\ f_1(X) + \epsilon(X)\left(f_2(X) - f_1(X)\right) & \text{if } X \geq 0 \end{cases} \\ \text{with,} \quad & f_1(X) = aX, \quad f_2(X) = bX^{\alpha} \\ & \epsilon(X) = \left(1 + \tanh\left(\frac{X-1}{\delta_t}\right)\right)/2 \end{aligned} \tag{17}$$

where $a = 0.3125$, $b \approx 0.3202$, $\alpha \approx 0.27$, $\delta_t = 0.1$. In Eq. (17), a linear form f_1 is prescribed up to a saturation radius and a power law form f_2 is proposed when TD instabilities saturate. A hyperbolic tangent function ϵ allows a smooth transition between the two functions. This formulation of the thermo-diffusive efficiency function distinguishes three regimes:

1. For $r_{\mathrm{f}} < r_{\mathrm{f,c}}$ ($X < 0$ in Fig. 8), $E_{\mathrm{TDS}} = 1$: the instability is absent for small flame radii and therefore no efficiency is needed;

2. As soon as the kernel reaches the critical size $r_\mathrm{f} \geq r_\mathrm{f,c}$, the TD instability appears and $E_\mathrm{TDS} > 1$. In the early stages of TD development ($0 < X < 1$ in Fig. 8), the efficiency linearly grows with the flame radius:
$$E_\mathrm{TDS} \approx 1 + a\left(\frac{r_\mathrm{f}}{r_\mathrm{f,c}} - 1\right) \tag{18}$$
3. After some saturation radius ($X > 1$ in Fig. 8), the growth of the instability becomes milder, following a power-law with a sub-unity exponent α:
$$E_\mathrm{TDS} \approx 1 + b\left(\frac{r_\mathrm{f}}{r_\mathrm{f,c}} - 1\right)^{\alpha} \mathrm{Le}_\mathrm{eff}^{\alpha-1} \tag{19}$$

Parameters $r_\mathrm{f,c}$ and Le_eff of course depend on the operating conditions (mixture composition, temperature, pressure) thereby impacting the value of the TD efficiency. In practice, the critical radius $r_\mathrm{f,c}$ can be obtained from experimental correlations [52, 53, 54, 55, 56, 57] (as explained in the previous section) whereas the mixture Lewis number is computed using theory (Equation (8)). For example, for lean hydrogen-air mixtures, when the equivalence ratio is increased (or when the mixture is diluted): (1) $r_\mathrm{f,c}$ increases (the onset of the TD instability is delayed because richer mixtures are more stable); (2) Le_eff increases to traduce the fact that hydrogen is "less deficient". The resulting TD efficiency function E_TDS is impacted: (1) it is activated at a greater flame radius (richer mixtures are more stable); (2) its rate of increase is reduced (the growth of the instability is slower for richer mixtures).

Fig. 7 shows that the TD-S-TF strategy, which splits Lewis number effects into global stretch and subgrid contribution of the instabilities, is the most effective in capturing all phases of the propagation.

4.2. Local analysis

Using the TD-S-TF model allows to retrieve a correct flame propagation at a macroscopic level. But if one looks at a smaller scale, the local flame speed in TF simulations can also be compared to that of the FRS. To that end, a local consumption speed is extracted following this procedure:

1. A progress variable is defined based on the fuel mass fraction: $c \equiv (Y_\mathrm{F} - Y_\mathrm{F,u})/(Y_\mathrm{F,b} - Y_\mathrm{F,u})$. This function continuously varies from 0 in the fresh mixture to 1 in the burnt products;
2. The flame front is then defined as an isolevel of progress variable $c = c^* = 0.85$ (corresponding to the maximum heat release rate loci);

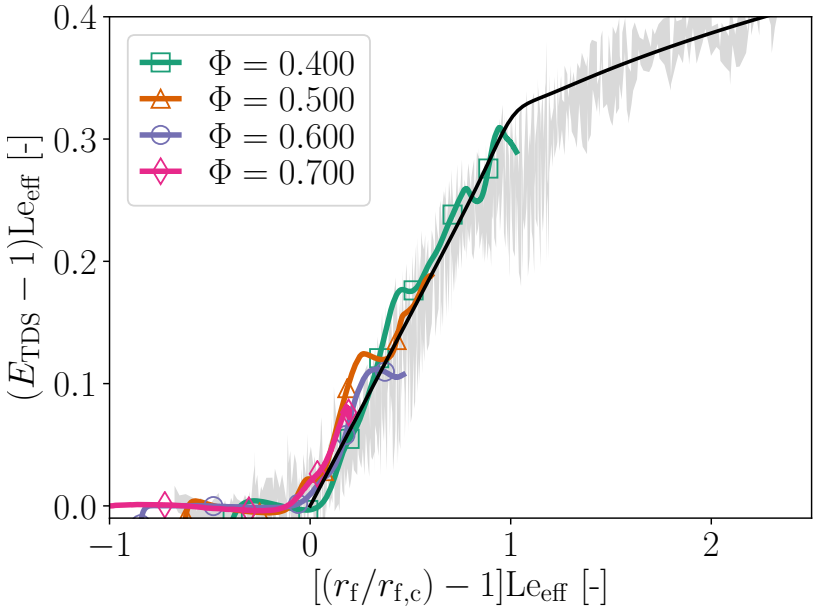

Figure 8: Evolution of the TD efficiency function E_{TDS} with flame radius, measured on 2D FRS. Abscissa and ordinate are scaled to match the self-similarity space identified in [54]. Light gray: experimental envelope covering mixtures at $\Phi \in [0.45, 0.95]$ from 3D experiments of Goulier [54]. Black line: extended correlation used in this study (Equation (17)).

3. For each flame point P along this surface, the streamline (Γ) following the gradient of progress variable $\nabla \mathbf{c}$ is computed;
4. The consumption speed of point P is defined as $S_{\mathrm{c}}^{\mathrm{P}} = -(\rho_{\mathrm{u}}(Y_{\mathrm{F,u}} - Y_{\mathrm{F,b}}))^{-1} \int_{(\Gamma)} \dot{\omega}_{\mathrm{F}} \mathrm{d}x$ where $\dot{\omega}_{\mathrm{F}}$ is the fuel consumption rate. Note that the integration is done over the streamline (Γ) instead of the straight line used in Equation (4) (which is valid for 1D flames).

Fig. 9 represents the consumption speed along the flame front normalized by the laminar flame speed $S_{\mathrm{c}}/S_{\mathrm{L}}^0$ for several instants for the FRS and the TD-S-TF simulation. The local curvature (hence stretch) generated by TD cells in the FRS directly affects the consumption speed: positive (resp. negative) curvature is linked to flame acceleration $S_{\mathrm{c}}/S_{\mathrm{L}}^0 > 1$ (resp. flame deceleration $S_{\mathrm{c}}/S_{\mathrm{L}}^0 < 1$). Negatively curved zones (commonly called cusps) represent a minor fraction of the flame surface area. The colormap has been clipped to values of $S_{\mathrm{c}}/S_{\mathrm{L}}^0 > 1$ to emphasize the fact that TD cells induce an overall acceleration of the flame. While this behavior is lost in the TD-S-TF sim-

ulation due to mesh coarsening and flame thickening, the local flame speed for $r_\mathrm{f} \geq r_\mathrm{f,c}$ is enhanced by the efficiency E_TDS.

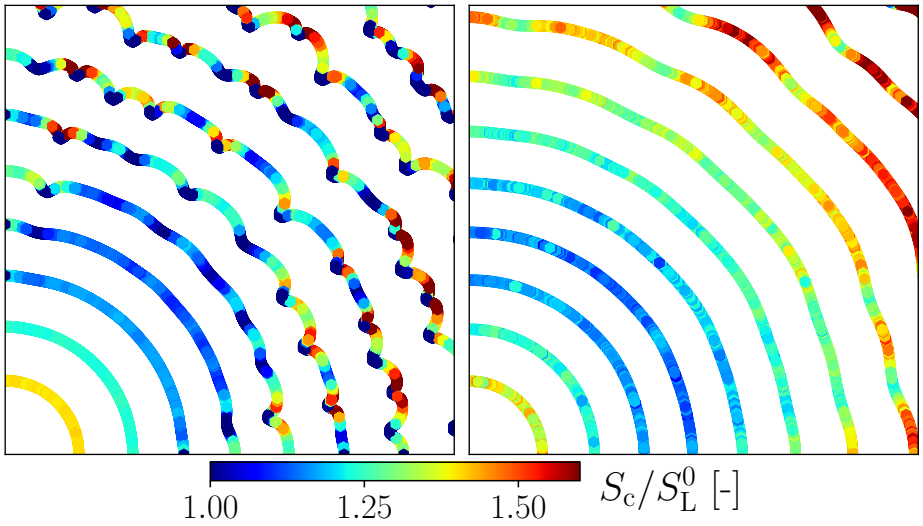

Figure 9: Superimposition of normalized local flame speed for several flame snapshots at $\Phi = 0.4$. Left: FRS. Right: TD-S-TF simulation at $F = 2$.

Although the distributions of local flame speed differ between the FRS and the TD-S-TF simulation, their integrated effect results in a similar acceleration. For example, the probability density functions (PDF) are compared in Figs. 10. During the first stage of propagation (top plot), the flame speed distribution of the FRS is concentrated around a given value because the flame is still globally smooth. This is also the case of the TD-S-TF simulation thanks to the S-TF accurate prediction of the global stretch effect. On the contrary, it is not correctly captured by the Fractal-TF and Planar-TF models as discussed in the previous sections. Later during the TD-dominated phase (bottom plot), the instabilities in the FRS generate a great variety of local flame speed correlated with local stretch. In comparison, the TD-S-TF flame speed distribution is much narrower but its mean correctly match that of the FRS ($\overline{S_\mathrm{c}}/S_\mathrm{L}^0 \approx 1.32$). Note that the Fractal-TF model has caught up with the FRS too while the Planar-TF PDF is still overpredicting the global flame speed.

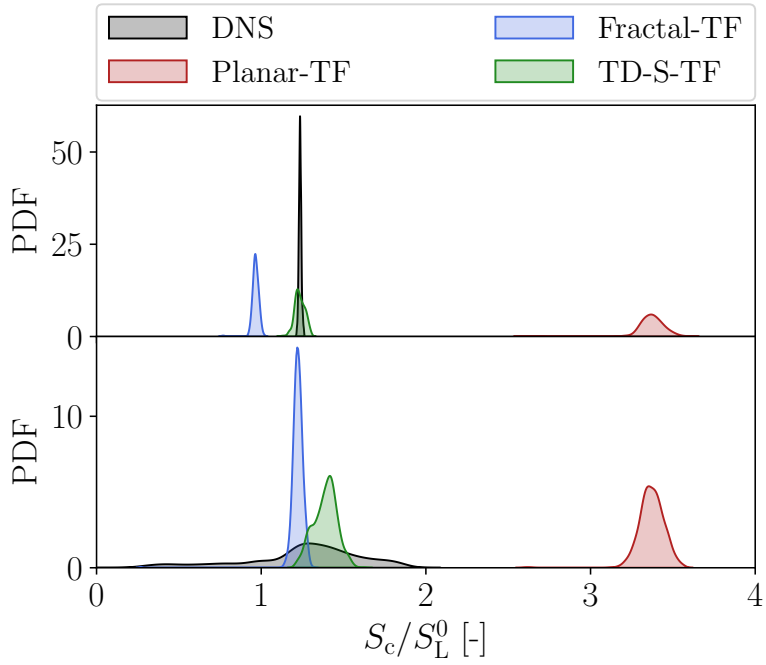

Figure 10: Probability density function of local flame speed for two flame snapshots. Top: in the globally-stretched phase ($r_f \approx 0.02\text{m} < r_{f,c}$). Bottom: in the TD-dominated phase ($r_f \approx 0.06\text{m} > r_{f,c}$). $\Phi = 0.4$. TF at $F = 2$.

4.3. TD-S-TF model at higher thickening levels

This section is dedicated to the application of the TD-S-TF modeling strategy at higher thickening levels, associated with coarser meshes. The big issue identified in Section 2.2 is the mesh dependency introduced by the classical TF approach. Fig. 11 clearly shows that the TD-S-TF model solves this problem, thereby strengthening its reliability for the TF simulation of lean H_2-air propagating flames. At high F, even if the initial radius is close to the TD onset radius, the S-TF is able to rapidly catch up with the FRS results. Note that the spurious effect identified in Section 3.2 (where the (TD-)S-TF flame is still unstable) disappears at higher thickening values.

4.4. TD-S-TF model at other operating conditions

To further demonstrate the genericity of the TD-S-TF correction model, this section evaluates its application for other operating conditions. Fig-

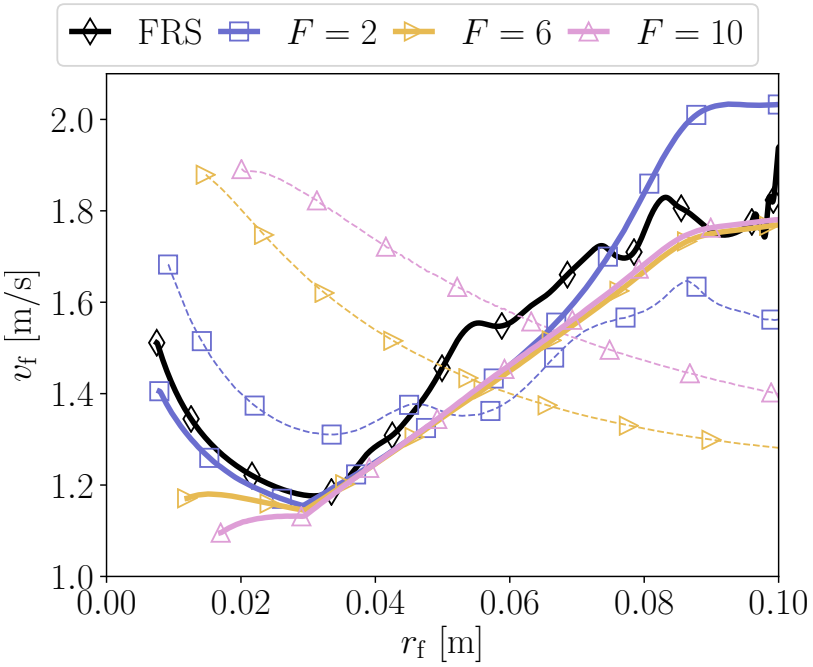

Figure 11: Flame speed as a function of flame radius for the FRS and TD-S-TF at various thickening levels. $\Phi = 0.4$. TF curves in dashed lines.

ure 12 shows the flame speed evolution for atmospheric H_2-air mixtures at equivalence ratios $\Phi \in [0.5, 0.7]$. Such mixtures albeit closer to stoichiometry than the previously-analyzed $\Phi = 0.4$ case, are still known to be strongly stretch-sensitive and TD-unstable. All TD-S-TF simulations are validated against their corresponding FRS and show a fairly good reproduction of the flame dynamics.

5. Conclusions and discussion

This investigation highlights the inability of the classical Thickened Flame model to accurately predict the propagation of lean H_2-air flames: (1) flame thickening amplifies the stretch response of flames, resulting in a considerable overprediction of the flame speed; (2) the use of a LES-type mesh depletes the contribution of TD instabilities. It also shows that the classical TF approach suffers from a mesh dependency problem that hinders its application for propagating lean H_2-air flames.

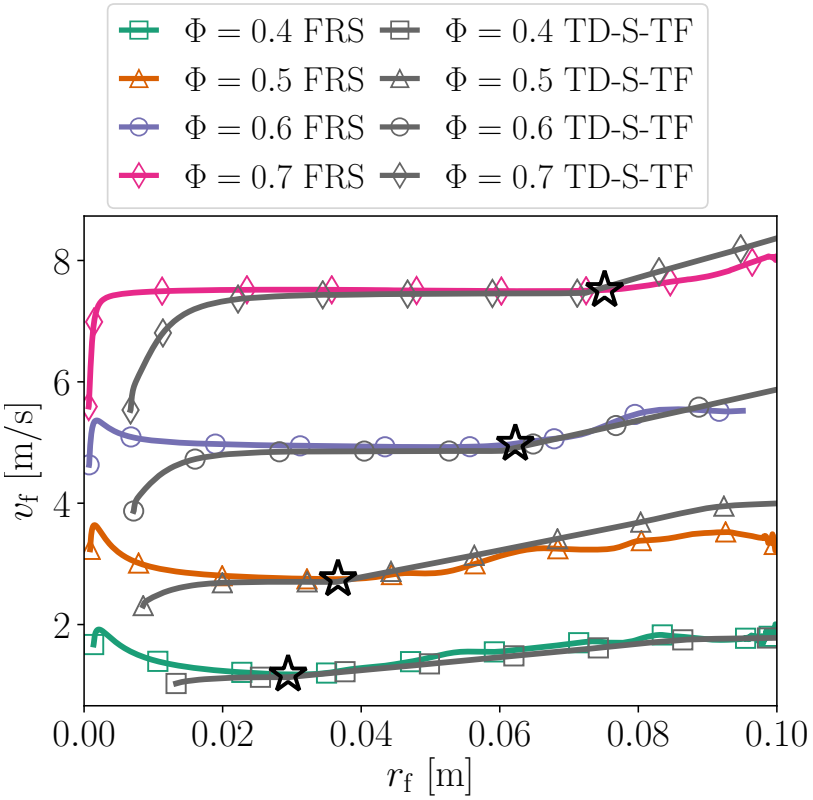

Figure 12: Flame speed as a function of flame radius for the FRS and TD-S-TF ($F = 10$) simulations at various equivalence ratios. Black star: onset of TD instabilities in the FRS.

Several strategies are assessed to correct the erroneous behaviors of the TF approach. It is concluded that the Thermo-Diffusive-Stretched-Thickened Flame (TD-S-TF) model is able to reproduce all phases of the propagation. It introduces a new paradigm by treating separately the problems of stretch response amplification and intrinsic flame front instabilities. The former is corrected thanks to the Stretched-Thickened Flame (S-TF) model which is validated in the present paper for H_2 flames. The latter is modeled through a thermo-diffusive efficiency applied to the laminar flame speed that contains both subgrid wrinkling and subgrid stretch due to the cellular patterns. The proposed approach is validated for propagating lean H_2-air flames with equivalence ratios ranging from 0.4 to 0.7. The TD-S-TF model outperforms the other strategies by retrieving the right flame propa-

gation both at the early stages and during the fully-developed-instabilities phase. The practical implementation of the TD-S-TF model is made through a modification of diffusive and reactive terms in the conservation laws, in a manner similar to the classical TF model which makes it easily reproducible on other CFD solvers. The model does not show any significant additional cost in comparison with the classical TF model. In practice, it constitutes an extension of the TF model, requiring: (1) an optimization step which is done in pre-processing to parameterize the S-TF component, prior to the LES; (2) a few additional scalar operations and only one MPI global reduction operation during its application in the LES (negligible cost in comparison with the other operations used for the classical TF model).

The validation of the TD-S-TF model presented herein constitutes a first step for the simulation of lean H_2-air explosions. The model has been developed in a 2D frame to allow the computation of the Flame-Resolved Simulation. Though, the fact that the expression of the thermo-diffusive efficiency function is based on experimental measurements from Goulier [54] gives confidence on the TD-S-TF model's representativeness of real flames. Even if it has been tested on atmospheric lean hydrogen-air mixtures, it is reasonable to expect that the strategy is readily applicable to spherical flame propagation in other mixtures and operating conditions (in particular higher pressures). Indeed, the two components of the TD-S-TF model have been formulated in a robust manner to ensure that: (1) the thermo-diffusive efficiency is expressed in a generic form which only requires the effective Lewis number of the mixture (theoretically computed) and the critical radius for the onset of TD instabilities (obtained from experimental correlations/measurements); (2) the thermo-diffusive efficiency function naturally degenerates to unity for stable flames allowing to correctly capture the impact of stretch on stable flames (i.e. TD-S-TF degenerates to S-TF which was already validated for stable stretched propane/air flames in [17]). For example, under a strong dilution, the mixture progressively becomes thermo-diffusively stable. This is traduced by an increased critical radius (thereby delaying the activation of the TD efficiency function). On the contrary, increasing the pressure reduces the critical radius (the flame becomes more unstable), both bringing forward the activation of the efficiency and strengthening its values.

While it is not directly applicable for complex cases, extensions can be explored. Many explosion scenarios begin with a fully laminar flame kernel that expands into a confined and obstructed area. As the flame loses its spherical shape, it can be expected that the subgrid contribution of TD cells

will saturate. This has been shown to hold for the first stages of flame acceleration in a tube (laminar phase) [13]. Therefore, as long as the flow remains laminar, a saturation of the TD subgrid component may enable the extension of the TD-S-TF model to flame acceleration in confined spaces. The case of flame propagation in turbulent flows is more complex. First steps for the modelling of turbulent lean hydrogen-air flames have been made [58], but their suitability for turbulent flame acceleration remains to be shown. Finally, the question of the transition between the model presented in this paper and turbulent phase models needs more in-depth analyses.

Funding

This work received financial support from TotalEnergies, GRTgaz, and Air Liquide as part of the LEFEX project, and from GENCI-IDRIS under the allocation 2023-A0132B10157.

Acknowledgments

The authors thank TotalEnergies, GRTgaz and Air Liquide for their financial support in the framework of the LEFEX project. This work was also granted access to the HPC resources of GENCI-IDRIS under the allocation 2023-A0132B10157.

References

[1] G. Ciccarelli, S. Dorofeev, Flame acceleration and transition to detonation in ducts, Progress in Energy and Combustion Science 34 (4) (2008) 499–550. doi:10.1016/j.pecs.2007.11.002.

[2] F. Williams, Combustion theory, Benjamin Cummings, Menlo Park, 1985.

[3] A. R. Kerstein, W. T. Ashurst, F. A. Williams, Field equation for interface propagation in an unsteady homogeous flow field, Physical Review A 37 (7) (1988).

[4] S. B. Pope, The evolution of surfaces in turbulence, International Journal of Engineering Science 26 (5) (1988) 445–469. doi:10.1016/0020-7225(88)90004-3.

[5] A. Trouvé, The evolution equation for the flame surface density in turbulent premixed combustion, Journal of Fluid Mechanics 278 (1994) 1–31. doi:10.1017/S0022112094003599.

[6] L. Vervisch, E. Bidaux, K. N. Bray, W. Kollmann, Surface density function in premixed turbulent combustion modeling, similarities between probability density function and flame surface approaches, Physics of Fluids 7 (10) (1995) 2496–2503. doi:10.1063/1.868693.

[7] S. B. Pope, PDF methods for turbulent reactive flows, Progress in Energy and Combustion Science 11 (2) (1985) 119–192. doi:10.1016/0360-1285(85)90002-4.

[8] D. C. Haworth, Progress in probability density function methods for turbulent reacting flows, Progress in Energy and Combustion Science 36 (2) (2010) 168–259. doi:10.1016/j.pecs.2009.09.003.
URL http://dx.doi.org/10.1016/j.pecs.2009.09.003

[9] P. O'Rourke, F. Bracco, Two Scaling Transformations for the Numerical Computation of Multidimensional Unsteady Laminar Flames, J. Comp. Phys. 203 (1979) 185–203.

[10] B. Rochette, E. Riber, B. Cuenot, O. Vermorel, A generic and self-adapting method for flame detection and thickening in the thickened flame model, Combust. Flame 212 (2020) 448–458. doi:10.1016/j.combustflame.2019.11.015.
URL https://doi.org/10.1016/j.combustflame.2019.11.015

[11] H. Terashima, Y. Hanada, S. Kawai, A localized thickened flame model for simulations of flame propagation and autoignition under elevated pressure conditions, Proceedings of the Combustion Institute 38 (2) (2021) 2119–2126. doi:10.1016/j.proci.2020.06.063.
URL https://doi.org/10.1016/j.proci.2020.06.063

[12] E. Sandoval Garzon, C. Mehl, O. Colin, Modeling of spark ignition in gaseous mixtures using adaptive mesh refinement coupled to the thickened flame model, Combust. Flame 248 (2023) 112507. doi:10.1016/j.combustflame.2022.112507.
URL https://doi.org/10.1016/j.combustflame.2022.112507

[13] J.-J. Hok, O. Dounia, O. Vermorel, T. Jaravel, Effect of Flame Front Thermo-Diffusive Instability on Flame Acceleration in a Tube, 28th International Colloquium on the Dynamics of Explosions and Reactive Systems, 2022.

[14] P. Quillatre, Simulation aux grandes echelles d'explosions en domaine semi-confine, Ph.D. thesis, Université de Toulouse, Toulouse, France (2014).

[15] S. Popp, G. Kuenne, J. Janicka, C. Hasse, An extended artificial thickening approach for strained premixed flames, Combust. Flame 206 (2019) 252–265. doi:10.1016/j.combustflame.2019.04.047.

[16] A. L. Comer, T. P. Gallagher, K. Duraisamy, B. A. Rankin, A modified thickened flame model for simulating extinction, Combust. Theory Model. 26 (7) (2022) 1262–1292. doi:10.1080/13647830.2022.2141138.

[17] N. Detomaso, J.-J. Hok, O. Dounia, D. Laera, T. Poinsot, A generalization of the Thickened Flame model for stretched flames, Combust. Flame 258 (2023) 113080.

[18] P. Pelce, P. Clavin, Influence of hydrodynamics and diffusion upon the stability limits of laminar premixed flames, J. Fluid Mech. (1982) 425–443doi:10.1016/b978-0-08-092523-3.50046-0.

[19] J. K. Bechtold, M. Matalon, Hydrodynamic and diffusion effects on the stability of spherically expanding flames, Combust. Flame 67 (1) (1987) 77–90. doi:10.1016/0010-2180(87)90015-0.

[20] G. I. Sivashinsky, Diffusional-Thermal Theory of Cellular Flames, Combust. Sci. Tech. 15 (3-4) (1977) 137–145. doi:10.1080/00102207708946779.

[21] Z. Y. Sun, F. S. Liu, X. C. Bao, X. H. Liu, Research on cellular instabilities in outwardly propagating spherical hydrogen-air flames, Int. J. Hydrogen Energy 37 (9) (2012) 7889–7899. doi:10.1016/j.ijhydene.2012.02.011.

[22] F. Wu, G. Jomaas, C. K. Law, An experimental investigation on self-acceleration of cellular spherical flames, Proc. Combust. Inst. 34 (1) (2013) 937–945. doi:10.1016/j.proci.2012.05.068.

[23] T. Katsumi, T. Aida, K. Aiba, S. Kadowaki, Outward propagation velocity and acceleration characteristics in hydrogen-air deflagration, Int. J. Hydrogen Energy 42 (11) (2017) 7360–7365. doi:10.1016/j.ijhydene.2016.06.165.
URL http://dx.doi.org/10.1016/j.ijhydene.2016.06.165

[24] C. R. Bauwens, J. M. Bergthorson, S. B. Dorofeev, Experimental investigation of spherical-flame acceleration in lean hydrogen-air mixtures, Int. J. Hydrogen Energy 42 (11) (2017) 7691–7697. doi:10.1016/j.ijhydene.2016.05.028.

[25] W. Kim, Y. Sato, T. Johzaki, T. Endo, Experimental study on the onset of flame acceleration due to cellular instabilities, J. Loss Prev. 60 (March) (2019) 264–268. doi:10.1016/j.jlp.2019.05.008.

[26] J. Grune, K. Sempert, M. Kuznetsov, T. Jordan, Experimental investigation of unconfined spherical and cylindrical flame propagation in hydrogen-air mixtures, Int. J. Hydrogen Energy 46 (23) (2021) 12487–12496. doi:10.1016/j.ijhydene.2020.09.062.
URL https://doi.org/10.1016/j.ijhydene.2020.09.062

[27] S. Huang, R. Huang, P. Zhou, Y. Zhang, Z. Yin, Z. Wang, Role of cellular wavelengths in self-acceleration of lean hydrogen-air expanding flames under turbulent conditions, Int. J. Hydrogen Energy 46 (17) (2021) 10494–10505. doi:10.1016/j.ijhydene.2020.12.124.

[28] N. Dentsel, V. Golub, A. Elyanov, V. Volodin, Experimental investigation of cell generation in an expanding spherical hydrogen-air flame front, Int. J. Hydrogen Energy 48 (76) (2023) 29461–29470. doi:10.1016/j.ijhydene.2023.04.105.
URL https://doi.org/10.1016/j.ijhydene.2023.04.105

[29] K. K. Ranga Dinesh, H. Shalaby, K. H. Luo, J. A. van Oijen, D. Thévenin, High hydrogen content syngas fuel burning in lean premixed spherical flames at elevated pressures: Effects of preferential diffusion, Int. J. Hydrogen Energy 41 (40) (2016) 18231–18249. doi:10.1016/j.ijhydene.2016.07.086.

[30] J. F. Yu, R. Yu, X. S. Bai, M. B. Sun, J. G. Tan, Nonlinear evolution of 2D cellular lean hydrogen/air premixed flames with varying initial

perturbations in the elevated pressure environment, Int. J. Hydrogen Energy 42 (6) (2017) 3790–3803. doi:10.1016/j.ijhydene.2016.07.059.

[31] P. E. Lapenna, R. Lamioni, F. Creta, Subgrid modeling of intrinsic instabilities in premixed flame propagation, Proc. Combust. Inst. 38 (2) (2021) 2001–2011. doi:10.1016/j.proci.2020.06.192.

[32] L. Berger, A. Attili, H. Pitsch, Intrinsic instabilities in premixed hydrogen flames: parametric variation of pressure, equivalence ratio, and temperature. Part 2 – Non-linear regime and flame speed enhancement, Combust. Flame 240 (2022) 111936. doi:10.1016/j.combustflame.2021.111936.

[33] T. L. Howarth, A. J. Aspden, An empirical characteristic scaling model for freely-propagating lean premixed hydrogen flames, Combust. Flame 237 (2022) 111805. doi:10.1016/j.combustflame.2021.111805.

[34] B. A. Aniello, D. Laera, L. Berger, A. Attili, Introducing thermodiffusive effects in LES of turbulent combustion for lean hydrogen - air flames, Center for Turbulence Research, Proceedings of the Summer Program (2022) 267–277.

[35] T. Schönfeld, M. Rudgyard, Steady and unsteady flow simulations using the hybrid flow solver AVBP, AIAA Journal 37 (11) (1999) 1378–1385. doi:10.2514/2.636.

[36] L. Y. Gicquel, G. Staffelbach, T. Poinsot, Large Eddy Simulations of gaseous flames in gas turbine combustion chambers, Progress in Energy and Combustion Science 38 (6) (2012) 782–817. doi:10.1016/j.pecs.2012.04.004.
URL http://dx.doi.org/10.1016/j.pecs.2012.04.004

[37] O. Vermorel, P. Quillatre, T. Poinsot, LES of explosions in venting chamber: A test case for premixed turbulent combustion models, Combust. Flame 183 (2017) 207–223. doi:10.1016/j.combustflame.2017.05.014.

[38] O. Dounia, Etudes des phénomènes d'accélération de flammes, transition à la détonation et d'inhibition de flammes, Ph.D. thesis (2013).

[39] B. Vanbersel, F. A. Meziat Ramirez, P. Mohanamuraly, G. Staffelbach, T. Jaravel, Q. Douasbin, O. Dounia, O. Vermorel, A systematic Adaptive Mesh Refinement method for Large Eddy Simulation of turbulent flame propagation, Flow, Turbulence and Combustion (2023) 0–48.

[40] A. Misdariis, O. Vermorel, T. Poinsot, A methodology based on reduced schemes to compute autoignition and propagation in internal combustion engines, Proceedings of the Combustion Institute 35 (3) (2015) 3001–3008. doi:10.1016/j.proci.2014.06.053.
URL http://dx.doi.org/10.1016/j.proci.2014.06.053

[41] A. Misdariis, O. Vermorel, T. Poinsot, LES of knocking in engines using dual heat transfer and two-step reduced schemes, Combust. Flame 162 (11) (2015) 4304–4312. doi:10.1016/j.combustflame.2015.07.023.
URL http://dx.doi.org/10.1016/j.combustflame.2015.07.023

[42] O. Dounia, O. Vermorel, A. Misdariis, T. Poinsot, Influence of kinetics on DDT simulations, Combust. Flame 200 (2019) 1–14. doi:10.1016/j.combustflame.2018.11.009.
URL https://doi.org/10.1016/j.combustflame.2018.11.009

[43] T. Jaravel, O. Dounia, Q. Malé, O. Vermorel, Deflagration to detonation transition in fast flames and tracking with chemical explosive mode analysis, Proceedings of the Combustion Institute 38 (3) (2021) 3529–3536. doi:10.1016/j.proci.2020.09.020.
URL https://doi.org/10.1016/j.proci.2020.09.020

[44] T. Poinsot, D. Veynante, Theoretical and Numerical Combustion, 3rd Edition, 2012.

[45] D. G. Goodwin, R. L. Speth, H. K. Moffat, Cantera: An Object-oriented Software Toolkit for Chemical Kinetics, Thermodynamics, and Transport Processes (2018). doi:10.5281/zenodo.1174508.

[46] M. A. Liberman, M. F. Ivanov, O. E. Peil, D. M. Valiev, L. E. Eriksson, Self-acceleration and fractal structure of outward freely propagating flames, Physics of Fluids 16 (7) (2004) 2476–2482. doi:10.1063/1.1729852.

[47] C. Altantzis, C. E. Frouzakis, A. G. Tomboulides, K. Boulouchos, Direct numerical simulation of circular expanding premixed flames

in a lean quiescent hydrogen-air mixture: Phenomenology and detailed flame front analysis, Combust. Flame 162 (2) (2015) 331–344. doi:10.1016/j.combustflame.2014.08.005.

[48] P. Saxena, F. A. Williams, Testing a small detailed chemical-kinetic mechanism for the combustion of hydrogen and carbon monoxide, Combust. Flame 145 (1-2) (2006) 316–323. doi:10.1016/j.combustflame.2005.10.004.

[49] A. L. Sánchez, F. A. Williams, Recent advances in understanding of flammability characteristics of hydrogen, Progress in Energy and Combustion Science 41 (1) (2014) 1–55. doi:10.1016/j.pecs.2013.10.002.
URL http://dx.doi.org/10.1016/j.pecs.2013.10.002

[50] Y. A. Gostintsev, A. G. Istratov, Y. V. Shulenin, Self-similar propagation of a free turbulent flame in mixed gas mixtures, Combust. Explos. Shock Waves 24 (5) (1988) 563–569. doi:10.1007/BF00755496.

[51] O. C. Kwon, G. Rozenchan, C. K. Law, Cellular instabilities and self-acceleration of outwardly propagating spherical flames, Proc. Combust. Inst. 29 (2) (2002) 1775–1783. doi:10.1016/S1540-7489(02)80215-2.

[52] E. Hu, Z. Huang, J. He, J. Zheng, H. Miao, Measurements of laminar burning velocities and onset of cellular instabilities of methane-hydrogen-air flames at elevated pressures and temperatures, Int. J. Hydrogen Energy 34 (13) (2009) 5574–5584. doi:10.1016/j.ijhydene.2009.04.058.
URL http://dx.doi.org/10.1016/j.ijhydene.2009.04.058

[53] F. Liu, X. Bao, J. Gu, R. Chen, Onset of cellular instabilities in spherically propagating hydrogen-air premixed laminar flames, Int. J. Hydrogen Energy 37 (15) (2012) 11458–11465. doi:10.1016/j.ijhydene.2012.05.013.

[54] J. Goulier, Comportements aux limites de flammes de prémélange hydrogène/air. Étude de la transition flamme laminaire-flamme turbulente, Ph.D. thesis, Université d'Orléans, Orléans, France (2015).

[55] W. Kim, T. Imamura, T. Mogi, R. Dobashi, Experimental investigation on the onset of cellular instabilities and acceleration of expanding

spherical flames, Int. J. Hydrogen Energy 42 (21) (2017) 14821–14828. doi:10.1016/j.ijhydene.2017.04.068.
URL http://dx.doi.org/10.1016/j.ijhydene.2017.04.068

[56] Y. Li, M. Bi, S. Zhang, H. Jiang, B. Gan, W. Gao, Dynamic couplings of hydrogen/air flame morphology and explosion pressure evolution in the spherical chamber, Int. J. Hydrogen Energy 43 (4) (2018) 2503–2513. doi:10.1016/j.ijhydene.2017.12.044.
URL https://doi.org/10.1016/j.ijhydene.2017.12.044

[57] X. Lu, E. Hu, S. Kokjohn, Q. Gao, G. Yin, K. Zeng, Z. Huang, Experimental and kinetic study of laminar flame characteristics of H2/O2/diluent flame under elevated pressure, Int. J. Hydrogen Energy 45 (56) (2020) 32508–32520. doi:10.1016/j.ijhydene.2020.08.142.
URL https://doi.org/10.1016/j.ijhydene.2020.08.142

[58] L. Berger, A. Attili, H. Pitsch, Synergistic interactions of thermodiffusive instabilities and turbulence in lean hydrogen flames, Combust. Flame 244 (2022) 112254. doi:10.1016/j.combustflame.2022.112254.
URL https://doi.org/10.1016/j.combustflame.2022.112254

A modeling strategy for the Thickened Flame simulation of propagating lean hydrogen-air flames

Jean-Jacques Hok*[1], Omar Dounia[1], Nicola Detomaso[1], Thomas Jaravel[1],
Quentin Douasbin[1], Olivier Vermorel[1]
[1]CERFACS, 42 avenue Gaspard Coriolis, 31057 Toulouse, France

1. Effect of domain geometry on flame propagation

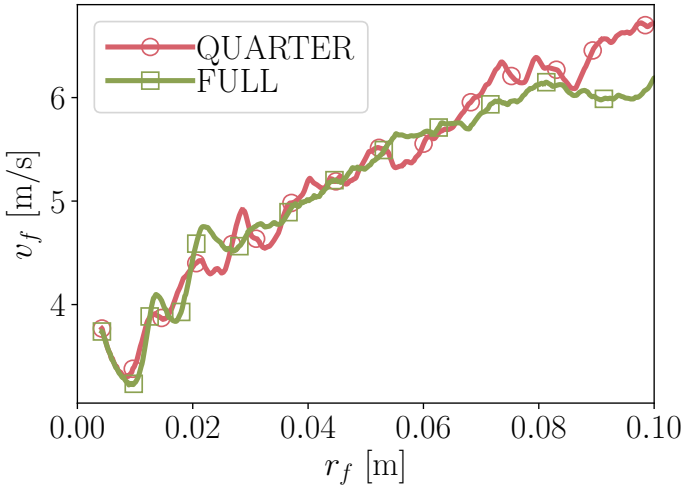

Fig. S1. Flame speed as a function of flame position for DNS at $\Phi = 0.5$ in quarter and full disk domains

7.2 Addendum

This section constitutes an addendum to the paper presented above. It provides details on specific features of the set-up and model that are not thoroughly discussed therein.

7.2.1 Strained flame initialisation procedure

The paper presented above has introduced a new initialisation procedure for propagating flame simulations. In the literature, most explosion simulations use one of the two following methods:

- an energy deposition in a small region of the domain [245, 295]. This method has the advantage of mimicking the mid-term effect of the laser or spark ignitions used in experiments (standard CFD codes cannot simulate the early plasma phase of a real ignition [303–307]). However, this model requires several parameters that can be hard to choose. In particular, the deposited energy does not necessarily come from experimental values. It must instead be set above a minimal value to ensure a successful ignition (the fresh mixture must be sufficiently heated by the deposition to trigger the reaction) and not too high to limit the extent of the transient phase;

- a hot gases kernel deposition [51, 53]. This second procedure does not suffer the need to choose an arbitrary amount of energy because it directly applies a spherical kernel of combustion products to initiate the reactions. Usually, the profiles (density, species mass fractions, energy/temperature) are taken from one-dimensional unstretched flame[1] computations (e.g. with CANTERA). As explained in Section 5.1.4, an analytical profile (depending on S_L^0) is imposed for the velocity field of the spherical flame (Equation (5.2) in a 2D set-up).

While the kernel deposition method is efficient to initialise simulations, the use of 1D unstretched flame profiles is problematic in the context of this thesis. As explained in Section 2.2.4, lean hydrogen-air flames are sensitive to stretch so that their structure departs considerably from their planar counterpart, especially for small initial radii (high stretch). In large-scale explosion simulations, the initial kernel radius being relatively big, the use of planar flame profiles is sufficient. However, the present analysis requires to start with small spherical flames, and the high curvatures at the early stages of propagation have a non-negligible effect on the flame dynamics. In an attempt to reduce as much as possible the initial transient duration, it is proposed to replace the unstretched planar flame profiles by strained flame profiles. To do so:

[1] The 1D unstretched flame is often simply called "planar flame", as introduced in Section 2.1.1.1.

1. the stretch rate of the initial spherical kernel is estimated by [62, 308]:

$$\mathbb{K}_0 \approx \begin{cases} \dfrac{\sigma S_\mathrm{L}^0}{r_{\mathrm{f},0}} \left[1 + \dfrac{F\delta_\mathrm{L}^0}{2r_{\mathrm{f},0}}\right]^{-1} & \text{for 2D cases} \\ \dfrac{2\sigma S_\mathrm{L}^0}{r_{\mathrm{f},0}} \left[1 + \dfrac{F\delta_\mathrm{L}^0}{r_{\mathrm{f},0}}\right]^{-1} & \text{for 3D cases} \end{cases} \tag{7.1}$$

2. a counterflow premixed flame is computed under this strain $\mathbb{K}_0$ (and the desired thickening F);

3. its profiles are interpolated on a spherical kernel for density, species mass fractions and enthalpy;

4. its consumption speed is computed and used to impose the analytical velocity profile (it replaces S_L^0 in Equation (5.2)).

The use of a 1D strained flame to initialise a 2D/3D curved flame may seem inappropriate. Nevertheless, it has the advantage of imposing profiles (species mass fractions, density, etc.) which account for stretch effects. In particular, the temperature profile is locally superadiabatic, representative of lean H_2 spherical flames.

To evaluate the effect of the new initialisation procedure, three DNS are carried out at $\Phi = 0.400$:

- a first case with initial radius $r_{\mathrm{f},0} = 2\delta_\mathrm{L}^0$ ($\mathrm{Pe}_{\mathrm{f},0} = 2$) using the classical planar profiles method. This flame starts with a smaller radius than the other two simulations described below. It is expected that the transient period is finished when the growing kernel reaches the same size as the other cases: the propagation of this flame serves as a reference;
- a second case with a greater initial radius $r_{\mathrm{f},0} = 5\delta_\mathrm{L}^0$ ($\mathrm{Pe}_{\mathrm{f},0} = 5$) using the classical planar profiles method;
- and a third case with the same initial radius $r_{\mathrm{f},0} = 5\delta_\mathrm{L}^0$ ($\mathrm{Pe}_{\mathrm{f},0} = 5$) but with strained profiles under the appropriate strain rate.

The results in terms of flame velocity versus flame mean radius and global stretch rate are presented in Figures 7.1 and 7.2. The overall outcome is that the simulation using an initialisation with strained flame profiles (blue curve with hexagons) converges faster towards the reference flame propagation (plain black curve): the transient period associated to ignition is cut shorter. The flame which is initialised with the new method burns more intensely at the beginning of the simulation thanks to the superadiabaticity due to strain (cf. comments below). Note that the subsequent differences between the three curves ($r_\mathrm{f} \gtrsim 0.03$ m) are due to the growth of TD instabilities which is chaotic by nature.

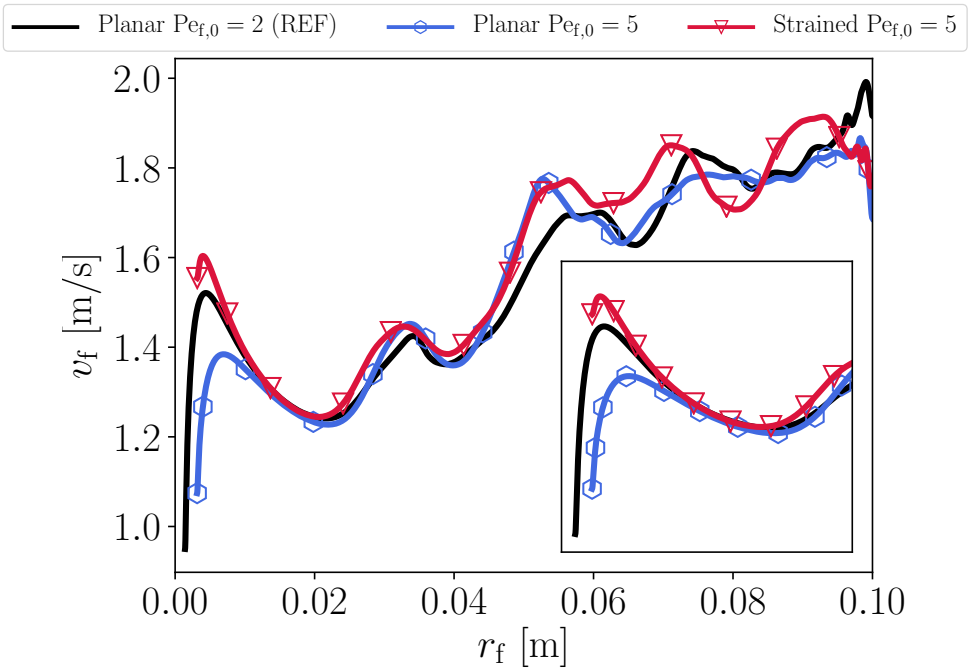

Figure 7.1: Flame speed as a function of flame mean radius for the three simulations using different initial kernels. Inset: zoom on the initial phase.

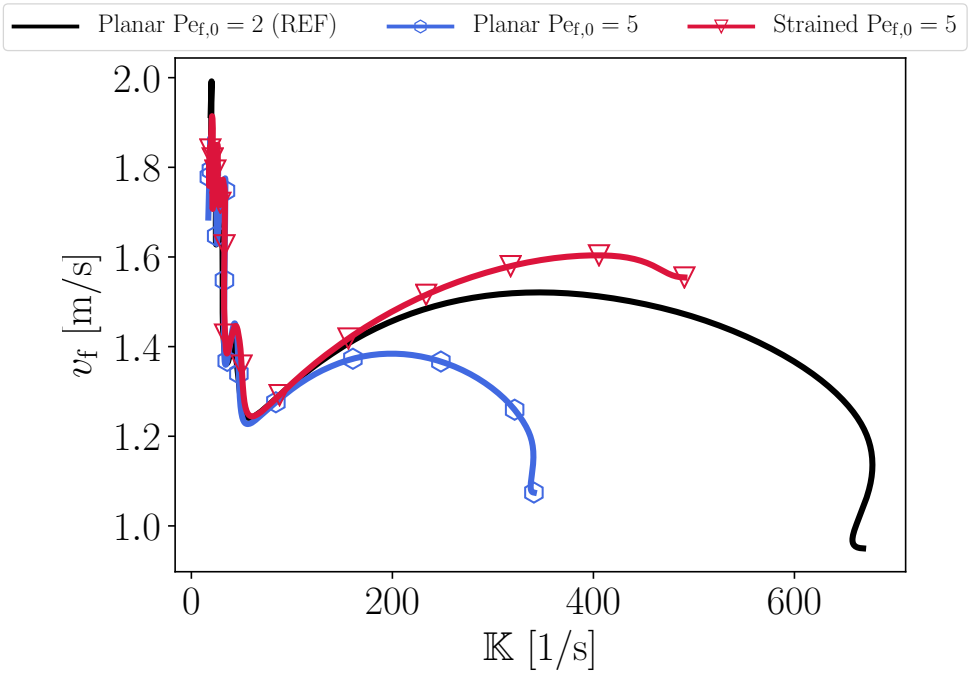

Figure 7.2: Flame speed as a function of global flame stretch for the three simulations using different initial kernels.

For a further justification of the strained flame initialisation procedure, the profiles of temperature and velocity magnitude of the three simulations are compared at $r_f = 5\delta_L^0$ in Figure 7.3. As explained above, at this radius, the reference simulation (initialised with $r_{f,0} = 2\delta_L^0$) has passed a transient phase (the duration of which is measured at

$\Delta t_{\text{transient}} \approx 0.55\delta_{\text{L}}^0/S_{\text{L}}^0$) and can be considered to represent "physical" profiles. Looking at the temperature profiles (Figure 7.3a), one can see that:

- the reference flame (black curve) shows an overall superadiabatic profile. This is naturally linked with positive stretch effects on lean H_2-air flames (cf. Section 2.2.4.3). The fact that the whole profile is hotter than the adiabatic temperature is due to history effects. Initially, the flame kernel has been deposited with an adiabatic temperature on the burnt side (see below and Appendix C) at a lower $r_{\text{f},0} = 2\delta_{\text{L}}^0$ radius. After the transient, the flame advances and the numerical profile adapts to the physical stretch effects by becoming superadiabatic just behind the flame front ($r \lesssim r_{\text{f}}$). In the meantime, heat diffusion progressively increases the temperature of the core ($r \ll r_{\text{f}}$);
- in the case $\text{Pe}_{\text{f},0} = 5$ using the planar profile initialisation, the temperature of the hot gases is perfectly adiabatic, leading to the lower flame speed observed above in Figure 7.1;
- when using a strained profile initialisation, the effect of strain on the counterflow flame generates a superadiabaticity which coincides with the reference case close to the flame front ($r \lesssim r_{\text{f}}$). Although the high temperature does not extend properly to the core of the sphere ($r \ll r_{\text{f}}$), this profile is sufficiently hot to increase the flame speed and get closer to the reference (Figure 7.1).

The gap between the three cases is similar on the velocity profiles (Figure 7.3b) but reported on the fresh gases side. The use of the strained consumption speed S_{c} instead of the laminar flame speed S_{L}^0 (red curve) in Equation (5.2) allows an appropriate reproduction of the velocity profile of the reference case which boosts the flame propagation. This behaviour is again not captured by the planar profile initialisation at $\text{Pe}_{\text{f},0} = 5$. All of this thus advocates for the adoption of strained profile initialisation for explosion simulations.

7.2.2 Details on the Stretched-Thickened Flame model for lean hydrogen-air flames

The Stretched-Thickened Flame model developed in Chapter 6 (see Section 6.1) requires several inputs:

- the effective Lewis number of the mixture: it is used to formulate the thickening factor F_{sp} applied to molecular diffusivities (Equation (6.25));
- either the exponent α or the exponent β carrying information on the sensitivity of the laminar flame speed S_{L}^0 to D_{th} and D_k respectively (knowing that $\alpha + \beta \approx 1/2$ from theoretical considerations given in Chapter 6): one of them is needed to compute F_{r} (Equation (6.25)) and ensure the correct extrapolation to S_{L}^0 as the stretch rates tends towards zero;

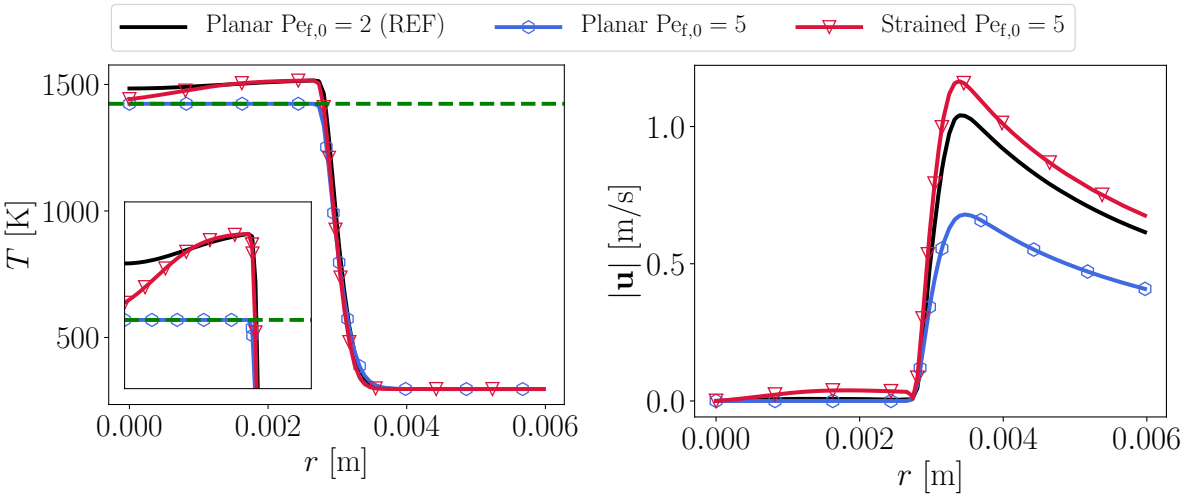

(a) Temperature. Dashed green line: adiabatic flame temperature.

(b) Velocity norm.

Figure 7.3: Flame profiles at $r_\mathrm{f} = 5\delta_\mathrm{L}^0$ ($\mathrm{Pe}_{\mathrm{f},0} = 5$) for the three simulations using different initial kernels. In abscissa, r corresponds to the radial coordinate.

- a target stretch rate $\mathbb{K}_\infty$ for the optimisation process.

The last parameter $\mathbb{K}_\infty$ is a user-input of great importance for the scope of applicability of the S-TF model. It indeed determines the range of stretch rates over which the correction is effective. Knowing that lean H_2-air flames are highly sensitive to stretch, an ill-chosen $\mathbb{K}_\infty$ value can lead to strong overshoots/undershoots of the stretch response (cf. Section 6.4.1). In the case of spherical flames, Equation (7.1) allows a direct evaluation of the global stretch experienced by the flame at a given radius. The stretch begins around $\mathbb{K}_0$ but rapidly declines as the kernel grows:

$$\mathbb{K} \approx \begin{cases} \dfrac{\sigma S_\mathrm{L}^0}{r_\mathrm{f} + (F\delta_\mathrm{L}^0)/2} \approx \dfrac{\sigma S_\mathrm{L}^0}{r_\mathrm{f}} & \text{for 2D cases} \\ \dfrac{2\sigma S_\mathrm{L}^0}{r_\mathrm{f} + F\delta_\mathrm{L}^0} \approx \dfrac{2\sigma S_\mathrm{L}^0}{r_\mathrm{f}} & \text{for 3D cases} \end{cases} \tag{7.2}$$

In both 2D and 3D cases, the global stretch rate quickly becomes of the order of $\mathbb{K} \approx \sigma S_\mathrm{L}^0 \kappa$ (where κ is the flame curvature, see Equation (2.32)). It can also be retrieved from Equation (2.32) based on the fact that the flame speed $\mathrm{d}r_\mathrm{f}/\mathrm{d}t$ can be approximated by σS_L^0 (thereby neglecting stretch effects on it). In every case, it is worth noting that the thickening applied to the flame in the TF formalism does not significantly alter the stretch rate globally experienced by the flame. It only modifies its sensitivity to it. This observation is checked in practice by examining the global stretch rate as a function of the flame radius for the DNS and several LES at $\Phi = 0.400$ in Figure 7.4. It also justifies the validity of using a single value for the S-TF target $\mathbb{K}_\infty$ (independent of the thickening level). To go further, in an attempt to make the TD-S-TF model developed in this chapter as generic as possible, the choice of $\mathbb{K}_\infty$ must be rendered consistent for

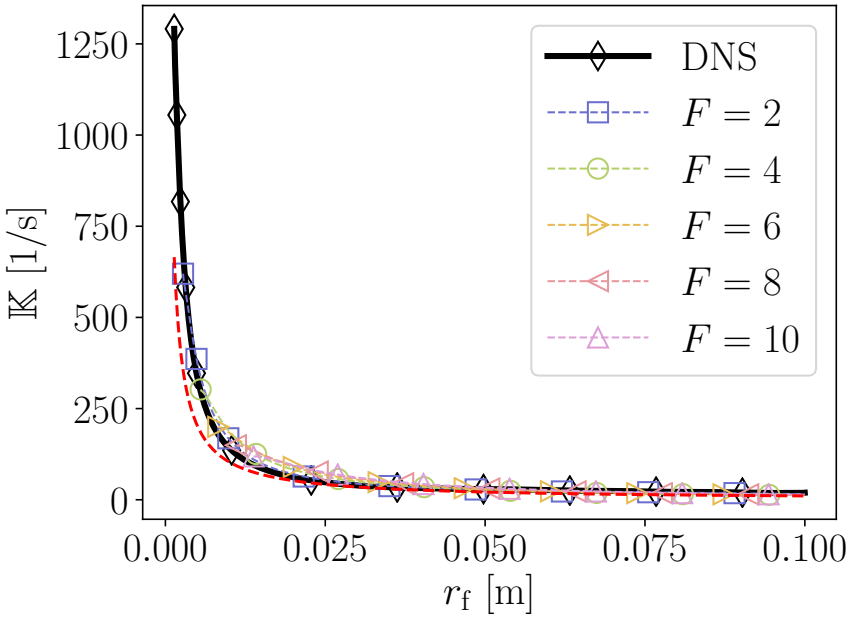

Figure 7.4: Global stretch rate as a function of flame mean radius for several meshes. $\Phi = 0.400$. LES use the classical TF model. Dashed red line: theoretical stretch rate (Equation (7.2)).

several operating conditions. To that end, the non-dimensional Karlovitz number (defined by Equation (2.43)) is considered. A value of $\mathrm{Ka}_\infty = 1/5$ (as analysed in the previous chapter, Section 6.4.1) is found to be best-fit to all the equivalence ratios considered in this thesis. It is indeed shown in Figure 7.5 that after a short transient phase, the stretch experienced by the flame is comprised in the S-TF range of optimisation $[0, \mathrm{Ka}_\infty]$.

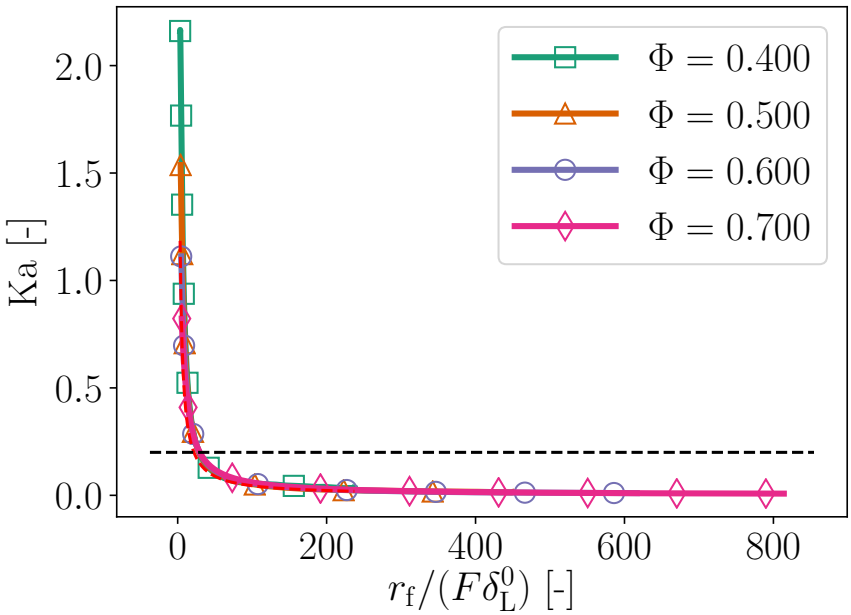

Figure 7.5: Global Karlovitz number as a function of normalised flame mean radius for DNS at several equivalence ratios. Dashed black line: $\mathrm{Ka}_\infty = 1/5$.

7.2.3 Stretch-fitted global chemistry

Also not explicitly mentioned in the article is the use of the novel 1S-LeFit chemistry developed in the previous chapter (Section 6.1). Instead of relying on the 1S-LeRe chemistry (detailed in Section 5.3.1) which has been shown ill-adapted for the LES of lean H_2-air flame propagation, the new 1S-LeFit chemical scheme provides a response to stretch fitted to the detailed mechanism [60]. While it has been built upon optimisation using counterflow premixed flames which are subject to pure tangential strain (see Figure 6.2), the chemistry needs further validation in the present 2D spherical flame set-up, subject to curvature effects. Following a similar rationale as in Section 6.3.3, one can state that: given that the set of species Schmidt numbers (or equivalently Lewis numbers) is uniquely linked to the flame stretch response, it is reasonable to expect that a flame which correctly reacts to strain will also properly react to any type of stretch. To verify this assumption, the 2D spherical flame DNS at $\Phi = 0.400$ is carried out for four chemistries: detailed, 1S-Le1, 1S-LeRe and 1S-LeFit schemes. Figure 7.6 shows that the new global mechanism best mimics the early stage of the propagation whereas the 1S-LeRe flame is too rapid. This gap between detailed and 1S-LeRe schemes was not observed in the 2D tube DNS of Chapter 5. It is reasonable to say that stretch (and more particularly curvature) plays a more important role in the present spherical flame set-up. The fitting of the response to stretch in the 1S-LeFit mechanism allows for an overall faithful reproduction of the detailed scheme flame propagation. Some small discrepancies are still observed during the TD phase of the propagation. The dynamics of TD cells development is indeed not solely dictated by the flame stretch response. It also depends on intermediary reactions and species not modelled in the global chemical scheme [293]. Figure 7.7 gives a complement-

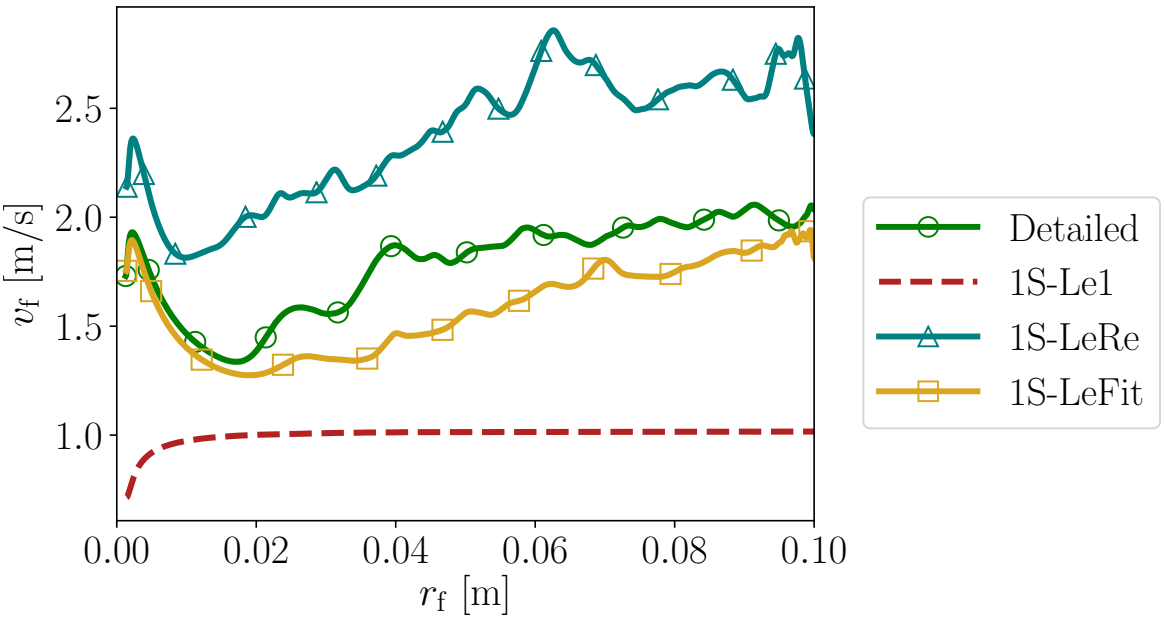

Figure 7.6: Flame speed as a function of flame mean radius for the detailed chemical scheme and global chemistries 1S-Le1, 1S-LeRe and 1S-LeFit.

ary view of the problem with the flame speed against its global stretch rate. The general

agreement of the 1S-LeFit stretch response with the San Diego mechanism is highlighted in this framework. Note also that the 1S-Le1 responds to stretch here. It is indeed not the consumption speed that is plotted but the flame displacement speed for which the asymptotic theory predicts a non-zero Markstein number (Equation (2.49)).

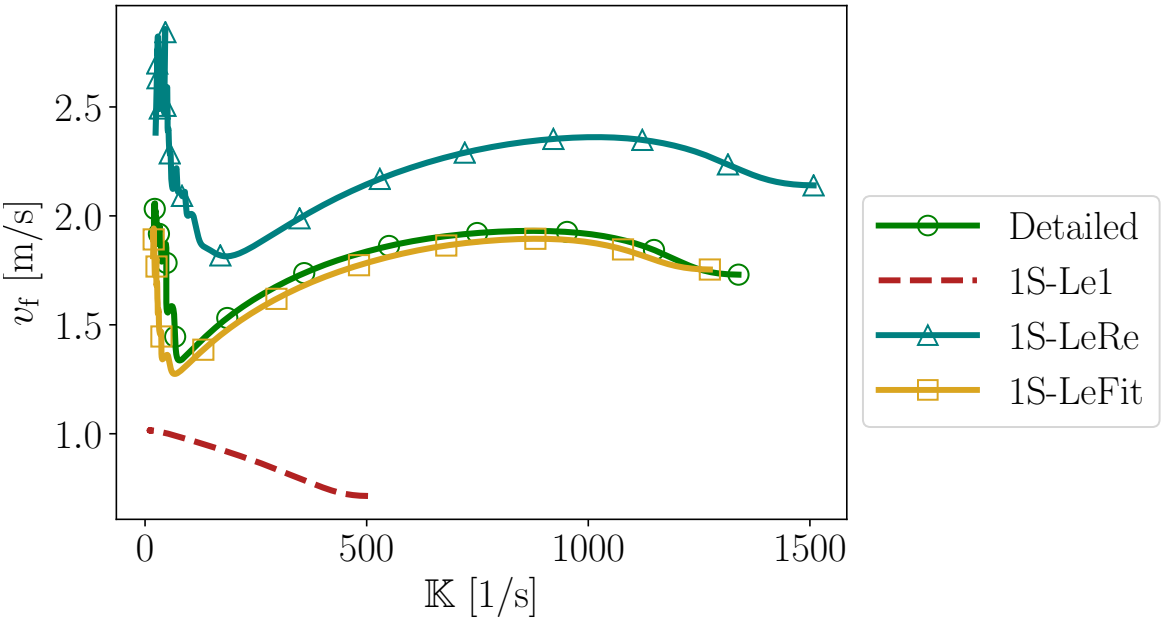

Figure 7.7: Flame speed as a function of global flame stretch for the detailed chemical scheme and global chemistries 1S-Le1, 1S-LeRe and 1S-LeFit.

7.3 Extension to three-dimensional spherical flames

The TD-S-TF model developed in the present chapter has so far only been validated against 2D spherical flame DNS data. This section is dedicated to the proof of the model's capacity to reproduce the correct flame propagation of real 3D spherical flames. To that end, Section 7.3.1 summarises a literature review that has been carried out in order to find suitable experimental data against which the simulations can be compared. The 3D spherical flame set-up used for the LES is then presented in Section 7.3.2. Details on the TD-S-TF model are given in Section 7.3.3 and its performance is assessed in Section 7.3.4.

7.3.1 Literature review

In order to compare simulation results with real flames, a literature survey of experimental measurements in spherical bombs has been carried out. Focus has been put on searching measures of flame propagation in terms of flame radius r_f, flame speed v_f and global flame stretch $\mathbb{K}$ for lean hydrogen-air mixtures under atmospheric conditions. Table 7.1 summarises the various papers (sorted by chronological order) along with the existing

data. Checkmarks indicate if one measure at least is available (most of the time, the quantitative data is not published for all cases). From this review, it has been decided to set-up a 3D spherical flame simulation for a lean hydrogen-air mixture at $\Phi = 0.6$. The numerical details are given in the next section.

Reference	**Equivalence ratio Φ**	$v_\mathrm{f}(r_\mathrm{f})$	$v_\mathrm{f}(\mathbb{K})$	$r_\mathrm{f}(t)$	**Additional comments**
Taylor [309]	0.3, 0.4, 0.5, 0.6, 0.7, 0.8, 0.9	✓			Other cases at $\Phi \in \{1.0, 1.1, 1.2, 1.3\}$
Aung *et al.* [97]	0.3, 0.45, 0.6, 0.75, 0.9	✓	✓		Other cases at $\Phi \in \{1.05, 1.5, 2.1, 3.5, 4.0\}$
Kwon *et al.* [123]	0.6, 0.9		✓		Other cases at $\Phi \in \{1.8, 4.5\}$
Lamoureux *et al.* [150]	0.28, 0.37, 0.6, 0.75, 0.82	✓	✓	✓	Other cases at $\Phi \in \{1.02, 1.59, 2.38, 3.57\}$
Verhelst *et al.* [157]	0.5	✓			Other cases at higher pressure and temperature
Bradley *et al.* [310]	0.4		✓		
Jomaas *et al.* [91]	0.6, 0.8, 1.0				Other cases at $\Phi \in \{1.4, 1.6, 2.0\}$ Measures of TD critical radii
Kelley *et al.* [311]	0.3	✓		✓	Other case at $\Phi = 5.1$ Measures of TD critical radii
Hu *et al.* [312]	0.4, 0.6, 0.8, 1.0	✓	✓	✓	Other cases at $\Phi \in \{1.8, 2.2, 3.0, 4.0\}$
Sun *et al.* [133]	0.6				Other cases at higher temperature
Kuznetsov *et al.* [152]	0.42		✓		Other cases at lower pressure
Wu *et al.* [313]					Measures of TD fractal excess
Goulier [134]	0.45, 0.6, 0.75, 0.95	✓	✓		
Sun and Li [314]	0.6	✓	✓		Other cases at higher pressure and temperature Measures of TD critical radii

Katsumi *et al.* [136]	0.3, 0.4, 0.5, 0.6, 0.7, 0.8, 0.9	✓	✓		Measures of TD critical radii
Beeckmann *et al.* [141]	0.5, 0.8, 1.0	✓			Other case at $\Phi = 1.5$ Measures of TD critical radii
Kim *et al.* [145]	0.5				Measures of TD critical radii
Kim *et al.* [143]	0.7	✓			Other cases at higher pressure Measures of TD critical radii
Liu *et al.* [315]	0.8, 1.0	✓			Other cases at $\Phi \in \{1.2, 1.5, 2.0, 2.5\}$
Grune *et al.* [316]	0.33, 0.36, 0.39, 0.45, 0.52, 0.6, 0.67	✓		✓	
Shu *et al.* [98]	0.4		✓		
Zhao *et al.* [317]	0.6				Laminar and turbulent cases

Table 7.1: Summary of available experimental spherical bomb measurements for H_2-air mixtures. All reported cases are done under atmospheric conditions.

7.3.2 3D spherical flame set-up

Geometry and boundary conditions

The global geometry of the numerical 3D spherical flame configuration is depicted in Figure 7.8. One eighth of the whole sphere is simulated using symmetries. Following the results of the 2D spherical flames analysed above (see Supplementary Material), the effect of symmetries is expected to be negligible. This is all the more justified as only LES cases are considered in this section (an asymmetry of the flame front could have been created by TD instabilities in DNS). Similarly to the 2D case, the domain size is set sufficiently large to avoid effects of the outlet on the flame propagation ($R = 1$ m). The outlet uses the Navier-Stokes Characteristic Boundary Conditions (NSCBC) formalism [282] with a zero relax coefficient so as to evacuate all pressure waves generated both by the flame (physical effect) and by the initialisation procedure (numerical effect).

Meshes and Adaptive Mesh Refinement

Following a rationale similar to that used for the 2D spherical flame (Section 7.1), several LES mesh resolutions are targeted. However, in the 3D simulation (eighth of sphere of radius R), to impose a given mesh resolution, the number of cells is considerably increased

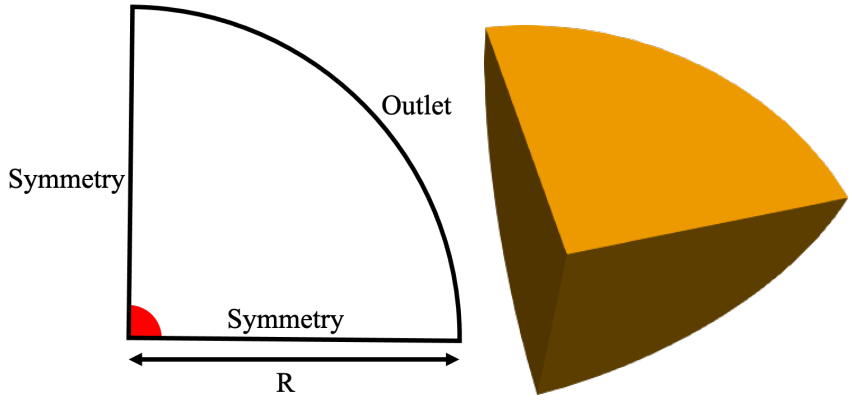

Figure 7.8: Schematic and render view of the 3D sphere configuration.

in comparison with the 2D equivalent (quarter of disk of same radius R):

$$\frac{N_{\text{cells}}^{\text{3D}}}{N_{\text{cells}}^{\text{2D}}} \approx \frac{\frac{\pi R^3}{6\Delta x^3}}{\frac{\pi R^2}{4\Delta x^2}} = \mathcal{O}\left(\frac{R}{\Delta x}\right) \tag{7.3}$$

The ratio $R/\Delta x$ being tremendous (e.g., $R/\Delta x \approx 3700$ in the DNS at $\Phi = 0.4$ presented in the 2D case), the computational cost associated to DNS and LES at high mesh resolution is prohibitive. Fortunately, in the present laminar spherical flame expansion scenario, the flame front is highly localised. This property advocates for the use of *Adaptive Mesh Refinement* (AMR) to increase the computation efficiency. AMR is a numerical technique consisting in dynamically adapting the mesh to refine targeted regions and coarsen the rest of the computational domain (see Figure 7.9). These targets are chosen based on the physics that one wants to resolve. In the current configuration, the mesh is progressively adapted to follow the flame front similarly to the TFLES flame sensor[1] (see Section 4.4.5). Provided that the mesh adaptation cost remains small, the overall computational cost is significantly reduced in comparison with a homogeneously refined case. The AMR method coded in AVBP has proved efficient for the simulation of explosion scenarios [249]. The reader may refer to the works of Sengupta [318] and Vanbersel *et al.* [249] for further details.

The properties of all considered meshes are summarised in Table 7.2.

Operating conditions

As explained in the previous section, the mixture considered here is a lean H_2-air premix at $\Phi = 0.6$ ignited under atmospheric conditions.

Initialisation

To initialise the flame, the strained profile procedure described in Section 7.2.1 is used. The initial global flame stretch is estimated using Equation (7.2) (3D case) with an initial

[1]Note that the refined region is extended towards the fresh gases in front of the flame. This buffer zone is added in anticipation of the flame propagation in that direction, to limit the number of necessary mesh adaptations.

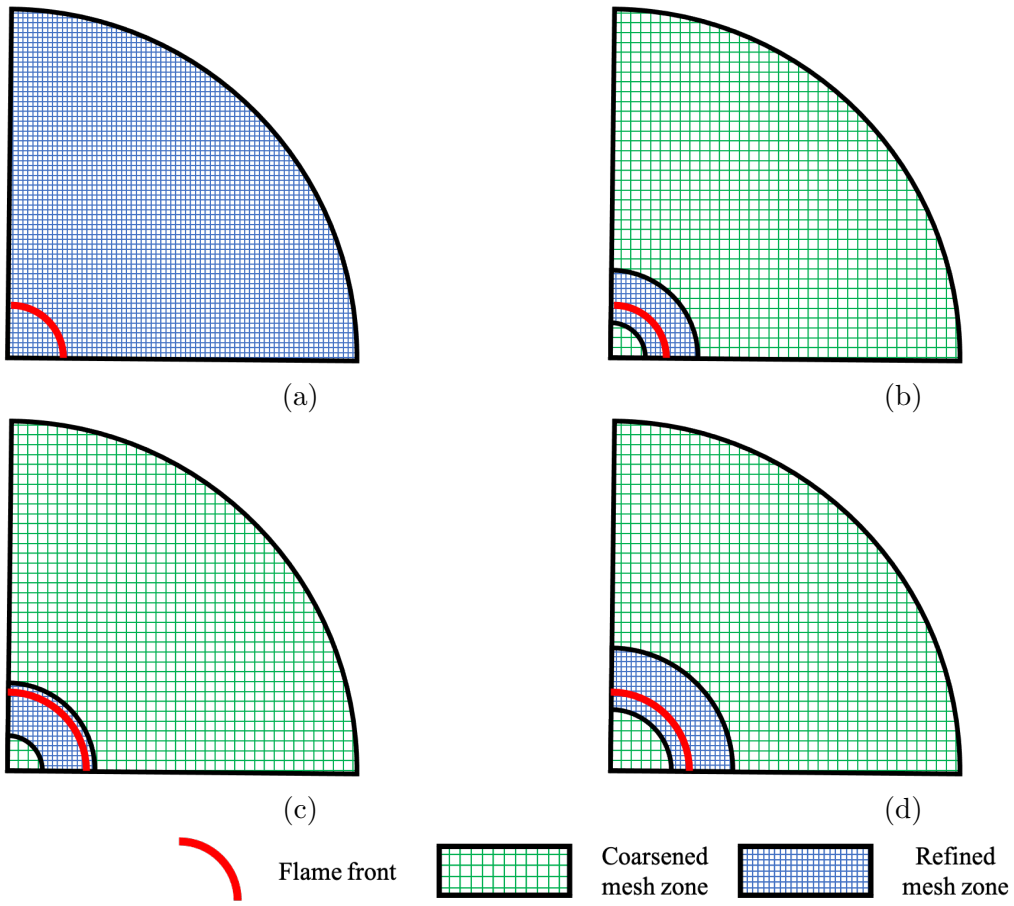

Figure 7.9: Schematic principle of Adaptive Mesh Refinement. a) t_0: initial solution on initial mesh: the mesh is refined everywhere. b) t_0: the mesh is adapted to the initial solution: the mesh is refined only in the vicinity of the flame front. c) $t_0 + \Delta t$: the flame has advanced close to the end of the refined area. d) $t_0 + \Delta t$: the mesh is adapted to the new flame front.

Thickening level F (imposed by the mesh resolution)	$\delta_{\mathrm{L}}^0/\Delta x$	$F\delta_{\mathrm{L}}^0/\Delta x$
2	3.50	7
4	1.75	7
8	0.875	7
16	0.4375	7

Table 7.2: Summary of mesh properties for the 3D spherical flame configuration.

radius set at $r_{\mathrm{f},0} = 2F\delta_{\mathrm{L}}^0$.

Flame tracking procedure

The flame advancement is tracked again using the radius of an equivalent perfect sphere containing the same mass of products as the real (potentially wrinkled) flame. For the eighth of sphere simulated here, it writes:

$$r_{\mathrm{f}} = \left(\frac{6}{\pi \rho_{\mathrm{b}} Y_{\mathrm{P,b}}} \int_{\Omega} \rho Y_{\mathrm{P}} \mathrm{d}\Omega \right)^{1/3} \tag{7.4}$$

where subscript P refers to properties of the product species (H_2O). From the flame radius temporal evolution, the flame speed is easily computed using $v_{\mathrm{f}} \equiv \mathrm{d}r_{\mathrm{f}}/\mathrm{d}t$ and the global flame stretch is estimated in this 3D spherical flame by (cf. Section 2.2.2, Equation (2.31)):

$$\mathbb{K} = 2\frac{v_{\mathrm{f}}}{r_{\mathrm{f}}} = \frac{2}{r_{\mathrm{f}}}\frac{\mathrm{d}r_{\mathrm{f}}}{\mathrm{d}t} \tag{7.5}$$

7.3.3 Thermo-Diffusive-Stretched-Thickened Flame model

On each of the meshes presented in Table 7.2, two simulations are run. One simulation uses the classical Thickened Flame transformation:

$$\begin{cases} D_{\mathrm{th}} \mapsto F D_{\mathrm{th}} \\ D_k \mapsto F D_k \\ \dot{\omega}_k \mapsto F^{-1}\dot{\omega}_k \end{cases} \tag{7.6}$$

and a second simulation uses the Thermo-Diffusive-Stretched-Thickened Flame transformation:

$$\begin{cases} D_{\mathrm{th}} \mapsto E_{\mathrm{TDS}} F_{\mathrm{th}} D_{\mathrm{th}} \\ D_k \mapsto E_{\mathrm{TDS}} F_{\mathrm{sp}} D_k \\ \dot{\omega}_k \mapsto E_{\mathrm{TDS}} F_{\mathrm{r}}^{-1}\dot{\omega}_k \end{cases} \tag{7.7}$$

where thickening coefficients F_{th}, F_{sp} and F_{r} are determined from the S-TF model to correct the flame response to stretch (cf. Chapter 6, in particular Section 6.3.2). The inputs of the S-TF optimisation (detailed in Section 7.2.2) are kept identical to the 2D case to test the genericity of the model. In particular, the target Karlovitz number is

conserved at $\mathrm{Ka}_\infty = 1/5$.

The expression for the thermo-diffusive efficiency function is recalled here:

$$(E_{\mathrm{TDS}} - 1)\mathrm{Le}_{\mathrm{eff}} = f\left(\left(\frac{r_{\mathrm{f}}}{r_{\mathrm{f,c}}} - 1\right)\mathrm{Le}_{\mathrm{eff}}\right) \tag{7.8}$$

using:

$$\begin{aligned} f(X) &= f_1(X) + \epsilon(X)\left(f_2(X) - f_1(X)\right) \\ \text{with,}\quad f_1(X) &= aX, \quad f_2(X) = bX^\alpha \\ \epsilon(X) &= \left(1 + \tanh\left(\frac{X-1}{\delta_{\mathrm{t}}}\right)\right)/2 \end{aligned} \tag{7.9}$$

where $a = 0.3125$, $b \approx 0.3202$, $\alpha \approx 0.27$, $\delta_{\mathrm{t}} = 0.1$. The evaluation of the thermo-diffusive efficiency from Equation (7.8) requires the mixture effective Lewis number (readily available from the theory, Equation (2.37)) and the critical radius for the onset of the instabilities. As explained in Section 7.1, the value of $r_{\mathrm{f,c}}$ in the 2D spherical flame TD-S-TF model is extracted from the DNS because its value is expected to differ from real flames. In the present case of 3D flames, it can directly be extracted from experimental measures [91, 136, 141, 143, 145, 311, 314]. In practice, it is computed from the correlation proposed by Goulier [134]:

$$r_{\mathrm{f,c}} = 198 X_{\mathrm{H_2}} - 18 \tag{7.10}$$

7.3.4 Results

The flame propagation using the TF and TD-S-TF models under the various resolutions are compared in the $(r_{\mathrm{f}}, v_{\mathrm{f}})$ space in Figure 7.10. First of all, if one looks only at the experimental data (symbols), a general collapse of all measures is observed. This gives confidence on the quality of the data.

As for the classical TF simulations, the analysis may be split between the first, stable, and the subsequent, unstable, stages of propagation (delimited by the black vertical line in Figure 7.10). The first phase is associated with a stable flame front subject to global stretch effects while the second phase is dominated by TD effects accelerating it (cf. Section 7.1). None of the TF curves predict the same propagation in the early stage. This has also been observed on the 2D spherical flames (which were at $\Phi = 0.4$) but here, the ordering of the curves with respect to thickening factor is reversed: the higher F, the slower the flame. This is discussed below. In the second stage of the propagation, all TF LES flames stay stable (due to the stabilising effect of the thickening and coarse mesh resolution, see Section 5.2.3) and the effects of stretch become negligible so that all curves collapse on a constant-speed propagation. This is contrary to the real behaviour given by the experiments which feature the acceleration of the kernel due to TD instabilities and confirms the inability of the classical TF model to predict unstable flame propagations.

Now, with regard to TD-S-TF LES simulations, several conclusions can be drawn:

- in the first phase of the propagation, the problem of mesh dependency is not solved. While the S-TF model has significantly reduced the discrepancies in the 2D sphere case, it does not improve the predictions in this 3D set-up. The difference between LES and experiments is probably due to the combination of two factors. On the LES side, some errors may be related to the initialisation of the simulations. The strained profile ignition procedure does not seem sufficient to correctly trigger the early high speeds observed in reality. Furthermore, on the experimental side, as mentioned by Goulier [134] and Kelley and Law [100], the energy that is deposited in experiments is usually higher than the minimum ignition energy (cf. Section 1.3 for its definition) to ensure successful ignition and this can cause the measured high speeds. In any case, this deficiency remains specific to the spherical set-up for which the problem of ignition is central;

- in the subsequent unstable phase of the propagation, the effect of the thermo-diffusive efficiency function is able to accelerate the flame and catch up with the experimental measurements. At this stage, as explained above, the effects of the resolved stretch become negligible and the small gap between TD-S-TF curves is only due to resolved TD instabilities.

The second point is illustrated in Figure 7.11 which displays several flame snapshots at the same mean flame radius for the cases $\delta_{\mathrm{L}}^0/\Delta x = 3.5$ ($F = 2$) and $\delta_{\mathrm{L}}^0/\Delta x = 0.4375$ ($F = 16$). The finer case still captures some TD structures (explaining the higher velocities in Figure 7.10) while the coarser is fully stable for the observed range of flame radius.

The same simulations can be compared to other experimental data in the $(\mathbb{K}, v_{\mathrm{f}})$ space (see Figure 7.12). As a reminder, in this framework, time goes from right (high stretch) to left (low stretch). The agreement between the various experimental measures is less obvious. While most curves approximately extrapolate towards $(\mathbb{K} = 0, v_{\mathrm{f}} = \sigma S_{\mathrm{L}}^0)$ as expected, their slope is strongly disparate from one publication to the other. Also, the onset of thermo-diffusive instabilities is not always visible except for the data of Sun and Li [314] and Katsumi *et al.* [136]. These differences may come from the combination of uncertainties on the measure both of v_{f} (as explained above) and of $\mathbb{K}$.

The stretch response scatter is also considerable both with the classical TF model and with the TD-S-TF model. Despite the spread of experimental data, most measures show an increase of flame speed with stretch. This behaviour is not captured in the simulations and may be due to initialisation effects cited above. It leads to an apparent negative response to stretch which is further amplified when thickening is increased.

The analysis in this framework also shows that the S-TF model does not significantly diminish the amplification of stretch effects. However, as soon as the critical radius is reached, the TD efficiency generates an acceleration of the flame front compatible with experimental observations.

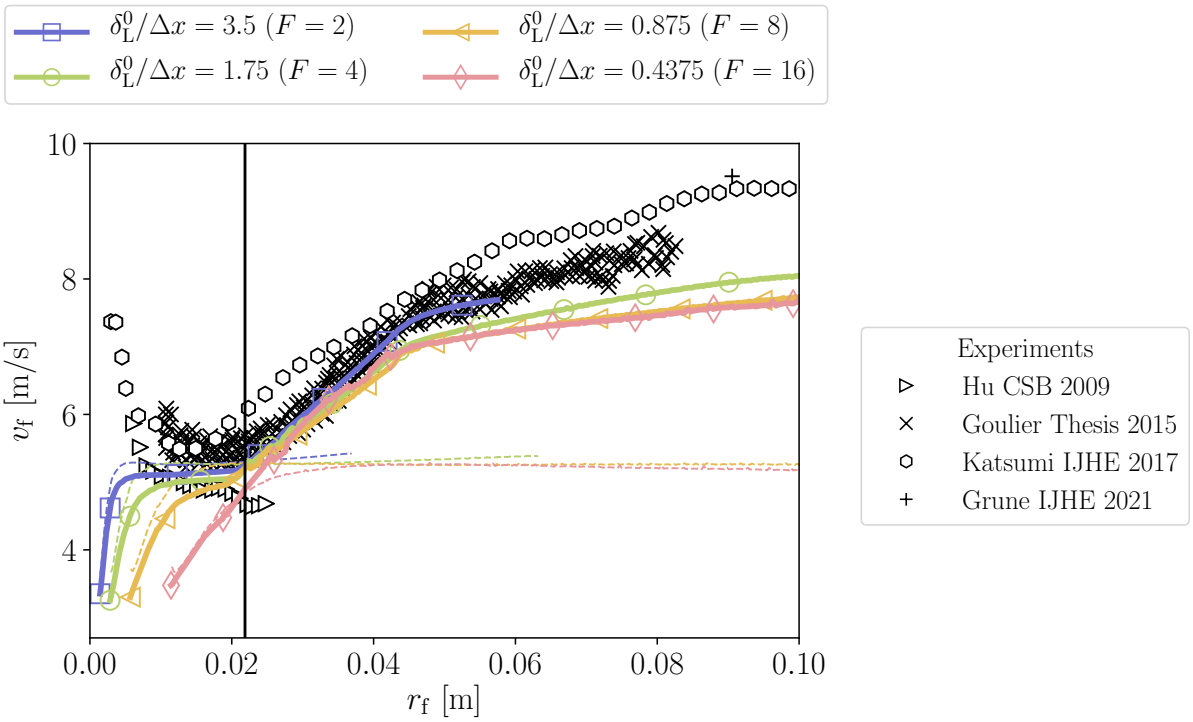

Figure 7.10: Flame speed as a function of flame mean radius for several meshes using TF and TD-S-TF models. $\Phi = 0.600$. 1S-LeFit chemistry. Dashed lines: classical TF LES. Solid lines: TD-S-TF LES. symbols: experimental data (Table 7.1). Black vertical line: delimitation of globally-stretched and TD-dominated phases.

7.4 Conclusion

This chapter has been dedicated to presenting the Thermo-Diffusive-Stretched-Thickened Flame (TD-S-TF) model. It constitutes the second step in solving the shortcomings of the classical Thickened Flame approach identified in Chapter 5, recalled here:

1. amplification of the flame sensitivity to stretch due to thickening;
2. inability to capture TD cells onset and development.

The TD-S-TF correction is built upon the Stretched-Thickened Flame (S-TF) model (see Chapter 6) aimed at fixing the coupling of stretch effects with thickening. A thermo-diffusive efficiency is added as a second ingredient to model all subgrid effects (stretch and wrinkling) induced by TD instabilities. In Section 7.1, the model principle has been demonstrated in a 2D spherical flame set-up. The TD-S-TF strategy requires:

- for the stretch response correction, the same inputs as the S-TF model (cf. Chapter 6, Figure 6.9): the mixture effective Lewis number, one parameter for the laminar flame speed sensibility to a perturbation of molecular diffusivities, and a target stretch rate determining the range of relevance for the model;

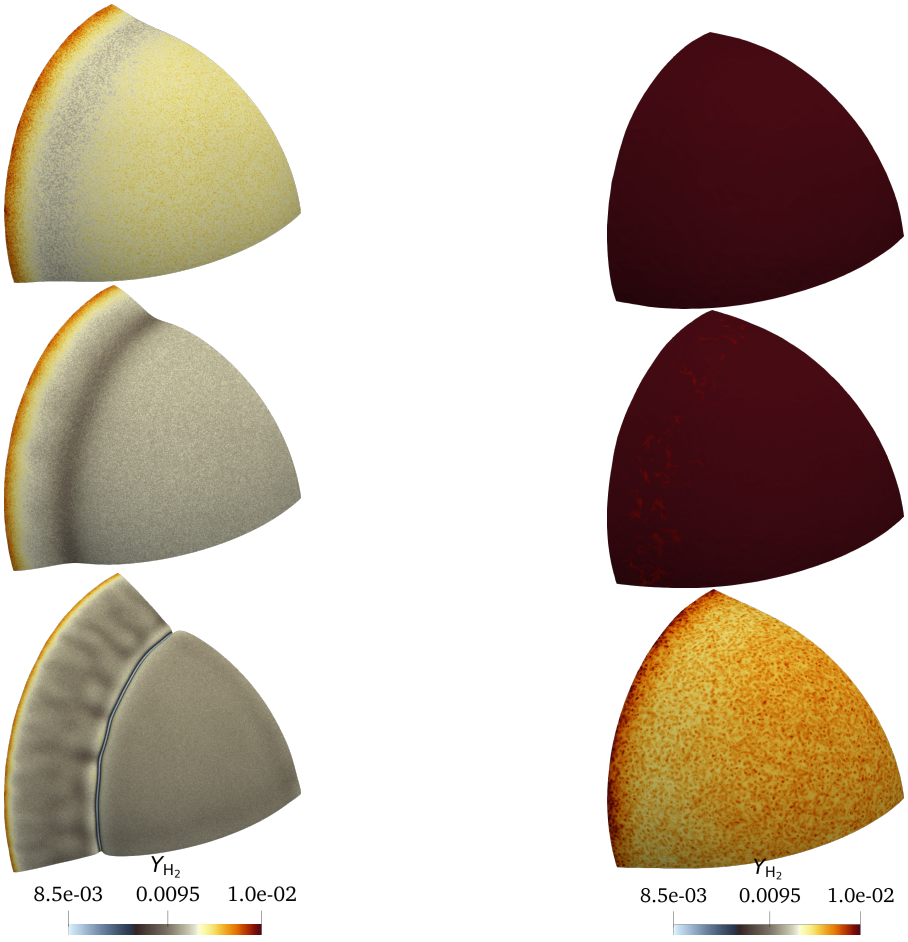

(a) $\delta_L^0/\Delta x = 3.5, F = 2.$ (b) $\delta_L^0/\Delta x = 0.4375, F = 16.$

Figure 7.11: Flame isocontour ($T = 800$ K) snapshots colored by hydrogen mass fraction at several flame radii for two TD-S-TF LES. From top to bottom: $r_f \approx 14 - 24 - 56$ mm. $\Phi = 0.600$. 1S-LeFit chemistry. The colormap is centered around the laminar value $Y_{H_2}^0(T = 800\text{K})$.

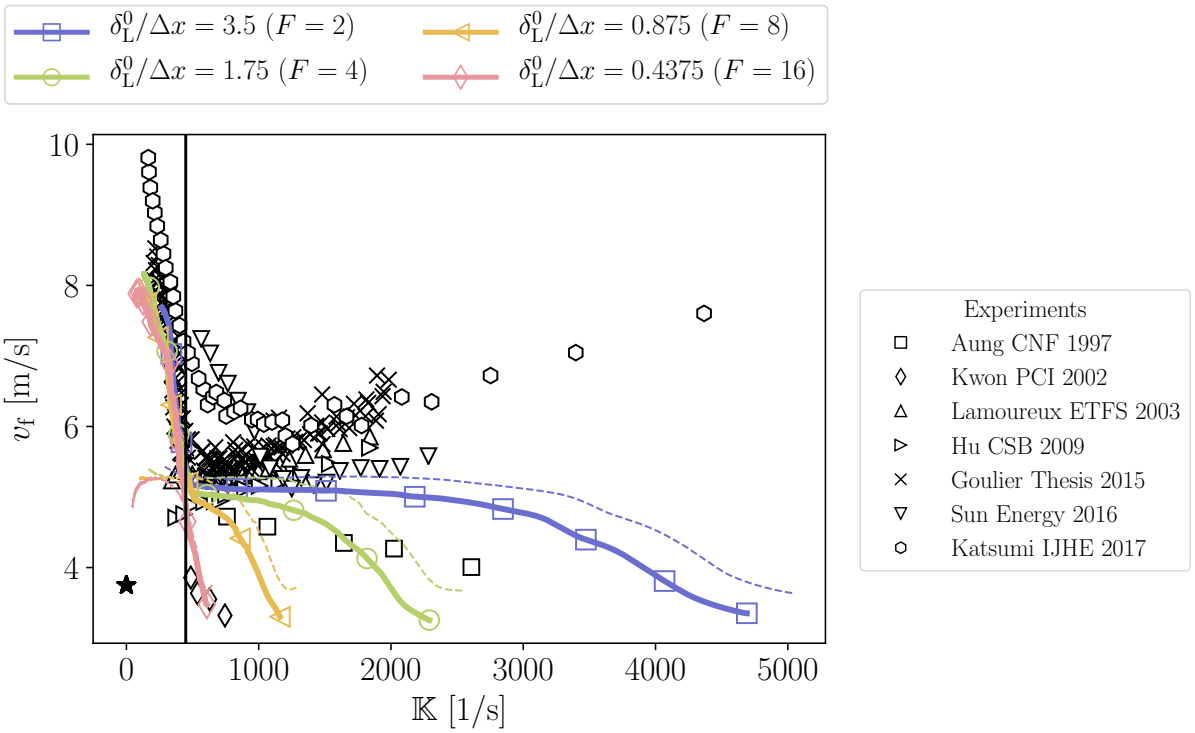

Figure 7.12: Flame speed as a function of flame mean radius for several meshes using TF and TD-S-TF models. $\Phi = 0.600$. 1S-LeFit chemistry. Dashed lines: classical TF LES. Solid lines: TD-S-TF LES. Symbols: experimental data (Table 7.1). Black star: unstretched laminar point.

- for the TD efficiency function: the mixture effective Lewis number (already given for the S-TF model) and the critical radius for the onset of TD instabilities (activation of the efficiency).

The correction has been successfully validated at several conditions (all atmospheric, Φ ranging from 0.4 to 0.7) and under several levels of thickening. At this stage, it was concluded that although the model has only been explicitly validated on 2D lean hydrogen-air flames, its scope of applicability is wider:

- the fact that the expression of the thermo-diffusive efficiency function is based on experimental measurements from Goulier [134] gives confidence on the TD-S-TF model's representativeness of real flames;
- even if it has been tested on atmospheric lean hydrogen-air mixtures, it is reasonable to expect that the strategy is readily applicable to spherical flame propagation in other mixtures and operating conditions (in particular higher pressures). This is supported by the robust manner in which the TD-S-TF approach has been formulated: (1) degenerating into the S-TF model for stable flames; (2) and relying only on two parameters for the TD efficiency (cited above), easily retrieved from theory or experimental data.

The first item has been addressed in Section 7.3 where the TD-S-TF approach has been applied to the LES of 3D lean H_2-air flames and confronted to experimental measurements. To switch from the initial 2D case to the 3D application, the TD-S-TF formulation remains unchanged, except for the critical radius for the onset of TD instabilities which is now based from experimental measures/correlations. The 3D LES has demonstrated the capability of the TD-S-TF model to correctly reproduce the kernel development as soon as the TD instability arises. In the early stages, the S-TF correction does apparently not significantly modify the flame speed evolution compared to the classical TF model. This shortcoming may be due not to a problem of stretch response per se, but rather to the difficulty of properly igniting a spherical flame in the simulations. This problem is therefore specific to the spherical set-up. It is indeed shown in the next chapter that the S-TF correction does represent an important correction for the LES of a confined explosion scenario where the early spherical stage is short.

Finally, it has also been stated that, while the model is not directly applicable for complex cases, extensions can be explored. Indeed, many explosion scenarios begin with a fully laminar flame kernel that expands into a confined (in the style of the 2D tube configuration used in Chapter 5) and obstructed area. As the flame loses its spherical shape, it can be expected that the subgrid contribution of TD cells will saturate. This has been shown to hold for the first stages of flame acceleration in a tube (laminar phase) [319] (see Section 5.3.6). This potential extension is now studied in the next chapter.

Part IV

Applications to Large-Eddy Simulation: confined and obstructed explosions

Chapter 8

Application to flame propagation in a confined environment

Sommaire

The last chapter has presented the basic principles of the Thermo-Diffusive-Stretched-Thickened Flame (TD-S-TF) model for the LES of lean hydrogen-air flames propagation. Its has been developed on the canonical 2D spherical flame set-up. This simplified approach has allowed to get rid of the finger flame phenomenon commonly found in explosion scenarios and to focus on the effects which are characteristic of lean H_2-air mixtures. Eventually, the TD-S-TF model has been validated on the larger 3D spherical configuration against experimental measurements. The next logical step towards a real explosion

scenario is to see whether the model is adapted for the LES of confined cases. It has indeed been shown in Chapter 5 that during flame propagation in a tube, several phenomena are coupled. The flame experiences a sudden acceleration due to the finger flame phenomenon. This latter interacts with intrinsic flame front instabilities by imposing a general shape of the flame (which drives curvature effects) and the main features of the flow (which drive strain effects). The instabilities, in turn, influence the overall acceleration as well as the duration of the finger flame phase. It has also been demonstrated that the classical Thickened Flame model does not provide predictive simulations and suffers from a mesh dependency. The present chapter deals with the application of the TD-S-TF model for flame propagation in a confined environment. It loops back to Chapter 5 to answer the challenges raised therein:

- is the TD-S-TF model capable of solving the erroneous behaviours observed with the standard TF formalism (amplification of stretch effects and lack of flame front instabilities) for the LES in a confined environment?
- does it produce a flame acceleration consistent with the reference DNS?

To do so, the main components of the set-up used in Chapter 5 are re-used. It is briefly reminded in Section 8.1 along with the main changes that have been made. In particular, the new global chemistry 1S-LeFit introduced in Chapter 6 is preferred to the 1S-LeRe chemistry of Chapter 5. Section 8.2 re-evaluates the effect of mesh resolution with this new chemical mechanism to show that the shortcomings of the Thickened Flame model remain the same as identified in Chapter 5, namely:

- the use of a coarse mesh depletes the resolution of TD instabilities. The loss of TD structures leads to the deceleration of the flame;
- in the meantime, thickening amplifies the stretch response of the flame, resulting in an overprediction of the consumption speed;
- the overall propagation results from the interaction of these two mechanisms respectively hindering and fostering flame propagation as the mesh resolution is decreased. The main consequence is the unpredictability of the classical TF model which presents a strong dependency to mesh resolution and thickening level.

The workflow chosen to address these issues is similar to the one of Chapter 7: (1) Section 8.3 evaluates the effectiveness of the Stretched-Thickened Flame (S-TF) model to dampen the amplification of stretch effects; (2) Section 8.4 adds the second component with the use of the TD-S-TF model to correct subgrid TD effects. Attention should be paid to this part which shows how geometrical parameters of a given explosion configuration can be fed to the model. Section 8.5 appraises the performance of the other TD models (introduced and discarded in Chapter 7) for the present 2D tube flame. Finally, an evaluation of the TD-S-TF model genericity is carried out in Section 8.6 by varying the tube radius.

8.1 Set-up reminder

Most characteristics of the set-up are kept the same as in Chapter 5. In particular, the 2D tube geometry is the same (see Figure 8.1) and both DNS and LES meshes are retained (they are all parameterised by the flame thickness, see Table 5.4). Focus is put on the lean hydrogen-air mixture at $\Phi = 0.400$. The boundary conditions remain unchanged: adiabatic slip wall for the ignition plate, adiabatic no-slip wall on the top, symmetry at the bottom and non-reflecting outlet on the right. The macroscopic flame propagation is quantified in terms of flame tip position x_f and velocity v_f (cf. Figure 2.3 and Equation (5.5)).

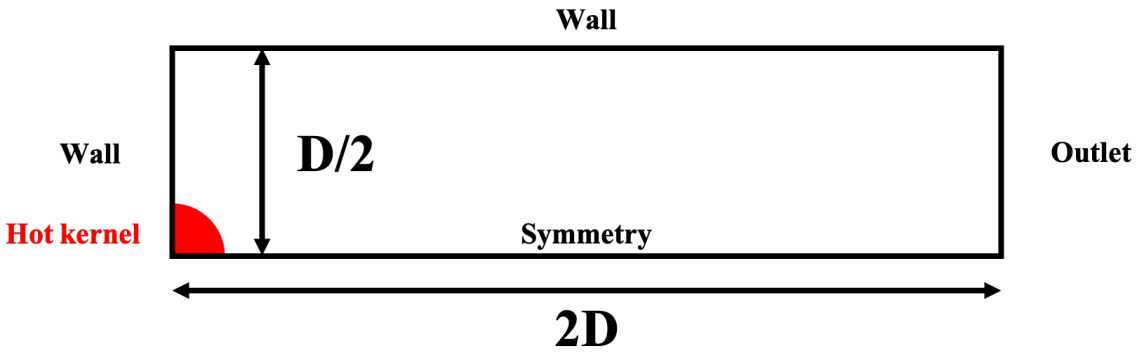

Figure 8.1: Schematic of the 2D tube configuration.

Now, the experience from the previous chapter has shown that some features of the configuration must be changed to get more realistic simulations. The strained profile initialisation (see Section 7.2.1) is used to limit the transient phase due to ignition. On top of that, the new global chemistry 1S-LeFit (see Sections 6.1 and 7.2.3) is also used in this chapter to guarantee a single-step scheme as close as possible to reality for explosion simulations.

8.2 Effect of mesh resolution

This section briefly re-illustrates the TF shortcomings for the LES of lean H_2-air flames identified in Chapter 5. It is indeed necessary to show that they are still present with the new 1S-LeFit chemistry. To do so, a mesh dependency analysis is carried out. Figure 8.2 compares the propagation of the various DNS and LES in the (x_f, v_f) space. If one looks at the average finger flame acceleration slope only, the same conclusions as before can be drawn:

- in DNS, the flame advances faster than predicted by the finger flame theory because of stretch effects and the thermo-diffusive instability;

- when the mesh resolution is decreased, so does the resolution of TD cells. The acceleration slope is reduced;
- as soon as no TD wrinkling is resolved on the mesh, as the mesh resolution is further decreased, the amplification of the flame stretch response enhances its acceleration.

Nevertheless, a major difference with Chapter 5 is noteworthy: the LES curves have a velocity offset which varies with the mesh resolution. This new characteristic of the flame propagation is directly linked to the novel initialisation procedure:

1. the use of strained flame profiles for the initial kernel is more consistent with the rest of the propagation;
2. but given that the TF model intensifies the response to stretch, this amplification also applies for the initial profile;
3. a faster initial flame ensues;
4. after the spherical transient phase, the finger flame phenomenon takes over with an exponential acceleration.

In the end, the coarsest LES propagates even faster than the DNS. This phenomenon was not observed in the previous TF mesh dependency analyses in Chapter 5.

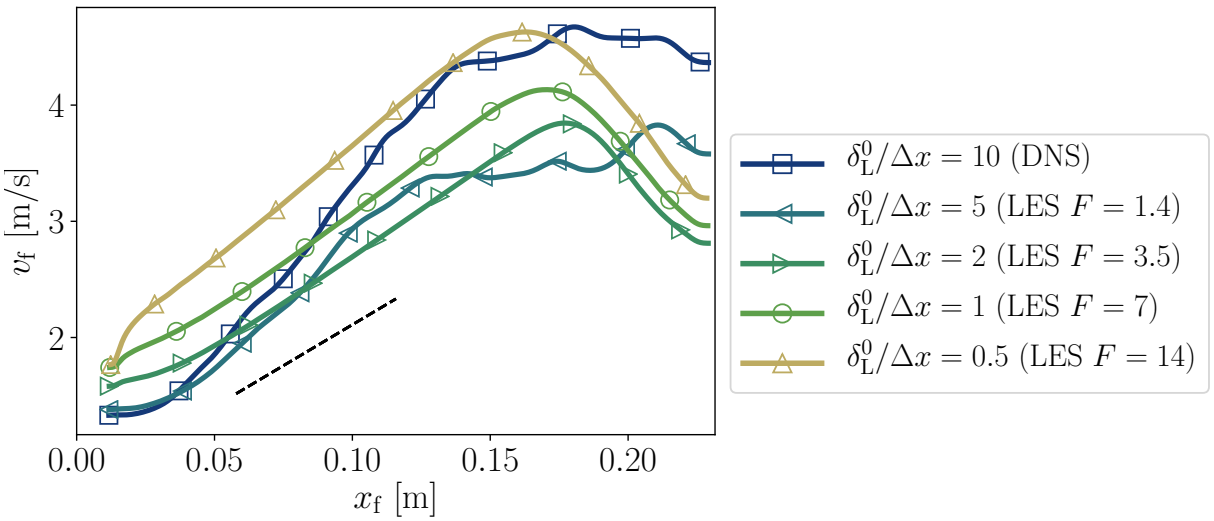

Figure 8.2: Flame speed as a function of flame tip position for several mesh resolutions (Table 5.4). DNS and TF LES. 1S-LeFit chemistry. Strained kernel initialisation (also thickened for the LES). Dashed black line: finger flame theoretical slope (Equation (3.11)).

To check that the velocity offset is purely due to the initialisation, the mesh dependency study is repeated with the standard initialisation based on unstretched flame profiles (also thickened for the LES). The resulting flame propagations are compared in Figure 8.3.

Now that the kernels are deposited using untretched profiles (the temperature of the hot kernel is completely adiabatic, cf. Appendix C), the flame speed is not boosted by the TF transform at the first instants. A behaviour similar to the former 1S-LeRe mechanism of Chapter 5 is retrieved.

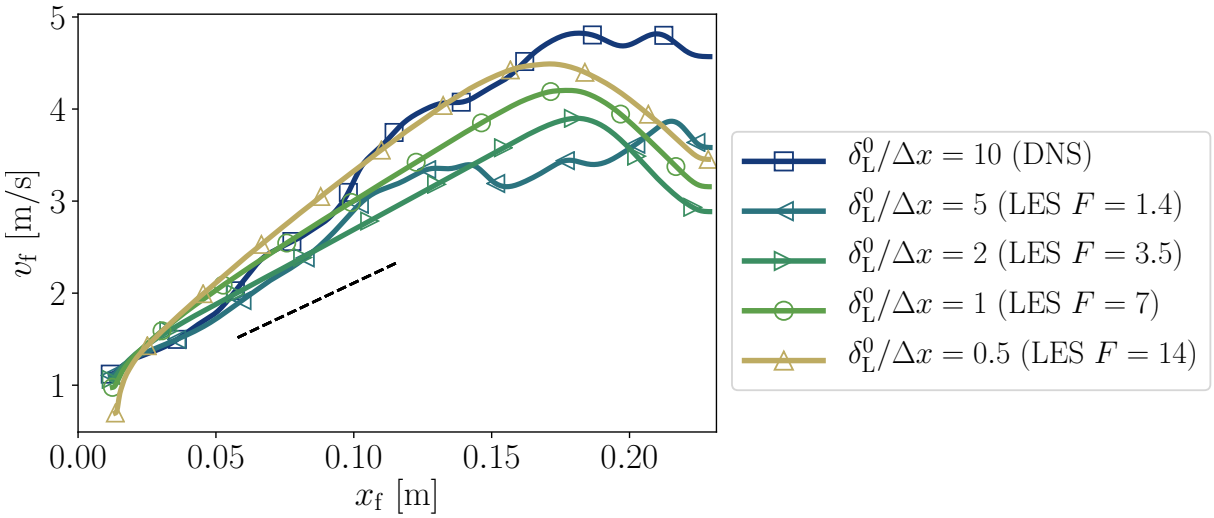

Figure 8.3: Flame speed as a function of flame tip position for several mesh resolutions (Table 5.4). DNS and TF LES. 1S-LeFit chemistry. Unstretched kernel initialisation (also thickened for the LES). Dashed black line: finger flame theoretical slope (Equation (3.11)).

8.3 Stretch response correction

Now that the shortcomings of the TF model have been re-demonstrated in the 2D tube set-up with the new 1S-LeFit mechanism, the correction models proposed in Chapters 6 and 7 can be tested. This section focuses on the Stretched-Thickened Flame (S-TF) model which aims at rectifying the response to stretch of thickened flames.

8.3.1 Application of the Stretched-Thickened Flame model

The Stretched-Thickened Flame model developed in Chapter 6 is evaluated, first on the LES at $\delta_L^0/\Delta x = 0.5$. This case is indeed thoroughly stable during the propagation but suffers a strong stretch amplification by the TF model ($F = 14$) which needs to be corrected. The parameters of the S-TF optimisation extended to lean H_2-air flames in Chapter 7 are used without any modification to validate their genericity. In particular, the target Karlovitz number is still fixed at $\mathrm{Ka}_\infty = 1/5$ (see Section 7.2.2). Figures 8.4 and 8.5 depict the field of local Karlovitz experienced by the flame in DNS and TF LES at $\delta_L^0/\Delta x = 0.5$ respectively. In DNS, the highly curved regions of the flame exhibit a Karlovitz which is higher than 1/5 but the rest of the flame front is stretched around and

below this target value. This choice is all the more justified as the S-TF model is meant for LES flames which do not present such highly stretched zones. Indeed, for instance, the case $\delta_L^0/\Delta x = 0.5$ (shown in Figure 8.5) exhibits stretch values at $\mathrm{Ka} < \mathrm{Ka}_\infty$.

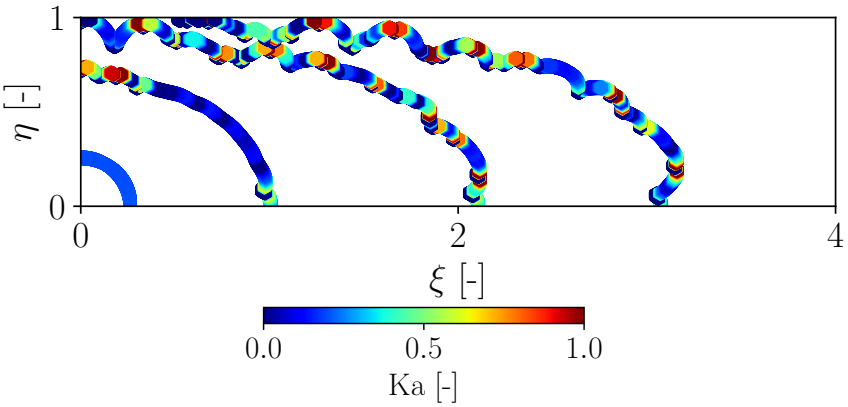

Figure 8.4: Local Karlovitz Ka at several instants during flame propagation for the DNS.

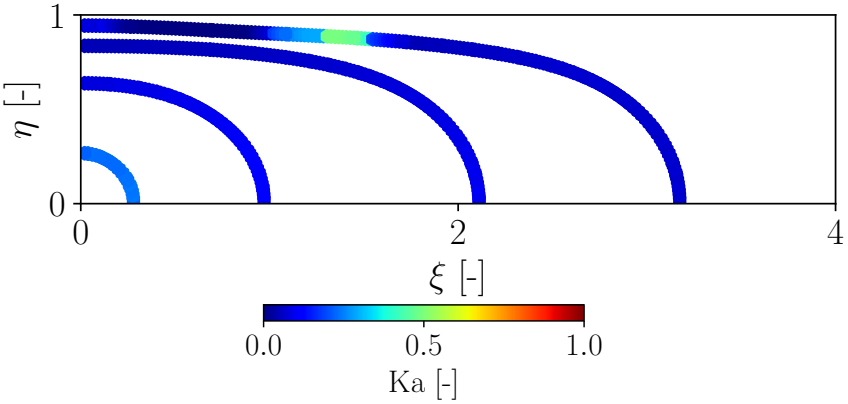

Figure 8.5: Local Karlovitz Ka at several instants during flame propagation for the TF LES at $\delta_L^0/\Delta x = 0.5$.

The LES corrected with the S-TF model is now compared with the reference DNS and the classical TF case in Figure 8.6. It is seen to recover a slower propagation in comparison with the uncorrected LES. However, the flame speed is now lower than in the DNS. This is because the effect of subgrid thermo-diffusive instabilities has not been added yet. Note also that the acceleration slope almost perfectly matches the theoretical finger flame slope.

To verify that the S-TF correction is effective, the local stretch response of the DNS, TF LES and S-TF LES flames are compared in Figure 8.7 for several positions of the flame tip corresponding to snapshots in Figures 8.4 and 8.5. While the I_0 distribution is greatly shifted upwards and concentrated around low stretch abscissas for the TF simulation (thereby highlighting the over-sensitivity to stretch), the S-TF model corrects this erroneous behaviour by reducing I_0 without affecting the range of stretch rates experienced by the flame.

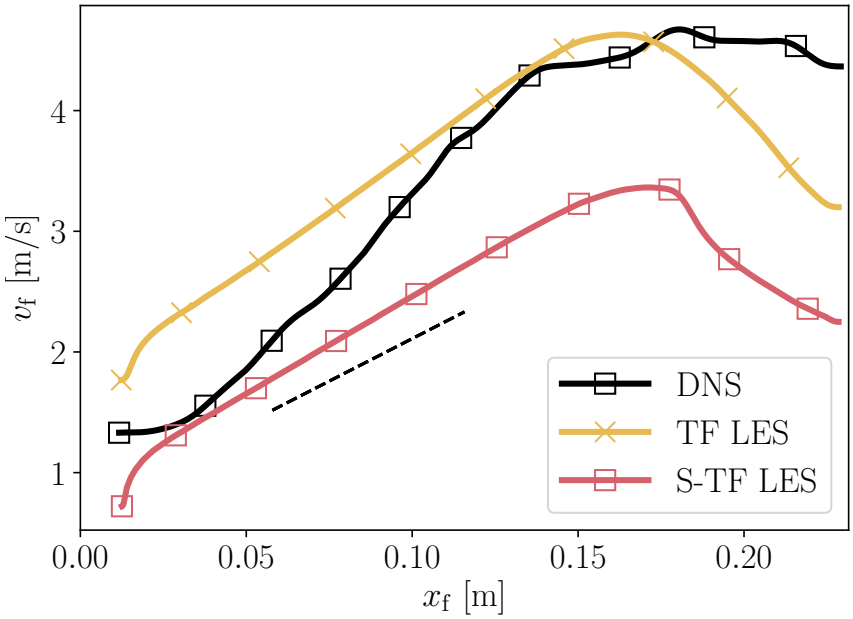

Figure 8.6: Flame speed as a function of flame tip position for the DNS and several LES models. 1S-LeFit chemistry. Dashed black line: finger flame theoretical slope (Equation (3.11)).

8.3.2 Mesh dependency check

The last check of the validity of the S-TF correction for the LES of lean H_2-air explosions is about mesh dependency. It must ensure that the stretch response is consistently rectified for all levels of F. The global flame propagation is again analysed in the phase space for the DNS and all LES corrected with the S-TF formalism in Figure 8.8. Similarly to what has been noted in Chapter 7, all LES curves collapse on the same propagation except the case at $\delta_L^0/\Delta x = 5$. This case constitutes an example of intermediary LES where TD effects are slightly captured, resulting in a visible speed-up around $x_f \approx 0.12$ m. Anyway, this kind of highly resolved LES is not usually encountered for large-scale explosion simulations. Similarly to what has been observed in the previous section, all S-TF curves display an acceleration rate corresponding almost exactly to the finger flame theory. It constitutes an important conclusion:

- in LES, provided that the response to stretch is correct, stretch effects do not substantially modify the flame acceleration exponent. In other words: when the S-TF model is activated, the flame follows more or less the propagation predicted by the finger flame theory (i.e. using a unity-Lewis number mechanism);
- the S-TF approach does not account for subgrid stretch effects induced by the thermo-diffusive instability: the resulting flame does not propagate like the DNS reference.

Figure 8.9a(resp. 8.9b) represents the $I_0(\mathbb{K})$ distributions for all meshes in the TF

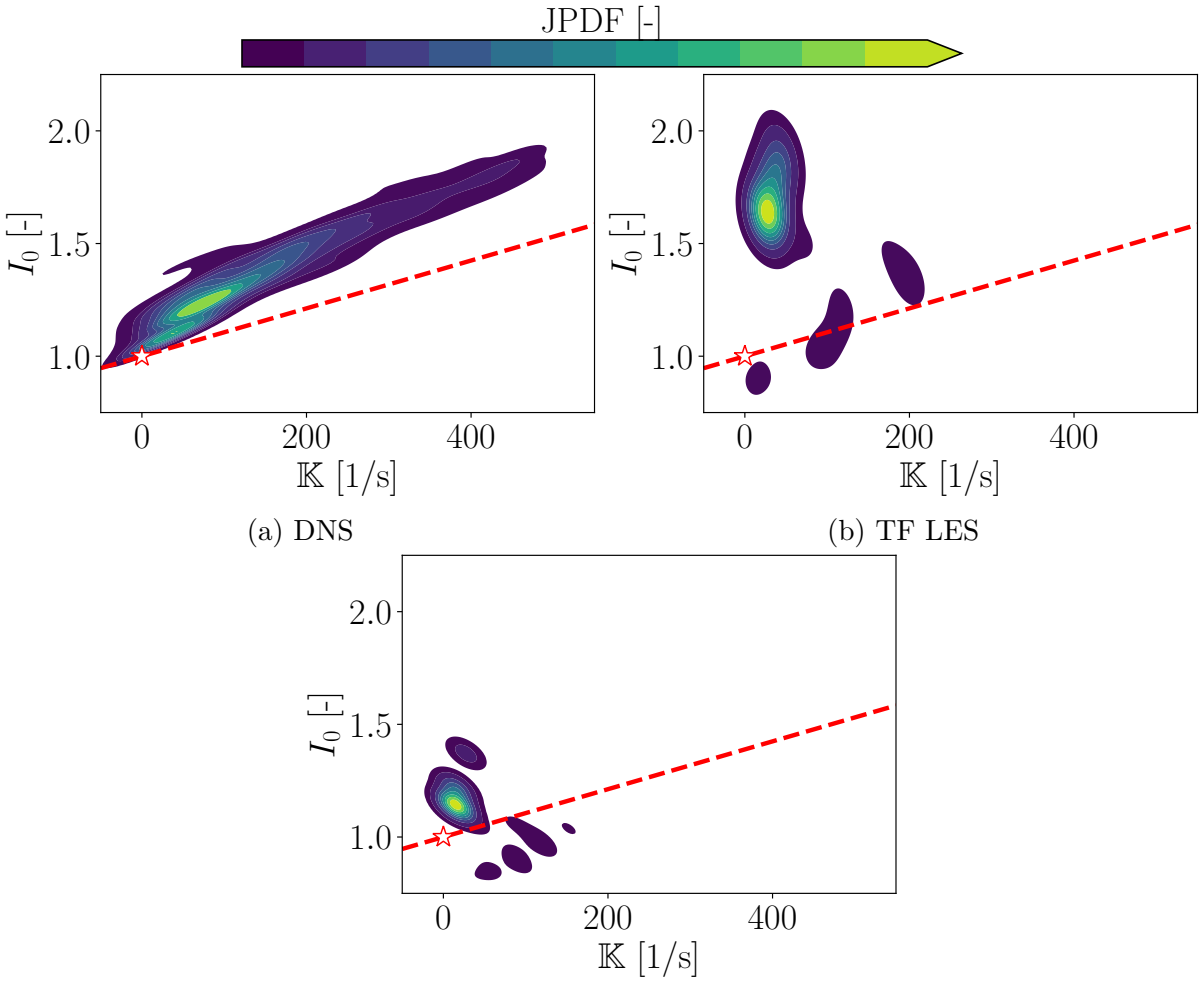

(a) DNS

(b) TF LES

(c) S-TF LES

Figure 8.7: Joint PDF of stretch factor I_0 as a function of total stretch $\mathbb{K}$ for the DNS, TF LES and S-TF LES. Distributions corresponding to snapshots shown in Figures 8.4 and 8.5. Dashed red line: asymptotic theory (Equation (2.44)). Red star: unstretched laminar value.

(resp. S-TF) approach at $x_\mathrm{f} \approx L_\mathrm{tube}/2 \approx 0.12$ m. The correction does not significantly modify the distribution of the intermediary case $\delta_\mathrm{L}^0/\Delta x = 5$ but it largely abates the levels of flame speed for coarser cases, leading to an overall agreement for the response to stretch. Note also that the stretch levels at this same x_f position are all concentrated around the same value for all stable flames.

8.4 Thermo-diffusive instabilities correction

Now that the response to stretch has been consistently corrected for all LES, this section treats of the second component of the TD-S-TF model: the subgrid correction of thermo-diffusive effects.

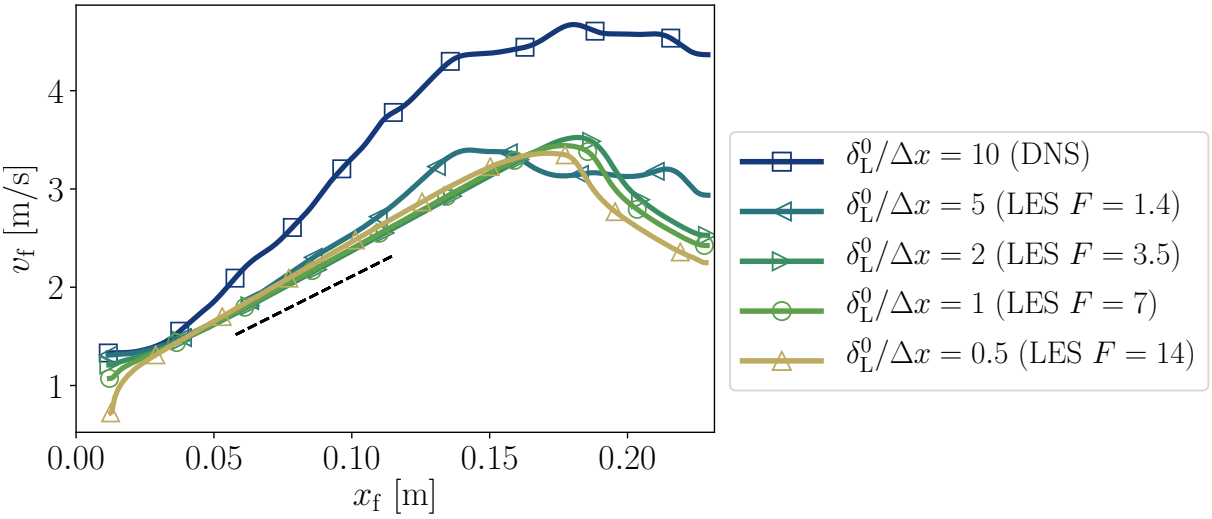

Figure 8.8: Flame speed as a function of flame tip position for several mesh resolutions (Table 5.4). 1S-LeFit chemistry. LES corrected with the S-TF correction. Dashed black line: finger flame theoretical slope (Equation (3.11)).

8.4.1 Application of the Thermo-Diffusive-Stretched-Thickened Flame model

Like what has been done for the S-TF component, the full TD-S-TF model is first assessed on the LES at $\delta_L^0/\Delta x = 0.5$. The S-TF parameters are again kept as they are. For the TD efficiency, the general form given in Chapter 7 represents a baseline. The onset radius for the activation of the efficiency is likewise extracted from the 2D spherical flame DNS, following the arguments explained in the preceding chapter. However, the interactions of the thermo-diffusive instability with the confinement is expected to modify its development. Several remarks can help generalise the TD-S-TF model to a tube flame propagation:

1. in the last section, it has been demonstrated that S-TF flames follow the finger flame acceleration theory, corresponding to a unity-Lewis assumption;

2. in Section 5.3.6, a comparison of 1S-Le1 and 1S-LeRe DNS has shown that non-unity Lewis number effects saturate in the finger flame phase at a value varying with the tube radius. Hok *et al.* [319] therefore advocate for a TD modelling accounting for the tube geometry.

In the genesis of the TD-S-TF model (Chapter 7), the TD efficiency has been developed for spherical kernels. The flame radius is estimated from the equivalent perfect sphere of burnt gases. In tube flame propagation, after the spherical stage, the finger flame phenomenon takes over, elongating the flame in the channel axis. It thus increasingly deteriorates the validity of the spherical assumption. This is verified by comparing three curves during the propagation: the flame tip position $\xi_f \equiv x_f/R_{tube}$, its skirt position

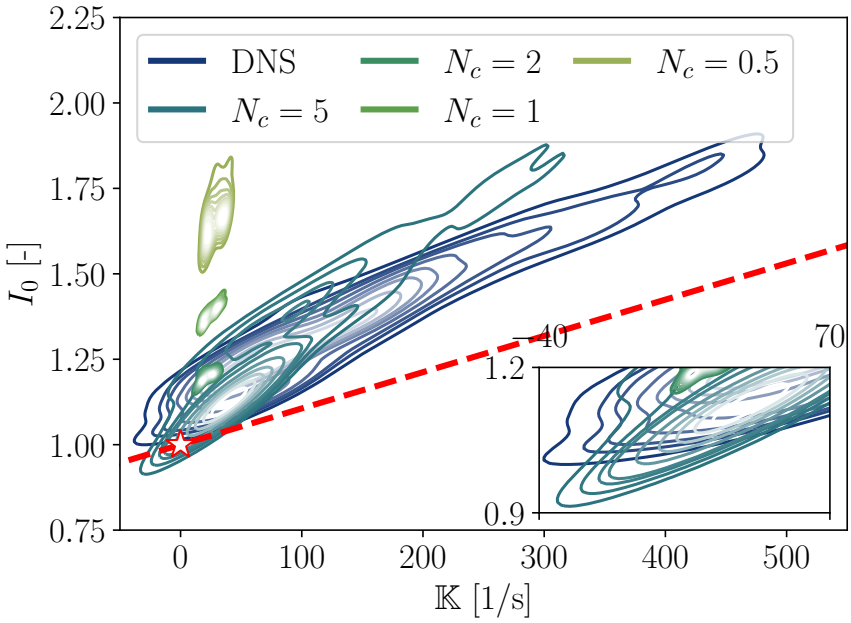

(a) TF LES

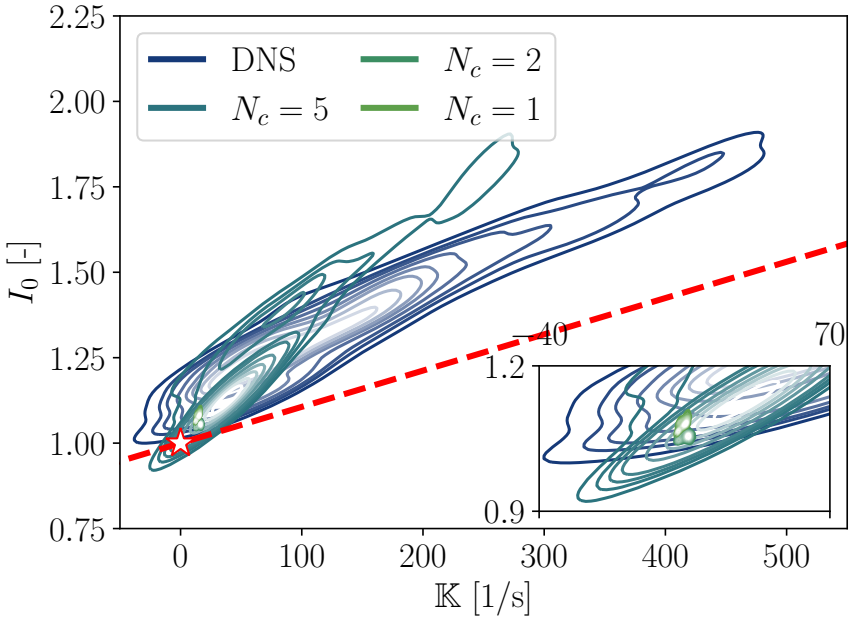

(b) S-TF LES

Figure 8.9: Joint PDF of stretch factor I_0 as a function of total stretch $\mathbb{K}$ for several mesh resolutions (Table 5.4). Distributions corresponding to snapshot at $x_\mathrm{f} \approx L_\mathrm{tube}/2$. Top: classical TF LES. Bottom: S-TF LES. Dashed red line: asymptotic theory (Equation (2.44)). Red star: unstretched laminar value.

$\eta_\mathrm{f} \equiv y_\mathrm{f}/R_\mathrm{tube}$ and the radius of the equivalent sphere of burnt gases $\psi_\mathrm{f} \equiv r_\mathrm{f}/R_\mathrm{tube}$. The results are depicted in Figure 8.10. Certain characteristics can be observed on this diagram:

- the non-sphericity of the kernel becomes visible as soon as the positions of the tip

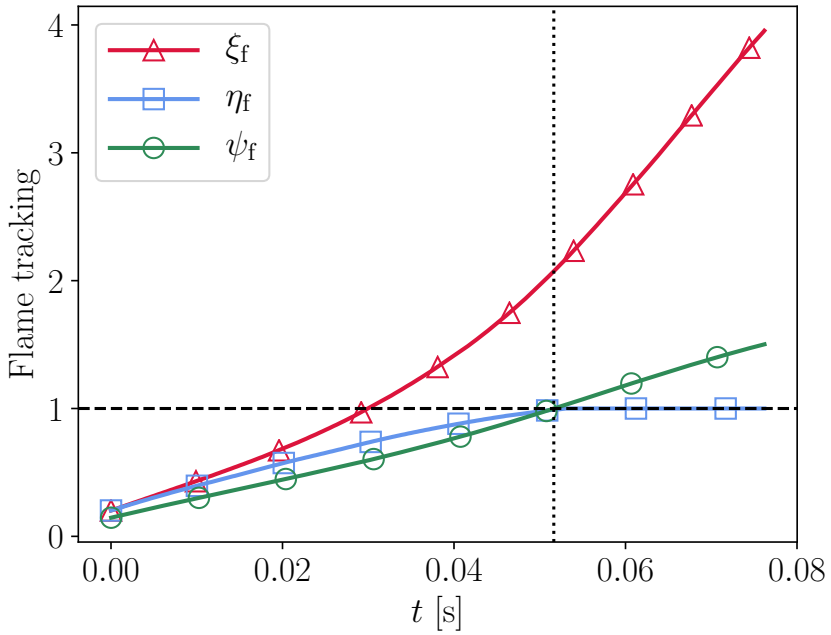

Figure 8.10: Various flame trackings of the DNS flame as a function of time. Dashed horizontal black line: R_{tube} limit. Dotted vertical black line: abscissa for $\psi_f = 1$.

and the skirt diverge;

- a slight vertical shift exists between ψ_f and ξ_f (or η_f) right from the beginning while the flame is still perfectly spherical. It comes from the fact that the kinematic tracking ξ_f (or η_f) is based on a flame isocontour (discrete information) whereas the mass tracking ψ_f is inherently based on an integral quantity;

- the instant $\psi_f = 1$ corresponds approximately to the skirt collapsing on the lateral wall. At this same moment, the flame tip is around twice farther in the tube direction. This feature has also been noted in Hok *et al.* [319].

From all these considerations, saturating the TD efficiency as soon as $r_f = R_{\text{tube}}$ seems a simple solution to account for the saturation of TD instabilities in a confined environment:

$$E_{\text{TDS}}(r_f) = \min\left(E_{\text{TDS,sph}}(r_f), E_{\text{TDS,sph}}(R_{\text{tube}})\right) \tag{8.1}$$

where $E_{\text{TDS,sph}}$ denotes the efficiency function developed in the spherical framework in Chapter 7 (Equation (7.8)).

To evaluate the performance of the TD-S-TF model with the saturated efficiency, its propagation is compared with the DNS reference, the classical TF LES and the S-TF LES in Figure 8.11. For the sake of completeness, the former unsaturated TD-S-TF model is also plotted. This latter follows the DNS propagation in the beginning but overtakes it afterwards. By contrast, the saturation at $r_f = R_{\text{tube}}$ mitigates the flame acceleration to fall back in accordance with the DNS. A slight gap is observed at the end of the

propagation (after the end of the finger flame phase). The DNS seems to maintain an almost constant speed due to interactions of TD cells with the side wall.

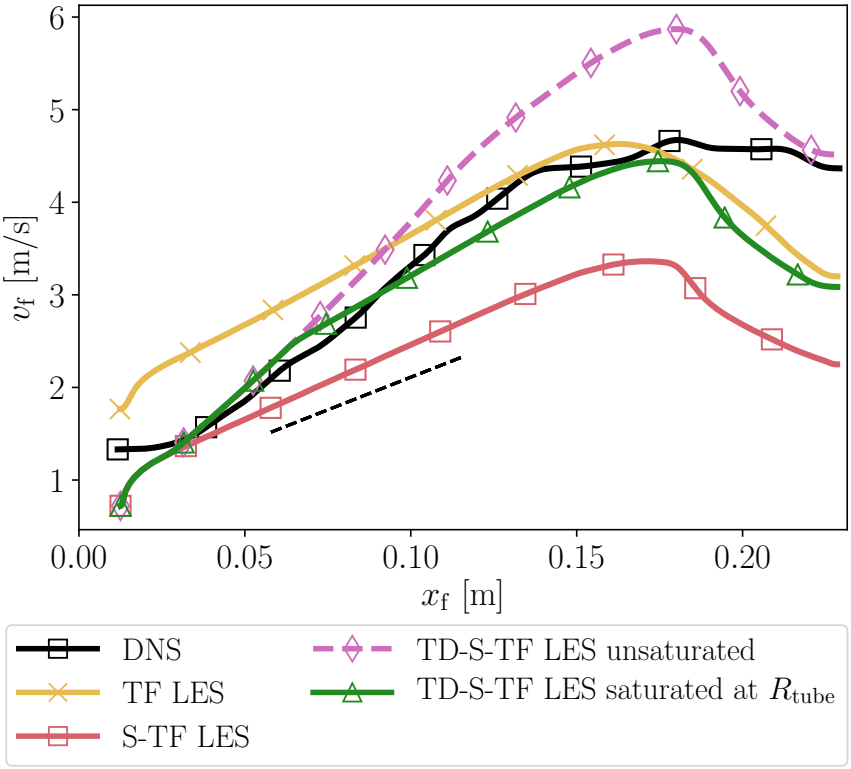

Figure 8.11: Flame speed as a function of flame tip position for the DNS and several LES models. 1S-LeFit chemistry.

8.4.2 Mesh dependency check

The dependency on the LES mesh resolution is also appraised for all TD-S-TF cases (with the saturated efficiency) in Figure 8.12. All curves are in relative good agreement with the DNS flame propagation. This is expected given that:

1. the S-TF model has solved the mesh dependency issue by aligning all stretch responses (Section 8.3.2);
2. the TD efficiency component is the same for all LES. It does not depend on the mesh resolution;
3. the saturated TD subgrid model has been proved able to correct the flame acceleration for one LES mesh in the last section.

Therefore, the TD-S-TF model as it has been extended in the present chapter proves relevant for the simulation of lean H_2-air explosions in confined environments, at least in the laminar regime.

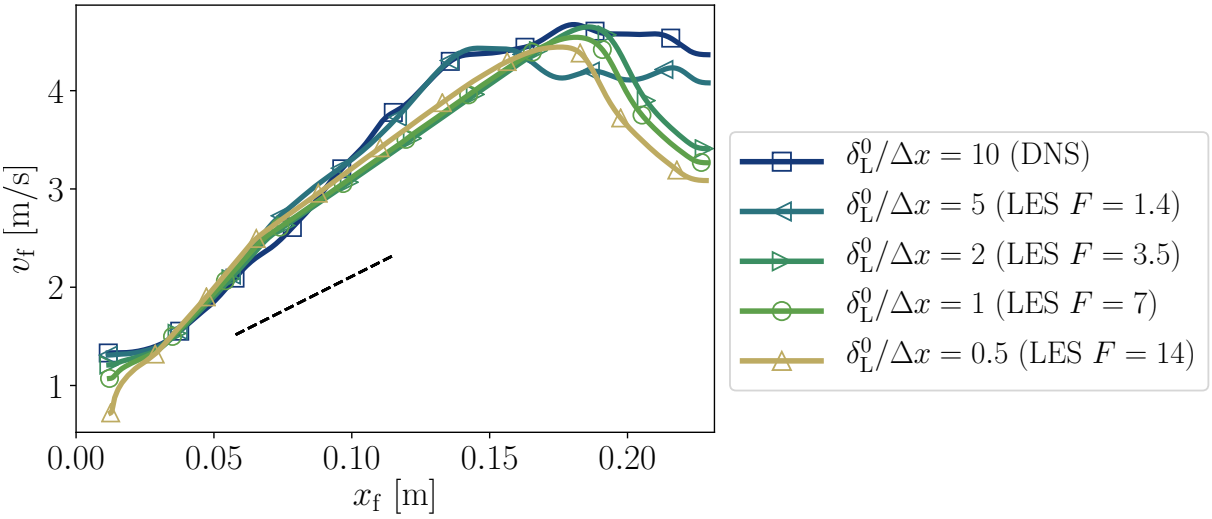

Figure 8.12: Flame speed as a function of flame tip position for several mesh resolutions (Table 5.4). 1S-LeFit chemistry. LES corrected with the TD-S-TF model with a saturated efficiency.

8.5 Comparison with other models

The TD-S-TF model can now be confronted to other models found in (or inspired from) the literature. These models have been thoroughly described in Chapter 7. They are briefly recalled and tested in the following sections.

8.5.1 Thermo-diffusive instabilities models reminder

Planar-TF model

The Planar-TF model is based on the work of Berger *et al.* [320] and Aniello *et al.* [321]. It relies on an efficiency factor extracted from the DNS of 2D planar lean H_2-air flames. In the present case of a fully premixed flame under ambient conditions, their correlation gives a constant value. It is used in conjunction with a unity-Lewis number chemistry 1S-Le1 thereafter. The laminar efficiency is activated right from the start of the simulations, thereby ignoring any unsteady development of the TD instability (in particular, the model does not include the notion of TD instability onset):

$$E_{\text{planar}} \approx 3.5 \tag{8.2}$$

Fractal-TF model

The Fractal-TF model originates from the fractal theory of flame front instabilities in a spherical flame context. A time evolution of the efficiency function is prescribed to mimic the dynamics of TD cells. It must also be used with a 1S-Le1 mechanism because the efficiency encompasses all effects of non-unity Lewis number. The function is saturated

at $r_\mathrm{f} = R_\mathrm{tube}$ like for the TD-S-TF model (cf. Equation (8.1)):

$$E_\mathrm{fractal}(r_\mathrm{f}) = \min\left[\max\left(1, \left(\frac{r_\mathrm{f}}{r_\mathrm{f,c}}\right)^d\right), \left(\frac{R_\mathrm{tube}}{r_\mathrm{f,c}}\right)^d\right] \tag{8.3}$$

8.5.2 Results

Both models are examined in contrast with the previously validated TD-S-TF approach in Figure 8.13. Like in the 2D spherical configuration of Chapter 7, the Planar-TF model largely overestimates the flame speed whereas the Fractal-TF model properly emulates the DNS propagation. The use of a constant subgrid efficiency (Planar-TF case) for the TD instabilities is once more inconsistent to describe accurately their evolution. On the other hand, the Fractal-TF approach performs better than in the previous chapter. This approach has been discarded in Chapter 7 for the simulation of spherical flames because stretch effects play an important role in the early, stable and globally-stretched phase of the propagation. In the present 2D tube set-up, the spherical phase of the propagation seems limited to the very first instants so that the TD-S-TF and Fractal-TF curves are superimposed. However, it is expected that in more complex cases, the use of the Fractal-TF model is not justified: the response to stretch remains wrong for the 1S-Le1 chemistry on which it relies. For instance, this may become important in situations where the laminar kernel pushes through an orifice and is thereby heavily stretched (see Section 3.2.3). In that case, the use of the TD-S-TF model is still valid (thanks to the S-TF correction) whereas the Fractal-TF approach becomes obsolete.

8.6 Variation of the tube radius

This last section is dedicated to substantiating the choice of saturation for E_TDS. So far, the strategy has been validated on a single geometry imposed by $R_\mathrm{tube} = 100\delta_\mathrm{L}^0$. A TD-S-TF LES is now performed in tubes with $R_\mathrm{tube} = 50\delta_\mathrm{L}^0$ and $R_\mathrm{tube} = 200\delta_\mathrm{L}^0$ on meshes at $\delta_\mathrm{L}^0/\Delta x = 0.5$ to verify that the model is able to account for the various intensities of flame front instability. It has indeed been demonstrated in Section 5.3.6 that the tube radius plays an important role in dictating the level of TD instability: a wider tube gives more room for cells to develop and also more time for the spherical flame stage. In a normalised framework, the effects of the TD instabilities on the macroscopic flame propagation are therefore stronger in larger tubes. The corresponding DNS and TD-S-TF LES are compared in Figure 8.14 along with TF and S-TF cases.

DNS

In DNS mode, the finger flame mechanism is stronger in the narrower tube (see Section 3.1.2) whereas TD effects are of lesser importance. TD effects become substantial in the larger tube as can be seen from the wiggles on the speed curve which result from the formation and destruction of TD "fingers".

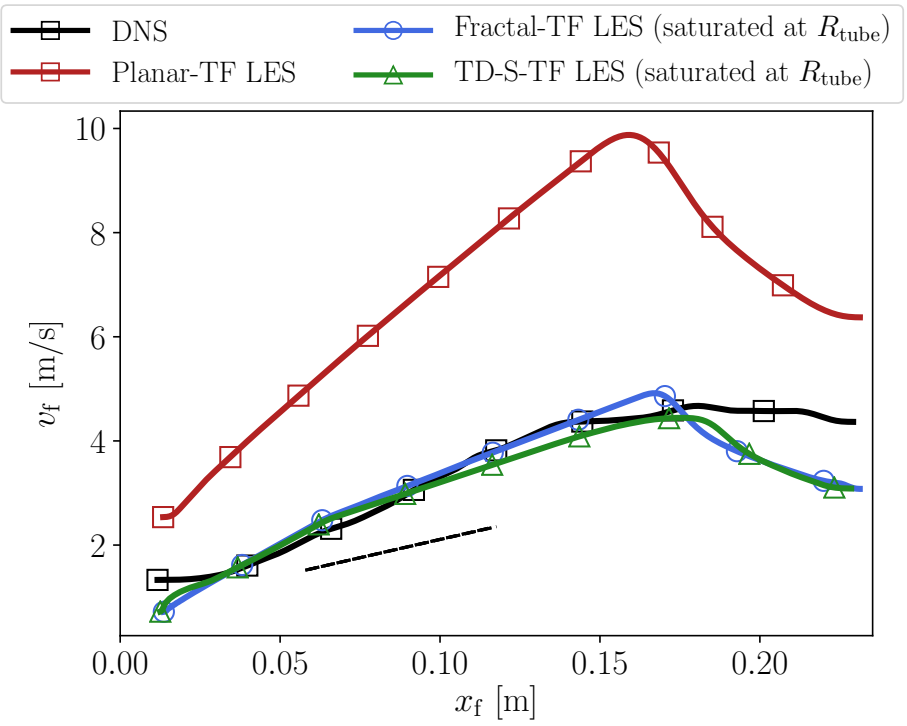

Figure 8.13: Flame speed as a function of flame tip position for several LES corrections.

TF LES

Comparing in each geometry the TF LES with the reference DNS suggests a different outcome of the TF shortcomings. These have been expressed many times so far and were summarised in Figure 5.22. A compensation mechanism is indeed observed between the loss of TD subgrid processes and the amplification of stretch effects when thickening the flame in a classical TF manner. The balance of both phenomena is in contrast for the two tubes considered herein:

- in the narrower tube, TD effects are small compared to the influence of the confinement as explained above. When one goes from DNS to LES, there is not so much cellularity to lose. The amplification of stretch is greater in comparison, thereby explaining the over-prediction of the acceleration;
- in the wider tube, the conclusions are opposite: the contribution of the thermo-diffusive instability to flame acceleration is considerably more important. This effect is lost in TF LES and is not compensated for by the amplification of stretch for the considered F value ($F = 14$). This explains the under-prediction of flame acceleration.

S-TF LES

In both tubes, the S-TF model brings down the flame speed compared to the TF model because of the correction of the stretch amplification by F. It is seen again that the smooth LES corresponding to the S-TF is very close to the DNS in the smaller tube because of the relatively negligible importance of TD effects in strongly confined cases.

TD-S-TF LES

Last but not least, the TD-S-TF model is able to catch up with the reference DNS flame propagation. This validates the use of this model along with a saturation at $x_\mathrm{f} = R_\mathrm{tube}$.

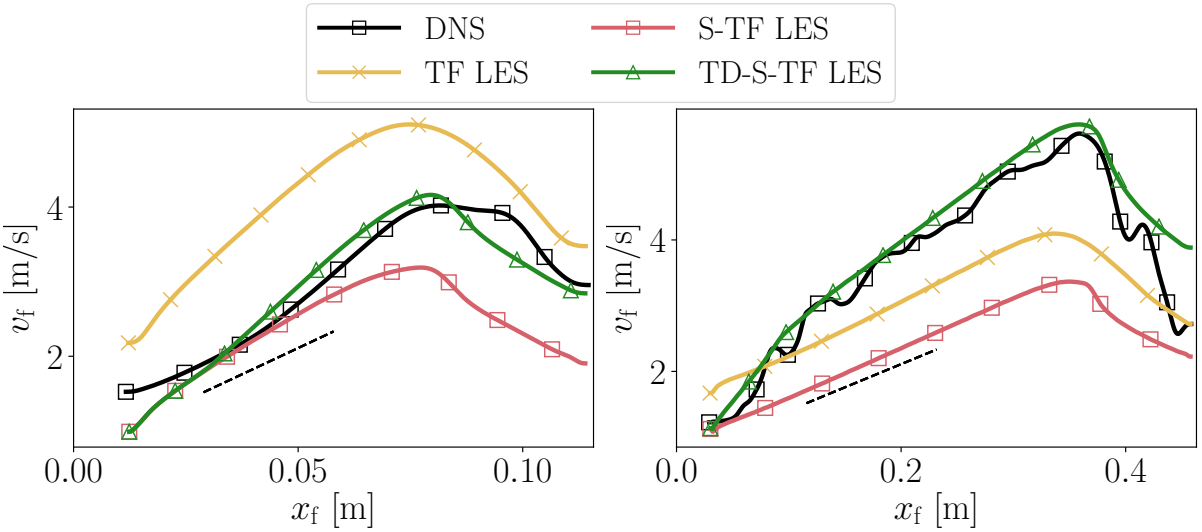

(a) $R_\mathrm{tube} = 50\delta_\mathrm{L}^0$ (b) $R_\mathrm{tube} = 200\delta_\mathrm{L}^0$

Figure 8.14: Flame speed as a function of flame tip position for tube geometry variants in DNS, TF LES and TD-S-TF LES approaches.

8.7 Conclusion

This chapter has dealt with the application of the Thermo-Diffusive-Stretched-Thickened Flame (TD-S-TF) model for the LES of lean hydrogen-air flames propagating in a tube. It has been aimed at answering the fundamental challenge raised in Chapter 5: to provide a correction to the classical Thickened Flame approach to produce predictive LES of lean H_2-air explosion in a confined environment.

The simple two-dimensional tube configuration of Chapter 5 has been re-used with novelties developed in Chapter 7. In particular, the new stretch-consistent global chemistry (called 1S-LeFit) is adopted.

In a validation procedure similar to Chapter 7, the two components of the model are distinguished. First, it has been shown in Section 8.3 that the Stretched-Thickened Flame (S-TF) model solves the mesh dependency by aligning the stretch response of all LES with that of the reference DNS flame. Then, Section 8.4 has treated of the TD efficiency function which encompasses all subgrid effects induced by the flame front instability. A modification of its expression has been designed to account for the confinement. Namely, it is shown that saturating its value when the flame mean radius approaches the tube radius proves effective. This traduces the fact that thermo-diffusive instabilities do not develop indefinitely in a confined geometry. All in all, the TD-S-TF model is able to reproduce the DNS flame propagation for all LES meshes considered in this chapter. In Section 8.6 the TD efficiency saturation strategy has been validated by performing DNS and TD-S-TF LES in tubes of various radii. In all cases, the TD-S-TF LES properly follows the acceleration of the DNS reference.

Even though saturating the TD efficiency at some value of flame radius remains a simple extension of the TD-S-TF model, it has broadened its scope of applicability. The step-by-step modelling strategy followed in Chapters 6, 7 and eventually the present one has laid down the fundamental components for the modelling of propagating lean H_2-air flames. The choice of the saturation parameter for confined cases other than the tube flame, however, remains to be determined. Simple options like the distance to the closest wall (except if the flame is ignited against a wall) must be evaluated. Another more important hurdle stands in the way to apply the TD-S-TF model to real complex explosions: turbulence-flame interactions. This issue is addressed in the next chapter.

Chapter 9

Application to flame propagation in a confined and obstructed environment: the ENACCEF2 case

Sommaire

The last chapter of this thesis deals with the application of the Thermo-Diffusive-Stretched-Thickened Flame (TD-S-TF) model to a full large-scale explosion configuration. However, the proposed correction strategy has only been developed and validated on laminar flame propagation so far. As detailed in Chapter 3, real explosion scenarios often involve several propagation regimes which can start from a slow deflagration in laminar mode and then transition towards a fast-flame regime correlated with strong turbulence-flame interactions. For example, the ENACCEF2 (*ENceinte d'ACCElération de Flamme 2*) explosion tube [57] has been designed to mimic such sequence of events for lean hydrogen-air mixtures. It thus represents an interesting last test case for the application and testing of the TD-S-TF model. The presence of turbulence considerably complicates the whole picture. Indeed, while turbulent efficiency functions exist to model the subgrid chemistry-turbulence interactions in classical mixtures, several issues arise when dealing with lean H_2-air flames:

- from a pure physical point of view: how do flame front instabilities and turbulent wrinkling interact? As briefly discussed in Section 3.2.3, this problem is still to this date an open issue and an active research topic;
- from the LES point of view: on the one hand, the turbulent efficiency function tries to model subgrid effects purely due to turbulence; on the other hand, the thermo-diffusive efficiency function is built for pure flame front instabilities. How should the two quantities be coupled in a real turbulent and TD-unstable LES?

The present chapter attempts to answer these questions. To do so, the ENACCEF2 experimental bench as well as its numerical twin are described in Section 9.1. In Section 9.2, a short digression is made to consider the practical effects of gravity in DNS and LES. In the ENACCEF2 experiments, the mixture is ignited at the bottom of a vessel and propagates upwards so that buoyancy effects linked to gravity (cf. Sections 2.3.3 and 2.3.4) are expected. This is further supported by the low values of unstretched laminar flame speeds

in the considered mixtures. Section 9.3 presents the phenomenology of the ENACCEF2 explosion using a classical Thickened Flame approach. Finally, Sections 9.4 and 9.5 assess the performance of the TD-S-TF model for two different lean mixtures.

9.1 Set-up description

The following section is dedicated to the description of the experimental ENACCEF2 test rig as well as the numerical procedure used for its simulation. Emphasis is put on the extension of the TF LES model to account for the pressure rise in the vessel.

9.1.1 Geometry and experimental diagnostics

ENACCEF2 experimental test rig is located at ICARE laboratory in Orléans [57]. It is composed of a 7.65-meter's long cylindrical tube fully closed with an inner diameter of $D_{\text{tube}} = 230$ mm. The tube is vertically installed and the flame ignited at the bottom, meaning that gravity potentially affects its propagation. For the sake of simplicity, the vertical coordinate corresponding to the tube axis of symmetry is noted x like what was done in the previous chapters and $x = 0$ corresponds to the bottom. 9 annular 4-mm's thick obstacles are placed inside the rig in order to obstruct the volume with a blockage ratio equal to 63% (leading to an inner diameter of $d_{\text{obs}} = 140$ mm). The first obstacle is located at $x^1_{\text{obs}} = 0.640$ m allowing a long laminar phase before the flame enters the obstructed region. All obstacles are equally spaced at a distance equal to D_{tube} (see Table 9.1 for the exact positions). The last obstacle is placed at $x^9_{\text{obs}} = 2.480$ m, the remaining part of the tube, representing approximately 2/3 of the tube, is obstacle free. A general overview of ENACCEF2 is given in Figure 9.1.

Obstacle #	1	2	3	4	5	6	7	8	9
Obstacle x^i_{obs} position [m]	0.640	0.870	1.100	1.330	1.560	1.790	2.020	2.250	2.480

Table 9.1: Obstacle positions in ENACCEF2. Note that $L_{\text{tube}} = 7.65$ m.

Experimental diagnostics include photomultipliers scattered along the channel height which measure the time of arrival of the combustion wave. A basic derivation then yields the flame tip velocity at a couple of locations in the tube. The uncertainty on this velocity has been determined at $\pm 8.81\%$ [57]. The pressure inside the vessel is monitored by 10 pressure probes, 9 of which are equally scattered in the vessel and the last one placed at the centre of the top plate. The reader may refer to Grosseuvres [57] for an exhaustive description of the experimental set-up.

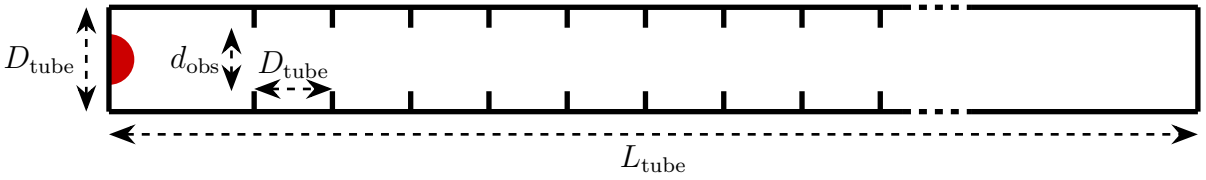

(a) 2D schematic with dimensions. Red half-disk: initial flame kernel.

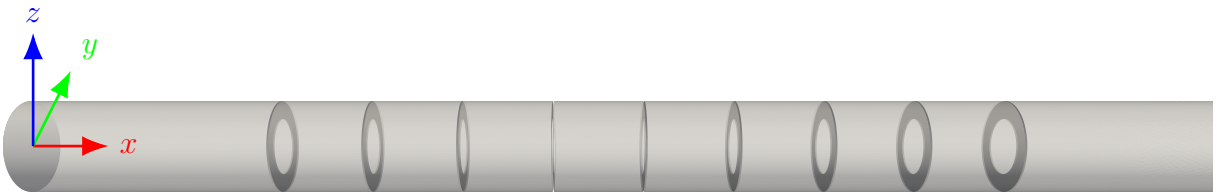

(b) 3D render view.

Figure 9.1: Overview of the ENACCEF2 explosion configuration. Both figures are rotated by 90° (the real set-up being vertical with ignition at the bottom).

9.1.2 Operating conditions

The original work of Grosseuvres [57] includes several experimental campaigns aimed at assessing the effect of initial temperature (homogeneous and temperature gradients) and water vapour dilution on flame propagation [322]. In this thesis, attention is focused on atmospheric initial temperature and pressure. Three H_2-air mixture compositions were studied in the experiments: $X_{H_2} = 11\%$ ($\Phi \approx 0.294$), $X_{H_2} = 13\%$ ($\Phi \approx 0.356$) and $X_{H_2} = 15\%$ ($\Phi \approx 0.420$). The gist of this chapter is focused on the last case at $\Phi = 0.420$. A leaner case ($\Phi = 0.356$) is also investigated in Section 9.5 and compared to the reference. Flame properties under such conditions are summarised in Table 9.2.

Φ	S_L^0 [m/s]	δ_L^0 [μm]	T_{ad} [K]
0.356	0.13	850	1320
0.420	0.29	515	1467

Table 9.2: Flame properties under ENACCEF2 operating conditions.

9.1.3 Boundary conditions

The ENACCEF2 vessel is fully closed so that one must only choose boundary conditions for the walls. The duration of the explosion is believed to be sufficiently short so that heat transfers from the flame to the walls is negligible: the walls are assumed to stay at their initial atmospheric temperature. For the flow, a no-slip condition is not suited to the present simulations given the low mesh resolutions considered herein in the near-wall regions (as will be detailed in Section 9.1.4). Instead, a law-of-the-wall formalism is

chosen [323].

9.1.4 Meshes

The whole 3D domain is discretised using tetrahedral elements. Particular attention is paid to the mechanisms responsible for the flame acceleration observed in ENACCEF2. Therefore the mesh strategy is designed to focus on the obstructed region of the tube and the resolution is piece-wise constant (see Figure 9.2):

- a general mesh resolution denoted Δx_{fine} is imposed from the ignition plate (bottom of the vessel) up to after the last obstacle. When the mesh resolution is mentioned from now on, it refers to Δx_{fine} because this first section of the tube is where the analysis is focused;

- around the obstacles, the cell size must be reduced in order to refine the "lip" of each obstacle: $\Delta x_{\text{lip}} = 0.8$ mm allows 5 cells within the obstacle thickness. Note that the thinness of these annular obstructions strongly constrains the minimal mesh cell size and thereby reduces the time step of the simulation;

- far after the regions of the obstacles, the mesh cell size is reduced back to a constant value at $\Delta x_{\text{coarse}} = 10$ mm. This is justified by the decrease of turbulence-flame interactions in this region (as will be shown in Section 9.3.1) and allows to reduce the computational cost.

Similarly to the previous chapters, several meshes are constructed to evaluate the impact of resolution on the numerical/physical models and the overall flame propagation. However, the mesh cell size is bounded by two effects:

1. the inner diameter of the obstacles d_{obs} constitutes an upper bound for Δx_{fine}. A maximum mesh cell size of $\Delta x \leq d_{\text{obs}}/(2F\delta_{\text{L}}^0) = d_{\text{obs}}/(2N_{\text{c}}) = 10$ mm is necessary to allow for at least two flame thicknesses to pass through the annular orifice and avoid potential flame extinctions;

2. the lower bound is simply imposed by computational costs.

Under these constraints, two mesh resolutions are considered: $\Delta x_{\text{fine}} = 2$ mm and $\Delta x_{\text{fine}} = 4$ mm. They allow for 10 and 5 flame thicknesses across the obstacles cross-section, yielding in total 77 million and 13 million cells respectively. Table 9.3 gives the resulting flame thickening factor in ENACCEF2 conditions under the initial atmospheric temperature and pressure.

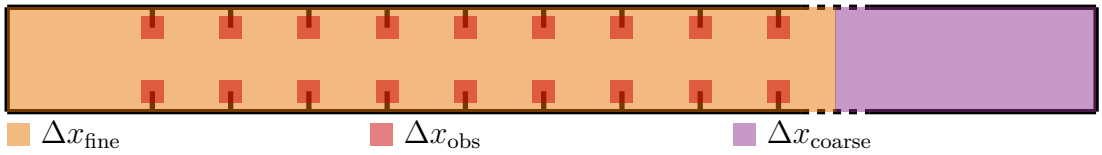

Figure 9.2: Schematic of the different mesh resolution zones.

Equivalence ratio Φ	**Mesh cell size** Δx_{fine} **[mm]**	**Thickening level** F **(imposed by** Δx_{fine}**)**	$\delta_{\text{L}}^0/\Delta x_{\text{fine}}$	$F\delta_{\text{L}}^0/\Delta x_{\text{fine}}$
0.356	2	16.5	0.424	7
	4	33.0	0.212	7
0.420	2	27.3	0.257	7
	4	54.5	0.128	7

Table 9.3: Summary of meshes and TF thickening factor (under atmospheric conditions) in ENACCEF2.

9.1.5 Initialisation procedure

In the experiments, the combustible mixture is ignited by a spark plug at the centre of the bottom plate. The fresh gases are approximately at rest. Following what has been argued in Section 7.2.1, the simulations are initialised by a hot kernel deposition rather than an energy deposition (see Figure 9.1a). The initial radius is fixed at $r_{\text{f},0} = 28$ mm to ensure at least 7 mesh cells across the hot kernel radius on the coarsest mesh (cf. Table 9.3). This value is still sufficiently far from the tube radius $R_{\text{tube}} = 115$ mm to justify the use of a spherical flame initialisation. Following the discussion detailed in Section 7.2.1, the profiles used for the initial kernel are taken from strained flames (1D counterflow premixed flames computed using Cantera) and the velocity profile is analytically determined from the consumption speed of the flame (see Section 7.2.1).

9.1.6 Chemistry

Following the strategy developed in Section 6.1, a global chemistry 1S-LeFit is tuned at the relevant operating conditions in terms of laminar flame speed, thermal thickness (Table 9.2) and response to stretch. In Section 7.1, it has been demonstrated that 1S-LeFit schemes provide a reliable response to stretch for operating conditions close to those encountered in ENACCEF2 (see Figure 2 of the publication). This is verified again for the present case $\Phi = 0.420$ in Section 9.1.8.

9.1.7 Turbulent combustion modelling in gas explosions

Flame thickening

In this chapter two approaches to flame thickening will be used for the ENACCEF2 test

case and compared with each other: (1) the TF LES model, corresponding the state-of-the-art modelling, (2) the TD-S-TF model specifically designed (Chapter 8) for the modelling of lean-hydrogen/air flames. The results for TF LES will be analysed in details in Section 9.3 and the impact of the TD-S-TF approach will be investigated in Section 9.4. The dynamic approach (DTF LES, described in Section 4.4.5) is needed to account for the variable mesh size.

Subgrid efficiency
All cases treated so far were laminar in nature. But in ENACCEF2, the presence of obstacles in the flame path generates turbulent wakes which progressively wrinkle the flame front, contributing to flame acceleration (see Section 3.2.2). To make up for the flame-turbulence interactions lost at subgrid scales, a turbulent efficiency function is used. The model of Charlette *et al.* [274] described in Section 4.4.6 is chosen with a standard $\beta = 0.5$ value. The goal of this study being to evaluate the TF and TD-S-TF LES approaches without further parameters variation, the value of β is kept constant for the entire chapter.

Model parameters
Both thickening and efficiency function need user inputs:

- to know to which extent the flame must be thickened, the DTF model requires the non-thickened flame thickness δ_{L}^0;
- the maximum thickening factor is imposed so as to guarantee $N_{\mathrm{c}} = 7$ points within the flame thickness (using Equation (4.68));
- on top of δ_{L}^0 and N_{c}, it also needs a reference reaction rate Ω_0 for the flame sensor (Equation (4.70));
- last but not least, the efficiency function of Charlette *et al.* [274] (Section 4.4.6) needs (in addition to the flame thickness δ_{L}^0) the laminar flame speed S_{L}^0 to compare with the flow velocity fluctuations at the LES filter size (Equation (4.78)).

In a standard premixed flame LES, all of these parameters are easily retrieved from a single 1D planar flame computation (using CANTERA for instance). However, in confined explosion configurations such as ENACCEF2, the propagation of the deflagration leads to a pressure increase in the whole combustion chamber. As explained in Chapter 3, it is related to the piston-like effect due to thermal expansion across the flame. This general pressure rise in the vessel affects the properties of the combustible mixture and that of the resulting flame. $(S_{\mathrm{L}}^0, \delta_{\mathrm{L}}^0, \Omega_0)$ must therefore account for these variations. In AVBP, this is done through the use of a table, referencing the model parameters as a function of $(T_{\mathrm{u}}, P, \Phi)$ for example. For ENACCEF2, mixture composition does not change, but temperature and pressure do. The latter do not vary independently. Instead, the preheating due to compression is assumed to follow an isentropic path. In practice, $(S_{\mathrm{L}}^0, \delta_{\mathrm{L}}^0, \Omega_0)$ are tabulated against $(P, T_{\mathrm{u}}(P))$. For a calorifically perfect gas compressed

from $(P_0, T_{\mathrm{u},0})$ to a pressure P, the Laplace relation reads:

$$T_{\mathrm{u}}^{\gamma} = \frac{P^{\gamma-1}}{P_0^{\gamma-1}} T_{\mathrm{u},0}^{\gamma} \tag{9.1}$$

where $\gamma \equiv C_p/C_V$ is the heat capacity ratio and P_0 and $T_{\mathrm{u},0}$ denote the nominal values. Even if γ is not constant in practice, Equation (9.1) provides compression results that are in excellent agreement with the more general implicit relation:

$$\frac{P}{P_0} = \exp\left(\frac{s^0(T_{\mathrm{u}}) - s^0(T_{\mathrm{u},0})}{R}\right) \tag{9.2}$$

where s^0 is the standard entropy of the fresh gases system, found in thermodynamic tables [215]. The isentropic hypothesis will be verified in Section 9.3.1. It is believed to be a good approximation as long as shock waves are not present in the vessel.

9.1.8 Isentropic compression for the global chemistry

Before going further, a quick check about the chemistry is necessary. Global mechanisms are indeed built to fit flame properties of a detailed scheme in a narrow range of operating conditions. The aforementioned compression (and preheating) of fresh gases may push them out of the 1S-LeFit scheme scope of applicability. To verify its suitability for ENACCEF2 simulations, the pressure response is evaluated for the detailed and global chemistries in Figures 9.3 to 9.5 (computed with 1D unstretched planar flames using Cantera). For the isentropic compression cases, the gases are considered to be pressurised from the nominal atmospheric conditions $(P_0, T_{\mathrm{u},0})$ up to $(P, T_{\mathrm{u}}(P))$. The maximum pressure has been set to 10 atm according to experimental measurements with pressure probes [57], but it will be shown in Section 9.3.1 that for most of the flame propagation, the pressure in the regions it crosses does not go beyond 5 atm. By construction, the 1S-LeFit properties at $(P_0, T_{\mathrm{u},0})$ perfectly match those of the detailed reference. When the pressure is increased without preheating of the gases, a deviation is observed. For a single-step irreversible reaction, the laminar flame speed response to pressure is fully determined by the pair of partial reaction orders of the fuel and oxidiser n_{F} and n_{O} (defined in Section 4.2.2) [62, 223]:

$$S_{\mathrm{L}}^0 \propto P^{n/2-1} \tag{9.3}$$

where $n = n_{\mathrm{F}} + n_{\mathrm{O}}$. Their value in the global chemical scheme has directly been chosen following the method of Sun *et al.* [101] to match:

$$\left.\frac{\partial S_{\mathrm{L}}^0}{\partial P}\right|_{P=P_0}^{(1\mathrm{S-LeFit})} = \left.\frac{\partial S_{\mathrm{L}}^0}{\partial P}\right|_{P=P_0}^{(\mathrm{Detailed})} \tag{9.4}$$

But given that this relation is constrained to pressure values close to P_0, the behaviour of $S_{\mathrm{L}}^0(P)$ at greater pressures is not guaranteed: it explains the deviation between global and detailed mechanisms at high pressure (Figure 9.3a). This difference is even more striking

for the flame thickness curves: the detailed scheme presents a non-monotonic trend which is not captured by the 1S-LeFit scheme (Figure 9.4a).

When one considers the preheating of the fresh mixture following an isentropic compression (Figures 9.3b, 9.4b and 9.5b), the agreement between 1S-LeFit and detailed schemes up to 5 bars is compelling. The gap in terms of laminar flame speed is reduced. The relative error at $P = 5$ atm is slashed from 68% to 6.8%. For the adiabatic flame temperature and the thermal flame thickness, curves are almost superimposed. This improvement is due to the fact that the dependency of S_L^0 with respect to T_u now also becomes important. Note that the activation energy of the global scheme has been set so as to match the thermal sensitivity of the detailed mechanism following the method of Sun *et al.* [101]:

$$\left.\frac{\partial \ln\left(\rho_\mathrm{u} S_\mathrm{L}^0\right)}{\partial(1/\mathrm{T_b})}\right|_{\Phi=\Phi_0}^{(\mathrm{1S-LeFit})} = \left.\frac{\partial \ln\left(\rho_\mathrm{u} S_\mathrm{L}^0\right)}{\partial(1/\mathrm{T_b})}\right|_{\Phi=\Phi_0}^{(\mathrm{Detailed})} \tag{9.5}$$

This is well visualised when the flame properties are plotted against temperature and pressure for the two chemistries (see Figures 9.6 and 9.7). Along the path of isentropic compression (white dashed curve), the flame speed and thickness follow the same evolution for both schemes. All these considerations justify the suitability of the global 1S-LeFit chemistry for the LES of the ENACCEF2 configuration. On top of that, the contour plots point out the importance of taking preheating of the gases into account: while S_L^0 decreases for a standard compression, it goes up for the isentropic transformation. The validity of the isentropic compression assumption is verified in Appendix D for the ENACCEF2 explosion at $\Phi = 0.420$.

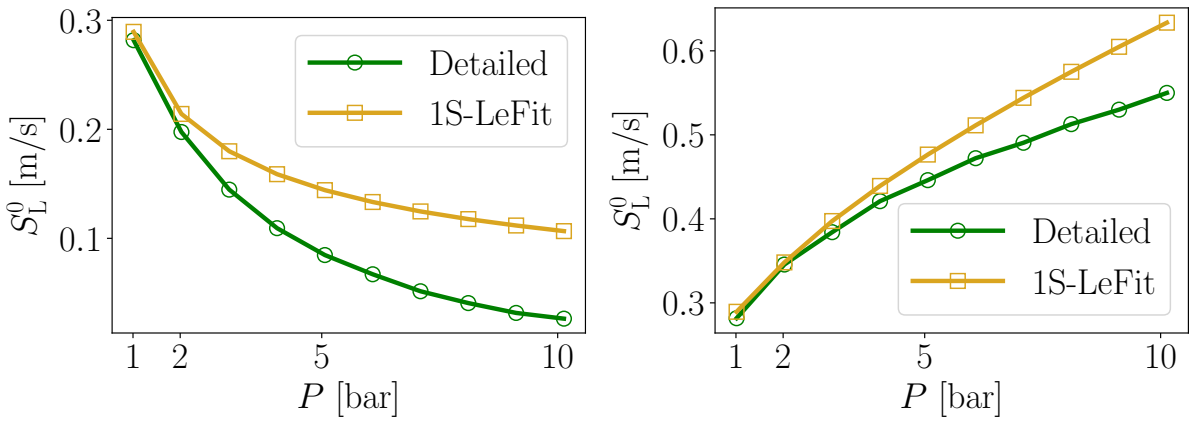

(a) Simple compression without preheating. (b) Isentropic compression (preheating).

Figure 9.3: Laminar flame speed as a function of pressure for a H_2-air premixed flame at $\Phi = 0.420$.

Now that the unstretched laminar flame properties of the global chemistry have been validated against the detailed scheme, the response to stretch in pressurised conditions must also be checked. The 1S-LeFit has indeed been developed to match the reference response to stretch of the detailed mechanism at atmospheric temperature and pressure $(P_0, T_{\mathrm{u},0})$. This is shown in Figure 9.8a where the consumption speed of 1D counter-

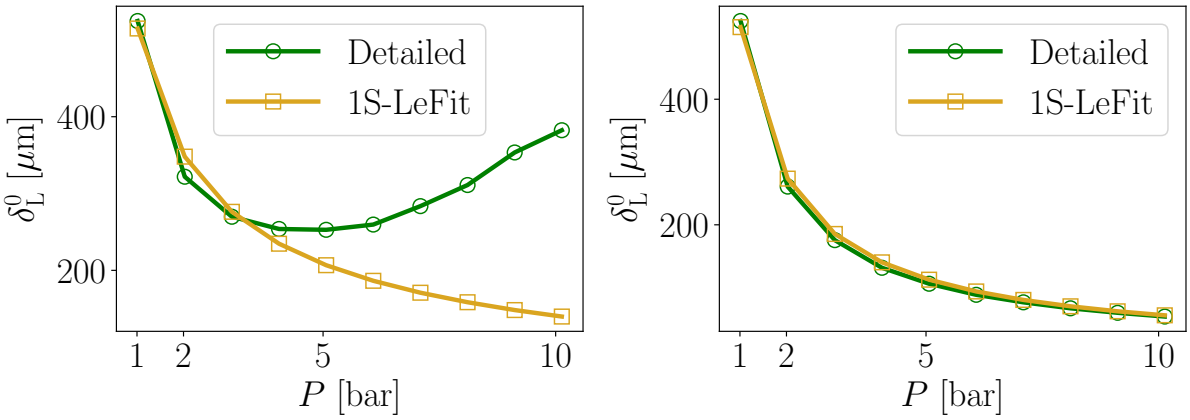

(a) Simple compression without preheating. (b) Isentropic compression (preheating).

Figure 9.4: Flame thermal thickness as a function of pressure for a H_2-air premixed flame at $\Phi = 0.420$.

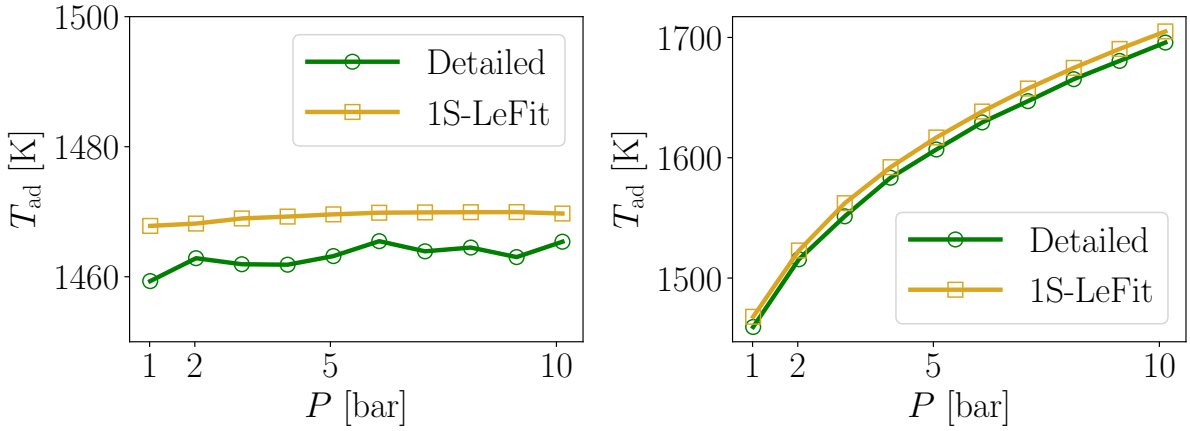

(a) Simple compression without preheating. (b) Isentropic compression (preheating).

Figure 9.5: Adiabatic flame temperature as a function of pressure for a H_2-air premixed flame at $\Phi = 0.420$.

flow premixed flames (computed with CANTERA) at different strain rates are compared. However, the behaviour at greater pressure is not guaranteed. Figure 9.8b shows that the response to stretch is still correctly predicted at $P = 3$ atm following an isentropic compression of the fresh gases. Despite a slight vertical shift, the curves have the same trend. Note that the maximum strain rate has been set at around S_L^0/δ_L^0 for both figures.

All the discussions of this section confirm that the 1S-LeFit chemistries are adapted to the simulation of the ENACCEF2 explosion scenario.

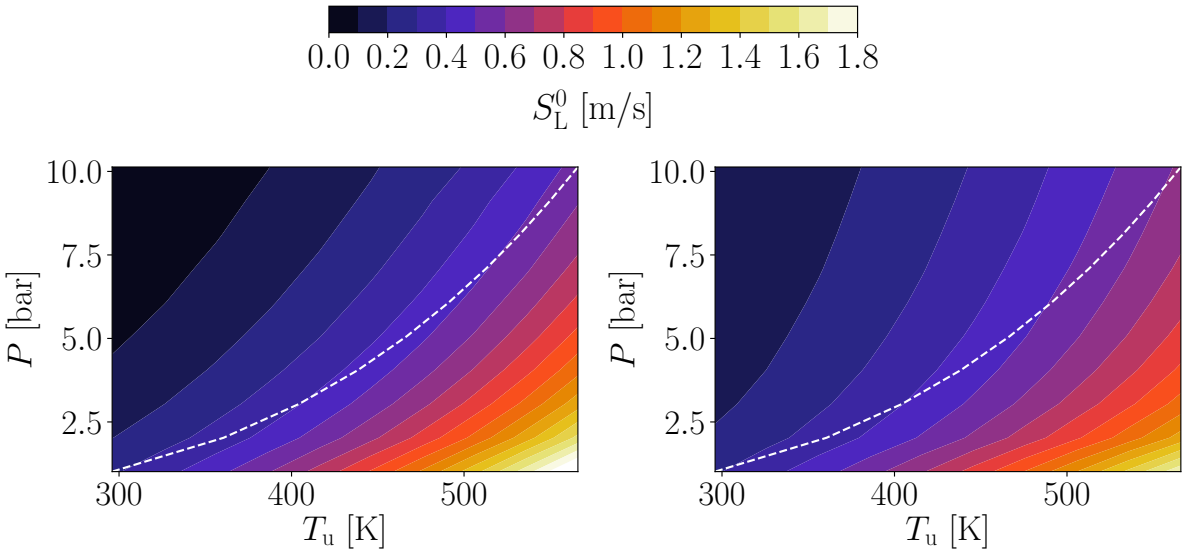

(a) Detailed scheme. (b) 1S-LeFit scheme.

Figure 9.6: Laminar flame speed as a function of pressure and temperature for a H_2-air premixed flame at $\Phi = 0.420$. White dashed line: isentropic compression curve (Equation (9.2)).

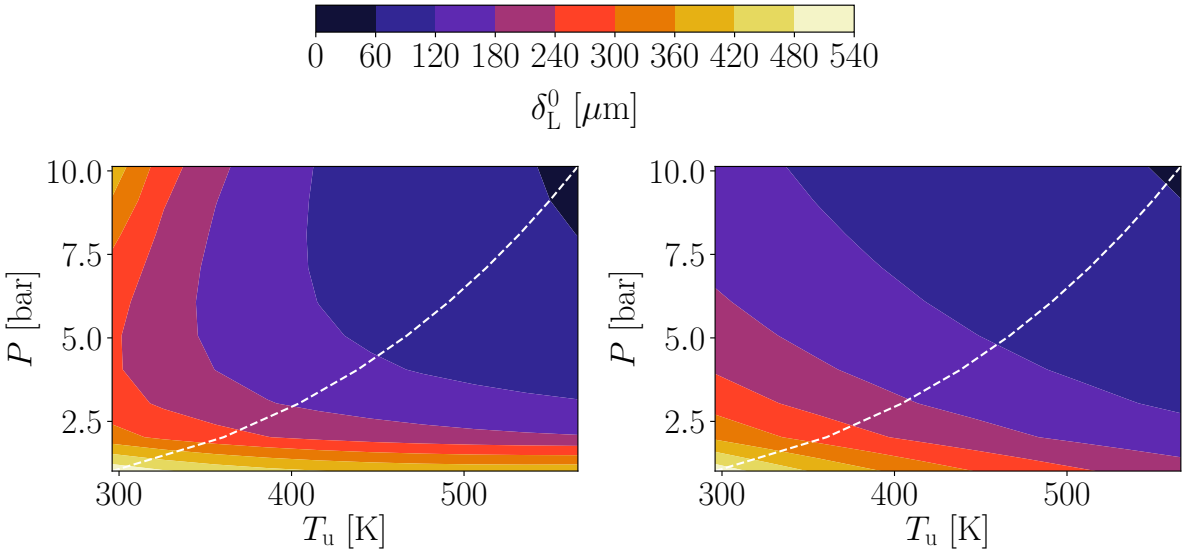

(a) Detailed scheme. (b) 1S-LeFit scheme.

Figure 9.7: Thermal flame thickness as a function of pressure and temperature for a H_2-air premixed flame at $\Phi = 0.420$. White dashed line: isentropic compression curve (Equation (9.2)).

9.2 On the importance of gravity

The following section deals with the potential effects of gravity in an explosion (from theoretical considerations in Section 9.2.1 and a practical assessment in Section 9.2.2)

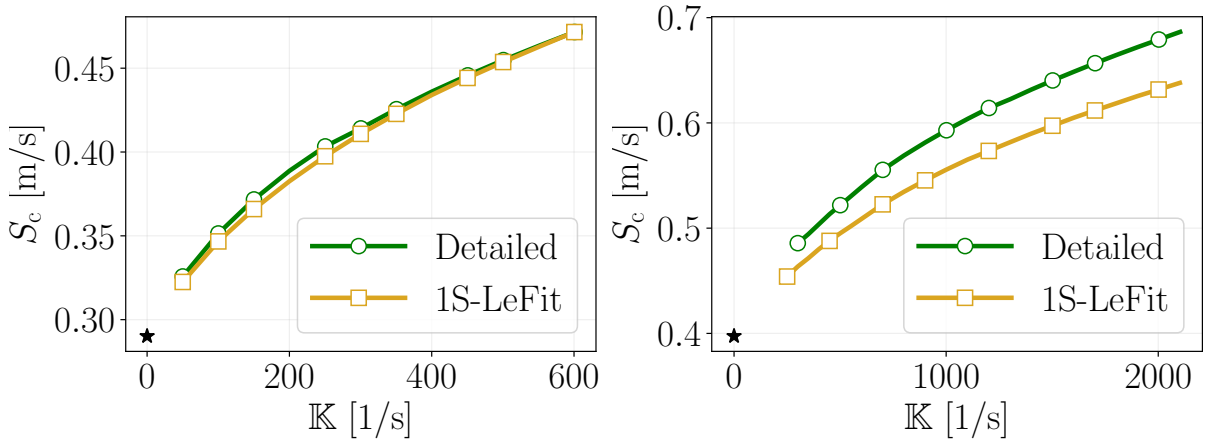

(a) Nominal conditions ($P_0, T_{u,0}$).

(b) Isentropically compressed conditions (P = 3 atm, $T_u(P)$).

Figure 9.8: Counterflow premixed flame response to strain for a H_2-air premixed flame at $\Phi = 0.420$. Left: nominal conditions of pressure and temperature. Right: isentropic compression up to 3 atm.

and the implications for the numerical modelling (Section 9.2.3).

9.2.1 Theoretical considerations

Apart from the presence of obstacles and the pressure rise, another phenomenon adds up to the complexity of the ENACCEF2 configuration: gravity. So far, its effects have been neglected in Chapters 5 to 8. Even though the density gap between the burning kernel and the fresh mixture is enormous, gravity is seldom accounted for in explosion simulations. This is often justified by a scales analysis using the Froude number [205, 324, 325]. This non-dimensional quantity measures the relative importance of gravity (natural convection) versus the flame propagation[1]:

$$\mathrm{Fr}_{\mathrm{bulk}} \equiv \frac{{S_L^0}^2}{gD} \tag{9.6}$$

where $g \approx 9.81$ m.s^{-2} is the acceleration of gravity and D represents a characteristic hydrodynamic size such as the tube diameter. In most situations, $\mathrm{Fr}_{\mathrm{bulk}}$ is high enough so that the time scale of flame propagation is shorter than that of buoyancy effects. Equation (9.6) suggests that the influence of gravity becomes more important for slow flames propagating in large tubes (leading to $\mathrm{Fr}_{\mathrm{bulk}} \ll 1$). However, the use of a single scalar quantity is not enough to thoroughly characterise the problem: the direction of the gravitational field also plays a crucial role. Several authors [324, 326] have indeed shown that even in narrow tubes, gravity substantially affects the flame dynamics when

[1] In the literature, some authors prefer using the square root of Equation (9.6) to define the Froude number. The analysis of orders of magnitude remains identical.

the propagation is horizontal. Due to buoyancy, the original symmetry of the flame is broken and a slanted flame is generated. In vertical tubes, the effects vary depending on whether one considers upward or downward propagation. The difference becomes all the more striking near flammability limits [327–329]. In upward propagation such as in ENACCEF2, a bubble-like flame front can arise, formed of light, hot matter pushed up into the denser fresh mixture. Such structure has been introduced in Section 2.3.4 in the context of spherical flames but is still present in confined explosions. Shtemler and Sivashinsky [330] have demonstrated that the main distinction with free-atmosphere explosions occurs near the lateral walls with the presence of an elongated flame skirt.

As previously shown in Sections 2.3.3 and 2.3.4, in addition to bulk effects, gravity is also at the origin of buoyancy-driven (or Rayleigh-Taylor) instabilities at a local level[1]. They are exaggerated for upward propagation like in the case of ENACCEF2. Nonetheless, in Large-Eddy Simulation, these wrinkles are no more resolved than thermo-diffusive instabilities. While TD effects focused the attention of this manuscript so far, the addition of gravity naturally leads to the following question: should buoyancy instabilities also be modelled for LES? The next sections give some insights to answer this problematic.

9.2.2 Practical assessment of gravity effects in a 2D tube

After the theoretical approach, this section is dedicated to quantitatively measuring the aforementioned effects of gravity. To properly resolve Rayleigh-Taylor instabilities (as well as thermo-diffusive instabilities), a DNS is needed. Given that a full DNS of ENACCEF2 is obviously not affordable, the 2D tube configuration of past chapters is used again here (cf. Section 5.1). It resembles the early laminar phase of the ENACCEF2 explosion. The numerical set-up introduced in Chapter 5 is recycled with some adaptations:

- the tube radius is adjusted to match ENACCEF2;
- the tube length is increased until the position of the first obstacle in ENACCEF2 ($L_{\text{tube}} = x^1_{\text{obs}}$);
- the operating conditions now correspond to the $\Phi = 0.420$ mixture used in ENACCEF2;
- the 1S-LeFit chemistry is used;
- the mesh resolution is accordingly adapted to impose $\delta^0_{\text{L}}/\Delta x = 10$ points within the flame thermal thickness.

Using this configuration, two DNS are carried out: one without gravity and the other with gravity (in the $-x$ direction like in ENACCEF2).

[1]Note that in Section 2.3.3, another Froude number based on the perturbation wave number has been introduced. It must not be confounded with the bulk Froude number defined by Equation (9.6).

Figure 9.9 compares snapshots of heat release rate at several instants of the propagation for the two DNS. The resemblance between both simulations is striking. The analysis can be split at several scales:

- at a local level, looking at instability cells for the same instant, one can conclude that the Rayleigh-Taylor instability does not significantly change the shape of the instability patterns;
- from a global point of view, one notices that for the few snapshots at the end of propagation, the flame front with gravity is slightly elongated in the direction of the tube axis. This is due to buoyancy effects as a bulk (cf. Section 2.3.4): the flame kernel rises towards the fresh gases due to its lesser density.

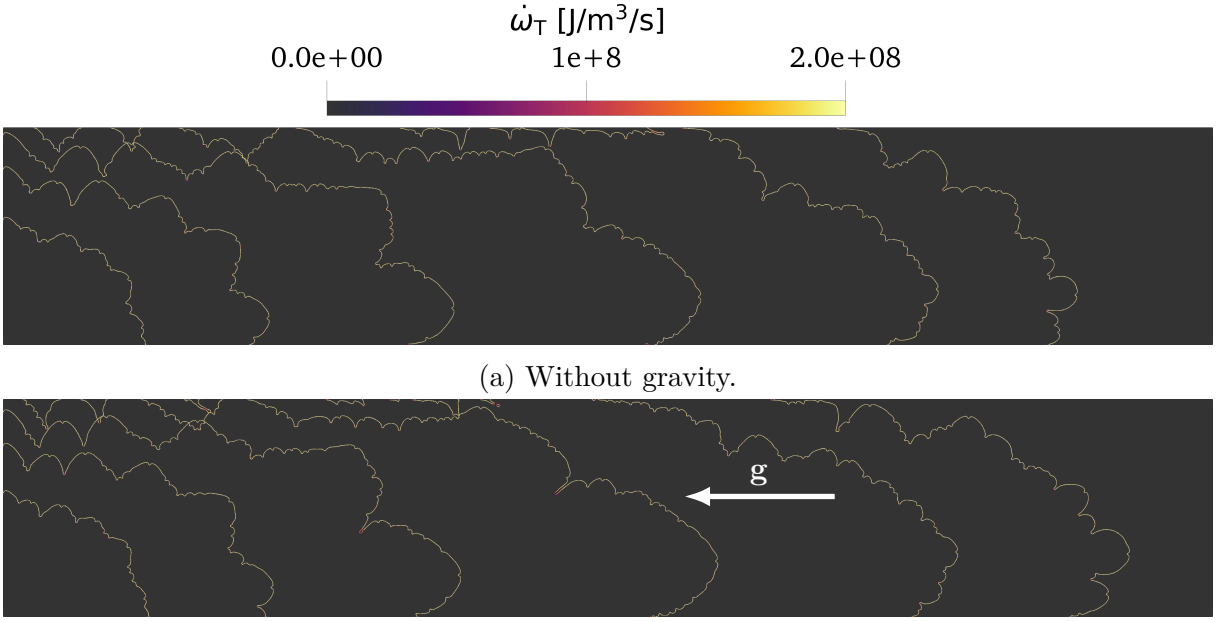

(a) Without gravity.

(b) With gravity.

Figure 9.9: Superimposition of heat release rate profiles at several instants of flame propagation in DNS. Top: without gravity. Bottom: with gravity.

The influence of gravity is quantitatively assessed in Figure 9.10. In the $x_f - v_f$ phase space (Figure 9.10a), the agreement between the two simulations is perfect during the initial transient (point 1) and the finger flame acceleration phase (point 2). At the end of it (point 3), the two curves diverge, indicating that gravity extends (albeit slightly) the duration of the finger flame stage. Note that the very end of the propagation (point 4) is not really of interest for the present study because it is close to the outlet of the tube whereas an obstacle is present at that position in ENACCEF2 ($L_{\text{tube}} = x^1_{\text{obs}}$) which would induce a flame acceleration depleting the impact of gravity (see Section 9.3 below). Now, Figure 9.10b shows similar conclusions, with an increased flame surface in the presence of gravity close to the end of the finger flame phase.

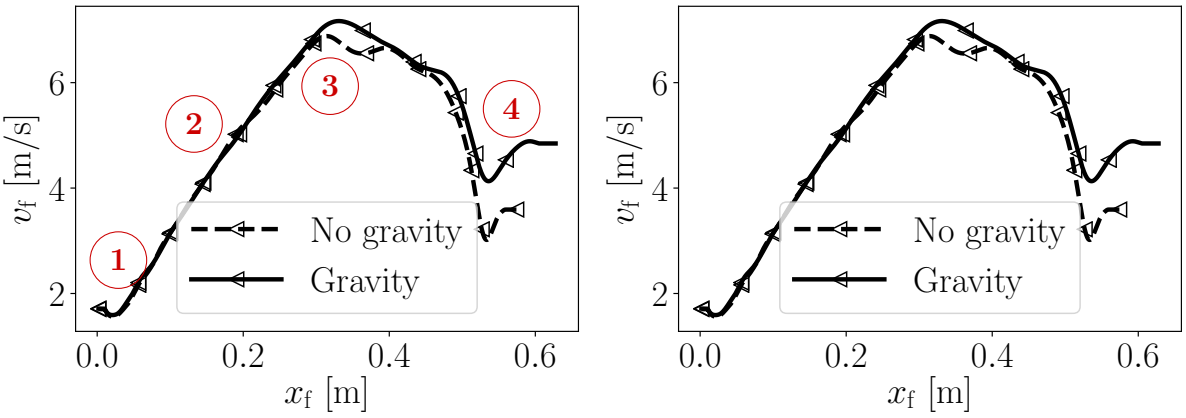

(a) Flame speed.

(b) Flame surface (Equation (2.71)).

Figure 9.10: Flame properties as a function of flame tip position for the DNS with and without gravity.

Except for the slightly prolonged finger flame phase, the results of this section seem to suggest that, in the operating conditions of ENACCEF2, gravity does not significantly affect the flame propagation in a DNS simulation. The next section evaluates its effects in LES using the classical Thickened Flame approach.

9.2.3 Influence of the Thickened Flame model on gravity effects

While gravity has a weak influence on the flame global evolution in DNS mode, its interaction with the Thickened Flame model in LES must be assessed. To do so, the numerical set-up of the previous section is adapted by coarsening the mesh. Given that the present study is in the end meant for ENACCEF2, LES resolutions considered in the following correspond to those used in the full 3D ENACCEF2 simulations (cf. Section 9.1.4), namely: $\Delta x = 2$ mm and $\Delta x = 4$ mm. On each of the meshes, one simulation without gravity and another with it are again carried out.

For the case $\Delta x = 2$ mm, a superimposition of heat release rate fields at several instants of the propagation is plotted in Figure 9.11. Without gravity (Figure 9.11a), the flame front follows the classical steps of tube propagation detailed in Chapter 5: a short initial hemi-spherical flame phase; a subsequent finger flame acceleration which ends when the flame skirt touches the lateral wall; finally, the beginning of a flame profile inversion is observed near the end of the vessel. The last step is often called the *tulip flame* mechanism [188, 331, 332]. It only happens for long enough tubes but stands out of the scope of this study. When gravity is added, the flame skirt portion close to the ignition plate (at the left in Figure 9.11) gradually becomes concave during the propagation: it is symptomatic of the bulk effect of gravity which generates this bubble-like structure through natural convection. At the end of the simulation, instead of starting a profile inversion to take the tulip shape as in the no-gravity case, the flame tip stays on the centerline of the tube,

which suggests a delaying effect of gravity on the position of flame front inversion. It seems relevant especially since the flame reaches very high propagating velocities as soon as it starts interacting with the first obstacles, thereby decreasing the impact of gravity in the remaining part of the tube. The importance of gravity will be further verified in the complete 3D ENACCEF2 configuration in Section 9.3.3.

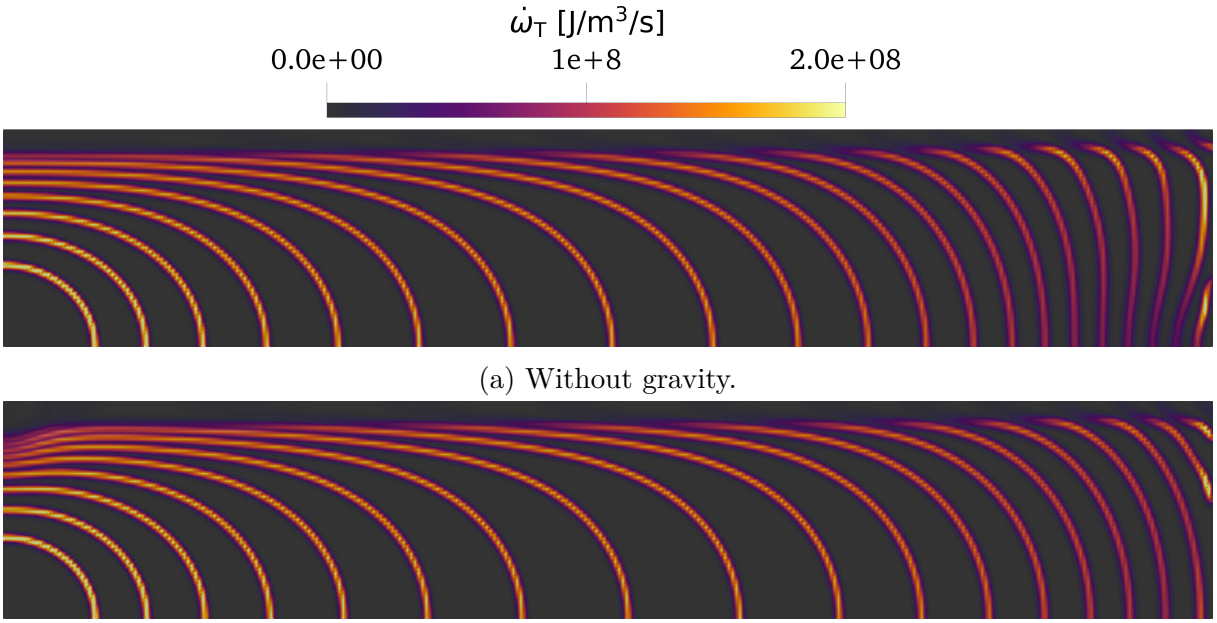

(a) Without gravity.

(b) With gravity.

Figure 9.11: Superimposition of heat release rate profiles at several instants of flame propagation in LES. Top: without gravity. Bottom: with gravity.

Now, the LES with and without gravity are again compared in terms of flame tip velocity versus flame tip position in Figure 9.12. The curves for the two DNS of the previous section are recalled for the comparison. One retrieves the mesh dependency associated with the use of the classical Thickened Flame model for the LES of lean hydrogen-air flames (Chapter 5). For each of the LES meshes, the conclusions are the same as in DNS mode: gravity slightly delays the end of the finger flame phase. Another important aspect arises from this diagram: the effect of gravity does not vary with the mesh resolution. In other words, gravity does not couple with the Thickened Flame model. The main practical implication is that no particular correction is needed for gravity in the full 3D ENACCEF2 simulations.

9.2.4 Conclusion on gravity effects

The analysis of gravity effects in the reduced set-up presented above allows to draw the following conclusions:

- in DNS mode, the additional instability due to buoyancy does not significantly change the distribution of flame front cells at a local level;

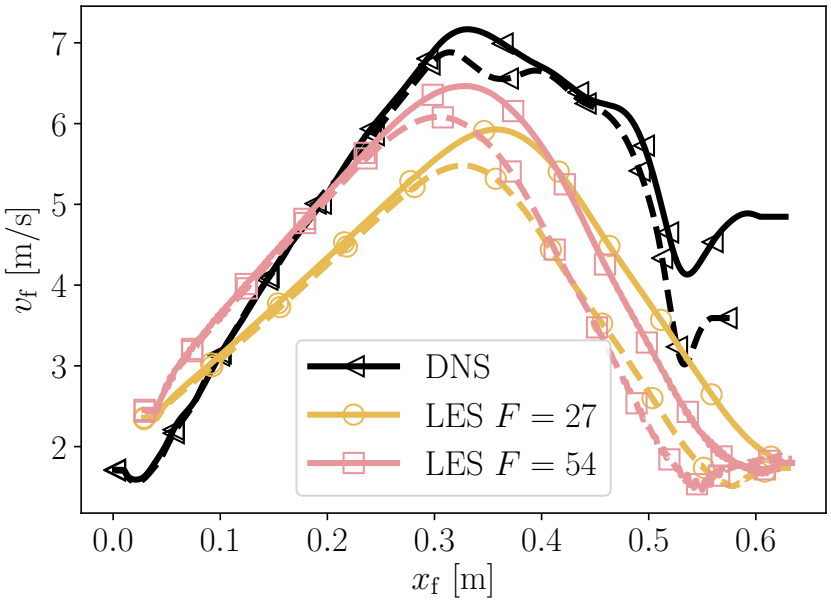

Figure 9.12: Flame speed as a function of flame tip position for several meshes. Solid lines: cases without gravity. Dashed lines: cases with gravity.

- at a macroscopic level, gravity acts on the burning kernel as a bulk, generating a bubble-like structure. The influence on the flame propagation starts to become visible when the flame skirt approaches the lateral wall: gravity delays the end of the finger flame phase;
- in LES mode, the effect of gravity is purely global (no flame front instability is observed) and does not depend on the thickening level.

Therefore, the shortcomings of the classical TF model (amplification of stretch effects, loss of TD instabilities, cf. Chapter 5) remain the same with or without gravity and no additional correction is necessary. Given that the computation of gravity-related terms (see Section 4.1.2) is not particularly tedious or computationally expensive, the simulations of ENACCEF2 include gravity. Its effect is quantitatively verified for the full 3D set-up in Section 9.3.3.

9.3 Classical TF LES of ENACCEF2 test case $\Phi = 0.420$

This section evaluates the performance of TF LES simulations of the ENACCEF2 explosion (case $\Phi = 0.420$). Numerical results are compared to experimental data. The classical TF LES model (dynamic flame thickening and turbulent efficiency model) is applied following the method detailed in Section 9.1.7. According to the discussion of the previous section, unless specified (in Section 9.3.3), gravity is activated.

9.3.1 Phenomenology of the ENACCEF2 explosion

First, a LES using the classical TF LES approach on the coarser mesh ($\Delta x_{\text{fine}} = 4$ mm) is used to delineate the phenomenology of the ENACCEF2 explosion along with the physical mechanisms at play. The propagation is first analysed from a qualitative point of view. Figures 9.13 to 9.15 depict longitudinal cuts (in the $x - z$ plane, $y = 0$, cf. Figure 9.1b for the axes definition) of temperature and vorticity fields at various instants of the propagation. The combustion wave undergoes several acceleration stages, in chronological order:

1. ($t \approx 10$ ms): the beginning of the simulation is very similar to what has been detailed in the half-open tube configuration (Chapters 5 and 8). Right after ignition, the flame stays hemi-spherical and advances in all directions at approximately the same speed;

2. ($t \approx 40$ ms): when the skirt approaches the lateral walls, the flame gets elongated in the x axis and progressively forms the typical finger flame shape (cf. Section 3.1). As soon as the flame starts accelerating, it acts as a permeable piston pushing the fresh gases in front of it and setting them in motion. The result of the interaction of this flow with obstacles is the formation of vortices, rolling up downstream of each obstacle;

3. the elongation of the flame front goes on until its skirt collapses on the lateral wall. At this moment ($t \approx 70$ ms), the flame tip is already close to the first obstacle, and a local elongation of the flame around the flame tip can be observed due to the influence of the obstruction. In the meantime, vortices continue to form and be convected dowstream in the obstructed region;

4. Because of the annular obstruction, a strong elongation of the flame is observed at ($t \approx 75$ ms) which further increases the flame surface area (cf. Section 3.2.1);

5. on top of the contraction effect, the flame surface area is increased due to the wrinkling by turbulence-flame interactions (cf. Section 3.2.2). This is evidenced in Figure 9.14 at $t = 77$ ms where the flame is wrinkled by the vortical structures;

6. the successive contraction/expansion and flame wrinkling by the vortices happens at each new obstacle ($t \approx 75 - 83$ ms) until the flame exits the obstructed area ($t \approx 83$ ms). The flow ahead of the combustion wave is constantly pushed forward and thereby accelerated. A shock wave progressively forms when the flame crosses the last obstacle (see the pressure field in Figure D.1, Appendix D). It is visible on the vorticity field and marks the limit between the high and low vorticity zones;

7. this shock wave advances faster than the flame and travels up the ENACCEF2 vessel ($t \approx 90$ ms). When reaching the top of the closed tube, it is reflected backward and ends up impacting the flame front. This flame-shock interaction pushes the combustion wave backward ($t \approx 105$ ms). The inverted flow is also visible on the same snapshot for example just before the first obstacle.

Following this complete qualitative description of the sequence of events in the ENACCEF2 explosion, it must be reminded that the stages after the combustion wave exits the obstructed region (step 8 described above, Figure 9.15) is not the focus of the analysis and will not be further discussed in the other sections of the chapter. It is indeed shown below that the flame decelerates in this part of the vessel.

Note that the displacement of fresh gases during flame acceleration is accompanied by a compression due to confinement. This is further analysed in Appendix D along with the validation of the isentropic compression hypothesis.

Now that the phenomenology associated to flame propagation has been detailed, it can be quantified and compared to experimental data. Figure 9.16 shows the flame tip velocity evolution against its position. First of all, an overall good agreement between the TF LES (solid line) and the experiments (symbols) is observed. Figure 9.16 highlights the strong acceleration that can be observed in the levels of obstruction in ENACCEF2, where the final flame propagation velocity is almost 1000 times that of the planar flame propagating away from a wall ($S_{\mathrm{f,max}} \approx 600$ m/s $\approx 1000\sigma S_{\mathrm{L}}^0$). Also, the acceleration mechanism is limited to the region of obstacles and as soon as the flame exits the obstructed region, a gradual deceleration of the flame is observed both in the LES and in the experiments. It is reasonable to say that the gap between the LES and experimental speed levels ($x_{\mathrm{f}} \in [4-6]$ m) is linked to the decreased mesh resolution in that region (cf. Section 9.1.4).

If one looks more into the details, the analysis can again be split into the initial, laminar regime of propagation (before the first obstacle) and the successive accelerations when the flame interacts with each obstacle.

Laminar phase

After the ignition, the flame undergoes an exponential acceleration in time (which translates into a linear slope in the $(x_{\mathrm{f}}, v_{\mathrm{f}})$ phase space). Note that the initial radius ($r_{\mathrm{f},0} = 28$ mm) is too large to correctly observe the early spherical stage so that the finger flame acceleration kicks in from the start. The slope of the effective finger flame acceleration is higher than the theoretical prediction (dashed line given by Equation (3.15)). According to the previous conclusions of Chapter 5, this must be linked with the combination between the absence of thermo-diffusive instabilities on the LES mesh and the amplification of stretch effects by the classical TF model. The second mechanism is very strong due to the high thickening factor considered here (the present LES sits on the far-right in Figure 5.22, $F \approx 54.5$ in the nominal conditions of pressure and temperature). The end of the finger flame phenomenon (skirt touching the lateral wall) is visible with the slight velocity decrease before the first obstacle (inset zoom).

Overall flame acceleration: the combined effect of obstruction and relatively small inter-obstacle spacing

As the flame passes an annular obstruction, a strong tip velocity increase ensues from the aforementioned flow contraction and flame surface area enlargement. The expansion of the flow right after causes the tip to decelerate as explained in Section 3.2.1. The spacing between the successive obstacles is low enough to generate an overall escalation of the

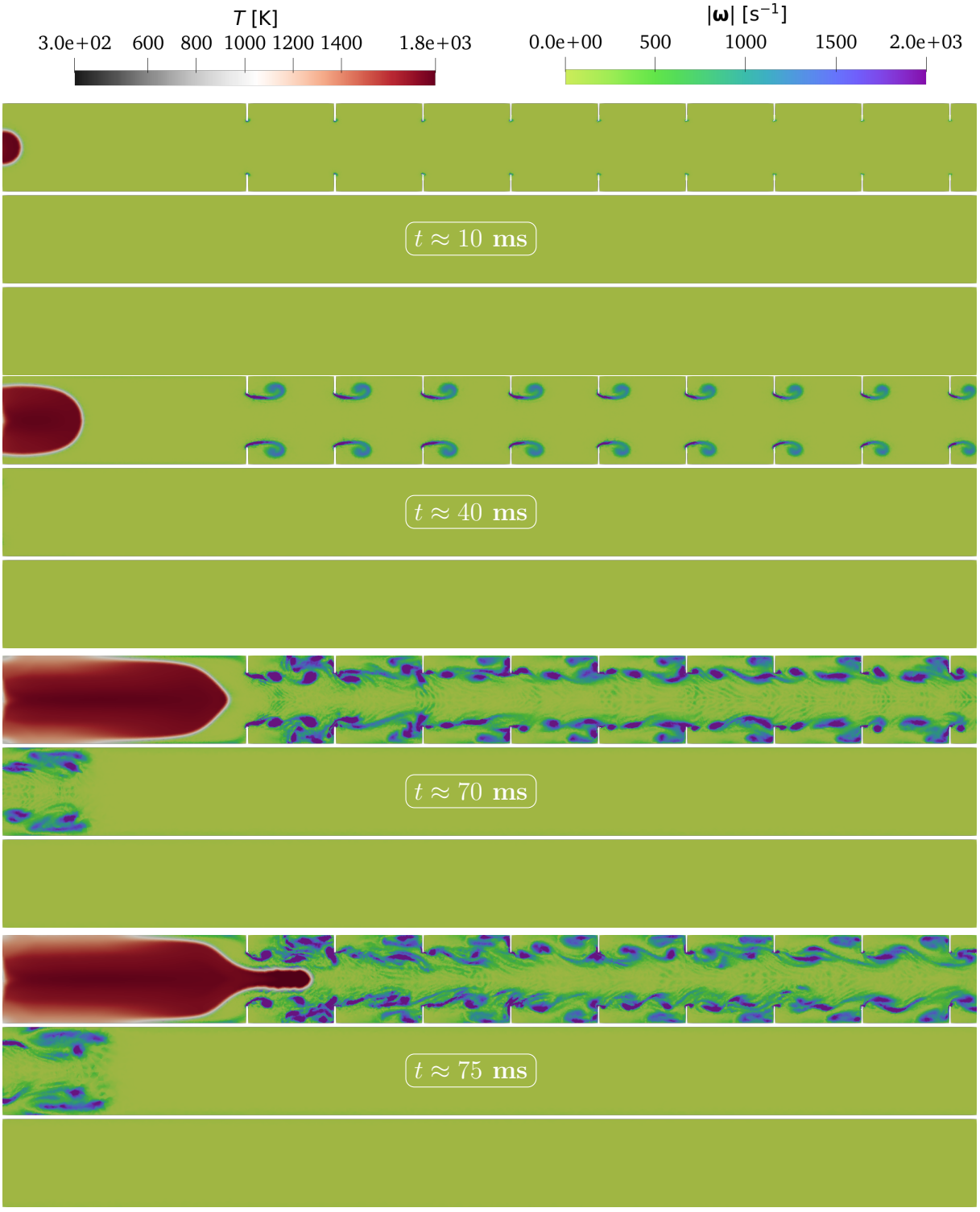

Figure 9.13: Snapshots of temperature and vorticity fields ($x-z$ plane) at several instants of the propagation for the TF LES on the mesh $\Delta x_{\text{fine}} = 4$ mm. Laminar regime before the first obstacle. From top to bottom: after 10, 40, 70 and 75 ms.

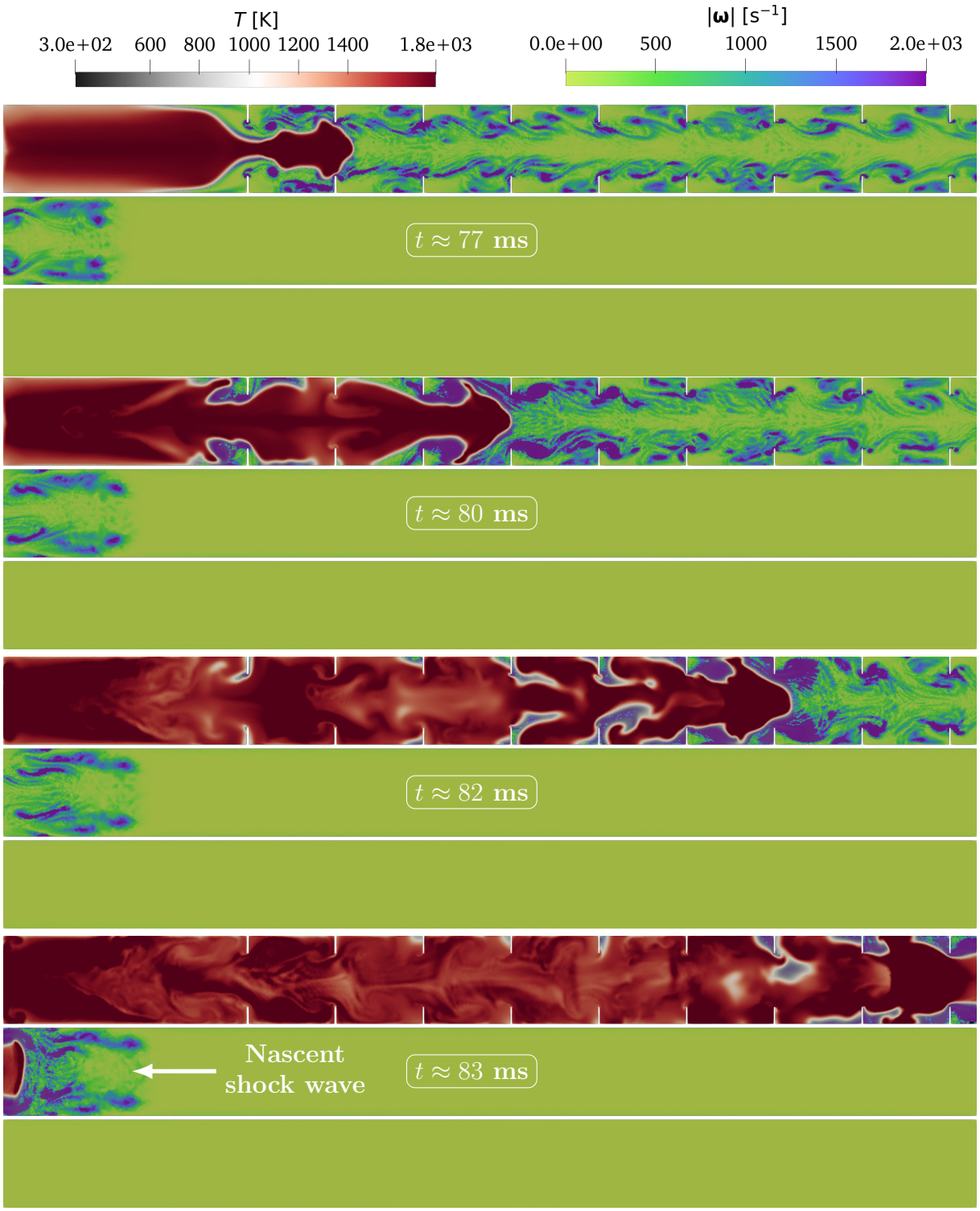

Figure 9.14: Snapshots of temperature and vorticity fields ($x-z$ plane) at several instants of the propagation for the TF LES on the mesh $\Delta x_{\text{fine}} = 4$ mm. Flame acceleration in the obstructed region. From top to bottom: after 77, 80, 82 and 83 ms.

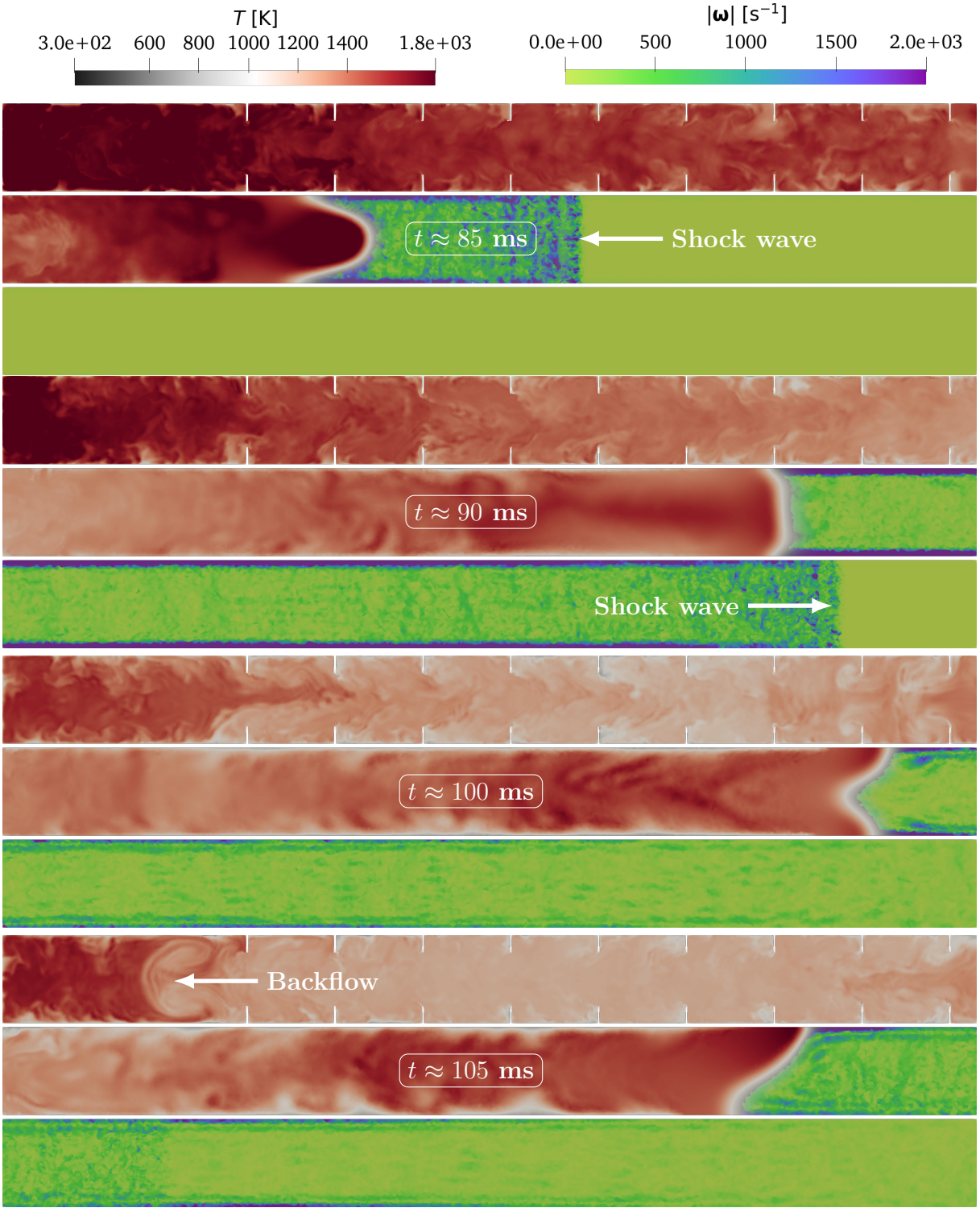

Figure 9.15: Snapshots of temperature and vorticity fields ($x-z$ plane) at several instants of the propagation for the TF LES on the mesh $\Delta x_{\text{fine}} = 4$ mm. Flame deceleration after the obstructed region. From top to bottom: after 85, 90, 100 and 105 ms.

flame tip velocity. This can be quantified by measuring the relative velocity increment at each obstacle. The flame impact velocity for an obstacle k is defined as $v_{\mathrm{f,imp}}^{k} \equiv v_{\mathrm{f}}(x_{\mathrm{f}} = x_{\mathrm{obs}}^{k})$. Figure 9.17 depicts the normalised velocity increment after the passage of each obstacle. For the two first obstacles, the acceleration lasts during the whole inter-obstacle spacing. For the third obstacle and the following ones, a deceleration is observed at a certain distance from the obstacle, suggesting that the acceleration becomes localised around the obstruction. Despite this deceleration, the acceleration across the successive orifices becomes stronger and stronger, explaining the global flame speed-up in the obstructed region.

When the flame exits the obstructed area, its velocity decreases again (Figure 9.16) because the acceleration feedback loop (cf. Section 3.2.1) is broken. Again, the events following this flame deceleration will not be further discussed in the rest of the chapter.

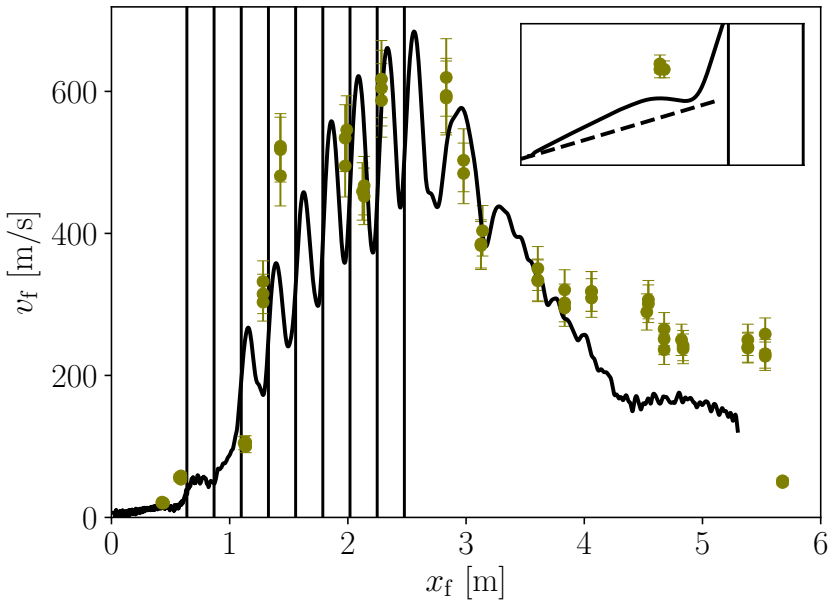

Figure 9.16: Flame tip velocity as a function of flame tip position for the TF LES on the mesh $\Delta x_{\mathrm{fine}} = 4$ mm. Inset: zoom on laminar phase. Vertical bars: obstacles. Symbols: experimental measures (with error bars). Solid line: TF LES simulation. Dashed line (inset): finger flame theoretical slope (Equation (3.15)).

The last quantity that can be compared with experimental data is the pressure increase during flame propagation. As explained in Chapter 3, the overpressure represents one of the main metrics used to evaluate the severity of an explosion. Large-scale experiments are also often limited to the data output from a couple of pressure probes. In ENACCEF2, 10 of them are scattered in the tube height (cf. Section 9.1.1). Figure 9.18 compares the TF LES results with the experimental measures. Both LES and experimental curves at each probe are shifted in time by $t_{\mathrm{reflection}}$ which corresponds to the moment the shock wave created during flame propagation reflects on the top plate of the vessel. The agreement between numerical and experimental pressure signals is satisfying both in terms of levels of overpressure and in terms of timing. The intensity of the shock wave is indeed correctly

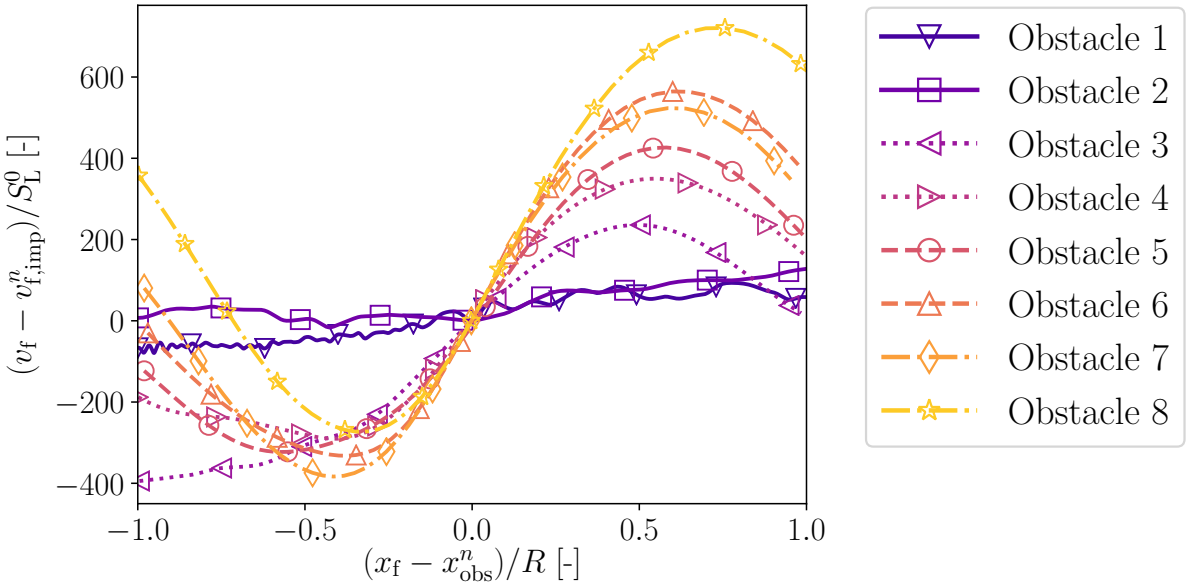

Figure 9.17: Relative flame tip velocity increment as a function of flame tip position at each row of obstacle. TF LES on the mesh $\Delta x_\mathrm{fine} = 4$ mm. Note that the axial coordinate covers the whole spacing between consecutive obstacles ($x^{i+1}_\mathrm{obs} - x^i_\mathrm{obs} = D_\mathrm{tube}$).

reproduced in the TF LES as well as its propagation in the vessel (cf. arrows denoting the main incident and reflected shock waves). The pressure increase in ENACCEF2 is directly related to the flame front acceleration (through the piston-like effect formerly described). Given that the TF LES captures the right flame dynamics (Figure 9.16), the corresponding overpressure is retrieved as well.

9.3.2 Turbulent flame speed analysis

Now that the main features of the ENACCEF2 explosion have been presented, an in-depth analysis on the different contributions to flame acceleration can be carried out. In Section 2.4, the global propagation speed of any combustion wave, called *turbulent flame speed* has been split into several factors (Equation (2.75), recalled here):

$$\begin{aligned} S_\mathrm{T} &= \Xi \overline{I_0} S^0_\mathrm{L} \\ &= \frac{\Sigma}{\Sigma_\mathrm{ref}} \overline{\left(\frac{S_\mathrm{c}}{S^0_\mathrm{L}}\right)} S^0_\mathrm{L} \end{aligned} \tag{9.7}$$

where the laminar flame speed S^0_L gives a baseline, the wrinkling factor Ξ carries all effects due to surface area enlargement and the global stretch factor $\overline{I_0}$ represents a macroscopic integration of all effects due to stretch on the consumption speed (see Section 2.2).

This approach provides a convenient way of understanding the most important elements of flame acceleration. In a TF LES framework, this relation is revisited to account

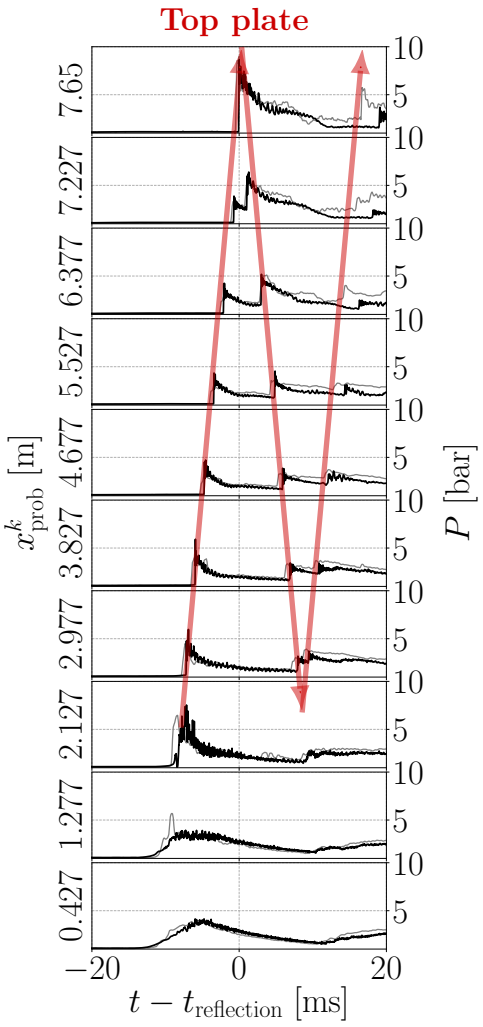

Figure 9.18: Pressure signals of different probes. Gray: experiments. Black: TF LES on the mesh $\Delta x_{\text{fine}} = 4$ mm. Red arrows: incident and reflected shock wave.

also for the different components of the total flame surface Σ_{tot}, namely the resolved part Σ_{res} and the enhancement contained in the turbulent efficiency $\mathcal{E}$ (cf. Section 4.4.6). It amounts to re-writing Equation (2.75) as:

$$\begin{aligned} S_{\text{T}} &= \Xi \overline{I_0} S_{\text{L}}^0 \\ &= \frac{\Sigma_{\text{tot}}}{\Sigma_{\text{ref}}} \overline{\left(\frac{S_{\text{c}}}{S_{\text{L}}^0}\right)} S_{\text{L}}^0 \\ &= \frac{\overline{\mathcal{E}} \Sigma_{\text{res}}}{\Sigma_{\text{ref}}} \overline{\left(\frac{S_{\text{c}}}{S_{\text{L}}^0}\right)} S_{\text{L}}^0 \end{aligned} \tag{9.8}$$

Note that, similarly to what has been done for $\overline{I_0}$ (Equation (2.73)), $\overline{\mathcal{E}}$ is a flame-surface-density-weighted average of the turbulent efficiency field (but over the whole domain V):

$$\overline{\mathcal{E}} \equiv \frac{\int_V \mathcal{E} |\nabla \mathbf{c}| \, \mathrm{d}V}{\int_V |\nabla \mathbf{c}| \, \mathrm{d}V} \tag{9.9}$$

This definition allows to simply relate the total and resolved flame surface areas through a global mean turbulent efficiency, reminding that (Equation (2.71)):

$$\Sigma_{\text{res}} = \int_V |\nabla \mathbf{c}| \, \mathrm{d}V \tag{9.10}$$

$$\Sigma_{\text{tot}} = \int_V \mathcal{E} |\nabla \mathbf{c}| \, \mathrm{d}V \tag{9.11}$$

Equation (9.8) depends on a reference flame surface Σ_{ref} which remains ambiguous and ill-defined in complex configurations like ENACCEF2[1] . Therefore, the analysis is restricted to the measurable components of the turbulent flame speed, namely Σ_{res}, Σ_{tot} and $\overline{I_0}$. Moreover, it has been shown in Section 2.4 that the global stretch factor can be retrieved from appropriate combinations of the different relations:

$$\begin{aligned}
\overline{I_0} &= -\frac{1}{\Sigma_{\text{tot}} S_{\text{L}}^0} \frac{1}{\rho_{\text{u}}(Y_{\text{F,u}} - Y_{\text{F,b}})} \int_V \dot{\omega}_{\text{F,tot}} \, \mathrm{d}V \\
&= -\frac{1}{\overline{\mathcal{E}} \Sigma_{\text{res}} S_{\text{L}}^0} \frac{1}{\rho_{\text{u}}(Y_{\text{F,u}} - Y_{\text{F,b}})} \int_V \mathcal{E} \dot{\omega}_{\text{F,res}} \, \mathrm{d}V \\
&= -\frac{1}{S_{\text{L}}^0} \frac{1}{\rho_{\text{u}}(Y_{\text{F,u}} - Y_{\text{F,b}})} \frac{\int_V \mathcal{E} \dot{\omega}_{\text{F,res}} \, \mathrm{d}V}{\int_V \mathcal{E} |\nabla \mathbf{c}| \, \mathrm{d}V}
\end{aligned} \tag{9.12}$$

The flame surface components are plotted against flame tip position in Figure 9.19 for the present state-of-the-art TF LES. As expected, in the initial laminar phase of the propagation (inset zoom), the total and resolved flame surface areas are exactly the same (overall no contribution of the turbulent efficiency model to flame acceleration). As the flame passes the first obstacle, the vortices generated behind it start to wrinkle it following the mechanism introduced in Section 3.2.2. The resolved flame surface does show a mild increase, but most importantly, the turbulent efficiency drastically departs from unity to model the contribution of subgrid turbulence-flame interactions to the total surface area. This phenomenon is repeated throughout the whole obstructed region of the tube and accumulates to produce the stupendous acceleration observed in Figure 9.16. Note that in the turbulent stage, most of the total flame surface is provided by the subgrid-scale turbulent model. This unsurprisingly has to do with the low mesh resolution (cf. Table 9.3, $\delta_{\text{L}}^0/\Delta x_{\text{fine}} = 0.128$). It is better visualised in Figure 9.20a where the ratio $\Sigma_{\text{res}}/\Sigma_{\text{tot}}$ is plotted against the flame tip position. While the total flame surface corresponds entirely to its resolved part up to the first obstacles, a drastic decrease of the resolved part contribution is observed inside the obstructed region, reaching values around 10% as soon as the flame passes the fourth obstacle. Similarly to other explosion studies using the TF LES approach at comparable geometric scales [49, 51, 53], the results depend heavily on the performance of the turbulence combustion model. It is important to note

[1]Note also that even the laminar flame speed S_{L}^0 in Equation (9.8) should be replaced by a FSD-weighted average along the flame surface $\overline{S_{\text{L}}^0}$ to account for the variations of operating conditions (isentropic compression). Given that S_{T} can anyway not be estimated, the relation using a constant nominal S_{L}^0 value is kept as-is. Here, the turbulent flame speed analysis is mainly used to separate the contributions of wrinkling and stretch effects.

that the parameters of the efficiency model are those classically used in the literature and have not been fitted to this case (cf Section 9.1.7).

The other contributor to flame speed, the global stretch factor $\overline{I_0}$, is plotted against the flame tip position in Figure 9.20b. During the early stages of flame propagation, $\overline{I_0}$ reaches rapidly a value around 2 showing the stretch sensitive nature of lean hydrogen-air flames. Potential amplification of this stretch effect by the thickening will be addressed in Section 9.3.4. $\overline{I_0}$ also increases progressively when the flame traverses the obstructed region of the vessel and reaches extreme values linked with the stretch rates experienced by the flame surface in the turbulent regime.

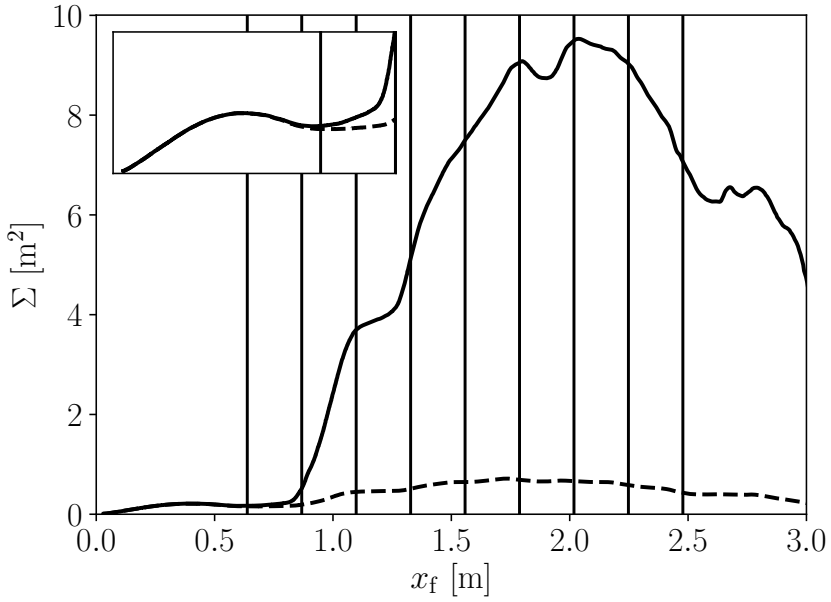

Figure 9.19: Flame surface as a function of flame tip position for the TF LES on the mesh $\Delta x_\mathrm{fine} = 4$ mm. Inset: zoom on laminar phase. Solid line: total surface (Equation (9.11)). Dashed line: resolved surface (Equation (9.10)). Vertical bars: obstacles.

The whole flame propagation, and its contributors (surface area, stretch effects, etc.) must be linked to the TF LES properties, namely: the thickening factor and the turbulent efficiency function (cf. Section 4.4.5). Figure 9.21 gives the evolution of the mean value for these quantities as a function of the flame tip position[1,2]. During the early

[1]Note that the $\overline{\bullet}^0$ notation is used to indicate that the mean is not weighted by the FSD (like it was done in the definition of $\overline{I_0}$ or $\overline{\mathcal{E}}$ for instance). This has been done for practical reasons because the FSD-weighted averages have not been computed here. It is not expected to bring out significant differences.

[2]Note also that the means have been computed using a mask based on the DTF LES flame sensor (Equation (4.70)):

$$\overline{\bullet}^0 \equiv \frac{\int_V \mathcal{H}(\mathcal{S} - 0.9) \bullet \, \mathrm{d}V}{V} \tag{9.13}$$

where V is the total volume, $\mathcal{S}$ is the DTF LES flame sensor and $\mathcal{H}$ the Heaviside step function (here equal to one for $\mathcal{S} > 0.9$)). The use of this mask allows to discard regions far from the flame where the thickening factor and efficiency function are equal to one, irrelevant for the analysis.

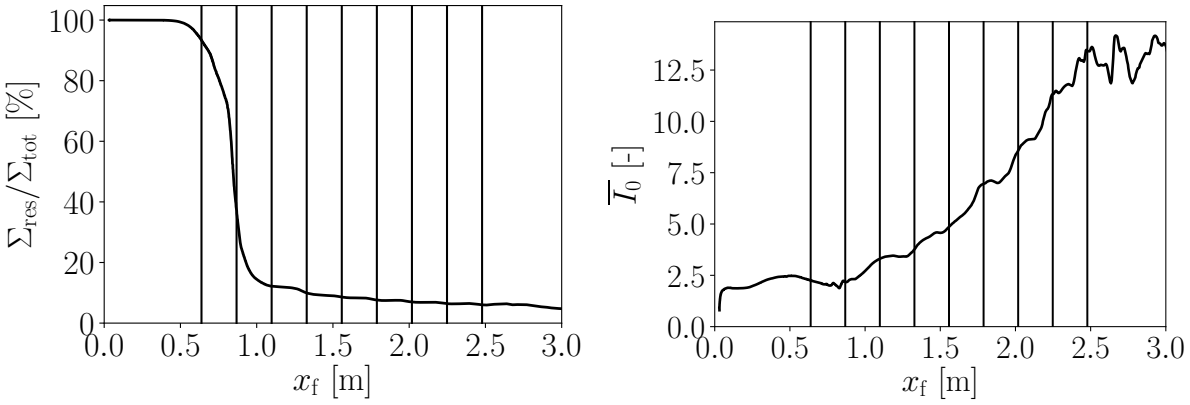

(a) Ratio of resolved flame surface over total surface

(b) Global stretch factor (Equation (9.12)).

Figure 9.20: Flame surface ratio (left) and global stretch factor (right) as a function of flame tip position for the TF LES on the mesh $\Delta x_{\text{fine}} = 4$ mm. Vertical bars: obstacles.

laminar phase of the explosion, the conditions of pressure and temperature still stick to the nominal values $(P_0, T_{u,0})$: the thickening is close to the predicted value ($F \approx 55$, cf. Table 9.3) and the turbulent efficiency $\mathcal{E}$ is equal to one everywhere. As soon as the flame enters a turbulent regime, $\overline{F}^0$ soars up due to the pressure rise and the preheating (the flame becomes thinner, see Figure 9.4b)[1], reaching values almost 6 times higher than the initial one at the end of the obstructed region. This thinning of the flame during its propagation in the obstructed region also contributes to the drastic increase of the contribution of the subgrid-scale turbulent model to the total flame surface $\overline{\mathcal{E}}^0$. Note that both thickening and efficiency factors are not homogeneous along the flame surface as depicted in Figure 9.22. The flame is very elongated and the pressure variations along the tube induce a heterogeneous distribution of flame parameters along the flame surface. This is highlighted by the laminar flame speed, where variations are observed even between two obstacles (close to the flame tip).

9.3.3 Effect of gravity

In Section 9.2, it has been shown in a 2D tube with the same radius as ENACCEF2 that gravity does not significantly modify the flame propagation both in DNS and LES. Here, this assumption is put to the test in the 3D ENACCEF2 set-up. Figure 9.23 shows the flame propagation in the (x_f, v_f) space for the previous TF LES with gravity and another one without gravity. The similarity of the two simulations is compelling: gravity does not affect the propagation in ENACCEF2. Note that, as seen in Section 9.2, gravity slightly extends the duration of the finger flame phase (inset zoom).

[1]The slope break around $x_f \approx 2.8$ is due to the decrease of the mesh resolution from Δx_{fine} to Δx_{coarse} (cf. Figure 9.2).

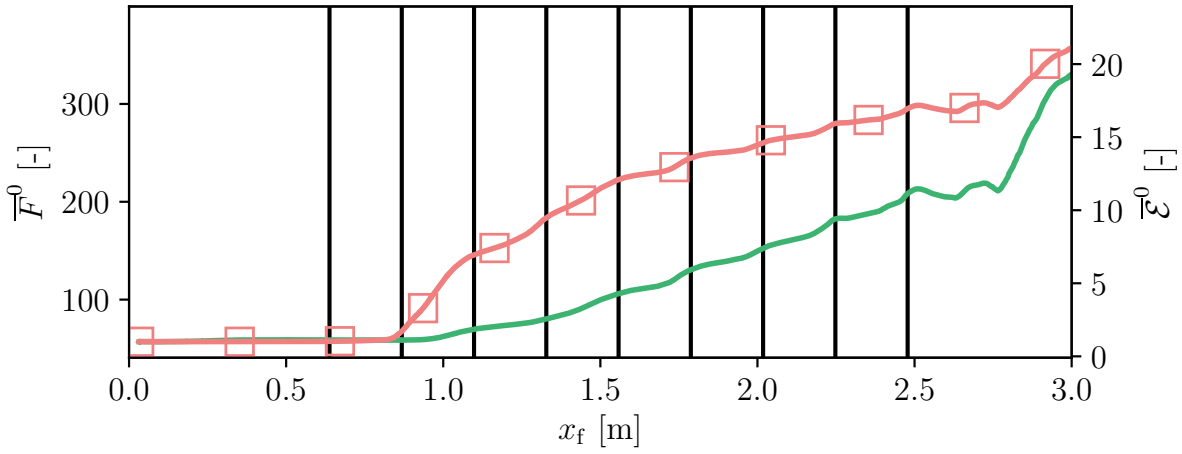

Figure 9.21: TF LES model outputs for the TF LES simulation on the mesh $\Delta x_{\text{fine}} = 4$ mm. Green solid line: mean thickening factor (left y-axis). Red solid line with squares: mean turbulent efficiency (right y-axis).

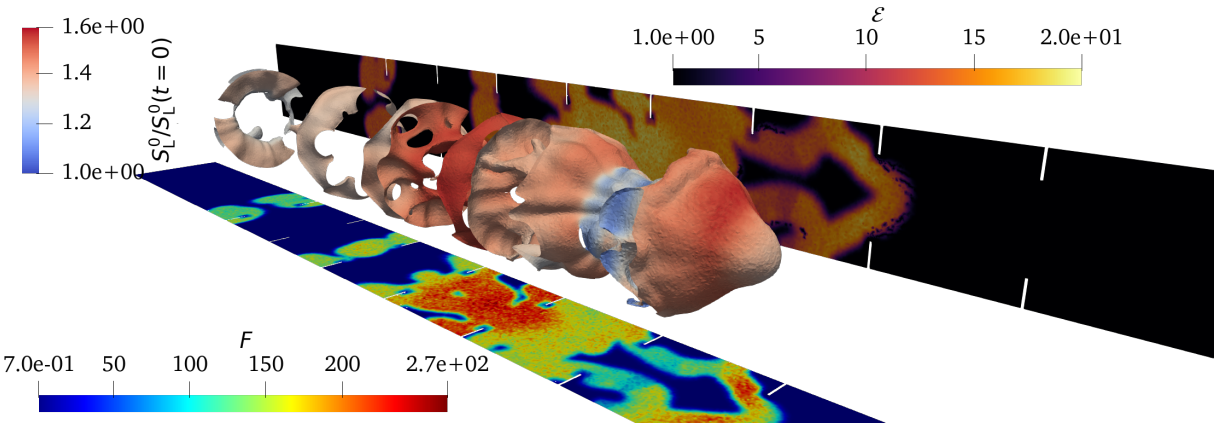

Figure 9.22: Snapshot of TF LES thickening and turbulent efficiency fields and isotherm ($T = 800$ K) coloured by the local laminar flame speed (normalised by the initial value $S_L^0(t=0)$). TF LES on the mesh $\Delta x_{\text{fine}} = 4$ mm. $t = 82$ ms ($x_f \approx x_{\text{obs}}^7 \approx 2$ m).

9.3.4 Effect of mesh resolution

The previous sections have demonstrated that the classical TF LES approach is able to faithfully reproduce the explosion evolution measured in experiments. However, in Chapter 5, important shortcomings of the classical TF model have been identified in the case of lean hydrogen-air flames: the inability to capture TD instabilities (decelerating effect) and the amplification of stretch effects by the thickening applied to the flame (accelerating effect for positive stretch). These undesired mechanisms lead to a strong mesh dependency in the 2D tube set-up studied therein. This section evaluates the effect of the mesh resolution on the ENACCEF2 TF LES by comparing the previously shown simulation ($\Delta x_{\text{fine}} = 4$ mm mesh) with a LES on the finer $\Delta x_{\text{fine}} = 2$ mm mesh.

Both flame propagations are compared in the phase space in Figure 9.24. The overall

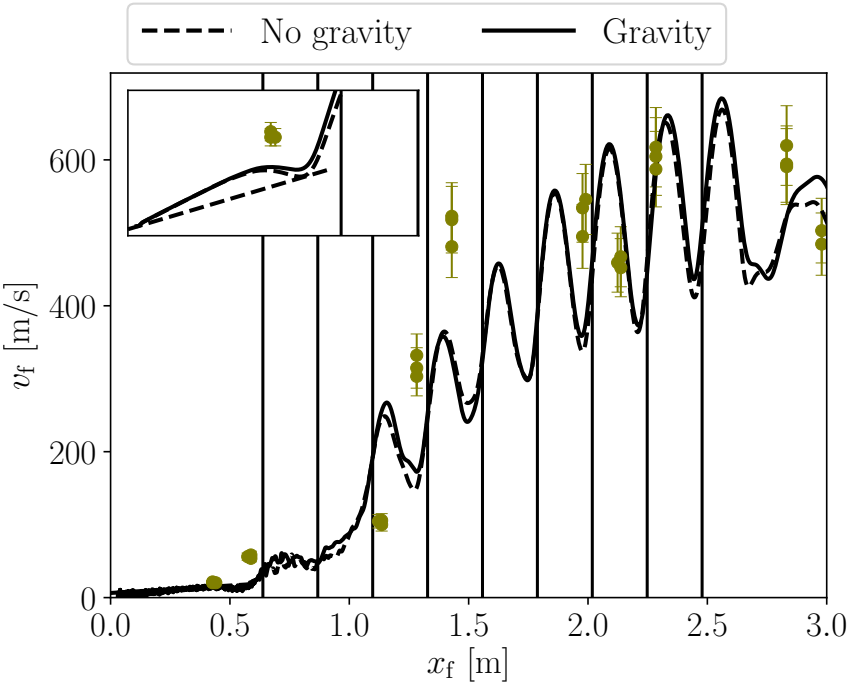

Figure 9.23: Flame tip velocity as a function of flame tip position for the TF LES on the mesh $\Delta x_{\text{fine}} = 4$ mm with and without gravity. Inset: zoom on laminar phase. Vertical bars: obstacles. Symbols: experimental measures (with error bars). Solid lines: TF LES simulations. Dashed line (inset): finger flame theoretical slope (Equation (3.15)).

flame propagation seems to be globally insensitive to the mesh resolution. During the laminar phase (inset zoom), the TF LES using $\Delta x_{\text{fine}} = 4$ mm has a higher acceleration slope. This is similar to the observations of Chapter 5 and results from the amplification of stretch effects. This discrepancy remains very limited and becomes totally imperceptible in the turbulent phase.

From the conclusions of Chapter 5 (see Figure 5.22), it could be expected that the LES on the $\Delta x_{\text{fine}} = 2$ mm mesh would yield lower flame speeds (because of the lower thickening levels). Note that for the two resolutions considered here, the mesh cell size is too large to resolve any TD instabilities. So now the question is: how is the classical TF model able to capture the right flame propagation on two thoroughly different meshes (with different thickening factors)? In an attempt to answer this issue, the flame speed is split into the effect of surface wrinkling and global stretch effect (cf. Section 9.3.2). Figure 9.25 represents the resolved and total flame surface areas as a function of the flame tip position. As expected, the resolved flame surface is always greater on the finer $\Delta x_{\text{fine}} = 2$ mm mesh. In the region with obstacles (Figure 9.25, bottom right plot), the turbulent efficiency again soars up to achieve a total surface area close to the simulation on the coarser $\Delta x_{\text{fine}} = 4$ mm mesh. Figure 9.25 shows that the resolved surface area does represent a larger proportion of the total area on the finer mesh, but the differences with the LES on the coarser mesh remain negligible. Therefore, the turbulent efficiency function completely fulfils its role of modelling subgrid wrinkling and yields the same total surface during the whole flame propagation for two different meshes. But for lean

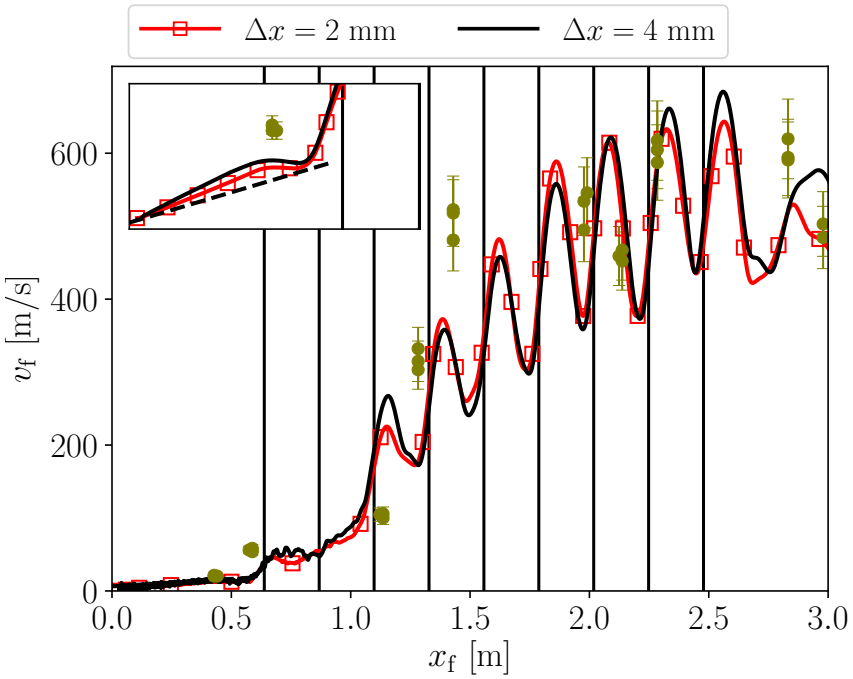

Figure 9.24: Flame tip velocity as a function of flame tip position for the TF LES on the two meshes $\Delta x_{\text{fine}} = 2$ mm and 4 mm. Inset: zoom on laminar phase. Vertical bars: obstacles. Symbols: experimental measures (with error bars). Solid lines: TF LES simulations. Dashed line (inset): finger flame theoretical slope (Equation (3.15)).

H_2-air flames, the amplification of stretch effects by the thickening factor also play an important role. Figure 9.26b depicts the evolution of the global stretch factor $\overline{I_0}$. In the laminar phase, the simulation on the coarser mesh (higher thickening factors) presents stronger values of $\overline{I_0}$ as expected (the levels are approximately 30-50% higher than the LES with finer mesh resolution), thereby confirming the conclusions of Chapter 5. But in the turbulent stage, the discrepancies between the two LES become negligible. The global analysis of the different components of the turbulent flame speed does not satisfactorily explain why the TF simulations on the two meshes yield a similar propagation. In the next paragraph, the analysis is led at a local level.

The flame response to stretch can be evaluated locally, by computing the consumption speed at each point of the flame surface. But contrary to Equation (2.10) used so far in the previous chapters, the effect of the turbulent efficiency must be accounted for. That being said, one can define two stretch factors, based on two consumption speeds:

$$\begin{cases} I_{0,\text{lam}} \equiv -\dfrac{1}{S_{\text{L}}^0 \rho_{\text{u}} (Y_{\text{F,u}} - Y_{\text{F,b}})} \displaystyle\int_{(\Gamma)} \dot{\omega}_{\text{F,res}} \, \text{d}s \\ I_0 \equiv -\dfrac{1}{S_{\text{L}}^0 \rho_{\text{u}} (Y_{\text{F,u}} - Y_{\text{F,b}})} \displaystyle\int_{(\Gamma)} \dot{\omega}_{\text{F,tot}} \, \text{d}s = -\dfrac{1}{S_{\text{L}}^0 \rho_{\text{u}} (Y_{\text{F,u}} - Y_{\text{F,b}})} \displaystyle\int_{(\Gamma)} \mathcal{E} \dot{\omega}_{\text{F,res}} \, \text{d}s \end{cases} \tag{9.14}$$

where (Γ) defines a streamline normal to the flame front. Note that for the normalisation, the laminar flame speed $S_{\text{L}}^0(t = 0)$ under the initial conditions $(P_0, T_{\text{u},0})$ is used. $I_{0,\text{lam}}$

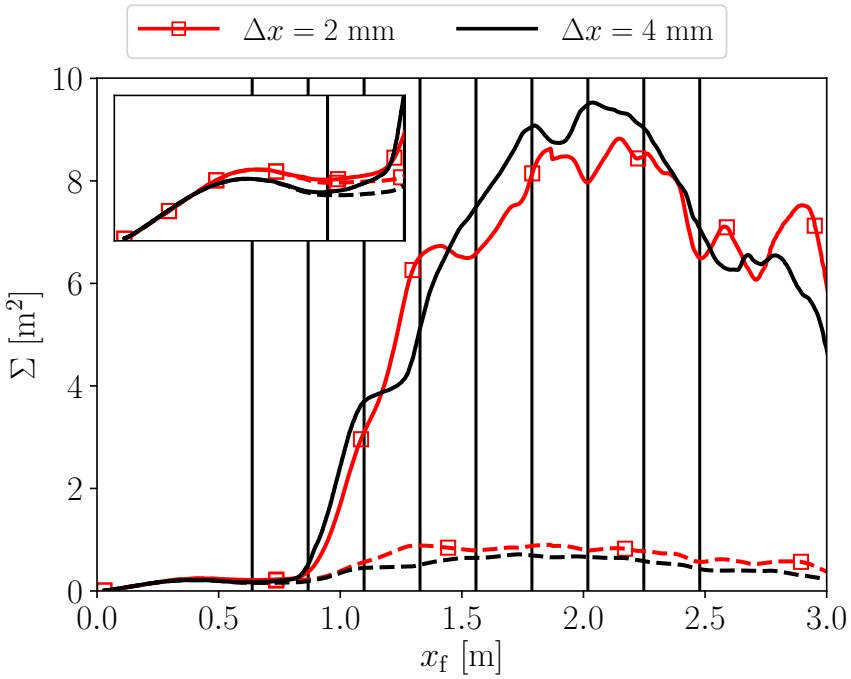

Figure 9.25: Flame surface as a function of flame tip position for the TF LES on the two meshes $\Delta x_{\text{fine}} = 2$ mm and 4 mm. Inset: zoom on laminar phase. Solid line: total surface. Dashed line: resolved surface. Vertical bars: obstacles.

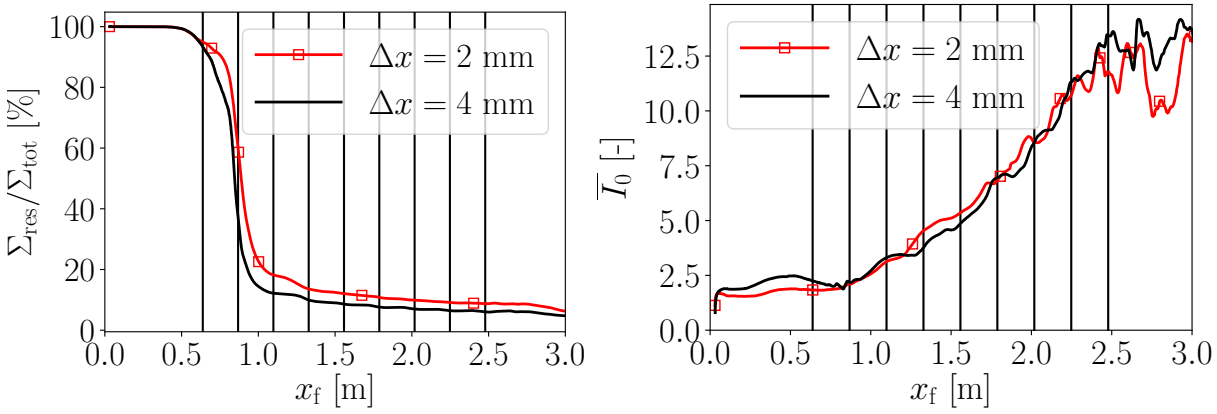

(a) Ratio of resolved flame surface over total surface

(b) Global stretch factor (Equation (9.12)).

Figure 9.26: Flame surface ratio (left) and global stretch factor (right) as a function of flame tip position for the TF LES on the two meshes $\Delta x_{\text{fine}} = 2$ mm and 4 mm. Vertical bars: obstacles.

represents a "laminar" stretch factor which does not account for the turbulent efficiency. On the contrary, I_0 includes the contribution of subgrid wrinkling effects by considering the total fuel consumption rate. In Figure 9.27, these two quantities are compared for the two TF LES. Each of the diagrams corresponds to a snapshot at a fixed flame tip position. In the early spherical stage of the propagation (Figure 9.27a), laminar and total consumption speeds are exactly the same because the turbulent efficiency is identity in

the whole vessel (cf. Figure 9.21). As expected, the TF simulation on the coarser mesh yields higher flame speeds due to the amplification of stretch effects. When the flame tip approaches the first obstacle (Figure 9.27b), the turbulent efficiency is still very weak ($S_{c,lam} \approx S_c$). The distribution of flame speeds remains higher for the LES at $\Delta x_{fine} = 4$ mm. When the flame enters the turbulent regime (Figure 9.27c), the turbulent efficiency function activates in some regions of the flame surface (see Figure 9.22), affecting the distribution of I_0 with respect to $I_{0,lam}$. Note the stupendous levels of total consumption speed S_c which show that the flame is hypothetically strongly wrinkled at the subgrid level ($\mathcal{E} \gg 1$). The stretch rates experienced by the flame (at the resolved scale) are noticeably higher due to the extreme strain generated by the flow field and the flame curvature. The spreading of the stretch range is associated to a spreading of the consumption speed levels. For the laminar part $S_{c,lam}$, the differences between the two LES are no more visible. Finally, when the flame tip further advances to the end of the obstructed region (Figure 9.27d), the discrepancies between the two LES are totally erased by the turbulent efficiency function. This may explain why the two flames undergo the same acceleration. Even though the flame response to stretch is amplified by the thickening of the TF model, the influence of the turbulent efficiency as well as the strong disparity of stretch rates wipe out the differences in local flame speed.

9.3.5 Conclusion on the classical TF LES of ENACCEF2 test case $\Phi = 0.420$

The present section was dedicated to assessing the performance of the classical TF LES model to reproduce the ENACCEF2 explosion, following a standard strategy (in particular for the turbulent combustion modelling). It has been shown in Section 9.3.1 with a preliminary simulation on a typical LES mesh ($\Delta x_{fine} = 4$ mm, $\delta_L^0/\Delta x_{fine} \approx 0.128$) that the TF approach is able to correctly reproduce the main features of the scenario, in particular the evolution of the flame tip velocity and the pressure rise in the vessel, yielding a quantitative agreement with experimental measures.

Section 9.3.2 has re-introduced the concepts of the turbulent flame speed decomposition into wrinkling (pure surface enlargement) and stretch effects. The turbulent combustion model activates during the turbulent phase of the propagation to model the subgrid flame-turbulence interactions and artificially boost the flame speed. The resolved part only represents 5 to 10% of the total surface area of the flame front in the fully turbulent regime. In this same analysis, the global stretch factor (representing the integrated outcome of all local stretch effects on the flame surface) has been measured and shown to gradually increase as the flame crosses the obstructed region.

Finally, a second TF LES is performed on a twice finer mesh ($\Delta x_{fine} = 2$ mm) and compared to the previous one in Section 9.3.4. The flame evolution is still properly recovered in this simulation, demonstrating the robustness of the classical TF LES model for the simulation of ENACCEF2. From the conclusions of Chapter 5, one could expect

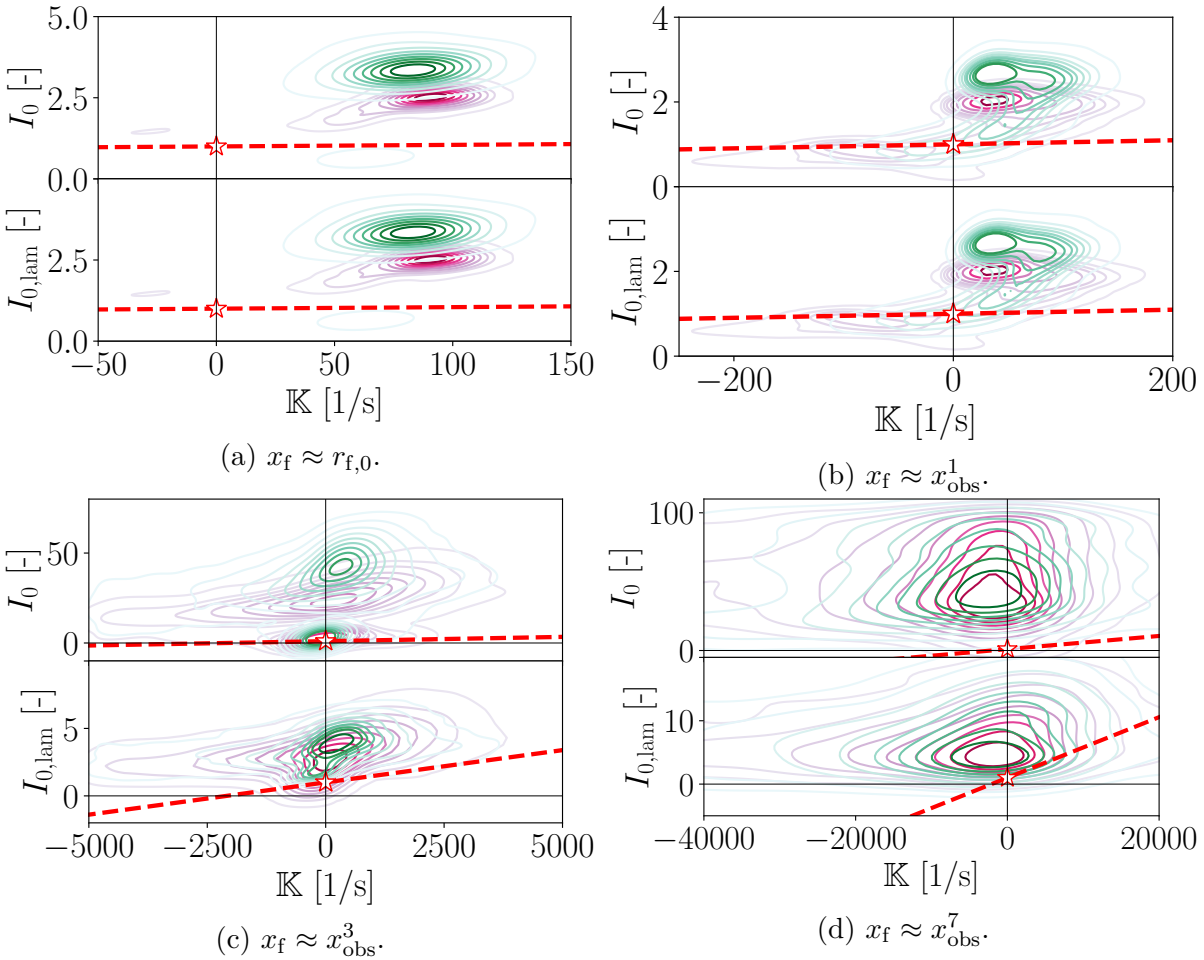

(a) $x_\mathrm{f} \approx r_{\mathrm{f},0}$.

(b) $x_\mathrm{f} \approx x^1_\mathrm{obs}$.

(c) $x_\mathrm{f} \approx x^3_\mathrm{obs}$.

(d) $x_\mathrm{f} \approx x^7_\mathrm{obs}$.

Figure 9.27: Joint PDF of stretch factor $I_{0,\mathrm{lam}}$ as a function of total stretch $\mathbb{K}$ for several flame tip positions. Pink contours: TF LES on the $\Delta x_\mathrm{fine} = 2$ mm mesh. Green contours: TF LES on the $\Delta x_\mathrm{fine} = 4$ mm mesh. Dashed red line: asymptotic theory (Equation (2.44)). Red star: unstretched laminar value.

the second LES flame ($\Delta x_\mathrm{fine} = 2$ mm) to be slower, owing to the decreased thickening factor (milder amplification of stretch effects). The global stretch factor indeed decreases in the initial laminar regime when switching to a finer mesh and the resolved surface area increases, but the discrepancies with the coarser LES become almost imperceptible in the turbulent regime of propagation. The turbulent efficiency function becomes the dominant contributor to flame acceleration and fulfils its role of modelling subgrid wrinkling: the total flame surface area (resolved + modelled) matches for the two TF LES. All of this may explain why, in spite of the gap in thickening levels between the two TF LES, they overall recover the same flame acceleration. Note that the study on the effect of the mesh resolution is very limited in ENACCEF2 and justifies why only two meshes were considered. The mesh cell size is indeed bounded by: (1) the computational cost for the higher resolutions (e.g. a TF LES using a mesh with $\Delta x_\mathrm{fine} = 1$ mm is technically feasible but astoundingly expensive); (2) the initial kernel radius, the tube radius and most critically the obstacle inner radius for the coarser resolutions (further reducing the mesh cell size below 4 mm, for instance $\Delta x_\mathrm{fine} = 8$ mm leads to a thickened flame front

which is almost as thick as the obstacles aperture).

Despite the apparent sufficient performance of the classical TF LES model to simulate the ENACCEF2 explosion, it is important to remind that the TF model remains conceptually wrong. The propagation in the present simulation is essentially driven by the turbulent combustion model which correctly compensates the gap in subgrid flame surface between the two mesh resolutions. This suggests that the results may be specific to the present type of configuration. Confrontation with the Thermo-Diffusive-Stretched-Thickened Flame (TD-S-TF) strategy developed during this thesis has to be carried out to fully understand how the turbulent combustion model behaves when resolved stretch effects are corrected.

9.4 Application of the TD-S-TF model to ENACCEF2 test case $\Phi = 0.420$

Even though the classical TF approach correctly captures the ENACCEF2 explosion dynamics, it is worth testing the Thermo-Diffusive-Stretched-Thickened Flame (TD-S-TF) model developed during this thesis. The computations presented below use the $\Delta x_{\text{fine}} = 4$ mm mesh. Section 9.4.1 provides a preliminary study to discuss the practical applicability of the TD-S-TF model for a complex turbulent explosion like ENACCEF2. The results of the TD-S-TF LES are presented in Section 9.4.2 and they are confronted to the Planar-TF model (introduced in Chapter 7) in Section 9.4.3.

9.4.1 Details on the use of the TD-S-TF model

This section aims at providing the reader with details on the practical applicability and use of the TD-S-TF approach for real turbulent explosion scenarios.

TD-S-TF model baseline
The TD-S-TF model developed in Chapter 7 and extended to confined geometries in Chapter 8 is not directly applicable in ENACCEF2 but the main components remain unchanged:

- for the correction of the amplification of stretch effects by thickening, the Stretched-Thickened Flame (S-TF) model developed in Chapter 6 is kept as-is. In particular, the target stretch/Karlovitz for the optimisation is chosen again at $\text{Ka}_\infty = 1/5$;

- regarding the subgrid effects induced by thermo-diffusive instabilities, the generic TD efficiency function formulation of Equation (7.8) is used in conjunction with the saturation of Equation (8.1) for the laminar phase of the explosion.

S-TF model under isentropic compression

As shown in Figure 9.21, the pressure and temperature conditions inside ENACCEF2 vary in time during flame propagation. Therefore, the S-TF correction must be able to account for the diverse thermodynamic conditions observed by the flame. The S-TF parameters built at $(P_0, T_{u,0})$ are tested as-are against thermodynamic conditions corresponding to an isentropic compression up to $P = 5$ atm in Figure 9.28[1]. It shows that even when built for P_0 and $T_{u,0}$, the S-TF model is able to account for isentropic compression of the fresh gases and reproduces the correct response to stretch. This owes to the fact that the S-TF transformation (Equation (6.25)) does not need any information about the laminar flame properties and automatically rescales its parameters to match the flame speed and the stretch response given a thickening factor F (which fixes the correction parameter $\widetilde{X_0}(F)$). Now, given that the thickening factor varies strongly during flame propagation (see Figures 9.21 and 9.22), a correlation for the dependence of $\widetilde{X_0}$ on F is still needed. As shown in Appendix B, the existence of a simple correlation is demonstrated (Equation B.2) and depends only on a limited set of parameters (γ, η, b) that is used in the code to retrieve the correction as a function of F in the whole domain. Therefore, the S-TF correction built only for the initial operating conditions P_0 and $T_{u,0}$, for various values of F, can be applied to the ENACCEF2 test case.

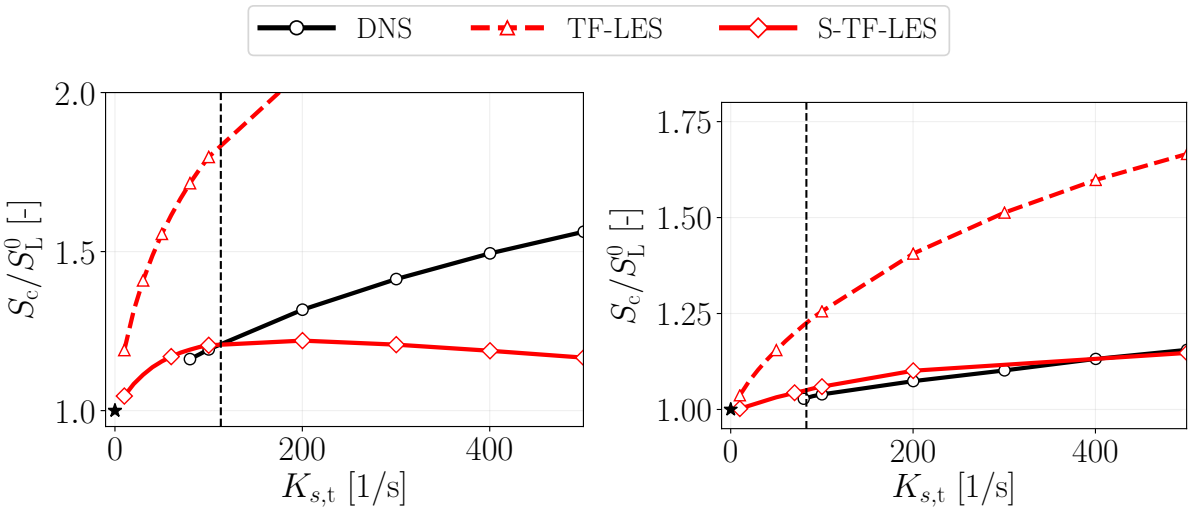

(a) $P = 1$ atm, $T_u = 296$ K. (b) $P = 5$ atm, $T_u(P)$.

Figure 9.28: Normalised consumption speed as a function of the strain rate applied to a counterflow premixed flame. TF and S-TF models at $F = 10$. Left: nominal conditions of pressure and temperature. Right: isentropic compression up to 5 atm. Dashed black line: $K_{s,t} = \mathbb{K}_\infty$ abscissa.

Thermo-diffusive and turbulent efficiencies coupling

The second component of the TD-S-TF model is the TD efficiency function aimed at

[1]Given that the unstretched laminar flame properties (S_L^0 and δ_L^0) are modified in the isentropically compressed case, the strain abscissa corresponding to $\mathrm{Ka}_\infty = 1/5$ is shifted (vertical dashed black line).

modelling the subgrid effects due to the TD instability. In Chapter 7, a generic functional form has been chosen (based on the measures of Goulier [134]) to model the unsteady development of TD cells in the early spherical stage of an explosion. In Chapter 8, this function has been generalised with a saturation parameter to mimic the observed saturation of TD development in a confined geometry. This work can be used here for the laminar phase of the ENACCEF2 explosion which corresponds to a genuine tube flame propagation. In practice, the critical radius for the onset of the TD efficiency function $r_{\mathrm{f,c}}$ is chosen from the experimental correlation of Goulier [134] as it was done for the 3D spherical flames (Section 7.3.2). Owing to the relative coarse mesh used for the LES ($\Delta x_{\mathrm{fine}} = 4$ mm), the initial flame radius $r_{\mathrm{f},0}$ is already greater than the TD critical radius: the TD efficiency function is activated right from the beginning of the simulation. Its value will increase until the flame size reaches the saturation radius, which is set at the tube radius (cf. Section 8.4.1). To sum up, one has:

$$r_{\mathrm{f,c}} = 12 \text{ mm} < r_{\mathrm{f},0} = 28 \text{ mm} < R_{\mathrm{tube}} = 115 \text{ mm} \tag{9.15}$$

Complexity arises in the subsequent turbulent phase. As briefly mentioned in Section 3.2.3, the influence of thermo-diffusive instabilities in a turbulent regime of combustion is still an open question. Some studies suggest that turbulence effects prevail over TD effects [207, 208] whereas others talk about a synergy between the two phenomena [146, 209, 210].

The nature of the interactions between thermo-diffusive instabilities and turbulence may also depend on the turbulent combustion regime where the flame sits. To further complicate things, in explosion scenarios like ENACCEF2, the flame traverses a large diversity of combustion regimes, ranging from the initial laminar phase to the strongly turbulent regime in the regions with the obstacles. To this date, it is still unclear whether thermo-diffusive instabilities can significantly change the flame acceleration in a turbulent explosion.

From a CFD perspective and in particular, within the LES framework, the effect of TD instabilities and turbulence-chemistry interactions must be modelled. For the latter, the turbulent efficiency function for the TF LES approach has been presented (Sections 4.4.6 and 9.1.7) and is classically used for stable mixtures (e.g. hydrocarbon flames) in various turbulent regimes [51, 248, 277]. The TD efficiency function uses a similar implementation to account for TD subgrid effects and has been validated in the laminar regime. In a complex case where the two effects are intertwined, several questions arise, such as: (1) should the turbulent and TD efficiency functions be modified? (2) how should they be coupled? In this thesis, it has been decided to stick to a simple solution: (1) none of the efficiencies functional forms is modified; (2) the efficiency values are multiplied to model their interactions. Therefore, the overall efficiency function reads $E = E_{\mathrm{TDS}}\mathcal{E}$, during the whole flame propagation. This choice mathematically traduces the independence between TD and turbulence effects. It corresponds to an extreme case, often used in combustion models where multiple contributions to flame acceleration are

assumed to be uncorrelated [54, 333–335]. In the case of TD instabilities and turbulence-flame interactions, this hypothesis has for instance been used by Aniello *et al.* [321].

9.4.2 Performance of the TD-S-TF model

Now that the practical use of the TD-S-TF model in ENACCEF2 has been detailed, the resulting LES flame propagation can be analysed. Figure 9.29 shows the flame tip velocity as a function of its position for the TD-S-TF model, the classical TF LES (presented in Section 9.3) and a last case where only the S-TF model has been activated (discarding the TD efficiency function). Starting the analysis at the global level, a satisfactory agreement of the TD-S-TF flame acceleration scenario and speed levels with experiments is noted. In the laminar phase (inset zoom), the stretch correction supplied by the S-TF model is recovered and yields an acceleration slope corresponding approximately to that of the pure finger flame phenomenon (like it was observed in the 2D tube case of Chapter 8). In the TD-S-TF approach, the activation of the TD efficiency function right from the start of the simulation mechanically increases the slope of the acceleration, close to that of the TF LES. In the obstructed region, the flame acceleration for the S-TF LES is too weak in comparison with the experiments, whereas the use of the TD efficiency re-establishes the correct speed levels. It is interesting to note that, while the classical TF LES case exhibits relatively high v_f fluctuations around each obstacle, this effect is reduced with the TD-S-TF model. This suggests that the strong accelerations and decelerations of the flame observed for TF LES around each obstacle are linked to the amplification of stretch effects, a mechanism mitigated by the S-TF model.

To go further, the flame propagation can again be analysed in terms of the turbulent flame speed components. Given that the TD efficiency function is aimed at modelling all subgrid effects induced by thermo-diffusive instabilities, Equation (9.8) must be re-written to account for its contribution to the turbulent flame speed. Following the discussion of the previous section, this new efficiency comes as a new multiplicative factor in the form:

$$S_\mathrm{T} = \overline{E_\mathrm{TDS}} \frac{\overline{\mathcal{E}}\Sigma_\mathrm{res}}{\Sigma_\mathrm{ref}} \overline{I_0} S_\mathrm{L}^0 \tag{9.16}$$

In the TD-S-TF model, the TD efficiency evolves during the flame propagation (at least in the laminar regime) but at each instant, it is constant in the whole domain so that $\overline{E_\mathrm{TDS}}$ is readily computed from Equation (7.8). Technically, $\overline{E_\mathrm{TDS}}$ should be split into a factor multiplying $\overline{\mathcal{E}}\Sigma_\mathrm{res}$ (i.e. TD cells contribute to the total flame surface) and another one multiplying $\overline{I_0}$ (i.e. TD cells generate stretch effects). Nevertheless, as explained in the previous section, the quantitative contribution of the TD instability to flame wrinkling and global stretch factor, and its relation with the turbulent efficiency remains complicated. Here instead, it is decided to show the relative contribution of each components to the

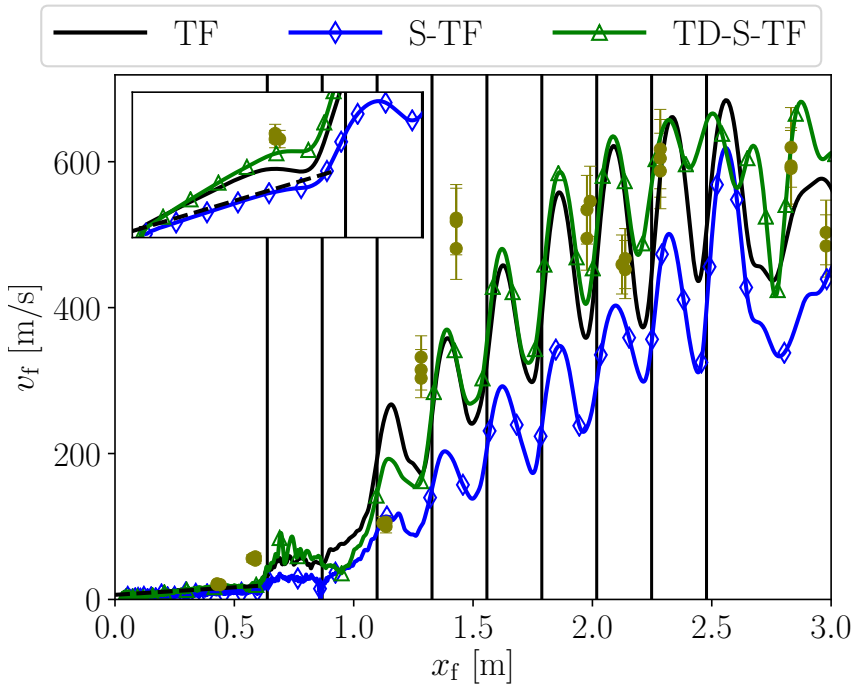

Figure 9.29: Flame tip velocity as a function of flame tip position for the TF, S-TF and TD-S-TF LES. Inset: zoom on laminar phase. Vertical bars: obstacles. Symbols: experimental measures (with error bars). Solid lines: LES simulations. Dashed line (inset): finger flame theoretical slope (Equation (3.15)).

total integrated fuel consumption rate. Namely:

$$\begin{cases} \dot{\Omega}_{\mathrm{F,res}} \equiv \displaystyle\int_V \dot{\omega}_{\mathrm{F,res}} \, \mathrm{d}V \\ \dot{\Omega}_{\mathrm{F,res+TD}} \equiv \displaystyle\int_V E_{\mathrm{TDS}} \; \dot{\omega}_{\mathrm{F,res}} \, \mathrm{d}V \\ \dot{\Omega}_{\mathrm{F,tot}} \equiv \displaystyle\int_V E_{\mathrm{TDS}} \; \mathcal{E} \; \dot{\omega}_{\mathrm{F,res}} \, \mathrm{d}V \end{cases} \tag{9.17}$$

The results are plotted in Figure 9.30a. As expected, during the laminar phase of the explosion, the resolved and TD parts represent 100% of the total fuel consumption rate because the turbulent efficiency is equal to one everywhere. If the TD efficiency is removed, the resolved part accounts for 50-60% of the total consumption (E_{TDS} rapidly saturates at around 1.9, see Figure 9.30b). When the turbulent efficiency kicks in, both contributions are reduced after the fourth obstacle to a mild 2-5% for the resolved part and 5-10% when the TD part is included.

9.4.3 Comparison with the Planar-TF model

To finalise the study on the ENACCEF2 explosion at $\Phi = 0.420$, the TD-S-TF LES model is compared to the Planar-TF model presented in Chapter 7. As a reminder, this model is composed of:

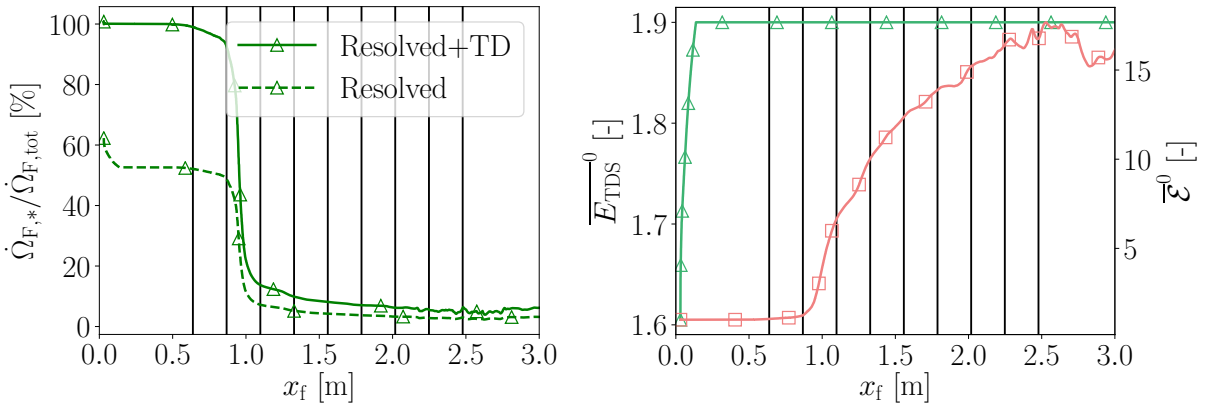

(a) (b)

Figure 9.30: Components of the total consumption rate as a function of flame tip position for the TD-S-TF LES. Left: integrated fuel consumption rate decomposition. Solid line: resolved and TD parts over total. Dashed line: resolved part over total. Vertical bars: obstacles. Right: Subgrid models evolution. Green solid line with triangles: thermo-diffusive efficiency value (left y-axis). Red solid line with squares: mean turbulent efficiency (right y-axis).

1. a unity Lewis chemistry: a 1S-Le1 scheme is constructed at $\Phi = 0.420$ (ambient temperature and pressure) following the procedure detailed in Section 5.3.1. Similarly to the 1S-LeFit used so far in this chapter (Section 9.1.6), the behaviour of the 1S-Le1 scheme is also validated in terms of laminar flame properties under an isentropic compression up to the conditions observed in ENACCEF2 (see Section 9.1.8);

2. a thermo-diffusive efficiency function, noted E_{lam}[1] is Chapter 7 based on the work of Berger *et al.* [320] and Aniello *et al.* [321]. In Chapters 7 and 8, this function took a constant value because the considered set-ups were at fixed operating conditions. In ENACCEF2 though, this function must locally vary to account for the isentropic compression of the combustible mixture.

The complete E_{lam} function is expressed as [320]:

$$E_{\text{lam}}(P, T_{\text{u}}, \Phi) = \left(\frac{P}{P_{\text{ref}}}\right)^{\gamma_P} \left(\frac{T_{\text{u}}}{T_{\text{u,ref}}}\right)^{\gamma_{T_{\text{u}}}} \left(\frac{\Phi}{\Phi_{\text{ref}}}\right)^{\gamma_\Phi} (E_{\text{lam,ref}} - 1) + 1 \tag{9.18}$$

where reference values are given by $P_{\text{ref}} = 1$ bar, $T_{\text{u,ref}} = 298$ K, $\Phi_{\text{ref}} = 0.5$, $E_{\text{lam,ref}} = 2.7$ and the power-law coefficients by $\gamma_P = 0.40$, $\gamma_{T_{\text{u}}} = -2.56$, $\gamma_\Phi = -1.62$. In practice for the present case, one has the following conditions: $\Phi = 0.420$; the pressure P varies at each location of the computational domain; and the fresh gases temperature T_{u} is evaluated following Equation (9.2).

[1]This notation is meant to make the difference with the E_{TDS} function of the TD-S-TF model, which assumes that the S-TF model already corrects the resolved response to stretch. Here the 1S-Le1 chemistry totally removes the consumption speed response to stretch.

The flame propagation of the Planar-TF LES is depicted in the phase space in Figure 9.31[1] along with the previous TD-S-TF LES for the comparison. The global evolution of the flame speed matches quite well with the experiments. In the laminar phase, the Planar-TF flame suffers a deceleration associated with the end of the finger flame phase. This is due to the absence of a correct response to stretch. On the contrary, the TD-S-TF flame keeps steadily accelerating past the first obstacle. In the subsequent turbulent regime, the Planar-TF simulation seems to correctly reproduce the various accelerations through each obstruction.

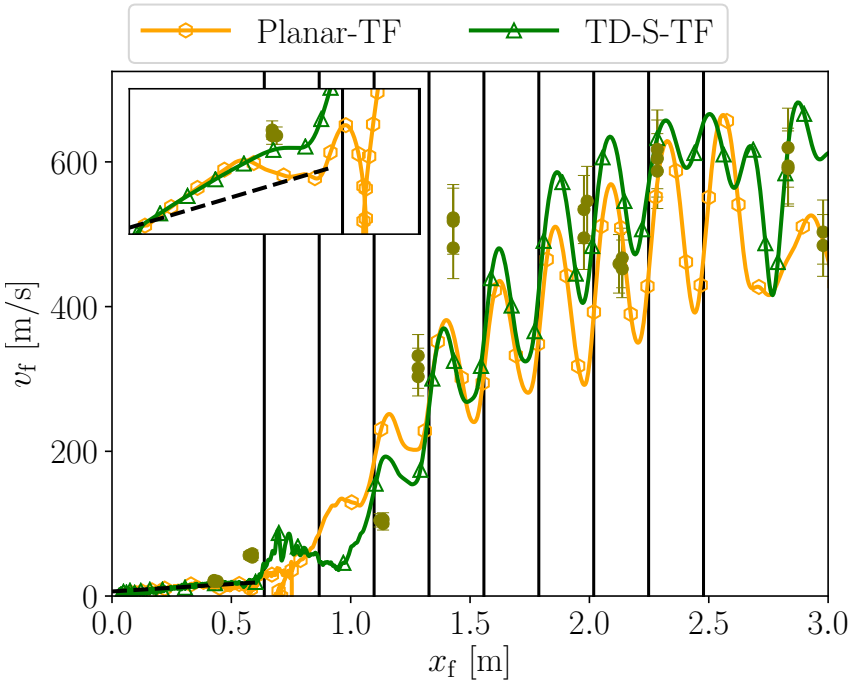

Figure 9.31: Flame tip velocity as a function of flame tip position for the Planar-TF and TD-S-TF LES. Inset: zoom on laminar phase. Vertical bars: obstacles. Symbols: experimental measures (with error bars). Dashed line (inset): finger flame theoretical slope (Equation (3.15)).

In an attempt to understand what makes these two different models work, the evolution of their thermo-diffusive efficiency mean values is depicted in Figure 9.32a. In the early laminar phase, the pressure rise in the vessel is still negligible (see Appendix D) so that the flame propagation can be considered to happen under constant-pressure. In that case, the Planar-TF model yields a constant value of efficiency all over the flame surface like the TD-S-TF model. Nevertheless, the efficiency levels are strictly different between the two LES: the Planar-TF model kick-starts the efficiency at a high value around $E_{\text{lam}} \approx 3.2$ whereas the TD-S-TF model begins at around $E_{\text{TDS}} \approx 1.6$ and saturates at $E_{\text{TDS}} \approx 1.9$. As explained in Chapter 7, the Planar-TF efficiency is a correlation based upon 2D planar

[1]Note that the velocity collapse of the Planar-TF case right after the first obstacle (inset zoom) is a spurious effect due to a pocket of hot gases which detaches from the main flame kernel and quenches. At this moment, the tracking of the flame front based on a temperature isolevel yields a discontinuity on $x_f(t)$.

flames DNS from Berger *et al.* [320] whereas the TD-S-TF efficiency is based on 3D spherical experiments from Goulier [134]. Then, in the region with the obstacles, the TD-S-TF efficiency stays at its saturated value while the Planar-TF efficiency decreases little by little. It can indeed be shown from Equation (9.18) that the Planar-TF efficiency decreases under an isentropic compression (see Figure 9.32b). All in all, this analysis shows how the two models work: the TD-S-TF model corrects the response to stretch and saturates the TD efficiency in the turbulent phase at a low 1.9 value; the Planar-TF approach is insensitive to stretch, but compensates it by higher efficiency levels.

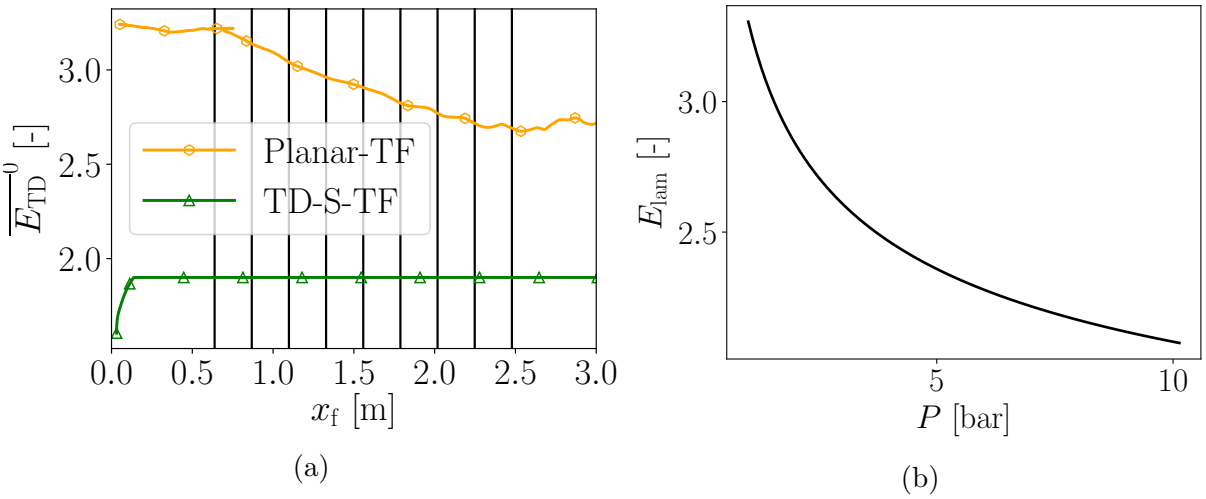

Figure 9.32: Analysis of the thermo-diffusive efficiencies for the Planar-TF and TD-S-TF models. Left: evolution of the thermo-diffusive efficiency mean values as a function of flame tip position for the Planar-TF and TD-S-TF LES. $E_{\mathrm{TD}} = E_{\mathrm{lam}}$ for the Planar-TF case (Equation (9.18)). $E_{\mathrm{TD}} = E_{\mathrm{TDS}}$ for the TD-S-TF case (Equation (8.1)). Right: theoretical evolution of the Planar-TF efficiency following an isentropic compression.

Although all models (even the classical TF approach) produce a satisfactory agreement with experimental measurements, they need further validation. In particular, the underlying conceptual mechanisms responsible for the flame acceleration differ between TF, TD-S-TF and Planar-TF LES. The next section is dedicated to the leaner $\Phi = 0.356$ operating point of ENACCEF2.

9.5 Application of the TD-S-TF model to ENACCEF2 test case $\Phi = 0.356$

The previous sections focused on the $\Phi = 0.420$ operating point of ENACCEF2. In this last section, the TD-S-TF model is tested on the leaner $\Phi = 0.356$ case. The resulting flame propagation is plotted against the classical TF LES and the Planar-TF LES models in Figure 9.33. If one starts by the analysis with the classical TF simulation, the maximum flame speed levels reached at the exit of the obstructed region seem correctly reproduced

along with the following deceleration and constant-velocity plateau for $x_f \in [3.5 - 5.5]$ m. For the early stages of the turbulent phase, the flame speed levels are a bit too low compared to the experimental data. In particular, the sudden acceleration of the flame measured between the third and fourth obstacles is not captured. These too-low velocities can be justified by the shortcomings of the classical TF model: the amplification of stretch effects might not be strong enough to compensate the lack of thermo-diffusive instabilities.

Now, looking at the two proposed correction models, none of them is able to reach the flame velocities observed in the experiments. The TD-S-TF and Planar-TF flames follow a similar acceleration scenario. The speed-up in the obstacles region is much weaker than for the classical TF approach. For the Planar-TF model, the absence of a proper response to stretch can explain why the flame front is too slow. Last but not least, the fact that the TD-S-TF LES flame does not capture the real flame acceleration in this explosion advocates for the reconsideration of the model's extension to turbulent flames (introduced in Section 9.4.1). In other words:

- the saturation of the TD efficiency function in the turbulent regime is not fully justified. While Hok *et al.* [319] have shown that TD effects do saturate during the finger flame phase, the contribution of TD cells in the turbulent phase remains unknown. In particular, the value of the TD efficiency could depend on the turbulent regime and vary locally along the LES flame surface;
- the coupling of the TD and turbulent efficiency functions by a simple multiplication operation may not be appropriate. Interactions between the two phenomena could induce a modification of their respective efficiency values. This result is not surprising as it is in accordance with recent DNS-based observations on the existence of synergistic effects between turbulence and TD instabilities, especially at very lean H_2-air mixtures like the one used here [209].

While these conclusions highlight some shortcomings of the TD-S-TF model as it is now, they open interesting discussions to extend the model. The TD-S-TF paradigm, separating the correction of resolved stretch effects and the modelling of subgrid TD effects, remains a strategy that is worth exploring.

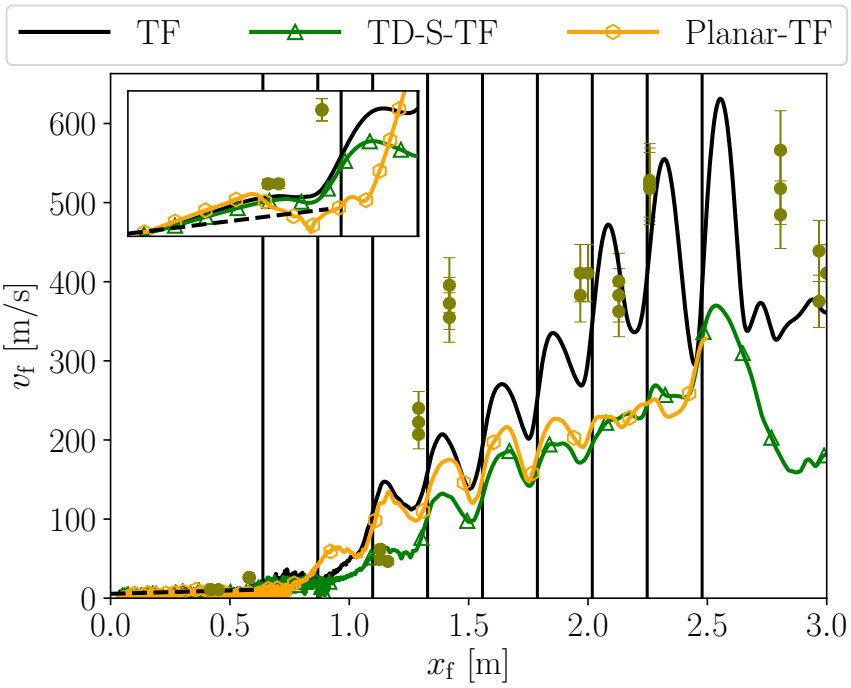

Figure 9.33: Flame tip velocity as a function of flame tip position for the classical TF, TD-S-TF and Planar-TF LES. Inset: zoom on laminar phase. Vertical bars: obstacles. Symbols: experimental measures (with error bars). Dashed line (inset): finger flame theoretical slope (Equation (3.15)).

9.6 Conclusion and implications for the modelling of very lean hydrogen-air propagating flames

The final chapter of this thesis was aimed at confronting the models developed throughout this thesis to a real explosion scenario. The ENACCEF2 vessel designed and tested at ICARE laboratory was chosen because its physics are perfectly in connection with the topics treated in the present work.

The ENACCEF2 explosion constitutes a challenging test case for the Thermo-Diffusive-Stretched-Thickened Flame (TD-S-TF) model for multiple reasons:

- the pressure rise induced by the flame acceleration in an enclosed environment affects the flame properties and generates a wide variety of operating conditions traversed by the flame front;
- the presence of obstacles in the way of the combustion wave generates turbulence and creates a broad spectrum of combustion regimes for the flame brush.

These issues have been progressively addressed throughout the chapter.

From a quantitative point of view, one of the major outcomes of this chapter is that the classical TF LES approach is able to capture the effective flame acceleration scenario

measured in the experiments for two lean H_2-air mixtures, with a weak dependency to the mesh resolution. The levels of flame speed as well as the overpressure are correctly reproduced. This somehow constitutes a surprising conclusion, given that in Chapters 5 and 8, several shortcomings of this model were identified for the simulation of lean hydrogen-air flames in a simplified tube configuration, notably its amplification of stretch effects and the strong dependence of the latter on the mesh resolution.

Nevertheless, even though a strong mesh dependence is indeed observed in the laminar phase of ENACCEF2, as soon as the flame enters the turbulent regime, the turbulent combustion model becomes the dominant contributor to flame acceleration, the amplification of stretch effects playing a supporting role for flame acceleration. The turbulent efficiency remarkably fulfils its role by adequately adjusting its values according to the mesh resolution to yield a similar total flame surface evolution independent of the mesh. It is believed however that for ENACCEF2 simulations at higher resolutions, the shortcomings of the TF LES model would be more observable as already demonstrated in Chapter 5. But the computational cost of such simulations remains prohibitive. Another result, not shown in this chapter, supports this conclusion. In Appendix E, it is indeed shown that when the classical TF model is used with a unity-Lewis 1S-Le1 chemical scheme (the other parameters such as the turbulent efficiency being unchanged, kept the same as in Section 9.3), the acceleration of the flame is much weaker and does not correspond to the experimental observations, enacting the importance of the response to stretch amplified by thickening.

In Section 9.4, the TD-S-TF correction strategy has been tested. When applied to the ENACCEF2 explosion at $\Phi = 0.420$, the S-TF model (without TD efficiency) yields flame speed levels below the experimental measures. In the laminar phase, the flame acceleration slope is brought back to the theoretical finger flame value (predicted by Equation (3.15)), as observed in Chapter 8. However, in the subsequent turbulent phase, the flame front remains too slow. The addition of the thermo-diffusive efficiency allows to retrieve the correct flame acceleration. This constitutes a significant feat for the TD-S-TF strategy which is validated here for a real lean H_2-air explosion scenario.

Apart from the TD-S-TF approach, the Planar-TF model presented in Chapter 7 is also tested. This model is based on the work of Berger *et al.* [320] which used DNS of 2D planar flames to build a correlation for the TD efficiency as a function of the operating conditions. This correlation is used with a 1S-Le1 chemistry which is insensitive to stretch effects. The Planar-TF LES also recovers the right flame propagation in ENACCEF2. Although the TD-S-TF and Planar-TF model are built upon different paradigms, they both reproduce the right flame propagation thanks to their respective components: the TD-S-TF model corrects the response to stretch and saturates the TD efficiency at a value around 1.9; the Planar-TF model does not respond to stretch at all, but compensates this lack by a stronger mean TD efficiency value staying above 2.6.

The last section of this chapter was dedicated to the study of the leaner $\Phi = 0.356$ case. Under this operating condition, neither the classical TF, nor the TD-S-TF, nor the Planar-TF approaches is able to satisfactorily reproduce the experimentally measured

flame tip velocity evolution. Although, the TF model seems to render the best results, all simulated flames are too slow. The velocity gap for the classical TF model can be explained by its aforementioned deficiencies (no TD effects and amplification of stretch effects being too weak here). For the Planar-TF model, the absence of a response to stretch can also explain the reduced velocity in the turbulent phase of the propagation. For the TD-S-TF case, the results advocate for further discussions on the assumptions that were used to extend the model to turbulent flames:

- the use of a saturated, constant value for the TD efficiency in the turbulent phase is not fundamentally justified. In the finger flame phase, Hok *et al.* [319] have shown that TD effects do saturate. But in the subsequent turbulent phase, their evolution remains unknown;

- the multiplication of the TD and turbulent efficiency functions may not be appropriate. Interactions between the two phenomena could induce a modification of their respective efficiency values. These results suggest a more complex interaction between the TD instability and turbulence, for which the community is still in search of a model. For instance, one may also expect synergistic effects between the two phenomena, as pointed out by Berger *et al.* [209]. Knowing that the dynamics of thermo-diffusive instabilities is closely related to the local curvature of the flame, turbulent motions interacting with the flame interface can reinforce the instability by generating such curvature. Besides, Chu *et al.* [336] have shown that the presence of turbulence can trigger the thermo-diffusive instability on flame kernels far below the critical size given in the laminar regime. Last but not least, Aspden *et al.* [337] indicate that the definition of Karlovitz and Damkhöler numbers, commonly used to characterise a turbulent regime, must be re-designed to account for thermo-diffusive effects. While these numbers are conventionally based on unstretched laminar flame properties, they suggest replacing these quantities by their freely propagating (i.e. unstable) flame counterparts to recover universal scalings.

This last case opens interesting discussions to extend the TD-S-TF model. As expected, the application of the model to a real turbulent explosion is not straightforward. Still, the TD-S-TF paradigm, separating the correction of resolved stretch effects and the modelling of subgrid TD effects, remains a strategy that is worth exploring.

Conclusion and perspectives

The works presented throughout this manuscript come within the scope of gas explosion studies led over the past few decades and in particular at CERFACS since the last ten years. It is part of the LEFEX (Large-Eddy simulation For gas EXplosions) project, a collaboration with TotalEnergies, Air Liquide, and GRTGaz which uses the expertise of CERFACS in the Computational Fluid Dynamics (CFD) field to develop numerical methodologies for accurately predicting gas explosions. This thesis proposes a modelling strategy for the Large-Eddy Simulation (LES) of lean hydrogen-air explosions.

The main particularity of lean H_2-air mixtures lies in their sub-unity Lewis number, which gives rise to: (1) a strong sensitivity of the flame to stretch; (2) the development of cells on the flame surface, characteristic of the thermo-diffusive (TD) instability. Both mechanisms are conducive to flame acceleration, which in turn determines the severity of an explosion. Correctly capturing these phenomena is therefore of paramount importance for an LES code to properly predict lean hydrogen-air explosion scenarios.

The main objectives of the present thesis were: (1) to assess the performance of existing LES methods for the simulation of lean H_2-air explosions; (2) to develop appropriate models to rectify potential deficiencies; (3) to apply these models in a realistic lean H_2-air explosion scenario. The final target configuration is the ENACCEF2 explosion from ICARE laboratory which is an academic mock-up of real lean H_2-air explosion events. That for, the work presented within this manuscript has been structured as follows:

1. in Chapter 5, the evaluation of classical models commonly used in the LES of explosions is carried out in a 2D tube configuration, representative of the early stages of an flame acceleration in a confined environment. It shows that neither stretch effects, nor the thermo-diffusive instability are correctly captured in the classical LES framework. The main outcome is a dependency to mesh resolution which calls for a reconsideration of the modelling strategy for lean H_2-air explosions;

2. the modelling strategy starts in Chapter 6: a correction, based on simple 1D flame simulations, is proposed to consistently capture the flame response to stretch;

3. in Chapter 7, this model is assessed first, in a 2D spherical flame configuration. On

top of that, Chapter 7 proposes a second block of correction with a model for the TD instability which is not resolved in LES. The two-component model (stretch effects and TD instability) is validated in a 3D spherical flame set-up representing the initial kernel development during an explosion;

4. in Chapter 8, the model is generalised to account for geometry effects and applied to the 2D tube flame of Chapter 5;

5. Finally, the modelling strategy is applied to the ENACCEF2 explosion scenario and confronted to the classical approaches in Chapter 9

The main findings of this thesis are now recalled.

This work starts with a state of the art on the classical modelling strategy applied to a reduced 2D tube lean hydrogen-air explosion. The various physical phenomena at play are first studied using DNS (rendered possible thanks to the reduced configuration size). Several hydrogen contents are studied under atmospheric conditions. The comparison of the various DNS shows that: for all mixtures, the flame tip follows an exponential acceleration characteristic of the so-called finger flame phenomenon linked with the confinement; on the lean side, the flame front cellular patterns characteristic of the thermo-diffusive instability are correctly captured and generate an acceleration which adds up to the finger flame baseline. In a second phase, the mesh resolution is decreased and the Thickened Flame (TF) model is activated. This approach is classically used for the LES of large-scale premixed flames. The flame front is artificially thickened by modifying the diffusion and reaction terms of the Navier-Stokes equations in order to resolve the flame structure on the coarse LES mesh. The classical TF model has already proved reliable for the simulation of explosion scenarios with classical fuels. However, during this thesis, several deficiencies have been identified when the TF model is applied to lean H_2-air flames:

- the thickening applied to the flame front amplifies its response to stretch. Under positive stretching, the consumption speed of the flame is exaggerated, resulting in an artificial acceleration of the flame front;

- thermo-diffusive instabilities are not captured in LES. This results from a "physical" stabilisation of the flame by thickening (a thicker flame is more resistant to the development of cells) and a numerical stabilisation (the small-scale cellular patterns cannot be resolved on the coarse LES mesh) which overall mitigates the flame acceleration.

The coupling of these two mechanisms generates a mesh dependency which questions the predictability of the classical TF model for lean H_2-air flames. Starting from these observations, this thesis follows a step-by-step plan to correct the shortcomings of the classical TF approach.

First, a strategy has been developed to properly capture the stretch response of thickened flames. To do so, this thesis proposes the construction of stretch-fitted global

chemistries, named *1S-LeFit*, which match a detailed chemical reference in terms of unstretched flame properties (laminar flame speed, adiabatic temperature, thermal thickness) and response to stretch. The use of this chemistry proves better-suited for the DNS of hydrogen flames than the classically used unity Lewis assumption (which generates stretch-insensitive flames). Then, in the LES framework, the amplification of stretch effects by the classical TF model is corrected by the introduction of the *Stretched-Thickened Flame* (S-TF) model. It uses the same formalism as the classical TF approach by modifying diffusion and reaction terms. In that sense, it preserves the simplicity of the TF model and offers a viable solution easy to implement in complex CFD codes. The model is based on an optimisation problem using 1D counterflow premixed flames at a reduced computational cost and tries to minimise the error at a given target strain rate. The choice of this target is essential to determine the range of applicability of the model for the highly sensitive lean H_2-air flames considered in this manuscript. But the overall error in stretch response is substantially reduced in comparison with the classical TF model.

Following the resolution of the stretch amplification issue, the next step studies the modelling of flame front instabilities. To this end, the *Thermo-Diffusive-Stretched-Thickened Flame* (TD-S-TF) model is proposed. As it name suggests, the TD-S-TF approach builds upon the formerly described S-TF model and adds an efficiency for the subgrid TD instabilities. This novel paradigm, separating resolved stretch effects and subgrid TD effects, differs from standard strategies encompassing all effects into a unique efficiency value. The TD efficiency is established on experimental correlations which account for the unsteady development of TD cells on the flame surface. The TD-S-TF model represents a convenient solution for the LES of lean H_2-air flames which only requires: the mixture effective Lewis number (given by theoretical relations), a critical kernel size for the onset of TD instabilities (obtained from empirical correlations). It is formulated in a generic manner which makes it readily applicable for other stable/unstable mixtures or operating conditions. After its development on 2D spherical flames, the strategy is validated against real experimental measurements of 3D spherical flames.

The next step towards realistic explosion scenarios is the application of the TD-S-TF model to a confined flame propagation. The 2D tube set-up (used previously for the evaluation of the classical TF approach) is reconsidered with the newly developed strategy. The S-TF component is conserved as-is, but the thermo-diffusive efficiency function is saturated at a certain kernel size. This choice is justified by DNS studies also carried out during this thesis which showed that the effects of TD instabilities saturate in a tube flame propagation. The extension of the TD-S-TF is successfully validated for several tube sizes and solves the mesh dependency of the TF model identified in the initial state of the art.

Finally, the last part of the manuscript confronts the classical TF LES model to the novel TD-S-TF strategy developed during this thesis in a real explosion scenario. The ENACCEF2 experimental test rig has been chosen: it is composed of a fully closed cylindrical tube in which 9 annular obstacles are placed. The vessel is vertically installed, filled with a H_2-air premix and ignited at the bottom plate. Two very lean H_2-air operating

conditions were investigated: $\Phi = 0.420$ and $\Phi = 0.356$. The phenomenology is similar for both explosions. The first part of the propagation resembles the laminar finger flame acceleration described beforehand. As the combustion wave advances in the vessel, fresh gases ahead of it are pushed forward due to the thermal expansion across the flame interface and the confinement (piston effect). When the flame traverses each orifice, it accelerates due to the flow contraction and the surface area increase imparted both by the geometry and by turbulence-flame interactions. The proximity of the obstacles creates a positive feedback loop progressively increasing the flame speed to reach several hundreds of meters per second at the exit of the obstructed region.

Regarding the simulations results, the classical TF LES model remarkably catches the flame dynamics measured in the experiments, with a weak dependency to mesh resolution. This observation must be linked to the fact that the turbulent combustion model represents the dominant contributor to flame acceleration in ENACCEF2 ($\approx 90\%$ of the total surface area in the obstructed region) and that the turbulent efficiency function seems to adequately adapt its values when the mesh resolution is modified. It is also believed that the amplification of stretch effects plays an important role for the flame acceleration. Despite its relatively good performance, the classical TF LES approach remains conceptually ill-posed.

For the TD-S-TF model, ENACCEF2 constitutes a challenging step forward in comparison with previous configurations treated in this manuscript because of the complexity of the explosion scenario. Indeed, the ENACCEF2 explosion involves new physical phenomena among which: a significant pressure rise due to the flame acceleration in an enclosed environment; and most importantly the presence of turbulence during the flame propagation. The intensity of the thermo-diffusive instability in a turbulent regime remains an open question in the research community. Furthermore, the coupling of the thermo-diffusive efficiency and the classical turbulent efficiency (modelling subgrid turbulence-flame interactions in the TF framework) is a thorny issue. In the present work, it has been decided to keep the TD efficiency saturated (as explained above) and to multiply it with the turbulent efficiency (e.g. the two phenomena occur independently). When applied to the test case at $\Phi = 0.420$, the TD-S-TF model is able to capture both qualitatively and quantitatively all phases of the propagation. Overall, the flame speed evolution and the levels of overpressure are correctly reproduced by the TD-S-TF LES, thereby constituting an important feat for the proposed modelling strategy.

In a last LES simulation of ENACCEF2, the hydrogen content has been changed to $\Phi = 0.356$. In this leaner mixture, the TD-S-TF model does qualitatively reproduce the various stages of flame acceleration, but the flame speed levels do not quantitatively agree with experimental data (the propagation is too slow). This observation puts in perspective the previous assumptions on the thermo-diffusive instability in a turbulent context. First, it is expected that the intensity of the TD instability can locally vary (in time and space) depending on the turbulent regime where the flame segment sits. One may expect synergistic effects between the two phenomena. Given that the dynamics of thermo-diffusive instabilities is closely related to the local curvature of the flame, turbulent

motions interacting with the flame interface can reinforce the instability by generating such curvature. On top of that, the definition of Karlovitz and Damkhöler numbers, commonly used to characterise a turbulent regime, must be re-designed to account for thermo-diffusive effects. While these quantities are conventionally based on unstretched laminar flame properties, the presence of thermo-diffusive instabilities locally affects the flame and calls for a reconsideration of general scaling laws. These final points open discussions on possible extensions of the TD-S-TF model for turbulent flames. They will be the subject of the PhD thesis of Francís Adrián Meziat Ramírez also part of the LEFEX project.

Appendix A

Interactions between the finger-flame mechanism and thermo-diffusive instabilities

The publication in the *Proceedings of the 28th International Colloquium on the Dynamics of Explosions and Reactive Systems* [319] about the interactions of flame front instabilities with the confinement due to lateral walls in a tube is included below.

Effect of Flame Front Thermo-Diffusive Instability on Flame Acceleration in a Tube

Jean-Jacques Hok, Omar Dounia, Olivier Vermorel, Thomas Jaravel
CERFACS
Toulouse, FRANCE

1 Introduction

Being decarbonated, hydrogen stands as an interesting candidate to reduce greenhouse gas emissions. However, its storage and transport in big quantities raise safety concerns. Following a leakage, mixed with the surrounding air, this hydrogen can form a highly flammable mixture. In case of accidental ignition of the hydrogen/air premix, different combustion scenarios and regimes are possible, depending on factors such as geometry (dimensions, presence of obstacles), mixture composition, temperature, pressure or turbulence level. These regimes range from slow deflagration to the transition to detonation in the worst case. However, even in the absence of a transition to detonation, the overpressure generated by the acceleration of the flame may threaten the integrity of people and facilities.

One specific case of interest for safety studies is the explosion scenario in a tube. This environment is indeed particularly conducive to flame acceleration leading to significant damage. The mechanism of flame propagation in tubes is well-documented. Among all, the studies of Bychkov et al. [1] and Valiev et al. [2] show three important properties of the early stages of flame propagation in tubes : (1) a flame acceleration phase is observed in the first instants after ignition; (2) this acceleration stage is limited in time and ends when the flame reaches the side walls; (3) the acceleration rate is inversely proportional to the tube radius.

The present study focuses on premixed mixtures of air and small concentrations of hydrogen, representative of leaks for instance. In these lean conditions, thermo-diffusive flame front instabilities are expected to develop. Indeed, the Lewis number of lean hydrogen-air mixtures is less than unity. It means that the unbalance between thermal diffusion of heat and molecular diffusion of reactants will lead to a flame instability enhancing the combustion processes and the flame acceleration. Following the pioneering work of Bechtold and Matalon [3] and Frankel and Sivashinsky [4], which gave the fundamental equations of linear stability theory, other papers provide more theoretical [5, 6], experimental [7, 8] and numerical [9, 10] investigations of flame front instabilities. These studies have all been conducted in canonical configurations such as planar flames and outwardly propagating spherical flames.

However, subunity-Lewis number flames in tubes will undergo the competing effects of both aforementioned acceleration mechanisms. Grosseuvres [11] and Katzy [12] have shown qualitatively from experimental measurements that flame front thermo-diffusive instabilities play a major role in the early propagation phase of a flame ignited in a tube. The question is now: how are both phenomena coupled ?

Correspondence to: hok@cerfacs.fr

The objective of the current paper is to provide a numerical study of the interplay between these two flame acceleration mechanisms: thermo-diffusive instabilities and finger-flame effects.

2 Numerical methods

It is usually agreed upon that thermo-diffusive instabilities result in cellular structures at scales ranging down to the flame thickness [9]. Due to computational cost constraints, Direct Numerical Simulations (DNS) of 3D tubes are impractical. Therefore, a 2D configuration is retained. A schematic of a characteristic set-up is depicted in Figure 1. A symmetry is imposed at the bottom to reduce the computational domain to half-a-tube. A slipping (resp. non-slipping) adiabatic condition is set on the left (resp. top) wall while an outlet is imposed at the right end to mimic the rest of the tube. The left side velocity assumption is meant to avoid any initial flame wrinkling at the wall which would force the development of thermo-diffusive instabilities. Instead, a free-slip hypothesis ensures they can appear anywhere along the flame surface. The length of the tube is chosen twice as long as the diameter to allow for finger-flame development without influence of the outflow condition. The flame is artificially ignited by imposing a hot kernel of burnt gases on the bottom left corner of the domain. Its radius is set to 1 mm for all cases, lower than the critical radius for the onset of instabilities which is estimated around 9 mm [13]. This value also ensures that the initial flame kernel can be considered perfectly spherical, devoid of the lateral walls confinement effect.

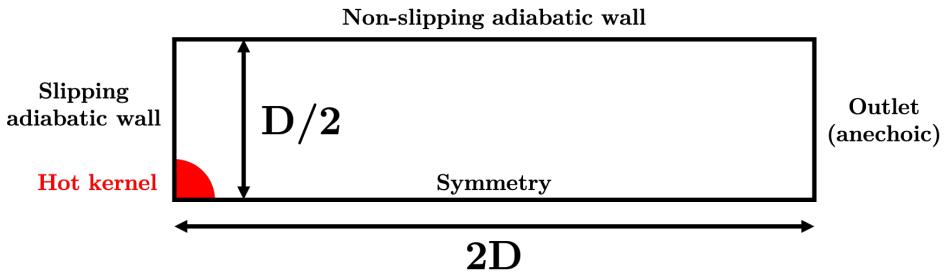

Figure 1: Schematic of tubes dimensions.

The chosen operating point corresponds to the exprimental conditions used by Grosseuvres [11] for which flame front instabilities are observed: homogeneous hydrogen-air mixture at $\Phi = 0.356$, $T_u = 296$ K, $P = 1$ atm.

To study the relative importance of thermo-diffusive instabilities versus finger-flame acceleration effects, three geometries are considered by varying the tube radius R_{tube} (while keeping the same aspect ratio). Each geometry is characterized by its adimensional radius defined as the ratio of R_{tube} over the flame diffusive thickness $Pe_{tube} = R_{tube}/l_f$. A summary of the different configurations is presented on Table 1.

Table 1: Test cases.

Name	Tube radius $\mathbf{R_{tube}}$ (mm)	Tube length (mm)	$\mathbf{Pe_{tube}}$
Tube S	54.2	216.8	250
Tube M	108.4	433.7	500
Tube L	216.8	867.4	1000

As for the chemistry, a 1-step scheme (four species, one reaction) following an Arrhenius law has been chosen. The advantage of such a scheme is to allow a direct choice of the Lewis number for species

involved in the global reaction whilst avoiding the complexity of intermediate species. To understand the interaction between flame instabilities and finger-flame effects, two chemistries are constructed. The first one assumes $Le_k = 1$ for each species k (noted "Le1") and allows a quantification of pure finger-flame propagation without any instability. The other uses realistic Lewis number values (noted 'LeRe'), retrieved from simulations using the detailed San Diego chemical scheme [14]. In both cases, the pre-exponential constant of the Arrhenius expression is tuned in order to fit the laminar flame speed to the San Diego chemical scheme [14]. The computations of laminar flame characteristics are performed using the CANTERA open-source code, yielding: $s_L^0 \approx 12$ cm/s (laminar flame speed), $T_{ad} \approx 1320$ K (adiabatic flame temperature), $\delta_{th} \approx 850$ µm (flame thermal thickness) and $l_f \approx 217$ µm (flame diffusive thickness).

To perform the DNS, quadrilateral meshes for the 3 tube diameters are generated with a resolution of about 85 µm, allowing around 10 grid points in the flame thermal thickness to resolve the instabilities. The 2D tube simulations are performed using AVBP [15], an in-house code developed at CERFACS solving the multi-species compressible Navier-Stokes equations on unstructured grids using parallelization for high-performance computing (HPC).

3 Results and discussion

3.1 Lewis number effects in the tube S configuration

The role of thermo-diffusive instabilities can be first highlighted by comparing the instantaneous flow fields over time for the two chemistries and for a given pipe diameter. Figure 2 depicts isotherms at $T = 600$ K computed every 10 ms using either the unitary Lewis (top) or the realistic Lewis scheme (bottom) in the tube S set-up. While the former front remains smooth throughout the propagation, the latter wrinkles soon after ignition. Significant flame acceleration results from this wrinkling as it substantially increases the flame surface area and thus the total reaction rate. This is evidenced by the increasing spacing of isocontours in the LeRe case.

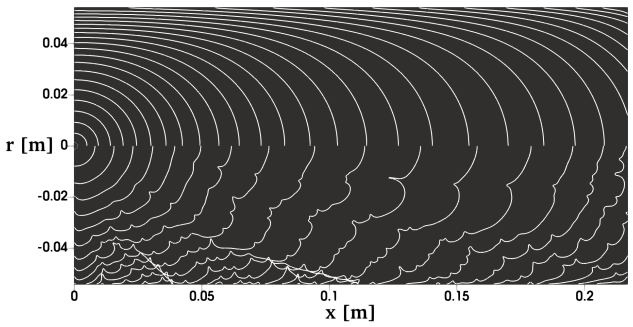

Figure 2: Snapshots of $T = 600$K-isotherms every 10 ms in the tube S. Le1 scheme (top) and LeRe scheme (bottom).

To assess more quantitatively the effect of instabilities on the propagation, the flame front speed v_{tip} is extracted, with the flame front position x_{tip} defined as the most advanced point in the tube in the x direction on the isotherm $T = 600$ K. Figure 3 shows the flame propagation in the $v_{tip} - x_{tip}$ frame. The kinematic model of Bychkov et al. [1] is represented by the dashed black line. According to their analysis:

$$v_{tip} = \sigma s_L^0 + \frac{s_L^0}{R_{tube}}(\sigma - 1)x_{tip} \tag{1}$$

where $\sigma = \rho_u/\rho_b$ is the thermal expansion parameter (ρ_u and ρ_b are respectively the unburnt and burnt gases density). The simulation with unitary Lewis chemistry follows properly that trend. This confirms that Bychkov's theory is valid for unitary Lewis mixtures. Furthermore, the flame decelerates around $x_{tip} = 0.16$ m, when the flame "skirt" touches the lateral walls. At that moment, the flame surface shrinks, explaining the strong speed reduction. On the other hand, during the first phase when the flame is far from lateral walls, the LeRe case exhibits a larger acceleration rate. It means that the flame front instabilities have a significant effect on the propagation. While the front still has an almost constant acceleration rate, as expected in the theory, the value of this acceleration is about twice as big compared to the Le1 case. It should also be noted that in this figure, the two curves do not start from the same initial flame speed. Indeed, the LeRe case starts at a greater velocity, due to stretch effects in the early spherical propagation. However, this phenomenon is rapidly overtaken by thermo-diffusive and finger-flame effects which contribute more significantly to flame acceleration.

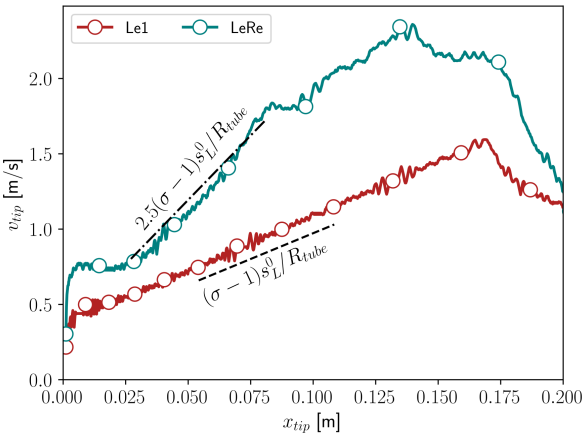

Figure 3: Flame front kinematic speed against flame front position in the tube S configuration. Dashed black line: asymptotic finger-flame acceleration slope [1]. Dot-dashed black line: 2.5 times the asymptotic finger-flame acceleration slope.

3.2 Competition between instabilities and finger-flame effects

To evaluate the prevalence of the effects of instabilities over finger-flame theory, flame kinematics for different tube radii are compared. Flame speeds are non-dimensionalized by s_L^0 to get s_{tip} whereas positions are divided by the tube radius R_{tube} to define ξ_{tip}.

First, the analysis in this non-dimensional $s_{tip} - \xi_{tip}$ phase-space on Figure 4 clearly demonstrates the similarity of all Le1 cases which collapse on a single curve. Indeed, following Equation 1, the asymptotic acceleration rate of the flame front in this space depends only on the thermal expansion ratio σ, namely:

$$s_{tip} = \sigma + (\sigma - 1)\xi_{tip} \tag{2}$$

To quantify the additional flame acceleration due to the thermo-diffusive instabilities described in Section 3.1, Figure 5 represents the flame tip non-dimensional speeds for the LeRe simulations divided by those obtained for the corresponding Le1 cases. Black stars on each curve denote the moment the flame skirt reaches the wall. It comes out that the influence of the instabilities depends on the tube radius. The larger the tube, the stronger the contribution of the instabilities to the flame acceleration. Indeed, widening the tube gives more room for instabilities to develop whereas the confinement effect of lateral walls weakens.

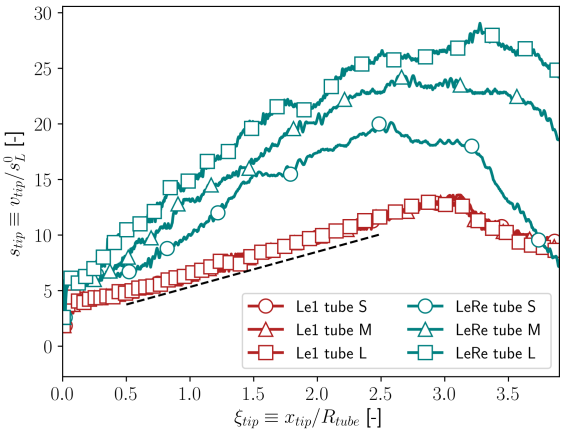

Figure 4: Non-dimensional flame front speed against non-dimensional position for several tube radii. Dashed black line: finger-flame acceleration slope [1].

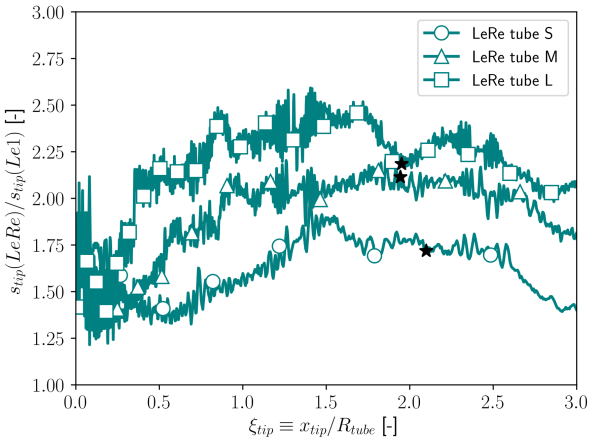

Figure 5: Non-dimensional flame speed for the LeRe cases divided by the corresponding Le1 cases against non-dimensional position for several tube radii.

4 Conclusion

Lean H_2-air flame propagation in a tube has been studied in order to understand the effect of flame front instabilities on flame acceleration occurring for mixtures at $Le < 1$. The comparison of simulations using unitary versus realistic Lewis numbers has given evidence for the additional acceleration due to the instabilities. Indeed, while the unitary-Lewis flames stay smooth and follow the finger-flame theory, the realistic-Lewis cases quickly form cells that contribute to combustion enhancement by supplementary wrinkling. A quantitative analysis has demonstrated that for a given tube radius, the acceleration rate of the thermo-diffusively unstable flame is considerably larger than that of the stable one. Besides, a variation in the tube radius has allowed for an analysis of the competing effects of instabilities and finger-flame. While small tubes are sufficiently narrow for finger-flame influence to be stronger than that of instabilities, larger tubes leave a broad channel in which instabilities develop longer before the flame takes on a tubular shape. It has also been shown on a similarity analysis that flame acceleration induced by the instabilities depend not only on the flame position, but also most importantly on the tube size. This means that, while conventional models developed in the spherical flame framework may be applicable to the initial short spherical phase, they cannot easily be extended to the finger-flame stage without a proper inclusion of the tube radius influence. Finally, it is worth mentioning that the current study of finger-flame and thermo-diffusive competition has been carried out by varying the tube radius, thus affecting the former effect. A perspective for future works would be to keep a single geometry and vary the chemistry so as to modify the thermo-diffusive influence.

5 Acknowledgments

This work was granted access to the HPC resources of TGCC and IDRIS under the allocation 2021-A0092B10157 made by GENCI. The authors are also grateful to TotalEnergies who funded the PhD thesis of Jean-Jacques Hok, within the framework of the LEFEX industrial partnership involving TotalEnergies, Air Liquide, GRTGaz and CERFACS.

References

[1] Bychkov, V., Akkerman, V., Fru, G., Petchenko, A., & Eriksson, L. (2007). Flame acceleration in the early stages of burning in tubes. Combustion and Flame, 150, 263-276

[2] Valiev, D. M., Akkerman, V., Kuznetsov, M., Eriksson, L. E., Law, C. K., & Bychkov, V. (2013). Influence of gas compression on flame acceleration in the early stage of burning in tubes. Combustion and Flame, 160(1), 97–111.

[3] Bechtold, J. K., & Matalon, M. (1987). Hydrodynamic and diffusion effects on the stability of spherically expanding flames. Combustion and Flame, 67(1), 77–90.

[4] Frankel, M. L., & Sivashinsky, G. I. (1982). The Effect of Viscosity on Hydrodynamic Stability of a Plane Flame Front. Combustion Science and Technology, 29(3–6), 207–224.

[5] Addabbo, R., Bechtold, J. K., & Matalon, M. (2002). Wrinkling of spherically expanding flames. Proceedings of the Combustion Institute, 29(2), 1527–1535.

[6] Matalon, M. (2007). Intrinsic flame instabilities in premixed and nonpremixed combustion. Annual Review of Fluid Mechanics, 39, 163–191.

[7] Bradley, D., Lawes, M., Liu, K., Verhelst, S., & Woolley, R. (2007). Laminar burning velocities of lean hydrogen-air mixtures at pressures up to 1.0 MPa. Combustion and Flame, 149(1–2), 162–172.

[8] Bauwens, C. R. L., Bergthorson, J. M., & Dorofeev, S. B. (2017). Experimental investigation of spherical-flame acceleration in lean hydrogen-air mixtures. International Journal of Hydrogen Energy, 42(11), 7691–7697.

[9] Altantzis, C., Frouzakis, C. E., Tomboulides, A. G., Matalon, M., & Boulouchos, K. (2012). Hydrodynamic and thermodiffusive instability effects on the evolution of laminar planar lean premixed hydrogen flames. Journal of Fluid Mechanics, 700(June), 329–361.

[10] Creta, F., Lapenna, P. E., Lamioni, R., Fogla, N., & Matalon, M. (2020). Propagation of premixed flames in the presence of Darrieus–Landau and thermal diffusive instabilities. Combustion and Flame, 216, 256–270.

[11] Grosseuvres, R., Bentaïb, A., & Chaumeix, N. (2019). Effect of initial temperature and temperature gradient on H_2/Air flame propagation in confined area. 27th ICDERS.

[12] Katzy, P., Hasslberger, J., Boeck, L. R., & Sattelmayer, T. (2017). The Effect of Intrinsic Instabilities on Effective Flame Speeds in Under-Resolved Simulations of Lean Hydrogen–Air Flames. Journal of Nuclear Engineering and Radiation Science, 3(4).

[13] Bradley, D. (1999). Instabilities and flame speeds in large-scale premixed gaseous explosions. Philosophical Transactions of the Royal Society A: Mathematical, Physical and Engineering Sciences, 358(1764), 3567–3581.

[14] "Chemical-Kinetic Mechanisms for Combustion Applications", San Diego Mechanism web page, Mechanical and Aerospace Engineering (Combustion Research), University of California at San Diego

[15] Colin, O., & Rudgyard, M. (2000). Development of High-Order Taylor-Galerkin Schemes for LES. Journal of Computational Physics, 162(2), 338–371.

Appendix B

Stretched-Thickened Flame model correlations

In Chapter 6, the Stretched-Thickened Flame (S-TF) model has been introduced to correct the amplification of stretch effects in a classical Thickened Flame framework. Under fixed operating conditions (T_u, P, Φ) and a given desired thickening factor F, the outputs of the model are the set of thickening factors ($F_\mathrm{th}, F_\mathrm{sp}, F_\mathrm{r}$) to be applied on the diffusion and reaction terms of the Navier-Stokes equations (see Figure 6.9). Provided that the coefficients containing the laminar flame speed sensitivity to D_th and D_k (noted α and β respectively) are correctly determined (see Appendix A of [295]), the S-TF model outputs can be described by the sole parameter $\widetilde{X_0}$ (all the thickening factors are computed following Equation (6.30)). In practice, in the LES of complex flames (e.g. the ENACCEF2 explosion considered in Chapter 9), the thickening factor greatly changes in space and time throughout the simulation. To account for these variations, the S-TF model is practically implemented by using a correlation of $\widetilde{X_0}$ with F. As can be seen in Figure B.1, their relation can indeed usually be represented by a simple correlation. In the work of Detomaso *et al.* [295], the functional form for propane-air flames was taken parabolic, of the type:

$$\widetilde{X_0} = \gamma(F-1)^2 + 1 \tag{B.1}$$

with γ representing a unique parameter to feed the LES code, along with $\mathrm{Le}^0_\mathrm{eff}$ and α (or β). For hydrogen-air flames, this function must be modified. Equation (B.1) imposes that $\widetilde{X_0}$ becomes extremal at $F = 1$, which seems not to be the case in Figure B.1. Instead, the functional form is generalised into:

$$\widetilde{X_0} = \gamma(F-1)^\eta(F-b) + 1 \tag{B.2}$$

Equation (B.2) allows a better representation of the $\widetilde{X_0}(F)$ relation for hydrogen-air flames and can degenerate into Equation (B.1) for propane-air flames (using $b = 1$ and $\eta = 1$).

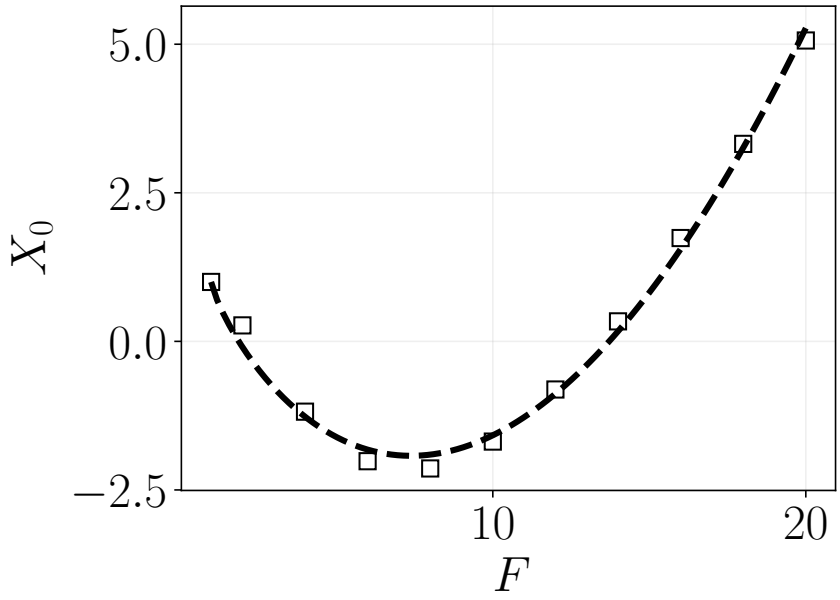

Figure B.1: Example of S-TF output $\widetilde{X_0}$ dependency to thickening F for a hydrogen-air flame at $\Phi = 0.400$ under atmospheric conditions ($\mathrm{Ka}_\infty = 1/5$). Symbols: results effectively obtained from an optimisation procedure (cf. Section 6.3.3). Dashed line: correlation (Equation (B.2)).

Appendix C

Transient from unstretched to stretched flame profiles

In Section 7.2.1 of the manuscript, the effect of using strained profiles for the initialisation of a spherical flame has been investigated. The reference case against which other simulations have been compared consists of a flame initialised with standard planar flame profiles but at a smaller radius. After a transient phase, these profiles have been considered close enough to realistic profiles. In this appendix, this transient period is analysed to see how the initial planar profiles adapt to the real physics of the problem. The same DNS at $\Phi = 0.4$ is considered. Figure C.1 depicts scatterplots of flame temperature and velocity magnitude as a function of the radial coordinate r for several instants of the propagation. Focusing first on the temperature scatterplot (Figure C.1a), several stages in the profile modification can be distinguished:

1. the initial profile (black scatterplot) is perfectly flat around T_{ad} on the burnt side as imposed by the unstretched planar flame;

2. then, as the simulation starts, during the early flame kernel growth (blue scatterplots), the profile progressively adapts to the stretch which heats up the flame front ($r \lesssim r_{\mathrm{f}}$). In the meantime, heat diffusion conveys the energy towards the core of the kernel ($r \ll r_{\mathrm{f}}$).

3. as the kernel gets bigger (reddish scatterplots), the curvature diminishes so the temperature behind the flame front reduces;

4. finally, when the flame size exceeds a critical radius (pink scatterplots), flame front instabilities kick in and broaden the distribution of temperature around the flame front ($r \approx r_{\mathrm{f}}$). The distribution loses its seemingly 1D shape. Some areas of the flame front (positively-curved) are heated up by thermo-diffusive effects and reach temperatures comparable to the preliminary highly stretched values.

These stages of the adaptation of numerical profiles to physical profiles is retrieved for the velocity field in Figure C.1b. The peak velocity ahead of the flame front is initially too low. It increases to adapt to the real physics and re-diminishes afterwards as curvature dies out. Note that the piston-like effect of the combustion wave is clearly illustrated on this diagram as well, with the escalation of the velocity field ahead of the flame front.

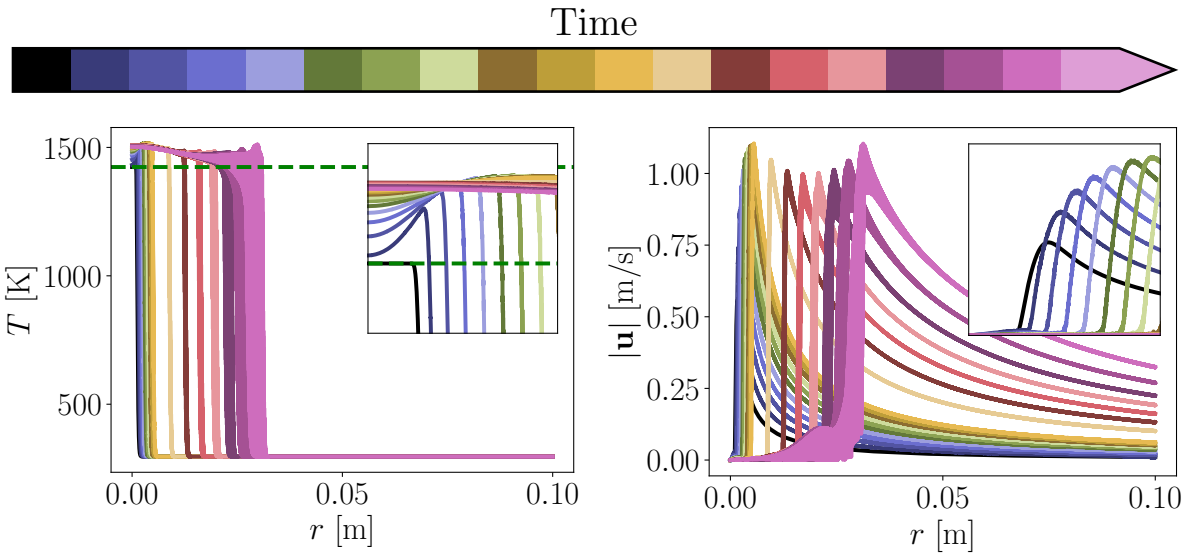

(a) Temperature. Dashed green line: adiabatic flame temperature.

(b) Velocity norm.

Figure C.1: Flame scatterplots of temperature and velocity magnitude as a function of radial coordinate r, at several instants of the propagation. DNS simulation at $\Phi = 0.4$ using a planar profiles initialisation at $r_\mathrm{f} = 2\delta_\mathrm{L}^0$ ($\mathrm{Pe}_{\mathrm{f},0} = 2$). All points of the 2D domain ($r < 0.1$ m) are plotted to reproduce the seemingly 1D profiles. Insets: zoom on the early propagation.

Appendix D

Pressure rise in ENACCEF2 and compression of fresh gases

In Section 9.3.1, the phenomenology of the ENACCEF2 explosion has been studied in terms of temperature and vorticity fields. Here, the pressure rise in the vessel is further analysed along with the preheating of the fresh gases induced by compression.

The displacement of fresh gases during flame acceleration is accompanied by a compression due to confinement. Figure D.1 depicts several snapshots of the pressure field during the explosion. At the beginning of the turbulent regime ($t = 80$ ms), the pressure rise is mild ($P - P_0 \approx 1$ bar). However, the flame front as well as some fresh gases ahead of it are thoroughly contained in a higher pressure zone which modifies the burning properties following the rationale in Sections 9.1.7 and 9.1.8. The pressure increase becomes substantial in the end of the obstructed region ($t \approx 82 - 83$ ms) where the flame tip reaches astonishing speeds (see Figure 9.16). The last snapshot ($t = 85$ ms) shows the shock wave that is formed ahead of the flame. Note that the compression is almost isentropic as assumed in Section 9.1.8. This is verified in Figure D.2 where a scatter plot of fresh gases temperature is plotted against pressure. The fresh gases are extracted by considering the progress variable segment $c \in [0, 0.1]$ (c being defined from the H_2 mass fraction, Equation (2.2)).

f

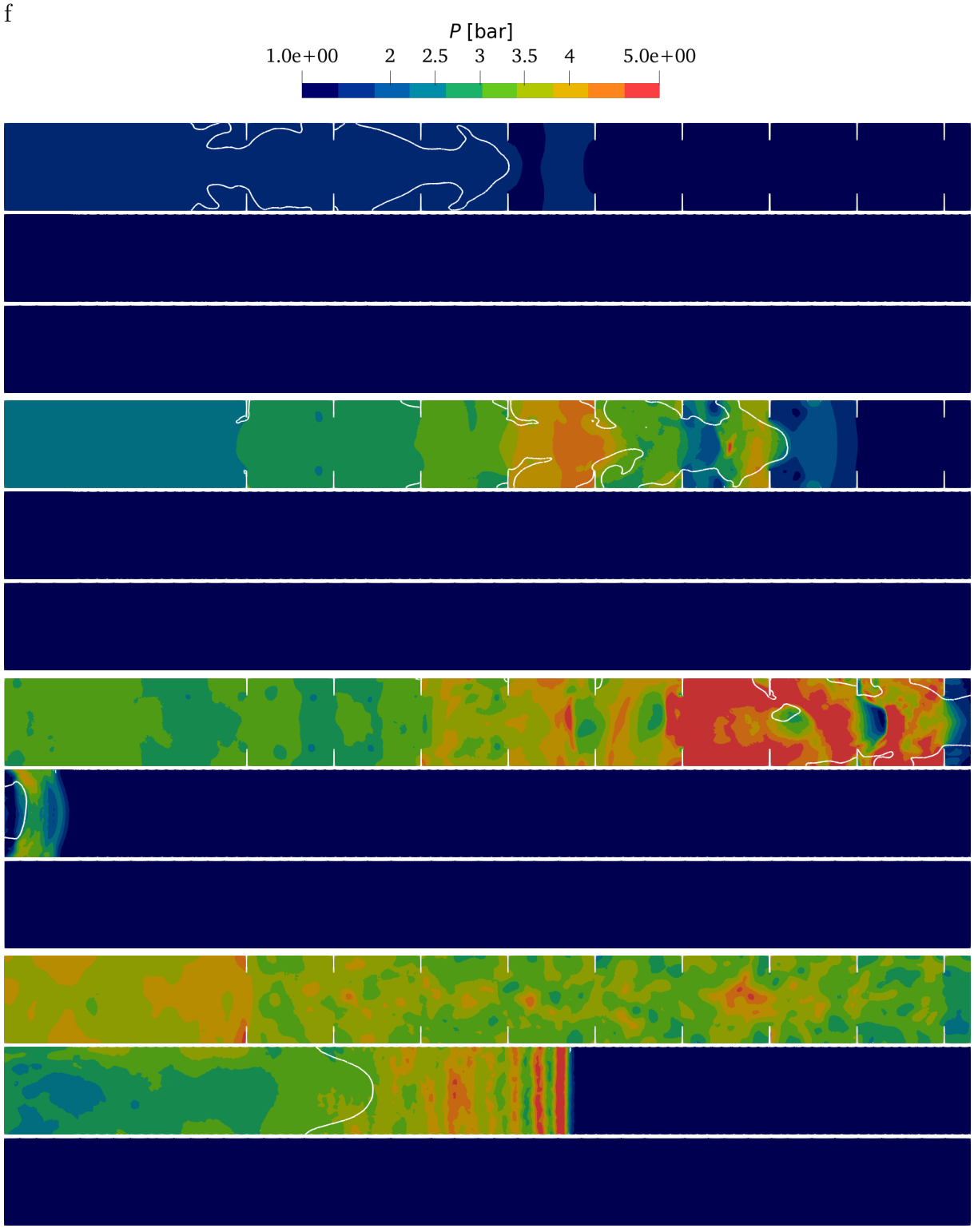

Figure D.1: Snapshots of pressure fields ($x-z$ plane) at several instants of the propagation for the TF LES on the mesh $\Delta x_{\text{fine}} = 4$ mm. White contour: flame front identified by isotherm $T = 800$ K. From top to bottom: after 80, 82, 83 and 85 ms.

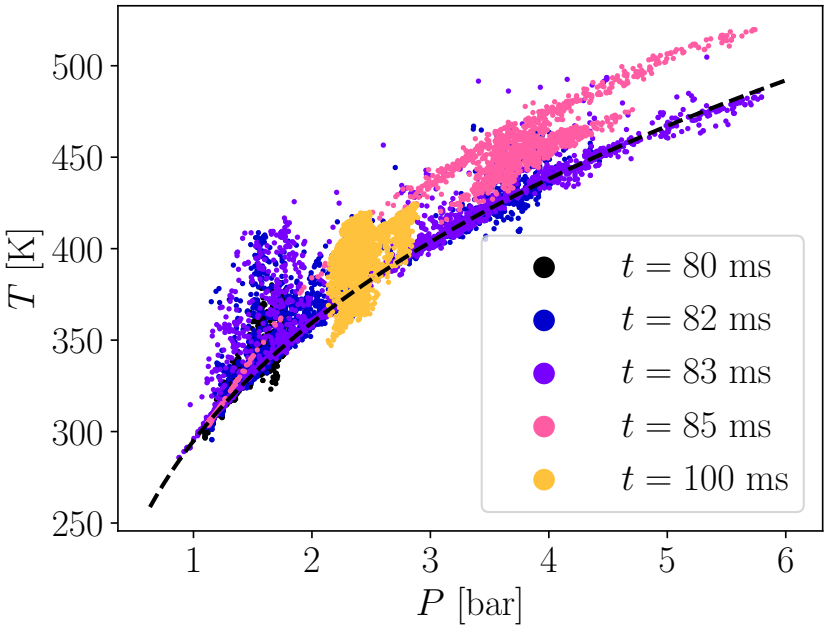

Figure D.2: Fresh gases temperature as a function of pressure for several instants of the propagation. TF LES on the mesh $\Delta x_{\text{fine}} = 4$ mm. Dashed black line: isentropic compression curve (Equation (9.2)).

Appendix E

Importance of the Lewis number in ENACCEF2 classical Thickened Flame simulations

In Chapter 9, it has been shown that the classical Thickened Flame (TF) approach, used with standard inputs (in particular for the turbulent efficiency function), is able to properly reproduce the flame acceleration dynamics in the ENACCEF2 explosion vessel, with a relatively weak dependency to mesh resolution. In the analysis (Section 9.6), it has been concluded that, as soon as the flame enters the turbulent regime (within the obstructed region of ENACCEF2), the turbulent combustion model becomes the dominant contributor to flame acceleration, with the amplification of stretch effects playing a supporting role. In this section, the contribution of stretch effects is further investigated by comparing the formerly described TF simulation which used a stretch-sensitive 1S-LeFit mechanism (cf. Section 9.1.6), with another TF LES using the unity-Lewis 1S-Le1 chemistry. The resulting flame propagations are depicted in Figure E.1. Contrary to the 1S-LeFit case which matches the flame speed evolution measured in the experiments, the 1S-Le1 LES is unable to reach such speed levels. As explained in Section 9.3.1, the flame acceleration in ENACCEF2 results from a positive feedback loop linked with the acceleration through each obstacle and the close spacing between two consecutive obstacles.

This feedback loop is further bolstered by the activation of the turbulent efficiency function, itself depending on the flow turbulence levels (u'). When the 1S-Le1 is used, the absence of stretch effects on the flame consumption weakens the initial acceleration, generating lower levels of u'. As a consequence, the turbulent efficiency function takes values that are overall smaller than in the 1S-LeFit LES (see Figure E.2). One link in the chain is made weaker thereby impacting the global flame acceleration. The present study highlights the importance of stretch effects in the ENACCEF2 simulation and demonstrates the incapacity of the classical TF LES to reproduce the correct flame dynamics with a stretch-effect-free chemistry.

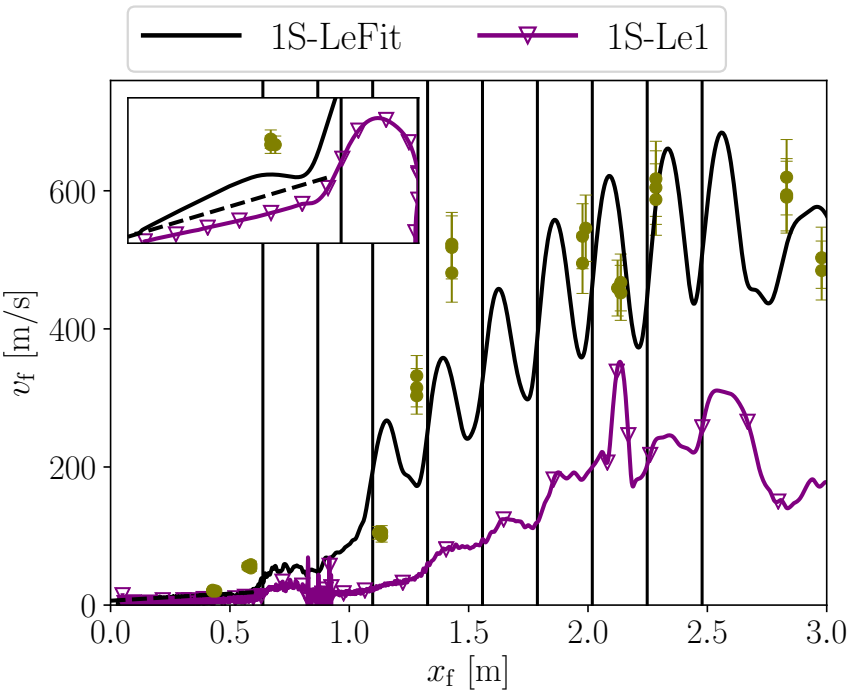

Figure E.1: Flame tip velocity as a function of flame tip position for the classical TF LES using a 1S-LeFit chemistry and a 1S-Le1 chemistry. Inset: zoom on laminar phase. Vertical bars: obstacles. Symbols: experimental measures (with error bars). Dashed line (bottom left diagram): finger flame theoretical slope (Equation (3.15)).

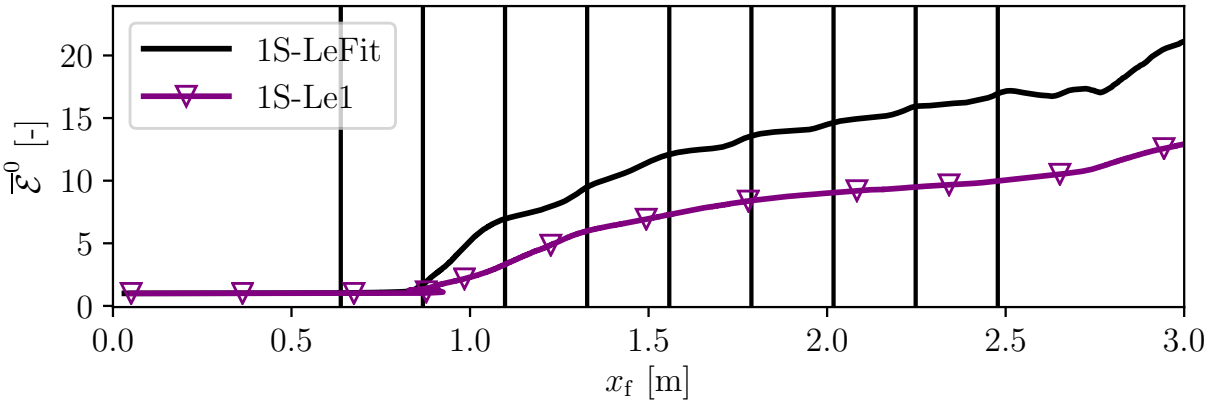

Figure E.2: Turbulent efficiency mean value (masked on the flame surface as explained in Section 9.3.2) for the TF LES simulation . $\Phi = 0.420$. Green solid line with circles: mean thickening factor (left y-axis). Red solid line with squares: mean turbulent efficiency (right y-axis).

Bibliography

[1] International Energy Agency, 'World Energy Outlook 2023,' Tech. Rep., 2023, pp. 1–355.

[2] OECD, 'Green economy and energy transition in emerging markets,' Tech. Rep., 2021, pp. 1–20.

[3] M. C. LaBelle, 'Energy as a weapon of war: Lessons from 50 years of energy interdependence,' *Global Policy*, vol. 14, no. 3, pp. 531–547, 2023.

[4] International Energy Agency, 'CO2 Emissions in 2022,' Tech. Rep., 2023.

[5] IPCC, 'Climate Change 2023: Technical Summary,' Tech. Rep., 2019, pp. 35–74.

[6] K. E. Cox and K. D. J. Williamson, *Hydrogen: Its Technology and Implications, Volume V*. 2018.

[7] E. Barbour, I. A. Wilson, J. Radcliffe, Y. Ding and Y. Li, 'A review of pumped hydro energy storage development in significant international electricity markets,' *Renewable and Sustainable Energy Reviews*, vol. 61, pp. 421–432, 2016.

[8] S. Ali, R. A. Stewart and O. Sahin, 'Drivers and barriers to the deployment of pumped hydro energy storage applications: Systematic literature review,' *Cleaner Engineering and Technology*, vol. 5, p. 100 281, 2021.

[9] S. Al-Thyabat, T. Nakamura, E. Shibata and A. Iizuka, 'Adaptation of minerals processing operations for lithium-ion (LiBs) and nickel metal hydride (NiMH) batteries recycling: Critical review,' *Minerals Engineering*, vol. 45, pp. 4–17, 2013.

[10] R. Deberdt and P. L. Billon, 'Conflict minerals and battery materials supply chains: A mapping review of responsible sourcing initiatives,' *Extractive Industries and Society*, vol. 8, no. 4, p. 100 935, 2021.

[11] A. G. Olabi, Q. Abbas, P. A. Shinde and M. A. Abdelkareem, 'Rechargeable batteries: Technological advancement, challenges, current and emerging applications,' *Energy*, vol. 266, no. November 2022, p. 126 408, 2023.

[12] International Energy Agency, 'The Role of Low-Carbon Fuels in the Clean Energy Transitions of the Power Sector,' Tech. Rep., 2021.

[13] P. Su-ungkavatin, L. Tiruta-Barna and L. Hamelin, 'Biofuels, electrofuels, electric or hydrogen?: A review of current and emerging sustainable aviation systems,' *Progress in Energy and Combustion Science*, vol. 96, no. January, p. 101 073, 2023.

[14] H. Ababneh and B. H. Hameed, 'Electrofuels as emerging new green alternative fuel: A review of recent literature,' *Energy Conversion and Management*, vol. 254, no. January, p. 115 213, 2022.

[15] D. Rusmanis *et al.*, 'Electrofuels in a circular economy: A systems approach towards net zero,' *Energy Conversion and Management*, vol. 292, no. February, 2023.

[16] J. M. Bergthorson *et al.*, 'Direct combustion of recyclable metal fuels for zero-carbon heat and power,' *Applied Energy*, vol. 160, pp. 368–382, 2015.

[17] S. Taamallah, K. Vogiatzaki, F. M. Alzahrani, E. M. Mokheimer, M. A. Habib and A. F. Ghoniem, 'Fuel flexibility, stability and emissions in premixed hydrogen-rich gas turbine combustion: Technology, fundamentals, and numerical simulations,' *Applied Energy*, vol. 154, pp. 1020–1047, 2015.

[18] A. Litheko, B. Oboirien and B. Patel, 'Life cycle assessment of Power-to-Gas (PtG) technology – Evaluation of system configurations of renewable hydrogen and methane production,' *Sustainable Energy Technologies and Assessments*, vol. 60, no. November, p. 103 527, 2023.

[19] S. R. Arsad *et al.*, 'Patent landscape review of hydrogen production methods: Assessing technological updates and innovations,' *International Journal of Hydrogen Energy*, vol. 50, pp. 447–472, 2024.

[20] International Energy Agency, 'Global Hydrogen Review 2023,' Tech. Rep., 2023.

[21] P. Muthukumar *et al.*, 'Review on large-scale hydrogen storage systems for better sustainability,' *International Journal of Hydrogen Energy*, vol. 48, no. 85, pp. 33 223–33 259, 2023.

[22] M. S. Sadaghiani, 'Introducing and energy analysis of a novel cryogenic hydrogen liquefaction process configuration,' *International Journal of Hydrogen Energy*, vol. 42, no. 9, pp. 6033–6050, 2017.

[23] U. Eberle, B. Mueller and R. von Helmolt, 'Fuel cell electric vehicles and hydrogen infrastructure: status 2012,' *Energy and Environmental Sciences*, vol. 5, no. 10, p. 8780, 2012.

[24] J. Yanez, M. Kuznetsov and A. Souto-Iglesias, 'An analysis of the hydrogen explosion in the Fukushima-Daiichi accident,' *International Journal of Hydrogen Energy*, vol. 40, no. 25, pp. 8261–8280, 2015.

[25] HYSAFE, 'Deliverable D113 Initial Guidance for Using Hydrogen in Confined Spaces - Results from InsHyde,' HYSAFE – Safety of Hydrogen As an Energy Carrier, Tech. Rep. January 2009, 2004, pp. 1–89.

[26] *ASTM E681-04*.

[27] J. H. Lee, *The Detonation Phenomenon*. Cambridge University Press, 2008.

[28] D. Bjerketvedt, J. R. Bakke and K. van Wingerden, 'Gas explosion handbook,' *Journal of hazardous materials*, vol. 52, no. 1, pp. 1–151, 1997.

[29] C. M. Galassi *et al.*, 'HIAD - Hydrogen incident and accident database,' *International Journal of Hydrogen Energy*, vol. 37, no. 22, pp. 17 351–17 357, 2012.

[30] ARIA, 'Accidentology involving hydrogen,' Tech. Rep., 2009, p. 18.

[31] F. Rigas and P. Amyotte, *Green Chemistry and Chemical Engineering: Hydrogen Safety*, S. Lee, Ed. 2012, p. 286.

[32] BARPI, 'Hydrogène et mobilité : risques à ne pas minimiser !' Tech. Rep., 2020, pp. 5–6.

[33] J. X. Wen *et al.*, 'Statistics, lessons learned and recommendations from analysis of HIAD 2.0 database,' *International Journal of Hydrogen Energy*, vol. 47, no. 38, pp. 17 082–17 096, 2022.

[34] F. Yang *et al.*, 'Review on hydrogen safety issues: Incident statistics, hydrogen diffusion, and detonation process,' *International Journal of Hydrogen Energy*, vol. 46, no. 61, pp. 31 467–31 488, 2021.

[35] S. De-León Almaraz, T. Kocsis, C. Azzaro-Pantel and Z. O. Szántó, 'Identifying social aspects related to the hydrogen economy: Review, synthesis, and research perspectives,' *International Journal of Hydrogen Energy*, vol. 49, no. August 2023, pp. 601–618, 2024.

[36] A. Bain and D. W. Van Vorst, 'Hindenburg tragedy revisited: The fatal flaw found,' *International Journal of Hydrogen Energy*, vol. 24, no. 5, pp. 399–403, 1999.

[37] M. Groethe, E. Merilo, J. Colton, S. Chiba, Y. Sato and H. Iwabuchi, 'Large-scale hydrogen deflagrations and detonations,' *International Journal of Hydrogen Energy*, vol. 32, no. 13, pp. 2125–2133, 2007.

[38] V. A. Petukhov, N. P. Bublik, P. A. Gusev, L. D. Gutkin and O. I. Solntsev, 'Influence of the initiation energy on development of hydrogen–air mixtures combustion in large spherical volumes,' *High Temperature*, vol. 54, no. 1, pp. 99–104, 2016.

[39] Z. Li *et al.*, 'Gas explosions of methane-air mixtures in a large-scale tube,' *Fuel*, vol. 285, no. September 2020, p. 119 239, 2021.

[40] R. Shen, Z. Jiao, T. Parker, Y. Sun and Q. Wang, 'Recent application of Computational Fluid Dynamics (CFD) in process safety and loss prevention: A review,' *Journal of Loss Prevention in the Process Industries*, vol. 67, no. March, p. 104 252, 2020.

[41] D. Baraldi *et al.*, 'An inter-comparison exercise on CFD model capabilities to simulate hydrogen deflagrations in a tunnel,' *International Journal of Hydrogen Energy*, vol. 34, no. 18, pp. 7862–7872, 2009.

[42] D. Baraldi *et al.*, 'An inter-comparison exercise on CFD model capabilities to simulate hydrogen deflagrations with pressure relief vents,' *International Journal of Hydrogen Energy*, vol. 35, no. 22, pp. 12 381–12 390, 2010.

[43] J. García *et al.*, 'An intercomparison exercise on the capabilities of CFD models to reproduce a large-scale hydrogen deflagration in open atmosphere,' *International Journal of Hydrogen Energy*, vol. 35, no. 9, pp. 4435–4444, 2010.

[44] D. Makarov *et al.*, 'An intercomparison of CFD models to predict lean and non-uniform hydrogen mixture explosions,' *International Journal of Hydrogen Energy*, vol. 35, no. 11, pp. 5754–5762, 2010.

[45] S. R. Gubba, S. S. Ibrahim, W. Malalasekera and A. R. Masri, 'LES modeling of premixed deflagrating flames in a small-scale vented explosion chamber with a series of solid obstructions,' *Combustion Science and Technology*, vol. 180, no. 10-11, pp. 1936–1955, 2008.

[46] S. S. Ibrahim, S. R. Gubba, A. R. Masri and W. Malalasekera, 'Calculations of explosion deflagrating flames using a dynamic flame surface density model,' *Journal of Loss Prevention in the Process Industries*, vol. 22, no. 3, pp. 258–264, 2009.

[47] C. R. Bauwens, J. Chaffee and S. B. Dorofeev, 'Vented explosion overpressures from combustion of hydrogen and hydrocarbon mixtures,' *International Journal of Hydrogen Energy*, vol. 36, no. 3, pp. 2329–2336, 2011.

[48] X. Wen, M. Yu, Z. Liu and W. Sun, 'Large eddy simulation of methane-air deflagration in an obstructed chamber using different combustion models,' *Journal of Loss Prevention in the Process Industries*, vol. 25, no. 4, pp. 730–738, 2012.

[49] P. Quillatre, 'Simulation aux grandes echelles d'explosions en domaine semi-confine,' Ph.D. dissertation, Université de Toulouse, Toulouse, France, 2014.

[50] M. A. Abdel-Raheem, S. S. Ibrahim, W. Malalasekera and A. R. Masri, 'Large Eddy simulation of hydrogen-air premixed flames in a small scale combustion chamber,' *International Journal of Hydrogen Energy*, vol. 40, no. 7, pp. 3098–3109, 2015.

[51] O. Vermorel, P. Quillatre and T. Poinsot, 'LES of explosions in venting chamber: A test case for premixed turbulent combustion models,' *Combustion and Flame*, vol. 183, pp. 207–223, 2017.

[52] P. S. Volpiani, T. Schmitt, O. Vermorel, P. Quillatre and D. Veynante, 'Large eddy simulation of explosion deflagrating flames using a dynamic wrinkling formulation,' *Combustion and Flame*, vol. 186, pp. 17–31, 2017.

[53] O. Dounia, 'Etudes des phénomènes d'accélération de flammes, transition à la détonation et d'inhibition de flammes,' Ph.D. dissertation, Institut National Polytechnique de Toulouse, 2018, pp. 1–162.

[54] I. C. Tolias and A. G. Venetsanos, 'An improved CFD model for vented deflagration simulations – Analysis of a medium-scale hydrogen experiment,' *International Journal of Hydrogen Energy*, vol. 43, no. 52, pp. 23 568–23 584, 2018.

[55] I. C. Tolias *et al.*, 'Numerical simulations of vented hydrogen deflagration in a medium-scale enclosure,' *Journal of Loss Prevention in the Process Industries*, vol. 52, no. August 2017, pp. 125–139, 2018.

[56] O. Dounia, O. Vermorel, A. Misdariis and T. Poinsot, 'Influence of kinetics on DDT simulations,' *Combustion and Flame*, vol. 200, pp. 1–14, 2019.

[57] R. Grosseuvres, 'Analyse de propagation de flammes Hydrogène-Air-Vapeur d'eau en milieu confiné,' Ph.D. dissertation, 2018.

[58] C. Law, *Combustion Physics*. 2006.

[59] P. Clavin and G. Searby, *Combustion waves and fronts in flows: Flames, shocks, detonations, ablation fronts and explosion of stars*. Cambridge University Press, 2004.

[60] P. Saxena and F. A. Williams, 'Testing a small detailed chemical-kinetic mechanism for the combustion of hydrogen and carbon monoxide,' *Combustion and Flame*, vol. 145, no. 1-2, pp. 316–323, 2006.

[61] N. Peters, *Turbulent Combustion*. Cambridge University Press, 2004.

[62] T. Poinsot and D. Veynante, *Theoretical and Numerical Combustion*, Third. 2012.

[63] F. H. Vance, Y. Shoshin, L. P. de Goey and J. A. van Oijen, 'A physical relationship between consumption and displacement speed for premixed flames with finite thickness,' *Proceedings of the Combustion Institute*, vol. 38, no. 2, pp. 2215–2223, 2021.

[64] G. K. Giannakopoulos, A. Gatzoulis, C. E. Frouzakis, M. Matalon and A. G. Tomboulides, 'Consistent definitions of "Flame Displacement Speed" and "Markstein Length" for premixed flame propagation,' *Combustion and Flame*, vol. 162, no. 4, pp. 1249–1264, 2015.

[65] G. K. Giannakopoulos, C. E. Frouzakis, S. Mohan, A. G. Tomboulides and M. Matalon, 'Consumption and displacement speeds of stretched premixed flames - Theory and simulations,' *Combustion and Flame*, vol. 208, pp. 164–181, 2019.

[66] L. R. Boeck, P. Katzy, J. Hasslberger, A. Kink and T. Sattelmayer, 'The GraVent DDT database,' *Shock Waves*, vol. 26, no. 5, pp. 683–685, 2016.

[67] M. Day, J. Bell, P. T. Bremer, V. Pascucci, V. Beckner and M. Lijewski, 'Turbulence effects on cellular burning structures in lean premixed hydrogen flames,' *Combustion and Flame*, vol. 156, no. 5, pp. 1035–1045, 2009.

[68] A. Bonhomme, L. Selle and T. Poinsot, 'Curvature and confinement effects for flame speed measurements in laminar spherical and cylindrical flames,' *Combustion and Flame*, vol. 160, no. 7, pp. 1208–1214, 2013.

[69] R. Borghi and M. Destriau, *Combustion and flames - chemical and physical principles*, Technip, Ed. 1998.

[70] N. Peters, 'The turbulent burning velocity for large-scale and small-scale turbulence,' *Journal of Fluid Mechanics*, vol. 384, pp. 107–132, 1999.

[71] S. Carnot, *Réflexions sur la puissance motrice du feu*. 1824.

[72] B. Karlovitz, D. Denniston Jr, D. Knapschaefer and F. Wells, 'Studies on Turbulent Flames : A. Flame Propagation Across Velocity Gradients, B. Turbulence Measurement in Flames,' *Symposium (International) on Combustion*, vol. 4, no. 1, pp. 613–620, 1953.

[73] S. M. Candel and T. J. Poinsot, 'Flame Stretch and the Balance Equation for the Flame Area,' *Combustion Science and Technology*, vol. 70, no. 1-3, pp. 1–15, 1990.

[74] M. Matalon, 'On Flame Stretch,' *Combustion Science and Technology*, vol. 31, pp. 169–181, 1983.

[75] M. Matalon, C. Cui and J. K. Bechtold, 'Hydrodynamic theory of premixed flames: Effects of stoichiometry, variable transport coefficients and arbitrary reaction orders,' *Journal of Fluid Mechanics*, vol. 487, no. 487, pp. 179–210, 2003.

[76] S. H. Chung and C. K. Law, 'An invariant derivation of flame stretch,' *Combustion and Flame*, vol. 55, no. 1, pp. 123–125, 1984.

[77] C. K. Law, 'Dynamics of stretched flames,' *Symposium (International) on Combustion*, vol. 22, no. 1, pp. 1381–1402, 1988.

[78] R. J. Kee, J. A. Miller, G. H. Evans and G. Dixon-Lewis, 'A computational model of the structure and extinction of strained, opposed flow, premixed methane-air flames,' *Symposium (International) on Combustion*, vol. 22, no. 1, pp. 1479–1494, 1989.

[79] R. J. Kee, M. E. Coltrin and P. Glarborg, *Chemically Reacting Flow: Theory and Practice*. John Wiley and Sons, 2003.

[80] C. Law, P. Cho, M. Mizomoto and H. Yoshida, 'Flame curvature and preferential diffusion in the burning intensity of bunsen flames,' *Symposium (International) on Combustion*, vol. 21, no. 1, pp. 1803–1809, 1986.

[81] P. Pelce and P. Clavin, 'Influence of hydrodynamics and diffusion upon the stability limits of laminar premixed flames,' *Journal of Fluid Mechanics*, pp. 425–443, 1982.

[82] P. Clavin and P. Garcia, 'The influence of the temperature dependence of diffusivities on the dynamics of flame fronts,' *Journal de Physique Théorique et Appliquée*, vol. 2, no. 2, pp. 245–263, 1983.

[83] G. Joulin and T. Mitani, 'Linear Stability Analysis of Two-Reactant Flames,' *Combustion and Flame*, vol. 40, pp. 235–246, 1981.

[84] J. K. Bechtold and M. Matalon, 'The dependence of the Markstein length on stoichiometry,' *Combustion and Flame*, vol. 127, no. 1-2, pp. 1906–1913, 2001.

[85] Y. Zel'dovich and D. Frank-Kamenetskii, 'Theory of thermal propagation of flame,' *Dynamics of Curved Fronts*, pp. 131–140, 1938.

[86] N. Darabiha, S. Candel and F. E. Marble, 'The effect of strain rate on a premixed laminar flame,' *Combustion and Flame*, vol. 64, pp. 203–217, 1986.

[87] W. B. Bush and F. E. Fendell, 'Asymptotic Analysis of Laminar Flame Propagation for General Lewis Numbers,' *Combustion Science and Technology*, vol. 1, pp. 421–428, 1970.

[88] P. Clavin and G. Joulin, 'Premixed flames in large scale and high intensity turbulent flow,' *Journal de Physique Lettres*, vol. 44, no. 1, pp. 1–12, 1983.

[89] J. K. Bechtold and M. Matalon, 'Hydrodynamic and diffusion effects on the stability of spherically expanding flames,' *Combustion and Flame*, vol. 67, no. 1, pp. 77–90, 1987.

[90] P. Clavin and F. Williams, 'Effects of molecular diffusion and of thermal expansion on the structure and dynamics of premixed flames in turbulent flows of large scale and low intensity,' *Journal of Fluid Mechanics*, vol. 116, pp. 251–282, 1982.

[91] G. Jomaas, C. K. Law and J. K. Bechtold, 'On transition to cellularity in expanding spherical flames,' *Journal of Fluid Mechanics*, vol. 583, pp. 1–26, 2007.

[92] N. Bouvet, F. Halter, C. Chauveau and Y. Yoon, 'On the effective Lewis number formulations for lean hydrogen/hydrocarbon/ air mixtures,' *International Journal of Hydrogen Energy*, vol. 38, no. 14, pp. 5949–5960, 2013.

[93] G. H. Markstein, *Nonsteady Flame Propagation*. 1964.

[94] F. N. Egolfopoulos, N. Hansen, Y. Ju, K. Kohse-Höinghaus, C. K. Law and F. Qi, 'Advances and challenges in laminar flame experiments and implications for combustion chemistry,' *Progress in Energy and Combustion Science*, vol. 43, pp. 36–67, 2014.

[95] C. K. Wu and C. K. Law, 'On the determination of laminar flame speeds from stretched flames,' *Twentieth Symposium (International) on Combustion*, vol. 20, no. 1, pp. 1941–1949, 1984.

[96] L. K. Tseng, M. A. Ismail and G. M. Faeth, 'Laminar burning velocities and Markstein numbers of hydrocarbon air flames,' *Combustion and Flame*, vol. 95, no. 4, pp. 410–426, 1993.

[97] K. T. Aung, M. I. Hassan and G. M. Faeth, 'Flame stretch interactions of laminar premixed hydrogen/air flames at normal temperature and pressure,' *Combustion and Flame*, vol. 109, no. 1-2, pp. 1–24, 1997.

[98] T. Shu, Y. Xue, W. Liang and Z. Ren, 'Extrapolations of laminar flame speeds from expanding spherical flames based on the finite-structure stretched flames,' *Combustion and Flame*, vol. 226, pp. 445–454, 2021.

[99] P. D. Ronney and G. I. Sivashinsky, 'A Theoretical Study of Propagation and Extinction of Nonsteady Spherical Flame Fronts,' *SIAM Journal on Applied Mathematics*, vol. 49, no. 4, pp. 1029–1046, 1989.

[100] A. P. Kelley and C. K. Law, 'Nonlinear effects in the extraction of laminar flame speeds from expanding spherical flames,' *Combustion and Flame*, vol. 156, no. 9, pp. 1844–1851, 2009.

[101] C. J. Sun, C. J. Sung, L. He and C. K. Law, 'Dynamics of weakly stretched flames: Quantitative description and extraction of global flame parameters,' *Combustion and Flame*, vol. 118, no. 1-2, pp. 108–128, 1999.

[102] C. K. Law and C. J. Sung, 'Structure, aerodynamics, and geometry of premixed flamelets,' *Progress in Energy and Combustion Science*, vol. 26, no. 4, pp. 459–505, 2000.

[103] C. D. Lind and J. C. Whitson, 'Explosive hazards associated with spills of large quantities of hazardous materials. Phase II.,' Department of Transportation, United States Coast Guard, Tech. Rep., 1977.

[104] J. Quinard, G. Searby, B. Denet and J. Grana-Otero, 'Self-turbulent flame speeds,' *Flow, Turbulence and Combustion*, no. 33, 2010.

[105] E. G. Groff, 'The cellular nature of confined spherical propane-air flames,' *Combustion and Flame*, vol. 48, no. C, pp. 51–62, 1982.

[106] S. Yang, A. Saha, F. Wu and C. K. Law, 'Morphology and self-acceleration of expanding laminar flames with flame-front cellular instabilities,' *Combustion and Flame*, vol. 171, pp. 112–118, 2016.

[107] G. Darrieus, 'Propagation d'un front de flamme,' *La Technique Moderne and Congrés de Mécanique Appliquée Paris*, 1938.

[108] L. D. Landau, 'On the theory of slow combustion,' *Acta Physicochimica*, 1944.

[109] G. I. Barenblatt, Y. Zel'dovich and A. Istratov, 'On diffusional thermal instability of laminar flame,' *Prikladnaya Mekhanika i Tekhnicheskaya Fizika*, vol. 2, no. 21, 1962.

[110] G. I. Sivashinsky, 'Diffusional-Thermal Theory of Cellular Flames,' *Combustion Science and Technology*, vol. 15, no. 3-4, pp. 137–145, 1977.

[111] G. Joulin and P. Clavin, 'Linear stability analysis of nonadiabatic flames: Diffusional-thermal model,' *Combustion and Flame*, vol. 35, no. C, pp. 139–153, 1979.

[112] M. L. Frankel and G. I. Sivashinsky, 'The Effect of Viscosity on Hydrodynamic Stability of a Plane Flame Front,' *Combustion Science and Technology*, vol. 29, no. 3-6, pp. 207–224, 1982.

[113] M. Matalon and B. J. Matkowsky, 'Flames as gasdynamic discontinuities,' *Journal of Fluid Mechanics*, vol. 124, pp. 239–259, 1982.

[114] J. Yuan, Y. Ju and C. K. Law, 'Coupled hydrodynamic and diffusional-thermal instabilities in flame propagation at subunity Lewis numbers,' *Physics of Fluids*, vol. 17, no. 7, pp. 1–10, 2005.

[115] Y. Rastigejev and M. Matalon, 'Nonlinear evolution of hydrodynamically unstable premixed flames,' *Journal of Fluid Mechanics*, vol. 554, pp. 371–392, 2006.

[116] M. Matalon, 'The Darrieus-Landau instability of premixed flames,' *Fluid Dynamics Research*, vol. 50, no. 5, 2018.

[117] C. Altantzis, C. E. Frouzakis, A. G. Tomboulides, M. Matalon and K. Boulouchos, 'Hydrodynamic and thermodiffusive instability effects on the evolution of laminar planar lean premixed hydrogen flames,' *Journal of Fluid Mechanics*, vol. 700, no. June, pp. 329–361, 2012.

[118] T. L. Howarth and A. J. Aspden, 'An empirical characteristic scaling model for freely-propagating lean premixed hydrogen flames,' *Combustion and Flame*, vol. 237, p. 111 805, 2022.

[119] M. Matalon and B. J. Matkowsky, 'On the stability of plane and curved flames,' *SIAM Journal of Applied Mathematics*, vol. 44, no. 2, pp. 327–343, 1984.

[120] R. Addabbo, J. K. Bechtold and M. Matalon, 'Wrinkling of spherically expanding flames,' *Proceedings of the Combustion Institute*, vol. 29, no. 2, pp. 1527–1535, 2002.

[121] A. G. Istratov and V. Librovich, 'On the stability of propagation of spherical flames,' *Journal of Applied Mechanics and Technical Physics*, no. 1, pp. 67–78, 1966.

[122] A. Istratov and V. Librovich, 'On the stability of gasdynamic discontinuities associated with chemical reactions. The case of a spherical flame,' *Acta Astronautica*, vol. 14, no. 5, pp. 453–467, 1969.

[123] O. C. Kwon, G. Rozenchan and C. K. Law, 'Cellular instabilities and self-acceleration of outwardly propagating spherical flames,' *Proceedings of the Combustion Institute*, vol. 29, no. 2, pp. 1775–1783, 2002.

[124] D. Bradley, C. G. Sheppart, R. Woolley, D. A. Greenhalgh and R. D. Lockett, 'The development and structure of flame instabilities and cellularity at low Markstein numbers in explosions,' *Combustion and Flame*, vol. 122, no. 1-2, pp. 195–209, 2000.

[125] M. Matalon, 'Intrinsic flame instabilities in premixed and nonpremixed combustion,' *Annual Review of Fluid Mechanics*, vol. 39, pp. 163–191, 2007.

[126] C. K. Law and G. M. Faeth, 'Opportunities and challenges of combustion in microgravity,' *Progress in Energy and Combustion Science*, vol. 20, no. 1, pp. 65–113, 1994.

[127] S. Ostrach, 'Natural Convection in Enclosures,' *Advances in Heat Transfer*, vol. 8, no. C, pp. 161–227, 1972.

[128] G. Patnaik and K. Kailasanath, 'Effect of gravity on the stability and structure of lean hydrogen-air flames,' *Symposium (International) on Combustion*, vol. 23, no. 1, pp. 1641–1647, 1990.

[129] L. Berger *et al.*, 'A DNS study of the impact of gravity on spherically expanding laminar premixed flames,' *Combustion and Flame*, vol. 216, pp. 412–425, 2020.

[130] H. Du, W. S. Chai, H. Wei and L. Zhou, 'Status and challenges for realizing low emission with hydrogen ultra-lean combustion,' *International Journal of Hydrogen Energy*, vol. 57, no. November 2023, pp. 1419–1436, 2024.

[131] N. B. Anikin, A. A. Tyaktev, I. A. Kirillov and V. A. Simonenko, 'Experimental Study of Early-Stage Dynamics of the Ascending and Descending Laminar Hydrogen-Air Flames in Vertical Closed Rectangular Tube,' *Proceedings of the 28th International Colloquium on the Dynamics of Explosions and Reactive Systems*, 2022, pp. 2–7.

[132] L. Leblanc, M. Manoubi, K. Dennis, Z. R. Liang and M. I. Radulescu, 'Dynamics of unconfined spherical flames: Influence of buoyancy,' *Physics of Fluids*, vol. 25, no. 9, pp. 5–7, 2013.

[133] Z. Y. Sun, F. S. Liu, X. C. Bao and X. H. Liu, 'Research on cellular instabilities in outwardly propagating spherical hydrogen-air flames,' *International Journal of Hydrogen Energy*, vol. 37, no. 9, pp. 7889–7899, 2012.

[134] J. Goulier, 'Comportements aux limites de flammes de prémélange hydrogène/air. Étude de la transition flamme laminaire-flamme turbulente,' Ph.D. dissertation, Université d'Orléans, Orléans, France, 2015.

[135] C. R. Bauwens, J. M. Bergthorson and S. B. Dorofeev, 'Experimental investigation of spherical-flame acceleration in lean hydrogen-air mixtures,' *International Journal of Hydrogen Energy*, vol. 42, no. 11, pp. 7691–7697, 2017.

[136] T. Katsumi, T. Aida, K. Aiba and S. Kadowaki, 'Outward propagation velocity and acceleration characteristics in hydrogen-air deflagration,' *International Journal of Hydrogen Energy*, vol. 42, no. 11, pp. 7360–7365, 2017.

[137] W. Kim, Y. Sato, T. Johzaki, T. Endo, D. Shimokuri and A. Miyoshi, 'Experimental study on self-acceleration in expanding spherical hydrogen-air flames,' *International Journal of Hydrogen Energy*, vol. 43, no. 27, pp. 12 556–12 564, 2018.

[138] X. J. Gu, M. Z. Haq, M. Lawes and R. Woolley, 'Laminar burning velocity and Markstein lengths of methane-air mixtures,' *Combustion and Flame*, vol. 121, no. 1-2, pp. 41–58, 2000.

[139] D. Bradley, M. Lawes and M. S. Mansour, 'Explosion bomb measurements of ethanol-air laminar gaseous flame characteristics at pressures up to 1.4 MPa,' *Combustion and Flame*, vol. 156, no. 7, pp. 1462–1470, 2009.

[140] D. Bradley, M. Lawes and R. Mumby, 'Cellular Flame Instabilities,' *Proceedings of 8th International Seminar on Fire & Explosion Hazards*, 2016, pp. 25–28.

[141] J. Beeckmann *et al.*, 'Propagation speed and stability of spherically expanding hydrogen/air flames: Experimental study and asymptotics,' *Proceedings of the Combustion Institute*, vol. 36, no. 1, pp. 1531–1538, 2017.

[142] X. Cai, J. Wang, Z. Bian, H. Zhao, H. Dai and Z. Huang, 'On transition to self-similar acceleration of spherically expanding flames with cellular instabilities,' *Combustion and Flame*, vol. 215, pp. 364–375, 2020.

[143] W. Kim, Y. Sato, T. Johzaki and T. Endo, 'Experimental study on the onset of flame acceleration due to cellular instabilities,' *Journal of Loss Prevention in the Process Industries*, vol. 60, no. March, pp. 264–268, 2019.

[144] W. K. Kim, T. Mogi, K. Kuwana and R. Dobashi, 'Self-similar propagation of expanding spherical flames in large scale gas explosions,' *Proceedings of the Combustion Institute*, vol. 35, no. 2, pp. 2051–2058, 2015.

[145] W. Kim, T. Imamura, T. Mogi and R. Dobashi, 'Experimental investigation on the onset of cellular instabilities and acceleration of expanding spherical flames,' *International Journal of Hydrogen Energy*, vol. 42, no. 21, pp. 14 821–14 828, 2017.

[146] T. L. Howarth, E. F. Hunt and A. J. Aspden, 'Thermodiffusively-unstable lean premixed hydrogen flames: Phenomenology, empirical modelling, and thermal leading points,' *Combustion and Flame*, vol. 253, p. 112 811, 2023.

[147] T. Iijima and T. Takeno, 'Effects of temperature and pressure on burning velocity,' *Combustion and Flame*, vol. 65, no. 1, pp. 35–43, 1986.

[148] D. R. Dowdy, D. B. Smith, S. C. Taylor and A. Williams, 'The use of expanding spherical flames to determine burning velocities and stretch effects in hydrogen/air mixtures,' *Twenty-Third Symposium (International) on Combustion*, vol. 23, no. 1, pp. 325–332, 199.

[149] S. D. Tse, D. L. Zhu and C. K. Law, 'Morphology and burning rates of expanding spherical flames in H2/O2/inert mixtures up to 60 atmospheres,' *Proceedings of the Combustion Institute*, vol. 28, no. 2, pp. 1793–1800, 2000.

[150] N. Lamoureux, N. Djebaïli-Chaumeix and C. E. Paillard, 'Laminar flame velocity determination for H2-air-He-CO2 mixtures using the spherical bomb method,' *Experimental Thermal and Fluid Science*, vol. 27, no. 4, pp. 385–393, 2003.

[151] C. K. Law, G. Jomaas and J. K. Bechtold, 'Cellular instabilities of expanding hydrogen/propane spherical flames at elevated pressures: Theory and experiment,' *Proceedings of the Combustion Institute*, vol. 30, no. 1, pp. 159–167, 2005.

[152] M. Kuznetsov, S. Kobelt, J. Grune and T. Jordan, 'Flammability limits and laminar flame speed of hydrogen-air mixtures at sub-atmospheric pressures,' *International Journal of Hydrogen Energy*, vol. 37, no. 22, pp. 17 580–17 588, 2012.

[153] G. Dayma, F. Halter and P. Dagaut, 'New insights into the peculiar behavior of laminar burning velocities of hydrogen-air flames according to pressure and equivalence ratio,' *Combustion and Flame*, vol. 161, no. 9, pp. 2235–2241, 2014.

[154] J. Goulier, N. Chaumeix, F. Halter, N. Meynet and A. Bentaïb, 'Experimental study of laminar and turbulent flame speed of a spherical flame in a fan-stirred closed vessel for hydrogen safety application,' *Nuclear Engineering and Design*, vol. 312, pp. 214–227, 2017.

[155] W. Han, P. Dai, X. Gou and Z. Chen, 'A review of laminar flame speeds of hydrogen and syngas measured from propagating spherical flames,' *Applications in Energy and Combustion Science*, vol. 1-4, no. October, p. 100 008, 2020.

[156] F. N. Egolfopoulos and C. K. Law, 'An experimental and computational study of the burning rates of ultra-lean to moderately-rich H2/O2/N2 laminar flames with pressure variations,' *Twenty-Third Symposium (International) on Combustion*, pp. 333–340, 1990.

[157] S. Verhelst, R. Woolley, M. Lawes and R. Sierens, 'Laminar and unstable burning velocities and Markstein lengths of hydrogen-air mixtures at engine-like conditions,' *Proceedings of the Combustion Institute*, vol. 30, no. 1, pp. 209–216, 2005.

[158] M. C. Krejci *et al.*, 'Laminar flame speed and ignition delay time data for the kinetic modeling of hydrogen and syngas fuel blends,' *Journal of Engineering for Gas Turbines and Power*, vol. 135, no. 2, pp. 1–10, 2013.

[159] L. Vervisch, E. Bidaux, K. N. Bray and W. Kollmann, 'Surface density function in premixed turbulent combustion modeling, similarities between probability density function and flame surface approaches,' *Physics of Fluids*, vol. 7, no. 10, pp. 2496–2503, 1995.

[160] M. Boger, D. Veynante, H. Boughanem and A. Trouvé, 'Direct numerical simulation analysis of flame surface density concept for large eddy simulation of turbulent premixed combustion,' *Symposium (International) on Combustion*, vol. 27, 1998, pp. 917–925.

[161] A. I. Gavrikov, V. V. Golub, A. Y. Mikushkin, V. A. Petukhov and V. V. Volodin, 'Lean hydrogen-air premixed flame with heat loss,' *International Journal of Hydrogen Energy*, vol. 44, no. 36, pp. 20 462–20 469, 2019.

[162] A. E. Dahoe, J. F. Zevenbergen, S. M. Lemkowitz and B. Scarlett, 'Dust explosions in spherical vessels: The role of flame thickness in the validity of the 'cube-root law',' *Journal of Loss Prevention in the Process Industries*, vol. 9, no. 1 SPEC. ISS. Pp. 33–44, 1996.

[163] E. S. Oran, G. Chamberlain and A. Pekalski, 'Mechanisms and occurrence of detonations in vapor cloud explosions,' *Progress in Energy and Combustion Science*, vol. 77, 2020.

[164] K. I. Shelkin, 'Influence of tube roughness on the formation and detonation propagation in gas,' *Zh. Eksp. Teor. Fiz.*, vol. 10, pp. 823–829, 1940.

[165] V. Akkerman, C. K. Law, V. Bychkov and L. E. Eriksson, 'Analysis of flame acceleration induced by wall friction in open tubes,' *Physics of Fluids*, vol. 22, no. 5, pp. 1–14, 2010.

[166] A. Adebiyi, R. Alkandari, D. Valiev and V. Akkerman, 'Effect of surface friction on ultrafast flame acceleration in obstructed cylindrical pipes,' *AIP Advances*, vol. 9, no. 3, 2019.

[167] Y. Xu, Y. Huang and G. Ma, 'A review on effects of different factors on gas explosions in underground structures,' *Underground Space*, vol. 5, no. 4, pp. 298–314, 2020.

[168] Q. Hu, X. Zhang and H. Hao, 'A review of hydrogen-air cloud explosions: The fundamentals, overpressure prediction methods, and influencing factors,' *International Journal of Hydrogen Energy*, vol. 48, no. 36, pp. 13 705–13 730, 2023.

[169] S. B. Dorofeev, 'Flame acceleration and DDT in gas explosions,' *Journal De Physique. IV : JP*, vol. 12, no. 7, 2002.

[170] R. K. Zipf *et al.*, 'Methane-air detonation experiments at NIOSH Lake Lynn Laboratory,' *Journal of Loss Prevention in the Process Industries*, vol. 26, no. 2, pp. 295–301, 2013.

[171] R. M. Kasmani, G. E. Andrews and H. N. Phylaktou, 'Experimental study on vented gas explosion in a cylindrical vessel with a vent duct,' *Process Safety and Environmental Protection*, vol. 91, no. 4, pp. 245–252, 2013.

[172] E. Vyazmina and S. Jallais, 'Validation and recommendations for FLACS CFD and engineering approaches to model hydrogen vented explosions: Effects of concentration, obstruction vent area and ignition position,' *International Journal of Hydrogen Energy*, vol. 41, no. 33, pp. 15 101–15 109, 2016.

[173] A. R. Masri, A. Alharbi, S. Meares and S. S. Ibrahim, 'A comparative study of turbulent premixed flames propagating past repeated obstacles,' *Industrial and Engineering Chemistry Research*, vol. 51, no. 22, pp. 7690–7703, 2012.

[174] R. K. Azadboni, A. Heidari and J. X. Wen, 'Numerical Studies of Flame Acceleration and Onset of Detonation in Homogenous and Inhomogeneous Mixture,' *Journal of Loss Prevention in the Process Industries*, vol. 64, no. March, p. 104 063, 2020.

[175] M. H. Shamsadin Saeid, J. Khadem, S. Emami and M. Ghodrat, 'Effect of diffusion time on the mechanism of deflagration to detonation transition in an inhomogeneous mixture of hydrogen-air,' *International Journal of Hydrogen Energy*, vol. 47, no. 55, pp. 23 411–23 426, 2022.

[176] H. Xiao, Q. Duan, L. Jiang and J. Sun, 'Effects of ignition location on premixed hydrogen/air flame propagation in a closed combustion tube,' *International Journal of Hydrogen Energy*, vol. 39, no. 16, pp. 8557–8563, 2014.

[177] J. Guo, X. Sun, S. Rui, Y. Cao, K. Hu and C. Wang, 'Effect of ignition position on vented hydrogen-air explosions,' *International Journal of Hydrogen Energy*, vol. 40, no. 45, pp. 15 780–15 788, 2015.

[178] S. K. Chow, R. P. Cleaver, M. Fairweather and D. G. Walker, 'An experimental study of vented explosions in A 3:1 aspect ratio cylindrical vessel,' *Process Safety and Environmental Protection*, vol. 78, no. 6, pp. 425–433, 2000.

[179] S. Rui, Q. Wang, C. Wang, J. Xiao, A. Zhang and T. Jordan, 'Effects of ignition location and vent area on the external explosion in vented hydrogen explosions,' *Process Safety and Environmental Protection*, vol. 183, no. November 2023, pp. 602–616, 2023.

[180] A. R. Masri, S. S. Ibrahim, N. Nehzat and A. R. Green, 'Experimental study of premixed flame propagation over various solid obstructions,' *Experimental Thermal and Fluid Science*, vol. 21, no. 1-3, pp. 109–116, 2000.

[181] V. N. Gamezo, T. Ogawa and E. S. Oran, 'Flame acceleration and DDT in channels with obstacles: Effect of obstacle spacing,' *Combustion and Flame*, vol. 155, no. 1-2, pp. 302–315, 2008.

[182] R. Hall, A. R. Masri, P. Yaroshchyk and S. S. Ibrahim, 'Effects of position and frequency of obstacles on turbulent premixed propagating flames,' *Combustion and Flame*, vol. 156, no. 2, pp. 439–446, 2009.

[183] C. T. Johansen and G. Ciccarelli, 'Visualization of the unburned gas flow field ahead of an accelerating flame in an obstructed square channel,' *Combustion and Flame*, vol. 156, no. 2, pp. 405–416, 2009.

[184] H. Xiao and E. S. Oran, 'Flame acceleration and deflagration-to-detonation transition in hydrogen-air mixture in a channel with an array of obstacles of different shapes,' *Combustion and Flame*, vol. 220, pp. 378–393, 2020.

[185] Y. Jiang, S. Qiu, W. Gao, B. Liang and Y. Li, 'Hydrogen flame acceleration and explosion overpressure characteristics in a closed obstructed duct,' *International Journal of Hydrogen Energy*, vol. 59, no. February, pp. 1–9, 2024.

[186] J. Kent, A. Masri, S. Starner and S. Ibrahim, 'A New Chamber to Study Premixed Flame Propagation Past Repeated Obstacles,' *5th Asia-Pacific Conference on Combustion*, 2005.

[187] K. G. Vollmer, F. Ettner and T. Sattelmayer, 'Deflagration-to-detonation transition in hydrogen/air mixtures with a concentration gradient,' *Combustion Science and Technology*, vol. 184, no. 10-11, pp. 1903–1915, 2012.

[188] C. Clanet and G. Searby, 'On the "Tulip Flame" Phenomenon,' *Combustion and Flame*, vol. 105, no. 225, 1996.

[189] V. Bychkov, V. Akkerman, G. Fru, A. Petchenko and L.-E. Eriksson, 'Flame acceleration in the early stages of burning in tubes,' *Combustion and Flame*, vol. 150, no. 4, pp. 263–276, 2007.

[190] D. M. Valiev, V. Akkerman, M. Kuznetsov, L. E. Eriksson, C. K. Law and V. Bychkov, 'Influence of gas compression on flame acceleration in the early stage of burning in tubes,' *Combustion and Flame*, vol. 160, no. 1, pp. 97–111, 2013.

[191] B. J. Arntzen, 'Modelling of turbulence and combustion for simulation of gas explosions in complex geometries,' Ph.D. dissertation, The Norwegian University of Science and Technology, 1998, p. 192.

[192] J. Daou and M. Matalon, 'Influence of conductive heat-losses on the propagation of premixed flames in channels,' *Combustion and Flame*, vol. 128, no. 4, pp. 321–339, 2002.

[193] D. K. Lee and K. Maruta, 'Heat recirculation effects on flame propagation and flame structure in a mesoscale tube,' *Combustion Theory and Modelling*, vol. 16, no. 3, pp. 507–536, 2012.

[194] G. P. Gauthier, G. M. Watson and J. M. Bergthorson, 'Burning rates and temperatures of flames in excess-enthalpy burners: A numerical study of flame propagation in small heat-recirculating tubes,' *Combustion and Flame*, vol. 161, no. 9, pp. 2348–2360, 2014.

[195] G. P. Gauthier and J. M. Bergthorson, 'Effect of external heat loss on the propagation and quenching of flames in small heat-recirculating tubes,' *Combustion and Flame*, vol. 173, pp. 27–38, 2016.

[196] C. Jiménez and V. N. Kurdyumov, 'Propagation of symmetric and non-symmetric lean hydrogen-air flames in narrow channels: Influence of heat losses,' *Proceedings of the Combustion Institute*, vol. 36, no. 1, pp. 1559–1567, 2017.

[197] M. Alkhabbaz, O. Abidakun, D. Valiev and V. Akkerman, 'Impact of the Lewis number on finger flame acceleration at the early stage of burning in channels and tubes,' *Physics of Fluids*, vol. 31, no. 8, 2019.

[198] V. V. Bychkov and M. A. Liberman, 'Dynamics and stability of premixed flames,' *Physics Report*, vol. 325, no. 4-5, pp. 115–237, 2000.

[199] P. Katzy, L. R. Boeck, J. Hasslberger and T. Sattelmayer, 'Application of high-speed OH-PLIF technique for improvement of lean hydrogen-air combustion modeling,' *Proceedings of the 2016 24th International Conference on Nuclear Engineering*, vol. 5, 2016, pp. 1–10.

[200] S. M. Frolov, I. V. Semenov, P. S. Utkin, P. V. Komissarov and V. V. Markov, 'Enhancement of Shock-to-Detonation Transition in Channels with Regular Shaped Obstacles,' *Proceedings of the 21st International Colloquium on the Dynamics of Explosions and Reactive Systems*, 2007, p. 8.

[201] L. R. Boeck, S. Lapointe, J. Melguizo-Gavilanes and G. Ciccarelli, 'Flame propagation across an obstacle: OH-PLIF and 2-D simulations with detailed chemistry,' *Proceedings of the Combustion Institute*, vol. 36, no. 2, pp. 2799–2806, 2017.

[202] V. Bychkov, D. Valiev and L. E. Eriksson, 'Physical mechanism of ultrafast flame acceleration,' *Physical Review Letters*, vol. 101, no. 16, pp. 1–4, 2008.

[203] A. M. Na'inna, H. N. Phylaktou and G. E. Andrews, 'The acceleration of flames in tube explosions with two obstacles as a function of the obstacle separation distance,' *Journal of Loss Prevention in the Process Industries*, vol. 26, no. 6, pp. 1597–1603, 2013.

[204] D. Valiev, V. Bychkov, V. Akkerman, C. K. Law and L. E. Eriksson, 'Flame acceleration in channels with obstacles in the deflagration-to-detonation transition,' *Combustion and Flame*, vol. 157, no. 5, pp. 1012–1021, 2010. arXiv: `1211.0655`.

[205] W. Breitung *et al.*, 'Flame Acceleration and Deflagration-to-Detonation Transition in Nuclear Safety,' *Nea/Csni/R(2000)7*, no. August, p. 455, 2000.

[206] G. Ciccarelli and S. Dorofeev, 'Flame acceleration and transition to detonation in ducts,' *Progress in Energy and Combustion Science*, vol. 34, no. 4, pp. 499–550, 2008.

[207] S. Huang, R. Huang, P. Zhou, Y. Zhang, Z. Yin and Z. Wang, 'Role of cellular wavelengths in self-acceleration of lean hydrogen-air expanding flames under turbulent conditions,' *International Journal of Hydrogen Energy*, vol. 46, no. 17, pp. 10 494–10 505, 2021.

[208] A. N. Lipatnikov, H. C. Lee, P. Dai, M. Wan and V. A. Sabelnikov, 'Transition from turbulence-dominated to instability-dominated combustion regime in lean hydrogen-air flames,' *Combustion and Flame*, vol. 259, no. November 2023, p. 113 170, 2024.

[209] L. Berger, A. Attili and H. Pitsch, 'Synergistic interactions of thermodiffusive instabilities and turbulence in lean hydrogen flames,' *Combustion and Flame*, vol. 244, p. 112 254, 2022.

[210] M. Rieth, A. Gruber, F. A. Williams and J. H. Chen, 'Enhanced burning rates in hydrogen-enriched turbulent premixed flames by diffusion of molecular and atomic hydrogen,' *Combustion and Flame*, vol. 239, p. 111 740, 2022.

[211] M. S. Kuznetsov, I. D. Matsukov, V. I. Alekseev and S. B. Dorofeev, 'Photographic study of unstable turbulent flames in obstructed channel.,' *International Colloquium on the Dynamics of Explosions and Reactive Systems*, pp. 10–12, 1999.

[212] M. Bambauer, J. Hasslberger and M. Klein, 'Direct Numerical Simulation of the Richtmyer–Meshkov Instability in Reactive and Nonreactive Flows,' *Combustion Science and Technology*, vol. 192, no. 11, pp. 2010–2027, 2020.

[213] H. Yang and M. I. Radulescu, 'Dynamics of cellular flame deformation after a head-on interaction with a shock wave: Reactive Richtmyer-Meshkov instability,' *Journal of Fluid Mechanics*, vol. 923, pp. 1–37, 2021. arXiv: 2009.02546.

[214] B. J. McBride, M. J. Zehe and S. Gordon, 'NASA Glenn coefficients for calculating thermodynamic properties of individual species,' Tech. Rep. September, 2002, p. 295.

[215] R. Stull and H. Prophet, 'JANAF thermodynamical tables, 2nd edition,' US National Bureau of Standards, Tech. Rep., 1971.

[216] F. A. Williams, *Combustion Theory*, Second. CRC Press, 1994.

[217] R. J. Kee, M. E. Coltrin, P. Glarborg and H. Zhu, *Chemically Reacting Flow: Theory, Modeling and Simulation*, Second. John Wiley and Sons, 2018.

[218] A. Ern and V. Giovangigli, *Multi-component transport algorithms*. Heidelberg: Springer Verlag, 1994.

[219] V. Giovangigli, *Multi-component Flow Modeling*. Boston: Birkhaüser, 1999.

[220] A. Ern and V. Giovangigli, *EGLIB A Multicomponent Transport Software for Fast and Accurate Evaluation Algorithms*, 2004.

[221] S. S. Penner, *Chemistry Problems in Jet Propulsion*. New York: Pergamon Press, 1957.

[222] J. Hirschfelder, C. Curtiss and R. Byrd, *Molecular theory of gases and liquids*. New York: John Wiley and Sons, 1969.

[223] R. A. Kenneth K. Kuo, *Fundamentals of Turbulent and Multiphase Turbulent Combustion*. 2012.

[224] V. Giovangigli and M. D. Smooke, 'Calculation of extinction limits for premixed laminar flames in a stagnation point flow,' *Journal of Computational Physics*, vol. 68, no. 2, pp. 327–345, 1987.

[225] R. Hilbert, F. Tap, H. El-Rabii and D. Thévenin, 'Impact of detailed chemistry and transport models on turbulent combustion simulations,' *Progress in Energy and Combustion Science*, vol. 30, no. 1, pp. 61–117, 2004.

[226] C. R. Wilke, 'A viscosity equation for gas mixtures,' *The Journal of Chemical Physics*, vol. 18, no. 4, pp. 517–519, 1950.

[227] R. Bird, W. Stewart and E. Lightfoot, *Transport phenomena*. New York: Wiley, 1960.

[228] S. Chandrasekhar, *Radiative Transfer*. New York; Dover, 1960.

[229] V. Kourganoff, *Basic Methods in Transfer Processes, Radiative Equilibrium and Neutron Diffusion*. New York; DOver, 1963.

[230] S. S. Penner and D. B. Olfe, *Radiation and Reentry*. New York: Academic Press, 1968.

[231] S. Mathur, P. K. Tondon and S. C. Saxena, 'Thermal conductivity of binary, ternary and quaternary mixtures of rare gases,' *Molecular Physics*, vol. 12, no. 6, pp. 569–579, 1967.

[232] E. A. Mason and S. C. Saxena, 'Approximate formula for the thermal conductivity of gas mixtures,' *Physics of Fluids*, vol. 1, no. 5, pp. 361–369, 1958.

[233] P. Paul, 'A Re-Evaluation of the Means Used To Calculate Transport,' *Twenty-seventh Symposium (International) on Combustion*, pp. 495–504, 1998.

[234] D. G. Goodwin, R. L. Speth and H. K. Moffat, *Cantera: An Object-oriented Software Toolkit for Chemical Kinetics, Thermodynamics, and Transport Processes*, 2018.

[235] M. Frenklach, H. Wang, M. Goldenberg, G. P. Smith and D. M. Golden, 'GRI-MECH: An optimized detailed chemical reaction mechanism for methane combustion. Topical report, September 1992-August 1995,' Tech. Rep., 1995.

[236] A. L. Sánchez and F. A. Williams, 'Recent advances in understanding of flammability characteristics of hydrogen,' *Progress in Energy and Combustion Science*, vol. 41, no. 1, pp. 1–55, 2014.

[237] J. Wirtz, 'Modelling the impact of fuel in aeronautical gas turbines,' Ph.D. dissertation, Institut National Polytechnique de Toulouse, 2022.

[238] F. Collin-Bastiani, O. Vermorel, C. Lacour, B. Lecordier and B. Cuenot, 'DNS of spark ignition using Analytically Reduced Chemistry including plasma kinetics,' *Proceedings of the Combustion Institute*, vol. 37, no. 4, pp. 5057–5064, 2019.

[239] A. Felden, E. Riber and B. Cuenot, 'Impact of direct integration of Analytically Reduced Chemistry in LES of a sooting swirled non-premixed combustor,' *Combustion and Flame*, vol. 191, pp. 270–286, 2018.

[240] P. W. Agostinelli, D. Laera, I. Boxx, L. Gicquel and T. Poinsot, 'Impact of wall heat transfer in Large Eddy Simulation of flame dynamics in a swirled combustion chamber,' *Combustion and Flame*, vol. 234, p. 111 728, 2021.

[241] P. W. Agostinelli, D. Laera, I. Chterev, I. Boxx, L. Gicquel and T. Poinsot, 'Large eddy simulations of mean pressure and H2 addition effects on the stabilization and dynamics of a partially-premixed swirled-stabilized methane flame,' *Combustion and Flame*, vol. 249, p. 112 592, 2023.

[242] T. Capurso, D. Laera, E. Riber and B. Cuenot, 'NOx pathways in lean partially premixed swirling H2-air turbulent flame,' *Combustion and Flame*, vol. 248, no. x, p. 112 581, 2023.

[243] V. Coulon, J. Gaucherand, V. Xing, D. Laera, C. Lapeyre and T. Poinsot, 'Direct numerical simulations of methane, ammonia-hydrogen and hydrogen turbulent premixed flames,' *Combustion and Flame*, vol. 256, p. 112 933, 2023.

[244] B. Franzelli, E. Riber and B. Cuenot, 'Impact of the chemical description on a Large Eddy Simulation of a lean partially premixed swirled flame,' *Comptes Rendus - Mecanique*, vol. 341, no. 1-2, pp. 247–256, 2013.

[245] G. Lacaze, E. Richardson and T. Poinsot, 'Large eddy simulation of spark ignition in a turbulent methane jet,' *Combustion and Flame*, vol. 156, no. 10, pp. 1993–2009, 2009.

[246] S. P. Bane, J. L. Ziegler and J. E. Shepherd, 'Investigation of the effect of electrode geometry on spark ignition,' *Combustion and Flame*, vol. 162, no. 2, pp. 462–469, 2015.

[247] A. Misdariis, O. Vermorel and T. Poinsot, 'LES of knocking in engines using dual heat transfer and two-step reduced schemes,' *Combustion and Flame*, vol. 162, no. 11, pp. 4304–4312, 2015.

[248] M. Boileau, G. Staffelbach, B. Cuenot, T. Poinsot and C. Bérat, 'LES of an ignition sequence in a gas turbine engine,' *Combustion and Flame*, vol. 154, no. 1-2, pp. 2–22, 2008.

[249] B. Vanbersel *et al.*, 'A systematic Adaptive Mesh Refinement method for Large Eddy Simulation of turbulent flame propagation,' *Flow, Turbulence and Combustion*, 2023.

[250] P. Moin and K. Mahesh, 'Direct numerical simulation: A Tool in Turbulence Research,' *Annual Review of Fluid Mechanics*, vol. 30, pp. 539–578, 1998.

[251] S. B. Pope, *Turbulent Flows*, 2000.

[252] B. H. Hjertager, 'Simulation of Transient Compressible Turbulent Reactive Flows,' *Combustion Science and Technology*, vol. 27, pp. 159–170, 1982.

[253] A. C. Van den Berg, 'Reagas-a code for numerical simulation of reactive gas dynamics in gas explosions,' Tech. Rep., 1989.

[254] N. R. Popat *et al.*, 'Investigations to improve and assess the accuracy of computational fluid dynamic based explosion models,' *Journal of Hazardous Materials*, vol. 45, no. 1, pp. 1–25, 1996.

[255] B. H. Hjertager and T. Solberg, 'A Review of Computional Fluid Dynamics (CFD) Modeling of Gas Explosions,' *Prevention of Hazardous Fires and Explosions*, 1999.

[256] D. Veynante and L. Vervisch, 'Turbulent combustion modeling,' *Progress in Energy and Combustion Science*, vol. 28, no. 3, pp. 193–266, 2002.

[257] F. Nicoud and F. Ducros, 'Subgrid-scale stress modelling based on the square of the velocity,' *Flow Measurement and Instrumentation*, vol. 62, pp. 183–200, 1999.

[258] R. W. Bilger, S. B. Pope, K. N. Bray and J. F. Driscoll, 'Paradigms in turbulent combustion research,' *Proceedings of the Combustion Institute*, vol. 30, no. 1, pp. 21–42, 2005.

[259] H. Pitsch, 'Large-eddy simulation of turbulent combustion,' *Annual Review of Fluid Mechanics*, vol. 38, pp. 453–482, 2006.

[260] S. B. Pope, 'Small scales, many species and the manifold challenges of turbulent combustion,' *Proceedings of the Combustion Institute*, vol. 34, no. 1, pp. 1–31, 2013.

[261] F. Williams, 'Turbulent combustion,' *The mathematics of combustion*, J. Buckmaster, Ed., Philadelphia, 1985, pp. 97–131.

[262] S. R. Gubba, S. S. Ibrahim, W. Malalasekera and A. R. Masri, 'An assessment of large eddy simulations of premixed flames propagating past repeated obstacles,' *Combustion Theory and Modelling*, vol. 13, no. 3, pp. 513–540, 2009.

[263] V. Di Sarli, A. Di Benedetto and G. Russo, 'Large Eddy Simulation of transient premixed flame-vortex interactions in gas explosions,' *Chemical Engineering Science*, vol. 71, pp. 539–551, 2012.

[264] B. Fiorina, R. Vicquelin, P. Auzillon, N. Darabiha, O. Gicquel and D. Veynante, 'A filtered tabulated chemistry model for LES of premixed combustion,' *Combustion and Flame*, vol. 157, no. 3, pp. 465–475, 2010.

[265] S. B. Pope, 'Lagrangian Pdf Methods,' *Annual Review of Fluid Mechanics*, vol. 26, pp. 23–63, 1994.

[266] T. D. Butler and P. J. O'Rourke, 'A numerical method for two dimensional unsteady reacting flows,' *Symposium (International) on Combustion*, vol. 16, no. 1, pp. 1503–1515, 1977.

[267] P. O'Rourke and F. Bracco, 'Two Scaling Transformations for the Numerical Computation of Multidimensional Unsteady Laminar Flames,' *Journal of Computational Physics*, vol. 203, pp. 185–203, 1979.

[268] J. P. Legier, T. Poinsot and D. Veynante, 'Dynamically thickened flame LES model for premixed and non-premixed turbulent combustion,' *Proceedings of the Summer Program, Centre for Turbulence Research*, pp. 157–168, 2000.

[269] C. Angelberger, D. Veynante, F. N. Egolfopoulos and T. Poinsot, 'Large eddy simulations of combustion instabilities in premixed flames,' *Proceedings of the Summer Program*, pp. 61–82, 1998.

[270] O. Colin, F. Ducros, D. Veynante and T. Poinsot, 'A thickened flame model for large eddy simulations of turbulent premixed combustion,' *Physics of Fluids*, vol. 12, no. 7, pp. 1843–1863, 2000.

[271] P. Flohr and H. Pitsch, 'A turbulent flame speed closure model for LES of industrial burner flows,' *Proceedings of the summer program*, pp. 169–179, 2000.

[272] W. W. Kim and S. Menon, 'Numerical modeling of turbulent premixed flames in the thin-reaction-zones regime,' *Combustion Science and Technology*, vol. 160, no. 1-6, pp. 119–150, 2000.

[273] H. Pitsch and L. Duchamp de Lageneste, 'Large-eddy simulation of premixed turbulent combustion,' *Proceedings of the Combustion Institute*, vol. 29, pp. 2001–2008, 2002.

[274] F. Charlette, C. Meneveau and D. Veynante, 'A power-law flame wrinkling model for LES of premixed turbulent combustion Part I: Non-dynamic formulation and initial tests,' *Combustion and Flame*, vol. 131, no. 1-2, pp. 159–180, 2002.

[275] I. B. Celik, Z. N. Cehreli and I. Yavuz, 'Index of resolution quality for large eddy simulations,' *Journal of Fluids Engineering, Transactions of the ASME*, vol. 127, no. 5, pp. 949–958, 2005.

[276] L. Selle *et al.*, 'Compressible large eddy simulation of turbulent combustion in complex geometry on unstructured meshes,' *Combustion and Flame*, vol. 137, no. 4, pp. 489–505, 2004.

[277] G. Kuenne, A. Ketelheun and J. Janicka, 'LES modeling of premixed combustion using a thickened flame approach coupled with FGM tabulated chemistry,' *Combustion and Flame*, vol. 158, no. 9, pp. 1750–1767, 2011.

[278] P. S. Volpiani, 'Dynamic wrinkling flame model for large eddy simulations of turbulent premixed combustion,' Ph.D. dissertation, 2017, pp. 1–212.

[279] M. Amerighi, 'LES investigation of a swirl stabilized technically premixed hydrogen flame with FGM and TFM models,' *Applied Thermal Engineering*, vol. 247, no. November 2023, p. 122 944, 2024.

[280] F. Proch and A. M. Kempf, 'Numerical analysis of the Cambridge stratified flame series using artificial thickened flame LES with tabulated premixed flame chemistry,' *Combustion and Flame*, vol. 161, no. 10, pp. 2627–2646, 2014.

[281] S. Yu and S. Navarro-Martinez, 'Modelling of deflagration to detonation transition using flame thickening,' *Proceedings of the Combustion Institute*, vol. 35, no. 2, pp. 1955–1961, 2015.

[282] T. J. Poinsot and S. K. Lele, 'Boundary conditions for direct simulations of compressible viscous flows,' *Journal of Computational Physics*, vol. 101, no. 1, pp. 104–129, 1992.

[283] A. Bonhomme, 'Numerical study of laminar and turbulent flames propagating in a fan-stirred vessel,' Ph.D. dissertation, 2014.

[284] C. Altantzis, C. E. Frouzakis, A. G. Tomboulides and K. Boulouchos, 'Direct numerical simulation of circular expanding premixed flames in a lean quiescent hydrogen-air mixture: Phenomenology and detailed flame front analysis,' *Combustion and Flame*, vol. 162, no. 2, pp. 331–344, 2015.

[285] M. Rieth, A. Gruber and J. H. Chen, 'The effect of pressure on lean premixed hydrogen-air flames,' *Combustion and Flame*, vol. 250, p. 112 514, 2023.

[286] P. E. Lapenna *et al.*, 'Data-driven subfilter modelling of thermo-diffusively unstable hydrogen–air premixed flames,' *Combustion Theory and Modelling*, vol. 25, no. 6, pp. 1064–1085, 2021.

[287] L. Berger *et al.*, 'Flame fingers and interactions of hydrodynamic and thermodiffusive instabilities in laminar lean hydrogen flames,' *Proceedings of the Combustion Institute*, vol. 39, no. 2, pp. 1525–1534, 2023.

[288] X. Wen, L. Berger, L. Cai, A. Parente and H. Pitsch, 'Thermodiffusively unstable laminar hydrogen flame in a sufficiently large 3D computational domain – Part I: Characteristic patterns,' *Combustion and Flame*, no. December, p. 113 278, 2023.

[289] D. A. Kessler, V. N. Gamezo and E. S. Oran, 'Simulations of flame acceleration and deflagration-to-detonation transitions in methane-air systems,' *Combustion and Flame*, vol. 157, no. 11, pp. 2063–2077, 2010.

[290] S. R. Gubba, S. S. Ibrahim, W. Malalasekera and A. R. Masri, 'Measurements and LES calculations of turbulent premixed flame propagation past repeated obstacles,' *Combustion and Flame*, vol. 158, no. 12, pp. 2465–2481, 2011.

[291] T. Jaravel, O. Dounia, Q. Malé and O. Vermorel, 'Deflagration to detonation transition in fast flames and tracking with chemical explosive mode analysis,' *Proceedings of the Combustion Institute*, vol. 38, no. 3, pp. 3529–3536, 2021.

[292] M. A. Liberman, M. F. Ivanov, O. E. Peil, D. M. Valiev and L. E. Eriksson, 'Self-acceleration and fractal structure of outward freely propagating flames,' *Physics of Fluids*, vol. 16, no. 7, pp. 2476–2482, 2004.

[293] O. C. Kwon and G. M. Faeth, 'Measurements and predictions of flame/stretch interactions of hydrogen-fueled laminar premixed flames,' *38th Aerospace Sciences Meeting and Exhibit*, vol. 2180, 2001.

[294] X. Lu, C. R. Kaplan and E. S. Oran, 'Predictions of flame acceleration, transition to detonation, and detonation propagation using the Chemical-Diffusive Model,' *Combustion and Flame*, vol. 235, p. 111 705, 2022.

[295] N. Detomaso, J.-j. Hok, O. Dounia, D. Laera and T. Poinsot, 'A generalization of the Thickened Flame model for stretched flames,' *Combustion and Flame*, vol. 258, p. 113 080, 2023.

[296] S. Popp, G. Kuenne, J. Janicka and C. Hasse, 'An extended artificial thickening approach for strained premixed flames,' *Combustion and Flame*, vol. 206, pp. 252–265, 2019.

[297] E. R. Hawkes and J. H. Chen, 'Comparison of direct numerical simulation of lean premixed methane-air flames with strained laminar flame calculations,' *Combustion and Flame*, vol. 144, no. 1-2, pp. 112–125, 2006.

[298] J.-J. Hok, 'Chemistry-flow interaction modelling for the Large Eddy Simulation of Explosions,' Ph.D. dissertation, Ecole Centrale de Lyon, 2020.

[299] A. L. Comer, T. P. Gallagher, K. Duraisamy and B. A. Rankin, 'A modified thickened flame model for simulating extinction,' *Combustion Theory and Modelling*, vol. 26, no. 7, pp. 1262–1292, 2022.

[300] S. Poncet, C. Mehl, K. Truffin and O. Colin, 'Modified diffusion model adapted to non-unity Lewis number mixtures for low flame stretch using the thickened flame model,' *11th European Combustion Meeting 2023*, 2023, pp. 1–4.

[301] P. Clavin and G. Searby, *Combustion waves and fronts in flows: Flames, shocks, detonations, ablation fronts and explosion of stars*. Cambridge University Press, 2016.

[302] R. Storn and K. Price, 'Differential evolution - a simple and efficient heuristic for global optimization over continuous spaces,' *Journal of Global Optimization*, vol. 11, pp. 341–359, 1997.

[303] R. Maly and M. Vogel, 'Initiation and propagation of flame fronts in lean CH4-air mixtures by the three modes of the ignition spark,' *Symposium (International) on Combustion*, vol. 17, no. 1, pp. 821–831, 1979.

[304] P. D. Ronney, 'Laser versus conventional ignition of flames,' *Optical Engineering*, vol. 33, no. 2, p. 510, 1994.

[305] T. A. Spiglanin, A. Mcilroy, E. W. Fournier, R. B. Cohen and J. A. Syage, 'Time-resolved imaging of flame kernels: Laser spark ignition of H2/O2/Ar mixtures,' *Combustion and Flame*, vol. 102, no. 3, pp. 310–328, 1995.

[306] J. L. Beduneau, B. Kim, L. Zimmer and Y. Ikeda, 'Measurements of minimum ignition energy in premixed laminar methane/air flow by using laser induced spark,' *Combustion and Flame*, vol. 132, no. 4, pp. 653–665, 2003.

[307] M. H. Morsy, 'Review and recent developments of laser ignition for internal combustion engines applications,' *Renewable and Sustainable Energy Reviews*, vol. 16, no. 7, pp. 4849–4875, 2012.

[308] F. Ruiz, G. Beardsell and G. Blanquart, 'Framework for simulating stationary spherical flames,' *Proceedings of the Combustion Institute*, vol. 000, pp. 1–9, 2020.

[309] S. Taylor, 'Burning Velocity and the Influence of Flame Stretch,' Ph.D. dissertation, University of Leeds, 1991, pp. 6–8.

[310] D. Bradley, M. Lawes, K. Liu, S. Verhelst and R. Woolley, 'Laminar burning velocities of lean hydrogen-air mixtures at pressures up to 1.0 MPa,' *Combustion and Flame*, vol. 149, no. 1-2, pp. 162–172, 2007.

[311] A. P. Kelley, G. Jomaas and C. K. Law, 'On the Critical Radius for Sustained Propagation of Spark-Ignited Spherical Flames,' *46th AIAA Aerospace Sciences Meeting and Exhibit*, no. January, pp. 1–10, 2008.

[312] E. Hu, Z. Huang, J. He, C. Jin, H. Miao and X. Wang, 'Measurement of laminar burning velocities and analysis of flame stabilities for hydrogen-air-diluent premixed mixtures,' *Chinese Science Bulletin*, vol. 54, no. 5, pp. 846–857, 2009.

[313] F. Wu, G. Jomaas and C. K. Law, 'An experimental investigation on self-acceleration of cellular spherical flames,' *Proceedings of the Combustion Institute*, vol. 34, no. 1, pp. 937–945, 2013.

[314] Z. Y. Sun and G. X. Li, 'Propagation characteristics of laminar spherical flames within homogeneous hydrogen-air mixtures,' *Energy*, vol. 116, pp. 116–127, 2016.

[315] Q. Liu, X. Chen, Y. Shen and Y. Zhang, 'Parameter extraction from spherically expanding flames propagated in hydrogen/air mixtures,' *International Journal of Hydrogen Energy*, vol. 44, no. 2, pp. 1227–1238, 2019.

[316] J. Grune, K. Sempert, M. Kuznetsov and T. Jordan, 'Experimental investigation of unconfined spherical and cylindrical flame propagation in hydrogen-air mixtures,' *International Journal of Hydrogen Energy*, vol. 46, no. 23, pp. 12 487–12 496, 2021.

[317] H. Zhao, G. Li, J. Wang, C. Yuan and Z. Huang, 'Effects of density ratio and differential diffusion on flame accelerative propagation of H2/O2/N2 mixtures,' *International Journal of Hydrogen Energy*, vol. 48, no. 24, pp. 9071–9081, 2023.

[318] S. Sengupta, 'Advanced methods for meshes in High Performance Computing of explosion simulations,' Ph.D. dissertation, Institut National Polytechnique de Toulouse, 2022.

[319] J.-J. Hok, O. Dounia, O. Vermorel and T. Jaravel, 'Effect of Flame Front Thermo-Diffusive Instability on Flame Acceleration in a Tube,' *Proceedings of the 28th International Colloquium on the Dynamics of Explosions and Reactive Systems*, 2022, pp. 1–6.

[320] L. Berger, A. Attili and H. Pitsch, 'Intrinsic instabilities in premixed hydrogen flames: parametric variation of pressure, equivalence ratio, and temperature. Part 2 – Non-linear regime and flame speed enhancement,' *Combustion and Flame*, vol. 240, p. 111 936, 2022.

[321] B. A. Aniello, D. Laera, L. Berger and A. Attili, 'Introducing thermodiffusive effects in LES of turbulent combustion for lean hydrogen - air flames,' *Proceedings of the Summer Program*, Center for Turbulence Research, 2022, pp. 267–277.

[322] R. Grosseuvres, A. Bentaïb and N. Chaumeix, 'Effect of initial temperature and temperature gradient on H2 / Air flame propagation in confined area,' *Proceedings of the 27th International Colloquium on the Dynamics of Explosions and Reactive Systems*, 2019.

[323] P. Schmitt, T. Poinsot, B. Schuermans and K. P. Geigle, 'Large-eddy simulation and experimental study of heat transfer, nitric oxide emissions and combustion instability in a swirled turbulent high-pressure burner,' *Journal of Fluid Mechanics*, vol. 570, pp. 17–46, 2007.

[324] K. Bioche, A. Pieyre, G. Ribert, F. Richecoeur and L. Vervisch, 'The role of gravity in the asymmetry of flames in narrow combustion chambers,' *Combustion and Flame*, vol. 203, pp. 238–246, 2019.

[325] F. Veiga-López, D. Martínez-Ruiz, M. Kuznetsov and M. Sánchez-Sanz, 'Thermoacoustic analysis of lean premixed hydrogen flames in narrow vertical channels,' *Fuel*, vol. 278, no. June, p. 118 212, 2020.

[326] A. Dejoan, C. Jiménez, D. Martínez-Ruiz, V. Muntean, M. Sánchez-Sanz and V. N. Kurdyumov, 'Flame propagation in narrow horizontal channels: Impact of the gravity field on the flame shape,' *Proceedings of the Combustion Institute*, vol. 39, no. 2, pp. 1535–1543, 2023.

[327] L. A. Lovachev, V. S. Babkin, V. A. Bunev, A. V. V'Yun, V. N. Krivulin and A. N. Baratov, 'Flammability limits: an invited review,' *Combustion and Flame*, vol. 20, no. 2, pp. 259–289, 1973.

[328] J. Jarosinski, R. A. Strehlow and A. Azarbarzin, 'The mechanisms of lean limit extinguishment of an upward and downward propagating flame in a standard flammability tube,' *Symposium (International) on Combustion*, vol. 19, no. 1, pp. 1549–1557, 1982.

[329] R. A. Strehlow, K. A. Noe and A. Brian, 'Extinction in a Vertical Standard Flammability Tube,' *Twenty-first Symposium (International) on Combustion/The Combustion Institute*, pp. 1899–1908, 1986.

[330] Y. M. Shtemler and G. I. Sivashinsky, 'On upward propagating flames,' *Combustion Science and Technology*, vol. 102, no. 1-6, pp. 81–93, 1994.

[331] X. Li, H. Xiao, Q. Duan and J. Sun, 'Numerical study of premixed flame dynamics in a closed tube: Effect of wall boundary condition,' *Proceedings of the Combustion Institute*, vol. 38, no. 2, pp. 2075–2082, 2021.

[332] S. P. Choudhury and R. Joarder, 'High-speed photography and background oriented schlieren techniques for characterizing tulip flame,' *Combustion and Flame*, vol. 245, p. 112 304, 2022.

[333] J. Hasslberger, P. Katzy and T. Sattelmayer, 'On the effect of pressure on intrinsic flame instabilities in lean hydrogen-air mixtures – Part I: Detailed chemistry based direct numerical simulation,' *Proceedings of the 26th International Colloquium on the Dynamics of Explosions and Reactive Systems*, 2017, pp. 1–6.

[334] P. Katzy, 'Combustion Model for the Computation of Flame Propagation in Lean Hydrogen-Air Mixtures at Low Turbulence,' Ph.D. dissertation, 2021.

[335] D. Zivkovic and T. Sattelmayer, 'Fractal-based RANS Modeling of Darrieus – Landau and Thermal-diffusive Instability Effects on Lean Hydrogen Flames,' *Proceedings of the 28th International Colloquium on the Dynamics of Explosions and Reactive Systems*, 2022, pp. 1–6.

[336] H. Chu, L. Berger, T. Grenga, Z. Wu and H. Pitsch, 'Effects of differential diffusion on hydrogen flame kernel development under engine conditions,' *Proceedings of the Combustion Institute*, vol. 39, no. 2, pp. 2129–2138, 2023.

[337] A. J. Aspden, M. S. Day and J. B. Bell, 'Characterization of low Lewis number flames,' *Proceedings of the Combustion Institute*, vol. 33, no. 1, pp. 1463–1471, 2011.

RÉPUBLIQUE FRANÇAISE
Liberté
Égalité
Fraternité

Université de Toulouse

Titre : Stratégie de modélisation pour la Simulation aux Grandes Echelles d'explosions de mélanges hydrogène-air pauvres

Mots clés : Combustion, Hydrogène, Explosions, Simulation aux Grandes Echelles, Instabilités de front de flamme

Résumé : La crise climatique à laquelle le monde est confronté aujourd'hui exige des actions immédiates pour réduire les émissions de carbone. En particulier, une transition énergétique rapide vers des sources plus propres est nécessaire. Parmi de nombreux candidats, l'hydrogène se distingue en tant que vecteur d'énergie décarboné. Cependant, son stockage et son transport en grandes quantités posent des problèmes de sécurité. Dans le cas d'une fuite accidentelle d'hydrogène, un mélange hautement inflammable peut se former. En cas d'allumage, différents scénarios et régimes de combustion sont possibles, en fonction de différents facteurs tels que la géométrie (dimensions, confinement, présence d'obstacles), la composition du mélange, la température, la pression ou le niveau de turbulence. Ces régimes vont de la déflagration lente à la transition vers la détonation dans le pire des cas. Pour prédire les dommages consécutifs à une explosion, la Mécanique des Fluides Numérique présente l'avantage d'être plus sûre que les expériences et de donner accès à des quantités difficiles ou impossibles à mesurer empiriquement. Cette thèse traite de la prédiction des explosions de mélanges d'hydrogène-air pauvres en utilisant l'approche de Simulation aux Grandes Échelles (SGE ou LES en anglais). Les mélanges pauvres d'H2-air sont caractérisés par leur nombre de Lewis subunitaire, qui traduit un déséquilibre entre les processus de diffusion moléculaire et thermique avec des conséquences majeures : (1) les flammes H2-air pauvres sont très sensibles à l'étirement ; (2) elles sont enclines à développer des cellules sur le front de flamme dues à l'instabilité thermo-diffusive. Les deux constituent des mécanismes d'accélération qui impactent la surpression générée lors de l'explosion. Dans ce travail, nous montrons que l'utilisation du modèle de Flamme Épaissie (TF en anglais) pour simuler les flammes à nombre de Lewis subunitaire : (1) induit une amplification de l'effet d'étirement sur la flamme ; (2) combinée à la faible résolution de maillage en LES, filtre les instabilités de front de flamme. Le couplage de ces mécanismes indésirables peut générer une propagation erronée de la flamme qui remet en question la capacité de prédiction de la LES pour les explosions de mélanges H2-air pauvres. Dans le cadre de cette thèse, une stratégie de modélisation est proposée afin de prédire de manière fiable et précise les explosions d'hydrogène-air pauvre. Un nouveau paradigme est envisagé pour corriger séparément l'amplification des effets d'étirement et modéliser les phénomènes de sous-maille dus à l'instabilité thermo-diffusive. Ces deux corrections sont d'abord développées sur des configurations canoniques, puis étendues et validées sur des configurations d'explosion plus réalistes.

Title: Modelling strategy for the Large-Eddy Simulation of lean hydrogen-air explosions

Key words: Combustion, Hydrogen, Explosions, Large-Eddy Simulation, Flamme front instabilities

Abstract: The climate crisis the world faces today calls for immediate actions to curb down carbon emissions. In particular, a rapid energy transition towards cleaner sources is necessary. Among many candidates, hydrogen stands out as a carbon-free energy vector. However, its storage and transport in big quantities raise safety concerns. Following a leakage, mixed with the surrounding air, this hydrogen can form a highly flammable mixture. In case of accidental ignition of this mixture, different combustion scenarios and regimes are possible, depending on factors such as geometry (dimensions, confinement, presence of obstacles), mixture composition, temperature, pressure or turbulence level. These regimes range from slow deflagration to the transition to detonation in the worst case. To predict the damage induced by an explosion, Computational Fluid Dynamics has the advantage of being safer than experiments and gives access to quantities hard or impossible to measure empirically. This thesis deals with the prediction of lean hydrogen-air explosions using Large-Eddy Simulation (LES). Lean H2-air mixtures are known for their distinctive sub-unity Lewis number, which characterises an unbalance between molecular and heat diffusion processes with major consequences: (1) lean H2-air flames are strongly sensitive to stretch; (2) they are prone to develop flame front cells due to the thermo-diffusive instability. Both constitute accelerating mechanisms which impact the overpressure generated during the explosion. In this work, we show that the Thickened Flame (TF) approach to simulate sub-unity Lewis number flames: (1) induces an amplification of stretch on the flame; (2) combined with the low grid resolution in LES, filters out flame front instabilities. The coupling of these undesired mechanisms can generate an erroneous flame propagation which questions the predictability of LES for lean H2-air explosions. In this thesis, a modelling strategy is proposed to reliably and accurately predict lean hydrogen-air explosions. A new paradigm is considered to separately correct the amplification of stretch effects and model subgrid phenomena due to the thermo-diffusive instability. These two corrections are first developed on canonical configurations and then extended and validated on more realistic explosion configurations.